Phosphor Thermometry on Surfaces - A Study of its Methodology and its Practical Applications

Knappe, Christoph

2013

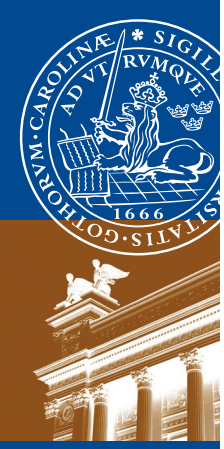

Phosphor Thermometry on Surfaces

A Study of its Methodology and its Practical Applications

Christoph Knappe

Division of Combustion Physics
Department of Physics
Faculty of Engineering LTH
Lund University

Phosphor Thermometry on Surfaces

A Study of its Methodology and its Practical Applications

Doctoral Thesis

Christoph Knappe

Division of Combustion Physics
Department of Physics

LUND 2013

Lund University

Printed by: E-husets tryckeri, Lund, Sweden
September 2013

Lund Reports on Combustion Physics, LRCP–169
ISBN 978–91–7473–615–1 (printed)
ISBN 978–91–7473–616–8 (pdf)
ISSN 1102–8718
ISRN LUTFD2/TFCP–169–SE

Christoph Knappe
Division of Combustion Physics
Department of Physics
Lund University
P.O. Box 118
SE-221 00, Lund, Sweden

For my parents
Ulrike and Bruno

Abstract

Phosphor thermometry is a term describing an optical measurement technique for remote temperature sensing. Its working principle is based on the temperature-sensitive emission characteristics of certain ceramic substances termed thermographic phosphors. These inorganic materials can either be coated on objects for surface thermometry or be seeded into the gas phase or into liquid flows as solid particles. After optical excitation, often achieved using pulsed laser systems, the phosphor emits an extended and typically red-shifted afterglow referred to as phosphorescence. As the temperature changes, either the temporal or the spectral composition of the phosphorescence emission can be used to determine temperatures through comparison with the results of a temperature calibration, carried out earlier. In many applications, temperatures both at various points and in two-dimensional fields have been characterized with a high degree of temporal and spatial resolution by use of thermographic phosphors. The combined sensitivities of different phosphors span a temperature range extending from cryogenic temperatures up to approximately 2000 K.

In the present study, the reader is introduced to the physical basics of phosphor luminescence and to utilization of the optical properties involved for temperature measurement. The thesis also examines various means of reducing measurement uncertainty in surface phosphor thermometry. This is done in a series of experimental studies concerned with the characterization and treatment of various error sources during temperature calibration, signal detection and data evaluation. A major factor considered here is that of the coating thickness. It appears to have an intrusive effect on surface temperatures in applications involving both high local and temporal thermal gradients.

The effects of instrumentation on signal detection are also investigated. The measurement accuracy was found to depend very much upon the consistency, achieved in the reproduction of the operating conditions from the temperature calibrations carried out to the experiments. This can be attributed to non-linear signal transformations that occur during detection. Even two detectors nominally identical were shown to exhibit large differences in the linearity of their signal response. Unfortunately, the linear workspace of many detectors is confined to very low signal values, the measurement precision being comparably poor due to the low signal-to-noise ratios involved. In order to improve the measurement precision without reducing the accuracy of the results, higher signal levels could be accessed through measures to compensate for detector-specific non-linearities. The signal responses to variations in operating conditions of several different point detectors and imaging devices were characterized, providing a basis for effective means of signal correction.

Interest in uncertainty reduction here also led to the investigation of means of signal processing enhancement. Temperature sensitivity was found to be a quantity which is not determined exclusively by the phosphor itself, it is also depending on the operator's choice of conditions for detection and evaluation. For evaluation schemes based on temporal decay transients, the proper choice of a time window for the evaluation was found to play an important role.

Finally, the versatility of phosphor thermometry as applied to surfaces was demonstrated in several industry-relevant applications, including a car engine, an aircraft turbine and a large-bore two-stroke diesel engine for marine vessels.

Populärvetenskaplig Sammanfattning

Eld och kontroll av denna samt dess användning anses vara en av människans äldsta och mest betydelsefulla teknologier som hjälpt till att bana väg för vår väsentliga framgång från stenåldern ända fram till vårt nutida samhälle. Det är därför inte konstigt att vi idag lever i en värld där mer än 90 % av vårt dagliga energibehov täcks genom förbränning av fossila och förnyelsebara bränslen. Men i takt med att Kina, Indien och de afrikanska länderna progressivt höjer sin levnadsstandard samtidigt som vi blir allt fler människor på jorden, ökar också behovet av energi i världen. För att kunna säkerställa en tillräcklig energiförsörjning framöver och för att minska den relativa mängden av de skadliga utsläppen, såsom växthusgaser och avgaser, är det av största intresse att öka vår kunskap om förbränning i alla dess former. Den stora mängd förbränningsenergi som används idag innebär att även små förbättringar kan ge enorma utslag i världsekonomin och i mängden skadliga emissioner. Forskning inom förbränning är därmed en mycket prioriterad verksamhet.

Temperatur är en särskilt viktig parameter i samband med förbränningsrelaterade processer. Livslängden hos en gasturbin avgörs t.ex. huvudsakligen av livslängden hos de komponenter som utsätts för högst temperatur. Temperaturen bestämmer även hastigheten av kemiska reaktioner vilka har stor betydelse för formering av skadliga utsläpp och är avgörande för värmefrigörelseprocesser. I förbränningsmotorer sker de största energiförlusterna just i form av värmeförluster till väggarna. Om man alltså lyckas minska dem, så minskar bränsleförbrukningen och utsläppen av växthusgaser med lika stor omfattning. Yttemperaturer är därför av stor betydelse, både för motordelarnas design och som inparameter i relaterade datorsimuleringar.

Förbränningsmotorer är dock rent allmänt sett relativt svåra att mäta temperaturer i. Att motorn består av en hel del rörliga delar som under drift kan röra sig flera tusen gånger per minut från och till sitt utgångsläge skapar huvudsakligen två svårigheter för motorforskarna. För det första så är det svårt att koppla in temperaturkänsliga sensorer i väggarna inuti den trycksatta förbränningskammaren där allt är i snabb rörelse. Det andra problemet är de höga varvtalen som skapar mycket snabba temperaturändringar. Under motorns drift kan dessa vara så pass snabba att konventionella temperaturmätare såsom termoelement ibland inte hinner med att upplösa temperaturens tidsförlopp.

Dessa problem kan till stor del undanröjas med hjälp av laserbaserade mättekniker. Den stora fördelen som sådana tekniker erbjuder är att man kan mäta på avstånd, utan att direkt påverka mätobjektet. På så vis kan man mäta realistiskt i annars besvärliga och svåråtkomliga miljöer. Laserdiagnostikska metoder möjliggör också att mäta många olika parametrar såsom temperatur, tryck, flödeshastigheter samt ämneskoncentrationer, i punkter och/eller tvådimensionella tvärsnitt av förbränningsrummet. De ämnen vars koncentration man kan mäta är bland annat bränsle, olika förbränningsradikaler och sot. Man kan även visualisera flamfronter och studera fenomen såsom blandning och bränsleförångning. Dessutom så kan man mäta flera av

dessa parametrar under mycket korta tidsförlopp. De lasrar som används är oftast pulsade, vilket innebär att de flera gånger per sekund genererar extremt korta laserpulser (omkring 10 nanosekunder, vilket motsvarar en 10-miljarddels sekund!). Under såpass korta tidsperioder kan förbränningsprocessen i princip anses som "stillastående". Nackdelen är att laser-baserade mättekniker ofta är relativt dyra och kräver optisk access till mätområdet genom optiska fiber eller genom fönster.

Laser-Inducerad-Fosforescens är en laserbaserad teknik för att mäta temperaturer upp till ca. 2000 K beröringsfritt på ytor, där konventionella mätmetoder med t.ex. termoelement är svåra att tillämpa. Fosfortermometri, som tekniken mera allmänt kallas för, bygger på att ett tunt temperaturkänsligt lager av ett fosforescerande ämne appliceras på en yta som sedan belyses med ljus. Det ljuset som fosformaterialet ger ifrån sig en mycket kort stund efter att ha blivit belyst av en kort och intensiv laserstråle kallas för fosforescens och för med sig egenskaper som i själva verket är temperaturberoende. Emission från termografiska fosforer kan vara temperaturberoende på olika sätt för olika fosforer. I huvudsak används två egenskaper hos emissionen för att erhålla information om temperaturen: Dels kan livstiden på emissionen minska med ökad temperatur och dels kan själva spektrumet förändras med temperaturen, vilket möjliggör mätning av intensitetskvotsvariationer för utvalda våglängder. Båda dessa metoder kräver att man först gör en kalibreringsmätning för att ta reda på vilket temperaturberoende ett visst material har. Detta görs oftast i en ugn där referenstemperaturen mäts med termoelement.

Denna avhandling är tänkt som faktakälla för nya forskare inom fosfortermometri. Teknikens metodik beskrivs med hjälp av olika praktiska exempel. Dessa exempel påvisar en del förväntade och oväntade felkällor som uppstår i samband med tillämpningen, sådana som både erfarna och mindre erfarna forskare lätt kan råka ut för. Dessa är exempelvis fosforns uppvärmning som följd av hög excitationsintensitet, temperaturgradienter tvärs över fosforlagrets tjocklek, icke-linjära effekter i detektionssystemet och flertydiga resultat från temperaturutvärderingen. Förutom själva mätmetodiken så har termografiska fosforer i samband med detta arbete även använts för tillämpade yttemperaturmätningar i en rad krävande industriella förbränningsmiljöer: i en lastbilsmotor, i efterbrännkammaren på en flygplansturbin och inuti en storskalig fartygsmotor.

Contents

List of Papers

This thesis is based on the following papers, which will be referenced by Roman numerals in the text. The papers are referenced and appended to the thesis in the order listed here.

[I] Abou Nada, F., **Knappe, C.**, Xu, X., Richter, M., Aldén, M. *Development of an automatic routine for thermographic phosphor calibration*, Submitted to Measurement Science and Technology, 2013.

[II] **Knappe, C.**, Andersson, P., Algotsson, M., Richter, M., Lindén, J., Tunér, M., Johansson, B., Aldén, M. *Laser-Induced Phosphorescence and the Impact of Phosphor Coating Thickness on Crank-Angle Resolved Cylinder Wall Temperatures*, SAE International Journal of Engines **4**(1):1689-1698, 2011.

[III] **Knappe, C.**, Algotsson, M., Andersson, P., Richter, M., Tunér, M., Johansson, B., Aldén, M. *Thickness dependent variations in surface phosphor thermometry during transient combustion in an HCCI engine*, Combustion and Flame **160**(8):1466-1475, 2013.

[IV] Lindén, J., **Knappe, C.**, Richter, M., Aldén, M. *Limitations of ICCD detectors and optimized 2D phosphor thermometry*, Measurement Science and Technology **23**(3):035201, 2012.

[V] **Knappe, C.**, Lindén, J., Abou Nada, F., Richter, M., Aldén, M. *Investigation and compensation of the nonlinear response in photomultiplier tubes for quantitative single-shot measurements*, Review of Scientific Instruments **83**(3):034901, 2012.

[VI] **Knappe, C.**, Abou Nada, F., Richter, M., Aldén, M. *Comparison of photo detectors and operating conditions for decay time determination in phosphor thermometry*, Review of Scientific Instruments **83**(9):094901, 2012.

[VII] Lindén, J., **Knappe, C.**, Richter, M., Aldén, M. *Precision in 2D temperature measurements using the thermographic phosphor BAM*, Measurement Science and Technology **23**(8):085205, 2012.

[VIII] **Knappe, C.**, Lindén, J., Richter, M., Aldén, M. *Enhanced color ratio calibration approach for two-dimensional surface thermometry using laser-induced phosphorescence*, Measurement Science and Technology **24**(8):085202, 2013.

[IX] **Knappe, C.**, Pfeiffer, K., Richter, M., Aldén, M. *A library-based algorithm for evaluation of luminescent decay curves by shape recognition in time domain phosphor thermometry*, Journal of Thermal Analysis and Calorimetry 1-10, 2013. DOI: 10.1007/s10973-013-3337-3.

Related Work

[A] **Knappe, C.**, Lindén, J., Richter, M., Aldén, M. *Decay-Time Analysis of Laser-Induced Luminescence for Phosphor Thermometry*, Paper presented at the Joint Scandinavian-French Section of the Combustion Institute, Snekkersten, Denmark 2009.

[B] Wagner, V., Paa, W., **Knappe, C.**, Triebel, W. *Extending the narrow-bandwidth tunability of a thin disk Yb:YAG laser regenerative amplifier*, Applied Optics **49**(6): 1020-1024, 2010.

[C] Algotsson, M., **Knappe, C.**, Tunér, M., Richter, M., Johansson, B., Aldén, M. *In-cylinder Surface Thermometry using Laser Induced Phosphorescence*, Proc. of the 8th International Conference on Modeling and Diagnostics for Advanced Engine Systems, Fukuoka, Japan, **MD1-4** 482-487, 2012.

[D] **Knappe, C.**, Abou Nada, F., Lindén, J., Richter, M., Aldén, M. *Response Regime Studies on Standard Detectors for Decay Time Determination in Phosphor Thermometry*, AIP Conference Proceedings **1552**:879-884, 2013.

[E] Pfeiffer, K., **Knappe, C.** *A new evaluation concept for phosphor thermometry based on shape matching of decay curves* Proc. of the European Combustion Meeting, Lund, Sweden, 2013.

Abbreviations

1D	one-dimensional ... 14
2D	two-dimensional ... 7
A/D converter	analog-to-digital converter ... 79
APD	avalanche photodiode ... 86
ATDC	after top dead centre ... 65
CAD	crank-angle degree ... 47
CCD	charge-coupled device ... 79
CMOS	complementary metal-oxide-semiconductor ... 79
CTS	charge-transfer state ... 17
CVD	chemical vapour deposition ... 58
EA-CVD	electrostatic-assisted chemical vapour deposition ... 58
EB-PVD	electron-beam physical vapour deposition ... 59
FWHM	full width at half maximum ... 109
HCCI	homogeneous charge compression ignition ... 65
IC	internal combustion ... 63
ICCD	intensified charge-coupled device ... 79
IR	infra-red ... 10
LED	light-emitting diode ... 42
LES	large eddy simulation ... 1
LIF	laser-induced fluorescence ... 49
LIP	laser-induced phosphorescence ... 1
LM	Levenberg-Marquardt ... 124
MCP	microchannel plate ... 80
Nd:YAG	neodymium-doped yttrium aluminium garnet ... 42
PIV	particle image velocimetry ... 159
PMT	photo-multiplier tube ... 27
PVD	physical vapour deposition ... 58
RANS	Reynolds-averaged Navier-Stokes ... 1
RLD	rapid lifetime determination ... 124
RS	Rayleigh scattering ... 80
SNR	signal-to-noise ratio ... 40
SSR	signal shape recognition ... 132
TBC	thermal barrier coating ... 10

TDC	top dead centre	65
TLAF	two-line atomic fluorescence	158
UV	ultra-violet	13

List of Chemical Compounds

(a) Molecules and Radicals

CH	methylidyne radical	158
CN	cyano radical	158
CO	carbon monoxide	1
CO_2	carbon dioxide	1
NO_x	nitrous oxides	1
OH	hydroxyl radical	158
SO_x	sulphur oxides	1
UHC	unburnt hydrocarbons	1

(b) Thermographic Phosphors

Al_2O_3:Cr	chromium-doped aluminium oxide	54
BAM	europium-doped barium magnesium aluminate	30
$CaWO_4$:Nd	neodymium-doped calcium tungstate	54
$CdWO_4$	cadmium tungstate	32
Gd_2O_2S:Tb	terbium-doped gadolinium oxysulfide	54
La_2O_2S:Eu	europium-doped lanthanum oxysulfide	33
$Mg_3F_2GeO_4$:Mn	manganese-activated magnesium fluorogermanate	34
YAG:Dy	dysprosium-doped yttrium aluminium garnet	35
YAG:Eu	europium-doped yttrium aluminium garnet	54
YAG:Tb	terbium-doped yttrium aluminium garnet	50
YAB:Cr	chromium-doped yttrium aluminum borate	54
Y_2O_3:Eu	europium-doped yttrium oxide	54
Y_2O_2S:Eu	europium-doped yttrium oxide sulfide	50
YSZ:Eu	europium-doped yttria-stabilized zirconia	54
ZnO:Zn	self-activated zinc oxide	36
ZnS:Eu	europium-doped zinc sulfide	54
Zn_2SiO_4:Mn	manganese-doped willemite	50

1 Introduction

This first chapter is concerned with the importance of developing and improving spectroscopic temperature measurements, including those of a laser-induced phosphorescence (LIP) type. In addition, the aims of the thesis work carried out are addressed. Finally, a brief outline of the different chapters is presented.

1.1 The Need for Spectroscopic Temperature Measurements

The ability to control fire, not only to harness it but also to adapt it to our needs, is one of mankind's oldest technologies. Heat generated by combustion has been our most important source of energy for about half a million years [1].
Today, more than 80 % of the world's energy demands are met by the combustion of fossil fuels [2]. At the present rate of growth of the world's population and with the increasing rate of industrialization in emerging and developing countries, the current energy demands are predicted to grow by more than a third by the year 2035 [3]. With nuclear energy on the decline and regenerative energies still limited in capacity, the combustion of fossil and renewable fuels can be expected to remain the primary source of energy for many years to come. The *International Energy Agency* has predicted that oil reserves present worldwide will be able to cover the expected increase in demand up to the year 2035, but the supply of other resources such as coal and gas is available in significantly larger amounts [3]. How complex and expensive it will be to access these resources in sufficient amounts to satisfy worldwide demands is less predictable, however. In addition, climate warming is closely connected with the emission of CO_2 in the combustion of fossil fuels [4]. Reaction by-products of combustion processes, such as CO, NO_x, SO_x, soot and unburnt hydrocarbons (UHC) are harmful to many living organisms and can lead to soil acidification, smog and an increase in the greenhouse effect. It is desirable and highly important, therefore, to enable combustion processes to be optimized through investigating means of increasing fuel efficiency and reducing the emission of harmful by-products. Even small enhancements in the design of the facilities involved, providing slight improvements in their efficiency, can have a huge impact if utilized on a global scale.

Due to the rapid advances in computer technology in recent years, numerical models have gained increasing importance over empirical, experimental optimization approaches in the development of combustion systems. At the same time, many predictive model approaches, such as LES (large eddy simulation) and RANS (Reynolds-averaged Navier-Stokes) are highly dependent upon the boundary conditions that are present and on various input parameters, all of which need to be determined experimentally. The availability of reliable data obtained through measurements is indispensable for the development and validation of accurate models here [5–7].

Temperatures, along with species concentrations and velocity fields are of central importance in this context. Since temperatures govern the rate of chemical reactions in combustion, they are closely interconnected with heat release and pollutant formation. Because of the temperature affecting the density and the viscosity of fluids,

it also affects the flow dynamics involved. The efficiency, that cyclic thermodynamic processes can theoretically achieve, depends primarily on the temperatures that are present. Surface temperatures govern different aspects of reliability, service life and thermal losses in combustion devices. Whereas the gas temperatures there can range from room temperature on up to adiabatic flame temperatures, surface temperatures are highly dependent upon the particular type of application and measurement location involved. Typical surface temperatures for combustion engines can be expected to be at around 500 K [8], whereas gas turbine parts can reach temperatures as high as 1600 K [9].

Conventional methods for measuring surface temperatures often rely on intrusive thermocouples or resistance thermometers. Such temperature probes are often comparably easy to implement. However, as they reach thermal equilibrium with the measurement object through becoming heated or cooled, thermal probes affect the object temperatures they are intended to measure. They also suffer from limited spatial and temporal resolution, which is a major drawback in fast-paced transient combustion environments. In need of electrical wiring, they also lack the ability to provide measurements of fast moving objects, such as turbine blades.

In recent years, much research has been directed towards the development of remote and non-intrusive optical measurement techniques for combustion applications [10,11]. In this context, thermographic phosphors have been shown to provide highly effective means of obtaining accurate and precise measurements of surface temperatures [12–15]. In addition, phosphor particles have been successfully seeded into both droplets [16,17] and gas flows [18–24] for studying the evaporation characteristics of sprays, velocity fields and gas temperature distributions. The research conducted within the framework of this thesis includes investigations concerning the optimization of measurement precision and accuracy for phosphor thermometry on surfaces. Major parts of this work are concerned with the effects of coating thickness in transient combustion, linearity-issues in connection with signal detection, as well as optimizations for current data evaluation schemes.

1.2 Personal Comments and Target Audience

The present work summarizes results of research on LIP as applied to surfaces that was conducted during the years 2008 to 2013 at the *Division of Combustion Physics* at *Lund University*.

In the course of work, curiosity drove me to investigate various factors of possible relevance to the results of phosphor thermometric research, factors that had before been largely ignored or had been taken for granted: Some of which turned out exactly as anticipated, while others showed unexpected effects which were earlier disregarded but in their presence influence the outcome of results by introducing systematic errors. Knowledge and awareness of such effects can prepare experimenters to circumvent potential error sources, or at least limit their impact to some extent. In the end,

as in the case of most other research disciplines, LIP involves considerably more complexity and depth than one might assume at first glance. As is common in scientific research, much time was spent making mistakes and learning from them. Some of these mistakes, I believe, were ones that keep being repeated in the course of time as new students arrive and embark on their work, unless they are properly reported. Experienced researchers too are by no means immune to making such mistakes, which motivated me to write this thesis from a practical point of view. My intention is to summarize the experience that I gained (though some of it may seem trivial to more experienced readers), and make it available for new and less experienced researchers in the field. Regarding the overall research area involved, it should be noted that several excellent and comprehensive review articles on phosphor thermometry have been published to date [12–15]. These provide a large number of references to original research articles for further reading and cover many theoretical matters, technological advances and practical applications of considerable interest that could not be taken up here.

1.3 Thesis Outline

Following the introduction to the thesis in Chapter 1, Chapter 2 describes some of the most important competing techniques for surface temperature measurements. Their advantages and disadvantages are briefly discussed in comparison with phosphor thermometry.

Chapter 3 then concerns thermographic phosphors. After a brief introduction to the basic theory involved two characteristics of phosphors which are most commonly exploited in thermometry – the emission lines ratio and the intensity decay characteristics – are discussed briefly. Finally, an overview is provided of the spectroscopic properties of several thermographic phosphors that were used in the course of this work.

Considerable attention is directed at optimising the outcome of experiments in terms of measurement precision and accuracy. In line with this, Chapter 4, which is the main chapter of this thesis, deals with the design, performance and data evaluation of a classical temperature calibration experiment. Many of these aspects offer considerable potential for customization of parameters and conditions involved so as to be able to optimize the experiment and adapt it to a specific given measurement task.

Chapter 5 takes up a number of combustion-related experiments that have been performed using LIP. Applications ranging from truck-engines and large vessel engines from container ships to aircraft turbines are described briefly.

Finally, future challenges and applications of phosphor thermometry are considered in Chapter 6.

2 Measurement Methods in Surface Thermometry

Temperature is the result of microscopic movements of the particles that constitute a material. The temperature increases as the motion of the particles increases, its being a measure of the thermal energy which is present. On a macroscopic scale, temperature can be interpreted as a numeric quantity used to scale the hotness of a body and be able to compare it with that of other bodies. An internationally agreed upon standard expresses temperature in units of Kelvin, K. This scale is directly connected to the *third law of thermodynamics*, in which the theoretically lowest possible temperature is that of zero Kelvin, where microscopic particle movement freezes and a thermodynamic system reaches the state of minimum possible energy. Internationally agreed upon temperature scales are based on fixed-point calibrations, employing triple-points of various elements [25].
The need for accurate and efficient temperature data in both industry and science has resulted in the continual advancement of existing measurement techniques and the development of new approaches to thermal analysis of various sorts. In principle, any temperature-dependent physical characteristic can be exploited for thermometric purposes. Temperature can be measured in a variety of ways, mechanically, electrically or through the analysis of thermal radiation, for example. Whereas industrial applications often require cheap, sturdy and reliable instrumentation equipment, in scientific research more precise and accurate techniques for temperature determination are generally preferred.

In this chapter, measurement approaches for surface thermometry that are commonly employed and can be used in conjunction with, or as an alternative to, phosphor thermometry are introduced. In addition, their particular advantages and disadvantages are described and assessed briefly.

2.1 Thermocouple Thermometry

Thermocouples are robust and low-cost contact thermometers that find wide use in a large variety of measurement situations. They are the most common sensors used to measure temperature since they can deliver readings of sufficient accuracy and precision over a large range of temperatures. A thermocouple is a device consisting of two dissimilar metal wires that are joined together in a junction. The junction end is immersed in the environment for which the temperature T_2 is to be measured. The other end of the thermocouple, which is called the reference end, is held at a different temperature T_1, e.g. at room temperature; see Figure 2.1.

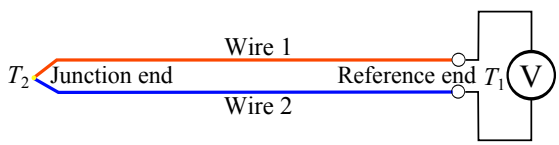

Figure 2.1: *Schematic diagram of a thermocouple, its consisting of two dissimilar metal wires that are joined at the junction end.*

Because of the temperature difference between the junction and the reference end, a voltage difference U can be measured between the two wires at the reference end in accordance with Equation (2.1)

$$U = \int_{T_1}^{T_2} (S_1 - S_2) \mathrm{d}T, \tag{2.1}$$

where S_1 and S_2 are the Seebeck coefficients of the two metals involved. The electromagnetic force gives rise to the voltage which is measured at the reference end and is induced by a thermoelectric current that arises when the electrons at the "hot" end of the wire gain thermal energy and diffuse towards the "cold" end, where their energy level can be lowered. The accumulation of negative charge at the colder end of the wire eventually creates an electric force that balances the charge distribution along the wire and creates a dynamic equilibrium. Two consequences follow from Equation (2.1):

1. If there is no temperature difference between both ends of the thermocouple, i.e. if $T_1 = T_2$, a null voltage will be measured at the reference end and electrons are distributed randomly along the wire. Increasing the temperature difference between junction and reference allows for a greater number of electrons to diffuse towards the cold end and results in a new equilibrium at a higher voltage reading.

2. If both wires are composed of the same material, i.e. if $S_1 = S_2$, electrons will diffuse symmetrically from the hot section of the wire into the cold reference end. Accordingly, there again will be no net voltage detected. Since only free electrons and holes contribute to the *Seebeck effect*, the coefficients S_1 and S_2 reflect the availability of charges that can be mobilized by their transition into the conduction band.

Seebeck coefficients are generally temperature dependent [26], since higher temperatures increase the probability of electrons being thermally excited and thus being able to more readily overcome the material-specific energy-band gap between the valence and the conduction band. Several types of thermocouples that differ in sensitivity and in temperature range have emerged through the combination of different metals and alloys. An overview of common types of thermocouples and the temperature-dependent tolerances they possess is provided in Table 2.1.

Table 2.1: *Properties of different thermocouple types for tolerance class 1* [27].

type	T_{Range} / K	ΔT / K	(low range)	ΔT / K	(high range)
K, N	230 … 1270	±1.5	(230 … 650)	$\pm 0.004 \cdot T$	(650 … 1270)
J	230 … 1020	±1.5	(230 … 650)	$\pm 0.004 \cdot T$	(650 … 1020)
R,S	270 … 1870	±1	(270 … 1370)	$\pm[1 + 3(\frac{T}{1000} - 1.1)] \cdot T$	(1370 … 1870)
B	870 … 1970	not available		$\pm 0.0025 \cdot T$	(870 … 1970)
T	230 … 620	±0.5	(230 … 400)	$\pm 0.004 \cdot T$	(400 … 620)
E	230 … 1070	±1.5	(230 … 400)	$\pm 0.004 \cdot T$	(400 … 1300)

Advantages: Thermocouples distinguish themselves in possessing a number of clear advantages. For one thing, they are both readily affordable and comparatively simple to utilize and to implement. In addition, they are known to be sturdy and to exhibit considerable resistance to shocks and vibrations. Finally, they require only limited space, which enables them to be used in very constricted environments.

Disadvantages: A major drawback of thermocouples is their invasive character, i.e. they change the temperature of the object that they measure. Since thermocouples measure the temperature at their tip against the reference end, they need to be in thermal equilibrium with the measurement object. Heat energy needs to be transferred to the junction end and is successively conducted away along the wire towards the reference end, this resulting systematically in the temperature readings obtained being too low. At high temperatures, also radiation losses become significant and need to be corrected for. If instead a cold object is to be measured, the inverse process results in the temperature values obtained being too high. In order to limit temperature intrusion, thermocouple probes are usually made very small, so that the amount of energy needed to reach thermal equilibrium with the object is very limited. In need for wired connectors, thermocouples often lack the ability to provide measurements of fast moving objects, such as turbine blades. Non-linear and weak output signals in the millivolt range sometimes need to be transmitted through long cables, making the signal prone to electromagnetic interference. Lead-outs require careful installation so as to minimize potential sources of noise. When operated at high temperatures, thermocouples tend to undergo irreversible changes in their physical and chemical properties, resulting in long-term drifts in the electromotive force. The effects of recrystallization, of residual strain, of the diffusion of atoms both from and into the thermocouple and not least of chemical reactions with the ambient atmosphere (such as oxidation) degrade the composition and purity of the material [26]. As a result, an increasing mismatch between the readout values and the true temperatures can be expected over time due to the effects of material ageing. This is a problem particularly in the case of long exposure times at high temperatures. The tolerance values shown in Table 2.1 only apply to new and unused thermocouples. Another restriction is that arising from the limited spatial and temporal resolution that can be attained. Thermocouples are devices for obtaining point measurements, which allow two-dimensional (2D) temperature information to be obtained only when several thermocouples are arranged in a matrix configuration. Thermocouple response times are an issue in connection with the observation of transient processes. Under fast temperature changes, where thermal equilibrium is not reached between the probe and the object, incorrect temperatures readings can be expected. Just as in the case of the thermal equilibrium conditions considered earlier, one finds here that less thermocouple material results in faster response times.

In order to reduce thermocouple response times and limit temperature intrusion, use is made of thin-film thermocouples, which have been developed since the beginning of the 1930s; reference inside [28]. They are manufactured by patterned sputtering of the material on a flexible circuit substrate. This allows the thermocouple to be in intimate

contact with the surface under examination. Thin-film thermocouples possess negligible thermal capacity and heat conduction from the surface via the film components is low. These two factors enable a relatively rapid response to fluctuating surface temperatures. However, thin-film thermocouples are extremely fragile and suffer from problems of electrical insulation and oxidation [29].

2.2 Pyrometry

Pyrometry, named after the ancient Greek word "pyr" for "fire", is a well established optical technique for surface thermometry. It is based on measuring the natural electromagnetic radiation released by heated objects [30–32]. In contrast to use of thermocouples, this technique is contact-free and thus does not perturb the measurement object. The electromagnetic radiation $R(\lambda, T)$ emitted by a body in thermal equilibrium with its environment is described by *Planck's law*

$$R(\lambda, T) = \varepsilon \cdot \frac{2\pi hc^2}{\lambda^5} \cdot \left[\exp\left(\frac{hc/\lambda}{kT}\right) - 1\right]^{-1}, \tag{2.2}$$

where ε is the emissivity, c is the speed of light, h denotes Planck's constant, k is Boltzmann's constant, λ denotes the radiation wavelength and T is the absolute temperature. The emissivity of a material is defined as the relative ability of its surface to emit energy by radiation. It is a unitless variable extending between 0 and 1, its value depending upon such factors as temperature, wavelength and material thickness. In Equation (2.2), R corresponds to the spatially integrated light intensity, emitted at a given wavelength and expressed in units of Wm^{-3}. Figure 2.2 shows the spectral composition of the light emitted by a perfect black body ($\varepsilon = 1$) at various temperatures, in accordance with Equation (2.2).

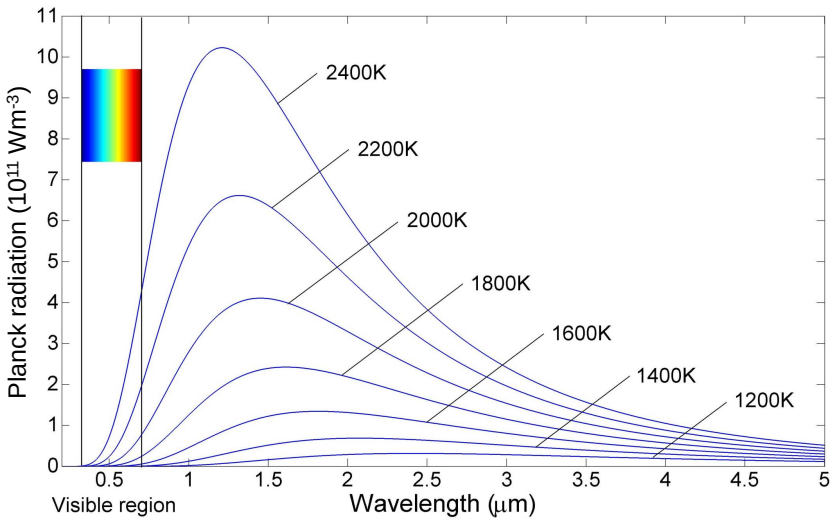

Figure 2.2: *Spectral composition of black body radiation for a set of different surface temperatures.*

Only a small proportion of the Planck radiation produced is visible to the human eye, as indicated by the spectral colour band in Figure 2.2. Two observations concerned with increases in temperature can be made on the basis of Figure 2.2:

1. The radiation intensity corresponding to the wavelength-integrated Planck radiation increases proportionally to the 4^{th} power of the temperature. This relation, given in Equation (2.3), is known as *Stefan-Boltzmann's law*.

$$I(T) = \int_0^\infty R(\lambda, T)\mathrm{d}\lambda = \varepsilon \cdot \frac{2\pi^5 k^4}{15h^3c^2} \cdot T^4 \tag{2.3}$$

2. The radiation maximum is shifting towards shorter wavelengths. A simple equation describing this relationship can be derived from Equation (2.2) and is known as *Wien's displacement law* (2.4).

$$\lambda_{\max} \cdot T = 2.898 \cdot 10^{-3}\,\mathrm{mK} \tag{2.4}$$

Accordingly, pyrometry provides a means for thermal sensing in two different ways:

1. Total radiation pyrometers measure the intensity emitted by an object over a broad spectral range, as based on Equation (2.3). Narrow acceptance angles (distance/spot ratios in the order of 30:1 [33]) allow the specific selection of measurement objects for determinations of point temperature. Some devices have a laser pointer to assist in the alignment. Cheaper pyrometers are set to assume $\varepsilon = 0.95$, whereas more expensive devices allow emissivity values to be adjusted in order to enhance the temperature accuracy if the surface emissivity is known. For commercially available broadband pyrometers, temperature accuracies of $\pm 2\,\mathrm{K}$ or of $\pm 2\,\%$, whichever is greater, are often specified [33].

2. Two-colour pyrometers are based upon the principle expressed in Equation (2.4), namely that the relative intensity of spectrally separated emission bands changes as a function of temperature. In contrast to the former technique, this method allows 2D temperature evaluation to be carried out if cameras equipped with spectral filters are used as detectors. In addition, this method is less prone to systematic errors introduced by unknown surface emissivities. By extracting two spectral bands from the Planck radiation (see Eq. (2.2) and Fig. 2.2), all effects of material-dependent emissivity, except for wavelength dependencies, are cancelled when the ratio is calculated. Hence, the two-colour approach is less prone to inaccuracies introduced by unknown and varying surface emissivities [34]. Interfering signals from spurious emission, such as scattered laser light, fluorescence, chemiluminescence or disturbance factors of other types can be spectrally suppressed by the appropriate choice of observation bands. Furthermore, the selection of suitable emission bands is a trade-off between achieving high signal values and a temperature-sensitive intensity ratio within the expected temperature range.

Advantages: In contrast to use of thermocouples, pyrometry is a remote and non-intrusive measurement technique offering high spatial and temporal resolution [35]. Remote access to surface temperature information enables measurements on moving objects that are either distant or unfavourable to contact (mechanically or chemically). There is also no upper temperature limit for this technique, the increase in the strength of the signal with temperature (see Eq. (2.3)) being beneficial for measurement precision at elevated temperatures.

Disadvantages: One major drawback of pyrometry lies in the uncertainty caused by unknown emissivity values. Since most objects are not perfect black or grey bodies constant in their emissivity, ε becomes a function of the emission wavelength, the observation angle and possibly also of the object thickness. In addition, coloured surfaces such as thermal barrier coatings (TBCs) may even exhibit temperature-dependent emissivities [31]. The weak radiation intensities obtained from cool surfaces result in poor accuracy within the low temperature region. Pyrometry is not selective and is sensitive to stray light. As Planck radiation is spectrally broadband, emission from nearby hot bodies can be superimposed on the measured signal, causing false temperature readings. For example, pyrometry of surfaces in the vicinity of sooty flames becomes very difficult, if not impossible to carry out. Many atmospheric molecules, such as CO_2 or water, absorb massively in the infra-red (IR) band. Their presence requires calibration in order to compensate for inaccuracies, caused by absorption effects. A problem arises if the chemical gas composition is also altered by independent variations in the experimental operating conditions. Finally, pyrometry relies on optical access to the surface under investigation, which could be difficult to achieve in some applications.

2.3 Thermometry involving Thermal Paints

Thermal paints can be used as temperature-sensitive coatings. The colour of thermal paints is irreversibly changed by thermal exposure. After application to the surface in question, the active sensor material in the paint records maximum operating temperatures across the coating. Temperature-induced colour changes can be compared to calibration colour charts in order to approximate the peak surface temperatures. Typical coatings possess an average thicknesses in the order of $30\,\mu$m [36], the use of thermal paints thus being a semi-invasive technique. Thermal paints have been applied successfully in hostile environments, such as combustor lining walls, turbine blades, nozzle guide vanes and fuel injector tips [37, 38]. They also are a standard tool for experimental research in the gas turbine industry [29]. The operating regions that are temperature-sensitive vary between different thermal paints. A combined temperature-sensitive interval ranges from about 320 K to approximately 1560 K [36].

Advantages: Use of thermal paints provides a cost-effective and practical means for obtaining high temperature measurements on surfaces containing both rotating and stationary components. They provide 2D surface temperature information concerning the temperature history, enabling hot spots to be identified either by the naked eye or

by automated electronic component analysis. After the coating has been applied, measurements on moving parts are possible with no further access to them being needed during experiments. The temperature information is stored inside the paint and can be read out at any time to ensure that thermal analysis can be easily integrated in scheduled work flows. In addition, thermal paint coatings can be effortlessly removed after test completion without this resulting in permanent modifications or damages to the target component.

Disadvantages: Many thermal paints exhibit only a single temperature change at a given threshold temperature. So-called "multi-change thermal paints" provide discrete temperature changes at a maximum of 7 to 10 points, which still results in poor temperature resolution [29, 36]. These colour changes are usually not observed precisely, but with an error margin of 8 K [36]. Due to the irreversible character of thermal paints, they can only be used once and provide only maximum temperatures, achieved at some point during the experiment, without the exact time when these temperatures occurred being specified. Calibration charts usually show the colours that can be expected after exposure to elevated temperatures for some specific period of time, usually 7 to 10 minutes [36]. Unfortunately, similar colours can be achieved by other temperatures for a different exposure time [29]. In order to avoid ambiguity, such temperature measurements thus require that the paint be exposed to steady temperatures for a known and well-defined period of time. This is impractical for a large number of applications, however. Certain thermal insulation can be expected to be produced by the painted surface layer itself, which can result in biased temperature readings. Paint coatings may also suffer damages and could possibly flake off during measurements in hostile environments [29].

2.4 Thermometry involving Fibre-Optical Sensors

Optical fibres are flexible light guides based on total internal reflection. They are of cylindrical design and are composed of a very pure and transparent fibre core in the centre, surrounded by a cladding having a lower refractive index in comparison. Outside the cladding, a fibre jacket is usually present that protects the fibre from physical and chemical damage. Optical fibres are primarily used for signal transmission in communication technology, but they can also serve as sensor probes for a wide variety of tasks, such as for monitoring strain, temperature, pressure, humidity or vibrations [39].

Thermometry with use of optical fibre probes based on various principles has been demonstrated, such as black-body radiation (see section 2.2 on page 8), fibre-Bragg gratings, Fabry-Perot interferometry and fluorescence thermometry [40–46]. In fibre-Bragg gratings that can be incorporated into the tip of an optical fibre, the temperature-induced fibre elongation causes a relative shift in the back-reflected Bragg wavelength. Such temperature probes, however, suffer from low sensitivity and are highly dependent upon material strain [40]. Fabry-Perot cavities provide greater thermal sensitivity than fibre-Bragg gratings do [40]. They involve the introduction of either a small air gap or a short transparent medium into the fibre, both providing a

different refractive index. However, Fabry-Perot gratings require the presence of highly parallel and polished surfaces. In addition, they are expensive, complicated to produce and suffer from low mechanical strength and poor reproducibility under precise control conditions [40]. Of the approaches to fibre-optic temperature sensing mentioned earlier, fluorescence thermometry appears to be one of the most successful and promising candidates [39]. This technique relies on use of a fluorescent coating applied to the sensing tip of the fibre. Excitation light travels through the fibre and hits the coated fibre tip, which is exposed to unknown temperatures. After excitation, the coating emits temperature-sensitive fluorescent light that is wavelength shifted and can thus be separated spectrally for detection at the opposite end of the fibre. Either the spectral composition of the fluorescence can be employed for thermometry [43,44] or, in the case of phosphorescent coatings, the signal decay rate can be analysed [45,46].

Advantages: Fibre-optic temperature sensors allow thermometry over extraordinarily long distances to be carried out. Use of high quality fibres enables high signal transmission levels to be achieved over distances of several kilometres. Already in the 1970s, optical fibres could be produced that had attenuation levels of less than 17 db/km [47]. Such fibres are very compact and are practically immune to electrical or magnetic disturbances. Thus, they can be deployed in areas in which electric sensors would either fail or would require expensive protection. In addition, optical fibres can be multiplexed, allowing several sensors to be attached to a single fibre end.

Disadvantages: Just as with thermocouples, fibre-optic probes are intrusive and need to be in contact with the measurement object. Holes need to be drilled for fibre inserts, which restricts the range of possible applications. As point detectors they lack the capability for mapping temperature gradients across surfaces unless they are arranged as multiples in a sensor-matrix configuration. In addition, fibre-optic sensors require the use of additional and expensive instrumentation equipment, such as optical excitation sources and signal detectors.

3 Thermographic Phosphors

The term "phosphor" originates from Greek and translates as "light bearer". It is used to classify solid luminescent materials that exhibit an extended afterglow upon excitation [48]. Most of the phosphors available today were the result of research aimed at finding highly efficient luminescent materials for the lighting and display industry [49]. Some of these phosphors were also found to have temperature-dependent luminescence characteristics, such as showing a decrease in intensity with increasing temperature. What was considered a drawback for fluorescent lighting, photocopy lamps, scintillation and X-ray conversion screens, however, also represented an opportunity for remote thermal sensing. Neubert suggested the use of phosphors for thermometry as early as in 1937 [50]. In terms of their composition, phosphors can be divided into two classes: organic and inorganic. It is the latter that have primarily found use in thermometry because they often survive high temperatures. Most thermographic phosphors are activator-doped ceramic crystals. They are commercially available in the form of white or brownish powder having typical particle-size distributions extending from 1 to 10 μm. Phosphorescent materials can be excited by exposure to X-rays, by ultraviolet (UV) radiation or by particle beams (electrons, neutrons or ions) and they emit mainly, though not exclusively, in the visible region of the spectrum [12].

In this chapter, the working principle of thermographic phosphors is introduced, which roughly follows the conceptual structure described in Ref. [51]. The basic emission characteristics of phosphors derive from physical interactions between the activator and the surrounding crystal lattice. Available methods for phosphor thermometry are also described here. Finally, specific thermographic phosphors that were employed in the research that led to the results presented here are discussed briefly.

3.1 Fundamentals of Phosphors

Many phosphors consist of host crystals doped with lanthanides or transition metals. The doping process replaces ions in the regular crystal lattice with the doped ions being referred to as activators or luminescence centres. Other luminescence centres include antinides, heavy metals, electron-hole centres and ZnS-type semiconductors. Lanthanides can be found in the sixth period of Mendelejew's periodic table. A specific property shared by these elements is the filling of the $4f$ shell after the $6s$ shell is already fully occupied.[1] Optically active $4f$ electrons are shielded by the outer, less energetic $5s$, $5p$ and $6s$ shells of electrons. The energy levels in the optically active $4f$ shell of the lanthanide ions are thus less affected by the surrounding ligands as a result. Hence, when mixed into a host lattice in low concentrations, lanthanide ions behave in a manner very similar to that of free ions. Although the external crystal field may lead to some energy state splitting (*Stark effect*), the overall distribution of energy levels of the ions in different host materials is very similar nevertheless. Thermographic phosphors used in high temperature applications usually consist of lanthanide activators in ceramic hosts [13].

[1] The elements Lanthanum and Lutetium constitute an exception to this statement. Both exhibit a partially filled $5s$ shell which is shielded by their fully occupied $6s$ shell.

The transition elements are also known as d-block elements, since whereas their outermost level contains at most two electrons, their next to outermost main levels contain incompletely filled d sub-orbitals, which become filled-up progressively. Similar to lanthanides, the active shell for electronic transitions here is shielded by completely filled outer electronic shells. The electromagnetic shielding effect for the $3d$ electrons, however, is less pronounced in comparison with electrons in the $4f$ shell. The luminescence properties of doped transition metals thus appear more dependent on the crystal field of the host material than in the case of lanthanide activators [15]. The strong interaction with the crystal field also broadens their emission spectra and activates further non-radiative transition paths [51].
Ceramic crystals are highly homogeneous and stable, even at high temperatures [52]. This makes them an excellent host material for thermographic luminescence centres. Host crystal and doping agent form a complex system, the components of each exhibiting their own energy levels. Electric and magnetic interplay lead to energy shifts and line splitting, resulting in a large amount of transitions being possible. Excitation energy can be absorbed either by the activator, by the host crystal, or by sensitizers, the latter being another doping component, one that is sometimes added to the host in order to increase the phosphorescence yield. During relaxation to the ground state, radiant and non-radiant transitions are in direct competition with one another due to interactions with the host material. Phosphor thermometry is based on the fact that this competition is temperature-dependent.

The sections that follow provide simplified descriptions of absorption, emission, non-radiative transitions and energy transport phenomenons in phosphors.

3.1.1 Configurational Diagram

Luminescent centres can be regarded as isolated the if doping concentrations are in the order of a few percent [12]. Although this most often the case, the host lattice has a profound effect on the thermal response of the phosphor [13]. Many properties of luminescent materials can be explained in principle by use of a simplified configurational diagram which represents the potential energy of a luminescence centre as a function of the configurational coordinate R. In such a diagram, which was originally utilized for interpreting colour centres [29], R denotes the distance from the atomic cores of the activator atom to the ligand with respect to a single vibrational mode. Such a one-dimensional (1D) model is usually not sufficient for quantitative observations. However it is able to describe the following key aspects of luminescence in a qualitative manner:

- **Stokes Shift:** the centre band of the emission wavelength is usually red-shifted in relation to the excitation wavelength.
- **Line Broadening:** the broadening of the absorption and the emission lines is temperature-dependent.
- **Thermal Quenching:** luminescence quenching by collisions and its temperature dependence.

The model is based on the assumption of there being a quantum-mechanical harmonic oscillator that exhibits a parabolic energy potential. Figure 3.1 shows the energy potentials of the ground state and of the excited state. The potential minimum R_0 denotes the equilibrium distance present in the ground state, whereas R'_0 denotes the minimum of the excited potential. In the excited state, the equilibrium distance is often shifted towards a slightly higher bonding distance $R'_0 \geq R_0$, because of electronic excitation weakening the strength of chemical bonds. This also results in the force constant being weaker in the excited potential, which results in a gentler slope of the curve there. The horizontal lines in the figure illustrate some of the vibrational energy levels that an atom can occupy. The lowest vibrational mode can be assigned to $v = 0$ and exhibits a probability density function that reaches its maximum at the equilibrium distance R_0. In analogy to the classical oscillator, the maximum value of the probability density function progressively shifts towards the boundaries of the parabola for populations of higher vibrational states, i.e. $v \to n$.
According to the *Franck-Condon principle*, the bonding distance R for electrons does not change upon excitation, this resulting in vertical excitation paths. This assumption is valid, since the mass, and hence the inertia of an atomic core is 10^3 to 10^5 times as high as that of an electron [51]. Absorption and emission are thus most likely to occur between two vibrational states that both exhibit a high probability density along a vertical line of $R = \text{const.}$ in Figure 3.1.

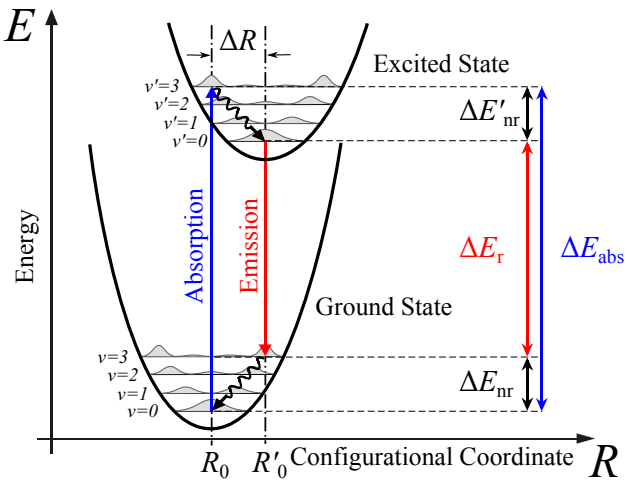

Figure 3.1: *Configurational diagram showing electronic transitions between the ground state and the excited state.*

3.1.2 Absorption

Light absorption in homogeneous and isotropic matter generally follows *Beer-Lambert's law* (3.1), whereas the absorption coefficient α is higher for wavelengths λ that closely match the energy gap in the absorber.

$$I(z, \lambda) = I_0(\lambda) \cdot \exp[-\alpha(\lambda) \cdot z] \tag{3.1}$$

In Equation (3.1), $I_0(\lambda)$ resembles the initial light intensity and z is the depth that the light has traveled into the material.
In the configurational diagram in Figure 3.1, the optical absorption path is highlighted by a vertical arrow. In the lowest vibrational state $v = 0$, the absorption most likely start from R_0, this corresponding to the bonding distance that exhibits the highest probability density. Due to the relative shift in potential between the ground state and the excited state, electronic excitation is most likely to populate the vibrational level $v' > 0$, which exhibits the highest probability density along the vertical transition line. Since this transition is the one most likely to occur, its corresponding energy difference represents a maximum on the absorption band. Other transitions, which start or stop at less probable positions and populate neighbouring vibrational levels, occur at lower rates and contribute to the line width of the absorption bands.
If the equilibrium distance between the ground state and the excited state remains unchanged ($\Delta R = 0$), such absorption bands become very narrow, since only transitions from $v = 0$ to $v' = 0$ achieve a decent overlap of the probability density functions in the ground state and the excited state. In contrast, an elevated shift between the potentials results in broad absorption bands that reach the excited state potential further off-centre, where the slope is steeper and the probability of interactions with multiple higher vibrational energy levels is higher. The width of the absorption bands found experimentally thus provide direct insights into the size of ΔR and also enable predictions to be made concerning the chemical bonds involved.

There are several mechanisms that can be responsible for light absorption in phosphorescent materials:

1. The doping agent can absorb and gain energy, which changes the electronic configuration of the orbitals that are not part of the chemical bond with the host ions. Hence, the bond under such conditions remains unchanged during transitions, i.e. $\Delta R = 0$. As discussed earlier, this results in narrow absorption bands.

2. The bond between dopant and host can absorb energy, this resulting in $\Delta R \neq 0$ upon excitation, followed by the broadening of absorption bands.

3. Finally, the energy can also be absorbed by the host material exclusively, this resulting in broad absorption bands, due to the large variety of chemical bonds involved.

If the dopant participates in the energy absorption process, the absorbed energies correspond mainly to the UV and the visible light spectrum, whereas the absorption of gamma and X-ray radiation is almost exclusively connected with energy absorptions by the host crystal [51].

The absorption process, which results in electronic transitions into a short-lived excited state, is always followed by relaxation processes that allow the absorbing medium to return to the ground state. These de-excitations can be divided into radiative and non-radiative relaxations as will be discussed in the sections that follow.

3.1.3 Emission

Figure 3.1 explains the processes of absorption and emission using a configurational diagram. After its transition into the excited state, the system first relaxes non-radiatively into the lowest vibrational level of the excited state by releasing part of the absorbed energy to the surroundings. Subsequently, the electron relaxes into the ground state by spontaneous emission of a photon. In the case of $\Delta R \neq 0$, as can be seen in Figure 3.1, the transition initially reaches a higher vibrational level of the ground state, in accordance with the *Franck-Condon principle*. From there, it again relaxes non-radiatively into the lowest vibrational mode of the ground state. This break-up into radiative and non-radiative transitions during the relaxation from the excited state to the ground state is responsible for the Stokes shift, which can be observed as a colour change between absorption and emission in the direction of the IR spectral region. Energy-wise, the Stokes shift between the absorption and the emission band is balanced by the sum of the energy differences that stem from the non-radiative relaxation processes that occur (see Figure 3.1). The configurational diagram suggests further that the Stokes shift is higher when ΔR is larger in size, since more energy needs to be bridged during non-radiative relaxations into the vibrational ground states. In addition, the emission line widths increase with an increase in ΔR, for reasons similar to those discussed previously in connection with the broadening of absorption bands.

3.1.4 Non-radiative Relaxation

As mentioned earlier, the de-excitation process from an excited state to the ground state is governed by the competition between radiative and non-radiative transitions. Whereas non-radiative transitions are unfavourable for applications in which phosphors serve as a light source, the temperature dependencies of non-radiative transitions in competition with phosphorescence emission are highly desirable characteristics within phosphor thermometry.

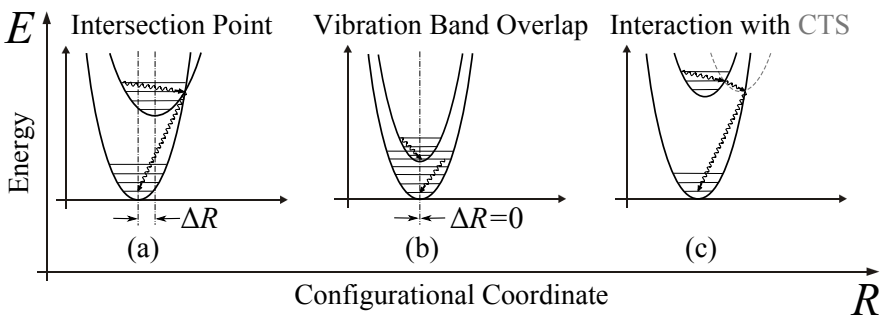

Figure 3.2: *Non-radiative transitions:* (a) $\Delta R \neq 0$ + *point of intersection between the ground state and the excited state potential,* (b) $\Delta R = 0$ + *overlap of the low energy vibrational levels due to a small energy gap between the ground state and the excited state,* (c) *interactions with the charge-transfer state (CTS) potential, connecting the ground state and the excited state.*

Figure 3.2 shows three major emission quenching processes that can be explained using configurational diagrams:

(a) In case $\Delta R \neq 0$, the potentials of the ground state and the excited state exhibit a common intersection point. At elevated temperatures, higher vibrational bands, those located above the intersection point may be populated in the excited state. From there, electrons pass downwards and reach the cross-over point, where they interact with the ground state parabola and can cross over, with a high probability, into an elevated vibrational level of the ground state. The absorption energy is thus released in an entirely non-radiative way into the host lattice as vibration energy. The process involved is termed thermal quenching, since its probability increases with temperature and with the relative potential shift ΔR.

(b) In the case of a potential configuration of $\Delta R = 0$ there is no intersection point between the ground state and the excited state that can be reached in a reasonable way by thermal excitation. However, if the energy difference between the two parabolas is sufficiently small to allow there to be an overlap of the vibrational levels between the ground state and the excited state, energy can be released from the excited state entirely by means of non-radiative vibrational relaxation. The probability of this relaxation process increases with an increase in temperature and a decrease in the size of the energy gap between the two potentials.

(c) Potentials of the ground state and the excited state can also be interconnected by a third potential, termed the charge-transfer state (CTS). This inter-system energy band, that connects the host lattice with the activator directly, was originally proposed by Fonger and Struck [53] to explain the luminescence characteristics of Eu^{+3} ions in different host materials. The CTS can be found at very low energy levels $\leq 40 \cdot 10^3\,\mathrm{cm}^{-3}$ for elements a with strong electron affinity such as Eu^{+3} or Yb^{+3} [48]. The probability of transition through CTS interactions is dependent upon both the temperature and on the positioning of each of the three potentials. Its spectrum is broadband and is highly dependent upon the host material.

3.1.5 Energy Transfer

Apart from radiative and non-radiative transitions in luminescence centres A into the ground state, the absorbed energy can also be transferred to another luminescence centre B in accordance with the relationship

$$A' + B \rightarrow A + B',$$

where the the apostrophe indicates an excited state. If B' relaxes radiatively, A is termed a sensitizer for B. Sensitizers are occasionally added to the host material in order to also feed the energy states of the dopant and to thus increase the overall phosphorescence yield. If B' relaxes non-radiatively, B is referred to as a quencher for A. Energy transfer can occur between both dissimilar and similar luminescence centres.

Energy transfer between dissimilar luminescence centres: Energy transfer between dissimilar luminescence centres occurs only if both energy systems are in a state of resonance, i.e. if they exhibit identical energy gaps between the ground state and the excited state. In addition, an electric or magnetic multipolar interaction between the two systems must exist [51]. Another mechanism connected to energy transfer in this category is that of resonant photon re-absorption between A and B.

Energy transfer between similar luminescence centres: Energy transfer between similar luminescence centres requires the the same prerequisites to be met as were discussed for the case of dissimilar luminescence centres. In contrast, however, energy transfer may occur multiple times between similar luminescence centres, allowing the energy to be transferred away from the original location at which the photon absorption took place. This can result in long migration paths. If an excited luminescence centre encounters a collisional quencher during the random migration process, the radiation is lost and is released into the lattice as vibrational energy. This mechanism is known as concentration quenching since its probability of occurring increases when further luminescence centres are introduced into the host. In the case of lower doping concentrations, the mean distances between activators in the crystal lattice can be too long for an effective migration of energy to the collisional quenching centres to occur. Related to this is the fact that a global luminescence maximum is usually reached at specific doping concentrations [54, 55]. Once this quenching point is reached, the addition of further luminescence centres no longer results in a relative increase in the phosphorescence yield, because of concentration quenching taking over there as the predominant process. Thus, concentration quenching through energy transfer between similar luminescence centres provides an explanation of the decline in phosphorescence yield with an increase in doping concentration that occurs once a critical doping concentration has been exceeded [12].

3.1.6 Temperature Dependency of Temporal Luminescence Properties

The decrease in electron population in an excited state becomes evident in the decay of an emission line that has been excited by a short excitation pulse. In a simple two-level system, the electron population in the excited state N' decreases in accordance with

$$\frac{\mathrm{d}N'}{\mathrm{d}t} = -N' \cdot (k_\mathrm{r} + k_\mathrm{nr}), \tag{3.2}$$

where k_r and k_nr are rates for radiative and non-radiative transitions [48]. A solution of the differential Equation (3.2), as presented in Equation (3.3), describes a single-exponential decay of the excited state population.

$$N'(t) = N'_0 \cdot \exp[-(k_\mathrm{r} + k_\mathrm{nr}] \cdot t) \tag{3.3}$$

This decay in the population of the excited state, with $N'_0 = N'(t = 0)$, is directly proportional to the observed phosphorescence intensity decay.

$$J'(t) = J'_0 \cdot \exp\left(-\frac{t}{\tau}\right) \tag{3.4}$$

In Equation (3.4), τ is the decay time required for the phosphorescence intensity to decrease by a factor of 1/e. The assumption of an isolated two-level system represents a very simplified approach, one which excludes for example, a proper consideration of interactions with other luminescence centres or with impurities in the host lattice (see section 3.1.5). In practise, however, such interactions allow additional relaxation mechanisms that introduce further de-excitation terms and are responsible for multi-exponential luminescence decays to occur. A comparison between equations (3.3) and (3.4) indicates the dependence of the decay time on the transition rates involved.

$$\tau = (k_\mathrm{r} + k_\mathrm{nr})^{-1} \tag{3.5}$$

The radiative transition rate k_r is also known as the Einstein coefficient for spontaneous emission. Non-radiative transitions are generally much more probable than radiative transitions are, because of radiative transitions being restricted by quantum mechanical selection rules. Whereas k_r is largely insensitive to temperature variations, the transition rate for non-radiative means of de-excitation is a temperature-dependent quantity. As discussed earlier in section 3.1.4, the probability of non-radiative excitation mechanisms occurring increases with temperature. Taking Equation (3.5) into consideration, this implies there to be a decrease in phosphorescence decay time with an increase in temperature.

The theory of multi-quantum emission provides a simple relationship as an example regarding the temperature dependency of non-radiative transitions in YAG hosts [56–58].

$$k_\mathrm{nr}^m(T) = k_\mathrm{nr}^m(T=0) \cdot \left[1 - \exp\left(\frac{\Delta E}{kT}\right)\right]^{-m} \tag{3.6}$$

In Equation (3.6), ΔE is the energy gap bridged by non-radiative transitions and m is the order of the multi-phonon process, e.g. $m = 2$ corresponds to a two-phonon process. When the temperature is low, the non-radiative decay is almost constant, whereas the decay rate becomes significantly higher as the temperature increases. The probability of higher order processes ($m > 6$) is very low, meaning that large energy gaps are unlikely to be bridged by multi-phonon processes [53, 56]. Noted that Equation (3.6) only holds in the case of a weak coupling between the activator and the host, requiring any interference caused by energy transfer processes (see section 3.1.5) to be negligible.

3.1.7 Temperature Dependency of Spectral Luminescence Properties

Host and activator form a complex bond in which each component has its own energy levels. These are dependent in each case on the proximity to neighbouring atoms and on the chemical bonds that are formed. The large number of possible transition lines that result from these interactions can be affected by thermal changes in various ways:

- **Emission Line Broadening:** Heat causes the crystal lattice to vibrate, which in turn creates a changing crystal field and produces a broadening of the line widths in the emission spectrum due to several mechanisms:

- **Inhomogeneous Broadening:** Spatial inhomogeneities in the crystal lattice result in shifts in the energy levels of the ions involved relative to a perfect crystal lattice. Such inhomogeneities can be introduced through defects in the lattice or through impurities. They might also stem from the edges of a crystal, where the influence of neighbouring ions on the electric potential is becoming increasingly asymmetric. The shifts thus produced interfere with one another, creating an inhomogeneous broadening effect [52].
- **Doppler Broadening:** Thermal vibrations in relative direction to the incoming electromagnetic excitation radiation lead to Doppler shifts of varying degree and sign during light absorption and emission, accumulating randomly and resulting in a macroscopic broadening of the emission lines [52].
- **Anisotropic Broadening:** Temperature-induced anisotropic expansions within the host lattice lead to changes in the distances between the involved ions. These in turn introduce spatially distributed changes in the energy potential, causing the emission lines to broaden [52].
- **Thermalization:** When the temperature increases, higher energy states ($v > 0$) become more densely populated. This can be understood as an increase in vibrational energy at elevated temperatures. At higher vibrational levels, the number of electrons N_e increases as compared with the number of electrons in the ground state N_g, as expressed by Equation (3.7), which can be derived from the *Boltzmann distribution* [29].

$$N_{\mathrm{e}} = N_{\mathrm{g}} \cdot \exp\left(-\frac{\Delta E}{kT}\right) \tag{3.7}$$

  According to Equation (3.7), higher vibrational levels become more densely populated both in the ground state and in the excited state. This increases the probability of additional transitions taking place. Accordingly, thermalization leads to a temperature-dependent broadening of the absorption and emission bands [29].

- **Spectral Intensity Shifts:** Another consequence can be derived from Equation (3.7). Since the electron population follows the *Boltzmann distribution*, it can also be predicted that excited vibrational states from higher energy transitions in the blue spectral region (having large ΔEs) are more difficult to feed thermally, and thus experience a greater relative increase in number density than it is the case for transitions occurring within the red end of the spectrum, where energy gaps are smaller. Thus as the temperature increases, luminescence is increasingly more likely to occur, i.e. more intense, in the blue part of the spectrum than in regions of longer wavelengths.
  In addition, frequency shifts in the spectral line structure can occur due to homogeneous thermal expansion in the host crystal. The greater average ion separation that is to be found at higher temperatures results in a reduced crystal field and a reduced Stark-component separation there [59].

- **Total Luminescence Intensity:** The wavelength-integrated luminescence intensity of many phosphors decreases at higher temperatures due to lattice vibrations having an impact on the phosphorescence yield there by increasing the probability of non-radiant de-excitation mechanisms occurring. There are exceptions to this general tendency, however. Some phosphors exhibit emission lines which experience an increase in intensity over a particular temperature range. This may occur due to effects that increase the absorption cross-section of specific wavelengths involved [12].

3.1.8 Terminology: Fluorescence and Phosphorescence

According to definitions of the terms phosphorescence and fluorescence employed up to late in the 20$^{\text{th}}$ Century, the two phenomena were distinguished in terms of the time scales involved in the luminescence decay that occurred. Fluorescence was used when referring to decay rates faster than $< 10^{-3}$s, whereas signal decay rates slower than this were termed phosphorescence [12]. Emission, luminescence, phosphorescence, and fluorescence are closely related terms sometimes used interchangeably. In recent years a new definition of the term phosphorescence and fluorescence, respectively, has come into wide use, one that stems from organic chemistry:
The physical process of phosphorescence is closely related to that of fluorescence and differs only from it in terms of the optical transition from an excited state to the ground state which is involved. Whereas, as shown in Figure 3.3, fluorescence is governed by a transition between two singlet states, phosphorescence is characterized by a much less probable type of transition from a triplet state to a singlet state.

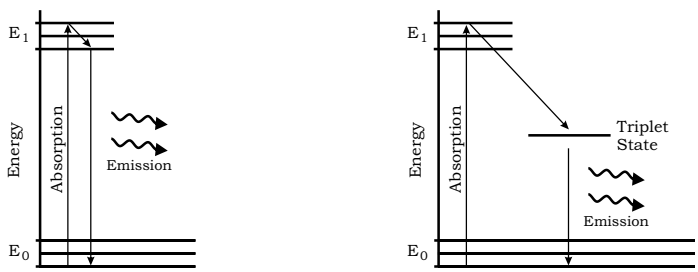

(a) Fluorescence (b) Phosphorescence

Figure 3.3: *Energy transition diagrams of* (a) *fluorescence and* (b) *phosphorescence, respectively* [60].

In theory, triplet-to-singlet transitions are spin-forbidden due to quantum mechanical selection rules. These rules apply more rigorously, however, to lightweight elements, in which the spin-orbit coupling is comparatively weak, than to the heavier elements that many phosphors consist of [51]. In addition, the selection rules can be considered to be more relaxed in solids [29], triplet-to-singlet transitions in solids being observed rather commonly. Nevertheless, their lower transition probabilities result in decay times usually being much larger than those observed for fluorescence transitions [48, 58].

3.2 Phosphor Thermometry

The emission properties of thermographic phosphors are sensitive to variations in temperature. Of the various measurement techniques for surface temperatures that are available (see section 2), LIP has drawn particular attention in the past few years, its being a versatile alternative to conventional probing techniques such as thermocouples and pyrometry [12, 14, 61–63]. The use of thermographic phosphors enables remote temperature sensing of comparatively high temporal resolution to be carried out, either in the form of point measurements or in 2D applications.
In its use for thermometry, the phosphor in question needs to be brought in physical and thermal contact with the measurement object, and optical access to it be maintained, both for its excitation and in the collection of emission signals. After optical excitation, the subsequent emission due to the relaxation of electrons from the excited state to the ground state is temperature-dependent. For a brief instant within this series of processes, the *Boltzmann distribution* in the ground state is perturbed by the feeding into the excited states that occurs. The thermal equilibrium is quickly restored, however, by vibrational relaxations. These occur on time scales in the order of 100 fs, which is very fast in comparison to typical phosphorescence decay rates [29]. Accordingly, any phosphorescence-based temperature measurement is conducted after thermal equilibrium has been restored and thus provides direct information on the internal temperature of the material.

Different approaches to temperature measurement that take advantage of the characteristics of thermographic phosphors have been utilized in the past. A comprehensive overview on a variety of such techniques has been presented by Khalid and Kontis in [13]. A schematic diagram of how these techniques are related to one another is provided by Figure 3.4.

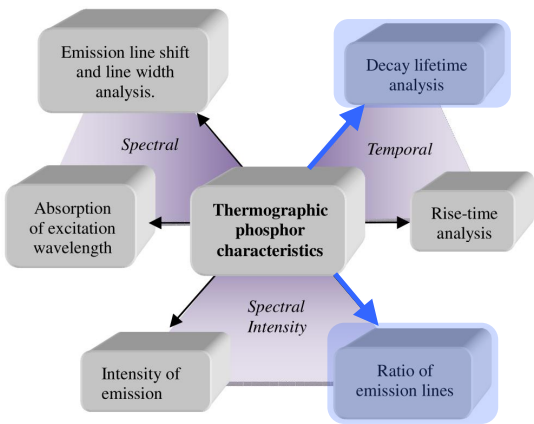

Figure 3.4: *Phosphor characteristics that can be utilized for thermometry. The two most common techniques are highlighted by bold arrows. This is a manipulated version of an original illustration, taken from [13] and replotted with permission of Prof. K. Kontis, Manchester University, UK.*

The temperature-sensitive characteristics of phosphorescence decay times and the ratio of the intensity of different emission lines to one another are most commonly exploited in phosphor thermometry, the first of these often being regarded as enabling higher measurement precision to be achieved [64, 65].

3.2.1 Analysis of Spectral Luminescence Properties

The intensity-ratio method concerns changes in the emission spectrum of a phosphor in response to changes in temperature (see section 3.1.7). Figure 3.5 is a schematic presentation of two spectral emission lines λ_1 and λ_2 that change in their relative intensities as a function of temperature. Three sets of observation temperatures are indicated there.

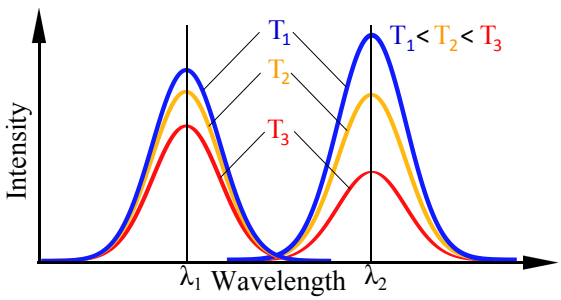

Figure 3.5: *Intensity of phosphorescence emission lines, changing as a the function of temperature.*

If only thermalization is considered, the absolute signal intensity $S_\lambda(T)$ from a transition is temperature-dependent and can be expressed as a function of the excitation pulse intensity I_0 and the energy of the emitting state above the ground state ΔE_λ [39].

$$S_\lambda(T) \approx C_\lambda t_{\text{exp}} T_\lambda I_0 \cdot \exp\left(-\frac{\Delta E_\lambda}{kT}\right) \tag{3.8}$$

In Equation (3.8), C_λ is the detection efficiency, t_{exp} corresponds to the signal exposure time and T_λ represents the filter transmission.
Direct measurements of the absolute intensities are difficult to achieve experimentally, however, without their suffering from various factors that contribute to an increased measurement error budget: Shot-to-shot variations in the excitation source, local differences in the thickness of the phosphor coating, contaminations of both the phosphor and the optical equipment, and the quality of alignment are just a few examples, giving rise to changes in intensity between calibration and measurement, which in turn hinder the achievement of accurate measurements. Many of these factors can be suppressed by dividing signals of one energy transition by the other, which results in a temperature-dependent intensity ratio $R(T)$ in accordance with Equation (3.9).

$$R(T) = \frac{S_{\lambda_1}(T)}{S_{\lambda_2}(T)} = \frac{C_{\lambda_1} T_{\lambda_1} \cdot \exp\left(-\frac{\Delta E_{\lambda_1}}{kT}\right)}{C_{\lambda_2} T_{\lambda_2} \cdot \exp\left(-\frac{\Delta E_{\lambda_2}}{kT}\right)} = \xi \cdot \exp\left(-\frac{\Delta E}{kT}\right) \tag{3.9}$$

The parameter ξ in Equation (3.9) denotes a constant factor, which can be determined experimentally, whereas ΔE corresponds to the energy difference between the two optical transitions involved. As based on Equation (3.9), a large energy gap ΔE between the emission lines selected appears beneficial to achieving a high level of temperature sensitivity for $R(T)$.

A typical setup for surface thermometry employing the two-colour ratio technique is shown in Figure 3.6, which involves use of two cameras, each equipped with a different bandpass filters. The two cameras take images of the measurement object simultaneously, enabling 2D temperature maps to be created. Since peak transmission levels of the filters are fixed in wavelength, temperature-activated line shifts can also contribute to the relative differences in measured intensities obtained.

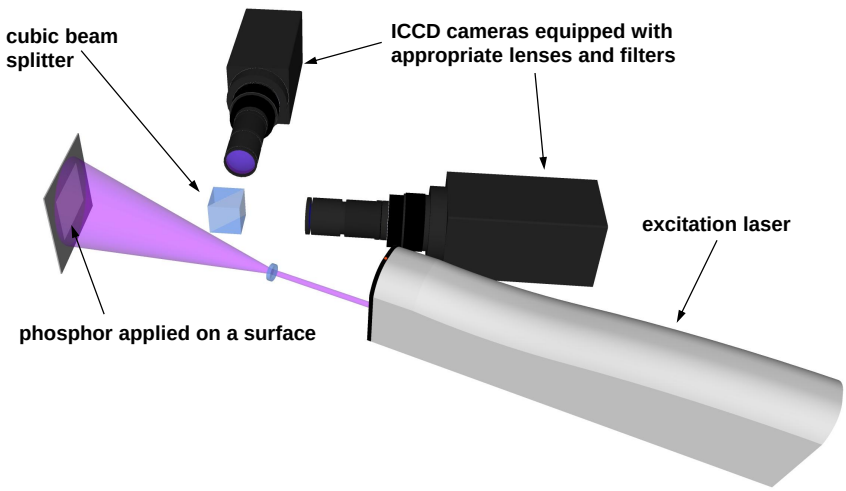

Figure 3.6: *The experimental setup for planar surface thermometry involving the analysis of spectral luminescence characteristic from thermographic phosphors.*

Figure 3.7 shows two camera images, (a) and (b), of a phosphor-coated target surface held at constant and uniform temperature ($T = 331\,\mathrm{K}$). A map of the intensity ratios is displayed in section (c) of the figure, corresponding at each point to the pixelwise overlap of the images of the two types (a) and (b), in accordance with Equation (3.9). Substantial inhomogeneities can be seen in the distribution of the absolute intensities in (a) and (b) of Figure 3.7. It is not possible without further effort, to judge whether these distributions stem from temperature gradients along the surface or whether they have some different origin instead. When an intensity ratio is calculated for each camera pixel by dividing image (a) by image (b), the resulting image (c) exhibits a fairly even distribution of the ratio values obtained, as can be expected for an object with a homogeneous surface temperature. Dependencies on the laser profile, inhomogeneities in the transmission optics and spatial variations in the intensity of the coating luminescence can be assumed to be largely cancelled out.

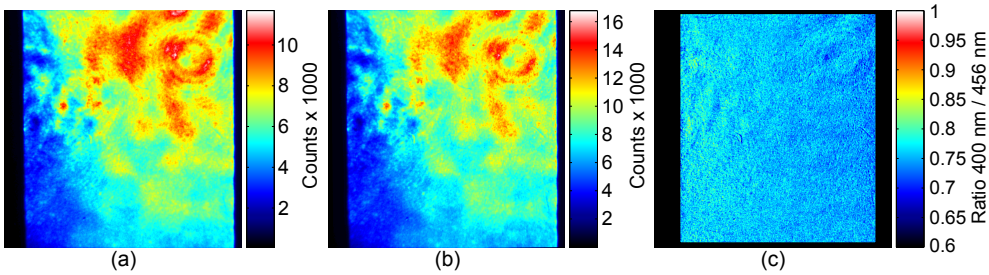

Figure 3.7: *Example of creating a two-colour ratio image from an inhomogeneously illuminated surface using BAM at* 331 K*. The first two images show absolute phosphorescence intensities at* 400 nm (a) *and* 456 nm (b)*, averaged over 10 laser shots. The resulting ratio image* (c) *is shown at the right.*

Although many error contributions have obviously been suppressed in obtaining such a set of intensity ratios in accordance with Equation (3.9), the image (c) in Figure 3.7 appears to not be free of random noise and local variations in these ratios, variations that are of virtual origin. A ring structure artefact, for example, is clearly visible in the ratio-based image (c), its mimicing the intensity ring structure found in images (a) and (b). A comprehensive discussion on the reduction of measurement errors achieved by means of the setup arrangement and the introduction of various image correction procedures can be found in section 4.7.2 (page 110).

3.2.2 Analysis of Temporal Luminescence Properties

Temporal methods for temperature determination involve the detection of phosphorescence decay times. Either of two known methods for measuring the decay lifetime can be employed here:

- The one technique utilizes pulsed excitation schemes to measure intensity decays directly through usage of optical detectors offering high temporal resolution.
- The other technique uses an amplitude-modulated excitation scheme to resolve low signals as phase shifts, that might otherwise be buried under a noisy background.

A more detailed account of each of these two methods follows.

Pulsed Excitation Scheme: As the temperature increases, the quenching rate increases too due to non-radiative processes gaining influence, as discussed earlier in section 3.1.6. This decreases the overall phosphorescence yield and results in shorter emission decays. Figure 3.8 shows the typical intensity-time relationship found for thermographic phosphorescence after pulsed excitation has taken place. Different lines with temperature labels are used to indicate the effect of temperature on the decay rate.

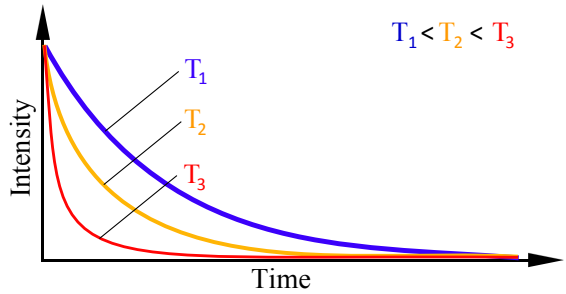

Figure 3.8: *Decay rate of thermographic phosphorescence after pulsed excitation, shown as a function of temperature.*

To obtain the decay time τ from a phosphorescence curve, a single-exponential model that accords with Equation (3.4) (page 19) is usually fitted to parts of the recorded signal. This results in a fitting function as seen in Equation (3.10)

$$J'(t) = J'_0 \cdot \exp\left(-\frac{t}{\tau}\right) + c, \tag{3.10}$$

where J'_0 denotes the initial phosphorescence intensity at time $t = 0$ and c is an optional offset constant.

Figure 3.9 is a diagram of the basic setup for point measurements, one involving use of the decay time technique. After excitation by a pulsed laser source, the phosphor coating emits phosphorescence, which is projected by a lens onto a detector. The detector, as in this case a photo-multiplier tube (PMT), records the decay as signal intensity over time and is equipped with an interference filter. The role of this bandpass filter is both to select a suitable spectral emission band and to increase the signal-to-background ratio. At the same time, one should note that radiative transitions from different energy levels in the phosphorescence spectrum usually exhibit dissimilar decay rates. The overlap of several such decay rates would introduce a multi-exponential character to the luminescence decay recorded. An attempt to evaluate such signals by use of Equation (3.10), would therefore suffer from ambiguities due to the mismatch between the assumed model equation and the recorded signal.[2] Yet the interference filter that selectively transmits a narrow segment of the wavelength here serves to limit signal contributions that would otherwise stand in the way of an unambiguous evaluation of single-exponential decay times. The use of a bandpass filter also enhances the overall temperature sensitivity of the signal by excluding certain transitions that are relatively insensitive to thermal changes.

[2] The errors in evaluation caused by multi-exponential signals are discussed further in section 4.7.3, page 123.

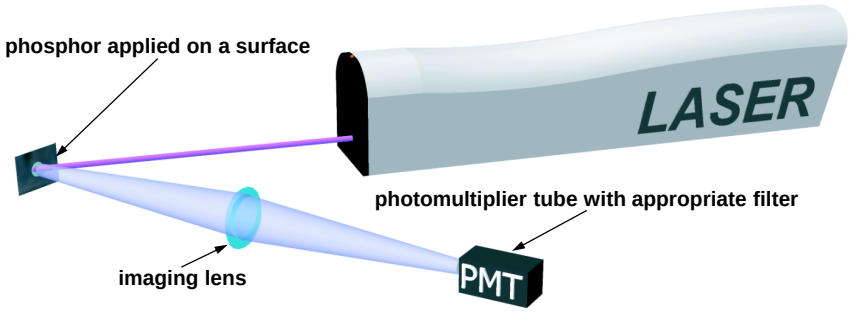

Figure 3.9: *The basic setup for point measurements of surface temperatures using the emission decay of a thermographic phosphor.*

Using the temporal approach instead of following an intensity-based approach in determining temperatures of the phosphorescent coatings has certain advantages, one of them being that decay times then are independent of the illumination intensity, so that the measurements do not suffer from spatial or temporal signal inhomogeneities [13]. However, a disadvantage of a method of this sort is that the signal strength is comparatively poor, since the excitation taking place is limited to the duration of short excitation pulses.

Amplitude-Modulated Excitation Scheme: This is another method of determining decay times, one which can be used in combination with continuously modulated light sources. Here, a continuous excitation signal $I(t)$ is modulated sinusoidally at an angular frequency of Ω, in accordance with Equation (3.11).

$$I(t) = I_0 \cdot (1 + a \cdot \sin \Omega t) \tag{3.11}$$

If it is assumed that phosphorescence emission $J'(t)$ is induced to a degree proportional to the strength of the signal $I(t)$ at all times and decreases exponentially in accordance with Equation (3.10), the following expression for the strength of the integrated phosphorescence response can be derived from Equation (3.11) [66, 67].

$$J'(t) = b \cdot I_0 \cdot \left[1 + \frac{a}{\sqrt{1 + \Omega^2 \tau^2}} \sin(\Omega t + \phi)\right] \tag{3.12}$$

According to Equation (3.12), the phosphorescence $J'(t)$ produced suffers from a gradual loss in contrast and is amplitude-modulated at the same angular frequency Ω as that of in the excitation signal. In addition, a phase shift ϕ is introduced in the equation, a phase shift related in size to the phosphorescence decay time τ, as expressed in Equation (3.13).

$$\Omega\tau = \tan \phi \tag{3.13}$$

Thus, there are two ways of extracting the phosphorescence decay time from the relation between excitation and emission:

1. One way is to determine the phase-shift ϕ by measuring the peak distance between the two signals in relation to the modulation frequency. This phase-shift can then be calibrated directly on the basis of the temperatures, as in the example shown in Figure 3.10.

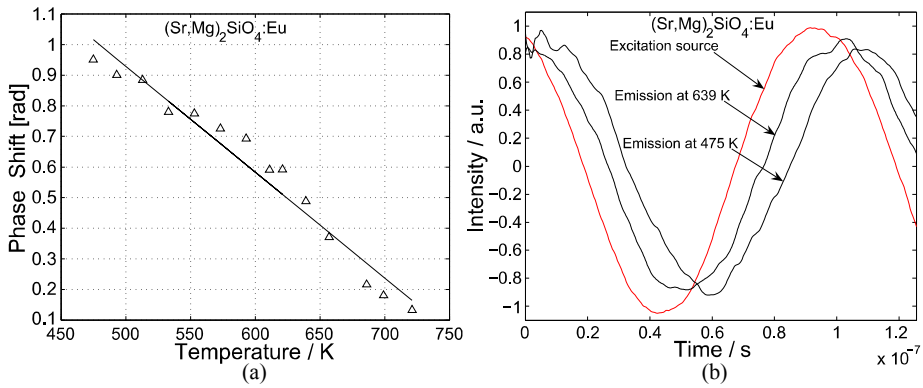

Figure 3.10: *Part* (a): *Temperature calibration of the emission phase shift of europium-doped magnesium silicate. A sinusoidally modulated laser diode at 415 nm and 10 MHz was used for excitation. Part* (b): *Examples of normalized phase-shifts, taken from* [14] *and replotted with permission of Dr. G. Särner.*

2. The other way of measuring decay times is more cumbersome, its involving the measurement of absolute amplitudes and offsets against the zero line or some other virtual signal reference. Doing so allows τ to be calculated from Equation (3.12) on the basis of the oscillation amplitude.

The phase shift method is less prone to errors caused by non-linearities in the detection line than short-pulsed excitation schemes are, as only peak positions are measured without signal shapes being of importance. A disadvantage of the phase shift method is that of its being of limited use if decay times smaller than $2\pi/\Omega$ are to be measured [15]. Also, the temporal resolution achieved is limited somewhat by the fact that several oscillations are needed in order to determine a phase shift accurately. A further limitation of this method is that of the phase shift measurements being very susceptible to signal interference. If contributions of the excitation source to the phase-shifted signals produced cannot be suppressed completely by means of filtering techniques, the observed phase-shifts are measured systematically as being shorter as they actually are. This can pose problems if the calibration and the experiment differ in their relative contributions of signal intensities involved, in which case performing in-situ calibrations directly on the measurement object itself is advisable.

3.3 Thermographic Phosphors used in this Thesis

A large number of thermographic phosphors are available to date, covering a combined temperature-sensitive range allowing measurements to be carried out that extend from cryogenic temperatures [68] up to 2000 K [69] without interruption [12, 70, 71]. This section only covers a small selection of thermographic phosphors, those that were used in conducting the research presented in the thesis. Figure 3.11 presents a combined temperature calibration chart of the decay times observed and the two-colour ratios obtained. The slope of a given set of phosphor calibrations is proportional to the temperature sensitivity over the given temperature range in question.

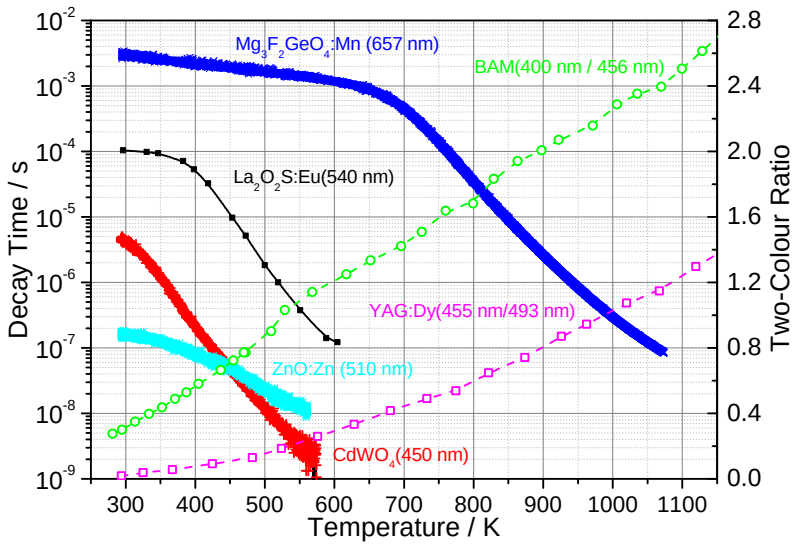

Figure 3.11: *A temperature calibration chart of thermographic phosphors used in the thesis. The filled symbols correspond to phosphorescence decay times, the hollow markers being associated with the two-colour ratio.*

In the sections that follow, a brief summary is provided of each of the thermographic phosphors, listed in Figure 3.11.

3.3.1 $BaMg_2Al_{16}O_{27}$:Eu

BAM is a blue-emitting phosphor that has a comparatively high quantum yield. It was developed for use in fluorescent lamps and is often found as the blue component in trichromatic plasma display panels [39, 70]. The luminescence properties of europium-doped barium magnesium aluminate (BAM) are governed by $4f^6 5d$ to $4f^7$ transitions of the activator ion Eu^{2+} [48]. The half-filled $4f$ shell provides greater stability and acts as the ground state. Europium ions are usually trivalent, although divalent compounds are readily formed as well, their type depending on the host material. Behaviour of this sort is unusual in most other lanthanides, which almost exclusively form compounds

with an oxidation state of +3. BAM can be readily excited by UV laser radiation at 355 nm. The types of electronic transitions thus induced are dependent upon the surrounding crystal field [72]. They result in a broadband emission spectrum, centered around 440 nm. The host lattice interactions that take place result in a temperature dependence of the phosphorescence spectrum, as is shown in Figure 3.12.

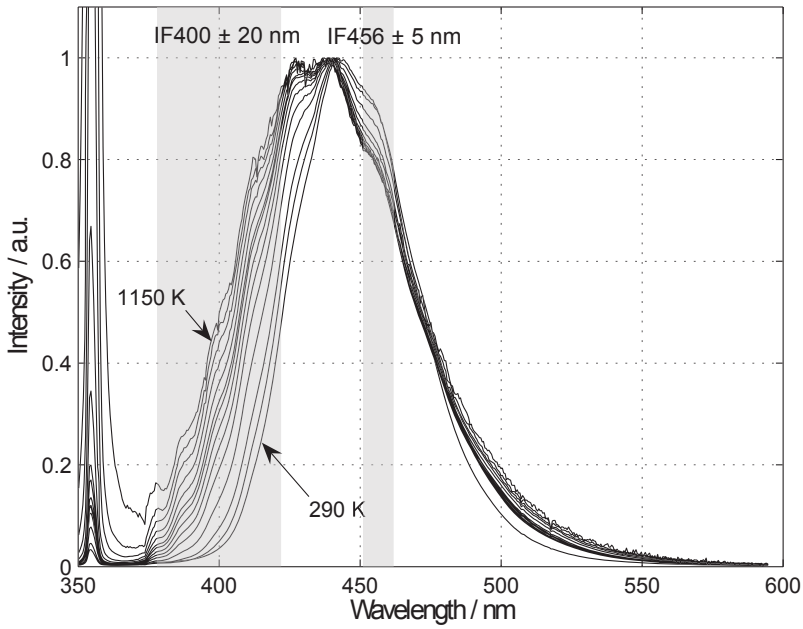

Figure 3.12: *BAM emission spectra at different temperatures following 355 nm laser excitation. The transmission intervals of the interference filters for a two-colour ratio are highlighted by the grey boxes.*

As the temperature increases, the emission band broadens and shifts towards the blue spectral region. This phosphor is thus suitable for thermometry of the type making use of the two-colour ratio approach. In addition, the temporal emission response displays a thermal sensitivity of between 700 K and 1150 K, the decay times ranging from 1 μs to 10 ns [70]. The phosphorescence of BAM is temperature-sensitive up to a level of 1200 K [73]. However, because of the degradation mechanisms involved being irreversible, great care should be taken in using BAM at temperatures in excess of 770 K. When BAM is kept at high and steady temperatures, trivalent Eu^{3+} is formed and corresponding changes in the emission spectrum alongside with an overall loss in emissivity occur. Bizarri and Moine identified three mechanisms as being responsible for this process [74]

- absorption of oxygen atoms into oxygen vacancies on the crystal surface,
- diffusion of Eu^{2+} along the conduction layer,
- and charge transfer of Eu^{2+} ions to adsorbed oxygen atoms.

Baking times of 150 min used in order to create this effect were reported in Ref. [74]. Thus it could be possible that BAM is able to withstand very high temperatures for short periods of time without noticeable signal perturbation [60]. Such applications of BAM can involve the application of gas-phase thermometry using seeded phosphor particles, this having been recently employed by research groups from *Eindhoven University* [23] and the *Imperial College of London* [75]. When long exposures of BAM to elevated temperatures are required, protective coatings of aluminium phosphate or lanthanum phosphate appear to be effective in blocking oxygen access to the phosphor. Unfortunately, the use of such protective coatings also reduces the overall emission efficiency [76]. In addition to the aforementioned temperature effects, high pressures, those above 1 kbar, may result in an increasing red-shift of the emission spectrum [77].

3.3.2 $CdWO_4$

The cadmium tungstate ($CdWO_4$) phosphor is a promising scintillation material for use in X-ray tomography, in the detection of slow neutrons, and in dosimetry [78]. Recently, this blue-emitting phosphor was discovered to be highly suitable for use in thermometry, due to its extremely sensitive decay time domain [79]. $CdWO_4$ is commonly excited by X-rays and also possesses a broad absorption band centred at 295 nm. Accordingly, it can be excited by 266 nm laser radiation at an efficiency of up to 65 % as compared to its absorption maximum [70]. The phosphorescence emission of $CdWO_4$ is characterized by a high quantum yield and a broadband spectrum. It exhibits a wavelength range extending from 350 nm up to 700 nm, with an emission peak at around 500 nm, as shown in Figure 3.13.

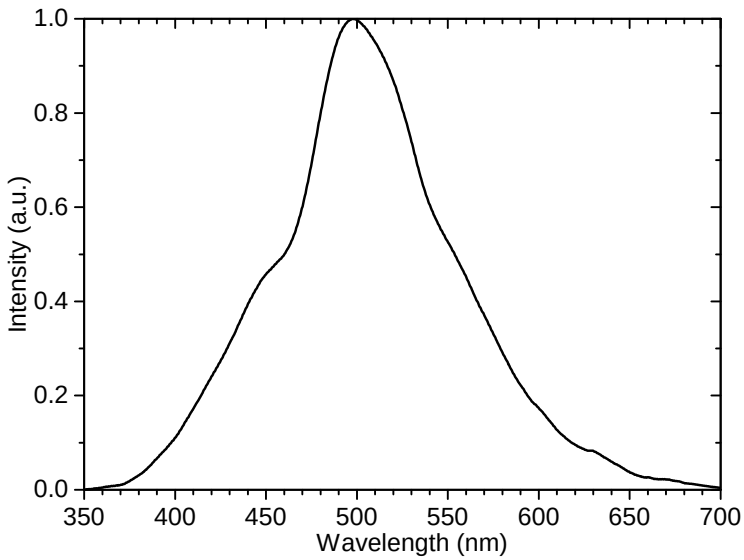

Figure 3.13: *The $CdWO_4$ emission spectrum following 266 nm laser excitation. The spectral distribution does not shift as a function of temperature.*

Although there are no spectral changes to be observed as a function of temperature, $CdWO_4$'s emission decay time changes from approximately 11 μm at room temperature down to a few nanoseconds at around 550 K. A saturation effect for $CdWO_4$ has been found in Paper [VI], its showing the decay rate of the phosphor to become shorter as the excitation light intensity increases.

3.3.3 La_2O_2S:Eu

Regarding its thermal sensitivity, europium-doped lanthanum oxysulfide (La_2O_2S:Eu) exhibits both luminescence decay times and emission lines that respond to temperature changes at anywhere between cryogenic temperatures [68] to about 600 K (see Fig. 3.11). It has a broad absorption band that extends towards the UV region, so that it can be readliy excited by laser radiations of 355 nm. Optical transitions occur between the ^5D and the ^7F bands of the Eu^{3+} doping agent, these resulting in narrow transition lines; see Figure 3.14.

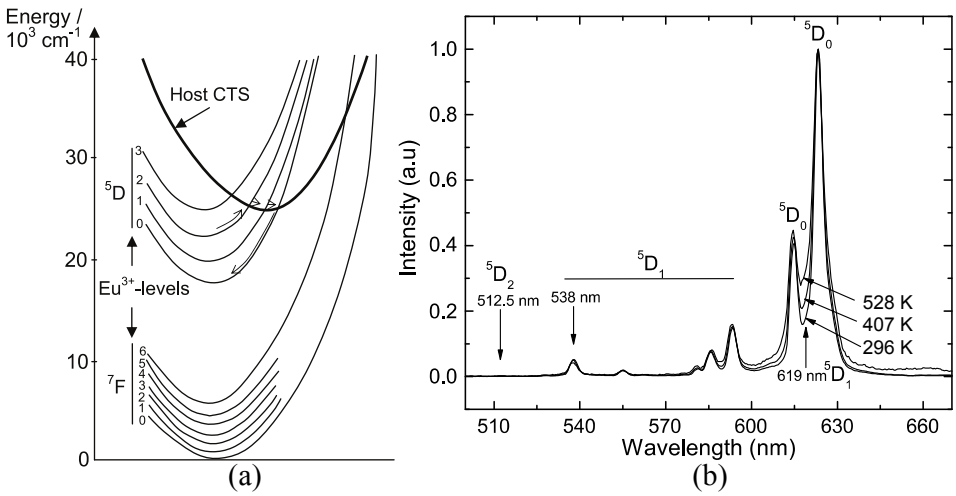

Figure 3.14: *A configurational diagram of La_2O_2S:Eu* (a) [53] *and the emission spectra obtained after* 355 *nm laser excition* (b)*. The intensities of the transition lines change as a function of temperature* [39].

As also indicated in that figure, a charge-transfer state (CTS) overlaps with the ^5D states of the trivalent activator ion [53]. This CTS, which is located in regions of unusually low potential energy ($< 40 \cdot 10^3$ cm^{-1}), allows a transfer of thermally excited ^5D state electrons to lower ^5D and ^7F states to occur. Because of the difference in activation energies needed for a crossover to the CTS, thermalization leads to the sequential quenching of emission bands, in the order of j = 3,2,1,0, with increasing temperature [68]. At room temperature, the $^5D_3$ emission is already fully quenched, but at temperatures below 100 K it is useful for thermometry [68]. In accordance with the spectral composition of La_2O_2S:Eu shown in Figure 3.14, major transition lines that can be observed at room temperatures are to be found in Table 3.1.

Table 3.1: *Observable emission wavelengths* (nm) *of* $^5D \rightarrow {}^7F$ *transitions in* La_2O_2S*:Eu at room temperature.*

ground state	$^5D_0$	$^5D_1$	$^5D_2$
$^7F_0$	580.7	527.0	—
$^7F_1$	593.0	537.0	—
$^7F_2$	614.5, 622.6	554.6, 561.9	—
$^7F_3$	—	585.0, 586.5	510.6, 511.7, 512.3
$^7F_4$	—	619.0	—
temperature response (K)	480–600 [68]	290–600 (Fig. 3.14)	200–430 [68,70]

La_2O_2S:Eu has been exposed to different gas atmospheres and to pressures of up to 10 bar over its entire temperature-sensitive range without any noticeable changes in the emission characteristics being observed [80]. However, the imposition of compressive strain can trigger changes in both the chemical bonds that are present and in the atomic-level orbital configurations found. At very high pressures, up to 450 bar, the decay time of La_2O_2S:Eu was found having increased by as much as 8 % [81], due to the intersection with the CTS shifting towards regions of higher energy in the configurational diagram.

3.3.4 $Mg_3F_2GeO_4$:Mn

The increase in the demand for efficient lamps in the late 1940s resulted in the development of many of the phosphorescent materials that are known today. One such phosphor is manganese-activated magnesium fluorogermanate ($Mg_3F_2GeO_4$:Mn). In 1950, Thorington investigated the excitation and emission spectra of Mg_3GeO_4:Mn, finding that the addition of F atoms to the compound resulted in an increase in emission efficiency by 3 orders of magnitude [82]. Ten years later, in 1960, Kemeny and Haake discovered that the emission from the luminescence centre Mn^{4+} in $Mg_3F_2GeO_4$:Mn is sensitive to temperature changes [48,83] and absorbs light over the entire UV region [51]. Phosphorescence emission was found to be generated exclusively by $^2E \rightarrow {}^4A_2$ transitions, whereas the excited state is split into two energy levels due to a distortion in the crystal symmetry (*Jahn-Teller effect*) [83]. This leads to the existence of two characteristic emission bands, represented by the peaks at around 631 and 657 nm in Figure 3.15. In the low-temperature regime, the emissions at these two levels are in thermal equilibrium. With an increase in temperature, however, a depopulation of the 657 nm band towards the more highly energetic 631 nm band takes place. This thermal interaction can be used for thermometry through employing a relative intensity ratio [84]. When exposed to 355 nm radiation, the absorption process depopulates a high phonon level in the ground state. As the temperature increases, more phonons populate this ground state level, absorption and emission increasing with temperature up to about 650 K. When the temperatures rise further, non-radiative de-excitation paths via CTS transitions become increasingly probable [85]. Hence, decreased emission intensities and a stronger temperature de-

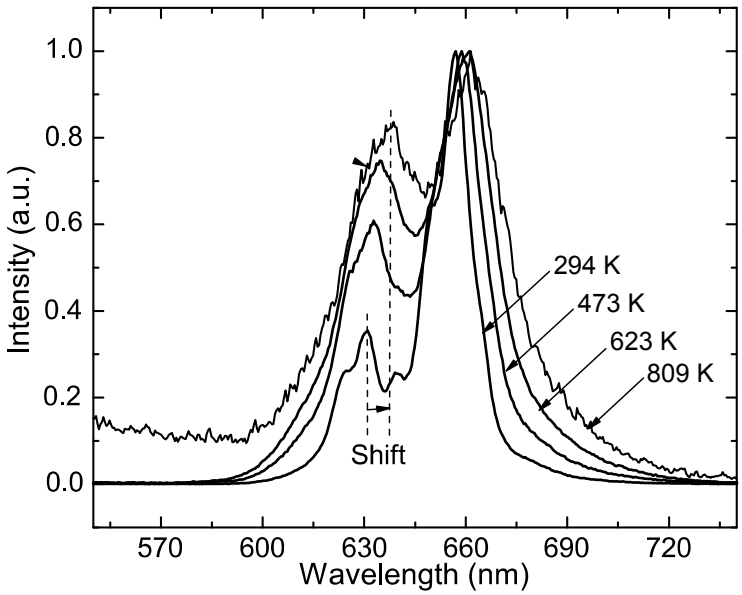

Figure 3.15: *$Mg_3F_2GeO_4$:Mn emission spectra following 355 nm laser excitation. The spectral distribution changes as a function of temperature. This figure was taken from [39] and was replotted with permission of Dr. A. Omrane.*

pendence of the decay time can be observed at temperatures above 650 K. The 657 nm emission line has a particularly strong temporal dependence on the temperature between 650 K and 1050 K, but it also allows thermometry to be carried out at cryogenic temperatures [86]. $Mg_3F_2GeO_4$:Mn has been exposed to different gas atmospheres and to pressures of up to 10 bar without being affected in its emission characteristics [80]. Phosphorescence decay rates of $Mg_3F_2GeO_4$:Mn have been found, however, to be affected by excitation irradiance, their decay time becoming smaller as the excitation energy increases [55]. In addition, this phosphor appeared to suffer from thermal history effects, when heated to above 970 K [55].

3.3.5 YAG:Dy

YAG:Dy (dysprosium-doped yttrium aluminium garnet) is very useful for high temperature thermometry [87] and marks today's upper temperature limit for phosphor thermometry of around 2000 K [69]. Phosphorescence emission occurs from the energy levels $^4I_{15/2}$ and $^4F_{9/2}$ following UV laser excitation at 355 nm [29]. Optical transitions that feed three electronic levels in the ground state, $^6H_{15/2}$, $^6H_{13/2}$ and $^6H_{11/2}$ correspond to emission bands at around 480, 580 and 680 nm, respectively [70]. When the temperature increases, emission also occurs at around 458 *nm* from the thermally populated $^4G_{15/2}$ state, which is found in close proximity to the $^4F_{9/2}$ state, their being an energy separation of only $\approx 1000\,\mathrm{cm}^{-1}$ [88].

Accordingly, a temperature-dependent relationship between the emission bands at 458 and 497 nm can be observed in Figure 3.16.

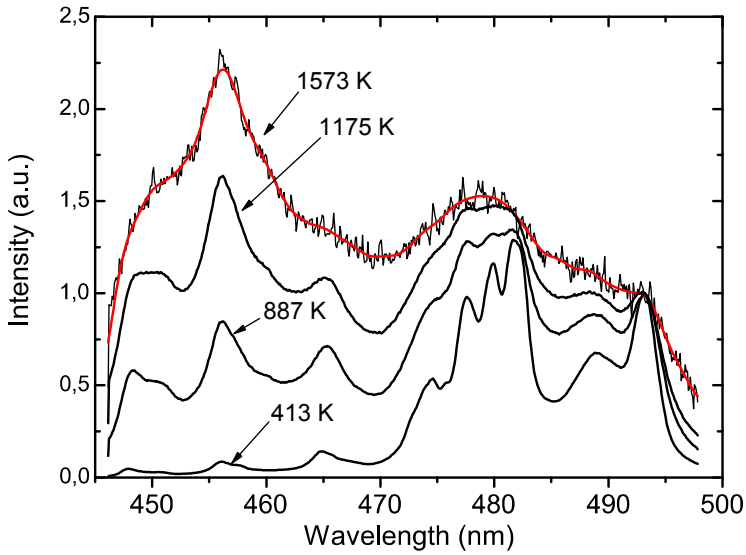

Figure 3.16: *YAG:Dy emission spectra following 355 nm laser excitation. The spectral composition changes as a function of temperature. This figure was taken from [39] and was replotted with permission of Dr. A. Omrane.*

Feist used an Arrhenius plot between 850 K and 1400 K to display and confirm the intensity ratio of YAG:Dy corresponding to the expected *Boltzmann relation* (Equation (3.9), page 24) [29]. Phonon quenching causes a decrease in signal intensities with an increase in temperature. Phosphorescence decay times are in the order of 1 ms at room temperature. In the 480 and 580 nm emission bands, a temporal response of YAG:Dy sets in between 1500 and 2000 K, resulting in progressively shorter decay times [69].

3.3.6 ZnO:Zn

ZnO:Zn (self-activated zinc oxide) consists of a zink oxide crystal with occasionally missing oxygen atoms that have been replaced by zink atoms in the lattice structure. When excited by 355 nm laser radiation, its broadband spectrum undergoes an exceptional shift towards the red spectral region; see Figure 3.17. This enables ZnO:Zn to be employed for precise temperature measurements using the two-colour ratio technique. Highly temperature-sensitive intensity ratios can be achieved by choosing spectral filter combinations, such as a 390 ± 5 nm bandpass filter in combination with a long-pass edge filter at 440 nm [70]. A one percent change in ratio corresponds to a temperature variation of about 4 K in the temperature range from room temperature up to almost 900 K. The spectral composition of ZnO:Zn, however, was found to change under variations in the excitation energy [89]. Decay time measurements for temperatures

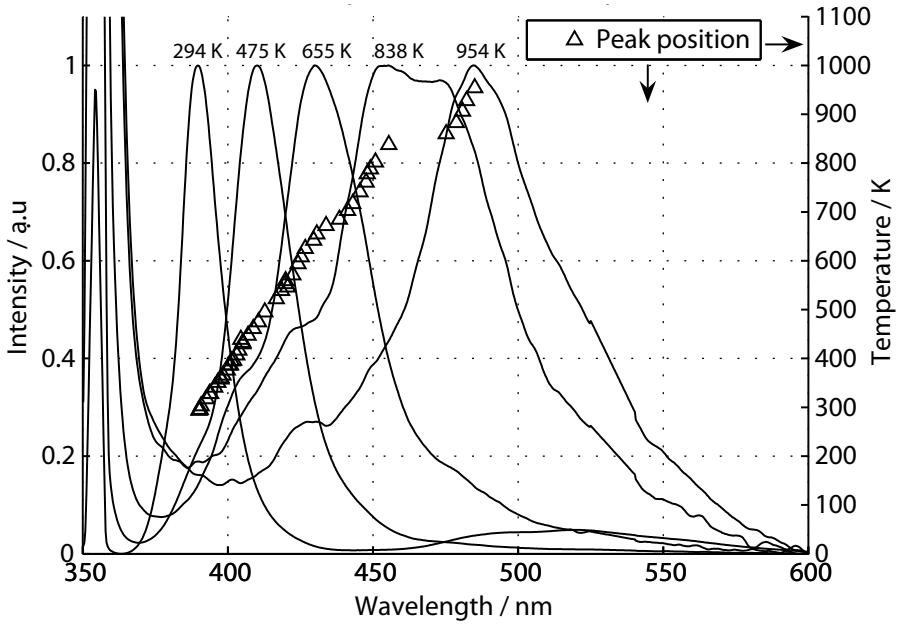

Figure 3.17: *ZnO:Zn emission spectrum following 355 nm laser excition. The spectral distribution changes as a function of temperature. This figure was taken from [70] and replotted with permission of Dr. G. Särner.*

below 550 K can be performed using a band pass filter centred at 510 nm. Studies by Särner et al. have indicated ZnO:Zn to be insensitive to the ambient oxygen concentration at pressures of up to 4.5 bar and temperatures of up to 400 K [70, 79].

4 Methodological Considerations

This chapter represents a kind of empirical guide for surface thermometry using LIP. Various sources of measurement errors are identified and discussed. These can stem from the phosphor employed, the experimental setup, or operation of the equipment, for example. Awareness of these errors and knowledge concerning them can help researchers to optimize their setups and avoid common mistakes in designing and performing experiments. The process of data evaluation and its optimization in terms of temperature precision is also taken up, as are details of possible improvements based on varying the boundary conditions and parameters for common or recently developed evaluation schemes.
Phosphor thermometry can be employed in a wide variety of measurement environments, many of which pose unique challenges to the experimental configurations and their operators. Despite such differences, all LIP applications share a common need for temperature calibration, a process which is little affected by the type of application intended. In addition, temperature calibrations make use of all the instrumentation devices needed for the final measurement task. A generic calibration setup is thus not only representative of a large number of applications, but also can pose the majority of potential challenges that experimenters will be faced with and need to overcome in applied phosphor thermometry. Altogether, this makes the calibration experiment a suitable candidate for outlining and identifying potential means of decreasing the overall measurement uncertainty. The way in which this chapter is organized was selected in accordance with the sequence of events found in connection with a typical temperature calibration setup of the type shown schematically in Figure 4.1.

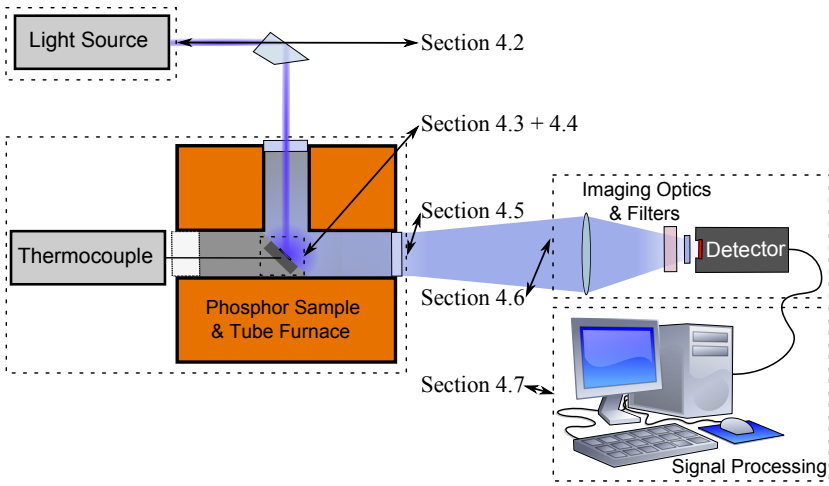

Figure 4.1: *An outline of this chapter, making use of the sequence of events in a generic temperature calibration setup. Particular setup components that are discussed in detail are labelled in accordance with the respective section numbers.*

The sections referred to in Figure 4.1 concern a number of different experimental

and analytical challenges, influencing measurement precision and accuracy in common applications of phosphor thermometry: A light source (4.2) illuminates a phosphor-coated target surface (4.3, 4.4) placed in an environment that provides controlled temperatures (4.5). In Figure 4.1, this environment is depicted in the form of a tube furnace, with thermocouples being attached to the phosphor-coated sample there. The emission of thermographic phosphorescence occurs as a consequence of electronic transitions, induced by optical excitation. Imaging optics are needed to direct this phosphorescence onto one or more photo-detectors (4.6). Spectral filters in front of the detectors select and isolate thermographic transitions from the residual spectrum of light. The signals that are recorded are digitized in order to be saved for later signal processing (4.7).
Additional challenges, not related to temperature calibration, that apply to combustion-related experiments and further increase the measurement uncertainty are addressed briefly in the final section of the chapter (4.8).

4.1 Definitions of Common Expressions

When discussing measurement errors, uncertainties and other commonly used terms can be understood in different ways, based on various definitions to be found in the literature. For consistency and in order to avoid confusions, the following definitions will be used in the thesis:

Signal-to-Noise Ratio: The signal-to-noise ratio (SNR) will be defined in the thesis in two different ways, depending on whether SNR is used for 1D decay curves or 2D signal matrices:

- For decay curves, the SNR is given by the ratio of the signal intensity $S(t)$ (at a given time t after the peak value $S_{\max}(t = 0)$) to the standard deviation of the vector elements of the zero signal prior to excitation.
- In the case of processed signal matrices, the SNR is defined locally for regions of quasi-constant signals. In such regions, the SNR is given by the ratio of the average signal to its standard deviation.

Precision: The term precision as used here is given by the absolute standard deviation of the parameter in question, which is proportional to the statistical spread of the accumulated measurement values. In case an ensemble of measurement values is normally distributed, ± one standard deviation from the ensemble average encompasses 68.2 % of all values. Accordingly, two and three standard deviations include 95.4 % and 99.9 % of all expected results. A high degree of precision corresponds to a low signal spread, i.e. a low standard deviation, respectively.

Accuracy: Whereas the term precision was defined to describe any particular random influence (e.g. the scatter of the measurement result), the discrepancy between the average measured value and the real value is denoted as the accuracy of the measured value. Similar to precision, accuracy is used as an absolute quantity, high accuracy corresponding to a small systematic error.

Uncertainty: The term uncertainty is used in the present work to describe the overall measurement error as the sum of absolute precision- and accuracy. Figure 4.2 shows how the definitions of the terms precision, accuracy and uncertainty, as used in the thesis, are interconnected.

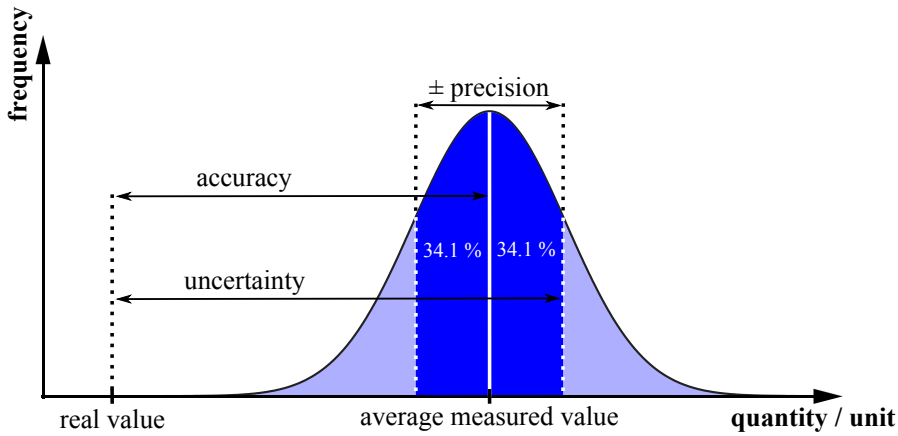

Figure 4.2: *A diagram, based on normally distributed results, showing how the terms precision, accuracy and measurement uncertainty are related to each other.*

4.2 Excitation Sources

A light source is needed in order to stimulate thermographic phosphorescence through optical excitation. Historically, pulsed UV lasers have been widely used for this purpose [13,15]. Current research, however, is pushing towards cheaper excitation devices in order to make phosphor thermometry accessible for a larger variety of practical applications. The present section provides a brief overview of a number of different light sources that can be employed for thermometry using thermographic phosphors. Finally, systematic errors due to optical heat transfer from the excitation source to the phosphor probe are discussed.

4.2.1 Pulsed Laser Systems

Pulsed laser systems deliver high peak powers during short time periods and are thus a preferred tool for the efficient excitation of phosphors. Continuous lasers generally deliver much smaller amounts of energy per time unit. This lack of power from continuous sources has encouraged researchers to use pulsed laser systems also in connection with time-integrated methods such as the two-colour ratio approach [13]. The length and temporal shape of the excitation pulse is of importance when measuring short emission decay times. The fall time of the pulses should be much shorter than the decay time of the phosphor, unless a deconvolution of the laser pulse shape from the signal is made.

Nd:YAG Lasers: In order to generate UV light at high pulse energies for phosphor thermometry, researchers most commonly make use of Nd:YAG lasers [13]. With the technology advances that have taken place in the past few decades, Q-switched Nd:YAG lasers in their higher harmonics can typically deliver 230 mJ at 355 nm and 90 mJ at 266 nm with repetition rates of 30 Hz and pulse durations of approximately 8 ns [90]. On the one hand, pulse energies that are too high per surface area can lead to such problems as sputtering or excessive optical heat transfer to the target surface. On the other hand, high laser energies are needed for 2D temperature imaging, which sometimes requires beam expansion in order for large areas to be illuminated. The gain medium in Nd:YAG lasers is usually pumped by flash lamps. Diode lasers have become available as an alternative, their providing better pumping efficiency, due to their spectrally narrow emission matching the peak absorption of the solid Nd:YAG rod. Diode pumps also provide extended service life and higher pulse repetition rates of up to several kHz [13, 91]. The pulse energies of diode-pumped Nd:YAG lasers are somewhat lower than those of flashlamp-pumped alternatives. Typical values for pulsed 266 nm emission are about 140 mJ at 10 Hz and 1 mJ at 1 kHz [91].

Excimer Lasers: Excimer laser are gas lasers that produce high power pulse outputs directly in the UV range. They consist of complexes, commonly formed between a noble gas and a halogen. Although having a stable bond in the excited state, these complexes are strongly repulsive in the ground state and dissociate in a matter of picoseconds. Pulse energies in the order of 200 mJ at wavelengths ranging from 157 to 351 nm are not uncommon [13]. Repetition rates are typically in the order of 100 Hz, but can be as high as 8 kHz [92], with pulse durations in the order of 10 ns [13]. Being effectively a two-level laser system that offers a high population inversion, the average number of resonator roundtrips for the laser photons is very small, leading to a high beam divergence. In addition, the beam shape is rectangular with a non-Gaussian beam profile. Due to its shape and intensity profile, transformations cannot be performed by use of the same optical systems as employed for round Gaussian beams. This can increase the complexity for many applications [13]. As of yet, applications making use of excimer lasers for phosphor thermometry have not been reported in the literature. However, the combination of high pulse repetition rates and high laser energies they involve makes them an attractive alternative for phosphorescence excitation in high-speed temperature imaging applications.

4.2.2 LEDs and Laser Diodes

Laser diodes and light-emitting diodes (LEDs) for the excitation of thermographic phosphors represent cost-efficient alternatives to expensive lasers devices. They are of compact and portable design and become increasingly available in the UV region, offering emission wavelengths down to 210 nm [93]. Laser diodes and LEDs can be operated, both in continuous and pulsed mode, their exhibiting fall times in the order of few ns. In addition, LEDs exhibit broadband emission, which can be absorbed better by some phosphors than narrow laser emission [13]. On the drawback side, their relatively low output power has restricted them for low-temperature applications

earlier, where background emission caused by black body radiation can still be considered being negligible. However, given the current rate of development of LEDs, there are predictions on the output power of LEDs increasing by a factor of 20 per decade [94]. If these predictions hold, then optimism is justified concerning phosphor thermometry becoming more practical in a variety of situations in the near future. Allison et al. were the first to report the use of UV LEDs in a phosphor thermometry application [95]. In another publication, the same authors carefully investigated the excitation of 14 different commercially available and customary prepared phosphors by LED emission [96]. Goedeke et al. reported LED-excited phosphor thermometry in excess of 1300 K using several yttrium aluminium garnet (YAG) and yttrium oxide based phosphors [97]. Currently, LEDs are commercially available that provide 3 W continuous output power at 365 nm [98].

Example: In relation to 10 ns pulsed lasers with output energies of 3 mJ, an LED with 3 W continuous output power would need a pulse length of 1 ms in order achieve a similar number of excitation photons.

If lower excitation intensities are to be compensated for by longer excitation pulses, it is apparent that LEDs work best for slow-decaying phosphors. In this context, Atakan et al. succeeded in measuring phosphorescent decay times of down to 30 μs using an UV-LED array with an output power of 285 mW at 375 nm [99].
Since pulse widths of LEDs can be modulated and fine-tuned, a phase-shift method can be used to measure decay times that would otherwise be too short to detect. Unlike pulsed excitation schemes, this method uses sinusoidal modulated light that illuminates the phosphor 50 % of the time. This can partially compensate for the generally lower output powers delivered by continuous light sources such as LEDs. Further details on amplitude-modulated excitation schemes can be found in section 3.2.2 (page 28). Phase-sensitive detection and frequency domain techniques have been characterized and applied less intensively than methods aimed at measuring the phosphorescence decay time directly. Due to the limited sensitivity of this method, only a few applications of it, such as [95, 100–102], have found their way into phosphor thermometry in the past. With increasing output powers that will become available, it could become more practical for future LED applications to rely on the well-established pulsed-excitation schemes as used in more recent studies [94, 99].
Similar to LEDs, laser diodes will continue to become both more powerful and less expensive. One advantage of them is the greater ease of coupling them to optical fibres. However, when implementing a broad array of light sources, such as in imaging applications, an LED array may be a more economical approach.

4.2.3 Optical Heating

The illumination of matter with light introduces heat as a consequence of light absorption. Whereas this is applied purposely in the welding industry, where e.g. CO_2 lasers are used, it is an undesired effect in optical thermometry. Energies of optical excitation sources should therefore be kept reasonably low in order to avoid their making significant contributions to the surface temperature of a measurement object.

Changes in surface temperature, induced by controlled variations of laser energies, have been observed in a number of recent publications on phosphor thermometry [I, 55, 62]. Incident light at the interface of two different media is either transmitted or reflected. For a given surface reflectivity $R \leq 1$, $(1-R)$ parts of the incident light are transferred from one medium into the other. Assuming the second medium to be a thermographic phosphor that absorbs all light that enters, the phosphorescence quantum yield q describes the fraction of absorbed photons at wavelength λ_1 that results in the emission of a phosphorescence photon at $\lambda_2 > \lambda_1$. It follows that the fraction of optical energy that is converted into heat in the phosphor then is described by Equation (4.1).

$$f_{\text{heat}} \approx (1 - R) \cdot \left(1 - \frac{\lambda_1}{\lambda_2} \cdot q\right) \tag{4.1}$$

Example: Values for R, q and the ratio of excitation to emission wavelength are needed in order to estimate the amount of heat being generated in the phosphor. Measurements of reflectivity on TBCs yielded surface reflectivities of 0.2 to 0.3 for UV radiation in between 266 and 355 nm [103]. These values, however, may vary substantially as a function of the surface roughness. For the quantum yield, an approximated value of $q = 0.5$ was stated as being typical for lamp phosphors [104]. Finally, the average wavelength ratio over all thermographic phosphors, as presented in section 3.3 (page 30), was found to be in the order of 0.6. Entering these values into Equation (4.1) results in $f_{\text{heat}} = 0.75 \cdot 0.7 = 0.525$. Consequently, ca. 70 % of the laser energy which is absorbed by the phosphor is transformed into heat energy. This heat accounts for more than half of the original light energy.

Experimentalists often find themselves confronted with the task of finding a trade-off between generating a signal from the phosphor sufficient for obtaining high SNRs and, at the same time, limiting the power of their excitation source in order to prevent surface temperatures from heating up through light absorption. In this context, the phosphorescence quantum yield q has a twofold effect on the trade-off: Phosphors with high q values provide the advantage of yielding a stronger signal while at the same time limiting the amount of light energy, which is transformed into heat.

The average temperature increase ΔT_+ per laser pulse (energy E) for a small target body with mass m and specific heat capacity c_v can be calculated using Equation (4.2).

$$\Delta T_+ = f_{\text{heat}} \cdot \frac{E}{m \cdot c_v} \tag{4.2}$$

The amount of heat which is lost per time interval $\mathrm{d}t$ over a surface area A corresponds to a decrease in temperature ΔT_- and is dependent upon the actual temperature difference ΔT between the sample and the surroundings; see Equation (4.3).

$$\Delta T_- = \frac{\alpha \cdot A \cdot \Delta T \cdot \mathrm{d}t}{m \cdot c_v} \tag{4.3}$$

The parameter α here denotes the heat transfer constant and may consist of contributions from heat transfer through convection and thermal radiation. Further details

regarding its calculation for a given example can be found in the appendix of [I] and in [105]. In Paper [I], the effect of laser-induced heating was studied experimentally on a calibration target surface (Hastelloy-C disc, diameter = 41 mm, thickness = 6 mm). Measured surface temperatures over time were compared with a model of lumped system analysis, using equations (4.2) and (4.3). Figure 4.3 shows the temperature drifts from a phosphor-coated Hastelloy disc, that were induced by pulsed laser illumination. The sample was exposed to 10 Hz pulses of 3 different laser energies: 1 mJ (thin line), 5 mJ (medium line) and 12 mJ (thick line). The corresponding dashed lines represent the temperature trend predicted by the model. The dotted line indicates the temperature increase of a corresponding black body with $R = 0$ and $q = 0$, that was exposed to a laser energy of 12 mJ.

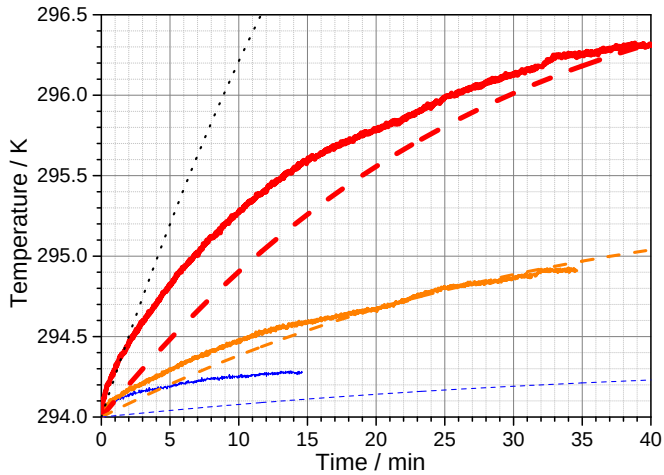

Figure 4.3: *The time-dependent heating of a $Mg_3F_2GeO_4$:Mn-coated Hastelloy calibration disc, induced by 10 Hz pulsed 355 nm laser illumination at room temperature. The solid lines represent measurement results at 1 mJ (thin line), 5 mJ (medium line) and 12 mJ (thick line). The corresponding model temperatures are indicated by dashed lines. The dotted line corresponds to a black body, optically heated by 12 mJ at a rate of 10 Hz.*

The modelled temperatures shown in Figure 4.3 agree fairly well with the measured values, when account is taken of the necessary assumptions that were made. There is a general tendency of the model to act more slowly than the measured values would suggest. This is particularly evident when one notes the disagreement of the model with the 1 mJ laser energy measurements. The following discussion attempts to shed light on the origin of mismatches between the model and the measurements:
The heating rate of the modelled black body in Figure 4.3 corresponds to the expected upper limit of the heat, absorbed by the object due to its exposure to light. In addition, the heating rate approaches its maximum at around $t = 0$, where the model is simplified significantly since according to Equation (4.3), heat losses can be neglected there. Figure 4.3 allows the modelled heating rate of the black body to be compared

with the measured heating rate of the phosphor target for values of light exposure being identical there (the dotted line and the thick line in Fig. 4.3). In the initial part of Figure 4.3, the experimental heating rate of the phosphor target exceeds its theoretical limit as given by the modelled heating rate of a corresponding black body. This behaviour was very likely caused by the local temperature gradients across the substrate, which could persist due to slow conduction. Since the temperature during the experiments was measured at the surface, the local heating rates may have been higher than what the lumped system analysis across the entire body predicts.
A lumped capacity approach was found to be of limited suitability for predicting the temporal change of the surface temperatures. More advanced and complex models are needed for this task, especially when attempting to accurately describe the heat transfer in large objects. Nonetheless, a simple heat tranfer model, as described by equations (4.1), (4.2) and (4.3), suffices to predict the order of magnitude of the heat, produced on surfaces through light exposure. In addition, it provides some crude understanding of the interplay of the different physical parameters that are involved in the process:

The effects of optical heating can be limited by choosing phosphors with high quantum yields and small stokes shifts (see Eq. (4.1)). For a given amount of heat introduced to a body, the temperature drifts are smallest in bodies of high mass having high specific heat constants (see Eq. (4.2)). High thermal conductivities help to disperse the heat equally across the body and limit local temperature gradients. A high surface-to-volume ratio (see Eq. (4.3)) is beneficial for transferring heat away to the surroundings by means of convection and thermal radiation. Limiting laser energies and pulse repetition rates, however, remains the most important parameter that experimentalists can influence in order to limit temperature drifts that are induced by optical heating.

4.3 Choice of Thermographic Phosphor

A large number of thermographic phosphors are available to date [12, 14, 15, 70, 71]. Combined together, they enable measurements to be made across a temperature interval ranging from cryogenic temperatures all the way up to about 2000 K [68,69]. There is often more than one thermographic phosphor available, which is sensitive in the desired temperature range. In this section, factors to consider in choosing an appropriate thermographic phosphor for a given measurement task are briefly discussed.

4.3.1 Temperature-Sensitive Emission Range

By far the most important choice criterion for finding a suitable thermographic phosphor for an LIP experiment is the temperature-sensitive emission range of the phosphor. Ideally, it should cover the entire interval of temperatures that can be expected from the experiment. The temperature-sensitive response range of different thermographic phosphors can be obtained most easily from calibration charts; see Figure 3.11, page 30. Comprehensive selections of the thermographic phosphors, that are available, are listed in [12, 14, 71].

4.3.2 Temporal Resolution

The temperature, extracted from the thermographic phosphorescence, is usually evaluated over a certain period of time Δt within the luminescence decay. For time-integrating methods, Δt can correspond either to the entire signal length or to the recorded camera gate width, depending on which of these is shorter. For intensity decay methods, Δt is given by the window length, for which temperature evaluation takes place. As the intensity contributions of phosphorescence and the laser pulse may change relatively between calibration and measurement, it is not recommended to start evaluating before the excitation pulse has fully passed. Evaluation windows are often expressed by a fixed number of decay times, which makes Δt a temperature-dependent parameter.
In order to obtain valid results from temperature calibrations, experimental temperatures should not be allowed to change over time scales of less than Δt. A sudden temperature change within the observation window would otherwise lead to altered decay transients, causing risks for misinterpretations and systematic errors. Thermographic phosphors with characteristics of long decays thus provide limited temporal resolution.[3]

Example: Temperature measurements using LIP are about to be performed inside a two-stroke motorcycle engine. The engine runs at 3600 rpm and surface temperatures are expected to lie within a range of 400 to 600 K: A typical time scale, for which temperature changes take place in such an engine environment corresponds roughly to the duration of one crank-angle degree, i.e. the time for which the crank shaft that moves the piston turns by one degree. At an engine speed of 3600 rpm, the duration of one crank-angle degree (CAD) can be calculated as $t = 60\,\mathrm{s}/(3600 \cdot 360) \approx 46\,\mu\mathrm{s}$. If evaluation windows in the order of $\Delta t = 4 \cdot \tau$ are desired, the phosphor selected for the task should exhibit decay times faster than $\tau = 46/4\,\mu\mathrm{s} \approx 10\,\mu\mathrm{s}$ over the entire range of expected temperatures.[4]

4.3.3 Temperature Precision

Another restriction in the choice of phosphor can be set by the required temperature precision that needs to be achieved in the experiment. The average measurement precision of a phosphor across a given temperature range T_{Range} can be compared with that of other phosphors as based on two quantities:

1. The range S_{Range}, over which the temperature-sensitive characteristic S of the phosphor extends, according to temperature calibration measurements. S could, for example, be either the phosphorescence decay time or a two-colour ratio. The temperature precision increases with an increase in S_{Range}.

[3] Other than by the phosphor involved, the temporal resolution can also be limited by the detectors that are used.

[4] Since phosphorescence decay times decrease with increasing temperature, it is usually sufficient to fulfill this criterion at the lower end of the expected temperature range.

2. The standard deviation ΔS_{Res} of the residuals of the measured values for S in the calibration fit . A high precision of S (low ΔS_{Res} values) also results in a high temperature precision.

Accordingly, the average temperature precision ΔT_{Prec} of a thermographic phosphor within a given temperature range can be expressed in accordance with Equation (4.4).

$$\Delta T_{\mathrm{Prec}} = \frac{T_{\mathrm{Range}}}{S_{\mathrm{Range}}} \cdot \Delta S_{\mathrm{Res}} \tag{4.4}$$

Example: According to Figure 4.4, a temperature calibration of ZnO:Zn between 300 and 550 K resulted in phosphorescence decay times that varied from $\tau = 95$ to 12 ns. The standard deviation of the decay time residuals to the fitted calibration model was found to be $\Delta\tau_{\mathrm{Res}} = 2.5$ ns. Thus, Equation (4.4) predicts an average temperature precision of $\Delta T_{\mathrm{Prec}} = 250\,\mathrm{K}/83\,\mathrm{ns} \cdot 2.5\,\mathrm{ns} \approx 7.5\,\mathrm{K}$.

Alternatively, individual temperature precisions $\Delta T_{\mathrm{Prec}}(T)$ of similar magnitude can be found by drawing horizontal lines in the calibration plot, as indicated in Figure 4.4.

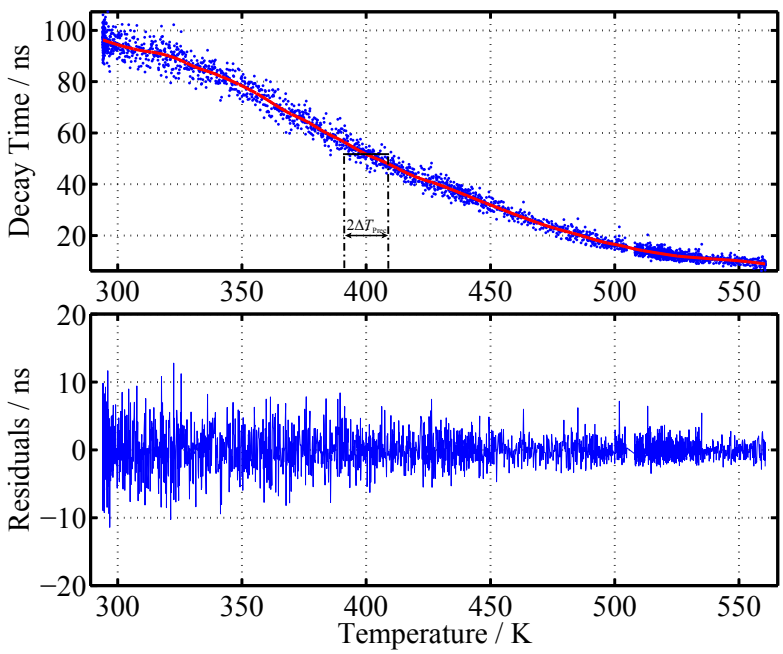

Figure 4.4: *Temperature calibration of ZnO:Zn (top). The lower part of the figure shows the residuals of the individual decay times in relation to the fitted model as a function of temperature.*

A similar calculation for $CdWO_4$ yields an average precision of 3 K during calibration, making it a far better choice for precise decay-based measurements within the temperature range in question.

4.3.4 Emission Wavelength and Spurious Background Radiation

In many practical applications, thermographic phosphorescence is not the only source of light present during signal collection. Spurious contributions from

- scattered laser light
- laser-induced fluorescence (LIF) from filters, windows, oil films, deposits or chemical species in the gas phase
- chemiluminescence and black body radiation in combustion-related environments

can be superimposed on the detected signal and give rise to signal perturbations. In some cases, it is possible to account for these perturbations by performing in-situ calibrations in the presence of all disturbances that could occur during the experiment. However, any additional signal contribution that is insensitive to temperature would likewise decrease the temperature sensitivity achieved during calibration.
Time-gating is a common approach taken to reduce the contributions of a constant background on top of a short-lived signal. In addition, optical bandpass filters can be used to select certain wavelength regions that carry the expected measurement signal while suppressing contributions from all other wavelengths.

4.3.5 Sensitivity to Experimental Quantities other than Temperature

The luminescence characteristics of certain thermographic phosphors can be affected by a number of additional quantities other than temperature. This can be problematical in situations, in which the temperature is not the only parameter to be varied. Inside combustion chambers, for instance, temperature, pressure and gas composition, all change in a correlated manner. It is thus important to be aware of these effects during selection of a suitable thermographic phosphor. Such effects need to be either avoided or carefully compensated for in order to limit the occurrence of systematic temperature errors. Some of the most common dependencies are discussed briefly in this section.

(a) Excitation-Energy Dependence: In principle, there are two distinct ways in which the luminescence properties of thermographic phosphors can be affected by variations in the intensity of the excitation source.

- The excitation source can transfer heat to the phosphor coating, this being followed by a temperature increase on the surface [I]. Thermodynamic properties, related to this effect, such as given in section 4.2.3 (page 43), need to be taken into account.
- Exposures to high incident fluxes may lead to luminescence saturation, which is when the phosphorescence efficiency changes dependent on the excitation intensities. If the impinging excitation intensity is increased to the point of saturation, this manifests itself in terms of spurious temperature changes [12].

Increasing the energy content of the excitation source results in a higher luminescence intensity, but it can also cause the occurrence of additional phonon quenching. Some cases have been studied, in which increasing irradiance above a certain intensity threshold were found to result in decreasing luminescence intensities and in shorter decay profiles [13]. In addition, the effect of luminescence saturation was found to increase with an increase in dopant concentration [12]. Moreover, saturation is itself a temperature-dependent phenomenon. For all concentrations, the saturation thresholds have generally been reported to be lower at higher temperatures [12].
Part of the effects induced by luminescence saturation can be explained by the following processes:

- The phosphorescence efficiency decreases with an increase in excitation light flux, because fewer luminescence centres are in their ground state so that the probability of resonant light absorption decreases for each photon.
- Phosphorescence decays become shorter due to an increase in the number of photons that can interact with already excited luminescence centres. This causes the latter to relax into their ground state prematurely through stimulated emission.
- Saturation effects can increase in importance at elevated doping concentrations, because of an increased probability of two luminescence centres in close proximity to one another being excited [12]. Their interactions can give rise to additional energy-loss mechanisms; see section 3.1.5 on page 18 for further information.
- The probabilities of various radiative and non-radiative transitions are often related to the thermal energy of the phosphor; see section 3.1 on page 13. Hence, the temperature can change the saturation of electronic states and affect the occurrence of internal energy transfer processes [15].

Example: Luminescence saturation has been observed in a wide range of phosphors, including $CdWO_4$ [VI], $Mg_3F_2GeO_4$:Mn [55], YAG:Tb [106], Y_2O_2S:Eu [107] and Zn_2SiO_4:Mn [106]. A change in laser energy between 0 and 500 μJ resulted in systematic temperature changes of up to 12 K in case of $Mg_3F_2GeO_4$:Mn, according to [55].

If thermographic phosphorescence characteristics are influenced by the excitation intensity of incident light, it is advisable to either keep the excitation energies between calibration measurement and application constant, or to calibrate and compensate for the intensity dependence of the phosphor. In most practical cases, however, the light impingement on the phosphor depends not only on the excitation source, but also on the optical components and the experimental setup. Dirt agglomeration on the phosphor and on optical components can hamper signal transmission in challenging environments and introduce a time dependence there. It is thus not a trivial task to account for all the systematic errors that can be induced by an intensity-sensitive phosphor. Hence, it seems prudent to either rely on phosphors thoroughly reported on in the literature in order to avoid any signal-intensity dependence, or to perform in-house tests with suitable phosphor candidates under the influence of deliberate intensity variations.

During the course of the thesis work, the excitation intensity dependence of $CdWO_4$ decay curves was investigated. The experimental setup, described in Figure 4.5, can be used to study additional phosphors in the future and provides the advantage of distinguishing between luminescence saturation and effects related to signal detection.

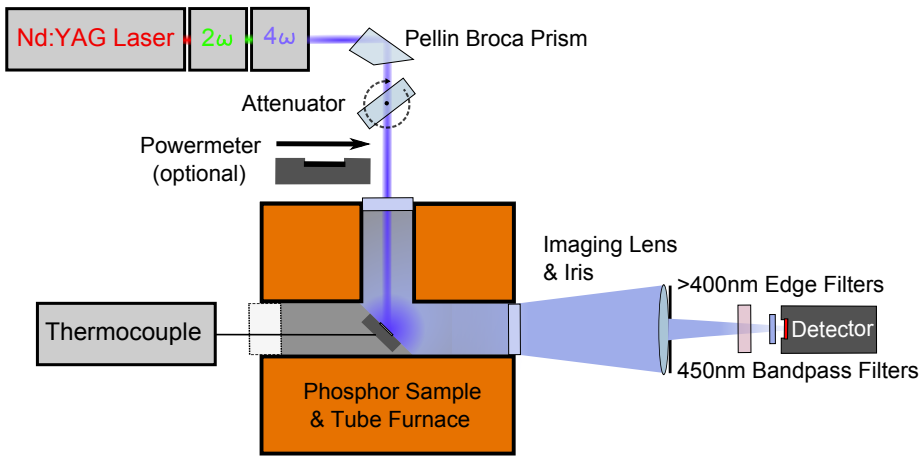

Figure 4.5: *Experimental setup for investigating the excitation-energy dependence of thermographic phosphors at arbitrary temperatures. The light intensity at the detector can be varied either by the attenuator located in the excitation beam path or by the iris in the path of the phosphorescence beam.*

A 266 nm 10 Hz pulsed laser was directed unfocused ($d = 8$ mm) at a $CdWO_4$-coated calibration target at room temperature. In case of the target being placed inside a tube furnace, as depicted in Figure 4.5, controlled measurements at any desired temperatures can be performed. The laser energy was varied from 15 μJ to 2 mJ by use of a polarizing beam attenuator so as to be able to study possible saturation effects on the phosphor. When signal intensities are varied this much, it appears important to ensure that the observed effects do not stem from any non-linear processes in the detection line (further information regarding this is to be found in section 4.6.5, page 91). In order to keep the detector response as linear as possible, it was decided to counteract any light intensity increase of the signal by a corresponding gain reduction. This kept the electrical output signal constant in amplitude. The phosphorescence signal was filtered spectrally by a combination of a $>$ 400 nm edge filter and a (450 ± 20) nm bandpass filter prior to detection of it by a *Hamamatsu* H11526-20-NF PMT. In a comparative study, this detector provided the most linear signal response of any of the point detectors that were available [VI]. The signal readout was carried out on a digital oscilloscope terminated by a 50 Ω input resistance. Figure 4.6 shows the evaluated signal decay as a function of light impingement on the detector. During variations in the phosphorescence intensity being collected, the peak signals recorded were kept constant in the one test at 30 mV (●/○) and in another test at 300 mV (■/□).

Various signal amplitudes can be achieved through changing the size of the collection lens by use of an adjustable iris. Signals at 300 mV had decay times that were assessed as being about 0.5 μs longer than signals with a maximum amplitude of 30 mV. This effect can be attributed to optical saturation in the PMT, that caused the decay times obtained to be longer [V]. More important, when the laser energies were increased, the decay times decreased from about 11 μs down to 7.5 μs (■/●). This corresponds to a virtual temperature increase of 11 K, which appears impossible to achieve just by heat transfer to the target surface at laser energies of less than 2 mJ (see section 4.2.3, page 43).

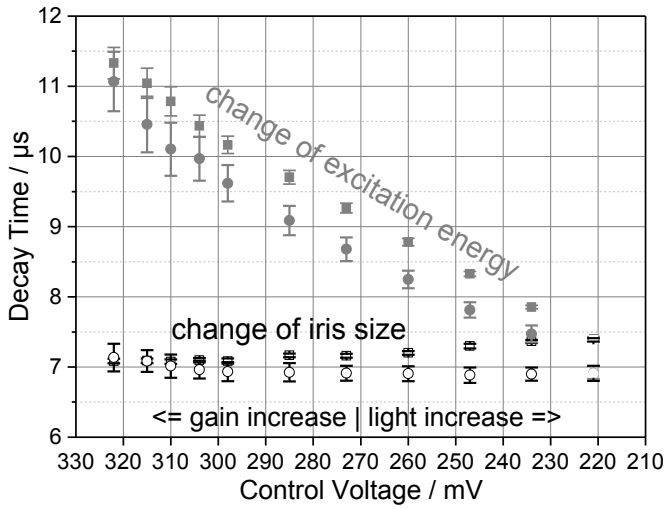

Figure 4.6: *Excitation energy dependence test for $CdWO_4$. The light intensity was either varied by means of the laser energy employed: 15 µJ... 2 mJ (■/●) or by changing the diameter of the imaging lens for a constant laser energy of 2 mJ (□/○). The maximum electrical output signal was kept constant at 30 mV (●/○) and 300 mV (■/□).*

In order to rule out the possibility, that the observed changes of the signal decay time ((■/●) in Fig. 4.6) were caused merely by changes in the detector response, another experiment was performed, for which the laser energy was kept constant at 2 mJ. The light intensity at the detector here being varied by changing the diameter of the imaging lens between the phosphor sample and the detector, by means of an adjustable iris. Although the PMT was exposed to similar light levels and gains as in the previous experiment, the results obtained ((□/○) in Fig. 4.6) show the decay time to be largely constant throughout the entire experiment.[5] Consequently, the decrease in decay times for increasing light intensities that $CdWO_4$ was exposed to is caused by saturation effects in the phosphor.

[5] One can observe the decay times of 30 mV and 300 mV signals drifting apart with increasing light intensities ((□/○) in Fig. 4.6.) This is an indicator of the onset of detector saturation with further details to be found in section 4.6.5, page 95.

(b) Oxygen Quenching: Oxygen is known to be an effective emission quencher [13]. It takes up energy by transfer processes through the interaction with excited luminescence centres nearby. The probability of this occurring is dependent upon the quenching substance involved and its concentration. The luminescence intensity of many oxygen-sensitive materials follows the *Stern-Volmer law*; see Equation (4.5)

$$\frac{I_{\mathrm{ref}}}{I} = 1 + K \cdot [O], \tag{4.5}$$

where I_{ref} is the signal intensity in the absence of oxygen, i.e. $[O] = 0$, and I is the signal intensity at a given oxygen concentration $[O]$. The Stern-Volmer quenching constant, as given by K, can be determined by calibration [108]. When the probability of oxygen quenching increases, the probability of radiative emission is reduced. This lowers the emission intensity and results in the decay times becoming shorter.

Phosphors that are quenched by oxygen usually exhibit also a pressure dependence. This can be made plausible by imagining a gas mixture that contains oxygen and that is contained within a closed space. When the gas is compressed by an outer force, its volume decreases and the gas pressure rises accordingly. At an elevated pressure, the same amount of oxygen molecules is now distributed over a smaller volume, which is equivalent to an increase in oxygen concentration. This principle is the basis for creating oxygen- and pressure-sensitive paints [109]. The *Stern-Volmer law* is often employed for measuring the air pressure (i.e. the partial pressure of oxygen) in aerodynamic applications [110]. A sensitivity to oxygen of thermographic phosphors is often problematic for thermometry in environments of temporally and spatially varying oxygen concentrations, for example in combustion environments. Särner and colleagues have shown that ambiguities arise for luminescence decay times in pressure-sensitive paints when temperatures and oxygen concentrations are changed simultaneously [111].

(c) Pressure Quenching: Apart from pressure causing an increase in partial oxygen levels, there is also evidence that the application of pressure or strain can affect the luminescent properties of thermographic phosphors. This phenomenon is not very well understood but becomes highly relevant when extreme pressures are involved. The application of pressure can be viewed as the imposition of compressive strain from all directions. It can result in changes, both in chemical bonds and in orbital configurations at the atomic level [13]. Thus, knowledge of a material's pressure dependence also provides insight into its strain dependence. At the atomic level, strain produces a change in chemical bond lengths and in atomic orbital configurations. This perturbs the electric and magnetic fields experienced by the activator, the spectral energy level thus becoming manifold. Such environmental changes modify the emission properties of phosphors, but the mechanisms involved vary from one phosphor to another [12]. The effects of pure pressure quenching usually do not become important before very high pressures in the order 1 kbar, and in excess of this are reached. La_2O_2S:Eu, for example, does not show any pressure dependence, when tested up to 10 bar [80], but if pressures of around 35 kbar are reached, its decay time increases by one order of magnitude [81]. A survey of the effects of high pressure on the luminescence characteristics of different fluorescent materials can be found in Ref. [12].

Examples:

- Oxygen dependence: Y_2O_3:Eu [80] and YAG:Eu [112]. Their dependency is supposedly caused by an interaction with the state of oxidation of the Eu activator ion [15].
- Pure pressure dependence:
  - Pressure-induced line shifts: BAM ($\gg$ 1 kbar) [77]; ZnS:Eu, Y_2O_2S:Eu and $CaWO_4$:Nd [12].
  - Pressure-induced decay time changes: La_2O_2S:Eu (35 kbar) [81], Gd_2O_2S:Tb (20 kbar) [13].
- Brübach et al. [15] tested the following thermographic phosphors for their cross-sensitivity to pressure and their ambient gas composition without any significant pressure dependence being shown: YAG:Dy, Al_2O_3:Cr, YSZ:Eu, YAB:Cr and $Mg_3F_2GeO_4$:Mn. Since these phosphors are only affected by thermal quenching, they are suitable for experiments in which changing gas environments are to be expected.

(d) Thermal History Effects: Chemical or physical interactions within the phosphor, or in between the phosphor and its binding agent or the substrate involved can be triggered or boosted at elevated temperatures. These interactions can permanently change the luminescence characteristics of thermographic phosphor coatings, causing thermal drifts in the temperature readings to occur. There are three major processes known, that can lead to irreversible changes of phosphorescence characteristics:

- **Chemical Reactions:** Most phosphors consist of ceramic hosts, which are chemically inert. Some of their doped activator ions, however, such as Europium, are known to change their oxidation state through redox-reactions [15]. The phosphor BAM falls within this category. When it is exposed to an air atmosphere at temperatures in excess of 770 K, thermal degradation sets in through gradual oxidation of the activator ions ($Eu^{+2} \rightarrow Eu^{+3}$), leading to permanent changes in its emission characteristics [74]. In addition, reactions of phosphor coatings with chemically active substrates or with gas mixtures are possible.
- **Diffusion:** The rates of ion diffusion between substrate, phosphor and binder tend to be higher at elevated temperatures. This can affect the luminescence characteristics of phosphors either through energy transfer processes or through its affecting the crystal field of luminescence centres nearby. Brübach and colleagues found the emission characteristics of $Mg_3F_2GeO_4$:Mn to be affected by the substrate (stainless steel) when the phosphor was heated to above 970 K [55]. The overall luminescence intensity decreased and the phosphorescence decay times were permanently reduced. The extent of this thermal history effect increased at higher temperatures and for longer exposure times.
- **Annealing:** The term annealing or curing generally refers to a form of heat treatment, involving the long-term exposure of a material to elevated tempera-

tures, which permanently alters the microstructure of the material. Annealing is an important post-process for coating deposition techniques, in which the phosphor is chemically recombined on the substrate (see section 4.3.6). After a phosphor coating has been deposited on the substrate, the activator ions are situated in a variety of positions and orientations within the crystal structure of the host. The activators involved thus experience a variety of crystal field effects, which results in the spectral emission lines becoming weaker and broader [113]. The annealing process enables the activator ions to re-position themselves more correctly within the host lattice, restoring the crystalline quality. In addition, small nano-crystals start to form larger crystals. Since this results in improvements in the coupling of excitation energy to the electrons, the intensity of the spectral emission lines is enhanced [113]. Annealing usually takes place during long-term exposure (several hours) to temperatures in excess of 800 K [54].

For phosphors that are known to suffer from thermal history effects, it is advisable to perform a curing process, in which prior to temperature calibration and measurement, the phosphor coatings are heat treated at high temperatures for several hours. Applying such heat treatments to coatings on measurement objects, however, may turn out very difficult (if not impossible) in many applications. In such cases, it can be advisable to rely on phosphor coatings instead, that do not change their emission characteristics as a result of annealing.
Thermal history effects can be easily detected during temperature calibration. One way of doing this is to calibrate thermographic phosphors during both the heating and the cooling phase of the calibration. A systematic difference in the phosphorescence response between the heating and the cooling phase of the calibration may be introduced, one that originates from the thermal treatment carried out. The detection of thermal history effects may be enhanced by keeping the phosphor at elevated temperatures for several hours, temperatures that exceed the maximum temperature being expected in a subsequent measurement application. If no systematic difference can be observed this way between phosphorescence characteristics from the heating and the cooling phase of the temperature calibration, possible errors induced by thermal history effects may be considered as negligible.

4.3.6 Bonding Techniques for Thermal Sensor Coatings

An ideal sensor coating should be very thin and in close thermal contact with the substrate so that it assumes the original surface temperature without perturbations. At the same time, the coating should be durable in order to withstand thermal shocks and vibrations that can occur during measurements in harsh environments, without developing cracks leading to the coating eventually flaking off. Dependent of the substrate in use, sandblasting the surface prior to the coating process usually increases the adhesiveness of the coating, by creating microscopic teeth. In addition, the substrate should be cleansed of contaminations and oil films using e.g. acetone. Finally, a high degree of homogeneity within the coating such that phosphorescence emission is equally intense throughout the coating surface is favourable.

Several methods are available today for creating thermal sensor coatings on surfaces of interest. Some of the most commonly employed techniques are discussed briefly in this section.[6]

(a) Adhesive Binder Coatings: For these, a slurry consisting of phosphor particles and a high-temperature resistant chemical binding agent is mixed and applied to the surface of interest. Phosphor particles are usually shipped in the form of powders, and can be ordered in specific narrow particle-size distributions. Typical diameter sizes range from a few nanometres to several micrometres.
An ideal binding material should be transparent to both excitation and phosphorescence radiation and form a stable bond between the substrate and the phosphor particles, while surviving high temperatures and thermal gradients. In addition, the binder should not interact with the phosphor particles chemically or by energy transfer. Organic binders can be used for temperatures up to 620 K [29]. For higher temperatures, silicates, silicones and water-mix refractories are typically employed. During this Ph.D. work, two different binders were used primarily, *HPC* and *Sauereisen* #14. *HPC* is composed of magnesium aluminium silicate and dries at room temperature in about 20 minutes. *HPC* coatings are soft and can handle temperatures of up to 1700 K. *Sauereisen* #14 is a water-based binder, producing hard coatings capable of withstanding temperatures of up to 1400 K [114]. A thorough comparison of various chemical binders for high-temperature application is given in [115].
The mixing ratio of the binder and the phosphor is usually not very critical. A higher phosphor-particle content enhances the emission intensity of the coating, but the bonding of coatings containing fewer phosphor particles is usually better. During the thesis work, the phosphor-to-binder mixing ratio was kept at approximately 1:20 by mass in line with experience gained empirically. Other research groups specify mixing ratios of 1:32 [116] or use 20 vol.-% of phosphor in the slurry [114].
Once the phosphor is mixed with the binder, the coating can be applied by use of either a paint brush or an airbrush. Coatings produced by an airbrush, however, are generally much more homogeneous and can be made significantly thinner than painted coatings [117]. When using an airbrush, it also seems wise to disperse the phosphor powder in ethanol before mixing it with the binding agent. This step helps to disperse the phosphor and contributes to maintaining a homogeneous particle distribution in each deposited layer. In addition, the risk of clogging the airbrush nozzle is reduced and the brush is less likely to spittle during the coating process. The production of the coating is carried out by applying a couple of thin layers to the surface, these being cured individually by exposure to elevated temperatures. In practise, a hot air gun can be used for this purpose, in order to dry off every freshly deposited layer of the coating. The dry-off process can often be witnessed as a slight colour transition on the surface. When a grey, wet finish turns dry, it often appears more whitish. Any residual ethanol in the mixture evaporates completely during the curing of each deposited layer. Different coating thicknesses can be achieved by varying the number of layers deposited. For coatings to remain intact and durable, it is important to keep the individual layers that are deposited thin and to dry them off thoroughly before

[6] All the experimental work presented in the thesis involves use of adhesive binder coatings.

applying another layer. As a general rule of thumb, thinner coatings are usually more durable and do not crack or flake off as easily as similar coatings of greater thickness.

Advantages: Adhesive binder coatings can be easily applied on-site to surfaces of arbitrary size and geometry. In addition, the required equipment can be purchased at negligible cost. The coated particles remain intact during application and generally do not require any additional annealing process prior to their use in remote temperature-sensing applications [12].

Disadvantages: Because binding agents do not actively contribute to the phosphorescence emission and may absorb part of the excitation and phosphorescence light, spray coatings usually produce less intense emissions than pure phosphor coatings of similar thickness do [54]. Another disadvantage of them is the poor control of coating thickness and homogeneity, the control of which depends primarily on the skill of the operator. The lower thickness limit for spray coatings is relatively large in comparison to other film deposition techniques and is defined by the phosphor particle size. The thickness was found to be on the order several micrometres, which makes spray coatings less durable than the thinner coatings of other competing techniques. Ranson and collegues managed to produce spray coatings of $\geq 10\,\mu$m in thickness [54], whereas independent studies in the framework of the thesis measured a thickness of $\approx 5\,\mu$m for the thinnest spray coating that could be produced and measured [III].

(b) Sol-Gel-Synthesis: The sol-gel synthesis is a wet-chemical process in which the phosphor is formed directly on the substrate during the deposition of the coating. In an initial step, all necessary precursors for the chemical compounds of the desired thermographic phosphor are dispersed in a solvent to form a homogeneous liquid, called sol. By carefully heating the sol, slow evaporation sets in and a gel is formed from the residual compounds [117]. The coating substrate needs to be brought into contact with the gel, usually by repetitive dipping or spin procedures [15,118], so as to create thin films of controlled thickness. Afterwards, thermal annealing at high temperatures is needed in order to remove the residual solvent and gel components and, more importantly, to allow the phosphor to re-organize into a multi-crystalline layer [119]. Film thicknesses on the order of about $1\,\mu$m can be achieved using sol-gel synthesis [117]. Further details concerning sol-gel processes can be found in [120].

Advantages: In comparison to most other film deposition techniques, the sol-gel method is still relatively cheap and does not require cost-intensive equipment. Pure crystalline phosphor coatings can be produced, which exhibit a high degree of homogeneity and allow for precise thickness control. In addition, the process customizes phosphors to be produced through the use of the appropriate proportions of precursor chemicals for the host the and activator.

Disadvantages: The measurement object needs to be of reasonable size and (if possible) to be detachable in order to be able to be dipped into the sol-gel bath. Closely reproducible pH values, temperatures and concentrations need to be achieved

for sol-gel baths, such that the emission characteristics of the calibration sample and the measurement object are maintained identical [119]. Also, the curing processes for the measurement object and that for the calibration sample need to be very similar, since phosphorescence emission also depends on the average crystal size. The annealing process requires very high temperatures in excess of 1000 K [120], both in order to enable crystal formation to take place and to avoid thermal history effects during experiments at high temperatures.

(c) Processes involving CVD: The chemical vapour deposition (CVD) process can be employed to produce high-purity, high-performance solid materials. It is often used in the semiconductor industry to produce thin films. Initially, one or more volatile precursors are transferred to the vapour phase before they are transported by a gas flow to the reaction chamber. The phosphor precursors need to have a reasonable vapour pressure at temperatures below 400 to 500 K [15] and usually enter the gas phase by evaporation or sublimation. Moderate pressures in the vapour phase are required, ranging from a few hPa to ambient pressure. This pressure regime only requires standard chemical process engineering techniques, instead of the high-vacuum techniques used in physical vapour deposition (PVD) processes [15]. In the reaction chamber, the precursors come in contact with the substrate and react to form a thin solid film of the desired phosphor on the surface [15, 117]. Frequently, volatile by-products are also produced, which have to be removed by the flow of gas through the reaction chamber. The activation energy for film growth can either be achieved thermally or by laser light, hot wires, flames, use of a plasma or by other means. The following two approaches have been employed successfully to produce thin and durable thermographic phosphor coatings [121–123].

- **Thermal CVD:** In thermal CVD the precursor reactions on the surface are triggered by applying heat to the substrate. Temperatures are kept high enough to allow crystallization to take place [121]. Alternatively the coating can be cured by heat treatment in a post-process [117].
- **EA-CVD:** The electrostatic-assisted chemical vapour deposition (EA-CVD) approach involves spraying atomized precursor droplets across an electric field, in which the droplets undergo combustion and chemical reactions in the vicinity of a heated substrate surface [29]. In contrast to other techniques, EA-CVD can be operated in an open atmosphere, which allows for a greater range of possible substrate geometries and applications. The process is able to produce thin solid adhesive films on the substrate that have a well-controlled stoichiometry, crystallinity and texture [122, 123].

Advantages: CVD techniques enable coatings, exhibiting high temperature tolerance, good impact strength, and excellent abrasion resistance and durability to be produced. At the same time, the deposition process not only results in homogeneous coatings but also provides accurate coating thickness control. Film thicknesses can be achieved on the order of one micrometre or less [124] and coatings are usually in good thermal contact with the substrate. Unlike adhesive binder coatings, the film that is deposited consists entirely of thermographic phosphor, which results in relatively high

luminescence efficiencies. In addition, the CVD process allows custom-made phosphors to be designed, that recombine at the surface of the substrate. Unlike other coating techniques, CVD depositions (as well as sol-gel coatings) do not suffer from any line of sight restrictions. This is because the phosphor precursors travel towards the substrate surface by diffusion or convection, which allows complex substrate geometries to be coated. Even porous materials, for example, can be infiltrated by this technique.

Disadvantages: The instrumentation required for this technique is more complex and expensive than for coatings produced from phosphor-binder mixtures or the sol-gel process. In addition, vapour deposition processes require a certain degree of experience and care on the part of the operator. Since the coating process also produces the phosphor, the reproducibility of the chemical stoichiometry between the calibration target and the measurement object is crucial for the avoidance of systematic temperature errors. Size constraints on the substrate and the necessity of exposing both the substrates and their coated films to high temperatures during the post-process of annealing may render CVD methods inappropriate for some applications.

(d) Processes involving PVD: The term PVD denotes a variety of different vacuum deposition methods, used to create thin films through the condensation of a vaporized film material onto the workpiece surfaces involved. PVD coating methods involve purely physical processes, such as high-temperature vacuum evaporation with subsequent condensation, or plasma sputter bombardment. Often, the film material itself is transferred to the vapour phase, meaning that the correct compound is present in the chamber but not yet on the substrate. In phosphor films created by vapour deposition, dopant atoms can be situated in a variety of different positions and orientations within crystal structure of the host and thus experience a variety of different crystal field effects, leading to both weaker and broader spectral emissions [113]. Post annealing for several hours at 900 to 1100 K is required to realign the ions, restore the crystalline quality and increase the luminescent intensity [12]. PVD processes are widely used in many manufacturing applications, such as in the automotive industries, in optics and during the production of semiconductor wavers.

- **EB-PVD:** In electron-beam physical vapour deposition (EB-PVD) a high-energy electron beam is used to heat and vaporize a pressed feed stock target, consisting of the thermographic phosphor to be coated. The vapour travels along the line of sight to the cooler substrate, on which it condenses atom by atom. EB-PVD requires high vacuum on the order of 10^{-13} bar for the atoms to reach the substrate [29]. The deposition rates are on the order of 0.2 to 2 μm/h [29].

- **Radio-Frequency Sputtering:** Similar to EB-PVD, a sintered or pressed feed stock from a commercially available phosphor is placed in a vacuum chamber together with the substrate which is to be coated. In this technique, the target achieves the vapour phase by momentum exchange: The phosphor target is bombarded by high-energetic ions (e.g. argon ions [54]) such that single atoms are ejected, those reaching the substrate and condensing to form a film of deposits.

Because ceramic phosphors are electrical insulators, a high-frequency alternating electric field is applied in order to support and enhance the creation of a plasma and thus increase the sputtering rate. The rate of film deposition can be increased by magnets being placed behind the substrate (magnetron sputtering) [125]. Since radio-frequency sputtering is a technique that is quite similar to EB-PVD, a general distinction or advantage of the one approach over the other in terms of bonding performance is not very likely [12].

- **Plasma Deposition:** In this method, a phosphor target is evaporated locally by a plasma, that almost instantaneously deposits high energies in a small-surface volume. The plasma can be created either by high-energetic laser pulses or by microwaves, causing local temperatures to rise in excess of 20 000 K [12, 117]. The ejected material hits the desired substrate at high speeds. An active temperature control through the substrate abets the diffusion processes and contributes to keeping the deposition rates constant [12, 117]. Since the stoichiometric composition of the target material remains largely intact during agglomeration, the crystalline structures can be formed directly on the substrate [117].

Advantages: PVD coatings have in common many of the advantages referred to in connection with the CVD technique. Very durable and long-lived coatings can be created, which are able to withstand thermal shocks and exposure to high temperatures. PVD techniques enable very thin films in the order of a few hundred nanometres up to a few micrometres to be deposited [54, 117]. Similar to the CVD technique and the sol-gel synthesis, the PVD process combines the creation of the phosphor with the film deposition process. This provides a high degree of freedom in defining the stoichiometric structure that is responsible for the thermographic properties of the phosphor. Since PVD coatings also consist of pure phosphor material, they possess an advantage in terms of luminescence intensity over coatings that partly contain binding agents: For example, Ranson and colleagues demonstrated that coatings, produced by radio-frequency sputtering, having a thickness of 0.7 μm were capable of emitting similar emission intensities as $\geq 10\,\mu$m spray coatings, that contain adhesive binders [54].

Disadvantages: PVD coating techniques suffer from all of the drawbacks, mentioned for CVD processes previously. Unlike CVD methods, however, PVDs are performed at high vacuum, which requires the use of far more complex and expensive equipment than needed for any other coating technique, that has been discussed earlier. In addition, the deposition process usually occurs along the line of sight, meaning that the flux of vapour atoms is along a single direction, so that shaded regions often are out of reach. The coating of substrates having complex geometries is thus rather difficult.

4.4 Temperature Gradients across Thermal Sensor Coatings

Thermographic phosphorescence emissions generally carry temperature information from the coated layer on top of the actual target surface, its being assumed implicitly, that the phosphor film is thin enough to adapt to the temperature of the covered surface without perturbation. This assumption is disputable, however, in thermal

non-equilibrium situations, in which altered time transients and systematic deviations of the coating temperature relative to the unperturbed wall may occur.
Thermographic phosphors are often described as (activator-doped) ceramics, which in turn are known to be thermal insulators. In fact, chemically similar coatings are used as TBCs in numerous applications. They have become integrated into advanced gas turbines, enabling hot-section components to operate at gas stream temperatures higher than the material melting point, whilst maintaining a reliable service life nevertheless [61,104,126]. Gentleman et al., for example, identified temperature differences in the order of 100 K for a 140 to 170 μm thick surface film of YSZ [127].
It is thus important to consider the thickness of thermal sensor coatings in certain types of applications as being a potential source of measurement error. The following sections discuss the existence and consequences of temperature gradients across thermal sensor coatings as a potential source of error in particular measurement environments.

4.4.1 Predicting the Existence of Thermal Gradients

This section introduces some useful tools that assist in predicting the relevance of temperature gradients across thermal sensor coatings prior to specific experimental applications.

According to the theory of thermodynamics, heat transfer in solid bodies is governed by conduction. Consider now a solid wall with a thickness d that on either side is in contact with two systems of different temperature, T_1 and T_2 ($T_1 > T_2$). Consequently, a linear temperature gradient $\Delta T_{12}/d = (T_1 - T_2)/d$ is to be expected across the wall, if the wall material is homogeneous. The amount of heat $\dot{Q}$ conducted through this wall, which can then be described by *Fouriers law* (4.6), is proportional to the surface area A, the wall's thermal conductivity λ and the existing temperature gradient:[7]

$$\dot{Q} = \lambda \cdot A \cdot \frac{\Delta T_{12}}{d} \tag{4.6}$$

This exchange of heat energy between system 1 and 2 has an immediate effect on the temperature since, depending upon the mass m and the specific heat c_v, a change in heat energy Q accompanies a temperature change ΔT in each system:

$$Q = m \cdot c_v \cdot \Delta T \tag{4.7}$$

Eventually, and if no heat sources or sinks are involved, thermal equilibrium is reached ($\lim_{t\to\infty} \Delta T = 0$) and the equilibrium temperature T_m can be calculated according to *Richmanns calorimetric mixing formula*:

$$T_m = \frac{m_1 \cdot c_{v1} \cdot T_1 + m_w \cdot c_{vw} \cdot \frac{1}{2}(T_1 + T_2) + m_2 \cdot c_{v2} \cdot T_2}{m_1 \cdot c_{v1} + m_w \cdot c_{vw} + m_2 \cdot c_{v2}} \tag{4.8}$$

In Equation (4.8), the subscript w corresponds to quantities associated with the wall. The previous considerations have consequences for the occurrence of measurement errors that may be introduced by the film thickness of thermal sensor coatings.

[7] In Equation (4.6), d represents the characteristic length, which is defined by the ratio of volume to surface in a body. For thin films on a substrate, however, this ratio converges to the film thickness d.

case A If the phosphor coating is in thermal equilibrium with surroundings that are nearby, temperature gradients across film coatings are insignificant and can thus be neglected.
Practical Example: The temperature calibration of phosphor coatings in a slowly heated furnace.

case B In the near presence of stationary heat sources and/or heat sinks, static temperature gradients may occur that could lead to systematic errors in the surface temperature reading, obtained from a thermal sensor coating.
Practical Example: Surface temperature measurements on gas turbine components during steady combustion.

case C In the presence of unsteady (e.g. oscillating) temperature distributions, dynamic temperature gradients may occur across thin film coatings, those having a biasing effect on the surface temperatures obtained.
Practical Example: Surface temperature measurements inside the combustion chamber of a reciprocating combustion engine during operation.

Whether or not the existence of temperature gradients across a thermal sensor coating are of significant relevance in a given application, can be determined on the basis of the Biot number Bi, which is defined as the ratio of the heat convection at the surface of a body to the heat conduction within the body. When a solid body is being heated by a hotter fluid surrounding it, heat is at first convected to the body and subsequently conducted within the body. According to Equation (4.6), a material with a comparatively high thermal conductivity is better able to transfer heat away from the surface of it. Therefore, a small Biot number represents a low degree of resistance to heat conduction, and thus the existence of only small temperature gradients within the body. The Biot number can be expressed as

$$Bi = \frac{\text{convected heat}}{\text{conducted heat}} = \frac{\alpha \cdot A \cdot \Delta T}{\lambda \cdot A \cdot \Delta T/d} = \frac{\alpha \cdot d}{\lambda}, \tag{4.9}$$

where α is the convective rate of heat transfer. The dimensionless ratio, described by Equation (4.9), determines whether or not the temperatures inside a body varies significantly in space while the body is being heated up or cooled down by a thermal gradient applied to its surface. The ratio is of special importance for temperature gradients during quasi-static experiments involving constant rates of convected and conducted heat; see **case B**. Values of the Biot number smaller than 0.1 imply that the heat conduction inside the body is much faster than the heat convection away from its surface, and that temperature variations across the body remain below 5 %. The opposite is also true: A Biot number greater than 0.1 indicates that one cannot make this assumption, more complicated heat transfer equations for "transient heat conduction" being required to describe the transient and non-uniform temperature field within the material body in question [128, 129].
After evaluating the potential existence of significant temperature gradients, another question arises, namely whether or not these gradients persist on time scales t, that are relevant to the experiment. This, along with the Biot number, can be of particular

relevance in systems of unsteady heat transfer; see **case C**. The situation involved can be assessed using the Fourier number $Fo(t)$, which is defined as the ratio of the heat conduction rate to the rate of thermal energy storage.

$$Fo(t) = \frac{\text{rate of heat conduction}}{\text{rate of thermal energy storage}} = \frac{\lambda \cdot A \cdot \Delta T/d}{\rho \cdot A \cdot d \cdot c_v \cdot \Delta T/t} = \frac{\lambda \cdot t}{\rho \cdot c_v \cdot d^2} \tag{4.10}$$

In Equation (4.10), ρ denotes the material density. For large Fourier numbers, the rate of conduction there being higher as compared with the rate of thermal energy storage, thermal gradients are more likely to have disappeared after a given characteristic time t as in the case of a small Fourier number. The Fourier number is frequently used as a non-dimensional time parameter in unsteady state conduction problems. For $Fo > 0.2$, conduction problems can be simplified using a one-term solution, approximation errors there remaining below 2 % [128, 129].

Example: This section will conclude with a numeric example of estimating the importance of temperature gradients across a $d = 60\,\mu$m thick thermographic phosphor coating applied to the inner wall of a reciprocating combustion engine (**case C** scenario). One problem arises from the lack of knowledge of the thermal properties of thermographic phosphor films (especially for adhesive binder coatings) so that only typical regimes can be assessed. Using an upper limit for the convection coefficient of $\alpha = 4500\,\mathrm{W/m^2K}$, found in [130], and a thermal conductivity of $\lambda = 1.5\,\mathrm{W/mK}$, which was measured for a chemically similar TBC coating in [127], one obtains a Biot number of 0.18 according to Equation (4.9). This resembles a regime, in which temperature gradients within the film begin to become important.
A typical time scale for which temperature changes take place in an engine environment corresponds to the duration of one crank-angle degree, i.e. the time during which the crank shaft connected to the piston turns by one degree. At an engine speed of 1200 rpm, a four-stroke engine fires every other cycle and one crank-angle degree (CAD) lasts for $t = 60\,\mathrm{s}/(1200 \cdot 360) \approx 138\,\mu$s. A further assumption, needed for calculating $Fo(t)$, is that the density and the specific heat of the coating is similar to that of the HPC binder material, which is the main component in spray coatings. HPC is a mixture of water and magnesium aluminium silicate [131]. Assuming that most of the water evaporates during the curing process, one obtains $\rho = 2100\,\mathrm{kg/m^3}$ and $c_v = 774\,\mathrm{J/kgK}$ [132]. With these values inserted into Equation (4.10), a very small Fo value of 0.035 is calculated. A Fourier number of unity is reached for time scales of about 3.9 ms $\hat{=}$ 28 CAD, which is not short for internal combustion (IC) engines. Hence, thermal gradients across the coating are likely to play a significant role. In the case of reducing the coating thickness from 60 μm to 20 μm, equations (4.9) and (4.10) yield $Bi = 0.06 < 0.1$ and $Fo = 1 \Leftrightarrow\ t = 433\,\mu\mathrm{s} \hat{=} 3\,\mathrm{CAD}$. This time, the temperature gradients across the coating are likely to remain below 5 % and the ratio of the energy conduction to the energy storage in the coating exceeds 1, already in the case of time scales that are characteristic of the present measurement environment.
Hence, it is advisable to limit the thickness of thermal sensor coatings to 20 μm or less in order to avoid measurement errors, caused by thermal gradients in engine experiments of similar nature.

4.4.2 Thermal Gradients across Phosphor Films in Engine Applications

In this section, the major results from Papers [II, III] are summarized, these being obtained from experiments that correspond closely to the numeric example discussed in the previous section.

Paper [II] reported for the first time the existence of significant temperature gradients across thin thermal sensor coatings. The experiments were performed in an optical car engine during motored and fired engine operation. Two La_2O_2S:Eu coatings with a surface area of approximately $20\,mm^2$ were applied to the inner side of a quartz cylinder liner for point measurements of temperatures using the phosphorescence decay time. The coating thickness was determined through microscopy, according to descriptions given in [III]. Both coatings yielded a film thickness $\geq 32\,\mu m$ and were affected by temperature gradients during motored- and fired engine operation. Figure 4.7 shows the experimental setup that was used, along with a magnified schematic view of the phosphor coating applied to the quartz liner and being exposed to the dynamic temperature gradient, present across the thermal boundary layer.

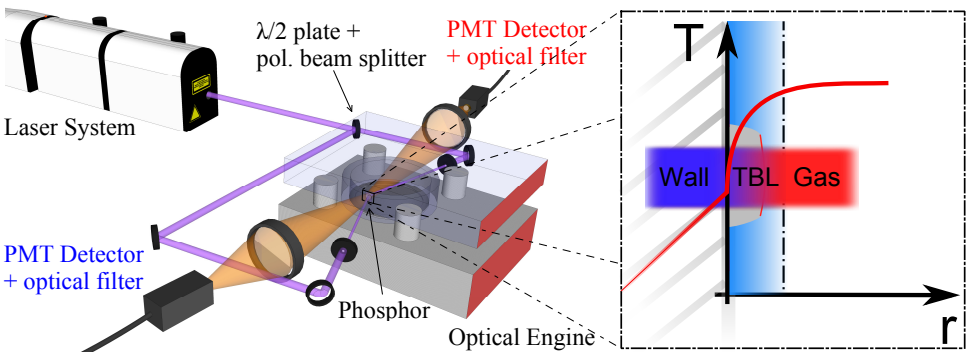

Figure 4.7: *Experimental setup for the determination of temperature gradients across thermal sensor coatings inside an optical engine.*

Choosing quartz as a coating substrate ensured both excitation and signal collection through the combustion chamber wall. In addition, the laser excitation beam was split in half by means of a $\lambda/2$ waveplate and a polarization beam splitter. This enabled the phosphor coating to be illuminated from two opposing directions, the gas side facing the inside of the combustion chamber and the wall side, which was in contact with the cylinder wall substrate. Irises were used to limit the area on the phosphor coating, to which the temperature-dependent phosphorescence was induced.
In a follow-up study, Paper [III], further coating thicknesses were investigated under test conditions similar to those described in [II]. In analogy to the predictions derived from the numeric example (see section 4.4.1, page 63), the experimental findings obtained did not indicate there to be significant gradients across the coatings $\leq 20\,\mu m$, this with an average measurement precision of 3 to 4 K. In addition, another phosphor ($CdWO_4$) was coated and was compared with La_2O_2S:Eu films of similar thickness.

Both phosphors showed consistent results, which led to the assumption that the thermal conductivity of spray coatings is dependent primarily on the binding agent. This result was expected due to the typically low phosphor-to-binder mass ratio of 1:20, that was used in [III].[8]
Figure 4.8 presents two examples of measurement results, obtained for La_2O_2S:Eu coatings (60 μm and 20 μm) under the influence of dynamic temperature fields close the surface of the combustion chamber in a homogeneous charge compression ignition (HCCI) engine. Temperature transients are shown here as a function of CAD after top dead centre (ATDC) and were evaluated on the basis of the overall phosphorescence signal that was recorded on either side of the thin film coating.[9]

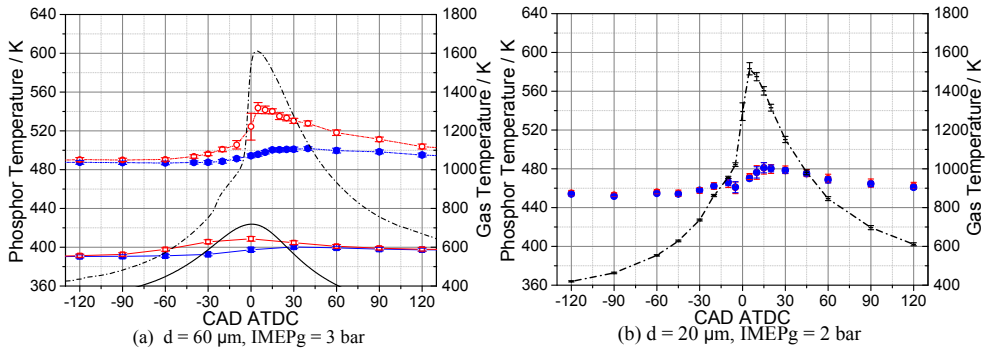

Figure 4.8: *Cycle-averaged wall temperatures obtained from La_2O_2S:Eu films, (●/■) = wall side, (○/□) = gas side, using two different coating thicknesses. Global gas temperatures are represented by lines, using separate y-axes on the right-hand side. All error bars indicate one standard deviation, based on 100 combustion cycles. Part* (a) *shows a comparison of temperature gradients obtained across a* 60 μm *thick phosphor film during motored* (□/■) *and fired* (○/●) *engine operation. Part* (b) *shows temperatures retrieved from a* 20 μm *thick coating during fired operation* (○/●).

According to experimental findings in [II, III], the maximum temperature difference measured across the thin thermal sensor films is dependent primarily on the engine load (compare motored vs. fired engine operation) and the film thickness (see ΔT across the coating for (a) and (b) in Fig. 4.8).
Another close look at Figure 4.8 (a) reveals a phase shift between the appearance of the maximum values for the front and back side of the coated film. This phase shift was anticipated, given the low Fo number of 0.035 that was previously found in case of a 60 μm coating and a time scale representing one crank-angle degree. In Figure 4.9, crank-angle (∼time) derivatives of temperature traces from both sides of the phosphor, as well as the bulk gas transient are displayed, based on measurements of a 60 μm thick La_2O_2S:Eu coating during HCCI combustion. This representation of data values was chosen in particular to indicate those crank-angle positions for which

[8] Since this ratio was obtained prior to the dry-heating process, the actual mass ratio of the sensor coating could be higher.
[9] TDC (top dead centre) refers to the situation, in which the piston reaches its uppermost position.

the temperature changes were the highest. Delays in the response, present between the individual temperature transients in Figure 4.8 (a) are highlighted by the chronological order of the individual maxima appearing in Figure 4.9.

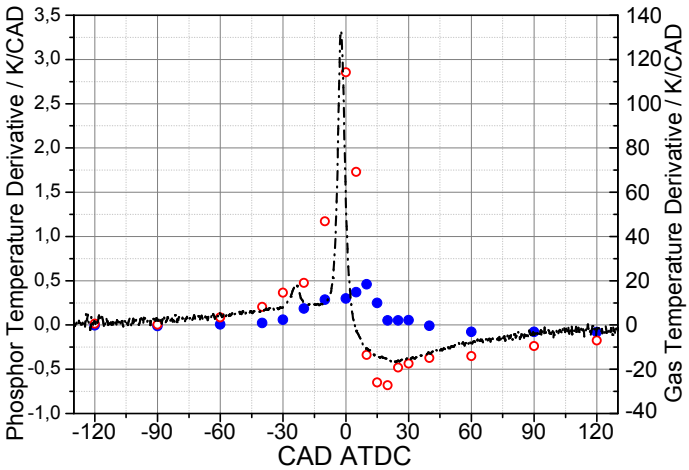

Figure 4.9: *Derivative of gas (···) and phosphor temperatures ((●) = wall side, (○) = gas side) from a 60 µm thick La_2O_2S:Eu film, displayed as a function of CAD during HCCI combustion* [III].

The time derivative of the gas temperature, shows two major peaks. The earlier and smaller one at -24 CAD corresponds to low temperature reactions. The latter one at -2 CAD characterizes the cycle position that coincides with the maximum temperature change per time interval. Slightly thereafter, the maximum gas temperature was reached at 2.4 CAD, as indicated by the dash-dotted line crossing the zero level. The top side of the coating experiences its fastest temperature change at around 0 CAD during the combustion cycle, followed by the bottom side having a peak at 10 CAD. This order of succession is characteristic for experimental time scales corresponding to low Fourier numbers, i.e. situations in which the rate of thermal energy storage exceeds the rate of heat conduction across the coating. In other words, the phosphor coating thermally insulates the substrate from high-amplitude and fast-paced gas temperature transients.

Very recently, Atakan and Roskosch published an interesting theoretical study of temperature gradients across thermographic phosphor coatings in a measurement regime, which is typical for combustion engines [133]. In their work, 1D heat transfer calculations were performed, based on the coating thicknesses and temperature gradients found in [II]. The experimental results from Paper [II] were largely confirmed by a model of transient conduction on a semi-infinite solid, experiencing surface convection. For cases of this particular type, a closed-form solution of the 1D-heat Equation (4.11) is derived in various textbooks, e.g. [128, 129].

Atakan and Roskosch suggested the use of Equation (4.11) in practical applications for estimating the approximate magnitude of temperature gradients, close to the surface [133].

$$\frac{T(x)-T_{\mathrm{w}}}{T_{\mathrm{g}}-T_{\mathrm{w}}} = \operatorname{erfc}\left(\frac{x}{2\sqrt{a\cdot t}}\right) - \exp\left(\frac{\alpha x}{\lambda}+\frac{\alpha^2 a\cdot t}{\lambda^2}\right)\cdot\operatorname{erfc}\left(\frac{x}{2\sqrt{a\cdot t}}+\frac{\alpha\sqrt{a\cdot t}}{\lambda}\right) \quad (4.11)$$

In Equation (4.11), x denotes an axis across the thickness of the coating, with $x = 0$ being at the surface of the coating. The parameter t describes the characteristic time, whereas T_{g} and T_{w} are mean temperatures of the gas phase and the wall. The parameter a corresponds to the thermal diffusivity, described by Equation (4.12).

$$a = \frac{\lambda}{\rho\cdot c_v} \quad (4.12)$$

The expression "erfc" in Equation (4.11), defined by Equation (4.13), denotes the complementary error function for which only numerical solutions exist.

$$\operatorname{erfc}(x) = 1-\operatorname{erf}(x) = 1-\frac{2}{\sqrt{\pi}}\int_0^x \exp(-u^2)\mathrm{d}u \quad (4.13)$$

In addition, the effect of different substrate materials was discussed in Ref. [133]. Interfaces made of quartz exhibit higher surface temperatures than steel substrates, due to their comparatively lower thermal conductivity. This decreases the temperature gradient in the thermal boundary layer and, as a consequence, across the phosphor coating. Figure 4.10 shows corresponding model results of thickness-dependent temperature gradients for a variety of coating/substrate combinations. This figure was originally presented in [133] and was replotted here with the permission from Prof. B. Atakan, *University of Duisburg-Essen, Germany*.

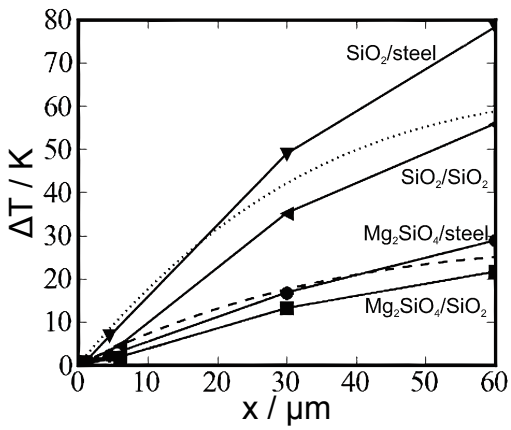

Figure 4.10: *Modelled effect of film and substrate materials on temperature gradients across phosphor films, shown as a function of coating thickness* [133]. *Two analytical solutions for semi-infinite bodies of quartz* (···) *and of steel* (---) *were calculated according to Equation* (4.11).

To conclude this section, the most important results from [II], [III] and [133] are summarized below. The extent of temperature gradients across sensor coatings in transient combustion depends on the ...

- **amplitude of temperature transients in the gas phase**, that are in direct contact with the coating surface. This is related directly to the discussion on the ratio of convection to conduction in the film coating, known as the Biot number [II, 133].
- **characteristic time scales of gas phase temperature transients**, that in combination with the coating material define the ratio of conducted heat to stored heat, known as the Fourier number [II, III, 133].
- **coating substrate material.** In analogy to wall surface temperatures, that depend largely on the material's thermal conductivity and heat capacity, gradients across thermal sensor coatings were also found to differ substantially, depending on the substrate material involved [133].
- **film thickness**. Film thickness remains the most important parameter that experimentalists can affect in a manner aimed at avoiding perturbations, caused by temperature gradients within thermal sensor coatings [II, III, 133].

Other parameters, such as the particular phosphor type and the involved differences in chemical and nano-crystalline composition, have not been shown to affect the gradient across thermal sensor coatings to a significant degree [III]. There is, however, yet another major effect to consider in the presence of temperature gradients along the thickness axis of a thermographic phosphor coating: It can be of interest to ask from what coating depth a phosphorescence signal that is detected originates. Accordingly, two different modelling approaches pertaining to this are outlined in the section that follows.

4.4.3 Light Propagation and Generation of Phosphorescence across the Thickness of a Thermal Sensor Coating

In measurement environments that induce thermal gradients across the thickness of thermographic phosphor coatings, the absorption coefficient of the film is also of importance. A high absorption coefficient results in temperatures measured close to the coating surface, whereas lower values result in a more thickness-averaged signal response [133]. In general, the overall phosphorescence signal $J'_{\mathrm{total}}(t)$, collected from a thermal sensor coating, consists of contributions integrated over all coating depths. Through dividing the coating into n adjacent and equally thick layers parallel to the substrate surface, the overall phosphorescence signal can be described as expressed in Equation (4.14).

$$J'_{\mathrm{total}}(t) = \sum_{\mathrm{i}=1}^{\mathrm{n}} J'_{0\mathrm{i}} \cdot \exp\left(-\frac{t}{\tau_{\mathrm{i}}}\right) \tag{4.14}$$

Hereby, each layer i from a depth $x(\mathrm{i})$ contributes with a temperature-dependent decay time τ_{i} and a scaling factor $J'_{0\mathrm{i}}$. The reconstruction of $J'_{\mathrm{total}}(t)$ from contributions of different coating depths is illustrated in Figure 4.11, taken from Ref. [134].

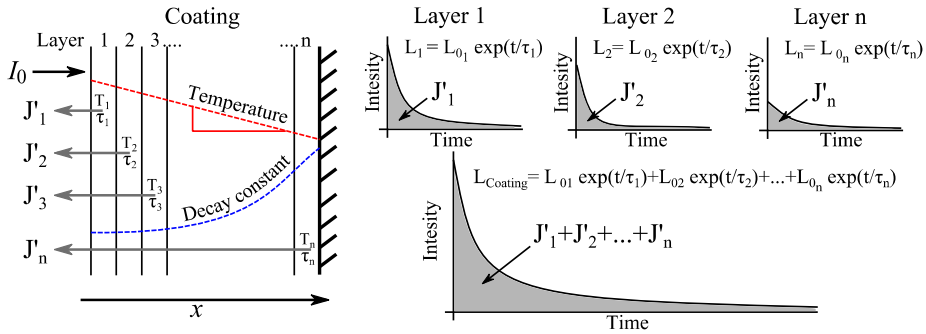

Figure 4.11: *Schematic diagram of the reconstruction of the overall phosphorescence signal from the decays of discrete phosphorescence layers throughout a film coating. The figure is taken from Ref. [134] and presented with permission of Dr. A. Heyes, Imperial College London, England.*

For decay time evaluations using Equation (4.14), it is sufficient to characterize the relative distribution of scaling factors J_i' along with the temperature-induced thickness dependence of τ_i. Atakan et al. modelled a thickness-integrated phosphorescence signal under the influence of a thermal gradient, considering absorption k as the main contributor [133]. Under this assumption, it can be shown that the scaling factors decrease exponentially along the x-axis, as described in Equation (4.15).

$$J'_{0i} \sim \exp[-k \cdot x(i)] \tag{4.15}$$

Unfortunately, absorption coefficients for porous ceramics are difficult to make out in the literature, especially if varying amounts of binder materials are added to the coating precursors. In Ref. [133], the investigators used the experimental data provided in paper [II] to determine k-values in the order of 10^{-6} to $10^{-7}\,\mathrm{m}^{-1}$.
Another, more elaborate approach to determining scaling factors for Equation (4.14) was presented recently by Pilgrim et al. [134]. In their study, the investigators describe light transport through TBC coatings using a model for scattering and absorption in coloured paint films, developed by Kulbelka and Munk in the early 1930s [135]. In contrast to the previously described absorption model, phosphorescence can increase up to a certain distance into the film due to its being augmented by the scattered emission from the surrounding coating.

4.5 Temperature Calibration

The highest level of possible temperature accuracy, that can be achieved in a phosphor thermometry experiment, is limited by the accuracy of the temperature reference measurement, obtained during calibration. A temperature calibration setup similar to that in Figure 4.1 is needed, one in which a phosphor-coated calibration target is exposed to a range of well-controlled and measured reference temperatures while temperature-dependent phosphorescence characteristics are being measured. In this section, various factors that are related to the optimization of measurement accuracy and to the avoidance of systematic errors during temperature calibration, are discussed.

4.5.1 Contact Test for Thermocouples during Temperature Calibration

Usually, the temperature during the phosphor calibration process is detected by use of thermocouples. In order to measure calibration temperatures correctly, it is necessary to maintain physical contact between the phosphor-coated object and the thermocouple. Figure 4.12 illustrates the error potential, that can arise when the thermocouple loses contact with the calibration object during temperature calibration.

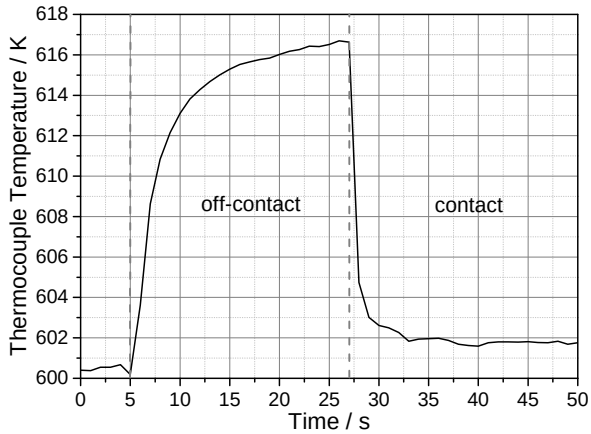

Figure 4.12: *The temperature reading, registered by a S-type thermocouple in a tube furnace heated to around 600 K. The thermocouple briefly looses contact with the phosphor-coated object (distance* $\approx 1\,mm$*) and gets in contact with it again.*

A phosphor calibration sample was placed into a tube furnace and was heated to approximately 600 K, the oven temperature being kept constant then for several minutes. An S-type thermocouple was pressed initially against the calibration object at the centre of the oven to measure its surface temperature. During the experiment, the thermocouple was pulled 1 mm away from the object briefly and was pushed against it again to re-establish physical and thermal contact. Although the oven was kept at around 600 K for several minutes prior to the experiment, one can observe in Figure 4.12 that the readout temperature increased markedly by 16 K during the time while a direct connection between the thermocouple and the object was lost.
In a general scenario, a temperature differences between the surface of an object and its surrounding atmosphere can occur for several possible reasons, including the following:

- Thermal equilibrium between the object and its surroundings may not yet be established, longer time scales being required.
- Local heat sources and sinks can create permanent temperature gradients. Decisive actions aimed at improving thermal insulation may thus be exercised to limit these effects: In a tube furnace, for example, open tube exits may need to be sealed by use of quartz windows, for example (for optical access) and by insulation wadding, as depicted in Figure 4.1. This also limits the heat transfer by convective air flow to the surroundings.

- Thermal radiation: Objects at elevated temperatures lose heat increasingly through thermal radiation. The effect scales by T^4 (see Eq. (2.3), page 9) and is the major source of error in thermocouple readings at elevated temperatures. Depending upon the vicinity to other hot bodies nearby, the effective heat transfer that occurs through radiation may either increase or decrease the surface temperature of any particular object.

The abovementioned effects, together with the example shown in Figure 4.12, suggest that thermocouples should always be kept in direct contact with the phosphor-coated object during temperature calibration in order to limit systematic errors in the temperature reading.

4.5.2 Thermocouple Reliability as a Referencing Device

In section 2.1, different thermocouple types are listed, together with their responsive temperature range and their expected tolerance limit. Already the choice of a certain thermocouple type affects the overall temperature accuracy, to be expected in an LIP experiment, since the minimum tolerance limits (tolerance class 1) vary from 0.5 K to 1.5 K, depending upon the thermocouple type involved (see Table 2.1, page 6). Those limits increase towards the high temperature regime. The tolerance of a thermocouple is not a systematic error exactly, but rather is the maximum expected systematic discrepancy between the real temperature and the measured temperature. Individual thermocouples within a given tolerance class thus experience different systematic reading discrepancies within the boundaries of their specified tolerances.
Since many thermocouples suffer from ageing effects, their original temperature tolerance may no longer apply after their long-term use and their exposure to elevated temperatures. Also, additional errors of individual thermocouples may occur, such as those introduced by improper wire connections. My own experience points to these errors not always being of obvious significance, especially if thermocouples are the only means of thermal feedback from the measurement device. It thus seems prudent to not rely on only a single thermocouple during the temperature calibration of a thermographic phosphor:

1. If only one thermocouple is used during calibration, the operator has no choice but to rely on the temperature given by the device. Unless the readings are completely off, there may be no evidence of the systematic errors involved being kept reasonably low.

2. If two thermocouples are being used at the same spot simultaneously, the operator can very likely trust the readings as long as both thermocouples show similar temperature values. However, if there is a significant difference between the temperatures that the two thermocouples provide, there is no indication of which of the two temperatures can be trusted.

3. As soon as three thermocouples are employed at the same measurement spot, one malfunctioning thermocouple within the ensemble can be identified as showing a temperature offset relative to the other two. This adds a certain degree of reliability to the temperature reading.

However, one particular accuracy issue remains, one which cannot be solved through use of several reference thermocouples. If all the thermocouples have a similar thermal history, it is quite possible that they are all affected in the same way by ageing effects. It is thus advisable to verify their flawless operation by testing them under physically defined fixed temperatures, such as an ice bath (273 K) or in boiling liquids, such as water (373 K), propylene glycol (461 K) or glycerol (563 K). Figure 4.13 shows measurement results from three thermocouples that all were submerged in boiling water at 373 K.

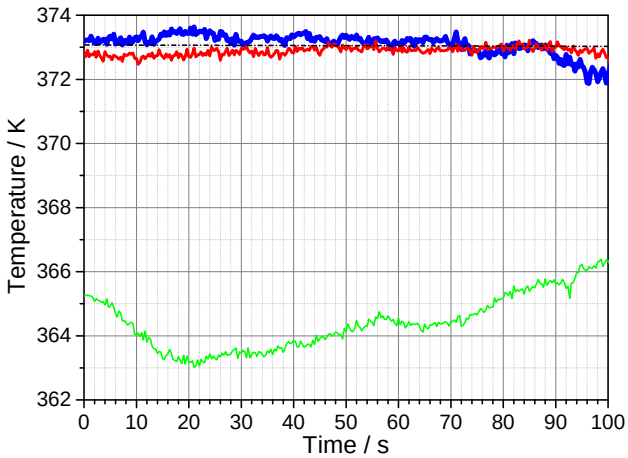

Figure 4.13: *Temperature measurements from three type S thermocouples, that were submerged in boiling water (T=373 K).*

Whereas two of the three thermocouples, when placed in boiling water, indicated approximately the correct boiling temperature, the third thermocouple showed relatively large variations in temperature, being systematically 7 to 10 K too low. Thus, Figure 4.13 is a good example in indicating the usefulness of thermocouple verification at known fixed-point temperatures. If it is supposed that this measurement was performed instead in a liquid with an unknown boiling point, one should note that only one thermocouple of the three showed temperatures that deviated appreciably from the others, this making the virtually common temperature of the other two thermocouples more reliable.

4.5.3 Calibration Substrate Design

Figure 4.14 shows a schematic of the basic design of in-house developed temperature calibration substrates. The substrate disc consists of Hastelloy-C, a nickel-based and heat-resistant alloy. Its melting point is specified as being above 1540 K [136], which is sufficient for most thermographic phosphors. In addition, Hastelloy-C exhibits a relatively low volumetric expansion coefficient ($\gamma = 11 \cdot 10^{-6} \mathrm{K}^{-1}$) [136], which reduces the risk of cracks in the phosphor coating due to the effect of thermal expansion of the substrate.

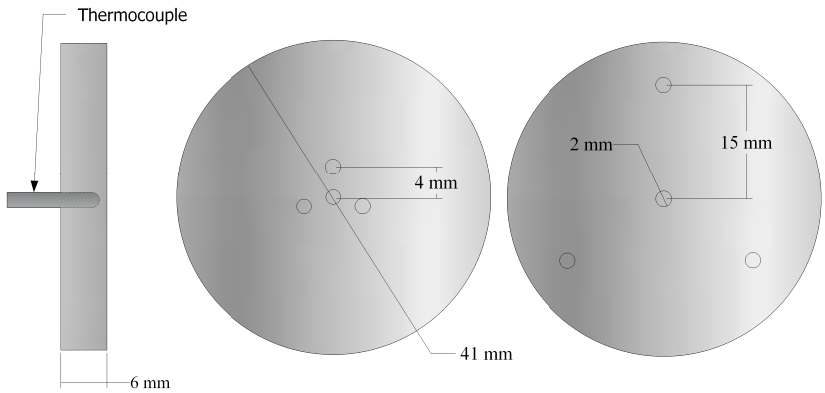

Figure 4.14: *Hastelloy-C calibration substrate disc designs for use in a tube furnace. Four K-type thermocouples establish thermal contact with the coated surface at the back end of the disc. The second design with the thermocouples spread out along the surface is intended for the calibration of temperature imaging techniques.*

Due to considerations of accuracy, discussed earlier in sections 4.5.1 and 4.5.2, four thermocouples were used for recording the surface temperature during phosphor calibration. As shown in Figure 4.14, they are so arranged that they are in close contact with the coated surface through their access to the back side of the disc. Two different designs were manufactured, one with the thermocouples arranged in a cluster at the centre of the disc and one with the thermocouples spread out more across the surface. Whereas the former design was intended for accurate point measurement calibrations, the latter design aimed at probing temperature gradients across the surface that would need to be considered during calibration measurements of surface-temperature imaging techniques. In the case of a (non-centre-symmetric) temperature gradient being measured across the surface, rotating the calibration disc around its axis of symmetry can indicate whether the gradient is real or is caused by a single malfunctioning thermocouple. The solid metal protection sheaths for the thermocouple wire outlets are used to keep the disc hanging freely in the furnace without its touching the inner walls of the tube. This precaution helps avoiding locally increased heat transfer, caused by conduction from the furnace walls to the calibration disc, which otherwise could increase the magnitude of thermal gradients occurring across the coated surface.

4.5.4 Automated Signal Recording during Temperature Calibration

Despite the importance of calibration measurements for the overall temperature accuracy in thermographic phosphor experiments, past research has not focused much on the development and improvement of experimental calibration designs in phosphor thermometry. In this section, an automated temperature calibration approach is described and is compared with a conventional calibration process. The content of this section is based on experimental findings, published in Paper [I].

(a) Conventional Discrete Temperature Calibration: A typical temperature calibration chart is usually composed of discrete and fixed temperature points.[10] At each of these points, the thermographic characteristic of the phosphor, such as the decay time or the spectral intensity ratio, was measured during calibration. If thermal equilibrium has been established prior to each measurement, averaging of the different phosphorescence characteristics can be performed to reduce statistical data noise. Most temperatures that are measured during an experiment, however, are likely to fall between these calibrated fixed points, where no direct comparisons with a calibration measurement can be made. In order to obtain a continuous translation of all possibly occurring phosphorescence characteristics into the temperature scale, a calibration chart is usually fitted or interpolated using non-linear algorithms. The probability of accurately matching the thermal phosphorescence behaviour with such interpolations or fits increases with the number of data points involved, as temperature gaps are successively closed. This accuracy benefit comes at the cost of longer experiment times, which can be particularly problematic when using calibration devices, that reach thermal equilibrium rather slowly. Achieving thermal equilibrium in a tube furnace, for example, is a rather tedious process, one that requires much attention by the operator in order to decide effectively when the oven has stabilized sufficiently.

Example: Figure 4.15 shows a fixed-point calibration of $Mg_3F_2GeO_4$:Mn phosphorescence decay times at 657 nm within a temperature interval of 290 K to 1100 K. The temperature chart consists of 17 measurement points (□) in Figure 4.15, which had an average temperature spacing of 50 K in between. Each of these fixed points consists of 100 measurements, which were first evaluated individually and then averaged. Since thermal equilibrium needed to be achieved before averaging signal decays at each temperature setpoint, the entire calibration took a total experiment time of 32 h (including a 12 h break during the night), as seen in Figure 4.16.

(b) Automated Continuous Temperature Calibration: As an alternative to the conventional calibration approach, an automated calibration method was developed during research related to the thesis [I]. Unlike the former approach, the automated calibration process does not rely on the establishment of thermal equilibrium for fixed temperature calibration points. Instead, the calibration furnace temperature is ramped up at a constant rate, while at the same time measurements of temperature and phosphorescence characteristics are undertaken continuously. The accumulation of thermocouple temperatures and phosphorescence signal waveforms was synchronized using LabVIEW. An embedded MATLAB script pre-processed every signal waveform on-the-fly to reduce file sizes before saving. With the tube furnace being specified for safe temperature ramping up to 4 K per minute and a maximum acquisition speed of one measurement per second, an average temperature separation of less than 100 mK can be achieved. At this rate, covering a calibration interval of 100 K is possible within a time interval of only 25 min. In addition, the automated calibration setup can be left on its own, once acquisition has started and the oven has been configured so as to ramp up at a suitable temperature rise rate.

[10] The plot for La_2O_2S:Eu in Figure 3.11 (page 30) is an example of a calibration of this kind.

Example: Figure 4.15 also shows an automated calibration of $Mg_3F_2GeO_4$:Mn phosphorescence decay times at 657 nm (·) within a temperature interval of 290 K to 1100 K. The oven was set at a moderate ramping speed of 1.6 K/min with an acquisition rate of 11 measurements per minute. This resulted in a total measurement time of a little more than 8 h (see Figure 4.16), 5500 decay curves being saved.

(c) Comparison of Calibration Approaches: Figure 4.15 shows the result of both the individually achieved temperature calibrations of $Mg_3F_2GeO_4$:Mn from the previous examples, presented in one chart.

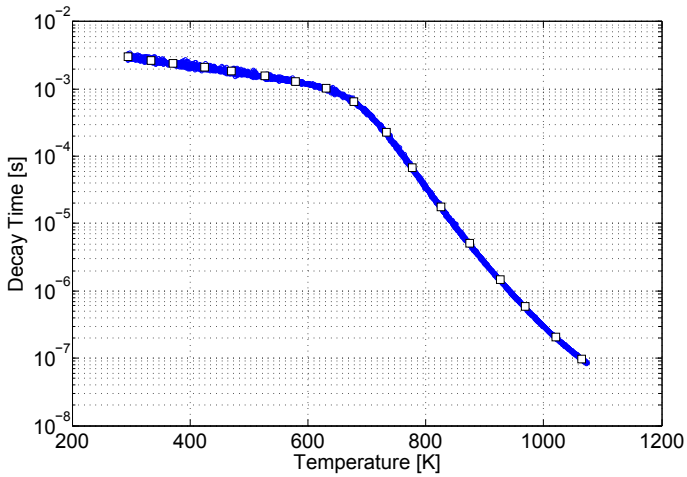

Figure 4.15: *Conventional (□) and automatic (·) temperature calibration plot, obtained from $Mg_3F_2GeO_4$:Mn in a temperature interval of 300 to 1100 K.*

According to Figure 4.15, the individual single-shot results from the automatic calibration procedure seem to agree fairly well with the averaged fixed points of the conventional approach. In a way, this verifies the necessary assumption that thermal equilibrium with the environment does not need to be maintained during temperature calibration, as long as the thermocouples are in direct contact with the coating substrate.
One obvious advantage of the automated continuous calibration measurement is the reduction in the duration of the experiment through eliminating the need for establishing thermal equilibrium. In the particular example presented here, the experiment time was reduced by a factor of 4 from 32 h to 8 h, as can be seen in Figure 4.16. In fact, the automated temperature calibration could have been performed in 4 h only, if the maximum heating rate of the oven had been exploited. For careful readers, an interesting detail can be revealed for the conventional calibration, when observing Figure 4.16 closely. The measurement speed of the discrete calibration increases slightly after the long measurement break during the night. This is a consequence of the energy losses to the surroundings, which play a larger role at elevated temperatures, allowing the oven to reach thermal equilibrium faster with every increase in temperature.

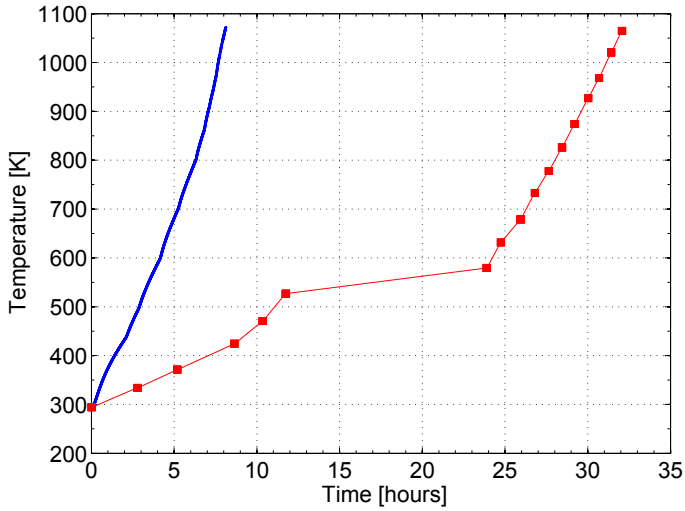

Figure 4.16: *Measurement of the time needed for achieving a temperature calibration of $Mg_3F_2GeO_4$:Mn within a temperature interval of 290 K to 1100 K using the conventional approach (−■−) and the proposed automatic routine (·).*

In Figure 4.15, it appeared that the reduced experiment duration and the continuous temperature information in the automated calibration approach were bought dearly through there being an excessive amount of measurement data to be stored. In fact, the entire continuous calibration consists of roughly 5500 single data points. However, it seems almost unexpected that the amount of detail, presented by the automated calibration graph in Figure 4.15, only requires three times as much disk space as the conventional discrete calibration does. One should keep in mind, that each fixed point from the discrete calibration also comprises 100 single measurements each, making it necessary to store a total of 1700 decay curves. In the automated approach, it is up to the operator to decide how many curves to save by individually setting the ramping speed of the oven and deciding on a desired acquisition rate. Instead of 17 fixed points (100 times averaged) with a temperature separation of 50 K each, for example, the same amount of data involved would allow the performance of a continuous calibration, consisting of 1700 temperature points with an average separation of only 0.5 K. Another concern that can be raised is whether the thermocouples are capable of following the temperature ramp fast enough without a time delayed response, relative to the phosphor readings, being introduced. Thus, the oven was ramped up and down quickly at different temperatures and with different heating and cooling rates. Whereas thermocouple temperatures were logged directly, the corresponding phosphorescence decay times needed to be converted to the temperature scale by use of a temperature calibration chart. Figure 4.17 displays several heating and cooling rates of thermocouples and the corresponding phosphor responses, plotted against each other. Heating and cooling rates from the thermocouples and phosphorescence decay times largely agree with each other within within the varied interval of $\approx \pm 10$ K/min; as seen in Figure 4.17.

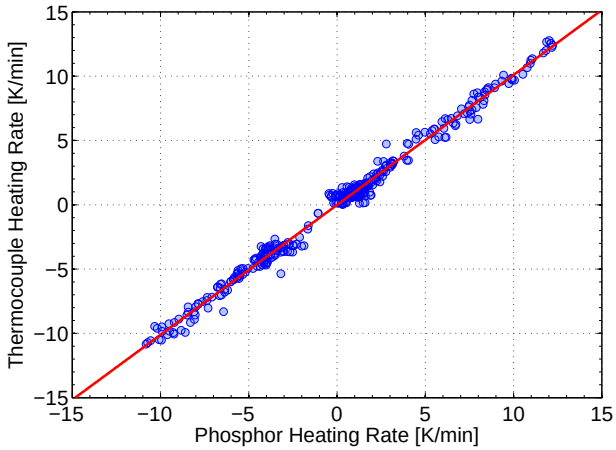

Figure 4.17: *Heating and cooling rates of thermocouples plotted against the corresponding phosphor temperatures. A linear fit of the data displayed is given by the straight line.*

This conclusion is based on the linear fit of the heating rates, which closely resembles a straight line with a slope of one and an offset constant of zero. Hence, it can be assumed that the thermocouples attached to the calibration substrate (see Fig. 4.14, page 73) are able to follow the maximum oven ramping speed of $\pm 4\,\mathrm{K/min}$ without systematic errors being introducing by a delayed temperature response.
Finally, the measurement accuracy of the two calibration approaches relatively to each other is compared in Figure 4.18. To study the accuracy of the calibration procedure developed, both calibration datasets were fitted by use of smoothing spline polynomials, that relate the temperature to the natural logarithm of the decay time. This is according to the usual procedure, so that the arbitrary decay times can be translated into temperatures later on. The fits for the calibrations achieved a satisfactory symmetrical distribution of the residuals, based on and judged by their individual datasets. To compare the two polynomials obtained in terms of accuracy, a dense array of generated decay times of between 3.3 ms and 60 ns was created and was inserted into both polynomials. The previous step assured that two similar, but not identical, temperature vectors were created, allowing insight into the difference between the two calibration approaches. How similar the two calibration polynomials appear in a calibration chart can be seen in Figure 4.18, in which they lie on top of each other, as indicated by the solid-line graph. Since no obvious deviations between the two fitting polynomials can be revealed in this way, the difference between the two virtually created temperature vectors is also shown by the dashed graph in Figure 4.18, indicating temperature deviations of $\leq \pm 1\,\mathrm{K}$. The effective temperature difference between the two calibration polynomials appears to oscillate around the zero line, which is an indication of the agreement of the two polynomials at certain temperatures. These temperatures closely correspond to the fixed points, that were measured in both calibration datasets.

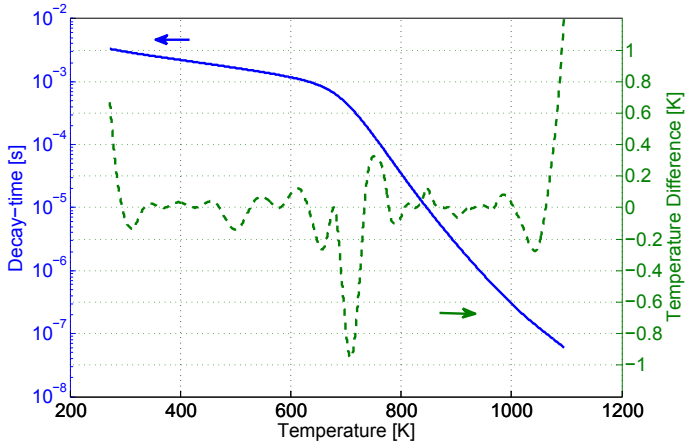

Figure 4.18: *Comparison of the fitting polynomials for conventional and for automatic temperature calibrations of $Mg_3F_2GeO_4$:Mn. The comparison is performed by showing the relative temperature difference between the two polynomials as a function of the calibration temperature (···). The solid line indicates the temperature calibration fits of the two approaches (—).*

The disagreement between the two polynomials appears to be largest at the edges of the calibrated temperature intervals, where the fits exhibit a loose end without being predetermined by data point constraints. The automated calibration dataset outreaches the conventional fixed-point calibration in both directions on the temperature scale. It is thus likely that the difference there is mainly caused by the polynomial of the fixed-point calibration, not following the phosphorescence behaviour well enough due to a lack of measured data. Although this observation underlines the fact that the calibration polynomials should not be extrapolated, one dataset outreaching another is an arbitrary criterion, that should not be used alone to judge the quality of the one approach over the other. Another significant disagreement of the two calibration polynomials can be found in the region of 700 to 800 K, coinciding with the quenching point of the calibration curve, i.e. the temperature region in which the thermal sensitivity of the phosphor changes. For this particular area, where the slope of the calibration curve changes, it can be assumed that the difference between the two calibration polynomials is most probably caused by an inaccuracy of the fixed-point approach, failing to find the exact quenching point location due to a lack of available data.

Summarizing this section, it can be concluded that the dashed line in Figure 4.18 largely corresponds to the errors in accuracy that are introduced by the fixed-point calibration. In order to achieve the best possible temperature accuracy for fitting polynomials during temperature calibration, a quasi-continuous calibration approach should be followed. Fixed-point calibrations suffer from relatively low temperature errors (a few hundred mK in Fig. 4.18), present within the interpolated temperature gaps. However, close to the quenching point, these accuracy errors can become significant in magnitude.

4.6 Signal Detection

In this section, different standard detectors for the signal collection of thermographic phosphorescence are described. In addition, a discussion of measurement errors caused by detector saturation and non-linear signal transformations is given, based on the Papers [IV, V, VI].

4.6.1 Imaging Detectors

In digital imaging applications, operators usually choose between the use of either charge-coupled devices (CCDs) or complementary metal-oxide-semiconductor (CMOS) sensors.

(a) CCD Cameras: CCD technology is important for digital imaging applications and can be found in digital cameras, optical scanners and video cameras as light sensing devices. A standard CCD chip consists of various pixels, arranged in a matrix. The electrons in each pixel detector are excited to higher electronic states while the pixel is exposed to light impingement. During light exposure, these excited electrons create a charge, that is stored and is read out from each pixel in the matrix. The CCD charge readout occurs via a shift register, that causes each pixel to transfer its content to its neighbour. The last pixel in the array transfers its charge to an amplifier that converts the charge into a voltage. By repeating this shift process, the entire content of an array is read out as a sequence of voltages, which then are sampled and digitized in the analog-to-digital converter (A/D converter). Conventional CCD cameras for scientific applications suffer from limited frame rates, caused by the sequential image readout process. However, current generation models have overcome this major drawback such that some CCD cameras are now capable of 1 MHz sustained repetition rate [137–139].

Advantages: The principal advantages of CCDs are their sensitivity, dynamic range and linearity. It is common for CCDs to achieve a quantum efficiency of about 70 to 80 %. Requiring just one A/D converter for the entire camera chip results in the response of the different pixels under identical illumination conditions being very uniform. These properties combined make CCD cameras a popular choice for two-colour-ratio imaging in phosphor thermometry [17, 20, 23, 68]. CCDs are also sensitive to a broad range of wavelengths and are much more sensitive to IR radiation than, for example, the PMTs used in photoelectric photometers are.

Disadvantages: When a CCD image is exposed to high intensities or to long exposures, charges from the brightest pixels can overflow and populate neighbouring pixels. This effect is known as blooming and requires specific engineering in order to be suppressed. In addition, CCD chips are not particularly sensitive in the UV region of the light spectrum. Enhanced UV sensitivity, however, can be achieved by image-intensifiers making use of intensified charge-coupled devices (ICCDs).

ICCD Cameras: Image intensifiers were developed initially by the military for night vision applications, but their development is being driven increasingly by scientific applications [140]. Most of the common intensifiers consist of three functional units: a photocathode, a microchannel plate (MCP) and a phosphor screen; see Figure 4.19.

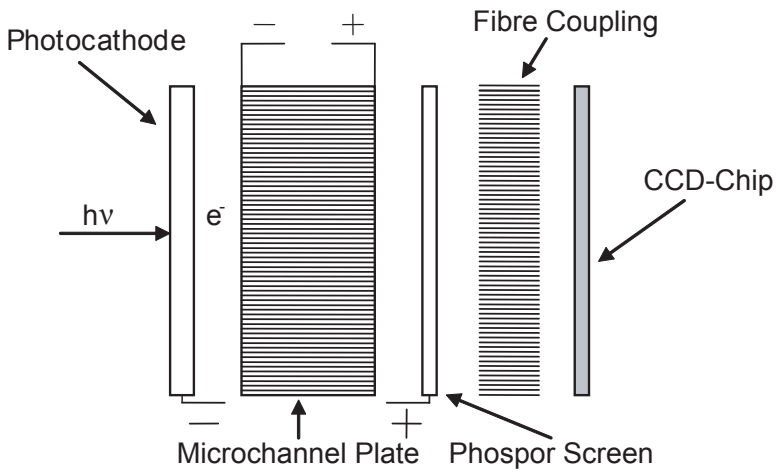

Figure 4.19: *A schematic of an ICCD camera with a fibre-coupled CCD chip.*

The photocathode converts the incident photons into photoelectrons, which are accelerated by an electrical field towards the MCP. This component part in turn multiplies these electrons, which are converted back into photons by the phosphor screen. Finally, these photons are directed at a CCD chip by either an optical fibre bundle or a lens system, and are read out as a digital image.

Advantages: The addition of an image intensifier is accompanied by certain benefits [IV]: Primarily, the MCP serves to intensify the signal by several orders of magnitude, enabling weak signal detection to take place. Signal amplifications in excess of 10 000 are not uncommon [140]. By pulsing the control voltage of the MCP with sub-nanosecond rise and fall times [140], the image intensifier can serve as a very fast electronic shutter, enabling time gating for short-lived signals to take place, which otherwise would have been drowned in the interfering background. Finally, the photocathode can be made sensitive to UV radiation, which most CCD detectors fail to detect. The phosphor screen converts all incoming electrons into photon radiation in the visible range, where the CCD exhibits high sensitivity. Hence, the spectral response of a ICCD camera is determined by the photocathode material used in the image intensifier. These features make ICCD cameras useful in pulsed-laser applications, where short laser pulses in the order of few nanoseconds are used for the visualization of various substances, either by detecting the scattered laser light itself, e.g. Rayleigh scattering (RS), or through a signal emitted being from a substance, induced by the laser light, e.g. LIF, LIP or laser-induced incandescence.

Disadvantages: Intensifiers increase the overall light sensitivity at the cost of further reducing the image quality and spatial resolution. In addition, ICCD cameras suffer from spatially non-uniform image gain factors and non-linear response functions [141]. The non-linearity is mainly due to the onset of saturation within the MCP, when the camera is subjected to high light intensities in combination with excessive gain settings. This falloff in response, or gain saturation, has to do with the MCP recovery process and is caused by the MCP's inability to produce enough secondary electrons from the original photoelectron [142, 143]. At high repetition rates, the intensifiers are susceptible to charge depletion, which can further undermine the quantification efforts [144]. In addition, bleaching of the photocathode, especially when collecting intense long-lived radiation, can contribute to saturation. The phosphor screen can also be subject to saturation, causing a non-linear output due to a response falloff at higher intensities. Although saturation effects within the intensifier are usually not a major issue when qualitative measurements are carried out, quantitative measurements, in particular with use of the two-colour ratio technique, are easily affected by small non-linear effects [IV].

(b) CMOS Cameras: CMOS is a technology for constructing integrated circuits, one which is commonly used in microprocessors, microcontrollers, and image sensors. In contrast to CCD cameras, CMOS sensors consist of an integrated circuit containing an array of pixel sensors, each pixel operating independently in active buffering and amplification. The overall light sensitivity of a CMOS chip tends to be lower than that of typical CCD chips. This is because each pixel on a CMOS sensor has several transistors located next to it, such that many of the impinging photons hit the transistors instead of the photodiode. One way to resolve this issue, is to place a micro-lens array in front of the camera chip. Traditionally, a CMOS camera without an intensifier was the best choice in high-speed imaging applications, as long as the signal strengths were reasonably high [145]. CMOS cameras for scientific applications often possess frame rates in the order of several hundred kHz [146, 147]. In phosphor thermometry, CMOS cameras thus gained attention in lifetime-imaging applications [21, 116, 146, 147].

Advantages: CMOS chips can be produced in standard silicon production lines, which keeps production costs low compared to more elaborately structured CCD sensors. Each pixel from a CMOS chip can be read-out individually, without charge-shifts being necessary, which creates greater flexibility and higher frame rates for CMOS sensors, as compared with their traditional CCD competitors. CMOS image sensors exhibit lower power consumption and offer the possibility of smaller system size as compared with CCD cameras. Unlike CCD sensors, the neighbouring pixels are not connected with each other, which makes CMOS sensors immune to blooming effects.

Disadvantages: Whereas CCD sensors traditionally create high-quality and low-noise images, CMOS sensors exhibit a slightly lower dynamic range and are commonly known to be more susceptible to noise. This is caused mainly by each pixel having its own A/D converter, so that there is a higher readout noise. Although today's CMOS cameras have improved tremendously in image quality, the image quality of

state-of-the-art CCD cameras is better yet [145]. The present CMOS chips suffer from non-linearity [145] and from high pixel-to-pixel inhomogeneity, i.e. there is a different, non-linear response for each pixel [144]. For their use in scientific applications, it is necessary to fully describe the behaviour and response of the pixels. Non-linear correction is thus essential for quantitative work being carried out through use of CMOS detectors [144].

4.6.2 Setup Configurations of Imaging Detectors

Whereas lifetime-imaging methods with fast framing cameras are straightforward to use, the two-colour ratio method for temperature imaging relies on the division of two simultaneously acquired images. There are different possible setup configurations, which permit the recording of such pairs of images, as presented in Figure 4.20. In the following, their advantages and disadvantages will be discussed.

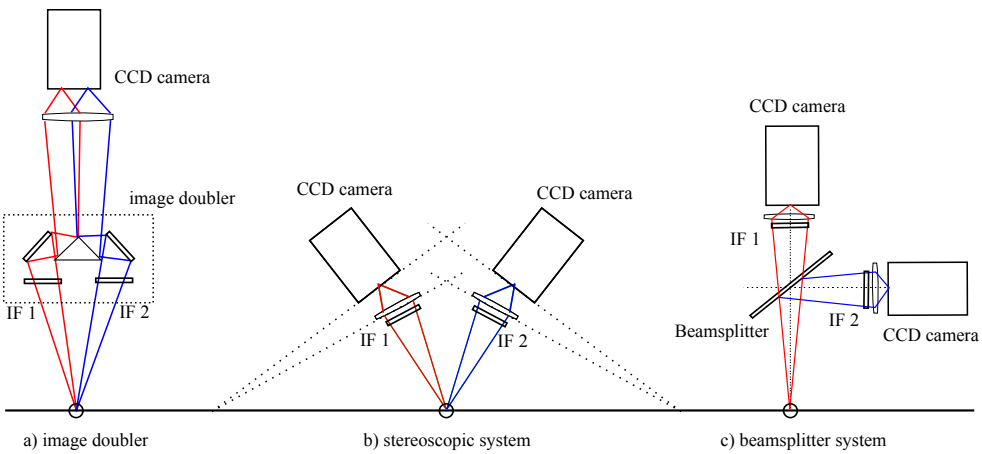

Figure 4.20: *Various detection schemes for two-colour imaging, taken from* [148] *and replotted with permission of Benoit Fond, Imperial College, UK.*

(a) Image Doubler System: A stereoscope or image doubler, as shown in Figure 4.20 (a), can be used in conjunction with a single camera. It consists of two mirrors and a prism, that can be fitted to a camera objective. Interference filters, for selecting suitable parts from the phosphorescence spectrum, are mounted directly on the stereoscope. Stereoscopes have been successfully employed in a number of LIP applications, e.g. [17, 149, 150].

Advantages: Stereoscopes can be used to reduce the number of necessary cameras needed, which decreases the degree of complexity in the setup and may be of advantage in cramped environments, in which the space for instrumentation is limited. In addition, a stereoscope is much cheaper than a camera, which helps in maintaining a cost-effective measurement setup.

Disadvantages: The recording of two images on one camera chip results in a loss by at least one half in the image resolution. In addition, a stereoscope decreases the amount of light impinging on the camera chip through its limiting the acceptance angle and the effective area of the camera lens. The two images also enter the camera at slightly different angles, causing perspective distortion and off-axis defocusing within the field of view [148]. Together with the use of one imaging lens for two different filters, theses effects could make it difficult to achieve a sharp focus for the two images simultaneously [IV]. Image distortions require transformation processes in order for a perfect overlap to be achieved (see section 4.7.2, page 110). These transformations, however, further degrade the image resolution. Stereoscopes are also known to introduce mechanical vignetting of collected light, which reduces the signal level locally and introduces intensity gradients within the field of view. Since the two optical paths differ in terms of these gradients, this introduces systematic errors, if they are left uncorrected. Another more critical problem arising from the use of stereoscopes is that of cross-talk. This is due to either internal reflections in the stereoscope, or scattered light originating from objects adjacent to the field of view. Such light is transmitted through each of the apertures onto the opposite side of the chip, which means that a source of light present outside the field of view can interfere with the measurement [148].

(b) Stereoscopic System: Another approach is to use two cameras, equipped with different optical filters, that view the object at an angle; see Figure 4.20.

Advantages: In contrast to method (a), this setup preserves full image resolution on the camera chip. Most of the problems with use of stereoscopes, such as vignetting and cross-talk, are eliminated. Similar to (a), the detection paths from the measurement object to each of the cameras do not require additional optics, which could limit the signal intensity.

Disadvantages: The use of two cameras adds additional costs and complexity to the experimental setup in comparison with the single-camera setup, shown in Figure 4.20 (a). Images are taken from a different angle, resulting in variations in magnification across the field of view. Differences in perspective of the recorded images may be substantially more pronounced than in a stereoscopic single-camera alignment, this depending upon the distance between the two cameras. To correct for this variation and also for rotation, translation or other distortions, an image registration routine (see section 4.7.2, page 110) needs to be used to map the pixels from the image to the object planes, providing a proper superposition of the two images. Finally, the detection paths of the two cameras differ. Hence, any difference arising from inhomogeneities in the optical path, such as dust or oil on windows, leads to a reduction in intensity in one of the images and thus to incorrect temperature readings.

(c) Beamsplitter System: Figure 4.20 (c) shows a two-camera setup in which the two cameras share a common optical path through employment of a beam splitter.

Advantages: Similar to alignment (b), images can be recorded with use of the full camera resolution for obtaining surface temperature maps with a high degree of de-

tail. Most problems arising from there being different beam paths are minimized in this arrangement. With careful alignment in this configuration, the collection paths of the two cameras are identical, meaning that further post-process of image registration may not be needed here.

Disadvantages: The requirement of having two cameras and a beam splitter makes this setup slightly more expensive than the two-camera setup (b). In addition, the beam splitter reduces the light intensity available by one half for each camera, which can be problematic under conditions of low signal level.

Significant intensity losses, introduced by use of the beam splitter can be largely circumvented if instead a dichroic beam splitter is employed, one which is designed with respect to the phosphor in use. If only spectral components from IF 2 are reflected (see Fig. 4.20), the entire residual spectrum is transmitted, so that almost no signal losses are introduced [148]. In contrast, a cubic beam splitter may sometimes be preferable over a semi-transparent mirror, due to the risk of artefacts caused by internal reflections in the mirror substrate [151].

4.6.3 Point Detectors

PMTs and photodiodes are common point detectors in phosphor thermometry, both characterized by offering rather high temporal resolution. They are predominantly employed in conjunction with measurements of the phosphorescence decay time [152–157] due to two major reasons.

1. The two-colour ratio approach would require either two point detectors or the presence of static temperatures, so that interference filters for wavelength selection can be switched.

2. Decay times of thermographic phosphors can vary many orders of magnitude, making this approach being superior to the two-colour ratio technique in terms of temperature sensitivity [64].

(a) PMTs: Photomultiplier tubes (PMTs) are perhaps the electronic tools most widely used in spectroscopy, their having been employed in every manner of optical measurement [V]. PMTs provide opto-electrical conversion combined with internal electrical amplification, making them suitable for low light level measurements. They are temporally resolving detectors; depending on their circuitry they can resolve the impingement of single photons on the photocathode in real time, but are also capable of measuring continuous streams of photons [158]. It is the ability of a PMT to operate continuously, that is utilized in phosphor thermometry for measuring temperature-dependent phosphorescence decays. Two different PMT models are common on the market, the dynode chain PMT and the MCP-PMT. Both are rather similar, but differ in terms of their means of internal signal amplification. Figure 4.21 shows a schematic of the dynode chain model, which consists of a photocathode, a dynode chain and an anode, contained inside an evacuated glass or metal tube.

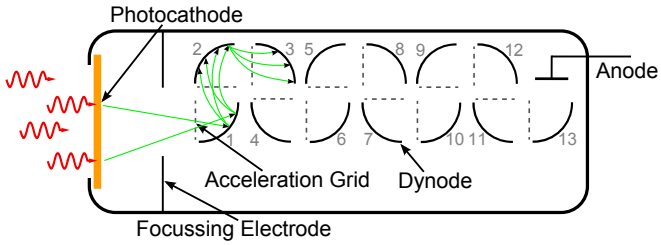

Figure 4.21: *The schematic construction of a PMT having 13 dynodes.*

The photocathode consists of photosensitive material, with a low work function. Upon light impingement, photons with energies above the work function level result in electrons being released from the photocathode. These photoelectrons are subsequently accelerated towards the first dynode by means of an applied voltage. Upon collision with a dynode, free secondary electrons are created. These secondary electrons are in turn accelerated to the next dynode by a strong electric field, the process being repeated until the electron cloud produced is collected at the anode. The dynode chain thus acts as an electrical amplification stage for the photoelectrons. Finally, the electrons leave the PMT via its anode as a time-dependent current signal.
An MCP-PMT is another type of photo-detector, one that works in a way similar to a normal PMT, except for the fact that the dynode chain present in the PMT is replaced by an MCP. Each microchannel is a continuous-dynode electron multiplier, in which the multiplication takes place under the presence of a strong electric field. Since MCPs drastically reduce the travelling distance of electrons between the photocathode and the anode, MCP-PMTs exhibit the fastest response times [13] of all PMTs and are thus often employed for the most demanding time-resolved measurements. The amplifications reached in the MCP are generally lower than for PMTs having discrete dynode chains.

Advantages: Due to their fast response and high sensitivity in the detection of low light levels, PMTs are very versatile photo-detectors. In fact, PMTs are the most sensitive photo-detectors currently on the market, their being capable of single photon detection [159]. Sensitive PMTs can amplify cathode signals by a factor of up to 10^9 [160]. Characteristics, such as large gain and low noise, make the PMT an attractive detector for many optical applications.

Disadvantages: PMTs are susceptible to shocks and vibrations. They are easily damaged, sometimes permanently, e.g. by overexposure to light. In addition, many PMTs are easily saturated and suffer from non-linear signal outputs as soon as anode currents higher than 100 μA are being detected [V, VI, 161–164].

(b) Photodiodes: A silicon photodiode is essentially a PN junction, consisting of a positively doped P region and a negatively doped N region. Between these, there exists an area of neutral charge, known as the depletion region. The impact of photons on a photodiode (hitting the P-side of the P-N junction) results in electron-hole pairs

if the energy of the photons is greater than the energy band gap of the semiconductor material, used in the photodiode. These electron-hole pairs are created throughout the device. When a potential is applied over the depletion zone, the electrons accelerate towards the N-side, whereas the holes accelerate towards the P-side of the P-N junction. This results in a positive charge build-up in the P-layer and a negative one in the N-layer. The amount of charge is directly proportional to the amount of light falling on the detector. A reverse bias is applied to the photodetector, which increases the electric field strength between the electrodes and increases the depletion zone. The advantages this provides are those of higher speed, lower capacitance and better linearity. However, also the dark current becomes greater through the employment of an external reverse voltage.
An avalanche photodiode (APD) is a specialized silicon PIN photodiode, designed to operate at high reverse bias voltages. Under the influence of an applied potential of sufficient size, the carriers accelerate and gain enough energy, that when they collide with the crystal lattice, they create a new electron-hole pair. If the newly created electron-hole pairs again acquire sufficient kinetic energy through acceleration, they create additional electron-hole pairs, thus resulting in a cascade effect. This is known as avalanche multiplication and is the mechanism, by which APDs produce internal signal amplification. Increasing the reversed voltage leads to an increase in the gain of the APD. A schematic of an APD is presented in Figure 4.22.

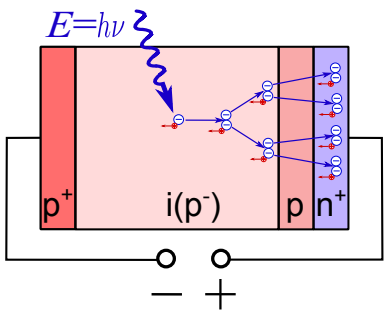

Figure 4.22: *The schematic construction of an avalanche photodiode.*

Advantages: APDs are characterized by their high sensitivity, high speed and internal gain mechanism. They are not as susceptible as PMTs are to shocks, vibration and damage.

Disadvantages: APDs exhibit lower sensitivities than their PMT competitors and are inferior in their internal signal amplification they achieve ($\leq 10^3$) [VI, 13]. The quantum efficiency of APDs is much higher than that of PMTs. However, APDs also have much smaller detection areas, and it is often the case that more light is lost in collection optics than is gained by their quantum efficiency [13]. In addition, the gain of APDs is inversely dependent upon the temperature, because elevated temperatures increase internal lattice vibrations, leading to collisions of the carriers before they have reached energy levels high enough to generate new electron-hole pairs.

4.6.4 Time Response and Bandwidth of Point Detectors

In a generalized description, the detected signal shape $S(t)$ corresponds to the time-transient of the phosphorescence $J'(t)$, folded with the spectral and temporal transfer function of the detection system $TF(t)$, i.e. its optical components, the detector, as well as additional electronics (e.g. amplifiers, oscilloscopes, ...).

$$S(t) = TF(t) \otimes J'(t) = TF(t) \otimes J'_0 \cdot \exp\left(-\frac{t}{\tau}\right) \tag{4.16}$$

An ideal detector would cause no distortion of the measured signal, i.e. $S(t) \sim J'(t)$, meaning that $TF(t)$ in Equation (4.16) would be replaced by a δ-function. In practice, however, the detection system is a lowpass filter with a certain cutoff frequency f_c, which compromises the measurement of short-lived decay signals $\tau \leq 1/(2\pi f_c)$. With current PMTs exhibiting rise times of less than 1 ns, most of the signal distortion is usually caused in the detection line after the photodetector [165,166]. The output of a PMT is a current I, whereas the external signal processing circuit is usually designed to handle a voltage signal U. Hence, the signal needs to be converted either by a load resistor or by a current-to-voltage amplifier.

(a) Load Resistor: Since a PMT can be thought of as an ideal constant current source, a load resistance with a considerably large value R_L can be used to obtain an output voltage in accordance with *Ohms law*.

$$U = R_L \cdot I \tag{4.17}$$

According to Equation (4.17), increasing the load resistance can be used to increase the readout voltage, when assuming a constant PMT anode current. However, if R is chosen unnecessarily large, the anode potential is decreased, causing the last dynode-to-anode voltage to decrease. This in turn increases the space charge effect and results in the degradation of the output linearity [158]. Another matter to consider is the avoidance of signal reflections in the cable, which occur if R_L from the readout device is not properly matched to the output resistor on the PMT side; see Figure 4.23.

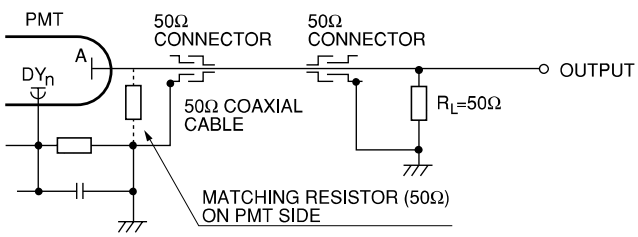

Figure 4.23: *Matching of the load resistance R_L to avoid ringing in the cable.*

Such a mismatch can be caused not only by the terminated resistance and the coaxial cable, but also by the connectors or the termination method of the coaxial cable. Thus, sufficient care needs to be taken in selecting a proper connector and also to

avoid creating an impedance discontinuity when connecting the coaxial cable to the photomultiplier tube or the connector [158]. If a matching resistor is not provided, only part of the signal dissipates through the output end, whereas the other part gets back-reflected. Depending on the length of the cable, a mirrored signal pulse can arrive somewhat time-delayed at the output and again gets partially reflected. The reflected part of the signal repeats its round trip until its total energy is dissipated. As a result, a ringing pattern is observed as a distortion of the output signal. Another matter to consider is that if a proper impedance match is not provided at the output end, the impedance in the photomultiplier tube varies with frequency.
Many PMTs are shipped with an internal load resistance of $50\,\Omega$, such that ringing can be avoided when connecting them via BNC cables to an oscilloscope with a matching input resistance of $R_\mathrm{L} = 50\,\Omega$ [V,158]. One reason for this can be a general dependence between R_L and the cutoff frequency f_c [167], as given in Equation (4.18).

$$f_\mathrm{c} = \frac{1}{2\pi\tau_\mathrm{c}} = \frac{1}{2\pi \cdot RC} = \frac{R_\mathrm{PMT}^{-1} + R_\mathrm{L}^{-1}}{2\pi \cdot (C_\mathrm{PMT} + C_\mathrm{cable})} \tag{4.18}$$

The fact that all the resistances and capacities are connected in parallel, see Figure 4.23, is already taken account of in Equation (4.18). It was assumed also, that the oscilloscope for reading out the signal at the output is electrically ideal, i.e. that $R_\mathrm{osc} = \infty$ and $C_\mathrm{osc} = 0$. The parameter τ_c can be viewed as the time constant at which an input signal of a δ–pulse would decay over time at the output. Such a pulse would have a rise time of $\approx 2.2\tau_\mathrm{c}$ (10 % to 90 %). When the resistances are matched at the output, i.e. when $R_\mathrm{PMT} = R_\mathrm{L}$, the time response of the detection line simplifies to

$$\tau_\mathrm{c} = \frac{1}{2} R_\mathrm{L} \cdot (C_\mathrm{PMT} + C_\mathrm{cable}). \tag{4.19}$$

Hence, a high input resistance of the oscilloscope leads not only to higher output voltages (see Eq. (4.17)), but also to a reduction in the time resolution.

Example: A *Hamamatsu* PMT (H6780-04 series) was measured to possess an output capacity of $C_\mathrm{PMT} = 60\,\mathrm{pF}$. Connector cables usually exhibit capacities in the order of $C_\mathrm{cable} = 10\,\mathrm{pF/m}$ (BNC type RG58). Three different load resistances for the oscilloscope were tested in conjunction with the PMT; $50\,\Omega$ (■), $500\,\Omega$ (○) and $5\,k\Omega$ (△). In accordance with Equation (4.19), the time response τ_c of the detection line was plotted as a function of the connector cable length; see Figure 4.24. The following conclusions can be drawn from Figure 4.24:

1. Only the $50\,\Omega$ resistance allows phosphorescence signals with decay times in the single ns regime to be resolved.[11]

2. Connecting cables should be kept reasonably short so as to achieve the best possible time resolution. In any case, the cable length should not be changed between experiment and calibration, in order to prevent systematic temperature errors from occurring.

[11] Due to this effect in the detection line, the calibation curve for $CdWO_4$, shown in Figure 3.11 (page 30), levels out for high temperatures at decay times of few nanoseconds.

There is one problem, however, arising from picking a low load resistance in order to maintain a highly responsive signal: Common PMTs are specified to be run at output currents $\leq 100\,\mu$A during DC operation [160, 165, 168]. According to Equation (4.17), this translates into a maximum output voltage of 5 mV being registered on the oscilloscope. Common digital oscilloscopes (such as the *Lecroy WaveRunner WA6030*), however, have a minimum voltage resolution of 2 mV/div [169]. Its screen offers eight divisions and an y-axis resolution of 8 bit, meaning effectively a maximum of $2^8 = 256$ possible y-bins for a full-scale signal [169]. At the highest possible voltage resolution, a 5 mV peak signal corresponds to 5 mV/(2 mV/div·8 div)= 5/16 parts of a full screen. Hence, there are only 80 possible bins available out of originally 256, which increases the digitizing noise of the signal and drives the oscilloscope towards operation close to its lower detection limit.

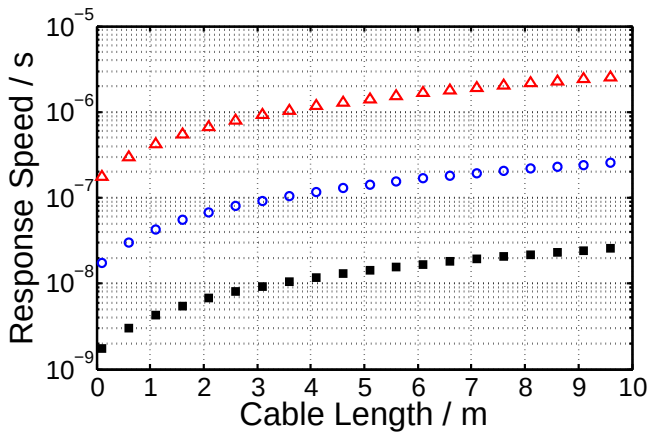

Figure 4.24: *The time response of a PMT detection line, shown as a function of the cable length. Three different load resistances were applied and were matched:* 50 Ω (■), 500 Ω (○) *and* 5 *k*Ω (△).

One way to solve this problem is to operate PMTs in excess of their specified output currents [V, VI, 167][12] These limits, after all, apply to DC operation, meaning that a linear output response for pulsed signals (as it is the case for most LIP applications) may be maintained at levels even above 100 μA. Although there are literature sources available, stating that output currents for PMTs can be as high as 50 mA (i.e. 2.5 V for 50 Ω!) during pulsed operation [168], great care needs to be exercised so as not to damage the PMT when operating at elevated output currents. A linear signal response may not be maintained at such high signal levels. Hence, the PMT response needs to be investigated carefully in order to avoid systematic errors caused by non-linear effects in the detector [V, VI]. Further discussion on this issue is given in section 4.6.5.

[12] An output current $\geq 300\,\mu$A is necessary in order to achieve a full-scale signal of 15 mV on the oscilloscope and utilize its entire bit range.

(b) Current-to-Voltage Amplifier: An alternative approach to increasing the output voltage, detected by the oscilloscope, is to implement a current-to-voltage amplifier in the detection line. Such amplifiers have a high impedance and provide gains, typically in the order of 10 to 100, at bandwidths of up to several GHz [160, 168]. A simplified schematic circuit for PMT current amplification can be seen in Figure 4.25.

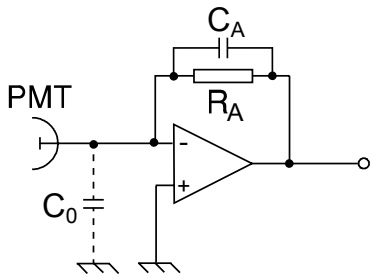

Figure 4.25: *An equivalent circuit for PMT current amplification.*

Figure 4.25 highlights the transformation, that can be made from a resistor, located in the anode to one located in the feedback path of the amplifier. By such means, the resistor R_A can be isolated from the unwanted effects of capacitance C_0 [160]. However, if the signal cable for a PMT is long, C_0 together with R_A can create a rolloff in the frequency response of the feedback loop, resulting in oscillations of the output signal [158]. Connecting C_A in parallel with R_A enables oscillations to be avoided, although this also degrades the bandwidth of the amplifier. Equation (4.20) provides an estimate of the amplifier bandwidth, expressed as the cutoff frequency f_CA:

$$f_\mathrm{CA} = \frac{1}{2\pi \cdot R_\mathrm{A} C_\mathrm{A}} \tag{4.20}$$

It is advantageous, therefore, to keep cables between detector and amplifier short and use a small capacitor C_A [158]. Since there is usually a trade-off between signal bandwidth and noise, it is advisable to dimension the amplifier bandwidth according to the response capabilities of the residual instruments in the detection line. For example, it would seem wise to choose a 500 MHz amplifier over one with 1 GHz in bandwidth, if the connected oscilloscope for signal readout exhibits a cutoff frequency of 350 MHz.
Since the input impedance of the amplifier is extremely high, the output current of the photomultiplier tube is blocked from flowing into the inverting input terminal (-); see Figure 4.25. Hence, most of the output current flows through the feedback resistance R_A and a voltage signal U_amp in accordance with Equation (4.21) can be measured at the amplifier output [158].

$$U_\mathrm{amp} = I \cdot R_\mathrm{A} \tag{4.21}$$

4.6.5 Non-linear Signal Response in the Detection Line

Quantitative measurements often rely on a linear relationship between the physical quantity and the detected signal. If this relation is no longer maintained, e.g. through effects of saturation in the detector, systematic errors may occur that hamper the retrieval of accurate temperature information from LIP experiments. Since most of today's photodetectors provide some sort of internal signal gain, a non-linear behaviour in these detectors may not only be caused by an inappropriate intensity of optical signals being detected, but could originate also from the electrical amplification stage. In this section, experiments are described that assist in understanding and quantifying the effects of a non-linear signal response [IV, V, VI].

Non-linearities in Two-Colour Image Ratios: The following discussion is based on experimental findings published in [IV] and deals primarily with signal saturation in ICCD detectors and its consequences for the temperature accuracy of the two-colour ratio technique. However, the experimental setup employed in this context is also well suited for other imaging devices, including lifetime imaging detectors that offer high frame rates, such as CMOS cameras. The effects of saturation on phosphorescence decay times, however, are discussed further in the section that follows; see page 95.

(a) Experimental Setup: Figure 4.26 shows an experimental setup that can be used to characterize a digital camera in terms of signal linearity [IV]. In principle, the linear workspace of a camera can be measured by use of a homogeneously intense and tunable light source, such as an Ulbricht sphere. Choosing a phosphor-coated surface as an object for the imaging process (as is the case in Figure 4.26), however, enables one in addition to understand how, and more importantly how much, signal non-linearities affect the accuracy of temperature measurements in phosphor thermometry.

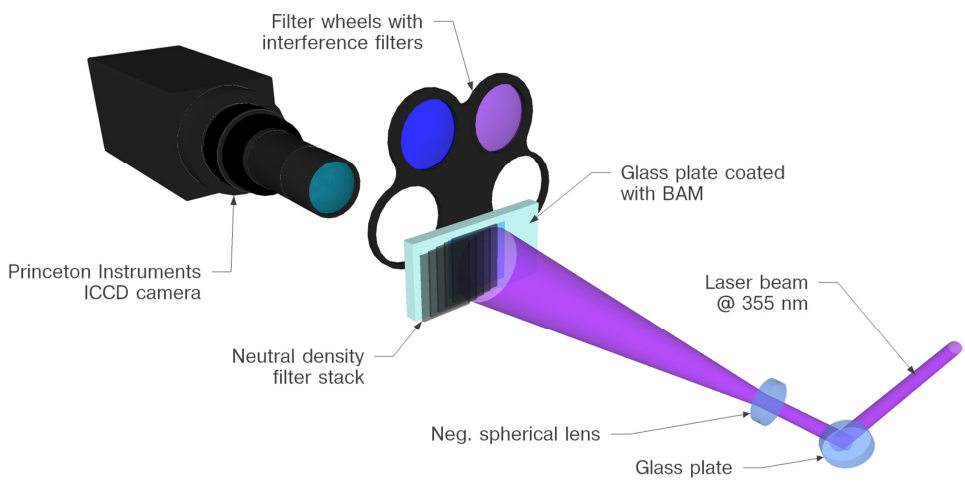

Figure 4.26: *Schematic setup for camera linearity investigations using LIP.*

A 10 Hz pulsed Nd:YAG laser, operating at its third harmonic at 355 nm, with an energy of ≈ 0.5 mJ/pulse was used as an excitation source. The beam was expanded by a spherical lens and illuminated a BAM-coated glass plate. Behind the plate, a filter wheel was placed, provided with optical bandpass filters [IF 456 = (456 ± 5) nm; IF 456 = (400 ± 20) nm]. Most of the laser light was converted into thermographic phosphorescence by the phosphor coating on top of the glass plate. The phosphorescence appeared in the visible part of the spectrum, and was recorded through the glass plate by a PI-MAX2 ICCD camera (*Princeton Instruments*). The glass plate provided also sufficient UV absorption to prevent residual laser contributions from entering into the camera.
Since this is a single-camera setup in which images recorded through different filters are taken consecutively, stability of temperatures and illumination levels over time is required. All the measurements were thus performed at room temperature, this providing a uniform and stable temperature distribution across the coated phosphor surface. In addition, an accumulation of ten images was made for each measurement, so as to cancel out laser shot-to-shot variations.
A stack of five partly overlapping neutral-density filters was placed in the expanded beam path (see Fig. 4.26). It introduced a step gradient of six discrete and parallel areas of different laser excitation energies to the phosphor coating. This in turn generated a similar step gradient of phosphorescence intensities to be recorded by the camera. The optical intensity was attenuated by the filter stack in transmission steps of 9 % (5 filters), 14 %, 22 %, 39 %, 67 %, and 100 % (no filter). The intensity gradient obtained this way made it possible to study the effects of optical saturation. In addition, the camera-internal signal amplification was also varied in steps of 10, from 0 to 250 (out of 255). With six areas of differing illumination intensities, this resulted in a total number of 156 different combinations of gains and laser fluences. Prior to the experiment, the laser energy was adjusted in a way that the maximum number of counts at gain 250 for the highest signal intensity is slightly below 65 535 counts, corresponding to the maximum count level of the 16 bit A/D converter in the camera.

(b) Signal Saturation: Each camera image from the experiment contained six areas of constant filter transmission, where average pixel count value could be calculated. Figure 4.27 (a) displays these average count values, as observed with use of the IF 456 filter, for all possible combinations of gain and intensity in form of a matrix. Because of the exponential behaviour of the camera gain, the signal intensity is displayed by use of a logarithmic scale.
Figure 4.27 (b) illustrates the camera's ability to reproduce the differences in filter transmission, indicated by the vertical bars, by relative proportions of averaged signal intensities (●/○). The blue (●)-markers show data values from (a), that were observed at gain 80 and that were scaled linearly in a way that the image segment with the lowest average signal matches a transmission value of 9 %, corresponding to 5 filters. As can be seen, these are in close agreement with the average filter transmission, indicating that the overall camera response is in its linear regime.
When the camera response is monitored for a gain value of 250 instead, see red (○)-markers, the signal counts for 2, 1 and 0 filters did not increase in a way which is

proportional to the increase in optical signal intensity. Instead, the measured signal levels out at only ≈ 35 % of the expected signal intensity and a state of non-linear camera response was found. The red (○)-markers begin to differ from the expected trend, as less than three filters were present, the signal level there exceeding 29 000 counts (or ≈ $10^{4.464}$). Since only the gain has changed between the two cases, displayed in part (b) of Figure 4.27, whereas the photon flux has remained constant, this behaviour must have been caused during signal amplification and can very likely be attributed to saturation effects in the MCP [IV, 142, 143].

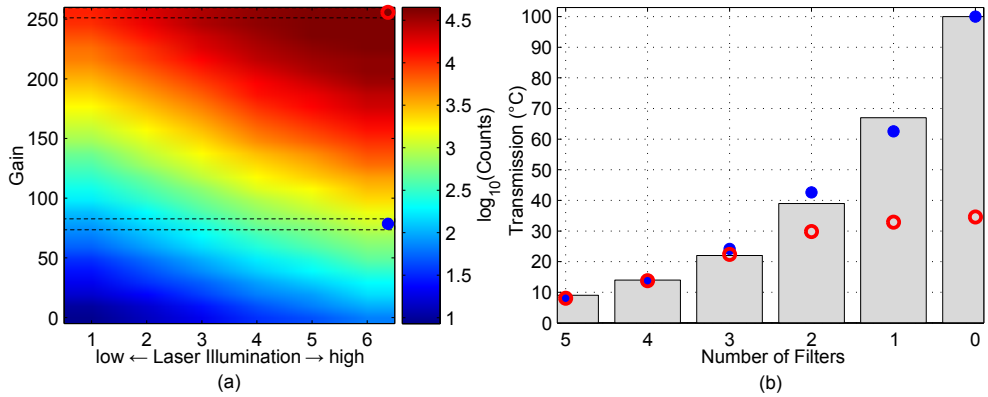

Figure 4.27: *Part* (a)*: Average camera counts, shown as a function of laser fluence and gain for images observed with the IF*456 *filter. Part* (b)*: Measured filter stack transmission* (*bars*)*, displayed with two scaled camera count examples with gain values of 80* (●) *and of 250* (○)*.*

Figure 4.27 (b) indicated a linear camera response to a gain of 250 for the first two to three lowest signal intensities. This observation is based on the close agreement of the camera signals with the filter stack transmission values; compare first 3 values of the circles and bar plots in Fig. 4.27 (b). Thus, it can be assumed that the entire first column of Figure 4.27 (a) is corresponding to measurements from the linear workspace of the camera. As BAM phosphorescence at room temperature was found to be generally less intense at 400 nm compared to its signal at 456 nm, low intensity segments from camera images observed through the IF 400 filter were also assumed to be linear over the entire range of gain values employed during the experiment. Hence, all of the measurements at the lowest laser fluence level have now been confirmed to stem from the linear operating regime of the camera.
In addition, the relative increase in transmission between different image segments, as defined by the optical filter stack, allowed the extrapolation of ideal camera count levels for higher intensity segments at each gain based on the image segment that was attenuated by a stack of 5 filters. By plotting these ideal camera counts against their corresponding values that were obtained from the experiments, a signal response function of the PI-MAX2 camera was achieved and plotted in Figure 4.28.

The information displayed in Figure 4.28 is based on the measured data shown in Figure 4.27 (a) (△), and on corresponding values measured at 400 nm (○); original data can be found in [IV].

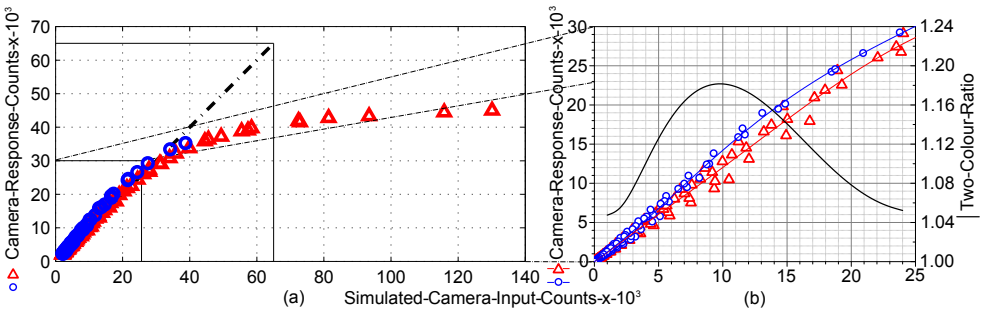

Figure 4.28: *Part* (a): *Camera response functions for the two filter wavelengths involved;* (○) *= IF 400* (△) *= IF 456). The straight dashed line shows an ideal linear response curve within the boundaries of the A/D converter. The second image part* (b) *displays a detail from the low-count region in* (a). *The line* (*right y-axis*) *shows the two-colour ratio as a function of the number of camera counts.*

For both wavelengths in Figure 4.28, the initially linear behaviour there tends to end between 20 000 and 30 000 counts, indicating the onset of electrical saturation. Hence, only 1/3 to 1/2 of the camera's nominal dynamic range can be utilized for quantitative measurements without there being a necessity for corrections of signal linearity. In addition, the results of recordings using the IF 400 filter (○) show a slightly steeper slope than those from the IF 456 filter (△). It appears as if the spectral sensitivity of the camera varies with signal level, even though the two wavelengths differ from each other by only ≈ 50 nm. This can be seen more clearly in part (b) of Figure 4.28, where the relative ratio of the two response curves is plotted (—, right *y*-axis). The relative spectral pixel sensitivity changed by approximately 11 % – a variation, which can be interpreted as a signal-dependent temperature error of the two-colour ratio technique, when experienced in context with thermographic phosphors.

Example: According to the calibration chart on page 30, an absolute variation of the intensity ratio of 11 %, i.e. ±5.5 % due to camera-internal effects corresponds to systematic temperature errors of ≈ ±20 K for BAM, or ≈ ±30 K if YAG:Dy is used as a thermographic phosphor.

(c) Systematic Temperature Errors: In order to show the effects of the previously discussed camera non-linearities on the measurement results of two-colour ratios in phosphor thermometry, each of the 156 averaged count values from the IF 400 image set (shown in [IV]) was divided by its corresponding signal counterpart from the IF 456 filter measurements; see Figure 4.27 (a). The result this provides is shown in Figure 4.29 (a), presenting a ratio matrix similar in structure to the intensity chart displayed in Figure 4.27 (c).

In part (b) of Figure 4.29, the ratio matrix (a) was translated into the temperature scale, using a temperature calibration chart obtained earlier, such as shown in Figure 3.11, page 30.

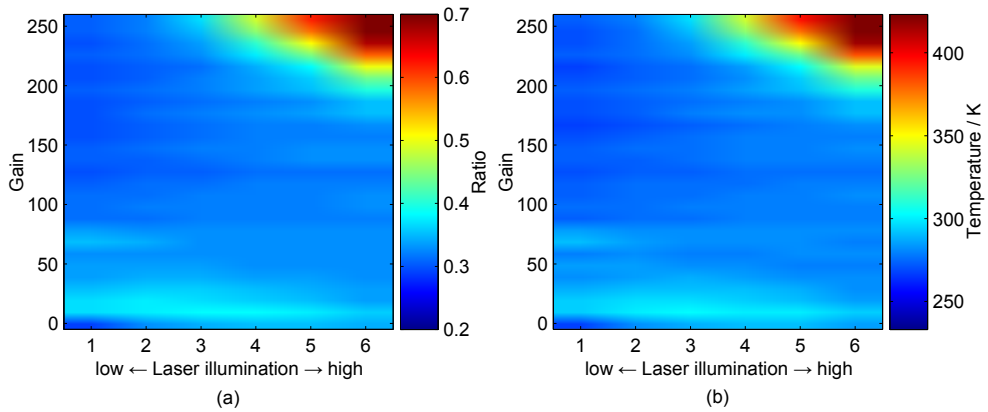

Figure 4.29: *Part* (a): *Evaluated two-colour ratio of BAM at room temperature as a function of different gains and laser illuminations. Part* (b)*: Translation of part* (a) *into virtual temperatures using a temperature calibration achieved earlier.*

As can be seen in Figure 4.29, the average ratio value, and hence their corresponding temperatures, are rather constant within the major part of the matrix, with exception of the upper-right corner. Despite all measurements being performed at constant room temperature, the evaluated temperatures shown in Figure 4.29 (b) are systematically too high, when acquired at high gain and high laser fluence. Whether temperatures are systematically higher (as in this example) or lower in response to non-linearities in the detection line depends very much on the shape of the signal response curve and the spectral characteristics of the phosphor. In Figure 4.29 systematic temperature deviations of almost 200 K were reached, underlining the importance of knowledge concerning the linearity of detectors.

The camera non-linearities discussed earlier may be associated with saturation effects inside the image intensifier [IV]. In contrast, there is also a distinct possibility of cameras being encountered, that act non-linearly also during the detection of weak signals [60]. In addition, familiar problems of long- or short-term drifts in camera detectors can occur and need to be taken into consideration as a source of systematic measurement error. For several camera types, it is advisable to keep them running a few hours before starting an experiment. Such precautions are tedious, but can contribute to avoiding signal drifts during operation. Further research on the detectors that are available may be desirable in order to allow more accurate measurements to be obtained in the future.

Non-linearities in Phosphorescence Decay Signals: In this section, the effect of non-linear signal detection on the decay time method is discussed on the basis of experimental studies [V, VI] and of unpublished work. Just as in the previous section, these effects could be observed by changing the electrical gain and the light intensities independently of each other. This time, however, the phosphorescence decay was studied and point detectors were employed. In addition, the temperature (e.g. the phosphorescence decay time) was varied to gain further insight into the transient nature of saturation effects in the detection line.

(a) Experimental Setup: Figure 4.30 shows an experimental arrangement, suitable for characterising signal linearity in point detectors.

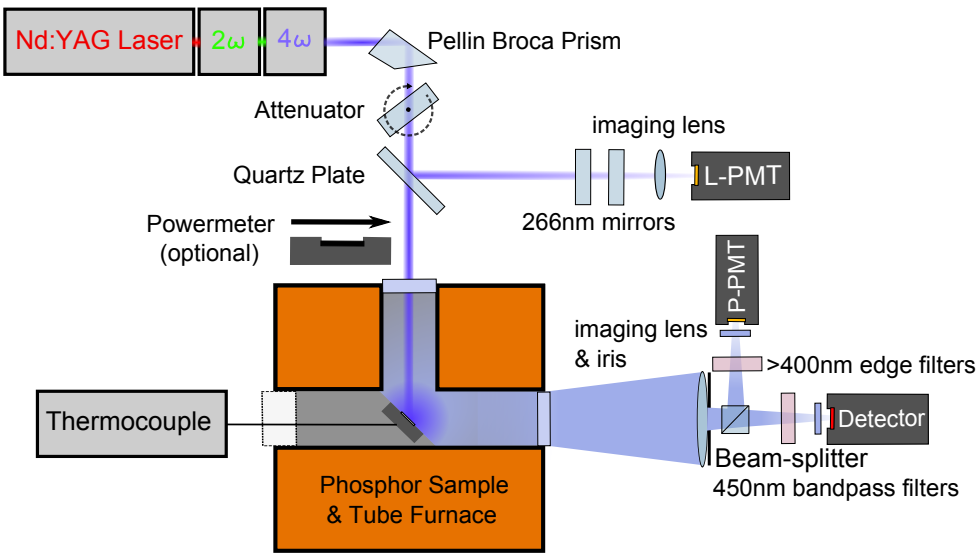

Figure 4.30: *Experimental setup for testing the temporal performance of a point detector under the influence of light intensity, gain and decay-time variation. L- and P-PMT are two identical PMTs used to estimate the amount of impinging photons per time interval on the detector, both being calibrated against the power meter.*

A substrate, coated with $CdWO_4$ was placed inside a tube furnace, the temperatures being measured by an array of three thermocouples. The phosphor was excited by a 10 Hz pulsed Nd:YAG laser operating at 266 nm. A polarizing beam attenuator was used to change the excitation energy from 15 μJ to 5 mJ.[13] Thermographic phosphorescence was collected by a spherical lens and imaged onto the detector under investigation. The effective lens diameter could be changed by an adjustable iris, which allowed the phosphorescence intensity on the detector to be varied independently of the laser excitation energy. Before entering the detector, the phosphorescence light

[13] From Fig. 4.3 (page 45), it is known that pulse energies on the order of 5 mJ already can have a moderate effect of laser heating of the substrate during long-term exposure [I].

passed through a combination of a $> 400\,\text{nm}$ edge filter (to eliminate any spurious laser contribution to the detected signal) and a $(450 \pm 20)\,\text{nm}$ bandpass filter. The signal was read out over a $50\,\Omega$ resistance on a 350 MHz digital oscilloscope. Two identical reference detectors (L-PMT and P-PMT) were aligned, in order to be able to continuously monitor the laser energy relative to the recorded phosphorescence intensity. Upon calibration, this allowed a rough estimate of the number of phosphorescence photons that impinge upon the detector during the first few nanoseconds of phosphorescence signal to be measured [VI].

(b) Signal Saturation: Phosphorescence decays under the influence of non-linearities in the detection line are affected differently than was discussed earlier in connection with the two-colour ratios. In order to demonstrate this effect, different states of signal saturation were simulated by creating artificial response functions $S_{\text{out}}(J'_{\text{in}})$ according to

$$S_{\text{out}}(J'_{\text{in}}) = S_{\max} \cdot \left[1 - \exp\left(-\frac{J'_{\text{in}}}{S_{\max}}\right)\right], \tag{4.22}$$

where J'_{in} is the incoming signal intensity and $S_{\max}$ is the highest possible signal output from the simulated detector [V]. Several such response curves based on Equation (4.22) are plotted in Figure 4.31 (a) together with the signal response of an ideal detector ($S_{\max} \to \infty$), indicated by the black solid line.

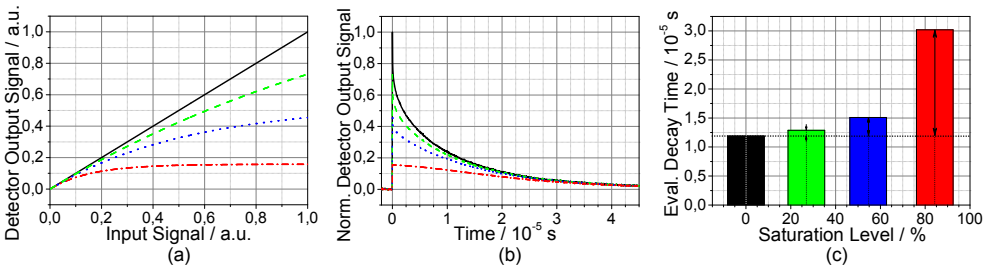

Figure 4.31: *Example of how different saturation states in the detector* (a) *change the shape of the output time-signal* (b) *and the evaluated decay time* (c)*. The original decay transient in* (b) (—) *corresponds to an average of 100 measured signal curves of* $La_2O_2S{:}Eu$ *at room temperature.*

The saturation effect becomes apparent when the measured phosphorescence decay curve is inserted as J'_{in} into Equation (4.22). Figure 4.31 (b) shows the original decay waveform (—) to be somewhat truncated by the saturated response curves displayed in part (a) of the figure. When a single-exponential decay in accordance with Equation (3.10) (page 27) is fitted to the distorted decay signals in (b), the evaluated decay time increases with increasing signal saturation.

Example: A saturated detector that reduces the original peak signal by 84 % due to the compression of elevated signal parts (red dash-dotted line Fig. 4.31 (b)) appears to exhibit decay times that are 2.5 times as long as those from an undistorted

signal (Fig. 4.31 (c)). This change would be experienced as an artificially decreased temperature readout, when calculated from an unsaturated temperature calibration. According to the calibration chart on page 30, an expected systematic decay-time error of this magnitude for $Mg_3F_2GeO_4$:Mn would result in temperature errors on order of 280 K (low temperature regime) and 54 K (high temperature regime). In contrast, the temperature error for $CdWO_4$ would be around 33 K over its entire temperature-sensitive range.

A detector operates in its linear response region, when the decay time being evaluated is dependent entirely on the transient shape of the optical signal, i.e. is insusceptible to changes in electrical gain and light intensity. It can thus be concluded, that the lifetime of exponential luminescence decays can be used as a measure for investigating non-linear effects in the detection line [V, VI]. This assumption has been later reconfirmed by Persvik et al., who utilized the single-exponential luminescence of two dyes (erythrosin B and eosin Y) for judging the performance of different PMTs [170]. Figure 4.32 presents an example of how the operator of an experiment perceives a PMT during the onset of saturation. Natural measurement characteristics, i.e. the signal peak voltage from the recorded luminescence decay and the knob number, which can be turned to increase or lower the internal gain are displayed.

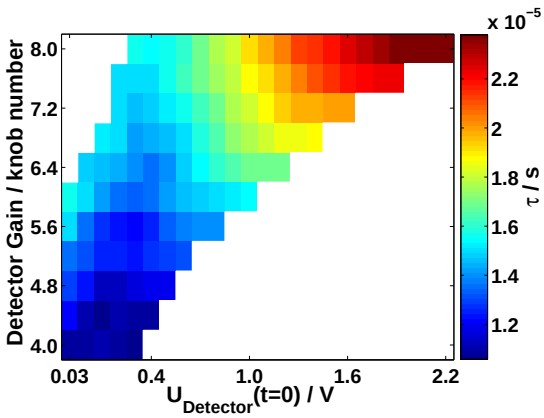

Figure 4.32: *Detector response matrix of a PMT (Hamamatsu H6780-04), measuring $CdWO_4$ phosphorescence at 294 K. The evaluated decay time is shown as a function of the gain knob number and the detector peak voltage.*

The arbitrary unit "knob number" translates into a control voltage and is used for driving the dynode chain. It can be converted into an approximate gain estimate for the PMT using data sheets provided by the manufacturer [171]. The phosphorescence was varied within the same intensity range for each of the displayed detector gains. This caused the phosphorescence peak signal to change within the interval of 0.03 to 2.2 V. The signal peak voltage depends on both incident light flux and detector gain, leaving large matrix parts empty in Figure 4.32. It is cumbersome in this plot, therefore, to distinguish the effects from gain and incident light intensity on the detected decay

time. However, having the actual reading values displayed offers an experimenter the advantage of using Figure 4.32 directly for judging the current saturation performance of a detector during measurements. It is also interesting to note that varying the signal intensities in experiments cannot be compensated for by changing the detector gain, without its affecting the shape of the decay signal. This becomes clear, when one follows a constant peak voltage (e.g. 0.3 V) across several gain columns with respect to the decay time. The discussed detector in its current configuration seems to be of limited use for quantitative measurements, judging from the lack of stability in the decay time.

(c) Systematic Temperature Errors: Figure 4.33 (a) shows the detector response surface from a H6780-04 PMT at 373 K, this time displayed as a function of gain and photon number, according to calculations detailed in [VI]. Every matrix element contains contributions from 10 to 500 single decays, each evaluated individually before averaging. The evaluated decays are longer in the upper right region of high gains and high photon numbers. Since this behaviour changes with gain and with light intensity, it can be associated with signal saturation. At low light levels visible in Figure 4.33, there is a gain-independent decay time gradient, which was later identified as being caused by the excitation-energy dependence of $CdWO_4$ (see section 4.3.5, page 52).

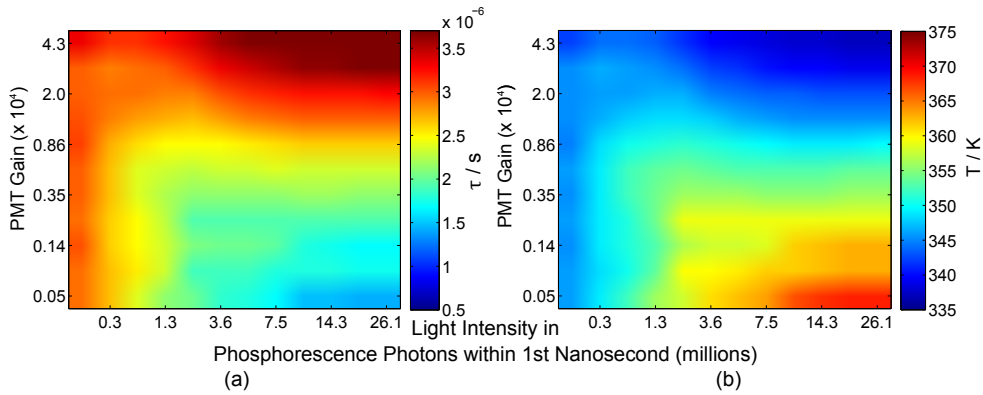

Figure 4.33: *Part* (a)*: Decay time response matrix of a Hamamatsu H6780-04 PMT, registering $CdWO_4$ phosphorescence at 373 K. Part* (b)*: Artificial temperatures, calculated from part* (a) *using previous temperature calibration data.*

Part (b) of Figure 4.33 is a translation of Figure 4.33 (a) into the temperature scale, using a calibration chart of the same type as found in Figure 3.11; page 30. It should be emphasized, that all of the measurement data that Figure 4.33 (b) is based on, was acquired at a constant temperature of 373 K. The temperature distribution presented here is consequently not real and only the result of a non-linear signal response, that was obtained from the PMT. A temperature distribution that spans across 40 K can be seen in Figure 4.33 (b), which represents more than 13 % of the phosphor's original temperature-sensitivity range.

(d) Comparison of Different Point Detectors: Besides the H6780-04 PMT, a number of other time resolving point detectors were compared in the experimental studies described in [VI]. These involved two gateable PMTs (one of which had an MCP as amplifying unit), an APD and the optional use of an in-house manufactured current-to-voltage amplifier with a 5 MHz bandwidth. Figure 4.34 provides an overview of the point detectors that were tested, together with their individual gain controls and modes of operation.

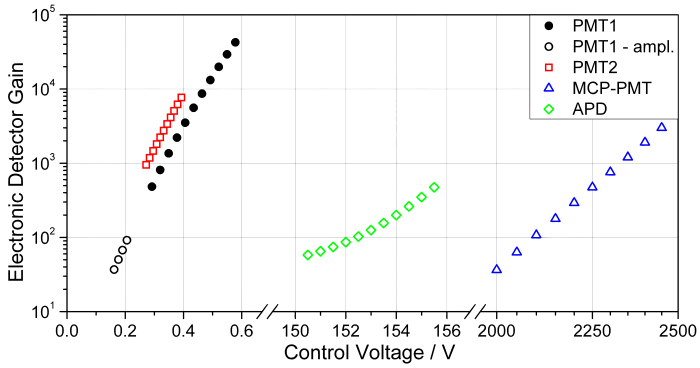

Detector type	Model number	Mode of operation	Gain range
PMT1	H6780-04	continuous	480-43000
PMT1	H6780-04	continuous + amplified	42-80
PMT2	H11526-20-NF	continuous	950-7700
MCP-PMT	R5916U-50	time-gated: −10 ns	36-3000
APD	S5343	continuous	62-470

Figure 4.34: *Detectors and operating modes as tested and compared in* [VI]. *Electrical amplification (gain) in each detector was achieved by varying the control voltages.*

The gain range represents the electrical amplification range that was tested for each detector as defined by peak voltages of the oscilloscope, ranging from ca. 5 mV up to several volts. Figure 4.35 presents temperature calibration charts for $CdWO_4$ while operating the individual detectors within the confines of their linear workspace. Of the detectors that were tested, the gateable H11526-20-NF PMT provided the best compromise between signal linearity, signal quality and time response. Operating the MCP-PMT was only possible in the time-gated mode with gate lengths limited to $\leq 10\,\mu$s. This could be a drawback for those phosphors having longer decay times in parts of their temperature-sensitive range. Performing external signal amplification appeared useful, helping to limit signal saturation in the H6780-04 PMT while at the same time maintaining reasonable signal outputs. The limited bandwidth of 5 MHz, however, was detrimental to its detection sensitivity for decays that were shorter than 200 ns. The APD's capability of reproducing short decays appeared superior to any of the other point detectors it was compared with. Nevertheless, signals acquired by the avalanche photodiode exhibited the lowest signal intensities that originated from a very limited gain range.

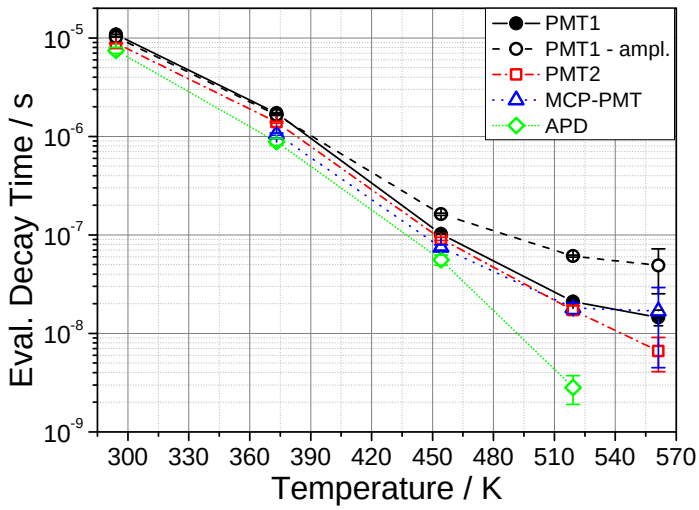

Figure 4.35: *$CdWO_4$ temperature calibrations for all the detectors from a fixed response matrix element. The error bars represent one standard deviation from the mean value.*

(e) Comparison of Similar Point Detectors: After comparing different point detectors, another question may arise, that of whether the earlier investigations of signal saturation are representative for other detectors of the same model type. If this were the case, there would be no need for testing and compensating detectors individually for any non-linear effect, since one could rely on analogies to a single representative measurement, such as provided in [V, VI]. Unfortunately, in Table 4.1 there is evidence that significant variations in the response behaviour of similar detectors are to be expected. Apparently, the luminous sensitivities of the photocathodes ($\sim$ amount of photoelectrons for a given number of photons arriving at the photocathode) and the gain response of the dynode chain to an externally applied control voltage vary considerably for individual detectors of a given production type.

Table 4.1: *Test sheet data values for H11526-20-NF PMTs, provided by Hamamatsu.*

Serial number	marker in Figure 4.36	cathode luminous sensitivity μA/lm	anode luminous sensitivity[14] A/lm
58590020	△/▲	499	606
58590039	□/■	326	1490
58590040	○/●	412	1920
58590043	◊/♦	460	6170
standard deviation:	–	75	2477

[14] control voltage: 0.8 V

Figure 4.36 confirms this in comparing the results of an experiment, in which the PMTs from Table 4.1 are exposed to $CdWO_4$ phosphorescence at 294 K and 454 K, respectively.

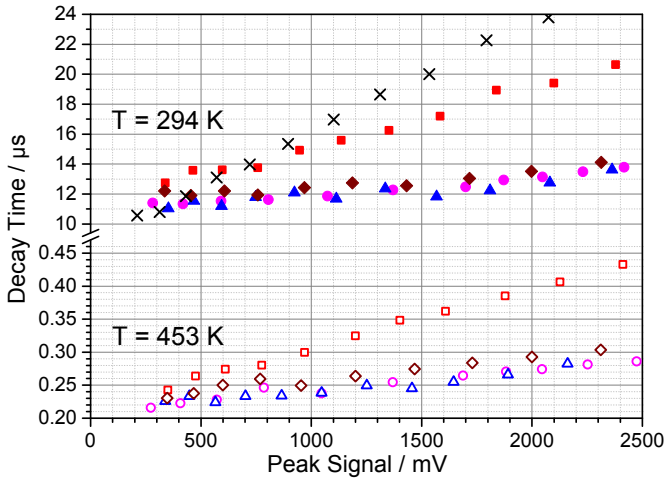

Figure 4.36: *Evaluated $CdWO_4$ decay times, shown as a function of the detector voltage as affected by variations in gain at constant light intensity for 294 K and 453 K. The △, □, ○ and ◊ markers represent results for the H11526-20-NF PMTs, listed in in Table 4.1. A measurement of PMT type H6780-04 at 294 K, displayed by using × markers, are presented for comparison purposes.*

As the PMT-internal signal gain was increased through changing the control voltage, the recorded phosphorescence peak signal increased accordingly from 300 mV to about 2500 mV. In addition, the decay times increased due to the onset of signal saturation, as predicted in discussing Figure 4.31, page 97. The temperature, and thus the length of the phosphorescence decay, did not appear to affect the saturation characteristics when the measurements at 294 K ($\tau \approx 4.5\,\mu s$) and at 453 K ($\tau \approx 43$ ns) were compared in Figure 4.36. All the H11526-20-NF PMTs that were tested experienced weaker signal distortions, due to saturation as compared with the H6780-04 PMT. This observation confirms the exemplary findings, presented in [VI]. However, responses of the H11526-20-NF type varied considerably, at least when comparing one individual model (serial number: 58590039, □) with the residual PMTs. This difference is consistent with the variations in the cathode luminosities of the detectors listed in Table 4.1. It appears that a high cathode sensitivity is conducive to a linear signal response, whereas the effects of differing luminous sensitivities of the anodes does not show any clear dependence of this sort. Further experiments may be needed to gain a better understanding of the saturation behaviour of point detectors.

(f) Non-linearities in the Oscilloscope: Oscilloscopes possess an internal signal amplification stage of their own, one which is used to zoom and to display the electrical signals that are fed into their input channels. It allows the user to change

manually the volts per division, that are shown on the screen. The operator does not perceive this signal alteration as an amplification process, however, since along with the scale of the signal the unit value per division changes as well. Figure 4.37 shows a test procedure, in which the input signal to an oscilloscope is changed in discrete steps, after each accumulation of 200 signals (upper graph, —). The signals, recorded by a PMT (serial number 5890040) and transmitted to an oscilloscope (*Lecroy WaveRunner WA6030*) via a 50 Ω input resistance, originated from $CdWO_4$ phosphorescence at 294 K. Since the peak signal from the phosphorescence increased by almost 60 times during the experiment (from 12 mV to 700 mV), the oscilloscope display needed to be adjusted accordingly through changing the volts/division settings (upper graph, ···). Since this change in the display was also performed after each accumulation of 200 signals, although with a delay of 100 signals, each of the 6 distinct signal voltage levels was measured 100 times at half and 100 times at full y-axis resolution.

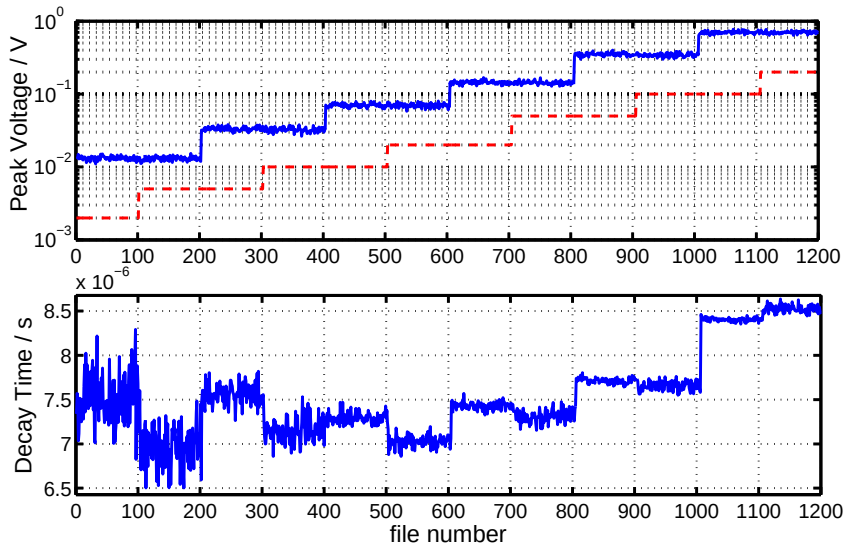

Figure 4.37: *Upper graph: Peak voltages recorded from $CdWO_4$ at 294 K using a H11526-20-NF PMT in combination with a 50 Ω terminated Lecroy WaveRunner WA6030 oscilloscope. The phosphorescence signal that was detected was stepwise increased (upper graph, —). In addition, the voltage/division on the oscilloscope (···) was adjusted so that each peak signal was measured 100 times at half and at full y-axis resolution. The lower graph shows corresponding $CdWO_4$ decay times.*

An immediate conclusion one can draw from Figure 4.37 is that the evaluated phosphorescence decay time changes after each set of 100 measured signal transients. This means that it is not only the increase in the detector signal (every 200 measurements) that contributes to non-linearities, i.e. distortions in the signal shape; but that also the oscilloscope's internal gain has an effect on them, its resulting in erratic decay time readings and thus being a source of systematic temperature errors in phosphor thermometry.

To analyse this problem further, two different experiments were carried out. In the one experiment, the detector signal was changed by varying the optical signal intensity (Fig. 4.38 (a)) and in the other one (Fig. 4.38 (b)), the detector signal was varied by gain. Both experiments were conducted using $CdWO_4$ phosphorescence at 294 K as the radiation source. However, in part (a) of Figure 4.38 input channel 2 was used, whereas the detector signals from (b) were fed to the oscilloscope via channel 3.

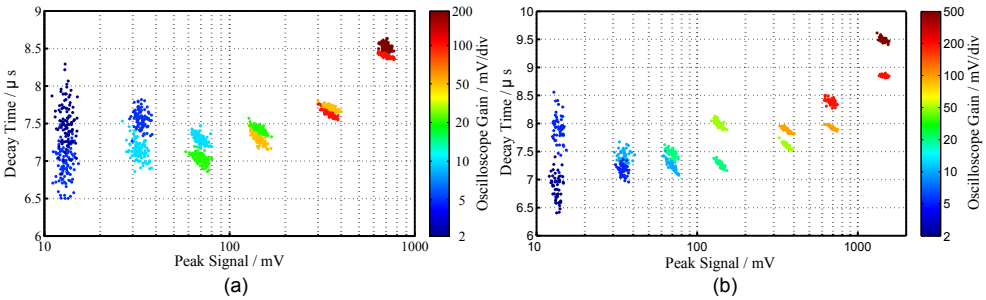

Figure 4.38: *Peak signals of $CdWO_4$ at 294 K versus its evaluated decay times. A colour bar indicates the current voltage/division amplification from the oscilloscope. Part* (a): *the peak signals detected via input channel 2 were increased by increasing the iris diameter of the imaging lens. Part* (b): *the peak signals detected via input channel 3 were and increased by increasing the internal gain of the detector.*

A considerable amount of information is provided by Figure 4.38, not exclusively specific to the distortions caused by the oscilloscope: Distinct clusters of individual colours there show a dependence of the decay time on the peak intensity of the phosphorescence signal. The colours can be associated with certain volts/division settings on the oscilloscope. As expected, the uncertainty of the decay times in such a cluster tends to decrease with an increase in the signal level. In addition, each individual cluster appears to have an uncertainty along the x-axis as well. This is caused by the uncontrollable shot-to-shot variations in the laser pulse energy. An especially interesting observation is that all point clusters, shown in Figure 4.38, possess a negative slope. This slope is another evidence for the dependence of $CdWO_4$ phosphorescence on the excitation energy, a matter discussed earlier (see Figure 4.6, page 52). In evaluating groups of two clusters each of identical colour, either the intensity dependence of the detector (Fig. 4.38 (a)) or the gain dependence of the detector (Fig. 4.38 (b)) can be observed. When one focuses instead on two point clusters of differing colour, that appear at similar peak voltages, the effect of the oscilloscope's zoom setting becomes apparent. In Figure 4.38 (a) one can observe a strong dependence of the signal decay time on the light intensity that impinges on the detector, its causing the decay time to rise regardless of the peak voltage level involved. This tendency was largely counteracted, however, by the effects on the oscilloscope of changing the volts/division, which led to the decay times decreasing (except in the case of the 700 mV point clusters). A change in detector gain, as shown in Figure 4.38 (b), initially caused the phosphorescence decay time to decrease. This tendency became progressively inverted towards

higher peak signals. Unlike channel 2 in (a), changing the mV/div scale from input channel 3 in (b) had the effect of increasing the phosphorescence decay time throughout the entire measurement interval. This observation is particularly unfortunate in the sense that it demands of the operator not only that such effects be compensated for, but also that one has to keep track of which of the channels were used during signal calibration and during the experiment. It is likely that changes in the time/division settings of the oscilloscope suffer from similar signal distortion effects. At this point, however, no such investigation has yet been performed.

(g) Fluorescence Peak Dependence: Unlike $CdWO_4$, decay transients of many thermographic phosphors exhibit a strong, but short-lived peak in the initial part of the signal. Such peaks are highly undesired as they limit the dynamic range of the recorded signal. Since they can be very strong as compared to the actual temperature-dependent phosphorescence afterglow, it is legitimate to wonder whether an intense peak in the initial part of the decay causes additional saturation in the detection line. Thus, an experiment was conducted that included several thermographic phosphors, such as La_2O_2S:Eu, $Mg_3F_2GeO_4$:Mn and ZnO:Zn. These phosphors exhibit different decay times at room temperature, which could play a role in the observed saturation effects. It may be assumed that shorter decays suffer more from highly intense peaks, since detectors can recover over time from a short exposure to high intensities. The recovery times may be short compared to long phosphorescence decays, meaning that only part of the phosphorescence decay could be affected in this way. The phosphorescence signals were registered by a *Hamamatsu* H11526-20-NF PMT. This type of PMT is especially useful for the experimental task here, since it can be operated in a time-gated mode, meaning that the electrical gain can be triggered to be active from a certain point in time on and during a desired timespan. The gate for signal amplification opens with a rise time of 180 ns [165]. Accordingly, if the gate has a sufficiently long gate length and is triggered to open $\geq$ 180 ns before the phosphorescence signal arrives, the PMT operates in a manner similar to a continuous device. However, if the delay between the trigger to open the gate and the arrival of the laser pulse is decreased, the initial part of the phosphorescence signal becomes gradually suppressed by the rising flank of the time gate. Figure 4.39 illustrates the effect, a sliding gate can have on the detected phosphorescence signal. If in addition the evaluation window for the decay time analysis always starts $\geq$ 180 ns after the initial peak of the signal, the peak can be completely suppressed without this affecting the residual part of the signal, where the evaluation of decay times takes place. The signal ratio between the peak $S_{\max}(t = 0)$ and the signal value at the start of the evaluation window $S_{\text{start}}(t = 180\,\text{ns})$ can be expressed through use of Equation (4.23), its changing under the influence of a moving time detector gate.

$$\text{Peak Ratio} = S_{\max}(t = 0)/S_{\text{start}}(t = 180\,\text{ns}) \tag{4.23}$$

A peak ratio of 8, for example means that the initial fluorescence peak is 8 times as strong as the residual phosphorescence is at 180 ns after the peak. In Figure 4.40 (a), the effect of different peak ratios for ZnO:Zn at 294 K in terms of the evaluated decay time is shown. Apparently, the peak ratio does not influence the evaluated decay time

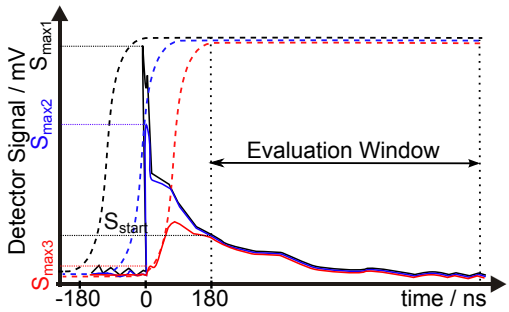

Figure 4.39: *Phosphorescence decay, as affected by a sliding gate with a rise-time of 180 ns. The peak can be suppressed completely without its affecting the signal within the evaluation window.*

within a range of peak ratios between 9 to 3. Once the peak ratio declined further, from 3 towards 2, a slight increase in the evaluated decay time from 72 ns to 75 ns can be observed. This observation in regard to Figure 4.40 (a) was somewhat unexpected: If an effect of signal saturation would have been observed in the fluorescence peak, it should be more likely to occur during the measurement of unsuppressed peaks, such as at higher peak ratios, for example.

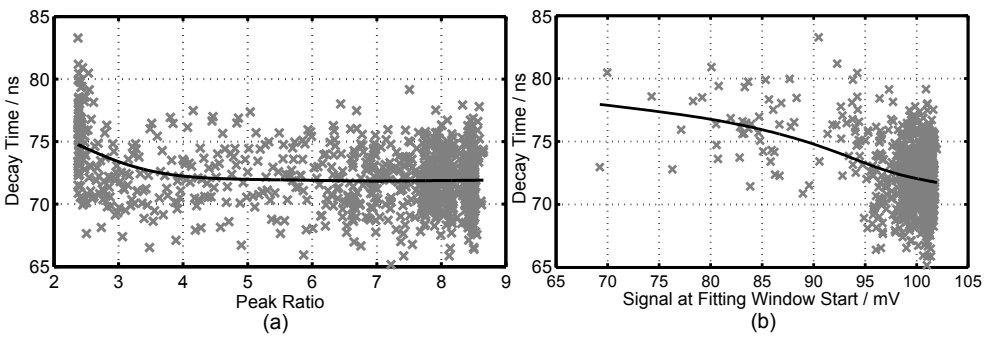

Figure 4.40: *Part* (a)*: Peak ratio vs. evaluated decay time for ZnO:Zn at 294 K when a sliding detector gate is employed. Part* (b)*: $S_{\mathrm{start}}(t = 180\,\mathrm{ns})$ vs. decay time using the same data as in* (a)*. A H11526-20-NF PMT was used and was read out over a 50 Ω resistance.*

The slightly different data representation in part (b) of Figure 4.40 sheds light onto this matter. There, instead of peak ratios, the same dataset is shown by a plotting of the signal voltage $S_{\mathrm{start}}(t = 180\,\mathrm{ns})$ in relation to the evaluated decay time. The trends displayed in Figure 4.40 (b) show clearly that any increase in decay time is associated with a decrease in the signal S_{start}. This decrease only affected a few of the measurements since the main data cluster appears at around $S_{\mathrm{start}} = 100\,\mathrm{mV}$. By the time the peak ratio goes below 3, it appears as if the gate has been moved too far, such that it has started to suppress the initial parts of the signal within the

evaluation window. As a consequence, the initial part of the signal after $t = 180\,\text{ns}$ was suppressed, which had a similar effect on the evaluated decay times as discussed earlier in connection with signal saturation (see Figure 4.31, page 97). Similar experiments, with longer decay times and using other phosphors, resulted in findings comparable to those presented in Figure 4.40. It can thus be concluded that intense fluorescence peaks[15] can occur during experiments without them posing a threat to the temperature accuracy in LIP experiments. Caution should be exercised, however, since the signal response of other detectors can lead to a different outcome of experiments [V].

Prevention of Systematic Errors caused by Non-linear Signal Detection: In section 4.6.5, several experiments were outlined, measuring signal non-linearities in the detection line in the context of systematic temperature errors during LIP experiments. The exact outcome from such measurements, however, appeared to be valid only for the very equipment in use and could differ even for detectors of similar production type. Accordingly, the previous discussions only serve as a means for a general and more qualitative understanding of non-linear signal transformations and their impact on LIP measurements. Nonetheless, the experiments presented here provide examples of how similar tests can be performed for quantifying such effects in various future setup configurations. Due to the sheer magnitude of certain temperature errors (which in some cases can be several tens to hundreds of Kelvin) and a current lack of linear detectors, it appears that signal detection is one of the key sources of measurement error in phosphor thermometry. Different strategies can be followed by operators to avoid or at least decrease the extent of systematic errors caused through non-linear signal detection:

- Non-linearity in detectors is generally not an issue in phosphor thermometry, as long as the signals are affected equally during measurement and calibration: Signal intensities, gains and any additional detector settings may be kept constant at all times during experiments and calibration. The use of beam homogenizers may help avoiding high intensity contrast across images, whereas high laser intensities that are externally attenuated exhibit a higher pulse-to-pulse stability.
- Response tests of gain and light-intensity variations may be performed in order to outline the linear workspace of the detection equipment. This may help avoiding measurement operation in regions of non-linear signal response [IV, VI].
- Once the response of the detection line is known from prior experiments stored in a library, the non-linear workspace may be exploited without causing systematic errors as long as the signals are properly compensated for [V].
- Imaging detectors take simultaneous measurements, one in every pixel. If a certain diversity of signal intensities is produced deliberately during calibration, these signals can be calibrated individually. The simultaneous calibration of a variety of signals provides a simple means of compensating for some of the systematic errors that may come about during an experiment. Further details concerning this approach are presented in Paper [VIII].

[15] Tested: $S_{\max} \leq 1\,\text{V}$ using a H11526-20-NF PMT in conjunction with a $50\,\Omega$-terminated oscilloscope.

4.7 Signal Processing

This section deals with a variety of theoretical considerations, empirical findings and experiments that can assist in the optimization of detection parameters during the recording of thermographic phosphorescence. Also, certain practical advise is given concerning the evaluation and processing of measured phosphorescence data and its conversion into the temperature scale.

4.7.1 Noise Reduction by Signal Averaging

Signal averaging can be used as a means of improving the quality of a signal, but this comes at the cost of reduced resolution. If n independent signals with uncorrelated noise (standard deviation σ) are averaged, the standard deviation of the resulting ensemble σ_n is given by

$$\sigma_\mathrm{n} = \frac{\sigma}{\sqrt{\mathrm{n}}} \tag{4.24}$$

according to the *Central Limit Theorem*. The SNR thus improves by the square root of n.

$$\mathrm{SNR}_\mathrm{n} = \mathrm{SNR} \cdot \sqrt{\mathrm{n}} \tag{4.25}$$

In addition to the increase in SNR, the bit range of digital signals, i.e. the number of signal values permitted, increases virtually through the process of averaging according to Equation (4.26).[16]

$$\mathrm{bit}_\mathrm{n} = \log_2 \left[(2^{\mathrm{bit}} - 1) \cdot \mathrm{n} + 1 \right] \tag{4.26}$$

Example: Imagine a 1-bit data storage, that only allows recorded signals to assume a value of either 0 or 1. The possible outcome for an average of two such signals might then be either 0, 0.5 or 1, whereas an average of 3 such signals could result in virtual signals 0, 1/3, 2/3 or 1. In the latter case, the bit range increases virtually to what corresponds to a 2-bit system.

Signal averaging can be employed as a noise reduction technique in two different ways:

- **Time Averaging** can be used during the measurement of stationary processes to enhance the signal quality. With increasing signal accumulations, the SNR increases in accordance with Equation (4.25). The temporal resolution of the measurement decreases, whereas the spatial resolution of 2D data information remains intact.
- **Spatial Averaging** increases the SNR of data images at the cost of spatial resolution. Locally sharp transitions in the image response are blurred, whereas the repetition rate of the measurement system is left unchanged. Noise filtering techniques based on spatial averaging may be suitable for increasing the SNR during measurements of transient systems that lack small scale details.

The spatial averaging of camera images can be achieved either by binning pixels directly during signal accumulation or by applying software filters to recorded images

[16] Equation (4.26) was discovered by the author through empirical deduction.

during data evaluation. As the camera readout noise is constant, there is a benefit of reduced signal noise when the pixels are binned directly on the camera chip. Pixel binning also decreases the time needed for reading out charges from the chip, which often results in higher camera frame rates.

Paper [VII] concerns a practical investigation of the trade-off between image resolution and temperature precision through use of two-colour image ratios from a BAM-coated surface that was heated to several different temperatures. Temperature profiles of the phosphor surface were generated to be uniform, showing spatial drifts and variations that were maintained below ±1 K, as verified by several K-type thermocouples placed at different surface locations. This established the basis for the assumption of regarding the standard deviation of the different pixel temperatures across the entire image as the overall temperature precision [VII]. The precision was increased by subjecting the original phosphorescence images to spatial smoothing during signal evaluation by means of a Gaussian filter. In order to measure the loss in spatial detail that comes about through the image filtration, a resolution test target such as shown in Figure 4.41 was subjected to an identical filtering procedure.

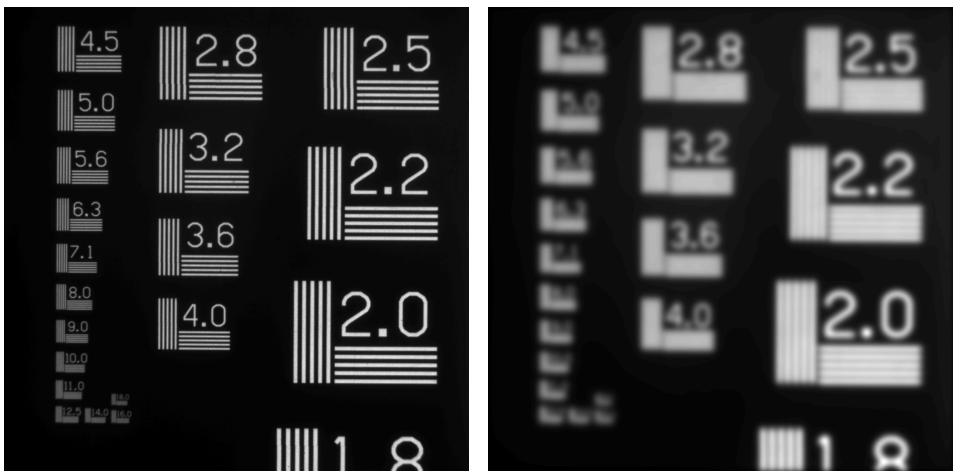

Figure 4.41: *A resolution test target prior to software filtering* [(b), 11 *lines/mm*], *and after software filtering* [(b), 2.2 *lines/mm*], *where the target has been subjected to a Gaussian filter* (*pixel area* = 50 × 50, *FWHM* = 16.5).

As the filter strength increases, the image resolution decreases, whereas the spatial data precision increases. This is illustrated in Figure 4.42, which shows the relationship between the gain in precision and the loss in resolution at each of three different operating temperatures of BAM. As can be seen, the precision at 281 K for the highest resolution (11 lines mm^{-1}) was measured to be ±3.9 K, corresponding to ±1.4 %. Since the phosphorescence images were subjected to spatial filtering, the resolution decreased gradually to 2 lines mm^{-1}, and the precision was increased to ±1.7 K (±0.6 %).

Similarly, for measurements performed at 455 K, the precision extended from ±12.5 K (±2.8 %) at the highest resolution to ±6.5 K (±1.4 %) at the lowest resolution.

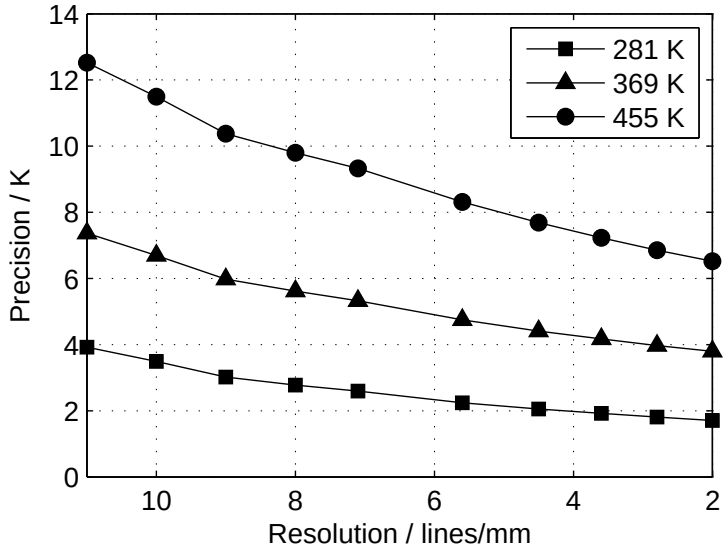

Figure 4.42: *Relation between spatial temperature precision and resolution of the two-colour ratio of BAM at three different temperatures.*

The employment of averaging routines to improve the SNR is highly recommended whenever the spatial or temporal resolution of the measurement system exceeds the requirements for accurately resolving the spatial and transient features of the measurement object. Otherwise, signal averaging should be avoided unless the signal quality is so poor that a trade-off has to be established between an acceptable signal-to-noise ratio and a sufficient image resolution.

4.7.2 Signal Processing and Optimization for Two-Colour Image Ratios

This section takes up signal processing issues that are specific to the evaluation of temperatures with use of two-colour image ratios. After describing several image corrections procedures (a), a number of considerations regarding the relationship between the intensity level and signal noise are examined from an error propagation point of view (b). In addition, an approach for combining spectral- and temporal phosphorescence thermometry is described in (c), and finally the effect of the fitting function on the calibration plot is discussed (d).

(a) Image Corrections: A number of image corrections are necessary for obtaining an image of intensity ratios from the overlap of two simultaneously recorded phosphorescence images. The following correction procedures are recommended for (1) reducing the effect of spurious signal contributions, (2) compensating for local variations in the detector sensitivity and (3) achieving an adequate overlap of images.

1. **Background Correction:** Dark noise, scattered light and interfering reflections can result in systematic errors through introducing non-resonant signal offsets. Hence, a background image BG should be recorded for each detector in the absence of the phosphorescence signal. It is of importance that background signals are recorded under identical circumstances in each case, in terms of ambient light, gain, exposure time, filters, etc., since the measurement images should be identical.

2. **Flat–Field Correction:** This correction involves obtaining a reference measurement at a uniform intensity that can be used to normalize the signals that are detected. The aim is to compensate for errors from variable detector sensitivities. It applies whenever different detectors or pixels are involved in the generation of individual intensity ratios, as was the case in the experimental setup presented earlier in Figure 3.6, page 25. To normalize camera images and account for different detection sensitivities, a flat-field image FF should be recorded. This usually involves use of a diffuse and highly uniform light source, such as provided by an integrating sphere (or Ulbricht sphere). Depending upon the detector employed, it may be that the flat-field correction is wavelength dependent and is affected by optical components located between the camera and the object, not least of all by the objective lens of the camera. It is thus advisable to keep interference filters mounted on the camera during the recording of flat-field images. Doing so enables possible inhomogeneities in the filter transmission to be taken into account. During the recording of FF images, it is advisable to maintain identical gain settings on the camera, just as during the measurements. In order to achieve light levels from the Ulbricht calibration light source that are similar to those obtained during the measurement, the camera exposure time can be varied instead. One should also note, that individual background corrections are necessary for all flat-field images.

3. **Image Registration:** In order to generate an image of pixel ratios from two independently achieved images, a perfect overlap of the two images needs to be obtained. Thus, it is necessary to perform a number of image transformations on at least one of the images. These corrections concern alignment errors, such as displacements, distortions of perspective and rotations, as well as barrel or pillow distortions caused by the optical equipment in use. Image registration is important in applications involving inhomogeneous intensities and/or temperature distributions in which significant variations in ratios are expected through imperfect image overlaps. Suitable reference images need to be recorded, these providing an object in the image plane possessing a recognizable pattern. Such objects can be either a grid of lines or of points. Their patterns aid in identifying a dense grid of reference points in each image, which dewarping tools (such as *cp2tform* in MATLAB) can use as input parameters to perform a transformation. The transformations are more accurate if a point target is used in combination with an automated reference point selector. This requires a high degree of image contrast and the absence of intensity gradients, however. The latter state can be achieved by means of a flat-field correction of the grid image, for example.

Figure 4.43 illustrates the process of image transformation, based on control point selection in a grid image: A camera equipped with a stereoscope was used here to record two images of a burning candle.

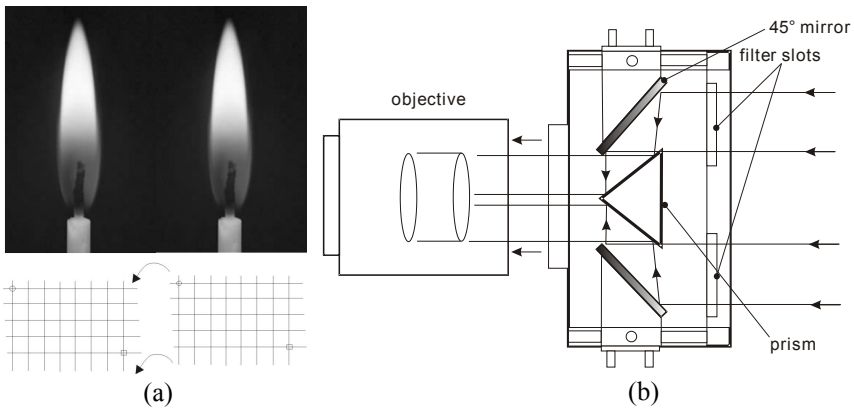

Figure 4.43: *Part* (a): *Image transformation using control points selected from a previously recorded grid image. Part* (b): *A schematic sketch of a stereoscope that was used to record a double image of a burning candle.*

It should be noted that dewarping routines that achieve subpixel alignment need to interpolate between the intensities of the neighbouring pixels. This results in a loss in resolutions in the image, which is perceived as a smearing of the distinct image structures [148]. In contrast, deliberate spatial averaging of highly structured image information prior to the registration process can limit the susceptibility to errors of two-colour ratios caused by imperfect image overlaps.

Equation 4.27 summarizes the aforementioned corrections of the two-colour image ratio (compare to Eq. (3.9), page 24). The superscript "*tr*" was used to identify the transformed images.

$$R(T) = \left(\frac{S_{\lambda_1}(T) - BG_{\lambda_1}}{FF_1 - BG_{FF_1}}\right) \cdot \left(\frac{[FF_2 - BG_{FF_2}]^{tr}}{[S_{\lambda_2}(T) - BG_{\lambda_2}]^{tr}}\right) \tag{4.27}$$

Note that it is not important whether image 1 or image 2 is transformed in Equation (4.27) to match the other image. Ideally, both images should be transformed so as to comply with a dewarped grid image in order to not only achieve a good overlap, but also remove most of the image distortions.

(b) Signal Level and Noise: In measurements using the two-colour-ratio technique, the temperature precision is expected to increase with increasing signal levels. An intuitive confirmation of this assumption can be obtained in estimating the error of the intensity ratio ΔR, which is generated by measurement errors on the two contributing signals ΔS_1 and ΔS_2 ($R = S_1/S_2$):

$$\Delta R = \sqrt{\left(\frac{\Delta S_1}{S_2}\right)^2 + \left(\frac{S_1 \cdot \Delta S_2}{S_2^2}\right)^2} = \frac{\sqrt{(S_2 \cdot \Delta S_1)^2 + (S_1 \cdot \Delta S_2)^2}}{S_2^2} \tag{4.28}$$

Since S_1 and S_2 are interconnected via $S_1 = R \cdot S_2$ with $R = \text{const.} \Leftrightarrow T = \text{const.}$, Equation (4.28) can be further simplified to

$$\Delta R = \frac{\sqrt{\Delta S_1^2 + (R \cdot \Delta S_2)^2}}{S_2} = \frac{R\sqrt{\Delta S_1^2 + (R \cdot \Delta S_2)^2}}{S_1} \tag{4.29}$$

Example: To analyse Equation (4.29) further and gain insight into the scaling of the ratio error together with the signal errors, two special cases are considered here:

- In situations in which the signal noise does not scale with the signal intensity ($\Delta S_1 = \text{const.}$ and $\Delta S_2 = \text{const.}$), for example if the signal noise is limited by either dark noise or readout noise, the error of the ratio scales with $1/S$.
- When one assumes the noise to be limited by the shot noise, i.e. $\Delta S_1 = \sqrt{S_1}$ and $\Delta S_2 = \sqrt{S_2}$, Equation (4.29) can be rewritten and further simplified to

$$\Delta R = \sqrt{\frac{R \cdot (1 + R)}{S_2}} = R \cdot \sqrt{\frac{1 + R}{S_1}}$$

  Hence, the error of the ratio in this scenario scales with $1/\sqrt{S}$.

Figure 4.44 shows experimental results of two-colour ratios obtained from BAM phosphorescence at 473 K, these being plotted against one of the background-corrected camera signals [VIII].

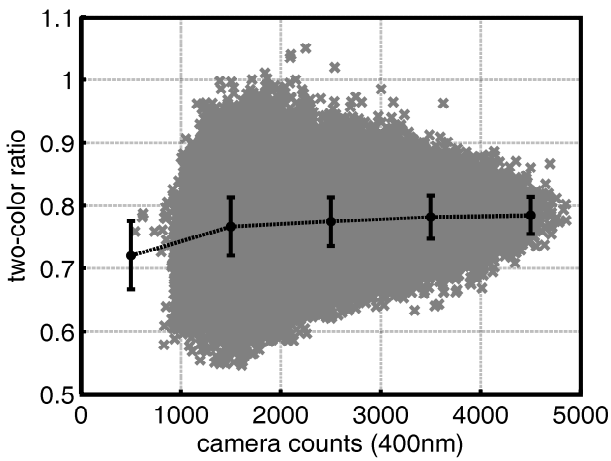

Figure 4.44: *Two-colour pixel ratios of BAM, expressed as a function of background-corrected signal intensity from a 400 nm centred camera image, recorded at an object temperature of 473 K. The black markers correspond to the average ratio within an intensity interval of ±500 counts. Their corresponding error bars show the ratio precision, expressed in terms of one standard deviation.*

A higher ratio variation is visible at the beginning of the plot, where signal intensities are low and image noise has a higher impact on the signal ratio. Hence, Figure 4.44

provides an experimental confirmation of the increase in precision that can be achieved by working at higher signal levels. The entire spread of the ratios within the plot extends from 0.55 to 1.05, which corresponds to a very high virtual temperature range of more than 100 K. In terms of variations in the pixel ratio, the total temperature spread decreases by more than a factor of 3 when instead only the highest 10 % of the camera counts are considered. Another observation related to Figure 4.44 is that of the ratio going up as the camera counts increase. This can be attributed to the non-linear signal response of the camera and agrees well with the predictions made in Figure 4.28 (page 94). In order to utilize the reduced statistical error of the image ratios that comes with higher signal values, systematic errors in the non-linear signal response of the camera need to be compensated for. One relatively simple and effective way to achieve this is to calibrate two-colour ratios separately according to their approximate pixel count value, as proposed in Paper [VIII].

The previous discussion suggests that high signal levels contribute to a low ratio error. Such signal levels can be achieved by various combinations of optical signal intensity and electrical gain. In general, it can be expected that high light intensities together with little electrical amplification results in the measurement errors for the signal S being smaller than with a combination of low light intensity and high gain. This is due to all useful information being stored in the optical signal, meaning that electrical signal amplification only scales the signal, without its effectively creating more information. Nonetheless, electrical signal amplification is very useful nevertheless in various situations, such as

- when the readout signal needs to be increased while the photocathode is at risk of optical saturation,
- or when the signal noise is limited mainly by the A/D converter.

Although no experimental proof is provided here to confirm these statements regarding two-colour image ratios, a similar relation between gain and light intensity for amplified point detectors is presented in Figure 4.48, page 121.

(c) Time-delayed Spectral Ratios: An interesting idea was developed in a recent study [14,70], its proposing to introduce a fixed time delay of one of the colour-filtered camera images relatively to the other in an attempt to increase the sensitivity of the two-colour ratio method. Such a time delay may be short in comparison with the exposure time of the image, but since decay times often become significantly shorter as temperatures increase, the loss in signal intensity in one of the images, due to the delay being introduced, increases with temperature. Such an approach can be seen as representing a combination of the intensity-ratio method and the decay time method. Depending upon the length of the delay and the changes in phosphorescence decay time produced by changes in temperature, introducing a time delay between the two images results in the intensity ratio coming to span an extended range for the temperature interval in question. Figure 4.45 shows a ratio calibration chart of BAM as affected by various time delays between the two camera images.

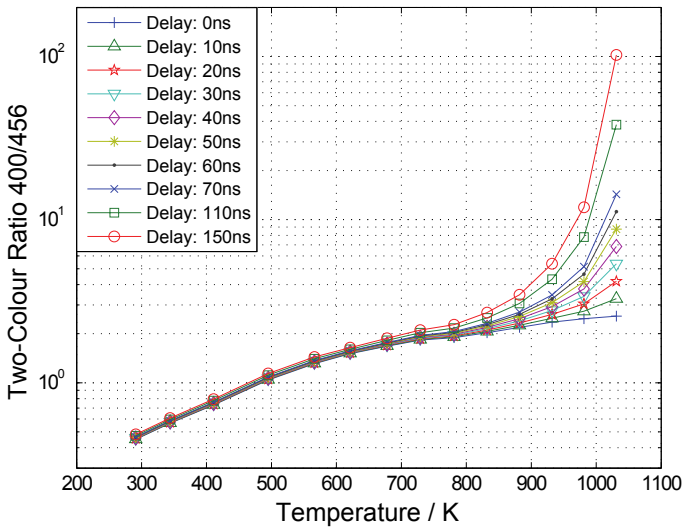

Figure 4.45: *Simulated effects of delaying one camera when performing two-colour ratio measurements on BAM, taken from [70] and replotted with the permission of Dr. G. Särner. The ratio of 400 nm to 456 nm is assumed for an exposure time of 10 µs. Different markers show alterations in the signal ratio, due to the exposure of the 456 nm image becoming progressively delayed.*

At the expense of signal level for one of the camera images, Figure 4.45 demonstrates the possibility of increasing the interval of temperature-calibrated image ratios. The introduction of a 150 ns time delay increased the maximum ratio value from 2.7 to about 100, which vastly improved the dynamic range of the intensity ratio within the given temperature interval.

Unfortunately, this increase in the range of the spectral ratios found does not improve the temperature sensitivity of the phosphor, as one might think at first glance. Instead, just the opposite is true, as the following calculations demonstrate. **It is** thus **not recommended to employ such an approach.** In general terms, the introduction of a time delay has a different effect on the calibration plot at one end of the temperature scale than compared to the other end:

1. For low temperatures that result in phosphorescence decay much longer in duration than the time delay which is introduced, the two-colour ratio remains largely unchanged, i.e. $R(T_{\mathrm{min}}) \rightarrow R'(T_{\mathrm{min}}) \approx R(T_{\mathrm{min}})$ (see Fig. 4.45)

2. At high temperatures, the introduction of a time delay increases the signal ratio (see Fig. 4.45) to a degree that can be expressed by the factor m, i.e. $R(T_{\mathrm{max}}) \rightarrow R'(T_{\mathrm{max}}) = m \cdot R(T_{\mathrm{max}})$. This increase in the ratio was achieved by decreasing one of the camera signals by a factor of m; see Equation (4.30).

$$R' = \frac{S_1'}{S_2'} = m \cdot R = \frac{S_1}{\frac{1}{m} \cdot S_2} \tag{4.30}$$

According to Equation (4.31) the abovementioned consequences result in the range of the temperature-calibrated signal ratios increasing by a factor f, where $0 < f \leq m$.

$$\left(\frac{R'_{\text{Range}}}{R_{\text{Range}}} = \frac{m \cdot R(T_{\max}) - R(T_{\min})}{R(T_{\max}) - R(T_{\min})} = f \right) \leq m \tag{4.31}$$

In order to evaluate whether or not the increased dynamic range of the signal ratios R_{Range} results into an increased temperature precision ΔT_{Prec}, use can be made of Equation (4.4) (page 48) presented earlier:

$$\Delta T_{\text{Prec}} = \frac{\Delta R}{R_{\text{Range}}} \cdot T_{\text{Range}}$$

By combining equations (4.4) and (4.31), the ratio of temperature precisions between the original and the enhanced ratio calibration can be obtained.

$$\left(\frac{\Delta T_{\text{Prec}}}{\Delta T'_{\text{Prec}}} = \frac{\Delta R}{R_{\text{Range}}} \cdot \frac{R'_{\text{Range}}}{\Delta R'} \cdot \frac{T_{\text{Range}}}{T_{\text{Range}}} = \frac{\Delta R}{\Delta R'} \cdot \frac{R'_{\text{Range}}}{R_{\text{Range}}} \right) \leq m \frac{\Delta R}{\Delta R'} \tag{4.32}$$

Equation (4.32) allows the temperature precision to be maintained as long as the absolute error of the signal ratio for a time-delayed case does not increase by more than a factor of m in comparison to the original ratio error.

$$\Delta T'_{\text{Prec}} = \Delta T_{\text{Prec}} \quad \Rightarrow \quad \Delta R' \leq m \cdot \Delta R \tag{4.33}$$

When it instead is the relative error which is taken account of, equations (4.30) and (4.33) yield the following expression

$$\Delta T'_{\text{Prec}} = \Delta T_{\text{Prec}} \quad \Rightarrow \quad \left(\frac{\Delta R'}{R'} = \frac{\Delta R'}{m \cdot R} \right) \leq \left(\frac{m \cdot \Delta R}{m \cdot R} = \frac{\Delta R}{R} \right), \tag{4.34}$$

which states that in order to maintain measurement precision the relative error of R needs to decrease as a result of the time delay that has been introduced. It is thus sufficient here to analyse the change in the relative ratio error in response to the introduced time delay, which effectively decreases one of the camera signals. The relative error of the two-colour ratio, which is given by Equation (4.35), can be obtained by dividing Equation (4.28) (page 112) by R.

$$\frac{\Delta R}{R} = \sqrt{\left(\frac{\Delta S_1}{S_1} \right)^2 + \left(\frac{\Delta S_2}{S_2} \right)^2} \tag{4.35}$$

If $S'_2 = \frac{1}{m} S_2$ is entered into Equation (4.35), the altered ratio error $\Delta R'/R'$ can be expressed as

$$\frac{\Delta R'}{R'} = \sqrt{\left(\frac{\Delta S'_1}{S'_1} \right)^2 + \left(\frac{\Delta S'_2}{S'_2} \right)^2} = \sqrt{\left(\frac{\Delta S_1}{S_1} \right)^2 + \left(m \cdot \frac{\Delta S'_2}{S_2} \right)^2} \tag{4.36}$$

Since the relative ratio error of the time-delayed measurement needs to be less than the relative ratio error of the unaltered measurement (see Eq. (4.34)), a comparison of Equation (4.35) with Equation (4.36) yields

$$\Delta T'_{\mathrm{Prec}} = \Delta T_{\mathrm{Prec}} \;\Rightarrow\; \frac{\Delta R'}{R'} \leq \frac{\Delta R}{R} \;\Leftrightarrow\; \frac{\Delta S'_2}{S'_2} \leq \frac{\Delta S_2}{S_2} \overset{S'_2=\frac{1}{m}S_2}{\Leftrightarrow} \Delta S'_2 \leq \frac{1}{m}\Delta S_2 \quad (4.37)$$

In order to expect an enhanced temperature precision for measurements that increase the dynamic range of two-colour ratios over a fixed range of calibration temperatures, one would need to assume the relative error of the camera signals to decrease with decreasing signal intensities. In other words, the temperature precision of the calibration only has a chance of improving if the camera-signal noise ΔS scales with $\Delta S \sim S^p$ $(p > 1)$. This assumption, does not hold in practise, however, since the SNR generally improves with signal intensity. Therefore, combining the spectral-image-ratio approach with the temporal decay time technique (as presented in Figure 4.45), unfortunately, degrades the overall temperature precision of the experiment.

(d) Temperature Calibration Fit and Measurement Uncertainty: The choice of a proper model R_{model} for fitting the measurement points in temperature calibration charts is of basic importance for measurement accuracy and also affects the temperature precision of phosphor thermometry measurements. In this context, a brief experimental study of the temperature calibration of uniformly distributed two-colour image ratios of BAM was performed, its being published in Paper [VIII]. The most important conclusions drawn from that study will be summarized below.
Before the effect of the fitting model on the temperature precision and accuracy can be discussed, a number of definitions need to be clarified: For a homogeneously illuminated camera image containing N pixels, the image-ratio precision $\Delta R_{\mathrm{prec}}(T_0)$ at a given temperature T_0 can be defined by the spatial standard deviation as

$$\Delta R_{\mathrm{prec}}(T_0) = \sqrt{\frac{1}{\mathrm{N}-1}\sum_{\mathrm{i}=1}^{\mathrm{N}}(R(T_0) - R_{\mathrm{i}}(T_0))^2}. \quad (4.38)$$

In this relationship, $R(T_0)$ denotes the arithmetic mean of all the individual image ratios $R_{\mathrm{i}}(T_0)$. Depending upon the fitting model R_{model} that best describes the relationship between calibration temperatures and the measured imaging ratios, the temperature precision can be linked to the ratio precision in (4.38) by Equation (4.39)

$$\Delta T_{\mathrm{prec}}(R(T_0)) \approx \left|\left(\frac{\partial T_{\mathrm{model}}(R)}{\partial R}\right)_{R(T_0)}\right| \cdot \Delta R_{\mathrm{prec}}(T_0), \quad (4.39)$$

In which $T_{\mathrm{model}}(R)$ is the inverted ratio model relationship R_{model} that was used to fit the data points in the ratio calibration plot. For describing the relationship between the temperature and the two-colour ratio in the temperature calibration chart shown in Figure 4.46 (a), two different model equations were employed:

1. The first approach (the dotted line in Figure 4.46 (a)) describes the correlation between temperature and the two-colour ratio as linear, using a slope factor $a_1 = (261.0 \pm 4.3) \cdot 10^{-5}\,\mathrm{K}^{-1}$ and a displacement constant of $a_0 = (-47.2 \pm 1.6) \cdot 10^{-2}$, as

$$\begin{aligned} R^{\mathrm{lin}}_{\mathrm{model}} &= a_1 T + a_0 \\ \Rightarrow\ T^{\mathrm{lin}}_{\mathrm{model}}(R(T_0)) &= \frac{R^{\mathrm{lin}}_{\mathrm{model}} - a_0}{a_1} \end{aligned} \tag{4.40}$$

2. The second approach (the solid line in Figure 4.46 (a)) uses a quadratic least-squares fit instead, its resulting in the fitting constants $a_2 = (22.5 \pm 2.7) \cdot 10^{-7}\,\mathrm{K}^{-2}$, $a_1 = (9.1 \pm 2.1) \cdot 10^{-4}\,\mathrm{K}^{-1}$ and $a_0 = (-16.1 \pm 3.9) \cdot 10^{-2}$:

$$\begin{aligned} R^{\mathrm{quad}}_{\mathrm{model}} &= a_2 T^2 + a_1 T + a_0 \\ \Rightarrow\ T^{\mathrm{quad}}_{\mathrm{model}}(R(T_0)) &= \frac{\sqrt{a_1^2 + 4a_2(R^{\mathrm{quad}}_{\mathrm{model}} - a_0)}}{2a_2} \end{aligned} \tag{4.41}$$

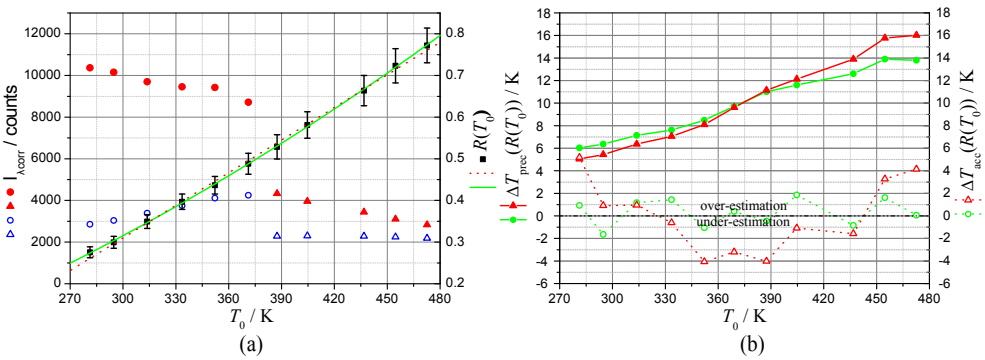

Figure 4.46: *Part* (a): *Temperature calibration plot for two-colour ratios of BAM (right y-axis). On the left y-axis, averaged signal intensities are shown that were used to calculate the signal ratio. Part* (b): *Temperature precision* (●/▲) *and accuracy* (○/△) *achieved by the two fitting models, as displayed by the solid and dotted line in* (a). *The* △*-markers in* (a) *correspond to the linear fitted model (4.40) and the* ○*-markers to the quadratic model (4.41).*

In order to calculate the temperature precision $\Delta T_{\mathrm{prec}}(R(T_0))$ from the ratio precision $\Delta R_{\mathrm{prec}}(T_0)$, model equations (4.40) and (4.41) need to be inserted into (4.39). This yields the temperature precisions according to Equation (4.42) for the linear case and Equation (4.43), when the quadratic model is employed:

$$\Delta T^{\mathrm{lin}}_{\mathrm{prec}}(R(T_0)) = \frac{\Delta R_{\mathrm{prec}}(T_0)}{a_1} \tag{4.42}$$

$$\Delta T^{\mathrm{quad}}_{\mathrm{prec}}(R(T_0)) = \frac{\Delta R_{\mathrm{prec}}(T_0)}{\sqrt{a_1^2 + 4a_2(R^{\mathrm{quad}}_{\mathrm{model}} - a_0)}} \tag{4.43}$$

In addition, the temperature accuracy ΔT_{acc} of a calibration model was defined by its capability to reproduce a calibration temperature T_0 from its corresponding image ratio $R(T_0)$.

$$\Delta T_{\mathrm{acc}}(R(T_0)) = T_{\mathrm{model}}(R(T_0)) - T_0, \tag{4.44}$$

This assumes a positive value when the model overpredicts the calibration temperature and gives a negative value for underpredicted temperatures. From these equations it can be concluded that the choice of a fitting model for calibration plots affects not only the accuracy of measurement results, but also the precision of the temperature obtained.
Figure 4.46 (b) shows a comparison between the linear model (▲/△) and the quadratic model (●/○) for the two-colour ratio of BAM regarding temperature precision (▲/●) and accuracy (△/○). The temperature precisions were calculated using (4.42) and (4.43), whereas the accuracies were derived by inserting equations (4.40) and (4.41) into (4.44). In Figure 4.46 (b), the temperature precision of the quadratic model shows there to be a weaker temperature dependence than with the linear model, the precision being slightly inferior there for the low calibration temperatures. On average, however, the temperature precision of the quadratic model is 0.2 K higher, extending from 6 K up to 14 K across a temperature interval of 200 K. The quadratic model shows a clear improvement in temperature accuracy as compared with the linear model, its having an average error of 1 K instead of 3 K. However, the overall measurement uncertainty appears to be limited by the temperature precision, caused by the spread of pixel ratios across the calibration images.

It should be noted that increasing the order of a fitting polynomial always improves the agreement between the measured data points and the fitted function. For this reason, the temperature accuracy at fixed calibration points can be expected to improve during the transition to more complex fitting polynomials. Employing a high order fitting polynomial, however, is often not meaningful, since high-order polynomials tend to oscillate between the measured data points and thus contain values that are implausible. The principle of parsimony suggests that in the case of multiple solutions to a problem one is obliged to choose the simplest one that still takes account of all important details. In many cases it can be prudent, therefore, to rely on interpolation algorithms that manage to describe physical trends of many kinds without producing undesired oscillations. Nevertheless, analysing the two previously presented fitting examples enabled better insight into the basic effects of different calibration models on temperature uncertainty in phosphor thermometry.

4.7.3 Signal Processing and Optimization for Phosphorescence Decays

Unlike signal optimization for two-colour ratios, which is based on a simple quotient of two signal quantities, the optimization of decay signals is more complex. It is involving the use of non-linear least-squares fitting procedures, that are applied to custom-defined sections of the signal vector that is recorded. To optimize the temperature precision of time-based phosphor thermometry, it is not only of interest to study how signal intensities and noise (a) enter into the equation, but it can also be worthwhile

to investigate how many vector elements need to be sampled (b) for each signal transient. In addition, phosphorescence decays can be analysed in various different ways, including use of multi-exponential (c) or single-exponential (d) approaches. Finally, the temperature sensitivity of phosphorescence decays was found to change, depending upon the part of the signal transient which is chosen for signal evaluation (e).

(a) Signal Level and Noise: Similar to the findings for signal level and noise in two-colour ratio applications, the relative precision of temperature measurements increases with increasing signal levels. Figure 4.47 shows an example of four different $CdWO_4$ phosphorescence decay curves, recorded at room temperature and characterized in terms of signal noise. During the recording of these curves, light intensity and electrical gain were set to binary states of either high or low, allowing for four unique combinations represented by four individual decay transients. Each of these decay signals was fitted by a smoothing spline polynomial, the residuals to the fit being plotted once over time and being collected once in histograms.

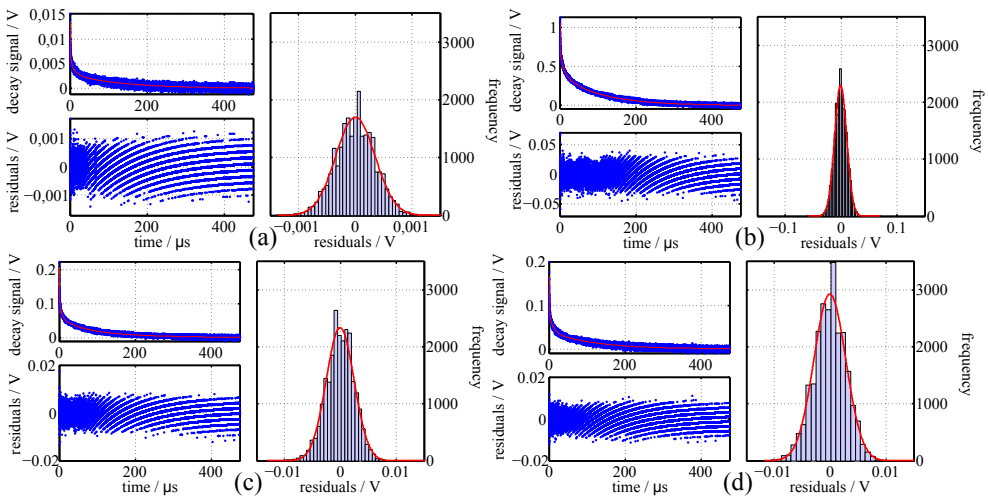

Figure 4.47: *Noise distributions obtained from four $CdWO_4$ phosphorescence decays at 294 K. Each decay was fitted, the residuals being analysed in separate histogram plots. Different combinations of gain (G) and intensity (I) were employed during signal recording.* (a): *low G, low I;* (b): *high G, high I;* (c): *low G, high I;* (d): *high G, low I.*

Figure 4.47 shows the noise amplitude to be distributed equally over time, without the intense part at the beginning of the signal and the signal tail differing. Corresponding histogram plots show the noise to follow closely a normal distribution. A comparison of the different curves in Figure 4.47 shows the signal-noise scales to represent approximately 5 % of the initial peak value. The line structure that is apparent in the residual plots marks the vertical resolution limit of the oscilloscope. It is of interest to note that all of the residuals stretch across approximately 10 lines, meaning that the scaling

of the signal on the oscilloscope must have been similar for all four phosphorescence curves in Figure 4.47. Taking into account the noise having been found on the order of ±5 % of the peak signal, the curve must have been scaled to 80 % of the vertical display axis on the 8-bit oscilloscope. Figure 4.47 is based on two contradictory observations.

1. The noise level in each curve is constant, even though each transient is comprised of a variety of signal levels.

2. When several curves with different peak levels are compared, the residuals are found to vary in proportion to the curve maximum.

The only viable explanation of this behaviour is that of the noise level being dominated primarily by the oscilloscope and its y-axis scaling. In addition, a careful observer can note a slight advantage here of operating at high light levels and low gain rather than the same signal intensity being achieved by low intensity and high gain (compare the fits at the tail of the histogram for the lower two images in Fig. 4.47).
This observation is confirmed in Figure 4.48 (a), displaying the results of investigations in which similar peak levels for $CdWO_4$ curves at room temperature were achieved by different combinations of gain and light intensity. Instead of looking at amplitudes of physical noise in the signal, as before, this time the relative decay time standard deviation of 100 curves was evaluated and was expressed in percentage, this providing more direct insight into the potential consequences for temperature precision that can be expected for variations in gain and intensity. As indicated in part (b) of Figure 4.48, each type of marker in (a) corresponds to a certain peak signal value.

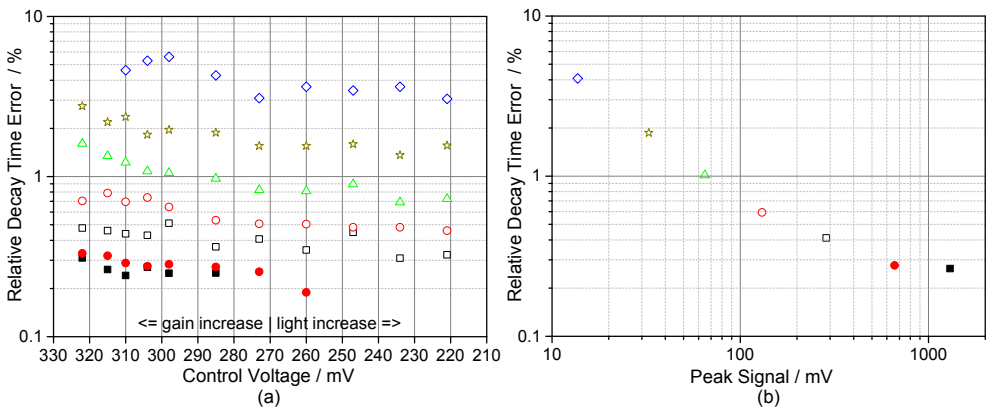

Figure 4.48: *Relative decay time errors of $CdWO_4$ signals at 294 K. In* (a)*, each type of marker corresponds to a certain peak signal and is achieved by several combinations of PMT gain and light intensity. Part* (b) *shows the average y-axis value of each marker type from* (a)*, this corresponding to their particular peak voltage* (*see x-axis*) *as read out over a* 50 Ω *resistor on the oscilloscope.*

There is a general tendency to be noted in Figure 4.48 (a) for there to be a slight decline in the relative decay time error when the PMT gain is decreased in favour

of an increase in light intensity. Primarily, however, the relative decay time error is related to the signal level; as seen in Figure 4.48 (b). The highest precision with a standard deviation of less than 0.27 % was reached for peak signals above 700 mV (read out over a 50 Ω resistor on the oscilloscope), whereas the lowest precision was reached for signals on the order of 14 mV having a precision of 4 %. One should bear in mind, however, the fact that phosphorescence curves with peak signals above 100 mV are likely to be biased by significant non-linearities in the detection line and need to be either avoided or properly compensated for.

(b) Vector Length and Bit-Range: Another interesting point of investigation is that of the trade-off between the vector length of a decay time transient and the precision of the evaluated decay time. In its simplest form, the length of a signal vector needs to be greater or equal to the number of unknown fitting parameters. A three-parameter fit of the initial intensity, the offset constant and the phosphorescence decay time thus technically requires there being a signal vector containing a minimum of three elements. However, if signal noise is present, as in every applied measurement, a vector of three noisy elements would result in a rather poor precision of the fitting parameters obtained. Since minimizing of the least squares between signal vectors and a fitted function is a non-trivial process, the discussion that follows involves use of statistics from simulated decay transients rather than performing an analytical assessment. Single-exponential decays with added Gaussian noise were simulated, such that three different signal-to-noise ratios were obtained. In addition, a large variety of different vector lengths were created in ensembles of 100 individual decay transients per SNR value and per vector length. Each signal from an ensemble was fitted individually to a single-exponential decay function, such that the relative statistical variation of the decay times that were obtained could be studied as a function of SNR and of vector length.

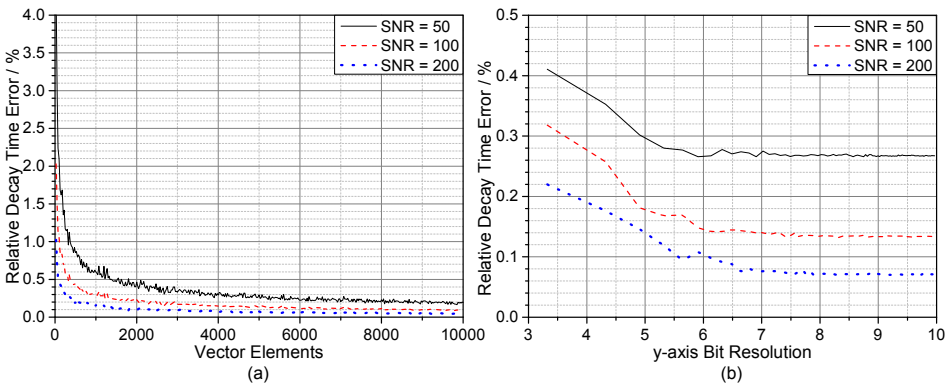

Figure 4.49: *Relative standard deviations of fitted decay times from simulated single-exponential phosphorescence transients with Gaussian noise being added. Part* (a) *shows the effects of the vector length as recorded on the relative standard deviation of the fitted decay times. In part* (b)*, the vector length was fixed to 4000 elements, their y-axis resolution there being changed instead.*

In Figure 4.49 (a), the relative standard deviations of the decay times is shown as a function of the vector elements of three different signal-to-noise ratios. An obvious and expected observation one can make regarding Figure 4.49 (a) is that the relative decay time error decreases with increasing signal quality. The decay time uncertainty also decreases when the number of vector elements in the decay transient increases. Interesting enough, the measurement precision does not appear to stabilize once some critical number of vector elements is exceeded. Even though reaching the point at which the slope of the dependencies displayed exceeds a value of -1 requires fewer vector elements at higher SNRs, it appears that determining the criterion for deciding on the number of vector elements the transients should be based on the trade-off between measurement precision vs. both file size and sampling speed. Part (b) in Figure 4.49 concerns a similar investigation of simulated signals at three different signal-to-noise ratios. Although here the vector length was fixed to 4000 elements, the y-axis resolution of the decay transients was varied by gradually increasing the bin size on the y-axis. In a way, part (b) complements the investigation of part (a) by sparsing the decay time transients in y-direction, whereas Figure 4.49 represents a sparsing in x-direction. Unlike the results shown in Figure 4.49 (a), part (b) shows the relative decay time error reaching a stable minimum for detectors that possess a y-axis resolution of 6 to 7 bits. It appears that low SNRs stabilize at lower y-axis resolutions simply because their noise amplitudes exceed the bin size on the y-axis much earlier than decay transients with high signal-to-noise ratiosdo. Since in most practical situations SNRs rarely exceed values of 100, there is no appreciable benefit to be expected through upgrading an 8-bit oscilloscope to one with 12-bits, for example.[17]

(c) Multi-Exponential Decay Analysis: In this paragraph, different approaches for the retrieval of temperatures from a given set of recorded phosphorescence intensity decays are discussed and compared. Phosphor scientists are usually confronted with the decision of whether to evaluate multi-exponential decays with the problem of finding a way of assigning calibration temperatures to a number of model parameters or instead to employ evaluation windows chosen in such a way that the decay time of a mono-exponential model can be fitted suitably to the recorded waveform.
In section 3.1.6 (page 19), a decrease in phosphorescence emission over time was explained in terms of the electron population of an excited state in a two-level system. In such an idealized system, the signal intensity over time decreases exponentially according to Equation (3.4). Most thermographic phosphors, however, are not necessarily best described in terms of a single-exponential decay rate and may instead exhibit an entire spectrum $J_0'(\tau)$ of decay components. These components can either stem from intrinsic material properties of the phosphor or be caused by thermal gradients across the film thickness of the phosphor coatings (see section 4.4.3, page 68). A generalized expression for multi-exponential decays is given by Equation (4.45).

$$J'(t) = \int_0^\infty J_0'(\tau) \cdot \exp\left(-\frac{t}{\tau}\right) \mathrm{d}\tau \tag{4.45}$$

[17] An exception to this statement is, of course, if experimenters are forced to keep the interesting part of the signal limited to only a small fraction of the actual screen size.

In cases in which the spectral function $J_0'(\tau)$ can be viewed as a sum over n discrete delta functions, Equation (4.45) can be rewritten as

$$J'(t) = \sum_{i=1}^{n} J_{0i}'(\tau) \cdot \exp\left(-\frac{t}{\tau_i}\right), \tag{4.46}$$

which again simplifies to a single-exponential decay function if $n = 1$. Since the signal ratio between two or more decay constants increases over time, the probability of resolving two similar decay constants from a measured signal increases if decay transients are monitored for as long as the signal amplitude exceeds the noise level. In practical applications, however, the SNR rarely exceeds 100 and is often limited by the experimental equipment.

Example: An experimental setup using an 8 bit oscilloscope digitizer (such as the *LeCroy Waverunner WA6030*) can only deliver SNRs of $2^8 \leq 256$. In such a case, it is not meaningful to record decay transients for time spans longer than $\ln(256) \approx 5.5$ decay times, unless the signals involved are averaged over time.

An attempt to resolve individual decay constants beyond the resolution limits of the detection system results in ambiguous and unreliable results, since variation in one of the decay rates might be compensated for by some other amplitude variation, and vice versa [172]. Due to this restriction, which affects most experimental situations in practical terms, multi-exponential analysis of decay rates provides very limited versatility in regard to related practical applications and is thus rarely employed in phosphor thermometry. Further information regarding the basic limitations of multi-exponential analysis and its resolution limit can be found in Istratov's and Vyvenko's review paper [172], which also features a comprehensive overview of algorithms for multi-exponential curve analysis.

(d) Single-exponential Decay Time Analysis: A more frequently used approach to the decay analysis in phosphor thermometry is the fitting of a mono-exponential model to experimental decay transients, where the decay time τ can directly and without confusion be attributed to a corresponding calibration temperature. Unlike multi-exponential curve analysis, reducing the number of model parameters involved to the initial signal intensity, the decay time and possibly an offset constant, enables non-ambiguous curve fitting within a chosen time interval (evaluation window) to be carried out. A large variety of methods are available for the fitting of single-exponential functions to recorded decay signals, such as algorithms based on rapid lifetime determination (RLD) [173–176], Fourier transform [177, 178] or successive integration [177–179]. Although these algorithms are time-effective and do not require the initial guess of the fitting parameters involved, several comparative publications have come to the conclusion that the best measurement precision is provided by least-squares fitting approaches, such as the Levenberg-Marquardt (LM) algorithm [173, 174, 177, 180].[18]

[18] Fitting parameters from methods previously employed can serve as an initial estimates.

(d1) Error Potential of Fitting Windows: In case of mismatches between experimental transients and the estimated single-exponential model function, the proper choice of an evaluation window has a biasing effect on the fitting parameters of a model [IX, 181]. Since phosphor thermometry relies on a calibration procedure rather than the determination of accurate luminescence quantities, evaluating a distorted decay time is not necessarily a problem as long as the biasing of results during calibration and measurement is similar. In the simplest case, this can be achieved by maintaining a fixed time window during the evaluation of all phosphorescence curves. Many phosphors, however, are very temperature-sensitive, meaning that thermographic phosphorescence can vary over several orders of magnitude in time. It is thus nearly impossible to define a general fitting window that is fixed in time and is also appropriate over the entire temperature-sensitive range of a phosphor. Instead, suitable evaluation windows for analysing phosphorescence decay times have to be found individually for each signal transient. Yet, regardless how this is achieved, automatic and manual procedures for determining the dimensions of the fitting window are generally prone to signal noise. Consequently, the reproducibility of the fitting window is usually reduced, which leads to variations in the evaluated decay times and introduces errors to the single-exponential decay-time analysis of phosphor thermometry.

Example: In Figure 4.50, evaluation window of different lengths were applied to the luminescent decay of $CdWO_4$ so as to demonstrate the mismatch between the data signal and the individually fitted models. The signal displayed in Figure 4.50 was recorded at a temperature of $T = 326\,\mathrm{K}$ and was fitted to mono-exponential models in accordance with Equation (3.10); see page 27. All fitting windows started 10 ns after the initial peak, i.e. slightly after the excitation laser pulse had passed. The end of each window is indicated in Figure 4.50 by vertical dashed lines.

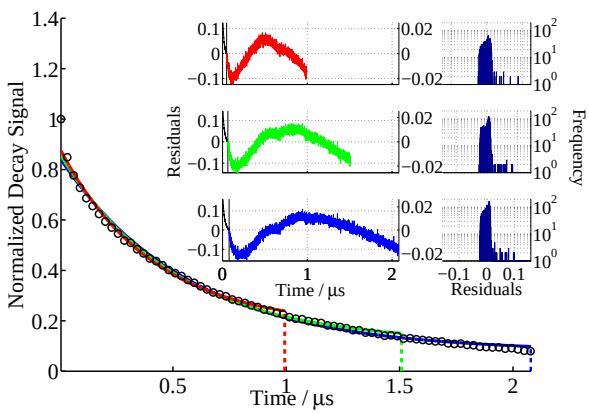

Figure 4.50: *Residuals of a single-exponential LM fit, applied to the decay signal of $CdWO_4$ at $T = 326\,K$. Different fitting window lengths, which end after the signal has decreased to 22.3 %, 13.5 % and 8.2 % are indicated by the vertical, dashed lines. Corresponding residuals between the decay signal and the fitted models and residual histograms are displayed in the upper right corner.*

At first glance, the fitted curves in Figure 4.50 appear very similar to each other and seem to follow the measured signal reasonably well. However, asymmetric distributions of fitted residuals, as displayed in Figure 4.50, suggest that a single-exponential model does not represent the measured data signal to a satisfactory extent. Mismatches between model and data values arise from the multi-exponential character of the recorded signal. As a consequence, it turns out that evaluated decay-time values are largely dependent upon dimensions of the fitting window. Figure 4.51 shows decay times (evaluated from the data displayed in Fig. 4.50) and their dependence on the length of the fitting window. In each time window selected, a single-exponential LM fit was adapted to the curve in order to compare the evaluated signal decay times. Extending the fitting windows towards the tail of the curve means that long-lived decay-time components of multi-exponential decays gain an increasing influence on the fitted function. Hence, a single-exponential fit under such conditions yields longer decay times as compared to a fit of the exact same curve performed within a shorter evaluation window. Although the same curve was evaluated several times and different fits in Figure 4.50 are difficult to tell apart, the evaluated decay times in Figure 4.51 show a shift by as much as ±20 % as a result of changing the fitting window length. If the evaluation windows are varied still further, as also shown in Figure 4.51, the evaluated phosphorescence decay times can change by a factor of 3 or greater in the case of $CdWO_4$.

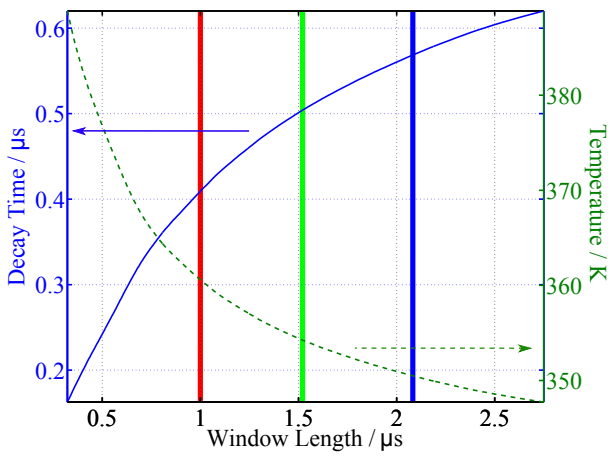

Figure 4.51: *Decay times and corresponding temperatures for a decay signal of $CdWO_4$ at $T = 326\,K$, estimated by an LM fit to a single-exponential model, are displayed as a function of different fitting windows. The different vertical lines correspond to the examples of evaluation windows, chosen earlier in Figure 4.50.*

Since decay signals from $CdWO_4$ become shorter as the temperatures increase, such virtual variations of the decay times can be translated directly into the temperature scale. The evaluated temperature stretches over an interval of more than 40 K in Figure 4.51, as compared with a temperature calibrations in which the fitting windows were not varied accordingly. Since there was only one calibration temperature for which the signal was measured, these temperature changes can be interpreted as

systematic errors. Depending on the multi-exponential character of the signal shape and the sensitivity of a chosen thermographic phosphor, temperature errors induced by uncertain fitting windows can vary from application to application. Other sources have used different phosphors in their measurement setup and have reported errors in the order of 10 K [181].

In the following, several strategies that aim at reducing the risk of errors caused by inaccuracies of the fitting window are presented.

(d2) Iterative Evaluation Window: An algorithm was introduced and characterized by Brübach et al. [181], who proposed relating the fitting window boundaries t_{start} and t_{stop} to the evaluated decay time constant τ as:

$$\begin{aligned} t_{\mathrm{start}} &= c_1 \cdot \tau \\ t_{\mathrm{stop}} &= c_2 \cdot \tau \end{aligned} \tag{4.47}$$

The optimization of c_1 and c_2 is considered to be a trade-off between high accuracy and high precision, since the signal-to-noise ratio is higher early on during presentation of the signal, where the curve is influenced more strongly by parameters other than the temperature (e.g. the laser pulse energy; see section 4.3.5, page 49).

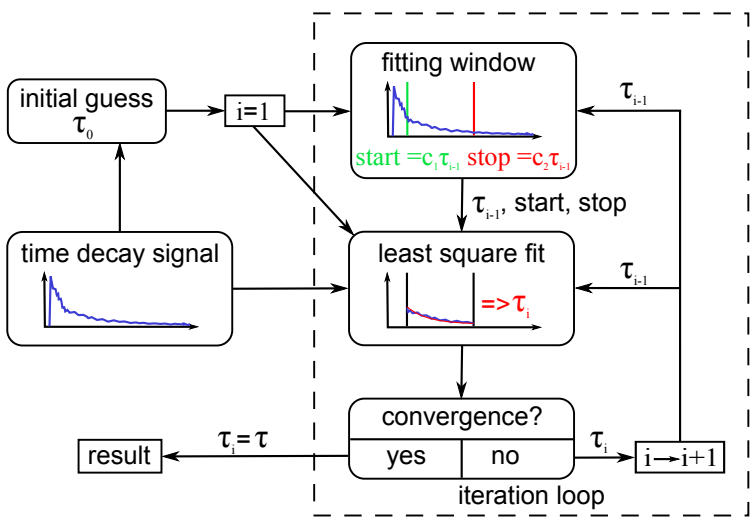

Figure 4.52: *Flow chart of the iterative window algorithm. The index* i *denotes the iteration step.*

The authors of [181] used $c_1 = 1$ and $c_2 = 4$, but it is advised to choose these values individually, based on the phosphor and the detection system involved [15]. For the LM fitting method employed, it is also necessary to find an initial guess value τ_0, which can be chosen so as to be related to the length of the fitting window Δt.

$$\tau_0 = c_0 \cdot \Delta t \tag{4.48}$$

Empirical studies by [181] suggest $c_0 = 0.1$ to be a suitable value for defining τ_0 in Equation (4.48). Since τ from (4.47) is an unknown quantity, the fitting routine has to be applied iteratively. A generalized flow chart describing the working principles of the algorithm is to be found in Figure 4.52. After the initial decay time estimate τ_0 has been found in accordance with Equation (4.48), the phosphorescence signal is submitted to the iteration loop. In each iteration step i, an evaluation window is applied to the signal, as defined by Equation (4.47), before a least squares fit is performed by use of a single-exponential function. The evaluated decay time from the fit serves as an input parameter in defining a new fitting window in the subsequent iteration step. This process continues until stability is reached and the results for τ converge.

Advantages: An advantage of the iterative windowing algorithm is its ability to eliminate the need for manual and arbitrary adjustments of fitting windows. These adjustments, if not performed consistently, would otherwise cause systematic evaluation errors, as indicated earlier in Figure 4.51. The automatic scaling character of this approach makes it very flexible in handling an indefinite range of signal time scales. In addition, parameters c_1 and c_2 are adjustable and leave the operator in control over the desired signal part in which the evaluation should be performed.

Disadvantages: One of the major problems with this algorithm is its stability. The authors of [181] mentioned the rare possibility of oscillations occurring and addressed this problem through use of another criterion, which comes into effect if the loop has processed 30 iterations without reaching a stable solution. In such cases, the final decay time is set to the algebraic average of the last 10 iterations, which effectively solves this problem. Another, much more crucial stability issue of the iterative algorithm is a distinct possibility of the evaluation window running off to either side of the detection window. This can happen because of multi-exponential phosphorescence signals decaying faster in the initial phase of the decay and exhibiting a slower decaying signal tail (see Fig. 4.51). In contrast to oscillating solutions, divergent fitting windows have not yet been discussed in the context of Brübach's iterative algorithm. Unpublished work by the author of the present thesis indicates, however, that multi-exponential phosphorescence decays from e.g. $CdWO_4$, La_2O_2S:Eu or ZnO:Zn suffer substantially from this limitation. Figure 4.53 shows a parameter variation of the fitting constants c_1 and c_2 that was performed over an entire temperature calibration dataset of ZnO:Zn signals. The colour scales in Figure 4.53 indicate the probability of fitting windows diverging, as displayed for individual combinations of c_1 and c_2. The white areas in Figure 4.53, framed by dashed lines, represent combinations of c_1 and c_2 that did not encounter occurrences of divergent fitting windows. The avoidance of such incidents essentially limits $c_1 \in [0, 0.5]$ whereas c_2 can be chosen more freely. Unfortunate combinations of c_1 and c_2 can result in divergence probabilities in excess of 80 %. Diverging fitting windows are more of a problem if phosphorescence decays exhibit a distinct multi-exponential character. Unfortunately, this is exactly where the iterative algorithm would be of most use, since it is the multi-exponential curvature in the signal that makes the evaluated decay time dependent upon the boundaries of the evaluation window in the first place.

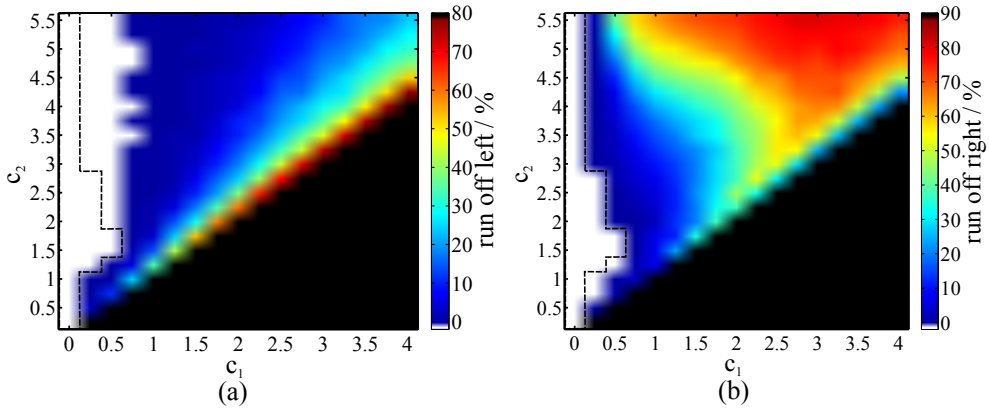

Figure 4.53: *Diverging fitting window probabilities for the iterative windowing algorithm, applied here to a calibration database of ZnO:Zn. Part* (a) *shows fitting windows walking off to the left, whereas part* (b) *shows fitting windows walking off to the right. The black areas represent impossible combinations of* c_1 *and* c_2.

The author has also observed multiple coexisting solutions caused by the algorithm being stabilized at different locations under the curve.[19] The risk of multiple solutions increases if evaluation windows are chosen to be short ($c_2 - c_1 \to 0$). Finally, the iterative algorithm suffers from the minor disadvantage of being slower than a single least-squares fit is. In relative comparison, Brübach's iterative algorithm is usually 4 to 8 times slower than a regular least-squares fit, how slow it is depending upon the number of iterations needed for the solution to converge.

(d3) Intensity-based Evaluation Window: This is an alternative approach to finding a suitable evaluation window for multi-exponential signal decays developed by the author [IX]. In contrast to the iterative-window algorithm, a fixed starting time $t_{\mathrm{start}} = 10\,\mathrm{ns}$ for the evaluation window is selected. This enables the signal parts that are still high above the noise level to be exploited, while reducing the window-allocation uncertainties caused by signal noise. The end of the window is defined by the time t_{stop}, for which the signal underruns a certain percentage value p of the intensity $J'_{\mathrm{w0}} = J'(t_{\mathrm{start}})$. However, instead of only picking the first data value that underruns the threshold intensity $p \cdot J'_{\mathrm{w0}}$ $(0 \leq p \leq 1)$, also the position of the last data point above the threshold is used for calculating the mean time value from both data points. This limits the effects of noisy signals falling systematically earlier below the intensity threshold, see Figure 4.54. However, such a mean time-value could still be biased by the accidental choice of outlier points which might be far off the actual threshold intersection. It seems prudent, therefore, to iterate and find the second point below and the second to last point above the threshold instead. This process reduces the time difference between the two data points in each iteration step. The iteration continues until the time difference is minimized, the process being terminated

[19] From a set of 100 similar decay curves, at least two distinct clusters of decay times were observed.

just before the ith point below the threshold comes for the first time just after the ith-last point above the intensity threshold. Finally, the value of t_{stop} is calculated from the mean time value of the last iteration step. Such an approach for terminating the evaluation window provides enhanced stability in terms of avoiding the influence of signal noise and of outliers. In addition, this method requires significantly less computational effort as compared with the alternative of noise-reduction algorithms such as use of smoothing filters or of curve fitting approaches.

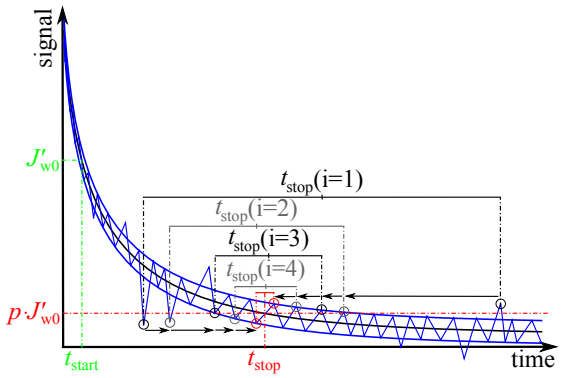

Figure 4.54: *A schematic illustrating the iteration process used for finding* t_{stop} *on the basis of a certain signal threshold* $p \cdot J'_{\mathrm{w0}}$.

It can be discussed whether t_{stop} is more accurately defined by an intensity threshold $p \cdot J'_{\mathrm{w0}}$ than by multiple decay times c_2. For a single-exponential transient with a zero background signal, a simple relationship between multiple of the decay time c_2 and the remaining percentage fraction p of the initial intensity I_{w0} can be expressed using Equation (4.49), as illustrated in Figure 4.55.

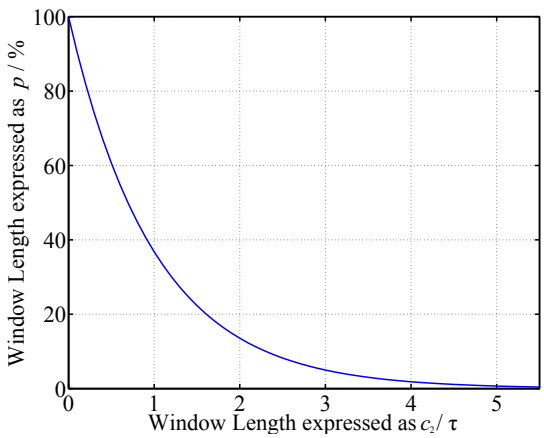

Figure 4.55: *Multiple of the decay time, converted into an intensity percentage fraction of a single-exponential decay curve in accordance with Equation (4.49).*

$$p = \exp(-c_2) \tag{4.49}$$

As evaluation window dimensions for functional fittings have to be found for individual and noisy decay signals, the repeatability of fitting windows is primarily governed by the SNR and the signal positions that were chosen to define the boundaries of the fitting window.
Figure 4.56 presents simulation results obtained by adding random Gaussian noise to simulated single-exponential decay curves. The beginning of the observation window was fixed to $t_{\text{start}} = 10\,\text{ns}$ after the initial peak. The window end t_{stop} was determined either by setting the length to being a multiple of the decay time (the reddish solid lines), evaluated through a least-squares fit over the entire signal, or by finding a curve position for which the signal falls below a certain percentage value (dashed lines of bluish colour). For the sake of comparison, decay time multiples were also expressed as threshold percentages (see the x-axis in Fig. 4.55), using the conversion described by Equation (4.49).

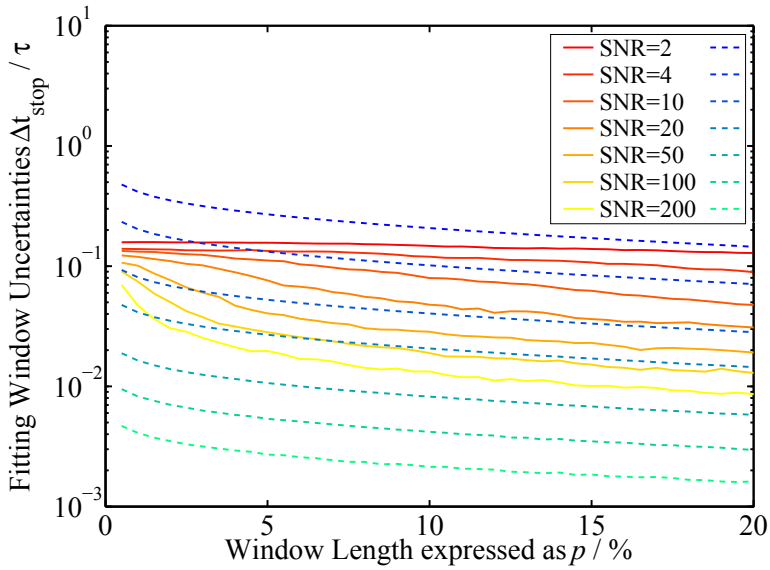

Figure 4.56: *Fitting window uncertainties, expressed as standard deviation of t_{stop} and normalized by the decay time of the signal (y-axis). The x-axis defines the choice of fitting-window length, represented by a percentage value that corresponds to either multiples of decay times (—, reddish) or intensity thresholds that the signal underruns after a certain period of time (···, bluish).*

The comparison of two different definitions used for setting equally long fitting windows in Figure 4.56 can be summarized as follows: For very noisy signals, in which the SNR is in the order of 2, the decay-time method delivers superior precision over the entire interval of window lengths. At SNR= 4, the percentage method is superior

to the decay-time method as long as observation windows remain reasonably short, i.e. $p \geq 4 \ldots 5\,\%$ (the windows being shorter than $3 \cdot \tau$). At signal-to-noise ratios in the order of 10, the percentage method is already superior over the entire range of fitting windows investigated. In fact, precision values were achieved that were not even matched by the decay time method when operating at an SNR value of 20. A SNR of 100 is necessary for the decay time method, in order to achieve a window precision similar to that achieved by use of the percentage method at SNR= 20.

Example: Experimental decay transients from $CdWO_4$ were measured as having a SNR value of between 40 and 70. For such measurement data, the percentage method is 3 to 10 times as accurate in defining t_{stop} (see Fig. 4.56).

Advantages: Intensity-based boundary conditions for evaluation windows achieve about the same degree of scalability to signal time scales as iterative evaluation windows defined in terms of multiple decay times do, and also eliminate the arbitrary influence of operators who otherwise would have to set the window boundaries manually. Unless phosphorescence transients are very noisy (SNR < 4), an intensity-based evaluation window can be employed with a higher degree of precision as that of a corresponding window defined in terms of multiple decay times. The reduction in statistical variations in the window boundaries should lead to an improvement in temperature precision. Finally, the intensity-based windowing algorithm does not require iterative decay-time fittings, this eliminating all previously discussed problems of stability and providing a significant advantage in terms of computational speed.

Disadvantages: Defining t_{start} directly by a fixed time after the signal peak eliminates errors in precision for the beginning of the fitting window. But in order to comply with both long and short phosphorescence decays, t_{start} needs to assume a value similar to or lower than the shortest phosphorescence decay time from the ensemble of calibration curves. Some phosphor coatings, however, can exhibit thermal history effects in the initial part of the decay, which become annealed after long thermal exposures. It might therefore be preferable to define t_{start}, similarly to t_{stop} as based on an intensity threshold. Since the signal slope is much higher in the beginning of the curve, the inaccuracies due to signal noise are expected to be much lower than those shown for t_{stop} in Figure 4.56.

(d4) A library-based Algorithm of Signal Shape Recognition: This paragraph deals with an alternative method for temperature determination that is largely insensitive to variations of the observation window. The signal shape recognition (SSR) algorithm, proposed in Paper [IX], compares the shape of the phosphorescence time transients with a number of decay signals from temperature calibration measurements. A generalized flow chart helping to explain the algorithm is presented in Figure 4.57. In an initial step, the measured signal is offset-corrected and is normalized to 1 at the start of the evaluation window, i.e. 10 ns after the peak signal. The entire calibration database was normalized in this way earlier, allowing differences between the signal and the individual calibration curves to be compared in terms of signal shape.

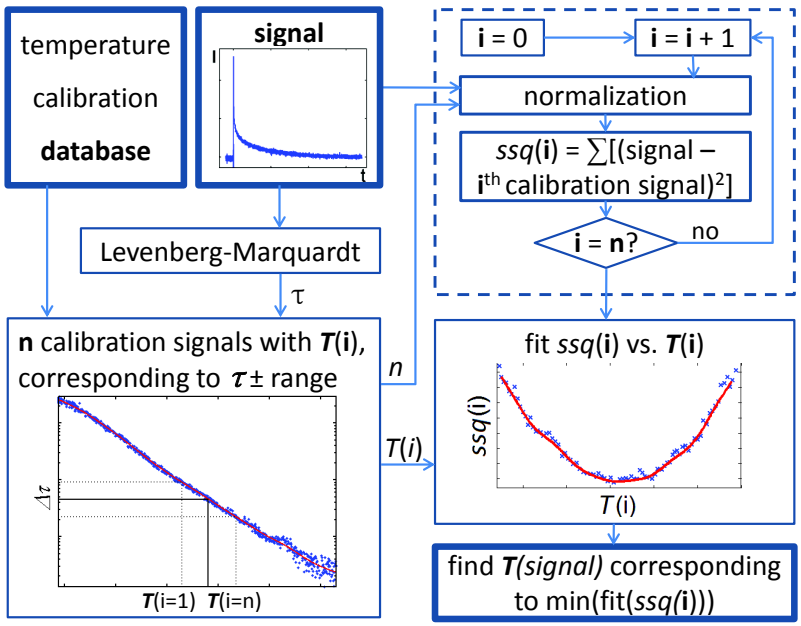

Figure 4.57: *A flow chart describing the basic working principle of the SSR algorithm. The signal from a measurement is scaled and overlapped with a selection of temperature-calibrated decay transients in order to identify a temperature from the calibration, whose corresponding waveform best matches the shape of the signal.*

In a subsequent step, a limited temperature interval ΔT needs to be selected, which comprises a number of calibration curves being compared with the signal. By all means, this interval should be large enough to contain the actual temperature of the signal. Alternatively, the signal could be compared with the entire calibration dataset. This may be very time-consuming, however, and is only meaningful if temperature calibrations are performed in a few discrete temperature steps.[20] In the present work, ΔT was found using a range of decay times $\Delta\tau$, see the lower left part of Figure 4.57. The temperature steps within the present calibration were small enough to allow $\Delta\tau$ to be defined as being $\pm 2.5\,\%$ of the signal's logarithmic decay time. All n calibration curves within this interval are then compared with the measured signal.
Figure 4.58 provides a comparison example showing a sample curve (red) together with the shortest calibration curve (blue) from the selected interval ΔT. The vertical dashed line indicates the end of the observation window, which is always fixed to the length of the shortest calibration curve within ΔT. This criterion was employed in order to maintain the longest constant window possible while comparing the transient shapes. An interpolation algorithm ensured that both the signals and all the calibration curves possessed m vector elements within the observation window.

[20] The SSR algorithm is capable of handling discretized fixed-point calibrations, but suffers from a lack of comparable signals, resulting in inferior precision as compared with conventional least squares fitting approaches [IX].

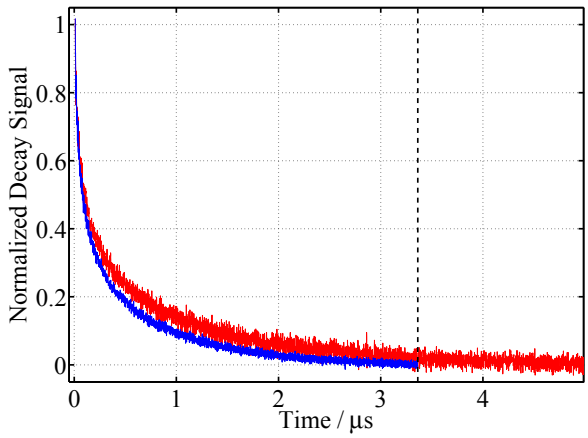

Figure 4.58: *A normalized measured sample curve (red) compared with a normalized calibration curve (blue). The vertical dashed line indicates the end of the observation window, as set by the length of the shortest calibration curve within* ΔT.

This allowed the signal shapes to be compared using the sum of squares ssq calculated from the difference between the signal vector Y and the calibration curve vector y; see Equation (4.50). In addition, the ssq was divided by the number of vector elements m involved in the comparison, this giving the mean squared distance ssq_{m}.

$$ssq_{\mathrm{m}} = \frac{1}{\mathrm{m}} ssq = \frac{1}{\mathrm{m}} \sum_{\mathrm{j}=1}^{m} (y_{\mathrm{j}} - Y_{\mathrm{j}})^2 \tag{4.50}$$

Since each calibration curve of the database is assigned to temperature value, the mean squared distance for each comparison can be plotted as a function of temperature, as represented by the crosses in the example shown in Figure 4.59. The mismatch between the two signals compared is large and results in higher ssq_{m} values if the signal shapes differ substantially from each other. A minimum value of ssq_{m} is reached for the closest match of signal shapes between the measured signal and a calibration curve. By applying a fit to all points (×) in Figure 4.59, a global minimum can be found which then corresponds to the signal's temperature, evaluated by the SSR algorithm. For comparison, the real temperature for the signal shown in Figure 4.59 was measured by a thermocouple and is indicated by a vertical dashed line.
Local variations in the ssq_{m} values in Figure 4.59 are caused mainly by errors occurring during the overlap of the measurement signals and the calibration curve, i.e. errors in connection with baseline corrections and amplitude normalization. Since any of these errors induces a systematic residual increase, the lower points (○) in Figure 4.59 are deemed to represent more reliable estimates of the mean squared distance. In order to verify this assumption, two different fitting strategies were followed in Figure 4.59: In the one case, all the points (×) were fitted, this being shown by the dashed line. In another case, only the lower ssq_{m} values (○) were selected for the fitting process, which resulted in the fit described by the solid line. The latter option was found to yield more reliable results in general.

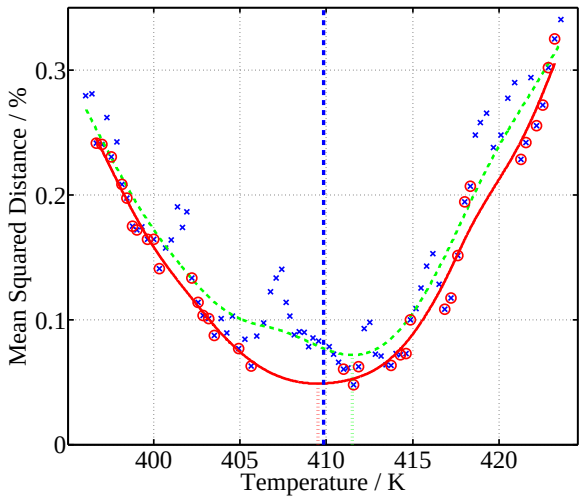

Figure 4.59: *Mean squared distances of the measured sample signal from $CdWO_4$ at 409.8 K compared with a set of averaged calibration curves. The dashed line corresponds to a fit that takes all data points into account (×), whereas the solid line only takes account of the lower points (○).*

Mono-exponential models often fail to describe a measured signal to a satisfactory extent and can induce errors connected with the precision of the fitting-window dimensions involved (see the residuals in Fig. 4.50, which are presented for comparison purposes again in Figure 4.60 (a)). In contrast to conventional curve fitting approaches, residuals of two similar signals, identified by the SSR algorithm, should be distributed equally. In Figure 4.60 (b) the decay transients of two separately acquired data curves are matched ($CdWO_4$ at 326 K).

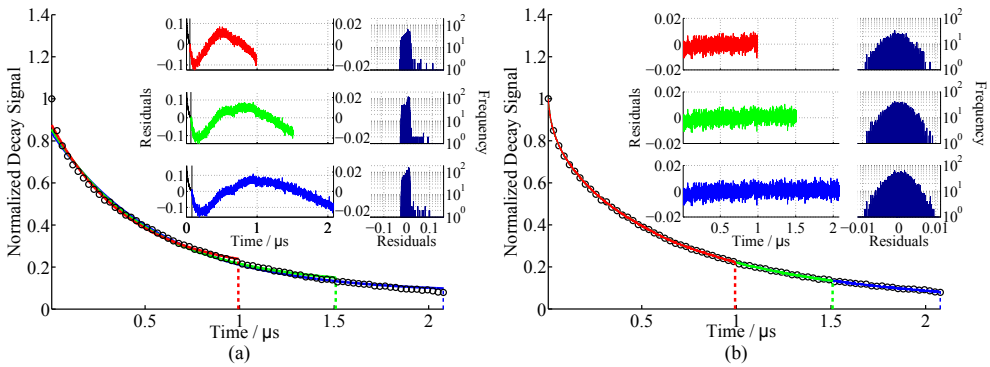

Figure 4.60: *Part* (a): *Reproduction of Figure 4.50, page 125. Part* (b): *Two separately obtained decay signals from $CdWO_4$ at $T = 326\,K$ and the corresponding residuals to the match of the curves, observed for different window lengths that end after the signal has decreased to 22.3 %, 13.5 % and 8.2 % of its original signal intensity.*

The residuals from matching two similar curves in Figure 4.60 (b) can be compared with the fitting residuals in (a) within the three previously defined observation windows. As expected, all the residuals and histograms show symmetrical distributions around zero, regardless the fitting window selected. Hence, the dependence of the window length can be largely eliminated through use of the SSR algorithm.
As pointed out earlier, it is important for conventional evaluation schemes that exactly the same fitting window is employed for calibrations and for experiments when a single-exponential model is fitted to multi-exponential decays. As soon as the size of observation window used for measurement and for calibration differ, systematic errors in the temperature readings are induced. The consequences of this are illustrated in Figure 4.61 (a), in which deviations from the calibrated temperature are shown for three different cases.

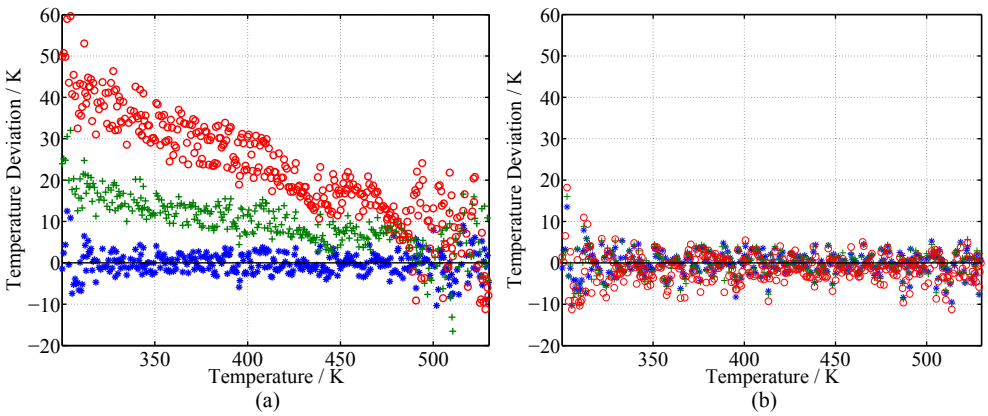

Figure 4.61: *Residuals of thermocouple temperatures to the temperatures that* (a) *were obtained through an LM fit to a single-exponential model and* (b) *that were determined using the SSR algorithm. The evaluation window during temperature calibration ended at 8.2 % of J'_{w0}. The window length during the temperature measurement varied from 8.2 % (∗) and 13.5 % (+) to 22.3 % (○).*

During this investigation, each curve from a calibration dataset was removed once and individually from the calibration and was instead treated as a measurement signal. Whereas the evaluation of the calibration signals was based on one particular definition of the fitting window, each measurement signal was evaluated using three different windows, resulting in three different decay times. Accordingly, three artificial temperatures per curve were obtained.
In the first case, indicated by the stars in Figure 4.61 (a), both the calibration and the measured curve were evaluated until the signal had decreased to 8.2 % (∗) of its initial value J'_{w0}. Since the evaluation of the calibration curve and the measured curve was performed using identical evaluation windows, the resulting temperature deviation fluctuates around zero. Within the observed temperature range of 300 K to 530 K, the standard deviation of the temperature is about 3 K. In the other two cases, the end of the fitting window for the calibration curves was kept at 8.2 % of J'_{w0}, but the window

length of the measured signal was decreased. The end of the window was set to the point in time when the signal had decreased either to 13.5 % (+) or to 22.3 % (○) of its initial value J'_{w0}. As Figure 4.61 (a) illustrates, the temperature deviation for different fitting windows changes. For low temperatures, i.e. longer decay times, the evaluated temperature accuracy decreases. At room temperature, the discrepancy from the true temperature is almost 52 K (○) and 25 K (+), respectively. Temperatures are overestimated as a result of only the short-lived part of the signal being registered. Although at higher temperatures the accuracy does not change, the precision achieved there is less. The observed effects become more pronounced as the differences in window size increases. The overall standard deviation of the temperature fit increases from 3.0 K (∗) to 3.97 K (+) and 5.33 K (○), respectively, as the fitting window for the measured curve becomes shorter.
For the SSR algorithm, this dependence upon employing the same evaluation window is not nearly as critical. As illustrated in Figure 4.61 (b), the temperature deviation fluctuates around zero in all three cases, indicating the level of measurement accuracy to be high regardless of any constraints on the fitting window. The large spread in the temperature deviations at around 300 K occurs in part due to the lack of calibration data below 295 K. This forces the best match between calibration and signal to occur at the edge of the compared interval, which reduces the chances of finding a pronounced and reliable minimum. Nevertheless, variations in the low temperature region are still of a magnitude comparable to the elevated data spread observed in Figure 4.61 (a) with use of the conventional algorithm. Within the calibrated temperature region extending from 300 K to 530 K, the temperature precision obtained by use of the SSR algorithm decreases somewhat as the observation window becomes shorter. The standard deviation was found to be 2.75 K for the evaluation window, which was determined to end after the signal has fallen below 8.2 % (∗) of the initial signal level J'_{w0}, 3.0 K for the window ending at 13.5 % (+), and 3.43 K (○) for the observation window ending at 22.3 %.

It has thus been shown that the SSR algorithm also provides slightly better temperature precision for a given set of measured data than the conventional fitting approach does. For the three scenarios that were investigated, the temperature precision improved by 9, 32 and 55 % respectively.

Advantages: The SSR algorithm relies on direct comparison of measured decay transients in order to associate temperatures with phosphorescence signals. This eliminates the risk of a mismatch between the fitted model and the physical signal, making the SSR algorithm effectively immune to systematic errors caused by uncertain boundaries of the evaluation window. One significant advantage of the SSR algorithm is the flexibility involved in being able to handle almost any type of measurement signal without introducing ambiguities arising from mismatches between a theoretical model and experimentally measured signals. The avoidance of intermediate fitting quantities, such as exponential decay times, reduces the amount of potential error sources. This is reflected in the values for the measurement precision, which are ≥ 9 % higher than the corresponding results obtained from a least-squares fitting approach.

Disadvantages: The SSR algorithm benefits from a dense grid of calibration measurements such as involved in Paper [I]. When used in combination with a discrete calibration consisting of few fixed points with large intermediate temperature gaps, the SSR algorithm suffers from inferior temperature precision as compared with conventional evaluation schemes. In addition, the performance of the SSR algorithm decreases towards the edges of the calibrated temperature interval. There, a well defined minimum of residuals is more difficult to achieve due to a one-sided lack of comparable decay transients.

(e) Fitting Window Selection for Single-Exponential Decay Evaluations: This paragraph takes a brief look at the potential for optimizing the sensitivity of given temperature calibrations through changing the boundaries of the evaluation window. Figure 4.62 displays two independently observed results that were obtained by systematically changing the length of the evaluation window over an entire temperature calibration database of ZnO:Zn. The evaluation window was changed by defining an intensity threshold for t_{stop}, while t_{start} was fixed to 10 ns after the initial peak, as proposed in paragraph (d3), page 129.

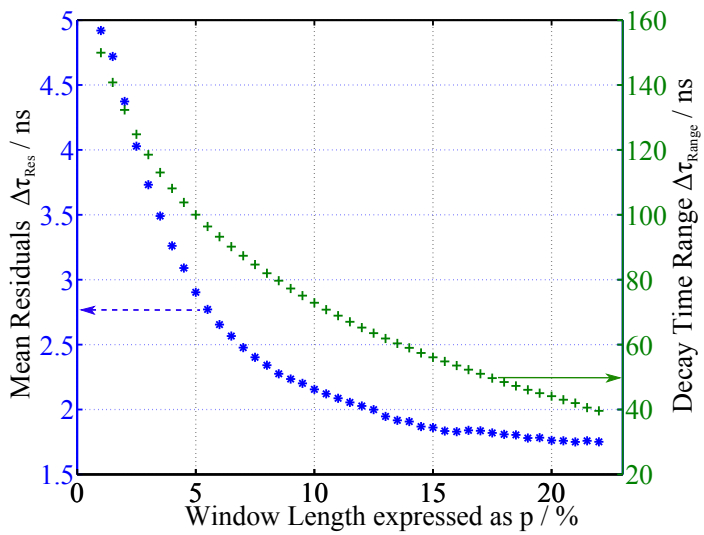

Figure 4.62: *Average effect of the evaluation-window length on the decay-time range* (+) *and the mean residuals* (∗) *of a ZnO:Zn temperature calibration.*

Figure 4.62 shows the mean value of the residuals ($\Delta\tau_{\mathrm{Res}}$, left y-axis), describing the average offset of all evaluated decay times to the fit of their corresponding temperature-calibration plot. Together with the range of evaluated decay times over the entire calibration ($\Delta\tau_{\mathrm{Range}}$, right y-axis), $\Delta\tau_{\mathrm{Res}}$ can be used for determining the overall temperature precision to be expected from the calibration; see Eq. (4.4), page 48. Both parameters, $\Delta\tau_{\mathrm{Res}}$ and $\Delta\tau_{\mathrm{Range}}$ increase for fitting windows that extend further in the direction of the signal tail (decreasing p values):

- The mean residuals $\Delta\tau_{\mathrm{Res}}$ increase due to the higher uncertainty in finding t_{stop} accurately as p decreases (compare with Fig. 4.56, page 131).
- An increase in $\Delta\tau_{\mathrm{Range}}$ can be observed because the single-exponential functions that are fitted to the multi-exponential transients generally result in larger decay times towards the signal tails (compare with Fig. 4.51, page 126). For longer phosphorescence decays at low temperatures, the shift towards longer decay times is greater than for shorter decays at high temperatures, which is why $\Delta\tau_{\mathrm{Range}}$ increases with a decrease in p.

Since a high temperature sensitivity in thermographic phosphor calibrations is a trade-off between a large signal range (large $\Delta\tau_{\mathrm{Range}}$) and a high signal precision (small $\Delta\tau_{\mathrm{Res}}$), Figure 4.62 predicts the existence of a precision-optimized p value that sets the length of the fitting window such that the calibration plot reaches its maximum temperature sensitivity S.

$$S(p) = (\Delta T_{\mathrm{Prec}}(p))^{-1} = \frac{\Delta\tau_{\mathrm{Range}}(p)}{\Delta\tau_{\mathrm{Res}}(p) \cdot \Delta T_{\mathrm{Range}}} \tag{4.51}$$

Figure 4.63 (a) shows examples of three temperature calibration plots from ZnO:Zn that were achieved by differences in the lengths of the evaluation window in combination with a single-exponential LM fit. All three plots stem from the same library of measured signals, their evaluations differing only in terms of their corresponding p values. Part (b) of Figure 4.63 shows the temperature sensitivity of the calibration according to Equation (4.51) over a variation of p. The three p values used for the plots in Figure 4.63 (a) are represented in (b) by colour matching circles.

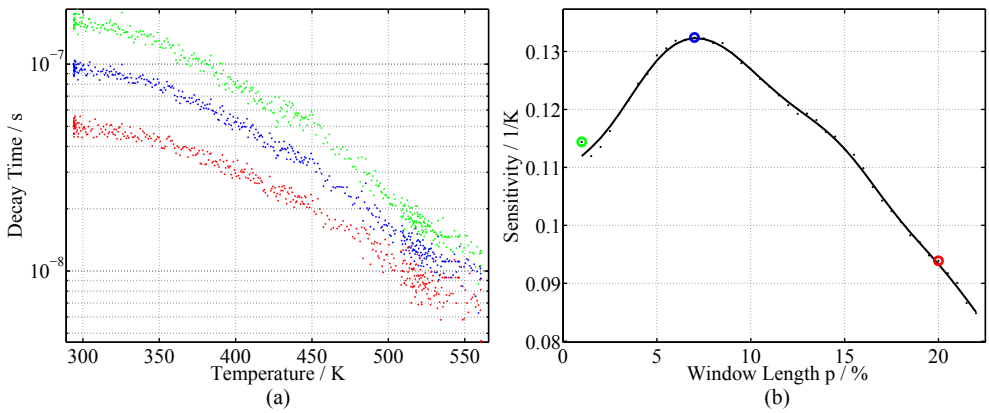

Figure 4.63: *Part* (a)*: Different ZnO:Zn calibration plots from the same data library, achieved by changing the length of the evaluation window. Part* (b) *shows the overall temperature sensitivity achieved as a function of the p-value.*

According to Figure 4.63 (b), the highest temperature sensitivity was reached for $p \approx 7\,\%$, which corresponds to an evaluation window length of about 2.66 decay times.

This sensitivity was achieved by the intermediate calibration plot in Figure 4.63 (a) (blue markers), which provides best compromise of a high level of data precision and a large range of decay times.

In addition to the optimization of evaluation-window dimensions for temperature calibrations of phosphorescence decays, it could be of interest to study how different fitting algorithms perform during the parametric variation of p. Not only the absolute value of the maximum sensitivity (which is achieved for one particular p value) may be of interest. If the maximum sensitivity extends over a broad region of the fitting window, there is a good chance that the algorithm is also robust in regard to inaccuracies in finding t_{stop} values from noisy decay transients. Figure 4.64 shows a comparison of the calibration sensitivities $S(p)$ of different algorithms based on a database of temperature-calibrated ZnO:Zn decay transients.[21]

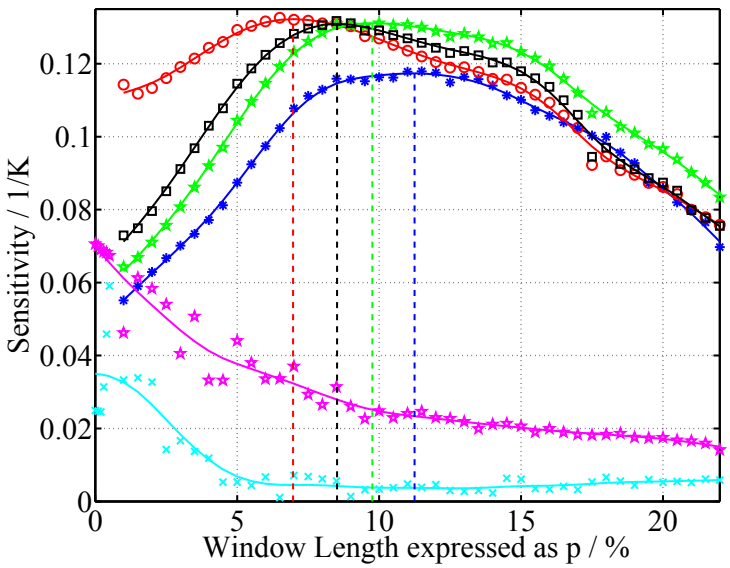

Figure 4.64: *Sensitivity plots of different algorithms, using temperature-calibrated ZnO:Zn decay transients: LM fit* (○)*; RLD* (∗)*; Fourier transform (green* ⋆*); successive integration* (□)*; multi-exponential decay components, retrieved from a LM fit* (×, purple ⋆).

The overall sensitivity changed as a function of the length of the fitting window, and was compared based on temperature-calibrated phosphorescence decay times, determined from:

1. a single-exponential LM fit (○)
2. a single-exponential RLD algorithm based on three equidistant integration sections (∗) [174]

[21] This is the same set of data values, that was previously made use of in figures 4.62 and 4.63.

3. a single-exponential algorithm based on a Fourier transform (green ⋆) [177, 178]
4. a single-exponential successive-integration algorithm (□) [177–179]
5. a double-exponential LM fit (×, purple ⋆)

Although the optimum fitting-window length (retrieved for each individual algorithm so as to achieve the maximum sensitivity of it) is generally dependent upon the transient shape of the phosphorescence decays, a few general conclusions can be drawn from Figure 4.64:
Most of the algorithms appear to show a similar trend regarding the calibration sensitivity, the LM fit exhibiting the highest possible temperature sensitivity of $S(p = 7,\%) = 0.1322\,\mathrm{K}^{-1}$ in the test. Although the RLD algorithm performed worst in the ensemble of single-exponential models, its maximum sensitivity of $S(p = 11.2,\%) = 0.1174\,\mathrm{K}^{-1}$ does not differ particularly much from the LM-fit results. In fact, the average benefit of employing an LM fit rather than carrying out an RLD evaluation corresponds to only about 1 K, which is an overall improvement in precision of about 12 %. The sensitivity results of the double-exponential LM fit, on the other hand, did not approach their optimum level of precision within the signal length that was recorded and remained well below the temperature sensitivity found for the single-exponential models. This reflects their dependence upon signal information from the signal tails in order for it to be possible to differentiate multiple decay constants from one another adequately. It is also assumed that a time-extension of the recorded phosphorescence transients would not result in any very applicable improvement in sensitivity with use of this approach, since the signal at the tail of the phosphorescence is small in comparison to the statistical noise from the background, and thus does not contain much meaningful information. The lowest p value for the test was set to 0.1 %, which according to Equation (4.49) (page 131) corresponds to almost 7 decay times.

The comparative results shown in Figure 4.64 should be understood as representing a qualitative indication of the performance of different algorithms in time-based phosphor thermometry. The optimum p values for termination of the fitting window are dependent upon not only the signal noise, but also on the multi-exponential character of the thermographic phosphorescence involved. Nevertheless, sensitivity plots of the sort shown in Figure 4.63 and Figure 4.64 can serve as useful tools for optimizing the temperature precision of phosphorescence signals that have already been recorded. The relative performance of the different algorithms as shown in Figure 4.64 can be regarded as exemplary of other phosphor calibrations.

4.8 Experimental Challenges in Combustion Research

In addition to the aforementioned issues concerning measurement precision and accuracy, laser-induced phosphorescence thermometry faces further challenges when employed in the hostile environments that combustion-related applications provide (see the examples presented in chapter 5). These challenges, however, do not apply simply to LIP but are shared by most other optical diagnostics techniques.

Optical Access: First and foremost, optical access to the measurement object is needed, however, such access is often very limited. In many applications, such as engines or constant-volume combustion chambers, combustion takes place in a closed environment that needs to be modified with windows in order for optical access to be attained. Such modifications, however, have an intrusive effect on the measurement object. Husberg et al. for example, removed one of the two existing exhaust valves of a diesel truck engine in order to measure piston temperatures [182]. Another common approach to measuring surface temperatures on the cylinder ceilings of IC engines is to gain access through use of an optical piston crown in combination with a cylinder extension [6, 62, 147, 154, 183].
Clearly, alterations of this sort have an effect on the combustion process itself and on the gas-wall interaction. Window inserts lower the stress resistance of construction parts and thus reduce maximum peak pressures allowed for safe operation. Not least of all, the window materials employed contribute to the altered experimental conditions: Quartz windows conduct heat in the order of 40 to 200 times slower than metals [C] do, this resulting in the surface temperatures on window parts being much higher than they would otherwise be.
Various approaches to compensating for the increase in wall temperatures in IC engines, are available, such as skip-fire operation [183] or alterations in the inlet air temperature [184]. A more expensive alternative for the window material employed is sapphire, which exhibits heat conduction characteristics similar to that of metal walls.

Flame Luminescence: Optical combustion diagnostics in the vicinity of flames suffers from the undesired contributions of flame emission to the detected signal. The fuel-rich flame zones that are present in Diesel engines, for example, exhibit intense black-body background emissions. Such background emissions can easily overwhelm the phosphorescence signals of interest during combustion, their suppression requiring the use of spectral and temporal filtering. Fast decaying phosphors emitting in the blue spectral region provide advantages for both of these filtering techniques [79].

Deposits: Deposit accumulation on windows and phosphor films stemming from both lubrication oil and flame-generated soot often poses a challenge so that optical access may need to be designed for convenient replacement of windows and the application of fresh phosphor coatings. This basically limits the time of operation available for a device in which reasonable SNR can be achieved. The challenges increase when experimenters aim at carrying out experiments under steady-state conditions, that could be required in order to average noisy signals over time, or in case temperature drifts need to be measured over extended periods of time. The warm-up times needed to reach steady surface temperatures in combustion engines, for example, often stretch over several tens of minutes, during which deposits on both windows and phosphor films grow. Contaminations on phosphor coatings (such as produced by films of UHC, by oil or by the agglomeration of soot particles) can act as sensitizers or collision centres and result in systematic errors in temperature readings.

Vibrations and Thermal Stress: Vibrations and thermal stress require that any equipment close to the measurement object is of rugged design. In the case of very limited optical access or of large-amplitude vibrations it may be of advantage to mount at least parts of the setup directly on the vibrating measurement object directly connected with it.[22]

Remote Control and Safety Precautions: A number of measurement facilities are located in large open halls for which experiments may need to be designed to ensure that strict safety requirements can be met in regard to laser hazards and catastrophic operation failure: Frequently, all the equipment involved needs to be entirely remote-controlled in regard to its operation and fine adjustments of it.

[22] Care should be exercised when such decisions involve sensitive equipment, such as lasers and detectors, that might not survive the occurrence of too violent vibrations.

5 Phosphor Thermometry in Practical Applications

In this section, a number of examples of the use of LIP in determining surface temperatures in combustion-related measurement environments are provided.

5.1 Piston Temperatures in an HCCI Truck Engine

The design and the performance of IC engines is mainly driven by aims of increasing efficiency and by legislative demands placed on exhaust emissions. The measurement of piston temperatures in diesel engines play an important role not only in improving current heat transfer models, but also in designing of piston geometry in a manner aimed at achieving increased thermal efficiency [182]. The reduction of thermal load and the avoidance of excessive surface temperatures reduces long-time wear on engine components and helps to extend their reliable service life [185].

Although thermographic phosphors have been used in a wide variety of experiments ever since their initial use by Urbach and Bradley in the early 1950s (cited in Ref. [12]), their use in IC engines was first reported in 1997, when Armfield et al. employed thermographic phosphors in a study of intake valve temperatures on the stem side of the valve [186].
To illustrate the versatility of phosphor thermometry and to examine the impact of its calibration accuracy within a typical industry-relevant application, crank-angle-resolved piston-temperature measurements in a single-cylinder heavy-duty research engine (*Scania Truck D12*) were carried out [C]. The engine was modified by placing a quartz window into one of the exhaust ports in the cylinder head, providing optical access to the piston head. The fact that the surface temperatures were not expected to exceed 600 K, made $CdWO_4$ a suitable thermographic phosphor for this task.
A schematic diagram of the experimental setup is shown in Figure 5.1. A 10 Hz pulsed Nd:YAG laser operating at 266 nm (4^{th} harmonic) was used as the excitation source, and was directed into the combustion chamber. The beam was expanded by a spherical lens (not shown in Fig. 5.1) so as to illuminate two phosphor dots on the piston surface simultaneously. One of these dots was placed in the squish area and the other on the outer side of the piston bowl, in accordance with the schematic diagram shown at the upper right in Figure 5.1. Thermographic phosphorescence was then collected by a lens and detected by two PMTs, that were mounted behind 450 nm interference filters (FWHM: ±20 nm). These filters blocked contributions from the laser and from stray combustion light, helping also in selecting a thermographic transition in the phosphor. The engine was run in HCCI mode at 1200 rpm. Three different engine loads were obtained by controlling the duration of fuel injection and varying the inlet air pressure. The average temperature transients of the global gas temperature were calculated from the pressure trace; see Figure 5.1.
Pointwise temperatures in the squish area and in the piston bowl, evaluated on the basis of measurements of the phosphorescence decay time, are displayed in Figure 5.2. The range of crank-angles around TDC that was investigated, was limited to ±20 and to ±30 degrees, respectively, depending upon the measurement point location involved. This limitation stems from the exhaust port, which forces the piston in motion to be

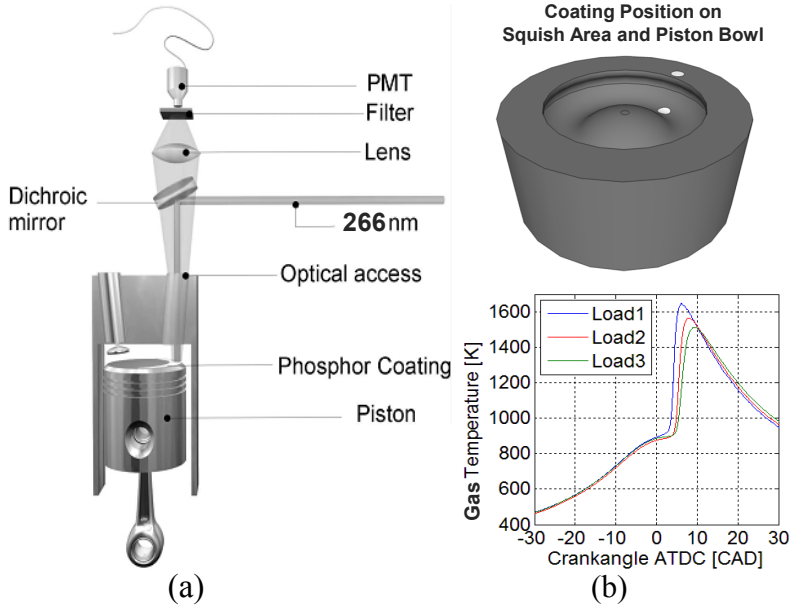

Figure 5.1: *Part* (a): *The experimental setup employed for obtaining dual-point measurements of piston temperatures through use of LIP. Part* (b): *Three different engine loads were compared, as shown in terms of the global gas temperature transients, which were extracted from the pressure trace inside the cylinder.*

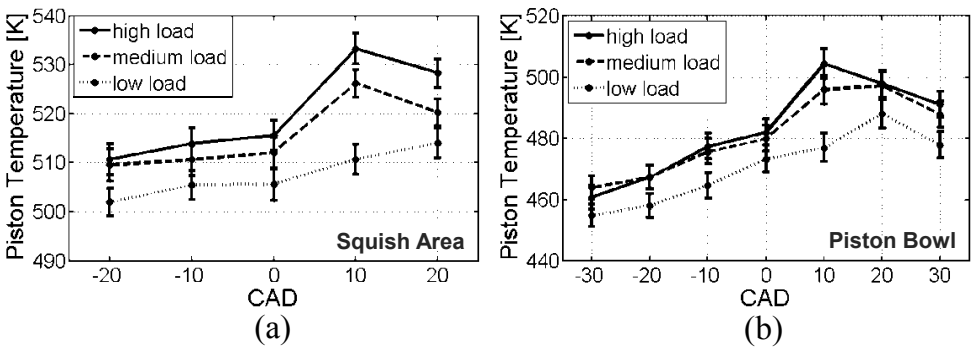

Figure 5.2: *Piston surface temperature transients of an optical heavy-duty research engine during HCCI combustion around TDC. Temperatures measured for three different loads, obtained in the squish area* (a) *and in the piston bowl* (b)*, are displayed. The temperature values and standard deviations* (*see error bars*) *correspond to measurements of 100 consecutive and averaged engine cycles.*

viewed at an angle; see Figure 5.1. Accordingly, the two dots of phosphor only appear within the field of vision for the crank-angles that were in the proximity of the TDC position of the piston.
As shown in Figure 5.2, the piston temperatures, as expected, rise when higher loads are applied. The difference in load results in a rise in temperature of about 10 K, its being highest at 10 CAD after TDC. Since it takes time to transfer heat from the gas phase to the thermally inert piston body, these surface temperatures are slightly delayed in relation to the peak values reached by the global gas temperature transient (see Fig. 5.1). The temperatures in the squish area were observed as generally being about 50 K higher than the corresponding piston bowl temperatures. This difference reaches its minimum of 30 K at around 10 CAD. This temperature difference could be caused by external oil cooling of the piston bowl, something which is common for diesel engines. It could also be caused by the gas velocities being higher in the squish area, this producing turbulence and thus distorting the thermal boundary layer, resulting in an increase in heat transfer. Within the investigated temperature range of 450 to 530 K, the shot-to-shot standard deviation between the different engine cycles was calculated to be in the order of ± 5 K. In comparison with the calibration curve, the uncertainty has thus increased by no more than one third within this particular temperature interval. Note that this increase also includes cycle-to-cycle variations of the engine, such that the measurement precision was not reduced appreciably by the experimental conditions, present in this application.

5.2 Surface Temperature Maps on a Gas Turbine Afterburner

During the past 50 years, a continuous development in terms of improvements in efficiency and the reduction of undesired emissions has taken place. Through efforts to improve fuel efficiency in advanced gas turbines, the operating temperatures employed are driven to a point at which they can exceed the melting temperatures of hot-section components. In order to achieve a favourable trade-off between thermal efficiency and operational safety it is important to measure and control the surface temperatures of turbine components that are in operation.

The use of thermographic phosphors in this context dates back at least two decades. Noel et al. in 1985 were the first to propose an experiment of this sort [187]. After several advances towards the application of thermographic phosphors to rotating turbine disks [188–190], their first use in an operating gas turbine was reported by Noel et al. in 1990 [152]. Today, ceramics and ceramic-coated components have become major elements in the development of advanced engines [191]. Such materials allow engines to run at much higher temperatures than those composed of the superalloys used in conventional engines. In order to prevent failure and maintain reliable service life, insulating TBCs have been used to an increasing extent. Recently, thermographic phosphors were embedded in thermal barrier coatings in order to produce smart TBCs having thermal sensing capabilities [126, 153, 192–194]. Accurate knowledge of the TBC operating temperatures makes it possible to optimize engine efficiency while maintaining an economic component lifespan [134].

In the present work, the surface temperatures of TBC-coated gas turbine parts were measured in a test rig at *Volvo Aero Corporation* in Trollhättan, Sweden. The measurement object, a *Volvo RM 12 engine*, was a low-bypass-ratio turbofan engine consisting of a total of seven modules, including a three-stage fan, a seven-stage compressor and an afterburner. Its design is based on that of the *General Electric F404 engine*, from which it was developed to meet single-engine operating criteria and achieve higher performance. It has a maximum thrust of 80.5 kN and an airflow of 68 kg/s. The *RM12 engine* is used to power the Swedish lightweight single-engine jet fighter *JAS 39 Gripen* (Griffin), that has been in service since 1997. The aim of the experiment carried out was to investigate the feasibility of performing phosphor thermometry under harsh conditions and to visualize the distribution of temperatures on the afterburner nozzle as a function of engine load.
A schematic diagram of the experimental setup is shown in Figure 5.3., which also displays a close-up photograph of the coated nozzle area, as well as another image showing the *RM12 engine* during high-load operation, involving the use of an afterburner.

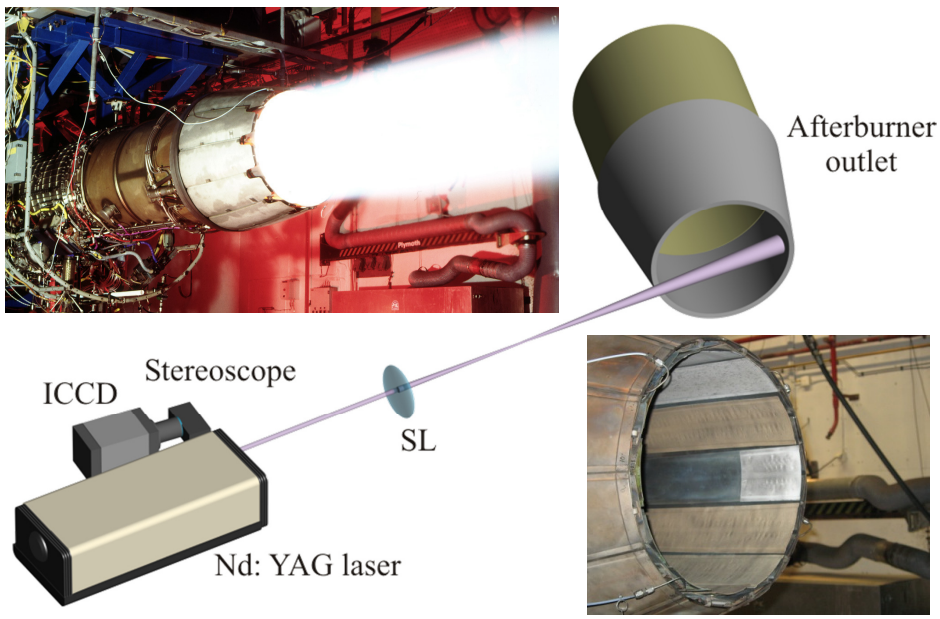

Figure 5.3: *Schematic of the experimental LIP setup used for obtaining 2D temperature maps of the outlet nozzle of a RM12 gas turbine. At the upper left, an image of the RM12 engine is shown during operation with the afterburner being active. At the lower right an image of the phosphor-coated nozzle segment is shown.*

The thermographic phosphor YAG:Dy was coated on a 10×10 cm large segment located on the outermost part of the variable outlet nozzle of the afterburner; see the photograph shown in Figure 5.3. A negative spherical lens expanded the laser to the approximate size of the phosphor-coated target area. After excitation at 355 nm by

the third harmonic of a 10 Hz pulsed Nd:YAG laser, the phosphorescence emission was recorded by an ICCD camera equipped with a stereoscope. The ICCD was gated at 100 μs to suppress the background radiation. Two-dimensional temperature maps were obtained using the temperature-sensitive ratio of two spectrally filtered phosphorescence emission lines at 455 and 493 nm. The stereoscope was equipped with two corresponding bandpass filters, each having a FWHM of 10 nm. The resulting intensity ratios were converted to the temperature scale, using temperature-referenced ratios from a separate calibration measurement.
Figure 5.4 presents temperature maps from the outlet nozzle, obtained at four different engine loads (loads increasing as their number increases). As expected, an increase in the average surface temperature (from 300 °C to about 800 °C) can be observed, shown as a function of engine load. Out of six operating loads being measured, the two lowest engine thrust levels (not shown in Fig. 5.4) had to be omitted, due to YAG:Dy not being temperature-sensitive below 300 °C.

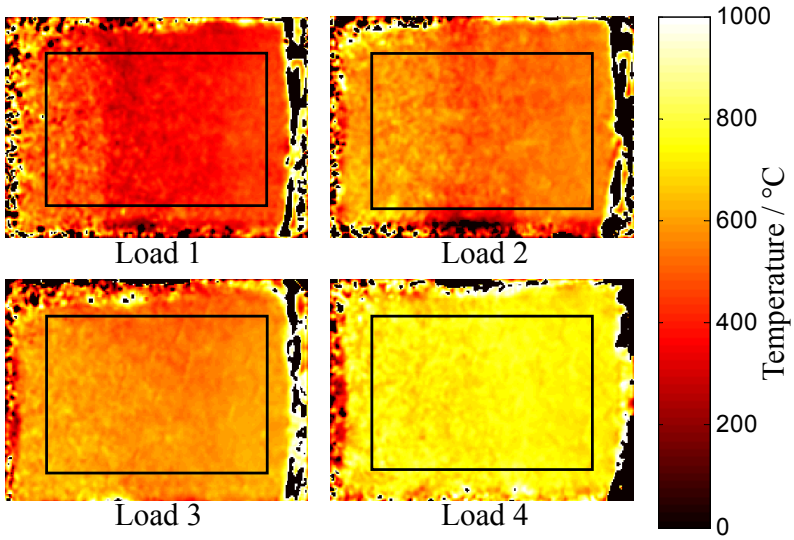

Figure 5.4: *Temperature maps of an outlet nozzle segment (see Figure 5.3), achieved through remote thermometry using a two-colour phosphorescence ratio of YAG:Dy. Conditions of engine operation at four different loads are displayed.*

In Figure 5.4 the spatial temperature deviations were found to be in the order of 40 °C across the entire nozzle segment, when concerned with the areas inside the black frames. These variations should be seen in relation to the temperature precision achieved during the calibration of the phosphor, which for YAG:Dy was found being in the order of ±7 to 10 °C. Hence, the observed variations in the results across different parts of the nozzle segment can be attributed to non-uniform temperature distributions during engine operation. LIP thermometry has thus demonstrated a clear potential for 2D surface temperature measurements in the adversely challenging environment of a jet engine under full-load operation.

5.3 Wall Temperatures in a Marine Two-Stroke Diesel Engine

At the present time, most large vessels all over the world operate on heavy fuel oil. New emission requirements and increasing fuel costs, however, led to the marine industry seeking alternative competitive fuels. In this connection, natural gas is considered to be an important clean source of energy for seagoing vessels. Using natural gas as fuel enables the CO_2 footprint of sea transportation to be further reduced, at the same time as close to zero SO_x emissions can be achieved. The volume of global natural gas resources together with the increasing availability of gas in many ports, contributes to making gas an attractive alternative. Two-stroke heavy-fuel-oil-burning engines have successfully been introduced to the liquefied natural gas carrier market offering high system efficiency at reduced emissions for ocean-going vessels [195].

The *4T50ME-X research engine* (*MAN Diesel & Turbo*, Copenhagen, Denmark) is a four-cylinder two-stroke engine specially designed to be modifiable for either diesel-fuel or natural-gas operation; see Figure 5.5. Its cylinders have a bore of 0.5 m and a stroke of 2.2 m, making the engine capable of delivering 7080 kW at a maximum speed of 123 rpm [196].

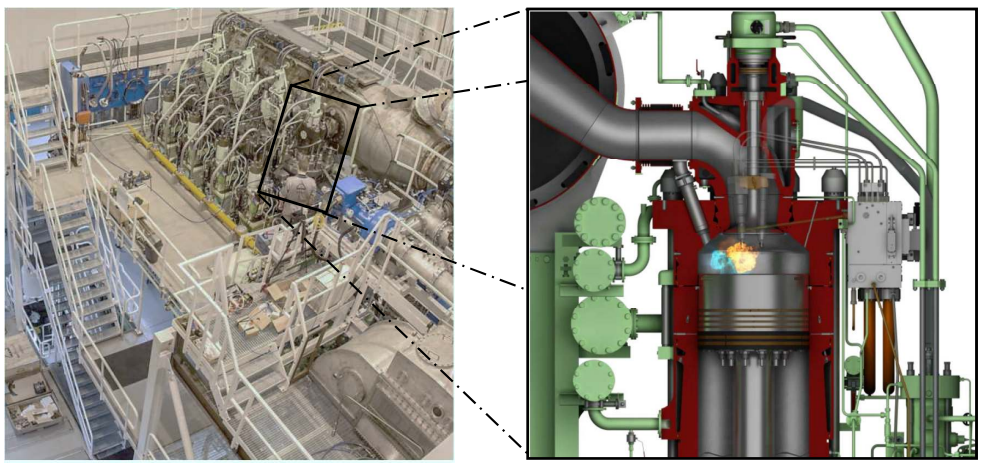

Figure 5.5: *Part* (a)*: A photograph of the 4T50ME-X research engine; Part* (b)*: A high pressure gas injection system making use of diesel pilot ignition. The images were provided with friendly permission of MAN Diesel & Turbo,* [196].

Information regarding the surface temperatures of large-bore marine engines is sparse and is as of yet either measured by use of thermocouples [197] or derived from sub-surface locations [198]. The present work shows LIP thermometry being applied to an operating large-bore marine engine for the very first time. A schematic diagram of the measurement setup is to be found in Figure 5.6.

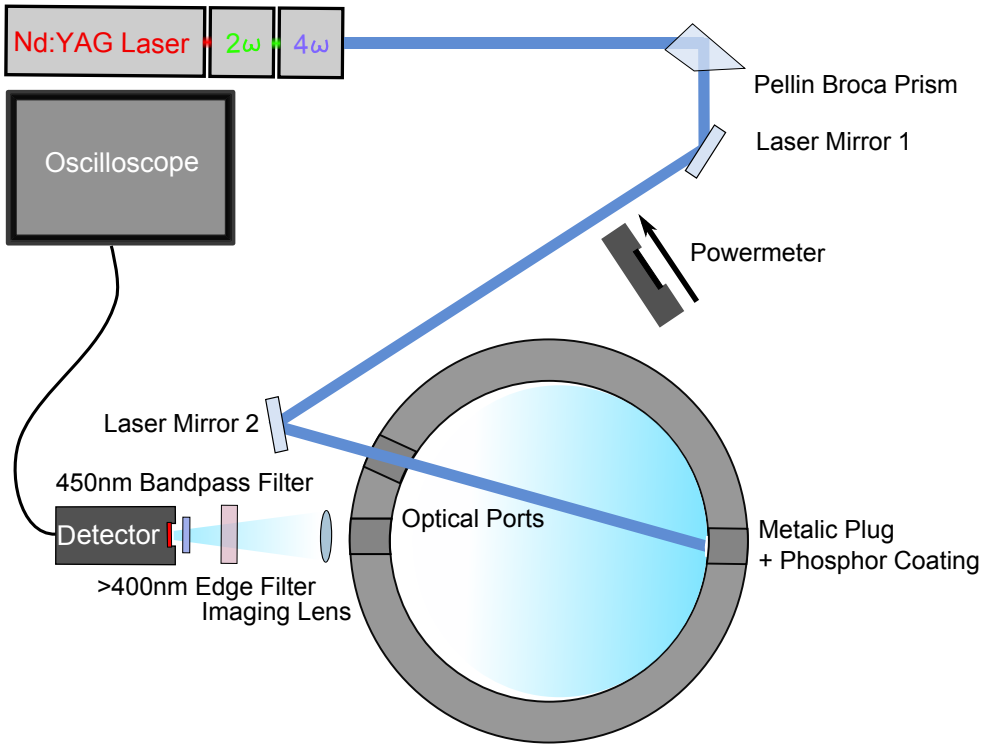

Figure 5.6: *An experimental setup for remote wall thermometry on a steel insert inside the 4T50ME-X research engine using* $CdWO_4$.

The *4T50ME-X engine* was fuelled with marine diesel oil and was run in scavenging uniflow mode. The cover of the cylinder head provided access to the combustion chamber by way of 24 optional ports. Two of these ports were equipped with sapphire windows, the one for laser excitation and the other for phosphorescence collection. One port on the opposite side was equipped with a phosphor-coated steel insert that could be removed for application of the coating without its being necessary to remove the entire cylinder cover. $CdWO_4$ with phosphorescence emission centred around 450 nm was excited by 10 Hz pulsed laser radiation at 266 nm. When the engine was running at between 75 to 100 rpm, depending upon the load, this allowed for the simultaneous observation of 6 to 8 temperatures per combustion cycle. A total of 100 single laser shots were accumulated for each CAD. To increase the crank-angle resolution for averaged wall temperatures during the combustion cycle, the trigger time delay between the piston position and the laser pulse was varied.
Figure 5.7 shows a comparison of wall temperatures from averaged combustion cycles at two different engine loads. In addition to the wall temperatures, which were derived from the decay time of $CdWO_4$, the global gas pressure is also shown as a function of CAD. When the engine load was increased from 23 % to 54 %, the peak pressure rose accordingly, from 62 bar to 110 bar. Due to the increase in gas pressures produced by

the combustion of more fuel, the cylinder wall temperatures rose by approximately 20 K on average. At 23 % engine load, the wall temperature swing went from 450 K at low compression to about 470 K around TDC. When the engine load was increased to 54 %, the wall temperatures increased and varied within an interval of 465 K to 485 K.

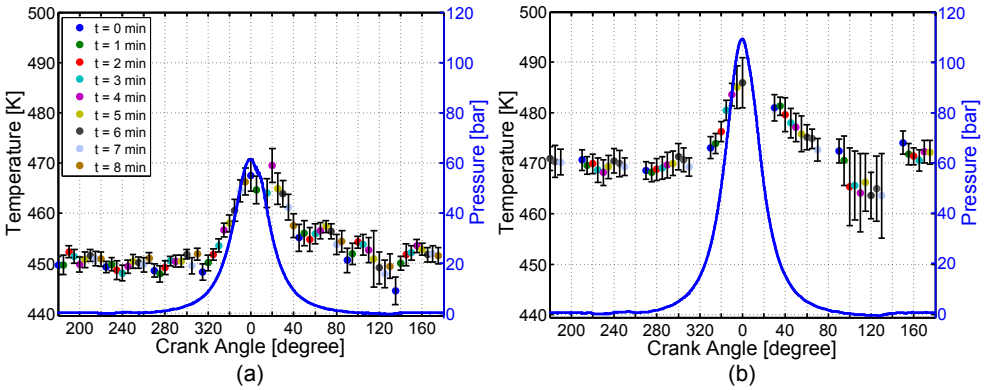

Figure 5.7: *Wall temperature during fired operation with use of a single-hole atomizer at an engine load of* 23 % (a) *and* 54 % (b). *Wall temperatures at each crank angle were averaged over 100 cycles, with error bars representing one standard deviation. Global gas pressures are represented by solid lines in connection with the right-sided y-axis scales.*

In experiments carried out at higher engine loads, the maximum cylinder wall temperatures that were expected during the cycle were exceeded. $CdWO_4$ was thus not sensitive enough to register the temperature transients as a whole during combustion at loads higher than 54 %. However, this false prediction of an expected surface temperature range simply underlines the importance of such measurements for the reassessment and improvement of today's predictive models and for the design of future engines. In addition, it should be noted that these results were obtained during an initial encounter with the *4T50ME-X engine* in which the time available for experiments was limited to 1.5 days, including time to setup and to dismantle all necessary equipment. Further experiments, in cooperation with *MAN Diesel & Turbo*, involving target areas on different engine parts and phosphors that are sensitive at higher surface temperatures are scheduled.
Nevertheless, the experiment carried out mark the first time of LIP thermometry being successfully carried out inside an operating large-bore two-stroke diesel engine. The results presented here indicate the prospects to be promising for successful experiments to be performed once the engine has been modified for the combustion of natural gas.

Free Telescope
This page, when rolled into a tube, makes a telescope with 1:1 magnification.

6 Outlook

This chapter concerns the prospects for interesting and worthwhile research on phosphor thermometry in the future. This is viewed mainly within the context of the investigations carried out within the framework of the thesis, what is taken up here being structured in accordance with the order of the articles that are appended.

6.1 Advances in Industrial Application

In the foreseeable future, laser diagnostics seem likely to maintain and expand their role as a major tool for studying the effects of different experimental input parameters in combustion. Their potential in performing remote and non-invasive measurements at high spatial and temporal resolution is hardly challenged by other diagnostic techniques in this area. One factor that does tend to limit the use of laser-based diagnostic techniques on a larger scale, such as in industrial applications, is their dependence upon expensive laser equipment.

Of the many laser-based techniques available, phosphor thermometry has a particularly high potential for the broader industrial use. Its simple, rugged design, involving few optical components, can withstand even the harshest environments and enables a wide variety of industry-relevant applications, including component inspection, control and further developments to be pursued. The comparatively high signal yields obtained from thermographic phosphors, increases the potential of using cost-effective instrumentation for excitation and detection. Recent research has shown the successful application of LEDs to be an alternative for excitation sources, replacing expensive pulsed laser systems at a fraction of their price. At present, UV LEDs having emission wavelengths as low as 210 nm are available. Given the current rate of advance in their development, their output powers can be projected to increase by more than one order of magnitude within the next decade.

Laser diagnostics suffer from a general drawback of being dependent upon optical access, which can be problematic in certain areas of application. In LIP, however, optical fibres can suffice for excitation of and signal collection from surface spots of interest, if neither endoscopic access nor the implementation of windows is feasible. Instead of large windows being created, only small holes need to be drilled, this creating fewer geometric distortions of the measurement object. Such access holes could be placed between cooling channels, for example. Fibre bundles can provide access to multiple objects at once, such as in the simultaneous measurement of piston temperatures from several different cylinders in ordinary production-type IC engines. In addition, the avoidance of optical windows allows phenomena occurring at high peak pressures, such as engine knock, to be observed. Several pre-studies including the construction and testing of suitable fibre adapters were carried out successfully during the research that led to the present work, which laid the foundation for further advances towards future applications of fibre-optic phosphorescence thermometry in combustion engines.

Another issue to address in efforts to achieve a more widespread use of phosphor

thermometry is that of automation. An automated data acquisition system can enable much quicker measurements of surface areas to be performed, reducing component stress and reducing the effects of long-term drifts in operating conditions. An automated calibration routine, such as that described in Paper [I] enables temperature calibrations to be conducted ca. four times as fast as earlier, with the additional advantage of increased measurement accuracy. Fast evaluation schemes, such as the RLD algorithm, can be utilized for obtaining user-friendly temperature results in real-time, using implemented libraries for the conversion of phosphorescence decay times into temperatures. Although it would be at the cost of reduced measurement precision, this alternative could be effective in reducing the amount of data and the evaluation efforts needed. A possibly even more interesting application of such a system would be its use for active feedback control. Initial tests with use of an in-house programmable oscilloscope have already provided promising results for real-time temperature determination during point measurements.

Finally, an international standard for phosphor thermometry used in high-temperature-turbine applications is currently under discussion by an international board of recognized phosphor scientists. Once it becomes publicly available, this standard can help gaining access to a broader audience of potential industrial end-users through providing useful guidelines and information. In this context, the development of smart TBCs for remote temperature or heat flux sensing, in which thermographic phosphors are embedded in thermal barrier coatings appears to be of particular interest. The implementation of such coatings on turbine parts that are in regular service would provide a desirable tool for inspection and overhaul applications in the turbine industry.

6.2 Film Thickness and On-Site Coating Techniques

Papers [II, III] demonstrated experimentally that coating films thicker than 20 μm, even if present only in a limited area, can have an intrusive effect on the surface temperatures observed in typical IC engine applications. Apparently, transient combustion at higher engine speeds or with larger temperature swings requires even thinner coatings in order to avoid temperature intrusion. In contrast to other thin-film deposition techniques, spray coatings are very cheap, fast and simple to apply on-site, without the necessity of employing tedious curing procedures at elevated temperatures. Surfaces of integrated parts that cannot be removed are comparatively effortless to access. However, regarding film thicknesses, it was found that coating cross sections smaller than 5 μm are very difficult, if not impossible, to produce by use of the spray coating technique. Also, the signal yield of spray coatings is considerably less than that of pure phosphor films of similar thickness, since these coatings consist to a large part of a non-emitting and to some extent signal-absorbing binding agent. It is desirable, therefore, to investigate alternative coating processes that can be performed on-site.

Of the various techniques for coating production that are available, the sol-gel process appears to be a particularly promising candidate, since it enables thin coatings of well controlled thicknesses to be produced in a liquid bath, there being no need of expensive

or bulky equipment, such as vacuum chambers. Another coating process of interest, currently used for TBCs in turbine applications, is that of electrostatic-assisted chemical vapour deposition (EA-CVD), which (unlike most other CVD or PVD processes) allows coatings to be produced at atmospheric pressure. To date, CVD processes have only very rarely been used for producing thermographic phosphor coatings, so that further progress in feasibility studies of CVD coatings in context with phosphor thermometry appear worthwhile and useful.

6.3 Signal Linearity in the Detection System

The issue of signal linearity in the detection system was investigated in detail for a number of different point detectors and CCD cameras; see Papers [IV, V, VI]. Non-linear detector behaviour was identified as being one of the major error sources in phosphor thermometry. In general, much care needs to be employed in choosing suitable operating conditions for electronic equipment during signal-collection. Even two devices of the same production type can exhibit distinctively different linearity characteristics. Thus, one cannot simply rely on linearity data concerning similar detector types published earlier. Instead, every detector needs to be characterized and corrected for individually, unless the operating parameters remain quite untouched between temperature calibration and experiment. In many practical applications, however, detection efficiency can be subjected to rather large changes that require gain, exposure-time, or laser energy adjustments in order to not lose the signal. Detailed knowledge of individual detectors is thus indispensable for accurate measurement results and should be assigned greater importance in future research.

Another issue that should be given further attention is that of long- and short-term drifts in detectors, which lead to difficulties in obtaining sufficiently similar results under identical measurement conditions. Thus, preliminary investigations with use of ICCD cameras have shown disturbing effects of instability that are believed to stem from the image intensifier. Further research should be directed at such problems of instability and how they can be avoided or compensated for.

Since 2009, scientific CMOS technology has been introduced on the market, which combines the advantages of classical CCD detectors with those of CMOS detectors. It is claimed that scientific CMOS cameras provide low noise, rapid frame rates, wide dynamic range, high quantum efficiency, high resolution, and a large field of view, in one and the same image. Of particular interest within the context of signal linearity is a special feature that provides automatic sensitivity correction algorithms that are unique for individual camera pixels in every CMOS detector. Clearly, this feature could reduce end-user efforts considerably through its avoiding errors caused by non-linear signals. Perhaps, suppliers of PMTs and photo-diodes could follow on a similar route in efforts to overcome the problem of signal linearity, that have been pointed out here. However, that would imply there to be a need for adding A/D converters to the detectors, a matter that would increase production cost and also prevent the signals to be read out on conventional oscilloscopes.

6.4 Data Reduction Algorithms

Papers [VIII,IX] and unpublished work carried out within the framework of the thesis have shown further potential to increasing measurement precision for a given set of recorded signals by means of adapting the data-evaluation algorithm. Such an increase in measurement precision can be attained by either changes in the evaluation algorithm being employed, or through the choice of evaluation window boundaries. With the various different evaluation approaches currently being in use, it could be desirable to guide research towards use of more standardized procedures. There may be no single approach that works best in all practical situations. Standardized guidelines, however, proposing use of various procedures for adapting data evaluation algorithms to specific measurement situations are desired in order to optimize precision of temperature results. During the course of the research for the thesis, fitting windows and the way they automatically adapted to individual changes in the signal curve, were seen as having particular potential for enabling improvements to be made in the precision of decay-time-based phosphor thermometry.

6.5 Gas-Phase Applications

An emerging area for use of thermographic phosphors (one not dealt with further in the thesis) is that of planar thermometry in gas flows and liquids through use of seeded phosphor particles. Lasers, because of their high pulse energies, will certainly continue to be major sources of excitation within this field, partly because of seeded particles producing weaker signals than coated surfaces do, and partly because pulse energies sometimes need to be distributed over large planar probing volumes. Current LEDs do not deliver sufficiently high emission intensities to excite seeded particles to a satisfactory extent.

Rayleigh scattering (RS), LIF and two-line atomic fluorescence (TLAF) are examples of competing techniques used in 2D gas phase thermometry. One of the most experimentally simple, yet useful, laser-based temperature techniques is that of Rayleigh scattering. The elastic scattering of light from molecules provides a measure of the total number density, which when coupled with the ideal gas law allows the temperature to be deduced. RS measurements can only be employed under very clean, particle-free conditions, because of the elastic nature of the process being highly susceptible to interference from Mie scattering and from spurious reflections on surfaces and on optical equipment. Filtered Rayleigh scattering is less susceptible to interference, yet the quantitative temperature measurements needed require knowledge of the Rayleigh cross sections of individual species, which are difficult to obtain in a 2D application, since this requires the mole fraction distribution to be known. Various LIF strategies for thermometry exist, all of them are based on the species population described by the Boltzmann distribution. The shift in wavelength associated with the fluorescence process is advantageous for reducing interference, especially as compared with Rayleigh scattering. LIF-based techniques can use either naturally occurring species or a seeded species. The use of in-situ species, such as OH, CH or CN, however, is restricted to limited temperature regions in which these species exist. Seeded LIF tracer

molecules such as toluene or acetone are also combustible and can disappear through taking part in chemical reactions. Pressure dependencies based on collisional effects have been observed in some LIF tracers, this disturbing pure temperature sensing without its providing additional knowledge on ambient pressures. Of the various techniques referred to TLAF has shown particular potential for thermometry conducted in sooty flames. TLAF is based on the excitation of Stokes and anti-Stokes transitions of seeded atoms, such as Indium. Temperature determinations are based on the relative intensities involved, a Boltzmann distribution of the populated electronic states being assumed. Although recent research has pushed the single-shot uncertainty of TLAF thermometry conducted in flames from around 250 K down to 100 K, through accessing the non-linear fluence regime, the degree of uncertainty involved is still rather high in comparison with the potential that thermographic phosphors have to offer.

The LIP technique is similar to LIF, but uses solid phosphor particles instead of liquid tracers. In contrast to LIF tracers, these particles are capable of surviving at high temperatures and yield comparatively high and long-lived emission signals. A field of application of special interest is that of combined studies of gas thermometry and flow turbulence, which can be achieved by use of phosphor particles in particle image velocimetry (PIV) experiments:

- One approach is to utilize phosphorescence traces from excited particles, making use of images having extended exposure times. For thermometry, this alternative can be expected to work best in combination with the two-colour ratio method, since the particle traces obtained may be too short to encompass a sufficient number of pixels for a reasonable decay time analysis to be carried out on the basis of the pixel intensities.

- The other, more promising, approach would involve recording two time-delayed images, as is common in conventional PIV systems. It has the possibility of utilizing both the two-colour ratio method and the RLD algorithm, which can be used to determine phosphorescence decay times on the basis of two integrated and time-delayed intensities.

A further example of a potential future area of application is the use of thermometry in connection with spray diagnostics. Known temperature distributions can contribute there to the explanation of experimentally observed spray patterns through use being made of local information concerning such temperature-dependent characteristics as viscosity and evaporation.

Given the current rate of advances in research and in instrumentation technology, many other exciting gas-phase applications will surely come within reach of phosphor thermometry in the near future.

Acknowledgements

Looking back at my past years of experience in Sweden, I count myself fortunate to have met so many great people that contributed to this work in one way or another. They all deserve being acknowledged for their continued care and support as colleagues and friends. In particular, I would like to express my gratitude to the following persons:

I wish to thank *Mattias Richter* and *Marcus Aldén* for admitting me as a Ph.D. student to the Division of Combustion Physics under their supervision. *Mattias* has been my main supervisor and shared his vast knowledge on laser diagnostics and combustion engines with me. He has always been a competent, funny and understanding project leader and his sharp scientific advice was often spiced with a good portion of humour, making our countless meetings not only informative, but also very enjoyable. I thank him especially for providing me with an enormous amount of freedom in choosing my research path within the boundaries of our projects.
Marcus has taken to the role of my co-supervisor and I'd like to express my deepest gratitude for countless proof-readings, his language advices and our discussions in connection with the writing of the included research articles. Besides, he showed a curious interest in German language and occasionally came to me with German proverbs that I, admittedly and to my own astonishment, had not heard of myself! As head of the Division, *Marcus* also provided an excellent, open minded, and very stimulating research environment.
My fellow colleague and predecessor *Johannes Lindén* deserves to be mentioned here for introducing me to the experimental basics of Laser-Induced Phosphorescence. His cheerful personality paired with his unique "German" sense of humour has left a long-lasting impression on me. I have never met anyone before in my life who has mastered the art of documentation and archiving to such a divine state of perfection.
Another thanks goes to my successional colleague and former master student *Fahed Abou Nada*. He is a great team player and his practical creativity in the lab is beyond imagination. I wish him the best of luck for his continued progress towards achieving his Ph.D. and pursuing a successful career as a researcher.
During my time of research as a Ph.D. student I had the opportunity to carry out a couple of engine measurements at the Division of Combustion Engines together with *Peter Andersson*, who has become a close friend of mine. One year later I had the pleasure to conduct another set of engine measurements together with *Martin Algotsson*. Thank you both for keeping the engine running, it was a fantastic experience to work with you guys.
Bengt Johansson, *Bengt Sundén* and *Helgi Fridriksson* have shared their detailed knowledge on heat transfer in numerous discussion meetings concerned with our engine related measurement results and helped us a great deal to make sense of the data obtained.
Within the HELIOS research project in close cooperation with *MAN Diesel & Turbo*, I had the chance to collaborate with *Stefan Mayer*, *Frank Jensen* and *Johan Hult*. Working with them has always been a smooth and inspirational experience and I hope that we get the opportunity to collaborate more in the near future.

Acknowledgements

I'd like to thank *Per-Erik Bengtsson*, *Mattias* and *Marcus* for putting enough faith in me to let me design and supervise five master- and bachelor projects. Thank you *Nawzad, Fahed, Robert, Xin* and *Kristin* for trying out new ideas and contributing to my research.
A lot of experiments would have been delayed or even discontinued at an early stage if it wasn't for the help of our friendly and very competent workshop technician *Rutger Lorensson*. Thanks for keeping both trash and treasure spare parts around every corner; there was always a quick and smart solution at hand thanks to his valuable, but terribly underestimated spare parts collection.
Another big thanks goes to *Susanne Dunér*, *Lennart Österman*, *Ronald Whiddon* and *Igor Buzug* for manufacturing the PMT control boxes and amplifiers that were used during the experiments involved.
Robert Collin and *Fredrik Ossler* should be acknowledged for keeping everyone safe in and around the Division. Especially on behalf of my mum, I'd like to thank them for making me write risk analyses that kept me unharmed and alive throughout my past years of research.
There has also been an administrative staff around the Division, professionals at keeping all the paper work at bay such that we could stay focused on our research projects instead. I am truly grateful for your kind efforts that make the Division work so smoothly *Minna Ramkull*, *Cecilia Bille*, *Eva Persson*, *Sara Holmgren*, *Anneli "fruktpolis" Nilsson* and *Nina Mårtensson*.
My next acknowledgement is connected with the potential risk of making some people's girlfriends jealous, but I think it is rather safe to claim that throughout the past years I have spent more hours awake with *Alexis Bohlin* and *Zheming Li* than anyone else did. I was very lucky getting the chance of sharing an office with you guys and I am deeply grateful for all sorts of inter-cultural, social- and scientific discussions that we had behind closed doors and during lunch breaks. They will be missed and never forgotten.
Jonathan Johnsson and *Edouard Beroccal* have over the years been faithful and much appreciated lunch companions. Together we shared many moments of great laughter and joy and it is needless to say that both of you have become valued friends of mine. On top of that, *Jonathan* is "cursed" with lots of competence and helped me out on numerous occasion troubleshooting when MATLAB and I had our differences. Apart from Ed's exquisite sense of humour, I truly admire his ability to get lots of people excited and involved in his projects when they really were to do something else instead.
Olof Johansson has been another valued lunch comrade and friend. His skill and dedication as a scientist seemed only to be matched by his kind and particularly Swedish modesty.
Apart from having shared lots of entertaining debates about gender issues, video games and the life in Sweden as a foreigner, I also like to express my sincerest appreciation to *Ronald Whiddon* for proof reading some of my documents on his free time. Even though I was mainly aiming for linguistic support, *Ron's* curiosity for scientific detail often made us end up in unexpected, but very fruitful discussions on matters of research instead. I'll miss the occasional Wednesday nights at *Pub Rydbergs* with him and *Peter Joo*, the Canadian guy who for some reason is doubting my nationality.

Johan Sjöholm was the first Ph.D. student from this Division that I met in 2008. I'll always remember how kind and helpful he was when I tried to set up my presentation for the job interview. I also very much enjoyed his company on our US road trip with *Mattias* in connection with the *SAE World Congress* in Detroit.
I would also like to express my gratitude to the former "Doktorandgänget", consisting of *Johannes*, *Jonathan*, *Johan*, *Ron*, *Elias Kristensson* and *Andreas Lantz*. Thanks for all the fun activities that made me feel welcome when I newly arrived in Sweden as a fresh Ph.D. candidate.
Now I almost forgot to sound a fanfare for *Håkan Fink*, my friend and Swedish teacher from Jena. There is no doubt that he and his funny Swedish lessons took a significant share in the events that eventually made me look for job opportunities in Sweden.
I would like to thank my colleagues at the Division that have enriched my experience through their own excellent work and pleasant company. In particular, I would like to mention *Henrik Bladh*, *Joakim Bood*, *Moah Christensen*, *Andreas Ehn*, *Bo Li*, *Zhongshan Li*, *Emil Nordström*, *Joakim Rosell*, *Zhiwei Sun*, *Nils-Erik Olofsson*, *Per Pettersson*, *Linda Vallenhag*, *Rikard Wellander* and *Bo Zhou*.
To the rest of you whose presence has been important, both within and outside the Division, whom I have not mentioned by name, I also express my sincere appreciation. I get by with a little help from my friends.

Of course, it is needless to say that neither me nor this thesis would exist, if it wasn't for my dear parents *Ulrike* and *Bruno*. I will never cease to be grateful for your love and care, for all your encouragement and support that I received throughout my life. Another big thanks goes to the rest of my family *Annette*, *Andreas*, *Siegfried*, *Friedrich* and *Mirabelle*. You were always there for me when I needed you and I consider myself very lucky to have you all in my life.

Finally, no words could suffice to fully express my appreciation for *Marion*, who has been there on the good days and the bad ones. Your passion and love has given me support, comfort and the strength to finish this work. Thanks for proofreading countless pages and, most of all, for being the best girlfriend in the world!

Ich liebe Dich !!! ♡

References

[1] Weinberg, F.J. *The first half-million years of combustion research and today's burning problems*. Proc. Comb. Inst., **15**:1–17, 1974.

[2] International Energy Agency. *Key world energy statistics 2012*, Retrieved May 26, 2013. URL http://www.iea.org/publications/freepublications/publication/kwes.pdf.

[3] International Energy Agency. *World energy outlook 2012*, Retrieved May 26, 2013. URL http://www.iea.org/publications/freepublications/publication/English.pdf.

[4] Intergovernmental Panel on Climate Change. *IPCC fourth assessment report*, 2007.

[5] Chang, J., Güralp, O., Filipi, Z., Assanis, D., Kuo, T., Najt, P., and Rask, R. *New heat transfer correlation for an HCCI engine derived from measurements of instantaneous surface heat flux*. SAE Tech. Pap., **2004-01-2996**:1–18, 2004.

[6] Wilhelmsson, C., Vressner, A., Tunestål, P., Johansson, B., Särner, G., and Aldén, M. *Combustion chamber wall temperature measurement and modeling during transient HCCI operation*. SAE Tech. Pap., **2005-01-3731**:1–11, 2005.

[7] Demuynck, J., De Paepe, M., Sierens, R., and Verhelst, S. *Heat transfer measurements inside a gas fuelled spark ignited engine for model validation*. In *Proc. of the FISITA World Automotive Congress, F2010-A-062*. 2010.

[8] van Basshuysen, R. and Schäfer, F. *Handbuch Verbrennungsmotor*. Vieweg + Teubner Verlag, Wiesbaden, 6 edn., 2011.

[9] Siemens Power Generation, Retrieved May 26, 2013. URL http://www.energy.siemens.com.

[10] Kohse-Höinghaus, K. *Applied Combustion Diagnostics*. CRC Press, 1989.

[11] Eckbreth, A.C. *Laser Diagnostics for Combustion Temperature and Species*. Gordon and Breach, 1996.

[12] Allison, S.W. and Gillies, G.T. *Remote thermometry with thermographic phosphors: Instrumentation and applications*. Rev. Sci. Instrum., **68**(7):2615–2649, 1997.

[13] Khalid, A.H. and Kontis, K. *Thermographic phosphors for high temperature measurements: Principles, current state of the art and recent applications*. Sensors, **8**:5673–5744, 2008.

[14] Aldén, M., Omrane, A., Richter, M., and Särner, G. *Thermographic phosphors for thermometry: A survey of combustion applications*. Prog. Energy Combust. Sci., **37**:422–461, 2011. ISSN 03601285.

[15] Brübach, J., Pflitsch, C., Dreizler, A., and Atakan, B. *On surface temperature measurements with thermographic phosphors: A review.* Prog. Energy Combust. Sci., **39**(1):37–60, 2013.

[16] Omrane, A., Särner, G., and Aldén, M. *2D-temperature imaging of single droplets and sprays using thermographic phosphors.* Appl. Phys. B, **79**:431–434, 2004.

[17] Brübach, J., Patt, A., and Dreizler, A. *Spray thermometry using thermographic phosphors.* Appl. Phys. B, **83**:499–502, 2006.

[18] Omrane, A., Petersson, P., Aldén, M., and Linne, M. *Simultaneous 2D flow velocity and gas temperature measurements using thermographic phosphors.* Appl. Phys. B, **92**(1):99–102, 2008.

[19] Lindén, J., Takada, N., Johansson, B., Richter, M., and Aldén, M. *Investigation of potential laser-induced heating effects when using thermographic phosphors for gas-phase thermometry.* Appl. Phys. B, **96**(2-3):237–240, 2009.

[20] Bai, S.Z., Zhao, H., and Li, G.X. *Two-dimensional gas-phase temperature measurements in engine using laser-induced phosphorescence thermometry.* Ranshao Kexue Yu Jishu/Journal of Combustion Science and Technology, **16**(6):515–518, 2010.

[21] Someya, S., Ochi, D., Li, Y., Tominaga, K., Ishii, K., and Okamoto, K. *Combined two-dimensional velocity and temperature measurements using a high-speed camera and luminescent particles.* Appl. Phys. B, **99**:325–332, 2010.

[22] Someya, S., Okura, Y., Uchida, M., Sato, Y., and Okamoto, K. *Combined velocity and temperature imaging of gas flow in an engine cylinder.* Opt. Lett., **37**(23):4964–4966, 2012.

[23] Van Lipzig, J., Yu, M., Dam, N., Luijten, C., and De Goey, L. *Gas-phase thermometry in a high-pressure cell using $BaMgAl_{10}O_{17}$: Eu as a thermographic phosphor.* Appl. Phys. B, **111**:469–481, 2013. Cited By (since 1996)0.

[24] Abram, C., Fond, B., Heyes, A., and Beyrau, F. *High-speed planar thermometry and velocimetry using thermographic phosphor particles.* Appl. Phys. B, **111**:155–160, 2013.

[25] Preston-Thomas, H. *The international temperature scale of 1990 (*ITS-90*).* Metrologia, **27**:3–10, 1990.

[26] Scervini, M. and Rae, C. *Thermocouple degradation mechanisms.* HEATTOP Lecture Notes, 2006.

[27] Pentronic. *Tolerance classes for thermocouples according to the* IEC 60 584-2:1995, Retrieved June 8, 2013. URL http://www.pentronic.se/media/26434/IEC_60584_TC_060210.pdf.

[28] Marshall, R., Atlas, L., and Putner, T. *The preparation and performance of thin film thermocouples.* J. Sci. Instrum., **43**:144–149, 1966.

[29] Feist, J.P. *Development of Phosphor Thermometry for Gas Turbines.* Ph.D. thesis, Imperial College of Science, London University, 2001.

[30] Profos, P. *Handbuch der industriellen Messtechnik.* Vulkan-Verlag Essen, 1974.

[31] Alaruri, S., Bianchini, L., and Brewington, A. *Effective spectral emissivity measurements of superalloys and* YSZ *thermal barrier coating at high temperatures using a* 1.6 μm *single wavelength pyrometer.* Opt. Las. Eng., **30**:77–91, 1998.

[32] Dunker, R. *Advances in Techniques For Engine Applications.* Wiley, 1996.

[33] Sentry Optronics Corp. ST685, ST688, ST689, ST688 Plus HDS Infrared Thermometer, Retrieved June 8, 2013. URL http://www.sentry17.com/st68x.htm.

[34] Anselmi-Tamburini, U., Campari, C., and Spinolo, G. *A two-color spatial-scanning pyrometer for the determination of temperature profiles in combustion synthesis reactions.* Rev. Sci. Instrum., **66**:5006–5014, 1995.

[35] Kerr, C. and Ivey, P. *An overview of the measurement errors associated with gas turbine aeroengine pyrometer systems.* Meas. Sci. Technol., **13**:873–881, 2002.

[36] TPTT, Inc. *Thermal paint - an essential tool for the accurate analysis of high temperature materials*, Retrieved June 10, 2013. URL http://www.thermalpaint.com.

[37] Bird, C., Mutton, J., Shepherd, R., Smith, M., and Watson, H. *Surface temperature measurements in turbines.* In *Symposium on Advanced Nonintrusive Instrumentation for Propulsion Engines; Brussels, NL.* 1992.

[38] Lefebvre, A. *Gas Turbine Combustion.* Taylor & Francis, 1983.

[39] Omrane, A. *Thermometry using Laser-induced Emission from Thermographic Phosphors: Development and Applications in Combustion.* Ph.D. thesis, Division of Combustion, Department of Physics, Lund University, 2005.

[40] Rong, Q., Sun, H., Qiao, X., Zhang, J., Hu, M., and Feng, Z. *A miniature fiber-optic temperature sensor based on a fabry–perot interferometer.* J. Opt., **14**:045002, 2012.

[41] Michalski, L., Eckersdorf, K., Kucharski, J., and McGhee, J. *Temperature measurement.* John Wiley & Sons, 2001.

[42] Grattan, K. and Zhang, Z. *Fiber Optic Fluorescence Thermometry.* Chapman and Hall, 1994.

[43] Wade, S., Collins, S., and Baxter, G. *Fluorescence intensity ratio technique for optical fiber point temperature sensing.* J. Appl. Phys., **94**:4743–4755, 2003.

[44] Sidiroglou, F., Wade, S., Dragomir, N., Baxter, G., and Collins, S. *Effects of high-temperature heat treatment on Nd^{3+}-doped optical fibers for use in fluorescence intensity ratio based temperature sensing.* Rev. Sci. Instrum., **74**:3524–3530, 2003.

[45] Grattan, K. and Palmer, A. *Infrared fluorescence "decay-time" temperature sensor.* Rev. Sci. Instrum., **56**:1784–1787, 1985.

[46] Shen, Y., Tong, L., Wang, Y., and Ye, L. *Sapphire-fiber thermometer ranging from 20 to 1800°C.* Appl. Opt., **38**:1139–1143, 1999.

[47] General Electric Company. *1971–1985 continuing the tradition*, Retrieved June 10. URL http://www.ge.com/about-us/history/1971-1985.

[48] Shionoya, S., Yamamoto, H., and Yen, W. *Phosphor Handbook.* CRC Press, 2nd edn., 2007.

[49] Butler, K.H. *Fluorescent Lamp Phosphors.* Pennsylvania State University Press, 1980.

[50] Neubert. US Patent No. 2071471, 1937.

[51] Brübach, J. Spektroskopische Methoden zur oberflächennahen Thermometrie in technischen Verbrennungsumgebungen. Ph.D. thesis, Technical University of Darmstadt, 2008.

[52] Kissel, T. Spektroskopische Methoden zur Charakterisierung wandnaher Verbrennungsvorgänge. Ph.D. thesis, Technical University of Darmstadt, 2011.

[53] Fonger, W. and Struck, C. Eu^{3+} ^5D *resonance quenching to the charge-transfer states in Y_2O_3S, La_2O_2S, and $LaOCl$.* J. Chem. Phys., **52**:6364, 1970.

[54] Ranson, R.M., Thomas, C.B., and Craven, M.R. *A thin film coating for phosphor thermometry.* Meas. Sci. Technol., **9**:1947–1950, 1998.

[55] Brübach, J., Feist, J.P., and Dreizler, A. *Characterization of manganese-activated magnesium fluorogermanate with regards to thermographic phosphor thermometry.* Meas. Sci. Technol., **19**:11pp, 2008.

[56] Weber, M. *Radiative and multiphonon relaxation of rare earth ions in Y_2O_3.* Phys. Rev., **171**:283–291, 1968.

[57] Hüfner, S. *Optical Spectra of Transparent Rare Earth Compounds.* New York, London: Academic Press, 1978.

[58] Henderson, B. and Imbusch, G. *Optical Spectroscopy Of Inorganic Solids.* Oxford University Press, USA, 2006.

[59] Goss, L.P., Smith, A.A., and Post, M.E. *Surface thermometry by laser-induced fluorescence.* Rev. Sci. Instrum., **60**:3702–3706, 1989.

[60] van Lipzig, J.P.J. *2D Temperature Measurements in the EHPC using Laser-Induced Phosphorescence.* Master's thesis, Combustion Technology Group, Eindhoven University, 2012.

[61] Skinner, S.J., Feist, J.P., Brooks, I., Seefeldt, S., and Heyes, A.L. *$YAG:YSZ$ composites as potential thermographic phosphors for high temperature sensor applications.* Sens. Actuators, B, **136**:52–59, 2009.

[62] Fuhrmann, N., Brübach, J., and Dreizler, A. *High-speed phosphor thermometry.* Rev. Sci. Instrum., **82**:104903, 2011.

[63] Khalid, A., Kontis, K., and Behtash, H.Z. *Phosphor thermometry in gas turbines: Consideration factors.* Proc. of the Institution of Mechanical Engineers, Part G: Journal of Aerospace Engineering, **224**(7):745–755, 2010.

[64] Fuhrmann, N., Brübach, J., and Dreizler, A. *Phosphor thermometry: A comparison of the luminescence lifetime and the intensity ratio approach.* Proc. Comb. Inst., **34**(2):3611–3618, 2013.

[65] Collins, S., Baxter, G., Wade, S., Sun, T., Grattan, K., Zhang, Z., and Palmer, A. *Comparison of fluorescence-based temperature sensor schemes: Theoretical analysis and experimental validation.* J. Appl. Phys., **84**(9):4649–4654, 1998.

[66] Duschinsky, F. Der zeitliche Intensitätsverlauf von intermittierend angeregter Resonanzstrahlung. Z. f. Phys., **81**(1-2):7–22, 1933.

[67] Svanberg, S. Atomic and molecular spectroscopy: basic aspects and practical applications. Springer-Verlag Berlin Heidelberg New York, 1991.

[68] Krauss, R., Hellier, R., and J.C., M. *Surface temperature imaging below* $300\,K$ *using* $La_2O_2S:Eu$. Appl. Opt., **33**:3901–3904, 1994.

[69] Cates, M., Allison, S., Jaiswal, S., and Beshears, D. *$YAG:Dy$ and $YAG:Tm$ fluorescence to* $1700\,°C$. In *Proc. of the 49th International Instrumentation Symposium; Orlando, FL; USA*, vol. 49, pp. 389–400. 2003.

[70] Särner, G. *Laser-Induced Emission Techniques for Concentration and Temperature Probing in Combustion.* Ph.D. thesis, Division of Combustion, Department of Physics, Lund University, 2008.

[71] Brübach, J., Kissel, T., Frotscher, M., Euler, M., Albert, B., and Dreizler, A. *A survey of phosphors novel for thermography.* J. Lumin., **131**(4):559–564, 2011.

[72] Swiatek, K., Godlewski, M., Niinistö, L., and Leskelä, M. *Optical recombination mechanisms in Eu^{2+}-doped CaS and SrS thin films.* J. Appl. Phys., **74**:3442–3446, 1993.

[73] Jeon, B., Hong, G., Yoo, Y., and Yoo, J. *Spherical* $BaMgAl_10O_17:Eu^{2+}$ *phosphor prepared by aerosol pyrolysis technique for* PDP *applications.* J. Electrochem. Soc., **148**:H128–H131, 2001.

[74] Bizarri, G. and Moine, B. *On $BaMgAl_{10}O_{17}$:Eu phosphor degradation mechanism: thermal treatment effects.* J. Lumin., **113**:199–213, 2005.

[75] Fond, B., Abram, C., Heyes, A., Kempf, A., and Beyrau, F. *Simultaneous temperature,mixture fraction and velocity imaging in turbulent flows using thermographic phosphor tracer particles.* Opt. Express, **20**:22118–22133, 2012.

[76] Lakshmanan, A. *Luminescence and Display Phosphors: Phenomena and Applications.* Nova Science Publishers Inc, 2007.

[77] Turos-Matysiak, R., Grinberg, M., Wang, J., Yen, W., and Meltzer, R. *Luminescence of BAM under high pressure: the Eu^{2+} sites.* J. Lumin., **122**:107–109, 2007.

[78] Rzhevskaya, O., Spasskiĭ, D., Kolobanov, V., Mikhaĭlin, V., Nagornaya, L., Tupitsina, I., and Zadneprovskiĭ, B. *Optical and luminescence properties of $CdWO_4$ and $CdWO_4 : Mo$ single crystals.* Opt. Spectrosc., **104**:366–373, 2008.

[79] Särner, G., Richter, M., and Aldén, M. *Investigations of blue emitting phosphors for thermometry.* Meas. Sci. Technol., **19**(12):125304, 2008.

[80] Brübach, J., Dreizler, A., and Janicka, J. *Gas compositional and pressure effects on thermographic phosphor thermometry.* Meas. Sci. Technol., **18**:764–770, 2007.

[81] Allison, S., Cates, M., Beshears, D., and Gillies, G. *Phosphor thermometry at ORNL.* In *Proc. of the 8th international temperature symposium.* 2003.

[82] Thorington, L. *Temperature dependence of the emission of an improved manganese-activated magnesium germanate phosphor.* J. Opt. Soc. Am., **40**:579–583, 1950.

[83] Kemeny, G. and Haake, C. *Activator center in magnesium fluorogermanate phosphors.* J Chem Phys, **33**:783–789, 1960.

[84] Omrane, A., Juhlin, G., Ossler, F., and Aldén, M. *Temperature measurements of single droplets by use of laser-induced phosphorescence.* Appl. Opt., **43**:3523–3529, 2004.

[85] Blasse, G. and Grabmaier, B. *Luminescent materials.* Springer-Verlag Telos, 1994.

[86] Cates, M.R. Beshears, D., Allison, S., and Simmons, C. *Phosphor thermometry at cryogenic temperatures.* Rev. Sci. Instrum., **68**:2412–2417, 1997.

[87] Edge, A., Laufer, G., and Krauss, R. *Surface temperature-field imaging with laser-induced thermographic phosphorescence.* Appl. Opt., **39**:546–553, 2000.

[88] Carnall, W., Fields, P., and Rajnak, K. *Electronic levels of the trivalent lanthanide aquo ions.* I. $Pr^{3+}, Nd^{3+}, Pm^{3+}, Sm^{3+}, Dy^{3+}, Ho^{3+}, Er^{3+}, Tm^{3+}$. J. Chem. Phys., **49**:4424–4442, 1968.

[89] Liu, Z., Jing, X., Song, H., and Fan, L. *The relationships between UV emission and green emission in ZnO phosphor.* Acta Phys. Chim. Sin., **22**:1383–1387, 2006.

[90] Quanta System. *Giant series specifications*, Retrieved May 13, 2013. URL http://www.quantasystem.com/root/gettechsheet.aspx?idtech=24&type=s&lang=en.

[91] EKSPLA. *Product specifications*, Retrieved May 14, 2013. URL http://www.ekspla.com/product/nl200-series-%E2%80%93-compact-air-cooled-short-pulse-duration-lasers.

[92] Christensen, C., Gordon, C., Moutoulas, C., and Feldman, B. *High-repetition-rate XeCl waveguide laser without gas flow.* Opt. Lett., **12**:169–171, 1987.

[93] Taniyasu, Y., Kasu, M., and Makimoto, T. *An aluminium nitride light-emitting diode with a wavelength of 210 nanometres.* Nature, **441**:325–328, 2006.

[94] Allison, S., Eldridge, J., and Jenkins, T. *Design issues for LED excitation of thermographic phosphors.* In *Proc. of the 58th International Instrumentation Symposium 2012, IIS, San Diego, CA, USA*, vol. 491, pp. 52–61. 2012.

[95] Allison, S.W., Cates, M.R., and Beshears, D.L. *Excitation of thermographic phosphors with a blue LED. 243-252.* In *Proc. of the 45th International Instrumentation Symposium, Albuquerque, NM, USA*. 1999.

[96] Allison, S., Cates, M., and Gillies, G. *Excitation of thermographic phosphors using a blue light emitting diode: Spectral characteristics and instrumentation applications.* Rev. Sci. Instrum., **73**(4):1832, 2002.

[97] Goedeke, S., Allison, S., Cates, M., Boudreaux, P., Valiga, R., and Mee, D. *LED excited phosphor thermometry in excess of* $1000\,^{\circ}C$. In *Proc. of the 53rd International Instrumentation Symposium 2007; Tulsa, OK; USA*, vol. 470, pp. 443–463. 2007.

[98] T-Tec. China (HK) Co., Limited. High Luminance 3W 365nm UV Power LED for Curing Machine, Retrieved May 14, 2013. URL http://www.uv-led-lights.com/china-high_luminance_3w_365nm_uv_power_led_for_curing_machine-180290.html.

[99] Atakan, B., Eckert, C., and Pflitsch, C. *Light emitting diode excitation of* $Cr^{3+} : Al_2O_3$ *as thermographic phosphor: Experiments and measurement strategy.* Meas. Sci. Technol., **20**:075304, 2009.

[100] Augousti, A.T., Grattan, K.T.V., and Palmer, A. *A laser-pumped temperature sensor using the fluorescent decay time of alexandrite.* IEEE/OSA J. Lightw. Technol., **LT-5**:759–762, 1987.

[101] Raja, R. and Cunningham, G. *Experimental investigation of phosphor thermography using a blue LED optical excitation source.* In *Proc. of the 48th International Instrumentation Symposium; San Diego, CA; USA*, vol. 48, pp. 55–62. 2002.

[102] Aizawa, H., Sekiguchi, M., Katsumata, T., Komuro, S., and Morikawa, T. *Fabrication of ruby phosphor sheet for the fluorescence thermometer application.* Rev. Sci. Instrum., **77**(4), 2006.

[103] Eldridge, J. Personal communication between C. Knappe and Dr. J.I. Eldrige. NASA Glenn Research Center, USA, April 5, 2013.

[104] Feist, J. and Heyes, A. *Photo-stimulated phosphorescence for thermal condition monitoring and nondestructive evaluation in thermal barrier coatings.* Heat Transfer Eng., **30**(13):1087–1095, 2009.

[105] Lee, S., Yovanovich, M., and Jafarpur, K. *Effects of geometry and orientation on laminar natural convection from isothermal bodies.* J. Thermophys. Heat Transfer, **5**(2):208–216, 1991.

[106] de Leeuw, D. and 't Hooft, G. *Method for the analysis of saturation effects of cathodoluminescence in phosphors; applied to* $Zn_2SiO_4 : Mn$ *and* $Y_3Al_5O_12 : Tb$. J. Lumin., **28**:275–300, 1983.

[107] Imanaga, S., Shigeru, Y., and Teruhiko, H. *Luminescence saturation effects in* $Y_2O_2S : Eu$ *phosphor.* Japanese Journal of Applied Physics, **19**:41–49, 1980.

[108] Hradil, J., Davis, C., Mongey, K., McDonagh, C., and MacCraith, B. *Temperature-corrected pressure-sensitive paint measurements using a single camera and a dual-lifetime approach.* Meas. Sci. Technol., **13**:1552–1557, 2002.

[109] Bell, J., Schairer, E., Hand, L., and Metha, R. *Surface pressure measurements using luminescent coatings.* Annu. Rev. Fluid Mech., **33**:155–206, 2001.

[110] Gouterman, M., Callis, J., Dalton, L., Khalil, G., Mebarki, Y., Cooper, K., and Grenier, M. *Dual luminophor pressure-sensitive paint:* III. *application to automotive model testing.* Meas. Sci. Technol., **15**:1986–1994, 2004.

[111] Särner, G., Göransson, U., Lindén, J., Richter, M., and Aldén, M. *Using oxygen-quenched pressure-sensitive paint for oxygen concentration measurements in low-temperature combustion environments.* Meas. Sci. Technol., **19**, 2008.

[112] Kissel, T., Brübach, J., Euler, M., Frotscher, M., Litterscheid, C., Albert, B., and Dreizler, A. *Phosphor thermometry: on the synthesis and characterisation of* $Y_3Al_5O_{12} : Eu(YAG : Eu)$ *and* $YAlO_3 : Eu(YAP : Eu)$. Mater. Chem. Phys., **140**:435–440, 2013.

[113] Rao, R. *Growth and characterization of* $Y_2O_3 : Eu^{3+}$ *phosphor films by sol-gel process.* Solid State Commun., **99**:439–443, 1996.

[114] Allison, S.W., Beshears, D.L., Bencic, T., Hollerman, W.A., and P., B. *Development of temperature-sensitive. paints for high temperature. aeropropulsion applications.* In *Proc. of the 37th AIAA/ASME/SAE/ASEE Joint Propulsion Conference and Exhibit.* 2001.

[115] Goedeke, S., Hollerman, W., Bergeron, N., Allison, S., Cates, M., Bencic, T., Mercer, C., and Eldridge, J. *Study of resbond ceramic binders used for high temperature noncontact thermometry.* In *Proc. of the 106th Annual Meeting of American Ceramic Society, Indianapolis, USA.* 2004.

[116] Someya, S., Uchida, M., Tominaga, K., Terunuma, H., Li, Y., and Okamoto, K. *Lifetime-based phosphor thermometry of an optical engine using a high-speed CMOS camera.* Int. J. Heat Mass Tran., **54**:3927–3932, 2011.

[117] Fuhrmann, N. Phosphor Thermometrie zur Bestimmung von Oberflächentemperaturen in Verbrennungsmotoren. Ph.D. thesis, Technical University of Darmstadt, 2013.

[118] Eckert, C., Pflitsch, C., and Atakan, B. *Sol-gel deposition of multiply doped thermographic phosphor coatings* $Al_2O_3 : (Cr^{3+}, M^{3+}), (M = Dy, Tm)$ *for wide range surface temperature measurement application.* Prog. Org. Coat., **68**:126–129, 2010.

[119] Brinker, J. *Sol-Gel Science: The Physics and Chemistry of Sol-Gel Processing.* Academic Press, 1990.

[120] Eckert, C.. Thermographische Phosphorschichten auf der Basis von dotiertem Al_2O_3 und dotiertem Yttrium stabilisiertm ZrO_2: Hergestellt mit CVD- und Sol-Gel-Verfahren. Ph.D. thesis, University of Duisburg-Essen, 2010.

[121] Pflitsch, C., Viefhaus, D., and Atakan, B. *CVD of thin ruby films on* $Si(100)$ *and stainless steel for surface temperature sensor applications.* Chem. Vap. Deposition, **13**:420–426, 2007.

[122] Feist, J.P., Heyes, A. L. Choy, K.L., and Su, B. *Phosphor thermometry for high temperature gas turbine applications.* In *Proc. of the 18th International Congress on Instrumentation in Aerospace simulation facilities.* 1999.

[123] Choy, K., Feist, J., Heyes, A., and Su, B. *Eu-doped* Y_2O_3 *phosphor films produced by electrostatic-assisted chemical vapor deposition.* J. Mater. Res., **14**:3111–3114, 1999.

[124] McClean, I., Simons, A., Thomas, C., and J.E., M. *Comparison between thin film and bonded powder phosphors for thermographic sensing in gas turbine engines.* IEEE T. Instrum. Meas., **49**:129–131, 2000.

[125] Ranson, R., Evangelou, E., and Thomas, C. *Modeling the fluorescent lifetime of* $Y_2O_3 : Eu$. Appl. Phys. Lett., **72**:2663–2664, 1998.

[126] Steenbakker, R.J.L., Feist, J.P., Wellman, R.G., and Nicholls, J.R. *Sensor thermal barrier coatings: Remote in situ condition monitoring of $EB-PVD$ coatings at elevated temperatures.* J. Eng. Gas Turbines Power, **131**(4):041301, 2009.

[127] Gentleman, M.M., Eldridge, J.I., Zhu, D.M., Murphy, K.S., and Clarke, D. *Non-contact sensing of TBC/BC interface temperature in a thermal gradient.* Surf. Coat. Technol., **201**:3937–3941, 2006.

[128] Engel, Y. *Heat and Mass Transfer: A Practical Approach.* McGraw-Hill, Inc., 2006.

[129] Incropera, F., DeWitt, D., Bergman, T., and Lavine, A. *Fundamentals of heat and mass transfer.* John Wiley & Sons, 2007.

[130] Merker, G. and Schwarz, C. *Grundlagen Verbrennungsmotoren, Simulation der Gemischbildung, Verbrennung, Schadstoffbildung und Aufladung.* Vieweg + Teubner Verlag, Wiesbaden, 2009.

[131] Zyp Coatings, Inc. *Material safety data sheet: HPC binder*, Retrieved April 1, 2013. URL http://www.msdshazcom.com/MSDS/A/ARCHIVE/WCD0000F/WCD00F0A.HTM.

[132] Thermtest, Inc. *Material property search*, Retrieved April 1, 2013. URL http://www.thermtest.com/material-property-search/.

[133] Atakan, B. and Roskosch, D. *Thermographic phosphor thermometry in transient combustion: A theoretical study of heat transfer and accuracy.* Proc. Comb. Inst., **34**(2):3603–3610, 2013.

[134] Pilgrim, C., Feist, J., and Heyes, A. *On the effect of temperature gradients and coating translucence on the accuracy of phosphor thermometry.* Meas. Sci. Technol., **24**:105201, 2013.

[135] Kubelka, P. and Munk, F. Ein Beitrag zur Optik der Farbanstriche. Z. tech. Phys., **12**:593–601, 1931.

[136] GoodFellow. Hastelloy C276®- Heat Resisting Alloy (Ni57/Mo17/Cr16/Fe/W/Mn), Retrieved July 19, 2013. URL http://www.goodfellow.com/E/Hastelloy-C276-Heat-Resisting-Alloy.html.

[137] Shimadzu Scientific Instruments. High-Speed Video Camera HPV-2, Retrieved July 21, 2013. URL http://www.shimadzu.com.au/high-speed-video-camera-hpv-2#hsvc1.

[138] Khalid, A.H. and Kontis, K. *2D surface thermal imaging using rise-time analysis from laser-induced luminescence phosphor thermometry.* Meas. Sci. Technol., **20**(025305):025305, 2009.

[139] Princeton Instruments. Imaging & Spectroscopy Cameras - PI-MAX4 -The Ultimate in Precision and Intelligence, Retrieved July 21, 2013. URL http://www.princetoninstruments.com/products/imcam/pimax/.

[140] Andor Technology. *Intensified CCD cameras*, Retrieved July 21, 2013. URL http://www.andor.com/learning-academy/intensified-ccd-cameras-the-technology-behind-iccds.

[141] Williams, T. and Shaddix, C. *Simultaneous correction of flat field and nonlinearity response of intensified charge-coupled devices.* Rev. Sci. Instrum., **78**:123702, 2007.

[142] Wiedwald, J. and Lerche, R. *Streak camera dynamic range optimization.* SPIE, **832**:275–282, 1987.

[143] Kruschwitz, C.A., Wu, M., Moy, K., and Rochau, G. *Monte carlo simulations of high-speed, time-gated microchannel-plate-based x-ray detectors: Saturation effects in dc and pulsed modes and detector dynamic range.* Rev. Sci. Instrum., **79**:10E911, 2008.

[144] Weber., V., Brübach, J., Gordon, R., and Dreizler, A. *Pixel-based characterisation of CMOS high-speed camera systems.* Appl. Phys. B, **103**:421–433, 2011.

[145] Hain, R., Kähler, C., and Tropea, C. *Comparison of CCD, CMOS and intensified cameras.* Exp. Fluids, **42**:403–411, 2007.

[146] Kissel, T., Brübach, J., and Dreizler, A. *Thermometry of surfaces: Application of a high speed camera as a detector for laser-induced phosphorescence.* In *Proc. of the Laser Applications to Chemical, Security and Environmental Analysis.* 2008.

[147] Fuhrmann, N., Schild, M., Bensing, D., Kaiser, S., Schulz, C., Brübach, J., and Dreizler, A. *Two-dimensional cycle-resolved exhaust valve temperature measurements in an optically accessible internal combustion engine using thermographic phosphors.* Appl. Phys. B, **106**:945–951, 2012.

[148] Abram, C., Fond, B., Heyes, A., and Beyrau, F. *Experimental considerations for simultaneous gas-phase thermometry and velocimetry using thermographic phosphors.* In *Proc. of the 6th European Combustion Meeting, Lund, SE.* 2013.

[149] Omrane, A., Juhlin, G., Aldén, M., Josefsson, G., Engström, J., and Benham, T. *Demonstration of two-dimensional temperature characterization of valves and transparent piston in a gdi optical engine.* SAE Tech. Pap., 2004.

[150] Seyfried, H., Särner, G., Omrane, A., Richter, M., Schmidt, H., and Aldén, M. *Optical diagnostics for characterization of a full-size fighter-jet afterburner.* In *Proc. of the ASME Turbo Expo; Reno, Nevada; USA*, vol. 1, pp. 813–819. 2005.

[151] Lindén, J. *Laser-Induced Phosphor Thermometry - Feasibility and precision in combustion applications.* Ph.D. thesis, Division of Combustion, Department of Physics, Lund University, 2012.

[152] Noel, B., Borella, H., Lewis, W., Turley, W., Beshears, D., Capps, G., Cates, M., Muhs, J., and Tobin, K. *Evaluating thermographic phosphors in an operating turbine engine.* In *Proc. of the International Gas Turbine and Aeroengine Congress and Exposition; Brussels, Belg.* 1990.

[153] Eldridge, J.I., Bencic, T.J., Allison, S.W., and Beshears, D.L. *Depth-penetrating temperature measurements of thermal barrier coatings incorporating thermographic phosphors.* J. Therm. Spray Technol., **13**(1):44–50, 2004.

[154] Särner, G., Richter, M., and Aldén, M. *Cycle resolved wall temperature measurements using laser-induced phosphorescence in an HCCI engine.* SAE Tech. Pap., **2005-01-3870**:1–7, 2005.

[155] Brübach, J., Zetterberg, J., Omrane, A., Li, Z., Aldén, M., and Dreizler, A. *Determination of surface normal temperature gradients using thermographic phosphors and filtered rayleigh scattering.* Appl. Phys. B, **84**:537–541, 2006.

[156] Seyfried, H., Richter, M., Aldén, M., and Schmidt, H. *Laser-induced phosphorescence for surface thermometry in the afterburner of an aircraft engine.* AIAA J., **45**(12):2966–2971, 2007.

[157] Brübach, J., Hage, M., Janicka, J., and A., D. *Simultaneous phosphor and CARS thermometry at the wall–gas interface within a combustor.* Proc. Comb. Inst., **32**:855–861, 2009.

[158] Hakamata, T., Kume, H., Okano, K., Tomiyama, K., Kamiya, A., Yoshizawa, Y., Matsui, H., Otsu, I., Taguchi, T., Kawai, Y., Yamaguchi, H., Suzuki, K., Suzuki, S., Morita, T., and Uchizono, D. *Photomultiplier Tubes - Basics and Applications.* Hamamatsu Photonics K.K. - Electron Tube Division, 2007.

[159] Becker, W. and Hickl, H. *Time-correlated single photon counting.* Tech. rep., Becker & Hickl GmbH, 2002.

[160] Wright, A. *Amplifiers for use with photomultipliers—who needs them?* Nucl. Instrum. Meth. A, **504**(1-3):245 – 249, 2003.

[161] Lush, H.J. *Photomultiplier linearity.* J. Sci. Instrum., **42**:597–602, 1965.

[162] Sauerbrey, G. Linearitätsabweichungen bei Strahlungsmessungen mit Photovervielfachern. Appl. Opt., **11**(11):2576–2583, 1972.

[163] Hartman, D.H. *Pulse mode saturation properties of photomultiplier tubes.* Rev. Sci. Instrum., **49**(8):1130–1133, 1978.

[164] Vicic, M., Sobotka, L.G., Williamson, J.F., Charity, R.J., and Elson, J.M. *Fast pulsed uv light source and calibration of non-linear photomultiplier response.* Nuc. Inst. Meth. A, **507**:636–642, 2002.

[165] Hamamatsu. Metal Package PMT with Gate Function – Photosensor Modules H11526 Series. Tech. rep.

[166] Hamamatsu. Si APD S5342 to S5345, S9073 to S9075. Tech. rep.

[167] Schip, L.J.B., Buzelatto, B.P., Batista, F.R., da Cunha, C.J., Dias, L.C., and Novo, J.B.M. *Photomultiplier nonlinear response in time-domain laser-induced luminescence spectroscopy.* Quimica Novo, **30**(1):214–218, 2007.

[168] Becker, W. and Hickl, H. *How (and why not) to amplify PMT signals.* Tech. rep., Becker & Hickl GmbH, 2000.

[169] LeCroy. Lecroy Waverunner® 6000A Series Oscilloscopes – Operators's Manual. Tech. rep., 2007.

[170] Persvik, O., Melo, T.B., and Razi Naqvi, K. *Pulsed-source time-resolved phosphorimetry: comparison of a commercial gated photomultiplier with a specially wired ungated photomultiplier.* Photochem. Photobiol. Sci., **12**:1110–1113, 2013.

[171] Hamamatsu. Metal Package PMT H5773/H5783/H6779/H6780 Series. Tech. rep.

[172] Istratov, A. and Vyvenko, O. *Exponential analysis in physical phenomena.* Rev. Sci. Instrum., **70**(2):1233–1257, 1999.

[173] Ballew, R.M. and Demas, J.N. *An error analysis of the rapid lifetime determination method for the evaluation of single exponential decays.* Anal. Chem., **61**:30–33, 1989.

[174] Ballew, R.M. and Demas, R.M. *Error analysis of the rapid lifetime determination method for single exponential decays with a non-zero baseline.* Anal. Chim. Acta, **245**:121–127, 1991.

[175] Waters, P.D. and Burns, D.H. *Optimizing detection for lifetime measurement over a wide range of single exponential decays.* Appl. Spectrosc., **47**(1):111–115, 1993.

[176] Chan, S.P., Fuller, Z.J., Demas, J.N., and DeGraff, B.A. *Optimized gating scheme for rapid lifetime determinations of single-exponential luminescence lifetimes.* Anal. Chem., **73**:4486–4490, 2001.

[177] Rosso, L. and Fernicola, V.C. *Time- and frequency-domain analyses of fluorescence lifetime for temperature sensing.* Rev. Sci. Instrum., **77**:034901, 2006.

[178] Everest, M.A. and Atkinson, D.B. *Discrete sums for the rapid determination of exponential decay constants.* Rev. Sci. Instrum., **79**:023108, 2008.

[179] Halmer, D., von Basum, G., Hering, P., and Mürtz, M. *Fast exponential fitting algorithm for real-time instrumental use.* Rev. Sci. Instrum., **75**:2187–2191, 2004.

[180] Dowel, L.J. and Gillies, G.T. *Errors caused by baseline offset and noise in the estimation of exponential lifetimes.* Rev. Sci. Instrum., **62 (1)**:242–243, 1991.

[181] Brübach, J., Janicka, J., and Dreizler, A. *An algorithm for the characterisation of multi-exponential decay curves.* Opt. Las. Eng., **47**:75–79, 2009.

[182] Husberg, T., Gjirja, S., Denbratt, I., Omrane, A., Aldén, M., and Engström, J. *Piston temperature measurement by use of thermographic phosphors and thermocouples in a heavy-duty diesel engine run under partly premixed conditions.* SAE Tech. Pap., **2005-01-1646**:1–13, 2005.

[183] Kashdan, J. and Thirouard, B. *Optical engines as representative tools in the development of new combustion engine concepts.* Oil Gas Sci. Technol., **66**:759–777, 2011.

[184] Aronsson, U., Chartier, C., Horn, U., Andersson, O., Johansson, B., and Egnell, R. *Heat release comparison between optical and all-metal HSDI diesel engines.* SAE Tech. Pap., **2008-01-1062**:1–10, 2008.

[185] Heywood, J. *Internal Combustion Engine Fundamentals.* McGraw-Hill, Inc., 1989.

[186] Armfield, J.S., Graves, R.L., Beshears, D.L., Cates, M.R., Smith, T.V., and Allison, S.W. *Phosphor thermometry for internal combustion engines.* SAE Tech. Pap., **1279**:55–59, 1997.

[187] Noel, B., Borella, H., Franks, L., Marshall, B., Allison, S., and Cates, M. *Proposed method for remote thermometry in turbine engines.* In *Proc. of the AIAA/SAE/ASME/ASEE 21st Joint Propulsion Conference.; Monterey, CA, USA*. 1985.

[188] Lutz, S., Turley, W., Borella, H., Noel, B., Cates, M., and Probert, M. *Remote temperature-measurement instrumentation for a heated rotating turbine disk.* In *Proc. of the 34th International Instrumentation Symposium; Albuquerque, NM, USA*, vol. 34, pp. 217–229. 1988.

[189] Dunphy, J. and Atkinson, W. *Development of advanced diagnostics for turbine disks.* In *Proc. of the International Gas Turbine and Aeroengine Congress and Exposition; Brussels, Belg*, p. GT390 7p. 1990.

[190] Stange, W. *Non-intrusive sensing techniques for advanced turbine engine structures.* In *Proc. of the International Gas Turbine and Aeroengine Congress and Exposition; Brussels, Belg*, p. GT389 5p. 1990.

[191] Allison, S.W., Beshears, D.L., Cates, M.R., Noel, B.W., and Turley, W. *Taking an engine's temperature.* Mech. Eng., **119**(1):72–74, 1997.

[192] Choy, K.L., Mei, J., Feist, J.P., and Heyes, A.L. *Microstructure and thermoluminescent properties of ESAVD produced Eu doped $Y_2O_3 - ZrO_2$ coatings.* Surf. Eng., **16**(6):469–472, 2000.

[193] Feist, J.P., Heyes, A.L., and Nicholls, J.R. *Phosphor thermometry in an electron beam physical vapour deposition produced thermal barrier coating doped with dysprosium.* Proc. of the Institution of Mechanical Engineers, Part G: Journal of Aerospace Engineering, **215**(6):333–341, 2001.

[194] Desai, S.K., Hansel, R.A., Pitz, R.W., and Walker, D.G. *Europium-doped pyrochlores for use as thermographic phosphors in thermal barrier coatings.* In *Proc. of the 48th AIAA Aerospace Sciences Meeting Including the New Horizons Forum and Aerospace Exposition; Orlando, FL; USA*. 2010.

[195] Juliussen, L.R., Kryger, M.J., and Andreasen, A. MAN B&W ME-GI *engines. recent research and results.* In *Proc. of the International Symposium on Marine Engineering (ISME), Kobe, Japan.* 2011.

[196] Juliussen, L.R., Kryger, M.J., and Mayer, S. *The* MAN ME-GI *engine: From initial system considerations to implementation and performance optimisation.* In *CIMAC Congress, Shanghai, China.* 2013.

[197] Christiansen, C.A., Mayer, S., and Schramm, J. *Simultaneous transient surface temperature and heat flux measurements in a large bore two-stroke diesel engine.* In *Proc. of the ASME 2012 Internal Combustion Engine Division Fall Technical Conference.* 2012.

[198] Boulouchos, K., Eberle, M., Ineichen, B., and Klukowski, C. *New insights into the mechanisms of in-cylinder heat transfer in diesel engines.* SAE Tech. Pap., **890573**, 1989.

Summary of Papers

Paper [I]: In this paper a routine for the simultaneous acquisition of temperatures and decay transients is described that enables the automated performance of temperature calibrations for thermographic phosphors to be carried out. Its being able to collect data continuously allows the operator to ramp up the temperature of the calibration device, while at the same time a dense grid of measurement values can be recorded over the entire temperature-sensitive-range of the phosphor. A procedure of this sort minimizes the experiment time and provides a temperature-accuracy advantage over conventional calibration procedures, which rely on fixed temperature points with larger temperature gaps to interpolate over. In addition, a brief investigation on the effects of laser-induced heating of the coating and of its substrate was carried out. A crude heat-transfer model based on lumped capacitance was found to be in satisfactory agreement with the experimental results and provided insights into the effects of laser-induced surface heating.

I initiated this study and worked on an early version of the LabVIEW data-acquisition routine. Xin continued my work and developed a first prototype of the code together with me, which we tested in various calibration experiments. Finally, Fahed took over the project and improved the program further. He performed most of the experiments that are presented in this paper. The figures included were designed by both Fahed and me. Fahed is also responsible for most of the manuscript, with exception of the heat transfer chapter, which I wrote.

Paper [II]: This paper concerns an investigation of the impact of the coating thickness on surface phosphor thermometry in transient combustion environments. A suitable combustion environment for a study of this type was provided by a Toyota car engine, one in which crank-angle resolved surface temperature measurements were performed during motored and fired operation. From the inside surface of a quartz liner which was inserted as a cylinder extension, La_2O_2S:Eu phosphorescence was detected from two opposite directions: One detector gathered information from the coating surface facing the in-cylinder gas, another detector recording phosphorescence temperature information from the coating surface facing the quartz liner. Two different coating thicknesses were investigated at various engine operating modes. Significant temperature differences between the "gas-side" and the "wall-side" of the phosphor coating were found for film thicknesses of 32 μm and above.

I initiated this project together with Mattias. It led to the conduction of experiments, that were carried out by Peter Andersson and me. The evaluation of global gas temperatures was performed by Martin Algotsson. I was responsible for the post-processing of all the phosphor-related data and wrote most of the manuscript.

Paper [III]: The aim of this study was to repeat measurements similar to those presented in Paper [II]. This time, however, thinner phosphor coatings were investigated and temperature gradients across thermal sensor films from $CdWO_4$

and La_2O_2S:Eu were measured. The results of this investigation suggest that coatings with a thicknesses of 20 μm and less do not experience any measurable temperature gradients. The critical thickness limit obtained in the study is believed to be approximately representative of surface thermometry applications in reciprocating combustion engines, although different thickness limits are likely to be found for other applications their size, depending upon the local and temporal temperature gradients that are present.

Martin Algotsson and I planned and conducted this study as a follow-up to the investigations presented in Paper [II]. Martin evaluated the gas temperatures and I was responsible for measuring the film thicknesses and evaluating the temperatures from the phosphorescence decays. The manuscript was written by me.

Paper [IV]: This paper presents investigations of nonlinear features caused by the intensifier of an ICCD camera, the effects these have on the results obtained in performing two-dimensional thermometry with use of thermographic phosphors, and how such effects can be avoided. It was concluded that for quantitative measurements there is an upper limit of camera counts that should not be exceeded.

Johannes carried out the experimental work, performed most of the data analysis and prepared large parts of the paper. I participated in the preparation of the study and took part in writing the manuscript. In addition, I contributed with ideas and additional data evaluations, such as those resulting in figures 6 and 7 and the discussion of them.

Paper [V]: The work presented in this paper is concerned with the detection of and compensation for non-linear PMT signals. The way of detecting signal nonlinearities, such as those produced by saturation, that was developed in the paper is based on the shape distortions that phosphorescence time transients experienced. An iterative correction scheme for distorted decay times was developed and presented in the paper. On the basis of the signal level present during calibration, distorted decay times at different signal levels can be corrected iteratively through use of a library of phosphorescence decays recorded under various different conditions.

I performed all the experiments, evaluated the results and prepared the manuscript.

Paper [VI]: This paper is a continuation of the investigations presented in Paper [V]. Four different point detectors for phosphorescence decay time measurements were studied and compared. Their signal response was measured as a function of electrical gain and light intensity by means of signal-shape distortions that biased the evaluation of phosphorescence decay times. None of the detectors investigated were found to act in an entirely linear way. Hence, a suitable operating workspace needs to be found experimentally for every each detector in order to ensure the reliability of the quantitative results obtained.

I planned this study and was responsible for the design of the experimental setup. Fahed conducted the experiments and evaluated large parts of the data during his master thesis under my supervision. I developed the algorithm that was used for

evaluating the phosphorescence decay times, derived the equations in connection with the photon number estimate and prepared the manuscript.

Paper [VII]: In this paper, the highest achievable precision in temperature when employing the two-colour ratio technique utilizing thermographic phosphors was investigated. The results obtained are valid for the setup that was involved and for the temperature range studied. The relationship between the precision and the spatial resolution obtained was studied, since these two properties involve a trade-off in this case. The results provide guidance concerning the precision to be expected in performing two-dimensional thermometry.

I performed a preparatory experiment for the study and assisted in the planning of the work. Johannes carried out all the measurements and evaluated the results. I took part in the discussion of results and made minor contributions to the manuscript, which was mainly written by Johannes.

Paper [VIII]: In this paper an alternative approach to calibrating spectral image intensity ratios is described, one that provides simple, yet effective means of compensating for systematic signal detection errors. The method relies on image segmentation by means of signal thresholds, the pixels being organized into different subgroups according to their corresponding signal count value. This enables the presence of high-intensity regions to be detected and to be exploited, this providing considerable advantages in terms of precision but suffering from various systematic errors caused by signal non-linearities. As compared with a conventional, such as a global calibration approach, significant accuracy improvements were achieved, even while keeping the average signal levels below 15 % of the detector's full dynamic range.

I developed the idea behind this study and used the measurement data recorded earlier by Johannes to test the simultaneous-calibration two-colour ratios in terms of the signal intensity of individual camera pixels. I carried out all the signal evaluations and prepared the manuscript.

Paper [IX]: The work presented in this paper describes and characterizes an algorithm for the non-ambiguous reduction of multi-exponentially decaying luminescence signals to the scalar values of corresponding calibration temperatures. The performance of the proposed signal shape recognition method (SSR) in terms of temperature precision and accuracy was compared with a conventional least-squares fitting approach, using a set of temperature-calibrated phosphorescence decay signals from $CdWO_4$. It was found that the SSR algorithm resulted in a reduction in the statistical temperature errors that occurred, provided a dense grid of temperature-calibrated decay transients was available (such as provided by the calibration routine proposed in Paper [I]).

I developed the idea behind this algorithm. Kristin did most of the programming work that resulted into the realization of the SSR code. As her supervisor, I provided her with my continued support, feedback and advice. Kristin also prepared most of the figures that I designed for the paper. The manuscript was written by me, with minor contributions being provided by Kristin.

Paper I

Development of an automatic routine for thermographic phosphor calibration

Fahed Abou Nada, Christoph Knappe, Xin Xu, Mattias Richter and Marcus Aldén

Submitted to: Meas. Sci. Technol. in 2013.

Development of an automatic routine for thermographic phosphors calibration

F. Abou Nada, C. Knappe, X. Xu, M. Richter and M. Aldén

Department of Physics, Division of Combustion Physics, Lund University, Box 118, S-22100, Lund, Sweden

E-mail: fahed.abou_nada@forbrf.lth.se

Abstract

An automated routine for the continuous calibration of thermographic phosphors was developed as a replacement for the conventional calibration scheme that relied on fixed temperature points. The automated calibration routine was validated using $Mg_3F_2GeO_4$:Mn as a calibration phosphor. Hardware and software aspects of the calibration process were addressed in this development. The hardware aspect included a new substrate design using a high performance alloy, the Hastelloy-C alloy, whereas the software aspect included an automated acquisition system which was capable to acquire simultaneous thermocouple temperatures and phosphor decay waveform in real time. The design of the calibration process eliminates the need for a system in thermal equilibrium during a phosphor calibration measurement. Temperature ramping rates of up to 4 K/min were employed in the oven without a delay in the response being measured between the phosphor and the thermocouples involved. In addition, the automated calibration setup allowed for detailed investigations on effect of heat being delivered to the phosphor coating by the laser, which were confirmed by a simple heat transfer model, based on lumped system analysis. In comparison to data acquisition performed at several fixed points with the conventional calibration scheme, the experiment duration was shortened by a factor of four with the overall accuracy improving by 1-2 K.

Keywords: Laser-induced phosphorescence, calibration, thermometry, thermographic phosphors

1. Introduction

Thermographic phosphors are materials for remote temperature sensing that have the capability of probing temperatures starting from cryogenic temperatures up to around 2000 K. Temperature probing applications using thermographic phosphors are extensive and include, but are not exclusive to, biological, electric, industrial and combustion research applications [1-9]. A thermographic phosphor consists of an inorganic host that is doped by an activator. The activator material can belong either to rare earth ions or transition metals [6]. Thermographic phosphors react to the change of temperature by altering their phosphorescence emission characteristics. The changing characteristics could be of a spectral or temporal nature. A spectral response for temperature changes is manifested as a wavelength shift of the emission distribution or intensity variations of spectral components, whereas a temporal response of the phosphor is detected as phosphorescence decay-time reduction with increasing temperature. Thermographic phosphor temperatures can be extracted by exploiting the different response mechanisms. Using 2-D detectors, e.g. CCD or CMOS cameras, the spectral ratios of two of the phosphorescence emission lines can be employed for 2-D temperature measurements [10, 11]. Similarly, by employing a detector to measure the phosphorescence decay-time, single-point and even 2-D temperature measurements can be achieved [7, 12].

Measuring temperatures using thermographic phosphors requires a calibration curve for the phosphorescent material being used. The calibration curve acts as a reference that maps the phosphorescence characteristics as function of temperature. In this article, the calibration of phosphorescence decay-time as function of temperature is discussed. A well-constructed calibration curve is important for an accurate thermographic phosphor temperature determination. The process of obtaining a phosphor calibration curve can be tedious and accompanied with effects such as detector nonlinearity [13, 14]. Despite of the importance of the calibration, no major development has occurred or been reported for the method by which a temperature calibration is achieved. A typical calibration curve is composed of several fixed temperature points acquired by averaging a number of decay curves at a single temperature. Measurements are usually performed with the system being in thermal equilibrium in order to avoid a potential mismatch between temperatures being measured by the thermocouples and those being measured by the phosphor. In order to obtain a calibration curve that is continuous over the entire calibrated temperature interval, subsequent data interpolation by means of smoothing polynomials can be used to fill the temperature gaps in between the data points acquired earlier. However, interpolating among calibration data points can pose a potential risk for accuracy errors, depending on deviations between the fit and the true phosphor behavior.

In this article, the development of an automated calibration routine is described and compared to the widely used conventional calibration process. Advantages, such as reduced acquisition time and higher temperature accuracy are the two improvements achieved with this setup. The aim is to continuously and simultaneously log the temperature measured by thermocouples and the associated phosphorescence decay waveform. This continuous acquisition runs while the phosphor was heated at a constant rate of 1.6 K/min. To evaluate the developed calibration scheme, manganese-doped magnesium fluorogermanate ($Mg_3F_2GeO_4$:Mn) [15] was chosen. This phosphor is sensitive over a wide temperature range, its decay-time extending from around 3 millisecond at 290 K to around 50 ns at 1100 K [16]. $Mg_3F_2GeO_4$:Mn was efficiently excited using pulsed UV laser radiation at 355 nm. The corresponding emission spectrum was composed of multiple peaks within a spectral range of 600 to 700 nm, the strongest emission peak being centered at 659 nm. Phosphorescence was detected at a central wavelength of 656 nm using an interference filter with a full width half maximum (FWHM) of 10 nm. $Mg_3F_2GeO_4$:Mn exhibits a quasi-single exponential decay form, as shown by the example decay in Figure 1.

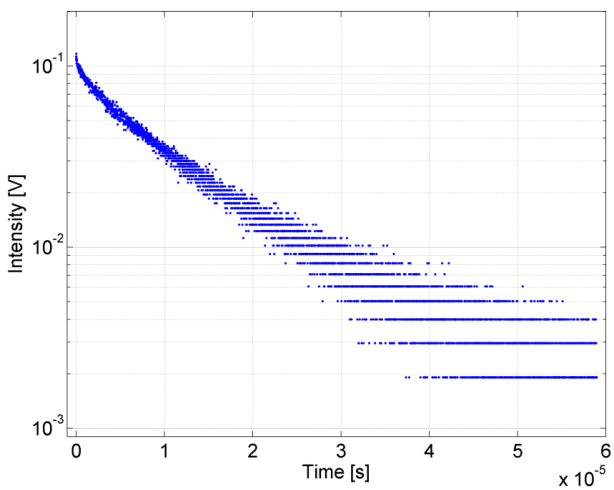

Figure 1: $Mg_3F_2GeO_4$:Mn phosphorescence decay curve at a temperature of 840.6 K. The horizontal gaps between single data points are a result of limited bit resolution in the oscilloscope's data acquisition software.

A single-exponential relation, provided by equation (1), is used to describe the exponential decay of $Mg_3F_2GeO_4$:Mn phosphorescence, where I(t) and I_0 are the intensity of the decay at any given time t and at $t = 0$ respectively. τ is associated with the decay-time and C is a constant signal offset.

$$I(t) = I_0 e^{-t/\tau} + C \tag{1}$$

2. Experimental Setup

The basic components of the experimental setup are shown in Figure 2. To excite $Mg_3F_2GeO_4$:Mn, a pulsed Nd:YAG laser was used, operating at 10 Hz and having a pulse duration of 6 ns at FWHM. $Mg_3F_2GeO_4$:Mn was effectively excited in the UV spectral region using the third harmonic of a Nd:YAG laser operating at 355 nm. Unfocused laser pulses excited a phosphor layer that was coated on Hastelloy-C alloy substrate. The laser beam is of circular profile and had a diameter of 12 mm and pulse energy of 10 mJ, this resulting in a laser energy density of 8.8×10^{-3} J/cm^2.

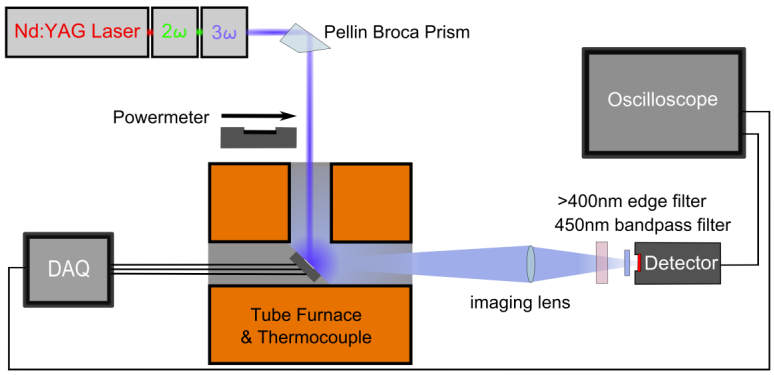

Figure 2: Experimental setup for the automated temperature calibration of a thermographic phosphor. Both the temperature logging and the phosphorescence detection are synchronized to realize simultaneous temperature-decay-time measurements.

Several in-house developed temperature calibration substrates were manufactured. The substrates of these were made of disks of Hastelloy-C alloy. Hastelloy-C alloy is a highly corrosion-resistant material with a relatively low expansion coefficient, which minimizes the risk of the phosphor coating flaking off due to thermal expansion of the substrate. Its high melting temperature (above 1550 K) makes Hastelloy-C a suitable substrate material for the majority of thermographic phosphors. The design of the Hastelloy-C substrates is shown in Figure 3. Each substrate was equipped with four type-K thermocouples. The thermocouples used are insulated by densely packed magnesium oxide and sheathed with an Inconel 600 alloy tube with 2 mm in diameter. The thermocouples were placed deep in the back of the substrate providing a close contact with the coated surface. For accurate point measurement calibrations, thermocouples were positioned in a cluster close to the center of the substrate, whereas for probing temperature gradients across the substrate surface, thermocouples can be arranged in a more spread-out configuration. The solid Inconel sheaths of the thermocouples allowed the substrate to be suspended in the furnace without touching the furnace ceramic walls. The suspension of the substrate prevents the occurrence of thermal gradients that could be caused by a local increase in heat transfer due to wall-substrate conduction. An oven of T-junction design (see Figure 1) with a maximum operating temperature of 1500 K was used to generate different temperatures for the calibration procedure. Quartz windows were installed at the front and side ports of the oven to increase the thermal stability by reducing convective flows through the oven tubes.

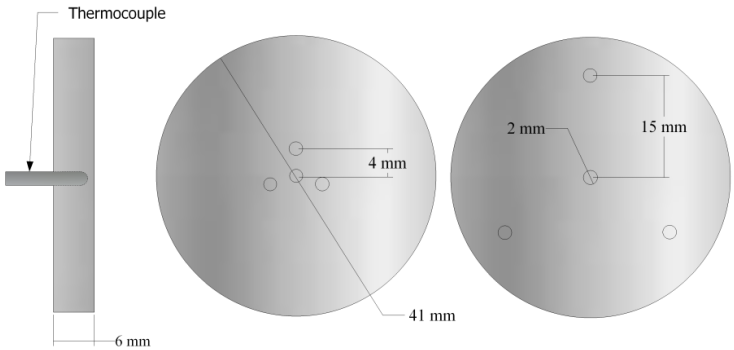

Figure 3: Hastelloy-C calibration substrate plate design.

Phosphorescence emission was collected and focused onto the detector window by a plano-convex lens with a focal length of 300 mm. A Hamamatsu H11526-20-NF photomultiplier tube was used as the detector. According to recent investigations by the authors, this PMT type showed superior signal linearity compared to other detector types [13]. A control voltage of 0.339 V set the photomultiplier gain constant throughout the entire experiment. The phosphorescence was spectrally narrowed by use of an interference filter centered at 656 nm with FWHM of 10 nm. To further suppress any scattered laser radiation, a long pass filter with a cutoff wavelength at 400 nm was mounted in front of the interference filter. The PMT output was connected via a BNC cable to the oscilloscope terminal with a 50 Ω termination resistance. A Data Acquisition system (DAQ) with a LabVIEW interface was used to log temperatures from the four thermocouples and synchronize them with decay signals, measured by the oscilloscope. The program design was focused on automated and simultaneous acquisition and processing of data needed to build a calibration curve for any selected phosphor. A flowchart illustrating the program design can be found in Figure 4.

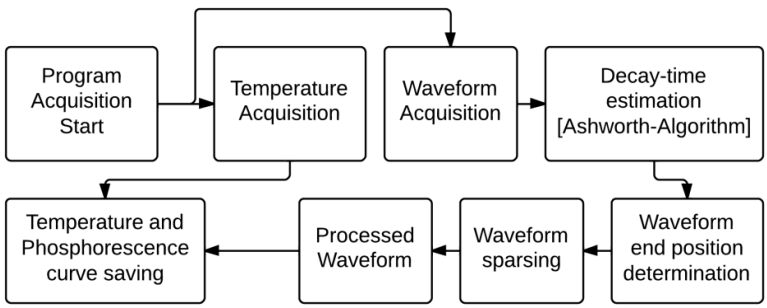

Figure 4: Program flowchart, for automated temperature calibration.

During a calibration both the decay-time and the emission signal strength varies with temperature as it increases. This requires the calibration routine to have the capability to accommodate to these changes by adjusting the base-time and voltage gain of the oscilloscope. The most suitable oscilloscope settings are automatically calculated and implemented onto the oscilloscope. Desired settings for time-base and voltage range can be set manually by the user prior to the calibration experiment. The automation process uses the decay-time and peak intensity of the latest acquired waveforms as input values for determining the suitable settings for the following waveform acquisition. The voltage range was computed by averaging the peak intensities of the last 5 acquired waveforms. To account for pulse-to-pulse variation, a value of 20 percent of the averaged peak intensities was added as a margin to the y-axis scale of the

oscilloscope, making sure that the phosphorescence peak is always contained in the acquired signal. This process is straight forward in contrast to the time-base resolution calculation method, which requires a fast and reliable decay-time estimate of the recorded phosphorescence decay waveform.
For this purpose, Ashworth's rapid lifetime determination (RLD) algorithm [17-21] was implemented. The RLD algorithm is estimated to perform three orders of magnitude faster than the weighted nonlinear least squares method [19]. Under the same noise levels, the RLD algorithm has a precision comparable to that of the weighted nonlinear least squares method. The decay-time calculated in real-time with the RLD algorithm from a curve being acquired was used to set the time resolution of the oscilloscope. Also, the RLD-computed decay-time was implemented by the waveform processing section of the program to define the end of the decay curve, which was set to 5 decay-times starting after the peak of the exponential decay of the phosphorescence signal.
Sampling 250k data points per curve is necessary for a proper time resolution of the phosphorescence peak, but at the same time weighs heavily in the size of the file when the waveform has to be saved for further post acquisition analysis. An adequate solution for file size reduction is the employment of variable sparsing of the decay-signal waveforms; which means saving only every n^{th} data point from an acquired waveform. To warrant a high resolution of the phosphorescence signal peak, selective sparsing was chosen which preserves the accurate peak position. In selective sparsing the decay curve is divided into three sections, the first section comprises the constant signal prior to the signal peak, the second is extending from the peak to a cutoff point set at 10 ns after the signal peak and the third section includes the residual part of the curve. Sparsing factors S_i for each section i can be varied individually, depending on the number of data points desired in each of the sections. For this study, S_1 was set to 300 data points, S_2 was set to the original number of data points and S_3, i.e. the temperature-sensitive part of the decay was set to contain 4000 data points. In case the number of data points in any segment is below the assigned value, the original number of data points is kept and no sparsing occurred. The main advantage of selective sparsing lies in the reduction of unneccessary information whilst preserving necessary curve features, needed for achieving results with satisfactory precision. An example of selective sparsing of a phosphor decay curve is displayed in Figure 5. In order to visually enhance the effects of sparsing on a curve, different sparsing settings were used to produce Figure 5 compared those which were used in the experiment. Assuming the sparsing settings used in the experiment to reduce the original waveform length of 250k points, the file size of the data saved in LabVIEW's default tdms file format was decreased by a factor of approximately 55 in relation to the original file size.

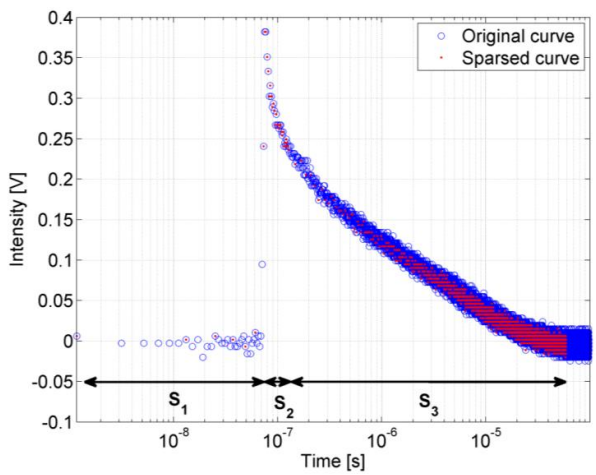

Figure 5: Selectively sparsed and original phosphorescence decay curve. The number of data points in each segment is given as follows: S_1 200 data points, S_2 original number of data points and S_3 3000 data points with 50k data points as the original number of points per curve.

After this kind of waveform processing, both temperature data and phosphorescence signals are saved within the same file, which allows the matching of each waveform and its corresponding decay-time with a temperature that was measured simultaneously. Upon completion of a temperature calibration measurement, the files containing the temperature value and phosphorescence waveform were evaluated in order to generate a phosphor-specific calibration curve. Temperatures were calculated from the mean value of the four simultaneously achieved thermocouple temperatures. Phosphorescence decay curves were processed according to pre-fitting conditions set globally for all of the curves. Those fitting conditions essentially define global criterions for the evaluation window, which are applied for each curve individually. Thus, the beginning of each fitting window is set to a constant time value of 10 ns after the phosphorescence peak. The fitting window end, in contrast, is determined as the time when the curve has reached 9 % of the initial peak value which is roughly around 2.5 decay-times after the start of the decay. After determining the fitting window for each curve, the segment of the curve that is meant to be fitted is passed on to the least-squares fitting algorithm. A baseline correction was applied by subtracting the mean of the constant signal prior to the peak from the entire curve thus reducing the number of fitted parameters to two instead of three. It is important to note that the RLD algorithm was used only during data acquisition for determining the end of individual waveforms being saved, this due to its fast execution which enabled the algorithm being used in real-time. For a higher precision of decay times being evaluated from the measurements a nonlinear least squares algorithm was used instead.

3. Results and discussion

An automated temperature calibration of $Mg_3F_2GeO_4$:Mn was realized and compared to a conventional calibration in order to establish a comparison in terms of measurement accuracy and experiment time. A plot showing both automatic and conventional calibration results is shown in Figure 6.

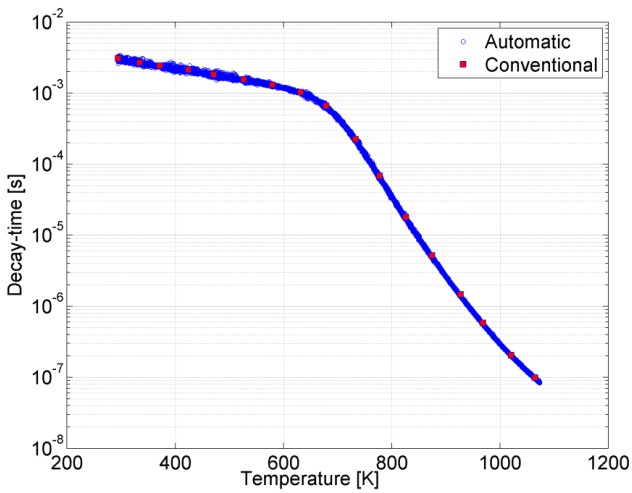

Figure 6: Automatic and conventional calibration curves for $Mg_3F_2GeO_4$:Mn.

The two calibrations were carried out within a temperature range starting around 290 K and ending around 1070 K. Both calibrations were conducted under similar experimental conditions, i.e. laser energy density and detector gain. The conventional calibration was produced by taking measurements at temperature intervals of around 50K. After reaching thermal equilibrium, 100 phosphorescence decay curves are saved and processed to get 100 decay-times and their corresponding temperatures which are then averaged to obtain a single data point. This procedure is repeated at every chosen calibration

temperature. However during automatic calibration, the oven was ramped up continuously on a constant heating rate of 1.6 K/min while acquiring phosphorescence decay curves at a rate of 1 waveform per second. These acquisition settings resulted in an average temperature separation of 0.027 degrees between two consecutive curves. The shortest possible time duration between two waveform acquisitions is limited to 1 s due to program speed limitations.

The speed at which the automated calibration curve can be run by is limited by the maximum heating rate of the oven and the acquisition rate of the system. A maximum heating rate of 4K/min and an acquisition rate of 1 acquisition per second for 800 K temperature range result in a calibration duration of at least 3.4 hours with an average temperature separation of 0.07 K. The automatic calibration of $Mg_3F_2GeO_4$:Mn required little more than 8 hours, bearing in mind that the oven was set to a heating rate of around 1.6 K/min. In comparison, the conventional calibration, with only 17 averaged measurement points, required almost 32 hours to complete (including a 12 hour break during the night). The prolongation is due to the requirement of establishing thermal equilibrium in the conventional calibration. Reaching thermal equilibrium takes more time at lower temperatures, where heat losses to the surrounding occur at a slower rate. The automated calibration achieved a reduction of the experiment duration by factor of four compared to the conventional calibration. This improvement in calibration duration could be further improved by setting the heating rate of the oven to a higher value.

To study the accuracy of the developed calibration procedure, the two calibration curves were subjected to a smoothing spline polynomial that relates the temperature to the natural logarithm of the decay-time. The benefit of the smoothing spline polynomial was evaluated by comparing the distribution of residuals around the zero line of the fitting polynomial. A fit is considered to be of good quality if the residuals are distributed symmetrically around the zero line. Two polynomials were obtained, one for each calibration curve. In order to compare the two obtained polynomials in terms of accuracy, an array of generated decay-times starting from a decay-time of 3.3 ms down to 60 ns was created. The natural logarithm of the generated decay-times was inserted into the automatic calibration polynomial, giving a simulated temperature. Then by using this generated temperature array, decay-times that correspond to the conventional calibration temperatures are found. A fitting polynomial was applied on the conventional calibration data and a temperature array was calculated from the fitting polynomial. The difference between the two temperature arrays was plotted against temperature along the generated automatic calibration curve see Figure 7.

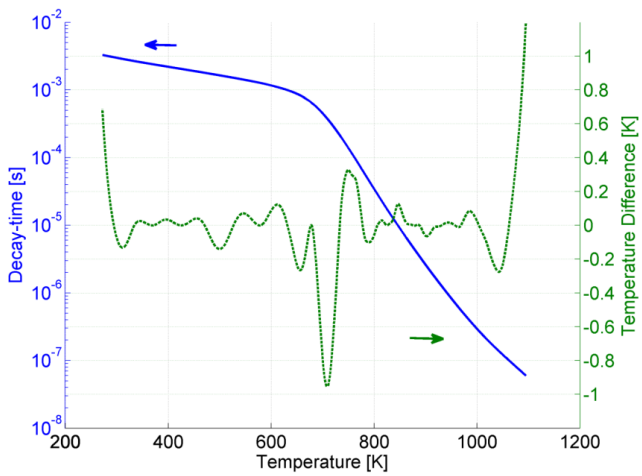

Figure 7: Comparison of conventional and automatic calibration polynomials by temperature difference analysis. A $Mg_3F_2GeO_4$:Mn calibration curve (solid-blue, left y-axis) and the temperature difference between the two calibration polynomials (dotted-green, right y-axis) are displayed.

Figure 7 shows that at the beginning of the calibration the temperature difference between the two polynomials is almost 0.7 K degrees. The most noticeable temperature difference is located at 710 K. This point marks the beginning of an increasing sensitivity of the phosphor due to its higher temperature dependence of the phosphor quenching rates. At this turning point, the automated calibration provided a better description of the phosphor's response due to a much higher data point density in the calibration curve. Also, the temperatures derived from the conventional and automatic fitting polynomials deviate from each other mostly at the extremes of the temperature range due to the failure of the polynomials to extrapolate out of the temperature range accurately. Even though the difference in temperature in the phosphor range of interest is small, it still shows that the automatic calibration introduces an improved accuracy compared to the conventional calibration method. This improvement in accuracy can be attributed to the high number of data points in the calibration curve achieved in with the automated measurement routine, which allows the calibration polynomial to accurately describe the behavior of the chosen phosphor with temperature throughout the entire temperature range that was measured.

Acquiring calibration data while continuously ramping the oven temperature meant that thermal equilibrium is not met. Thus, it is critical to check whether the thermocouples are responding without any delay being introduced between the registered thermocouple temperatures and the phosphor coating temperature. To test this aspect, temperature oscillations were generated in the range between 805 and 880 K creating a wide range of heating rates while heating and cooling the phosphor. Figure 8 represents the thermocouple temperature profile along with the evaluated phosphor temperature. The difference between the two measured temperatures is provided in a sub-plot. Two heating and two cooling cycles were applied to provide measurement replicas. The phosphor and the thermocouple temperatures match very well, giving an indication that the thermocouples respond quickly to phosphor coating temperature changes.

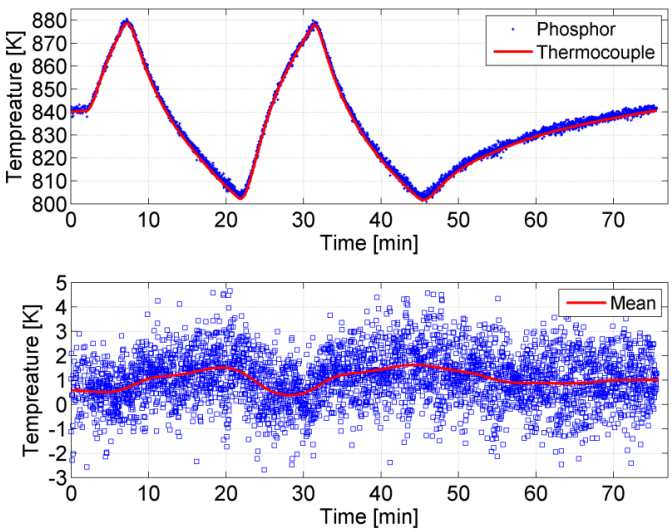

Figure 8: *(Top)*-Phosphor response plot to an induced temperature oscillation. *(Bottom)*- Temperature difference between evaluated phosphor temperature and average thermocouple temperature along with the corresponding smoothing average.

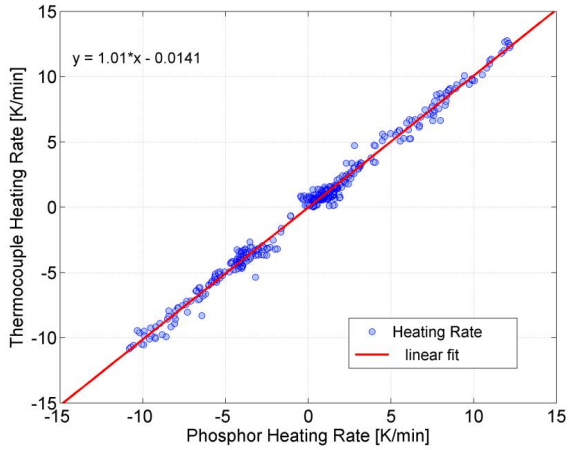

Figure 9: Cooling and heating rates of averaged thermocouple temperatures versus the corresponding phosphor coating heating rates.

To further confirm the absence of thermocouple response delay, the heating rates of the averaged thermocouple temperatures were plotted against the corresponding phosphor heating rates (see Figure 9). Heating rates extending over a range of ±10 K/min where achieved. This range spreads well beyond the maximum heating rate of 4 K/min which was specified by the oven manufacturer for safe operation.. The heating rate of the averaged thermocouple temperature agrees well with the phosphor's heating rate. A linear fit with a slope of nearly 1 and an offset constant of about 0 confirms the previous conclusion that the response of the thermocouples is quick enough to track the temperature changes experienced by the phosphor coating.

One possible application of the automated calibration setup is the measurement of heat transferred optically to the phosphor sample by the laser. Figure 10 shows temperature development of the phosphor sample over time, measured by the center thermocouple. While the surrounding environment was kept at room temperature (T = 294 K), the sample was exposed to 10 Hz pulses of 3 different laser energies: 1 mJ (thin line), 5 mJ (middle line) and 12 mJ (thick line). Corresponding dashed lines represent the lumped system analysis model. The black dotted line indicates the temperature increase of a corresponding black body with $R = 0$ and $q = 0$, exposed to a laser energy of 12mJ.

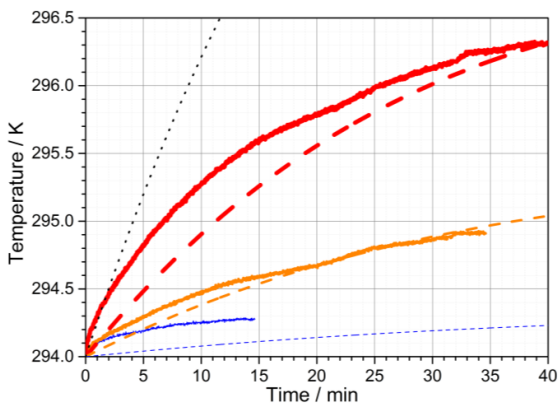

Figure 10: Comparison of measurement (lines) and model (dashed lines) on the effect of laser-induced heating of the calibration target. Three different laser energies were chosen: 1 mJ (thin blue line), 5 mJ (orange line) and 12 mJ (thick red line). The dotted line corresponds to a blackbody, heated with 12mJ.

In the following, a few more details on the model are given: The model acts on the assumption that 20 % of the laser energy gets reflected by the white phosphor-coated surface. This value is close to the reflectivity of YSZ TBC coatings, reported in [22], which was approximated by known values for UV absorption in TBC spray coatings. In addition, it was assumed that the residual laser energy transforms to 100·(1-q) % into heating the phosphor target, assuming a phosphorescence quantum yield of q = 0.5, which is typical for lamp phosphors [23]. The phosphorescence quantum yield q describes the fraction of absorbed photons at wavelength λ_1 that results in the emission of a phosphorescence photon at $\lambda_2 > \lambda_1$. In terms of mass, the existence of a few micrometer thick phosphor film [24] was neglected in comparison to the much larger substrate mass.
The average temperature increase ΔT_+ per laser pulse with an energy E can then by calculated according to equation (2).

$$\Delta T_+ = (1 - R) \cdot \left(1 - \left({}^{\lambda_1}/_{\lambda_2}\right) q\right) \cdot E/(c_v \cdot \rho \cdot \pi r^2 h) \tag{2}$$

In equation (2), ρ denotes the density, c_v the specific heat, r the radius and h the height of the Hastelloy substrate disc. For the highest laser energy in the test, this corresponds to ΔT = 171 µK per laser pulse. After the first laser pulse, the target is not in thermal equilibrium with the ambient air anymore and transfers heat energy to the surroundings. The amount of heat, which is lost per time interval dt corresponds to a decrease in temperature ΔT_- and is dependent on the actual temperature difference ΔT between the sample and the surrounding air. ΔT_- was calculated using equation (3).

$$\Delta T_- = \alpha \cdot 2(h + r) \cdot \Delta T \cdot dt/(c_v \cdot \rho \cdot r \cdot h) \tag{3}$$

The parameter α hereby denotes the heat transfer constant and comprises contributions from heat transfer through natural convection and radiation. It was calculated according to equation (4).

$$\alpha = \frac{0.68072 \cdot \lambda}{\left[1+(2Pr)^{-\frac{9}{16}}\right]^{\frac{4}{9}}} \cdot \left\{\frac{Pr g \beta \Delta T}{[2\pi r(r+h)]^{\frac{1}{2}} \cdot \upsilon^2}\right\}^{\frac{1}{4}} + \varepsilon \cdot \sigma \cdot (2T_r + \Delta T) \cdot [(\Delta T + T_r)^2 + T_r^2] \tag{4}$$

In equation (4), g denotes the gravitational constant, σ the Stefan-Boltzmann constant, ε the emissivity of the substrate, T_r is the ambient air temperature, λ the thermal conductivity of air, β the volumetric thermal expansion coefficient of air, υ the kinematic viscosity of air and P_r the Prandtl number of air. Further details on the assumption of α and the lumped system analysis can be found in the appendix.
The modeled temperatures in Figure 10 agree fairly well with the measured values, considering the amount of necessary assumptions. Generally, there is a trend in the model to act slower than the measured values would suggest. This stands especially out when comparing the agreement of the model to the 1 mJ laser energy measurement. The model of the black body exposed to 12 mJ expresses an upper limit of heat transfer to the sample. Around t = 0, also $\Delta T \approx 0$ applies and also the heat transfer to air approaches zero, see equation (3). However, the corresponding measured data (red thick line) still exhibits a higher heating rate in comparison. This behavior may have been caused by local temperature gradients across the substrate due to slow conduction. Since the thermocouple measured the temperatures very close to the laser illumination area, local heating rates might be higher than the lumped system analysis projected across the entire body.

4. Conclusions

An automated system for achieving fast and continuous temperature calibrations of thermographic phosphors is is decribed in this paper and compared to a discrete calibration approach using $Mg_3F_2GeO_4$:Mn. The broad temperature and decay-time range of $Mg_3F_2GeO_4$:Mn was deemed suitable

for evaluating the capabilities of the presented calibration approach. A phosphor substrate made from high-performance alloy embedded with four thermocouples was designed with a concern towards phosphor and thermocouple temperature gradient minimization. Ashworth's RLD algorithm was applied by the acquisition software to estimate the length of each waveform being saved during data acquisition.
The automation of the phosphor calibration process yielded an improvement in the accuracy of the obtained calibration curve and shortened the experiment duration significantly. A temperature range of 100 K could be covered in 25 minutes if the maximum heating rate of the oven was applied. A high data point density of several measurements per Kelvin, as achieved by the automated calibration procedure, provided a better description to the response of phosphor decay-time to temperature and hence resulted in improvements of the temperature accuracy by ca. 1 K as compared to a corresponding fixed-point calibration.In addition, the automated calibration setup was used to measure the effect of laser-induced heating with high temporal resolution, which allowed for verification of a crude heat transfer model for estimating the temperature offset, introduced by the excitation source.

5. Acknowledgements

The research leading to these results has received funding from the European Union Seventh Framework Programme (FP7/2007-2011) under grant agreement no. 265861 (Helios).

6. References

1. S.W. Allison and G.T. Gillies, *Remote thermometry with thermographic phosphors: Instrumentation and applications.* Review of Scientific Instruments, 1997. **68**(7): p. 2615-2650.
2. M. Aldén, A. Omrane, M. Richter, and G. Särner, *Thermographic phosphors for thermometry: A survey of combustion applications.* Progress in Energy and Combustion Science, 2011. **37**(4): p. 422-461.
3. J. Brübach, C. Pflitsch, A. Dreizler, and B. Atakan, *On surface temperature measurements with thermographic phosphors: A review.* Progress in Energy and Combustion Science, 2013. **39**(1): p. 37-60.
4. H.A. Feist JP, Seefeldt S, *Thermographic phosphors for gas turbines: instrumentation development and measurement uncertainties.* 11th International symposium on Application of Laser Techniques to Fluid Mechanics, Lisbon, Portugal,, 2002.
5. S.W. Allison and G.T. Gillies, *Fluorescence excitation and propagation through brain phantom gelatins: measurements and potential applications.* Measurement Science and Technology, 2010. **21**(8): p. 085802.
6. A. Khalid and K. Kontis, *Thermographic Phosphors for High Temperature Measurements: Principles, Current State of the Art and Recent Applications.* Sensors, 2008. **8**(9): p. 5673-5744.
7. S. Someya, M. Uchida, K. Tominaga, H. Terunuma, Y. Li, and K. Okamoto, *Lifetime-based phosphor thermometry of an optical engine using a high-speed CMOS camera.* International Journal of Heat and Mass Transfer, 2011. **54**(17–18): p. 3927-3932.
8. N. Fuhrmann, E. Baum, J. Brubach, and A. Dreizler, *High-speed phosphor thermometry.* Review of Scientific Instruments, 2011. **82**(10): p. 104903-4.
9. M. Salem, S. Staude, U. Bergmann, and B. Atakan, *Heat flux measurements in stagnation point methane/air flames with thermographic phosphors.* Experiments in Fluids, 2010. **49**(4): p. 797-807.
10. A. Omrane, G. Särner, and M. Aldén, *2D-temperature imaging of single droplets and sprays using thermographic phosphors.* Applied Physics B, 2004. **79**(4): p. 431-434.
11. A.L. Heyes, S. Seefeldt, and J.P. Feist, *Two-colour phosphor thermometry for surface temperature measurement.* Optics & Laser Technology. **38**(4-6): p. 257-265.

12. M. Euler, T. Kissel, A. Dreizler, and J. Brübach, *The spectrally resolved luminescence decay of thermographic phosphors.* Measurement Science and Technology, 2011. **22**(8): p. 083001.
13. C. Knappe, F.A. Nada, M. Richter, and M. Alden, *Comparison of photo detectors and operating conditions for decay time determination in phosphor thermometry.* Review of Scientific Instruments, 2012. **83**(9): p. 094901-10.
14. C. Knappe, J. Linden, F.A. Nada, M. Richter, and M. Alden, *Investigation and compensation of the nonlinear response in photomultiplier tubes for quantitative single-shot measurements.* Review of Scientific Instruments, 2012. **83**(3): p. 034901-7.
15. J. Brübach, J.P. Feist, and A. Dreizler, *Characterization of manganese-activated magnesium fluorogermanate with regards to thermographic phosphor thermometry.* Measurement Science and Technology, 2008. **19**(2): p. 025602.
16. J. Brübach, J. Zetterberg, A. Omrane, Z.S. Li, M. Aldén, and A. Dreizler, *Determination of surface normal temperature gradients using thermographic phosphors and filtered Rayleigh scattering.* Applied Physics B: Lasers and Optics, 2006. **84**(3): p. 537-541.
17. R.J. Woods, S. Scypinski, and L.J.C. Love, *Transient digitizer for the determination of microsecond luminescence lifetimes.* Analytical Chemistry, 1984. **56**(8): p. 1395-1400.
18. R.M. Ballew and J.N. Demas, *An error analysis of the rapid lifetime determination method for the evaluation of single exponential decays.* Analytical Chemistry, 1989. **61**(1): p. 30-33.
19. R.M. Ballew and J.N. Demas, *Error analysis of the rapid lifetime determination method for single exponential decays with a non-zero baseline.* Analytica Chimica Acta, 1991. **245**(0): p. 121-127.
20. P.D. Waters and D.H. Burns, *Optimized Gated Detection for Lifetime Measurement Over a Wide Range of Single Exponential Decays.* Applied Spectroscopy, 1993. **47**(1): p. 111-115.
21. C. Moore, S.P. Chan, J.N. Demas, and B.A. DeGraff, *Comparison of Methods for Rapid Evaluation of Lifetimes of Exponential Decays.* Applied Spectroscopy, 2004. **58**(5): p. 603-607.
22. D. Liu, O. Lord, O. Stevens, and P.E.J. Flewitt, *The role of beam dispersion in Raman and photo-stimulated luminescence piezo-spectroscopy of yttria-stabilized zirconia in multi-layered coatings.* Acta Materialia, 2013. **61**(1): p. 12-21.
23. J.P. Feist and A.L. Heyes, *Photo-stimulated phosphorescence for thermal condition monitoring and nondestructive evaluation in thermal barrier coatings.* Heat Transfer Engineering, 2009. **30**(13): p. 1087-1095.
24. C. Knappe, M. Algotsson, P. Andersson, M. Richter, M. Tunér, B. Johansson, and M. Aldén, *Thickness dependent variations in surface phosphor thermometry during transient combustion in an HCCI engine.* Combustion and Flame, 2013. **160**(8):p. 1466-1475.
25. Y.A. Çengel, *Heat and Mass Transfer: A Practical Approach, SI Version*2006: McGraw-Hill Education.
26. F.P. Incropera, *Fundamentals of heat and mass transfer*. 6th ed / ed2007, Hoboken, NJ: John Wiley. xxv, 997 p.
27. S. Lee, M.M. Yovanovich, and K. Jafarpur, *Effects of geometry and orientation on laminar natural convection from isothermal bodies.* Journal of thermophysics and heat transfer, 1991. **5**(2): p. 208-216.

Appendix: Lumped System Analysis

A prequisite for using the lumped system analysis approximation is the evaluation of the Biot number *Bi*, which describes the ratio between conduction and convection rate. If $Bi < 0.1$, temperature gradients across the solid material stay well within 5% [25]. The Biot number *Bi* describing this system is given by equation (A1):

$$Bi = \frac{\alpha_{conv} \cdot r}{\lambda_h} \tag{A1}$$

Coefficients for convective heat transfer in gases vary from 2 to 25W/m^{2}K [26]. Thermal conductivity of Hastelloy at room temperature was found to be λ_h=10.1W/mK. These values, together with the sample radius r yield a Biot number in between 0.004 and 0.051 and legitimate the lumped system analysis assumption.
The actual heat transfer coefficient for natural convection (first summand in equation (4)) was estimated as follows according to empiric models, summarized in [27]. It can be described using the Nusselt number Nu using equation (A2)

$$\alpha_{conv} = \frac{\lambda}{L} Nu \tag{A2}$$

The variable L in (A2) denotes the characteristic length of the body. It was chosen to be the square root of the body surface as described in equation (A3)

$$L = \sqrt{A_{cyl}} = \sqrt{2\pi r(r+h)} \tag{A3}$$

The Nusselt number for natural convection is defined by the Prandtl number Pr, the body-gravity function G_L = 1.016 (for a flat cylinder disc with horizontal axis and L according to (A3)) and the Rayleigh number Ra for natural convection in equation (A4).

$$Nu = \frac{0.670}{\left[1+(2Pr)^{-\frac{9}{16}}\right]^{\frac{4}{9}}} \cdot G_L \cdot Ra^{\frac{1}{4}} \tag{A4}$$

The Prandtl number of air was estimated to be Pr = 0.713 = const. at room temperature due to the expectation, that ΔT remains small. The Rayleigh number Ra is similar to the Reynolds number in corresponding forced convection scenarios and is defined as given by equation (A5).

$$Ra = Pr \cdot \frac{g\beta\Delta T L^3}{\nu^2} \tag{A5}$$

Tabular values for air parameters were used, such that β = 0.00343 K^{-1} and ν = 15.11·10^{-6} m^2/s. Combining equations (A2) - (A5), finally yields the convective heat transfer coefficient, given in equation (4). For a maximum temperature increase of ΔT = 5K, α_{conv} yields a maximum value of 4.1354 W/m^2 K. This again is within the expected range for convective gases and results in a better estimate for the Biot number of 0.008, which again justifies the estimation of a lumped capacity model.

Paper II

Laser-Induced Phosphorescence and the Impact of Phosphor Coating Thickness on Crank-Angle Resolved Cylinder Wall Temperatures

Christoph Knappe, Peter Andersson, Martin Algotsson,
Mattias Richter, Johannes Lindén, Martin Tunér,
Bengt Johansson and Marcus Aldén

Published in: SAE Int. J. Engines **4**(1):1689-1698, 2011.

SAE International®

Laser-Induced Phosphorescence and the Impact of Phosphor Coating Thickness on Crank-Angle Resolved Cylinder Wall Temperatures

2011-01-1292
Published
04/12/2011

Christoph Knappe
Div. of Combustion Physics, Lund Institute of Technology

Peter Andersson and Martin Algotsson
Div. of Combustion Engines, Lund Institute of Technology

Mattias Richter, Johannes Linden and Marcus Alden
Div. of Combustion Physics, Lund Institute of Technology

Martin Tuner and Bengt Johansson
Div. of Combustion Engines, Lund Institute of Technology

doi:10.4271/2011-01-1292

ABSTRACT

In order to further improve the energy conversion efficiency in reciprocating engines, detailed knowledge about the involved processes is required. One major loss source in internal combustion engines is heat loss through the cylinder walls. In order to increase the understanding of heat transfer processes and to validate and generate new heat transfer correlation models it is desirable, or even necessary, to have crank-angle resolved data on in-cylinder wall temperature.

Laser-Induced Phosphorescence has proved to be a useful tool for surface thermometry also in such harsh environments as running engines. However, the ceramic structure of most phosphor coatings might introduce an error, due to its thermal insulation properties, when being exposed to rapidly changing temperatures. In this article the measurement technique is evaluated concerning the impact from the thickness of the phosphorescent layer on the measured temperature. Experiments with different layer thicknesses are performed both during motored and fired operation of a HCCI engine. The results reveal a need for caution when applying the technique for in-cylinder measurements.

INTRODUCTION

Increasing fuel prices and more stringent legislation on emissions of greenhouse gases, such as CO_2, have driven the requirement for engines with higher efficiency. The upper limit has been pushed forward and is now approaching 60% indicated thermal efficiency (ITE) [1, 2]. In order to reach 60% ITE and beyond, all losses in combustion engines need to be considered. Heat loss through the cylinder walls is one major source of losses in internal combustion engines [3]. To gain knowledge about the heat transfer processes it is crucial to have information about the boundary conditions, including the wall temperature. In-cylinder wall temperature studies have previously been performed by e.g. Woschni et al [4] and Chang et al [5].

Homogeneous Charge Compression Ignition (HCCI) is a combustion process that can be described as a hybrid between the Spark Ignition (SI) and Compression Ignition (CI) engines. During the last decade the HCCI concept has been more intensively studied due to its higher efficiency at lower loads, compared to SI engines, and having lower emission of nitrogen oxides and soot than the CI engines [6, 7]. There are, however, drawbacks such as difficulty of controlling the combustion phasing and the heat release rate which is

globally high and thus resulting in high pressure rise rates. The pressure rise rate can, to some extent, be reduced by for example using diluted mixtures of air or recirculated exhaust gas.

Besides giving structural stresses and high noise, the high pressure rise rates also have an effect on the heat transfer to cylinder walls [8]. Similar observations have also been made for partially premixed combustion engines where high pressure rise rates lead to strong pressure oscillations and increased heat losses [9]. The thermal boundary layer (TBL) is a layer of fluids that to some extent insulates the cylinder walls from the high temperature of the burned gas during combustion, figure below. With high pressure rise rates and the resulting severe pressure oscillations, the TBL can be reduced or even broken exposing the relatively cooler cylinder walls to the hot gas and thus the heat transfer increases.

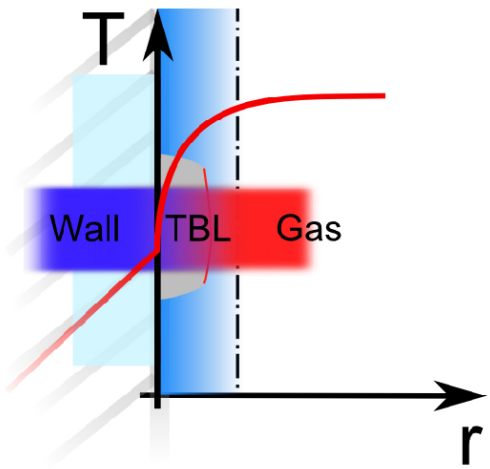

Figure 1. Schematic temperature gradient in a combustion engine showing the TBL near the chamber surface as well as a phosphor dot on top of the surface.

Understanding of the behavior of the TBL will aid the development of all combustion systems with high pressure rise rates. For understanding which variables and to what extent they will affect the TBL, the temperature within and near the TBL is of high interest. In recent experiments Laser-Induced Phosphorescence combined with other optical techniques, such as Filtered Rayleigh Scattering or Coherent Anti-Stokes Raman Spectroscopy proved its potential to measure temperature transients near and on surfaces [10, 11].

During the past years the technique of using LIP for thermometry has been proven to be an alternative to thermocouples and infrared pyrometry for surface temperature probing. The phosphor technique is believed to be non-intrusive and capable of remote probing while still offering high spatial and temporal resolution with good accuracy [12, 13, 14].

Cylinder wall temperature measurements have previous been studied at Lund University, for instance by Särner et al [15] and Wilhelmsson et al [16]. In both cases the aim was to measure the temperature on the valves and the cylinder head. Särner and Wilhelmsson showed that the phosphor technique was capable of providing crank-angle resolved temperature data.

The aim of this paper is to evaluate the LIP technique with respect to different phosphor layer thicknesses. When applying LIP for surface thermometry it is common practice to apply what is considered a “thin” layer of phosphor material to the surface of interest. Ideally, the measured temperature should reflect the temperature of the coated surface. However, one should keep in mind that the active elements are often embedded in a ceramic host material. As familiar, ceramics are used as thermal barrier coatings (TBC) in for example gas turbines [17, 18]. Although the TBC coatings are significantly thicker compared to what is found in LIP thermometry, it is relevant to ask if the thermal insulating properties of the ceramic host material influence the measured temperatures. This is especially important in extreme environments such as in a reciprocating engine where the temperature gradients across the surfaces/in-cylinder gas interface are severe and subject to rapid oscillations during operation.

EXPERIMENTAL SETUP

ENGINE

The engine used in this experiment was a 2 liter port injected in-line 4 cylinder Toyota engine that was running in single cylinder operation and in HCCI mode. The combustion chamber was in the shape of a disc, i.e. no bowl in the piston.

Figure 2 shows a picture of the engine used in the experiments, whereas table 1 presents some vital engine parameters.

The engine was equipped with a piston extension (Bowditch) and a metal piston. The location of the phosphor dot was chosen to be on the inside of a quartz liner right below the combustion chamber ceiling, covering the full squish height of 3 mm (see fig. 3). This position enabled optical access throughout the whole cycle without being restricted to a certain range of Crank-Angle Degrees (CADs). The width of the phosphor dot was chosen wide enough (ca. 7 mm) to account for vibrations during engine operation and to assure laser illumination at all times.

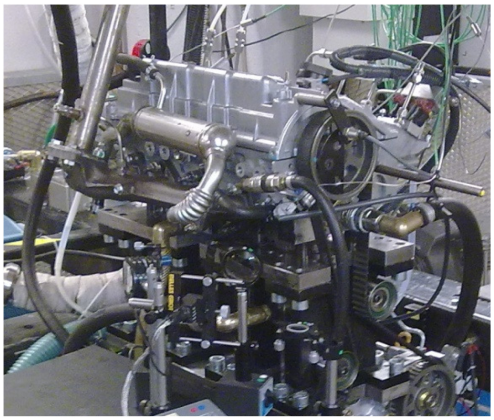

Figure 2. The Toyota engine with piston extension and a quartz liner.

Table 1. Geometric properties of the Toyota engine.

Displacement volume	499 cc
Stroke	94 mm
Bore	82.2 mm
Compression ratio	11.2:1
Number of Valves	4

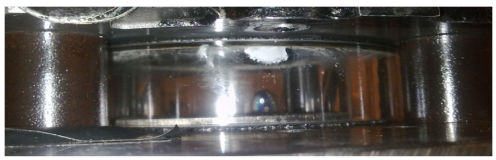

Figure 3. Outside view of the phosphor dot below the cylinder ceiling, sprayed onto the quartz ring's inner side surface.

The fuel used in this work was PRF 50, i.e. Primary Reference Fuel consisting of 50% iso-octane and 50% n-heptane. The engine was controlled by a LabView computer program, developed in-house. The engine control software also triggered the laser in order to timely adjust laser pulses to desired CADs. During combustion the inlet air was heated to around 120-125 °C with a manually controlled Leister heater to ensure HCCI combustion. The gas temperatures are calculated from recorded pressure traces by taking an average over 100 cycles and then use the ideal gas law to calculate the gas temperature for a given CAD.

$$\frac{p \cdot V}{T} = \text{const.} \;\Rightarrow\; T_{\text{CAD}} = T_{\text{ivc}} \cdot \frac{p_{\text{CAD}} \cdot V_{\text{CAD}}}{p_{\text{ivc}} \cdot V_{\text{ivc}}} \tag{1}$$

In equation (1) (p_{ivc}, V_{ivc}, T_{ivc}) are variables for pressure, volume and temperature after inlet valve closing whereas (P_{CAD}, V_{CAD}, T_{CAD}) are corresponding variables at any given CAD during the cycle. Equation (2) was used to estimate the uncertainty for T_{CAD} from the errors of all input parameters in (1):

$$\Delta T_{\text{CAD}} = T_{\text{CAD}} \cdot \left(\frac{\Delta p_{\text{CAD}}}{p_{\text{CAD}}} + \frac{\Delta p_{\text{ivc}}}{p_{\text{ivc}}} + \frac{\Delta V_{\text{CAD}}}{V_{\text{CAD}}} + \frac{\Delta V_{\text{ivc}}}{V_{\text{ivc}}} \right) \tag{2}$$

ΔT_{CAD} was therewith estimated to be below 5 °C before TDC, then reaches up to 60 °C around TDC and decreases to 10 °C after TDC.

However, the ideal gas law approximation estimates the mean gas temperature and does not take the spatial temperature profile seen, in figure 1, into account. It also implies a number of limitations: It considers changes of states to happen instantaneously and thus energy transfer with the environment can only be taken into account as a subsequent process. Particle interactions are neglected such that it applies best for small molecules with a long mean free path (high temperature, low pressure). Moreover it does not hold for thermodynamically open systems, which means that it applies only when the inlet and outlet valves are closed, i.e. from -149 CAD ATDC to 129 CAD ATDC (ATDC = After Top Dead Center).

LASER-INDUCED PHOSPHORESCENCE

By utilizing the well known phosphorescence from thermographic phosphors, temperatures can be measured remotely and non-intrusively with high accuracy in the range between cryogenic temperatures up to 1700 °C [19,20]. An appropriate phosphor is applied on the surface area of investigation using an appropriate non-fluorescent binder, e.g. HPC [14]. The surface is then irradiated with pulsed UV laser radiation for excitation of the phosphor material. The resulting emission intensity will decay exponentially according to

$$I = I_0 \cdot e^{-\frac{t}{\tau}} \tag{3}$$

where I_0 is the initial emission intensity, t is time and τ is the lifetime of the phosphorescence, i.e. the time after which the intensity has decreased to $1/e$ of the initial emission I_0 [12]. The phosphorescence time-decay depends on the temperature of the thermographic phosphor. Temperature can thus be

calibrated and determined by calculating the phosphorescence lifetime from the measured intensity decay. This is normally done by fitting the intensity decay to the theoretical model (eq. 3), using a non-linear fitting procedure. The error in such a measurement can ideally be less than 1% [18].

In the present measurement series the phosphor La_2O_2S:Eu was used. The light emitting substance is the Eu^{3+} ion doped into the host La_2O_2S. The Eu^{3+} ion has a broad absorption spectrum in the UV-region and mainly emits from its ^5D state to its F ground state. The host, La_2O_2S, interacts with the Eu^{3+} ion via its Charge Transfer State, making the emission temperature dependent according to the Boltzmann distribution [21].

Several of the spectral emission peaks originating from the ^5D - F transitions have a temperature dependent lifetime [22]. For these measurements the $^5D_2$ - F relaxation producing emission at 538 nm was used as it is very sensitive in the range 100 - 300 °C. Interference filters centered at 540 nm with a full width half maximum of 10 nm were used to suppress emission wavelengths other than the phosphorescence peak of interest.

The calibration of the thermographic phosphor was made in a controlled environment, in this case an ENTECH oven, where the temperature was constantly logged by a type S thermocouple (specified error: $\Delta T = \pm 1$ °C). The lifetime was measured for a number of temperatures in the expected temperature range, i.e. 100 - 300 °C. Lifetime versus temperature from the calibration is plotted in figure 4.

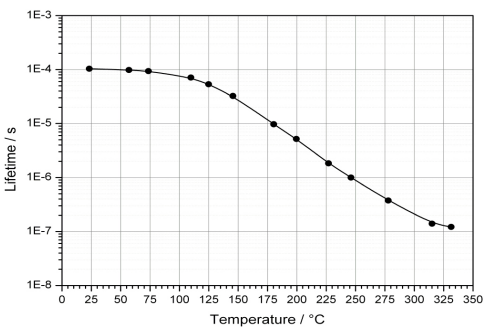

Figure 4. Phosphorescence lifetime as a function of temperature for the La2O2S:Eu 538 nm emission line.

As shown in figure 3 a phosphor dot was sprayed onto the inner side of the quartz liner right below the cylinder ceiling. Since point measurements of the temperature were intended, the size of the phosphor dot was kept reasonably small (3 mm × 7 mm) to prevent the phosphor from insulating a larger surface area. Also the laser beam cross section was reduced to 1 mm and centered onto the phosphor dot. By doing so, the collected temperatures originate from a limited area and thus surface temperature gradients over the probed area are reasonably small and less likely to modify the collected decay curves. HPC was used as a binding agent. The piston extension mentioned earlier greatly facilitated the phosphor applying procedure as it enabled convenient access to the combustion chamber without needing to dismantle the cylinder head every time a new phosphor was about to be applied.

The phosphor was excited by UV-light laser radiation at 355 nm produced by a pulsed Nd:YAG-laser working at its third harmonic. The laser operated at 10 Hz with pulse duration of 5 ns per pulse. The pulse energy was kept as low as 70 µJ throughout all experiments and illuminated a circular phosphor dot size of 8 mm in diameter. Thus errors from heating the wall locally by laser absorption can be neglected whereas the signal-to-noise level for phosphorescence decays maintains reasonably high. The phosphor dot was excited by the laser from two opposing directions, i.e. the phosphor's wall-side and the gas-side were illuminated simultaneously. To achieve this, a polarizing beam splitter was used in combination with a λ/2-plate as shown in figure 5. It creates two beam paths whose intensities can be tuned relatively to each other.

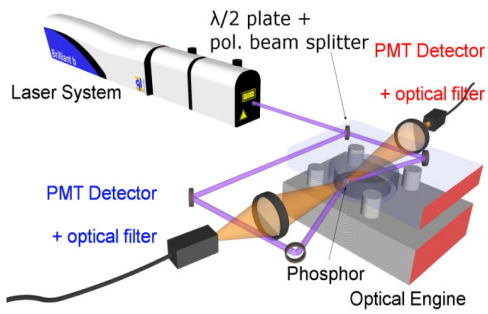

Figure 5. Experimental setup for two-face phosphor temperature determination in an optical engine.

Due to very short absorption lengths of UV light in ceramic materials (such as the phosphor's host material), two separate temperature readings can be obtained from the phosphor, i.e. one from each side of the substrate. In principle, although the excitation light is heavily absorbed, the generated red-shifted phosphorescence could to some extent leak trough the substrate. To quantify this effect, the beam path has been blocked either way before each experiment. The amount of signal that leaked through the phosphor into the opposite detector was at the order of 20% or less. Clearly distinct temperature results shown later indicate that the overhearing

was of none or at least only marginal effect. The induced phosphorescence was collected with quartz glass lenses (f_1 = +100 mm, f_2 = +200 mm, $d_{1,2}$ = 50 mm) and focused on two Photo Multiplier Tubes (PMTs). Interference filters, centered at 538 nm, were placed in front of the PMTs for spectral filtering. The PMT signal passed through a current-to-voltage amplifier and then was sampled and saved by a Lecroy 3 GHz oscilloscope.

Ten measurements were sampled and saved every second to obtain cycle-to-cycle resolution at 1200 rpm, corresponding to 10 Hz.

ENGINE OPERATION PROCEDURE

The measurement procedure contains three measurement cycles. Before the first cycle, the engine was warmed up by motoring the engine. After a warm-up time of 13 minutes a stable temperature of 87±1 °C was obtained for the outer surface of the quartz liner. Also the temperature of the phosphor was continuously monitored during the whole warm-up process using an integrated fast evaluation routine. Measurements were not started before the phosphor temperatures appeared to be stable in time. CAD-resolved temperatures were measured consecutively in steps of 30 CADs from −180 to +180 CAD ATDC. This measurements cycle took about 12 minutes. After this, the engine was heated up and run in HCCI mode. Once the combustion was stable the second measurement cycle was started. A list of operating temperatures during stable HCCI combustion is summarized in table 2.

Table 2. Typical operating temperatures during steady-state HCCI combustion.

Oil temperature	87±2 ˚C
Coolant temperature before engine	76±1 ˚C
Coolant temperature after engine	79±1 ˚C
outer quartz liner temperature (outside - thin phosphor layer)	111±2 ˚C
quartz liner temperature (outside - thick phosphor layer)	115±2 ˚C

As combustion was expected to cause significantly bigger and faster temperature changes than observed during motoring the CAD-resolution was increased down to steps of 5 CADs around TDC. The third and final measurement cycle was started directly after the fuel injection had been terminated and thus measured the cool-down of the engine during motoring for two different CADs, −180 and +5 CAD ATDC. This entire procedure has been repeated for the comparison of two different layer thicknesses of the La_2O_2S:Eu phosphor, one at 32±3µm and another one at 59±2µm. The error numbers indicate the uncertainty of the average thickness at a 95% confidence level. Local thickness variations in the order of ±10 µm have been observed for each phosphor.

RESULTS & DISCUSSION

Crank-angle resolved wall temperature measurements in an HCCI engine have been performed using Laser Induced Phosphorescence. Temperature was measured on a quartz liner slightly below the combustion chamber ceiling, giving simultaneous access to two opposing sides of the phosphor. To illustrate the impact of the phosphor coating thickness on the temperature reading, experiments have been performed comparing a layer of 32µm with a 59µm thick phosphor layer. A Crank-angle range between −180 CAD and 180 CAD ATDC has been investigated for fired and motored engine operation. This makes it possible to compare how different gas/wall temperature gradients have an effect on the phosphor's two-face response.

In figure 6 the CAD-resolved phosphor surface temperatures is shown for the two different thicknesses during HCCI combustion (second measurement cycle). It is obvious that there is a strong influence from the layer thickness. The thicker phosphor (59 µm) clearly indicates an insulating effect when compared to the thinner coating (32 µm). The difference in measured temperature between the two sides is significantly greater for the thicker coating. Furthermore, the side towards the wall shows a smaller temperature increase during combustion for the thicker coating. This implies that there is a stronger shielding effect for the thicker phosphor.

The corresponding measurements for the motored case are presented in Fig. 7. The gas temperature is here reaching 450 °C at TDC, hence, the gas temperature oscillations are significantly reduced compared to the fired operation. With the thin layer of phosphor, the temperature on both sides of the phosphor material increases by 20 °C during the motored compression stroke. With the thicker layer of phosphor, the temperature on the gas side of the phosphor increases by 20 °C during the motored combustion stroke but only by 10 °C on the glass side of the phosphor. For the thinner coating the temperature difference between wall-side and gas-side reaches a maximum of 5 °C for this case, in spite of the gas temperature oscillating with an amplitude ∼400 °C. These results are consistent with the findings from the fired operation presented above. There is definitely an insulating effect, especially for the thicker coating, but it is significantly less pronounced during motored operation.

Figure 8 shows an excerpt of the raw data from the 59 µm phosphor that is presented in figure 6. Single-shot temperatures for 100 successively recorded cycles are displayed. For the figures 6, 7 and 10, series like these have been averaged and are displayed together with their standard deviation as error bars. The dataset for figure 8 was chosen to provide a closer look on how the single-shot temperatures are

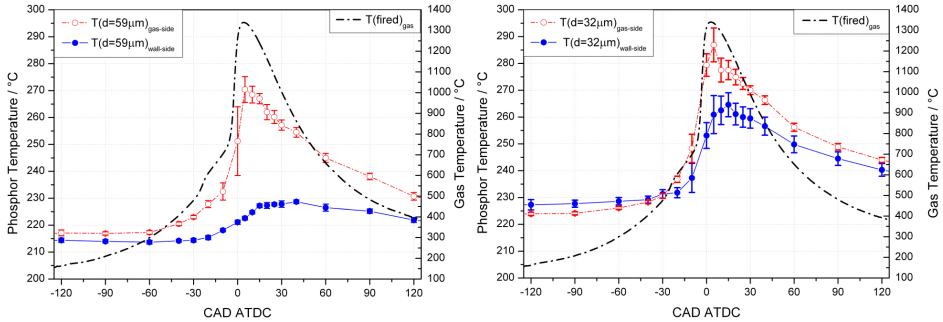

Figure 6. CAD-resolved phosphor surface temperatures during HCCI combustion set into relation to the in-cylinder gas temperature. The thicker phosphor coating (left hand side) can be compared to the thinner phosphor coating (right hand side).

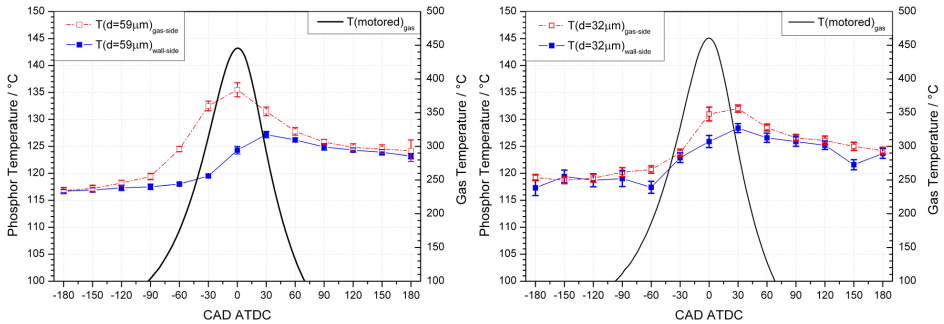

Figure 7. CAD-resolved phosphor surface temperatures during motored operation set into relation to the in-cylinder gas temperature. The thicker phosphor coating (left hand side) can be compared to the thinner phosphor coating (right hand side).

distributed at TDC during combustion - as this was the point with the highest temperature spread for the gas-side temperatures in figure 6. Cycle-to-cycle variation in combustion timing clearly show an effect on the phosphors gas-side temperature ($T_{gas\text{-}side}$=(251±13)°C) as expected. The standard deviation in CA50, i.e. 50 % of heat released, is 0.5 CAD for each series of 100 cycles. From looking at the phosphor's wall-side it is clear that not only the temperature is significantly lower here, but also the standard deviation ($T_{wall.side}$=(221.1±0.8)°C). This indicates the walls to be much more resistant to cycle-to-cycle variations in combustion phasing, i.e. the gas-side of the coating is much more affected by the varying gas temperature. It should also be mentioned that the insulating effect of this thicker phosphor helps dampening the temperature response measured on the wall-side.

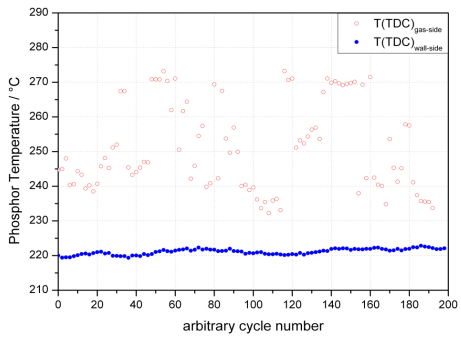

Figure 8. Single-shot phosphor temperatures at TDC during HCCI combustion, obtained for 100 consecutive cycles with the 59 µm phosphor coating.

In order to check whether there is a visible connection between the phosphor's two surface temperatures, they have been overlapped in figure 9 by using a double y-axis plot with different temperature scalings. Additionally, a sliding average filter over 20 neighboring values has been performed to reveal the overall time trend in temperature.

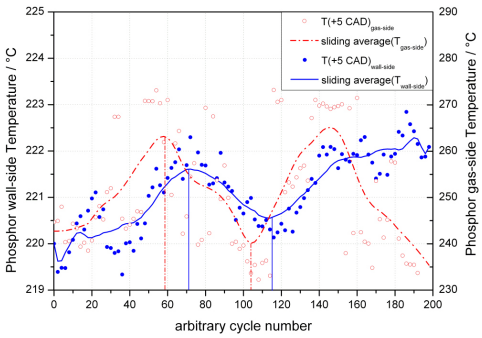

Figure 9. Rescaled single-shot temperatures that have been previously displayed in figure 7. Sliding averages over 20 neighboring points are displayed as lines for both temperatures.

The filtered curves in figure 8 show the wall-side to lag roughly 12 cycles behind the gas-side temperature. This conclusion was drawn by comparing and matching the turning points in the averaged temperature trends (see vertical lines in figure 9). The time delay between the curves has been measured twice, yielding $\Delta t = 0.67$ s for the first maximum, and $\Delta t = 0.53$ s for the first minimum.

In figure 10 the crank-angle resolved phosphor temperatures are set into relation to the gas temperature for the two running conditions. Here the combustion case can, more easily, be compared to the results obtained during motored operation.

As a result of the steeper gas temperature gradients during combustion, the heat transfer through the 59 µm phosphor layer does not keep up with the pace of the engine cycle speed (1200 rpm). This is expressed by the greater temperature differences between the two phosphor surfaces, which are significantly higher during HCCI combustion.

The absolute temperature differences between each side of the phosphor coatings (extracted from figures 6 and 7) are plotted in figure 11 as a function of CAD.

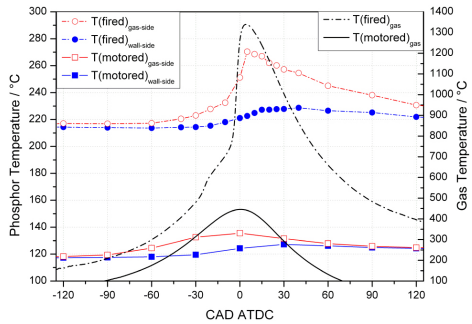

Figure 10. Gas- and phosphor temperature comparison between fired- and motored operation using the example of the 59 µm phosphor coating experiment.

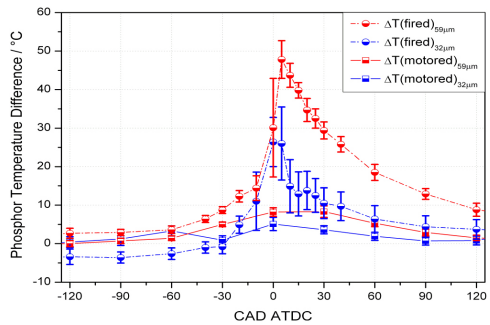

Figure 11. Temperature difference between the phosphor's gas- and wall-side as a function of CAD during fired- and motored engine operation Results for both coating thicknesses are displayed.

Clearly, one can determine differences between the motoring case and the combustion case. For the 59 µm layer during HCCI operation, the maximum temperature difference is almost as high as 50 °C whereas for the 32 µm layer the difference between the gas side and the wall side is only 25 °C. When comparing these results to the motoring case with a much lower average temperature and where the changes in gas temperature are both smaller and slower one can observe that the difference between both sides of the phosphor remain below 10 °C for the thick-, and about 5 °C for the thin phosphor, which is again roughly half of the difference that has been observed for the thicker phosphor coating. The highest temperature difference was observed around 0 CAD regardless of the phosphor coating thickness and mode of engine operation. The lowest temperature differences can be found around the edges of both plots in figure 11. Obviously this is where gas and wall temperatures change the slowest (see figures 6, 7). For the combustion case, the temperature

differences show an asymmetric behavior yielding higher differences at positive crank-angle degrees. This can be explained by the higher temperatures of the burnt gases after combustion that introduce a steeper gradient to the TBL in contrast to their corresponding negative CADs. Error bars plotted in figure 11 correspond to the superposition of the single temperature errors according to the laws of error propagation.

In figure 12 the cool-down behavior of the phosphor coatings is illustrated for −180 CAD and +5 CAD as a function of time after terminating the fuel injection, going from fired operation to external motoring. Displayed are single shot temperatures of two subsequent measurement series as only one CAD position could be monitored at a time. The two time axes have been overlapped such that the fuel termination takes place after 12 s, meaning that there are up to 120 single shot temperatures for each measurement to verify that walls were warmed up sufficiently such that the phosphor temperatures did not drift in time.

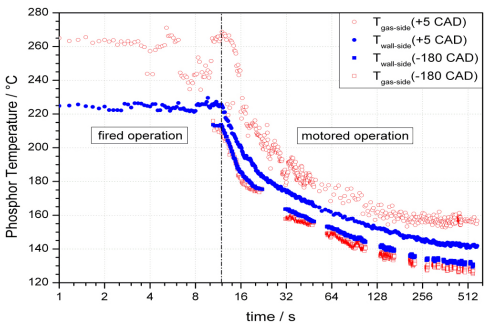

Figure 12. Phosphor temperature (thick coating) at −180 CAD and +5 CAD as a function time, passing from stable combustion on to motored operation.

Figure 12 shows that during a monitored time frame of 10 minutes, each temperatures converged towards a constant temperature T_{const}, reaching T_{const} + 10 % after 95 s (for +5 CAD) and 108 s (−180 CAD). The time difference of 13 s between the two measurements is relatively small and thus indicates that the subsequent measurements had been performed under quite similar conditions. Also comparing the temperatures prior to fuel extinction for +5 CAD ($T_{gas\text{-}side}$=265 °C; $T_{wall\text{-}side}$=225 °C) with the measurement taken earlier in figure 6 ($T_{gas\text{-}side}$=270 °C; $T_{wall\text{-}side}$=222 °C), shows that the temperatures could be reproduced quite accurately.

The cycle-to-cycle variations during combustion at +5 CAD had a clear effect on the spread of the gas side phosphor temperature, which had a standard deviation of about ±4.0 % before combustion was terminated and a value of only ±0.7 % after 10 minutes cooling time while motoring the engine externally. As the wall temperature decreases during the cooling, the difference between the two faces of the phosphor coating becomes less pronounced. In accordance to previous observations in figure 6, figure 12 shows the phosphor's temperature to be colder for −180 CAD compared to the +5 CAD case, regardless the engine's mode of operation.

A final conclusion that can be drawn in figure 12 is again the wall-side of the phosphor clearly to be less affected by the CAD-dependent, fast changing gas temperatures. This conclusion is based on the observation that for +5 CAD (where the gas temperature is close to its maximum) the phosphor's gas-side is hotter than its corresponding wall-side, whereas it is the other way round for −180 CAD, where the gas temperature is rather low. The wall-side phosphorescence thus reflects the inert/tardy characteristics of the cylinder wall as a heat reservoir much more accurate than the gas-side does.

SUMMARY & CONCLUSIONS

Crank-Angle resolved wall temperatures have been measured on the quartz liner close to the cylinder ceiling in an optical Toyota engine during motored and fired operation. According to our knowledge all previous experiments using LIP to determine surface temperatures rely on the assumption that the phosphor coating is non-intrusive to the surface, and sufficiently thin to attain the same temperature as the wall it is attached to without altering it.

For the first time, surface temperatures from phosphors were collected from two sides simultaneously, revealing differences that show a clear dependency on the thickness of the phosphor coating. This difference can be related to the steep temperature gradient that the phosphor coating experiences through the TBL close to the walls. Therefore the temperature difference can be observed to increase for thicker phosphors and with higher temperature gradients in time. The wall-side is believed to reflect the actual wall temperature more accurately than the gas-side of the phosphor coating. This observation is strengthened by the fact that it is much less sensitive to thickness variation of the phosphor compared the gas-side. In fact, the cylinder wall seems by far less sensitive to cycle-dependent gas temperature variations than assumed from previous experiments. It acts tardy and oscillates with lesser amplitude around the time-weighed average of the gas temperatures.

However the amount of heat transfer from the gas through the phosphor towards the wall-side is yet unknown and also the disturbance of the TBL that is introduced by the phosphor dot. This could have an impact on the wall-side temperature reading as the phosphor layer might shield the wall locally and the disturbance of the TBL could introduce some

inhomogenity to the surface temperature distribution (=intrusiveness of the phosphor technique).

In most applications access to the phosphor is solely possible from the gas-side as engine walls are usually non-transparent to laser radiation. This implies that the presented results reveal a need for caution when applying the technique for in-cylinder measurement. For engine experiments in similar temperature regimes as the results presented here, the phosphor coating thickness should be kept as thin as possible and well below 30um if it is of importance that systematic errors in the order of up to +30 °C are to be avoided.

For thinner phosphor coatings the temperature readings from the gas-side and from the wall-side should converge. However, the layer cannot be made infinitely thin since that would compromise the signal-to-noise ratio and also the durability of the coating. Unlike sprayed phosphor coatings, very thin phosphor coatings in the range of 0.1 µm to 5 µm can be produced using methods such as RF magnetron sputtering or Electrostatic Assisted Combustion Chemical Vapor Deposition [18, 23]. Ranson et al. showed, that the thickness of such a layer can be made as thin as 1 µm without compromising phosphorescence intensity [23]. It should be noted that the corresponding limit is probably higher for phosphors that have been applied using the spray technique, where phosphor particles are embedded in a transparent binding agent.

Nevertheless are sprayed phosphor coatings widely used in combustion engine research, where the access to internal surface areas is limited. Future work includes more detailed experiments in order to define how and under which restrictions the phosphor technique is applicable for accurate temperature measurements in engine environments.

REFERENCES

1. Splitter, D., Reitz, R., and Hanson, R., "High Efficiency, Low Emissions RCCI Combustion by Use of a Fuel Additive," *SAE Int. J. Fuels Lubr.* **3**(2):742-756, 2010, doi: 10.4271/2010-01-2167.

2. Manente, V., Zander, C., Johansson, B., Tunestal, P. et al., "An Advanced Internal Combustion Engine Concept for Low Emissions and High Efficiency from Idle to Max Load Using Gasoline Partially Premixed Combustion," SAE Technical Paper 2010-01-2198, 2010, doi:10.4271/2010-01-2198.

3. Heywood, J. B., "Internal Combustion Engine Fundamentals", McGraw-Hill, New York, ISBN 0-07-100499-8, 1988.

4. Woschni, G. and Fieger, J., "Determination of Local Heat Transfer Coefficients at the Piston of a High Speed Diesel Engine by Evaluation of Measured Temperature Distribution," SAE Technical Paper 790834, 1979, doi: 10.4271/790834.

5. Chang, J., Güralp, O., Filipi, Z., Assanis, D. et al., "New Heat Transfer Correlation for an HCCI Engine Derived from Measurements of Instantaneous Surface Heat Flux," SAE Technical Paper 2004-01-2996, 2004, doi: 10.4271/2004-01-2996.

6. Vressner, A., "Studies on the Load Range of an HCCI Engine using In-Cylinder Pressure, Ion Current and Optical Diagnostic," Ph.D. thesis, Lund Institute of Technology, Lund, 2007.

7. Christensen, M., "HCCI Combustion - Engine Operation and Emission Characteristics," Ph.D. thesis, Lund Institute of Technology, Lund, 2002.

8. Tsurushima, T., Kunishima, E., Asaumi, Y., Aoyagi, Y. et al., "The Effect of Knock on Heat Loss in Homogeneous Charge Compression Ignition Engines," SAE Technical Paper 2002-01-0108, 2002, doi:10.4271/2002-01-0108.

9. Manente, V., Johansson, B., Tunestål, P., "Half Load Partially Premixed Combustion, PPC, with High Octane Number Fuels. Gasoline and Ethanol Compared with Diesel," *SIAT 2009* **295**, 2009.

10. Brübach, J., Zetterberg, J., Omrane, A., Li, Z.S., Aldén, M., Dreizler, A., "Determination of surface normal temperature gradients using thermographic phosphors and filtered Rayleigh scattering," *Appl. Phys. B* **84**, 2006.

11. Brübach, J., Hage, M., Janicka, J., Dreizler, A., "Simultaneous phosphor and CARS thermometry at the wall-gas interface within a combustor," *Proc. Combust. Inst.* **32**, 2009.

12. Eckbreth, A.C., "Laser Diagnostics for Combustion Temperature and Species, 2nd edition," Gordon and Breach, ISBN 9056995324, 1996.

13. Allison, S.W., Gilles, G.T., "Remote thermometry with thermographic phosphors: Instrumentation and applications," *Rev. Sci. Instrum.*, **68**(7): 2616, 1997.

14. Allison, S.W., Beshears, D.L., Bencie, T., Hollerman, W.A., Boudreaux, P., "Development of temperature sensitive paints for high temperature aeropropulsion applications," *AIAA-2001-3528*, 2001.

15. Särner, G., Richter, M., Aldén, M., Vressner, A. et al., "Cycle Resolved Wall Temperature Measurements Using Laser-Induced Phosphorescence in an HCCI Engine," SAE Technical Paper 2005-01-3870, 2005, doi: 10.4271/2005-01-3870.

16. Wilhelmsson, C., Vressner, A., Tunestål, P., Johansson, B. et al., "Combustion Chamber Wall Temperature Measurement and Modeling During Transient HCCI Operation," SAE Technical Paper 2005-01-3731, 2005, doi: 10.4271/2005-01-3731.

17. Cao, X.Q., Vassen, R., Stoever, D., "Ceramic materials for thermal barrier coatings," *J. Eur. Ceram. Soc.* **24**:1-10, 2004.

18. Feist, J.P., Heyes, A.L., Choy, K.L., Su, B., "Phosphor thermometry for high temperature gas turbine applications," *IEEE-0-7803-5715-9*, 1999.

19. Krauss, R.H., Hellier, R.G., McDaniel, J.C., "Surface temperature imaging below 300 K using," *Appl. Opt.* **33**:3901, 1994.

20. Cates, M.R., Allison, S.W., Jaiswal, S.L., Beshears, D.L., "YAG:Dy and YAG:Tm fluorescence to 1700°C," *The 49th International Instrumentation Symposium - The Instrumentation, Systems, and Automation Society*. Orlando, Florida. May 2003.

21. Shionoya, S., Yen, W.M., "Phosphor handbook", CRC Press, 1999.

22. Husberg, T., Gjirja, S., Denbratt, I., Omrane, A. et al., "Piston Temperature Measurement by Use of Thermographic Phosphors and Thermocouples in a Heavy-Duty Diesel Engine Run Under Partly Premixed Conditions," SAE Technical Paper 2005-01-1646, 2005, doi: 10.4271/2005-01-1646.

23. Ranson, R.M., Thomas, C.B., Craven, M.R., "A thin film coating for phosphor thermometry," *Meas. Sci. Technol.* **9**, 1998

CONTACT INFORMATION

Christoph Knappe, Dipl.-Phys.
christoph.knappe@forbrf.lth.se
Telephone: +46 46 22 23733
Fax: +46 46 22 24542
Department of Physics
Division of Combustion Physics
Lund University
P.O. Box 118, SE-221 00, Lund, Sweden

ACKNOWLEDGEMENTS

This work has been performed within the "D60 - The 60% efficient diesel engine" -project, an integrated part of the Centre of Competence for Combustion Processes (KCFP) at Lund Institute of Technology, Sweden. The authors kindly acknowledge the funding from the Swedish Energy Agency.

DEFINITIONS/ABBREVIATIONS

(A)TDC
(After) Top Dead Center

CAD
Crank-Angle Degrees

CI
Compression Ignition

HCCI
Homogenous Charge Compression Ignition

ITE
Indicated Thermal Efficiency

LIP
Laser-Induced Phosphorescence

PMT
Photo Multiplier Tube

SI
Spark Ignition

TBL
Thermal Barrier Layer

TBC
Thermal Boundary Coating

Thickness dependent variations in surface phosphor thermometry during transient combustion in an HCCI engine

Paper III

Christoph Knappe, Martin Algotsson, Peter Andersson,
Mattias Richter, Martin Tunér, Bengt Johansson and Marcus Aldén

Published in: Combust. Flame **160**(8):1466-1475, 2013.

Combustion and Flame 160 (2013) 1466–1475

Contents lists available at SciVerse ScienceDirect

Combustion and Flame

journal homepage: www.elsevier.com/locate/combustflame

Thickness dependent variations in surface phosphor thermometry during transient combustion in an HCCI engine

Christoph Knappe [a,*], Martin Algotsson [b], Peter Andersson [b,1], Mattias Richter [a], Martin Tunér [b], Bengt Johansson [b], Marcus Aldén [a]

[a] Department of Physics, Division of Combustion Physics, Lund University, Box 118, SE-221 00 Lund, Sweden
[b] Department of Energy Science, Division of Combustion Engines, Lund University, Box 118, SE-221 00 Lund, Sweden

ARTICLE INFO

Article history:
Received 19 October 2012
Received in revised form 18 January 2013
Accepted 25 February 2013
Available online 2 April 2013

Keywords:
Laser-induced phosphorescence
Thermographic phosphor
Surface thermometry
Film thickness
Thermal boundary layer
Internal combustion engine

ABSTRACT

Phosphor thermometry is a semi-invasive measurement technique which is commonly used for temperature determination in combustion applications. Surface temperature measurements using thermographic phosphors rely on the assumption that the phosphor layer is thin enough in order to adopt the surface temperature non-intrusively. This work compares the temperature information, recorded from two opposing sides of phosphor films, coated on a translucent part of the combustion chamber wall inside a car engine. The film thickness was varied between 5 and 72 μm and two different phosphors were studied; $CdWO_4$ and La_2O_2S:Eu. For both phosphors, the results showed no significant differences. Being subject to unsteady heat transfer during fired engine operation, phosphor coatings above 20 μm in thickness experienced a significant temperature gradient between the front- and the backside of the coating, whereas thinner layers did not seem to be affected within the limits of measurement accuracy and precision. Cycle-to-cycle variations of the global gas temperature were not found to correlate with phosphor temperature variations. However, a strong temperature correlation between opposite sides of the phosphor coating was observed for film thicknesses below 20 μm during engine cycle-to-cycle variations.

1. Introduction

The temperature of combustion chamber walls is an important parameter for the generation and validation of predictive models describing heat transfer in internal combustion engines [1–3]. Amongst measurement techniques for surface temperatures, laser-induced phosphorescence has drawn increasing attention in the past few years, being a versatile alternative to conventional probing techniques such as thermocouples and pyrometry [4–8]. Thermographic phosphors allow remote temperature sensing with comparatively high temporal resolution by collecting the commonly red-shifted phosphorescence emission from an optically excited thin film that has been coated onto a target surface. Typical excitation sources are usually pulsed UV lasers, but also laser diodes and light emitting diodes have recently been employed as they continue to improve in terms of both price and output power [9–11]. In order to determine surface temperatures, the decay time or the relative spectral intensity distribution of the phosphor emission are most commonly exploited, the former one often regarded to allow a higher measurement precision [12,13].

The phosphorescence emission is generally carrying the temperature information from the coated layer on top of the actual target surface, followed by the implicit assumption that the phosphor film is thin enough to adopt the temperature of the covered surface without perturbation. This assumption, however, is critical in thermal non-equilibrium situations as thermographic phosphors often are described as ceramic materials, which in turn are known to be thermal insulators. As for chemically similar thermal barrier coatings, Gentleman et al. identified temperature differences in the order of 100 K for a 140–170 μm thick surface film of YSZ [14].

In a previous study the authors have shown for the first time that temperature gradients can occur throughout a phosphor film, meaning that the phosphor temperature no longer corresponds to the wall surface temperature below. More precisely, this behavior has been observed for $\geqslant$30 μm thick spray coatings of La_2O_2S:Eu which were applied inside an internal combustion engine [15]. Very recently, a theoretical study by Atakan et al. confirmed these measurement results by thoroughly investigating the optical cross-talk between spatial layers of the phosphor film and by performing a heat transfer analysis based upon our previous experimental results [16]. Another recent study used experimental surface temperatures from thin film thermocouples in an HCCI engine

* Corresponding author.
E-mail address: christoph.knappe@forbrf.lth.se (C. Knappe).
[1] Present address: HRM Engineering AB, Eriksbergstorget 11, SE-417 64 Gothenburg, Sweden.

0010-2180/$ - see front matter © 2013 The Combustion Institute. Published by Elsevier Inc. All rights reserved.
http://dx.doi.org/10.1016/j.combustflame.2013.02.023

(Homogeneous Charge Compression Ignition) for modeling the influence of combustion chamber deposits (e.g. soot, hydrocarbons) on the wall temperature [17]. Similarly to thermographic phosphors these deposits can have a thermally insulating effect, and as they are globally present, they even influence the combustion process.

In this work a wider range of thicknesses from 5 μm up to 72 μm has been investigated experimentally to remedy a general lack of experimental data needed to quantify this effect and verify theoretical models. Especially, film thicknesses below 30 μm seem a worthwhile target for further investigations in order to study if-, and to which degree, accurate measurements can be obtained by thermographic phosphors in applications with rapidly changing spatial- and temporal temperature gradients. Another question to be addressed in this study is whether and how the temperatures from the front- and backside of phosphor coatings correlate with each other and with cycle-to-cycle variations of the global gas temperature for various film thicknesses. Finally, a second thermographic phosphor ($CdWO_4$), was investigated along with La_2O_2S:Eu in order to study whether or not temperature gradients for different film thicknesses have a phosphor-specific dependency.

2. Experimental and analytic section

2.1. Engine environment

Phosphor film thickness experiments have been performed inside a Toyota diesel engine utilizing an experimental setup similar to the one which was used in preceding publications [15,18]. Out of four cylinders, the engine was operated on only one cylinder that has been modified for optical access by employing a quartz liner and a piston extension of Bowditch design [19]. The engine was run in HCCI mode using PRF50 fuel, i.e. a fuel-mixture of 50% isooctane and 50% n-heptane. Further engine details can be found in Table 1.

In order to maximize repeatability, the engine warm-up procedure was performed in the same way for all measurement series. Prior to data acquisition in each experiment, the engine was operated continuously for approximately 30 min in order to prevent temperature drifts. Oil and cooling water temperatures were monitored to ensure that the engine was running stable at the same overall temperature. Crank-angle resolved global gas temperatures were calculated in reference to known values during inlet valve closing using the in-cylinder pressure trace and employing the ideal gas law.

2.2. Thermographic phosphors

Two different thermographic phosphors (supplied by Phosphor Technology) were used under similar experimental conditions in this study, cadmium tungstate ($CdWO_4$) and lanthanum oxy-sulfide with a dopant concentration of 2% Eu (La_2O_2S:Eu). After being excited by pulsed UV light, these phosphors undergo an optically red-shifted relaxation process with a constant transition probability that results in an exponential intensity–time relation. A certain time t after laser excitation, the initial phosphorescence intensity I_0 at a time $t_0 = 0$ decays with a time constant τ such that the current phosphorescence emission $I(t)$ approximately follows a relation according to $I(t)/I_0 = \exp(-t/\tau)$.

Table 1
Engine properties of the optical engine.

Property (unit)	Value
Cylinder volume (l)	0.5
Bore (mm)	82
Stroke (mm)	92
Speed (rpm)	1200
Load (IMEPg) (bar)	2–3
Inlet pressure (bar)	1
Inlet air temperature (K)	390
Compression ratio	11
Injection system	Port fuel injection
Fuel	PRF50
Piston geometry	Pancake (flat)

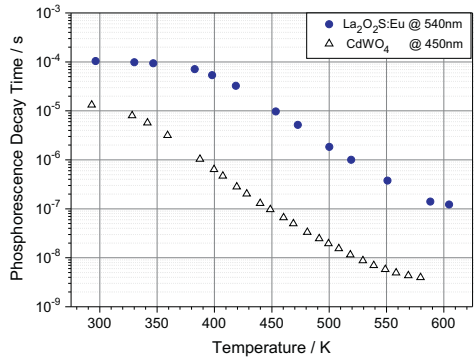

Fig. 1. Phosphorescence lifetime for $CdWO_4$ and La_2O_2S:Eu as a function of temperature.

Both phosphors exhibit a decay time which changes several orders of magnitude as a function of temperature in a region between 300 and 600 K (see Fig. 1).

At an engine speed of 1200 rpm, one crank-angle degree corresponds to a time interval of 139 μs. As displayed in Fig. 1, both phosphors decay in time intervals shorter than 100 μs. Moreover, their decay times decline towards elevated temperatures, which increases temporal resolution further and thus allows the retrieval of precise, crank-angle-resolved surface temperatures. $CdWO_4$ requires an excitation wavelength of 266 nm, whereas La_2O_2S:Eu can be suitably excited by 355 nm. Both wavelengths have been supplied by a 10 Hz pulsed Nd:YAG laser (Quantel, Brilliant B) with 5 ns pulse duration, operating either at its 3rd or 4th harmonic.

Decay times have been determined using the Levenberg–Marquardt algorithm. For the fitting window position and width, two different approaches were followed in this study.

(1) The first approach had a fixed starting position at 10 ns after the curve maximum which was given by the laser peak, retaining the highest quality signal and avoiding contributions of laser scattered light. The end of the fitting window was determined individually for each curve by the time, for which the phosphorescence signal had decreased to 5% relatively to the phosphorescence intensity at the start of the fitting window. This approach is preferable if temperatures change a great deal in between individual measurement events since the phosphorescence decay time varies several orders of magnitude for a given temperature range (see e.g., Fig. 1).
(2) A second evaluation approach was chosen for measurements addressing the resolution of single-shot based temperature variations, observed for individual crank-angles. In this experimental case, temperature changes were small compared to the full temperature transient of the engine. As most phosphors exhibit a multi-exponential emission behavior, noise-based variations of the fitting window position and length (as present when using approach 1) can

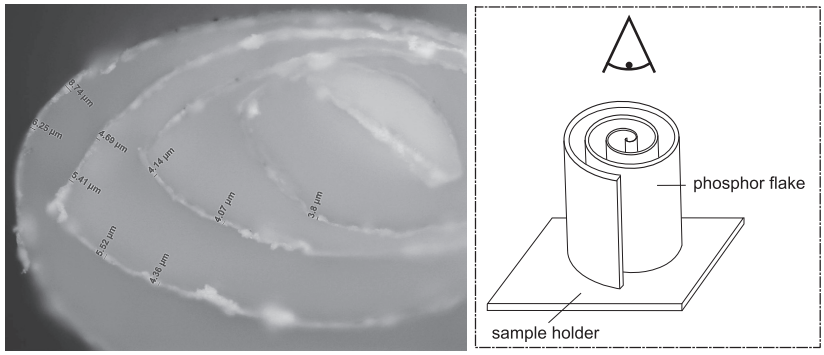

Fig. 2. Microscope image of a 5 µm thick La_2O_2S:Eu film that was earlier used for surface temperature measurements in an optical engine (see left hand side). Fuzzy edge areas, appearing locally thicker, originate from parts of the flake which bended into the focal plane. The phosphor flake was carefully removed from the quartz liner, cut, and finally attached to a sample holder in an upright position for thickness determination using optical microscopy (see schematic sketch on the right hand side).

cause random artificial temperature variations. When investigating cycle-to-cycle correlations, these variations could become a significant interference factor. Hence, a constant time window was first chosen individually for each crank-angle and then applied for the evaluation of multiple phosphorescence decays. While all evaluation windows started 10 ns after the curve maximum, the end of each fitting window was for this scenario chosen by the time, where the average decay curve of the entire ensemble underruns that 5% margin. The employment of such a fixed fitting window removes random noise that hampers the observation of minor temperature changes of equal or smaller magnitude. However, it should be noted that slight systematic errors are added to the most dissenting temperature values, where a fixed fitting window does not fully comply with the evaluation window that was previously used during calibration.

2.3. Coating procedure and thickness determination

In order to provide a set of different phosphor layers ranging from 5 to 72 µm, a spray coating technique was used. There are other and more precise methods for creating thin phosphor films, such as chemical vapor deposition, Sol–Gel growth or sputtering techniques [20–22]. However, the improved precision of such processes comes along with difficulties when being applied on-site in an industrial environment where target surfaces often are large in size or hard to remove.

Several measures were taken to create and control film thicknesses as accurate as possible with the given spray technique. The phosphor and a HPC binding agent, consisting of 2% magnesium aluminum silicate ($Mg_3Al_2(SiO_4)_3$) and 98% water, were premixed in larger quantities (phosphor-to-binder mass ratio: 1:20) to ensure that each experiment relies on the same relative composition between binder and thermographic phosphor. The phosphor was applied using an air brush, held at constant air pressure of 1.5 bar. All coatings were created layer-wise by spraying for a time interval of 1 s from a constant distance of 3 cm in front of the target surface. In between each layer deposition, the freshly applied phosphor-binder mixture was dry-heated by a hot air gun. Variations in the amount of spray intervals per film coating allowed the creation of different layer thicknesses.

The coating thickness determination was performed using an optical method, developed by the authors. After each finished engine run the combustion chamber was opened and the phosphor coating was removed from the surface using the sharp edge of a razor blade. Small flakes of phosphor were collected and prepared for thickness determination with an optical microscope (Zeiss, Axio Imager M1m). Each measurement resulted on average in three flakes that had high enough structural quality to be mounted upright on a sample holder such that the film diameter could be viewed and measured from above. For every mounted sample, approximately four microscope images covering different object regions were obtained, each revealing about five spots suitable for thickness readings on average. This yielded a total number of several tens to hundreds of thickness measurements per coated phosphor film. A typical microscope image, including thickness measures from a La_2O_2S:Eu coating after being removed from the engine interior, can be seen in Fig. 2.

In addition to applying each phosphor film on the quartz liner, a reference film was coated onto a steel substrate simultaneously, i.e. by alternating the two coating targets in between each applied layer. Since it is possible that phosphor coatings from the quartz liner were sometimes not fully removed by the razor blade, some optical thickness investigations might result systematically in too low values. Therefore, the order of magnitude for all optical thicknesses was reconfirmed by corresponding reference coatings from the steel substrate. The availability of these reference coatings allowed for a different thickness determination method, using an electromagnetic thickness gauge (Elcometer 456). In this method, the electric field between the gauge head and the steel substrate is measured and thicknesses of dielectric coatings on metal substrates can be measured without separating the film from the substrate. In practice, electromagnetic thickness results from reference surfaces varied in a random manner from the optical thickness results, giving no indication of a systematic bias in the optical method. Deviations were found in the order of ±3 µm for thicknesses below 20 µm and ±10 µm for thicknesses up to 72 µm and are mainly due to a lack of thickness precision when producing replica coatings on reference substrates. It was thus deemed important to mainly rely on optical measurements, which could be performed on the original coatings, used during the actual engine runs. However given the modest amount of variation, reference coatings served as a back-up value for reconfirming the optically determined thickness results.

2.4. Experimental setup

The laser energy was kept below 1 mJ and further reduced by irises that limited the excited area to a circular spot with a diameter of 2 mm, preventing both laser heating and spatial averaging of

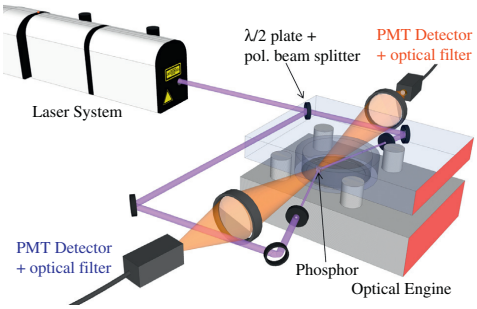

Fig. 3. Experimental setup for two-face phosphor temperature determination on the transparent part of the combustion chamber wall of an optical engine.

wall temperatures. The phosphor spot was of about 7 mm in diameter to allow for engine vibrations relative to the fixed laser beam position without losing the phosphorescence signal. Throughout this study $CdWO_4$- and La_2O_2S:Eu coatings of different layer thicknesses have been applied in consecutive experiments on the uppermost part of the quartz liner, approximately 4 mm below the cylinder head. The experimental setup is displayed in Fig. 3.

The quartz liner allowed for phosphor excitation and collection from the two opposing sides of the coating, i.e. the chamber wall-side (blue text) and the gas-side (red[2] text). Hence, the laser beam path was split into two using a $\lambda/2$-plate in combination with a polarizing beam splitter. Irises were used to limit the area on the phosphor coating, over which the temperature dependent phosphorescence was extracted. Two lenses (f_1 = +100 mm, f_2 = +200 mm, $d_{1,2}$ = 50 mm) imaged the phosphorescence on two PMT (photo multiplier tube, Hamamatsu H11526-20-NF) detectors. Interference filters were placed in front of the detectors. These filters were fit to isolate the phosphorescence wavelength from spurious laser- and background radiation. A 450 nm ± 20 nm bandpass filter was chosen for $CdWO_4$ and a 540 nm ± 10 nm bandpass filter for La_2O_2S:Eu. Finally, the PMT signal was read out over a 50 Ω input resistance of a 350 MHz oscilloscope (Lecroy, Waverunner WA 6030). The resistance value was chosen in order to maintain a high time resolution in the detection line. This was required for measurements at high temperatures using $CdWO_4$, where signals decay within just a few nanoseconds (see Fig. 1).

The measurement accuracy in this experiment is determined by the calibration process, in which the oven temperature was sampled by a K-type thermocouple, having a specified temperature accuracy of ±1–2 K. The accuracy was checked prior to experiments in boiling water and in an ice bath and was found to agree within the boundaries of ±0.5 K.

The measurement precision can vary a great deal throughout the experiment as it mainly depends on the signal-to-noise ratio of individually taken phosphorescence signal curves. These vary as a function of coating thickness (thinner coatings produce weaker signals) as well as the cleanliness of the optical excitation and detection paths. In the course of experiments, deposition of oil and soot on the quartz liner as well as interferences by background signals from the combustion reaction may compromise signal quality and thus precision. Error bars for standard deviations as well as cycle-resolved shot-to-shot variations are indicators of measurement precision.

[2] For interpretation of color in Figs. 1, 6–9, the reader is referred to the web version of this article.

3. Results and discussion

Crank-angle resolved wall temperatures between −120 CAD (crank-angle degree) and 120 CAD ATDC (After Top Dead Center) have been measured in an HCCI engine using Laser-Induced Phosphorescence. Measurement points were varied in steps of 5 CAD around TDC and had a wider spacing early and late in the cycle. At a speed of 1200 revolutions per minute, the 10 Hz laser system limited the data acquisition to one measurement per combustion cycle at a specific crank-angle. Phosphor film temperatures from two opposing sides of the phosphor were simultaneously measured along with corresponding global temperatures of the bulk gas that have been extracted from the in-cylinder pressure trace. Several engine runs have been performed for comparing phosphor films with a thickness in between 5 and 72 μm.

3.1. Cycle-averaged results

Figure 4 shows cycle-averaged temperatures for each crank-angle, originating from engine runs using La_2O_2S:Eu coatings with film thicknesses of 5 (a), 20 (b), 40 (c) and 72 μm (d).

For La_2O_2S:Eu coatings that had a thickness of 40 μm or more (Fig. 4c and d), a thermal gradient between the gas- and the wall-side of the phosphor was identified, reconfirming results for thicknesses $\geqslant$30 μm that have been obtained in [15,16]. This temperature difference between wall- and the gas-side of the phosphor film was caused by unsteady heat transfer and a steep temperature gradient in the gas region close to the chamber surface, also referred to as thermal boundary layer.

From the 40 μm phosphor film, the mean phosphor temperature at −120 CAD appears to be about 30 K lower, compared to corresponding measurements using a 72 μm thick coating. This observation is somewhat surprising and can only in parts be explained as a consequence of the inlet air temperature, which also was lower during measurements with the 40 μm coating. The inlet air temperature difference was ≈6 K, which caused the maximum gas temperature to change by 40 K. This temperature increase also advanced the combustion phasing, resulting in a gas temperature difference of 110 K at TDC (Top Dead Center), and thus contributed to the wall temperature difference (45 K at TDC).

Another observation from Fig. 4d is that the gas-side of the phosphor remains cooler than its corresponding wall-side until late in the cycle at −30 CAD, whereas the global gas temperature already exceeds the temperature of the phosphor at around −72 CAD. Clearly, a coating this thick acts perceptibly as a thermal insulator, which is additionally expressed by the distinct up- and downswing of the gas-side temperature compared to the mere temperature upswing, visible for the wall-side of the phosphor coating.

Phosphor film thicknesses of 20 μm and below (Fig. 4a and b) followed the gas temperature trends very well and showed no significant difference in the temperature reading of the gas- and wall-side of the phosphor. The temperature information from these thin films is thus a more reliable estimate of the true surface temperature. However, model-based predictions by Atakan et al. concluded that temperature gradients might be still important for coating thicknesses around 10 μm [16]. The presence of a temperature gradient along the surface normal for coated films with a thickness below 20 μm is therefore still possible, but hidden in the data due to the contribution of two factors:

(1) The first factor is the optical crosstalk of intermediate layers throughout the phosphor film that leads to contributions from different depths and temperatures to the total phos-

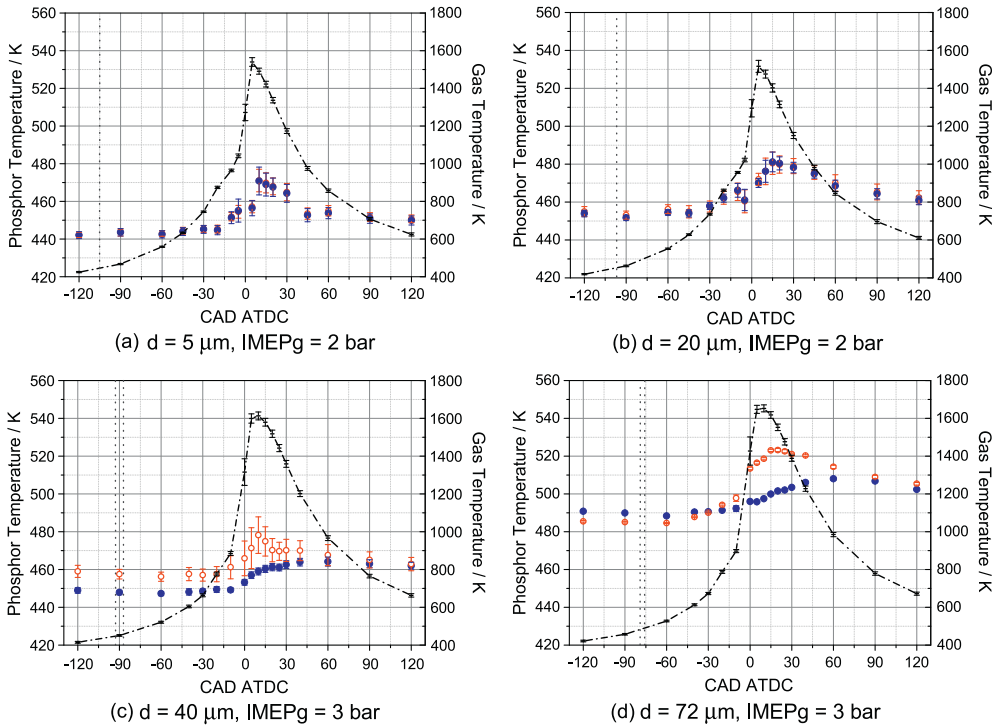

Fig. 4. Cycle-averaged wall temperatures from La_2O_2S:Eu films (blue dots = wall side, red hollow circles = gas side) using four different coating thicknesses. Global gas temperatures are represented by the dash-dotted black lines using a separate *y*-axis on the right-hand side. All error bars indicate one standard deviation, based on 100 combustion cycles. The vertical dotted lines indicate crank-angle positions, where gas- and phosphor temperatures intersect.

phorescence signal. The more translucent the phosphor layer becomes, the more the phosphorescence signal represents an average of temperatures across the film thickness. A demonstrative model using Beer–Lamberts law was proposed for this by [16], helping to predict this effect on a calibrated phosphor with a known laser absorption coefficient. In practice, however, these absorption coefficients are unknown and for spray coatings dependent on the mixing ratio between binder and phosphor. Future modeling work aiming at revealing further details could include effects of reabsorption, scattering and stimulated emission of phosphorescence photons.

(2) The second factor comprises overlapping errorbars as a result of increased measurement uncertainty, caused by weaker light signals from thinner phosphor coatings. Throughout this study, 5 µm phosphor films turned out to be the lower limit for spray coatings in terms of thickness and acceptable signal level. This value is close to the lower limit of 10 µm for spray coatings that was approximated by Ranson et al. [22]. His publication also demonstrated that the RF-sputtering technique could produce durable phosphor coatings of 0.7 µm, which were capable of emitting similar phosphorescence intensities as $\geqslant$10 µm spray coatings.

Finally, it should be noted, that during the measurements (a) and (b) in Fig. 4, the indicated mean effective pressure (IMEPg) was lower, which can be seen both by a delayed combustion phasing and maximum gas temperatures to be about 100 K lower compared to the measurement cases (c) and (d). This load dependent change in transient gas temperatures also has an effect on the temperature gradient across the phosphor coating, as reported earlier in [15] by the authors: Studies of motored and fired engine cycles with comparatively huge temperature differences (880 K) regarding the gas temperature transients resulted in moderate changes of the temperature gradient across the phosphor films. These findings give confidence to the assumption that the minor gas temperature transient changes, caused by variations of engine load could have only introduced a slight bias to the evaluated temperature gradients presented in Fig. 4.

Figure 5 shows temperature results obtained from a 14 µm thick $CdWO_4$ coating.

In accordance to phosphor films of La_2O_2S:Eu with thicknesses below 20 µm, no significant difference can be observed from the two opposite sides of the $CdWO_4$ phosphor film. Both, the temperature transient as well as absolute temperature values are very similar. This observation confirms the presumption that different phosphors probably exhibit a similar behavior in terms of thermal insulation and optical translucency.

Figure 6 illustrates measurement data extracted from Figs. 4 and 5 as a function of phosphor film thickness. Crank-angle positions for which the maximum temperature was reached are displayed for the bulk gas (black squares) and both phosphor sides (circles and dots).

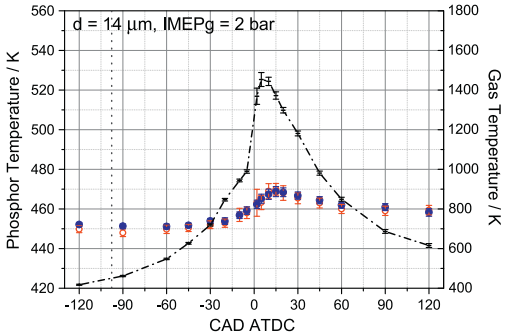

Fig. 5. Cycle-averaged temperatures of a 14 µm thick $CdWO_4$ coating as a function of crank-angle (blue dots = wall-side, red hollow circles = gas-side). Global gas temperatures are represented by the dash-dotted black line using a separate *y*-axis on the right-hand side. All error bars indicate one standard deviation, based on 100 combustion cycles. The vertical dotted line indicates the crank-angle where gas- and phosphor temperatures intersect.

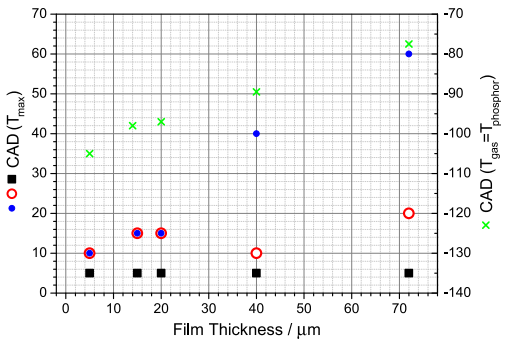

Fig. 6. Film thickness dependency of the crank-angle that yielded a temperature maximum (gas: black squares, phosphor wall-side: blue dots, phosphor gas-side: red circles). The right-sided *y*-axis, corresponding to the green crosses, indicates the crank-angle position where the gas temperature starts exceeding the thickness-averaged phosphor temperature. Data values were extracted from Figs. 4 and 5. (For interpretation of the references to colour in this figure legend, the reader is referred to the web version of this article.)

The maximum gas temperature appeared at approximately 5 CAD after TDC and was not affected by different engine runs and phosphor film thickness.

Concerning the maximum temperature, measured at the phosphor wall-side and indicated by blue dots, corresponding crank-angle positions were progressively delayed with increasing phosphor film thickness. Clearly, it can be understood, that the influence of high gas temperatures close to the chamber wall becomes less noticeable behind a thicker, thermally insulating surface coating.

The phosphor as a thermal insulator exhibits signs of inertia, making the gas-side react earlier to temperature changes than the wall-side. However, since local insulation of the chamber wall behind the phosphor film against hot- and fast gas temperature transients should increase for thicker coatings, the gas-side of the phosphor should react progressively faster and more drastic to gas temperature changes as the film thickness increases and the thermal cross-talk with the combustion chamber wall loses impact on the phosphor's gas-side. This assumption could not be confirmed by the trends in Fig. 6 (see red circles), most likely because of too low crank-angle resolution (±5 CAD) and measurement precision.

The crank-angle position for which the gas temperature exceeds the average phosphor temperature (displayed as green crosses, right hand side *y*-axis in Fig. 6), shows a clear dependency on the film thickness getting increasingly delayed for thicker coatings. This means that relatively to the gas temperature, the phosphor coating increases its temperature with increasing coating thickness. Assuming that the wall-side of the phosphor should be more and more shielded against the gas-temperature transients for thicker coatings, the overall phosphor temperature increase relative to the gas temperature has to be explained by a thickness-biased temperature increase on the gas-side of the phosphor.

Figure 7 displays the maximum temperature difference between both phosphor sides (blue dots) along with corresponding crank-angles (black squares). Both values are increasing as a function of film thickness, due to the phosphor film acting thermally insulating in between the hot gas region and the engine wall.

In summary, Figs. 6 and 7 give rise to the conclusion that neither side of a thick phosphor film is able to reproduce the surface

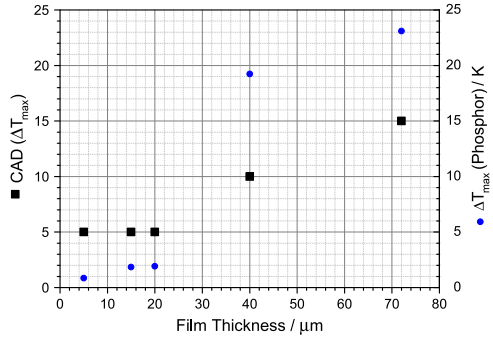

Fig. 7. Maximum temperature difference across the phosphor coating (blue dots, right *y*-axis) displayed together with its corresponding crank-angle (black squares, left *y*-axis) as a function of film thickness. All data was extracted from Figs. 4 and 5. (For interpretation of the references to colour in this figure legend, the reader is referred to the web version of this article.)

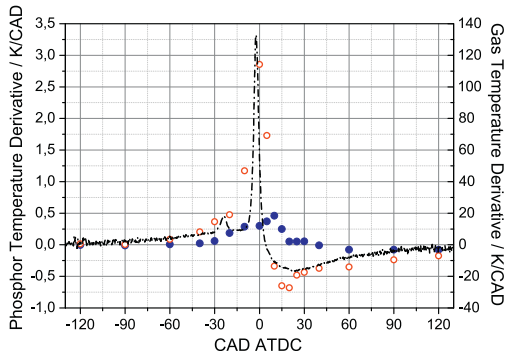

Fig. 8. Derivative of gas- (black) and phosphor temperatures (blue dots: wall-side, red circles: gas-side) from a 59 µm thick La_2O_2S:Eu film as a function of crank-angle during HCCI combustion. (For interpretation of the references to colour in this figure legend, the reader is referred to the web version of this article.)

temperature correctly due to the intrusive behavior of the coating: The phosphor wall-side becomes highly insulated from the hot gas region, hindering and delaying the heat transfer to the wall, whereas the gas-side of a thick coating is expected to follow the gas temperature changes more pronounced, leading to temperature swings that are greater and faster than the thermally inert engine block. However, for coating thicknesses $\leqslant 20$ µm the maximum temperature difference between the phosphor's front- and the back-side corresponds to approximately 2 K or less, which is below the measurement uncertainty and thus an insignificant result.

In Fig. 8, the crank-angle (∼time) derivative of temperatures from both phosphor sides and the bulk gas are displayed for a thick phosphor coating during HCCI combustion. The data originates from a 59 µm La_2O_2S:Eu phosphor film, that had been presented earlier in [15].

The time derivative of the gas temperature indicated in black shows two major peaks. The earlier and smaller one at −24 CAD corresponds to low temperature reactions. The latter one at −2 CAD characterizes the cycle position that coincides with the maximum temperature change per time interval. Slightly thereafter, the maximum gas temperature was reached at 2.4 CAD, indicated by the black curve crossing the zero line. The phosphor gas-side experiences the fastest temperature change around 0 CAD, during the combustion cycle followed by the wall side having a peak at 10 CAD. The order of succession is evidential for the inertness of the phosphor coating thermally insulating the surface below and confirms the conclusions drawn in the discussions around Figs. 6 and 7.

3.2. Cycle-to-cycle variations

In order to investigate how the phosphor responds to gas temperature changes from cycle-to-cycle, single-shot temperatures from adjacent engine cycles are shown and correlated in Figs. 9 and 10. The strength of correlation was determined by calculating the *Pearson product-moment coefficient R*. It is +1 in the case of a perfect positive linear relationship and −1 in the case of a perfect decreasing linear relationship, indicating the degree of linear dependency in between two sets of variables. As it approaches zero, there is less of a relationship.

In contrast to earlier results, the phosphor temperatures in this section were evaluated using a fixed time window, avoiding random noise contributions due to uncertain fitting window lengths (see Section 2.2).

Figure 9a shows phosphor temperatures over 90 engine cycles, recorded at 20 CAD ATDC from a 40 µm thick La2O2S:Eu film. Part (b) of Fig. 9 shows the temperature correlation between two opposite sides of the phosphor.

As discussed in the cycle-averaged results section, see Fig. 4c, there is a clear offset visible between the wall- and the gas-side of the phosphor due to spatial and temporal temperature gradients to which the coating was exposed to. The phosphor wall-side experiences much weaker temperature oscillations, compared to the gas-side. From part (b) in Fig. 9, the linear correlation coefficient was calculated to $R = 0.392$, indicating a very weak linear link between the two faces of the phosphor (see fitted red line).

Figure 10 shows temperatures and correlations from experiments using two thinner film thicknesses of La_2O_2S:Eu, 5 and 20 µm. When cycle-averaged, both coatings were earlier found to have no significant temperature difference between wall- and gas-side, see Fig. 4a and b. Compared to Fig. 9, both thinner coatings exhibit a stronger correlation between the temperatures at each side of the phosphor, see Fig. 10b and d. Being exposed to similar spatial temperature gradients from the thermal boundary layer as the 40 µm phosphor film from Fig. 9, the temperature difference between the two phosphor sides has decreased for thinner wall coatings. In fact, both sides of the phosphor now experience temperature oscillations around the same mean value with comparable magnitude. The 5 µm film resulted in a correlation coefficient of $R = 0.872$, whereas the 20 µm coating had a slightly higher correlation value of $R = 0.891$, probably due to an increased signal-to-noise ratio. The overall phosphor-intrinsic temperature correlation is also partly increased by the optical signal crosstalk, which thinner coatings are prone to. Both phosphor films exhibit a similar linear temperature relation between wall- and gas-side. Actually, both red fitted lines in Fig. 10b and d have similar slopes and offsets with small- and overlapping error bars (±5%). Because of measurement uncertainties, an ideal correlation coefficient of 1 is unlikely to be reached using experimental data.

When it comes to comparing local phosphor temperatures with variations in the global gas temperature (see cross + circle markers

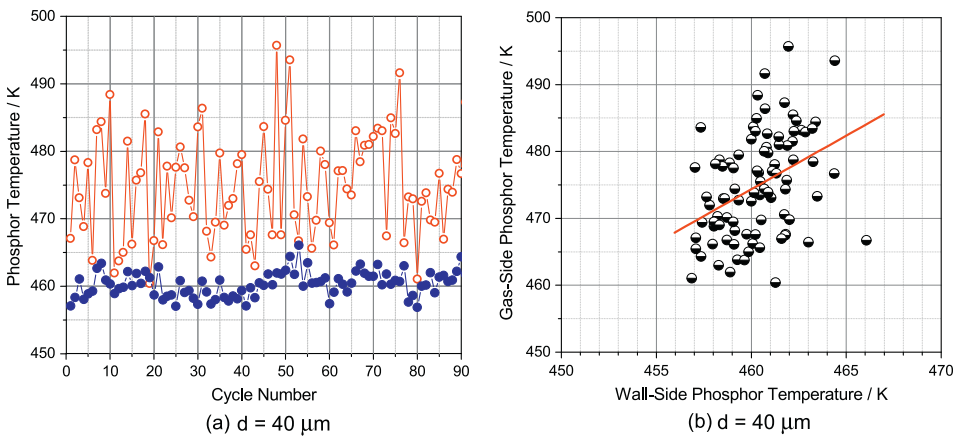

Fig. 9. Part (a): Cycle-to-cycle temperature variations from a 40 µm thick La_2O_2S:Eu phosphor coating, measured at 20 CAD ATDC during fired engine operation. Red circles correspond to the phosphor gas-side and blue dots refer to the wall-side temperature of the phosphor. Part (b): Correlation of temperature between two phosphor sides. (For interpretation of the references to color in this figure legend, the reader is referred to the web version of this article.)

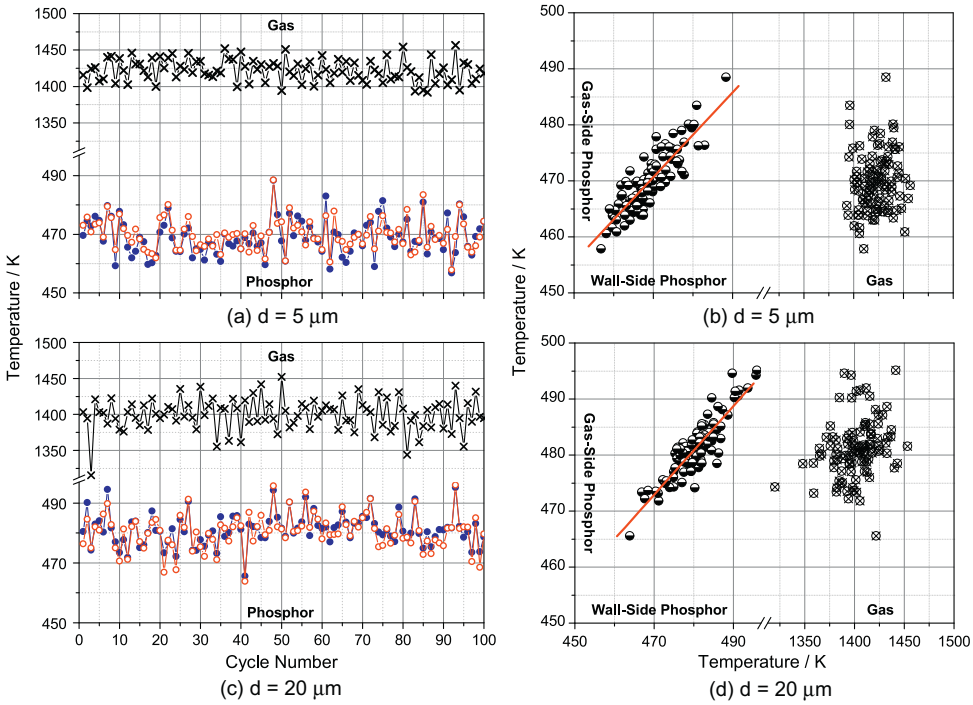

Fig. 10. Cycle-to-cycle variations of gas and phosphor temperatures, measured at 20 CAD ATDC during fired engine operation using La_2O_2S:Eu coatings. The upper figure part, (a) and (b), originates from data taken with a 5 µm coating whereas the lower part, (c) and (d), shows temperatures from a 20 µm coating. Data indicators: cross = global gas temperature, circles/dots = phosphor temperature (red circle = gas-side, blue dot = wall-side), half-hollow circle = phosphor temperature correlation, cross + circle = gas vs. phosphor-gas-side temperature correlation.

in the (b) and (d) part of Fig. 10), no obvious dependency could be found. This is reflected by very low correlation coefficients of $R = 0.101$ (b) and $R = 0.267$ (d). A lack of correlation between local wall temperatures and global gas temperatures is also in accordance to findings by J.E. Dec and W. Hwang using tracer-based single line PLIF imaging to derive gas temperature maps in an HCCI engine. Their study revealed that the spatial distribution of thermal non-uniformities during HCCI combustion shows no consistent pattern from cycle to cycle. Random temperature distributions were observed, suggesting a turbulent nature to the flow structures producing them [23]. Also, the random occurrence of initial ignition islands and the local temperature history contributes to a non-uniform temperature field.

Since correlations are best observable for high oscillations coinciding with high temperatures, results from 20 CAD ATDC were chosen to be presented in this study. This cycle position marks the temperature maximum of the phosphor wall coating on average (see Figs. 4–6). At 20 CAD ATDC, the combustion of the fuel/air mixture has already ended. However, the global bulk gas temperature still remains well above 1000 K. Cycle-to-cycle variations for all other crank-angles have been studied but did not result into obvious correlations between gas- and phosphor temperatures.

3.3. Gas-wall-temperature correlation during combustion termination

This part of the paper discusses gas- and phosphor temperatures at 5 and −180 CAD ATDC during the transition from steady HCCI combustion to motored operation, resolved on a combustion cycle basis. Surface temperature measurements, origination from the two phosphors in this study are compared in Fig. 11.

Apart from terminating the fuel supply after roughly 100 cycles, also the inlet air heater was switched off. Due to data noise, there is no clear breaking point visible from the phosphor temperatures that could mark the switch-off event more precisely than ±3 cycles in order to be compared with the pronounced switch-off event, clearly visible as a steep gas temperature drop during measurements at 5 CAD. The gas temperature in these measurements switches instantly to lower temperatures when the fuel was terminated and then decreases slowly. This is due to the fact that the gas gets exchanged every cycle. Once combustion is terminated and the engine is motored, the incylinder gas temperature at 5 CAD is instantly reduced due to the induction of fresh and uncombusted air. However, gas temperatures from the externally motored case still stay well above 800 K at 5 CAD due to heat induced by air compression and small contributions of the hot engine walls releasing heat to the gas phase. A further decrease in temperature over cycle number (about 60 K over 200 motored cycles) can be explained by the engine block cooling down over time as well as the inlet air heater, which was switched off. The phosphor, being attached to the quartz liner as a part of the hot and inert engine block, cooled down exponentially once the fuel injection was terminated.

A second observation from the same phosphor coatings, this time performed at −180 CAD (see case (c) and (d)), shows gas temperatures being colder than the corresponding phosphor tempera-

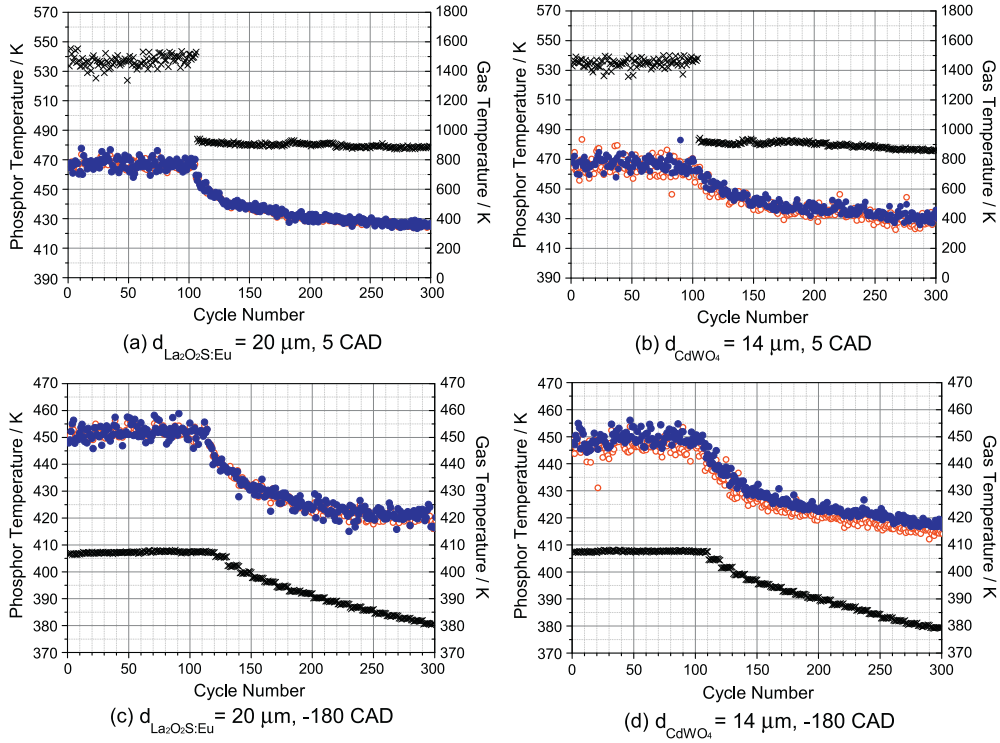

Fig. 11. Cycle-to-cycle variations of gas- and phosphor temperatures before- and during the cooldown period after fuel termination. The black crosses correspond to the gas temperature (right *y*-axis) whereas circular markers represent the phosphor temperatures (left *y*-axis: blue dots = wall-side, red circles = gas-side). The upper two plots show a temperature comparison of engine runs at 5 CAD using La_2O_2S:Eu (20 µm, (a)) and $CdWO_4$ (14 µm, (b)), whereas the lower two plots illustrate temperature results compared at −180 CAD from the same phosphor layers ((c) La_2O_2S:Eu and (d) $CdWO_4$).

tures in each cycle. This is a consequence from the thermal inertness of the engine block, which keeps it on an intermediate temperature with only a few tens of Kelvins in variation when being exposed to cyclic gas temperature changes on an order of about 1000 K. The exponential decrease of the phosphor temperatures is thus mainly due to the permanent termination of combustion in one of the preceding engine cycles. Moreover, the exponential drop in gas temperature is of equal magnitude (about 30 K for cases (c) and (d)). It decreases to 380 K towards the end, and first starts declining a couple of cycles after the phosphor temperatures decreased. A reasonable explanation for this is that the gas temperature drop in Fig. 11c and d was mainly caused by the deactivation of the inlet air heater which was switched off shortly after the fuel was terminated (inlet air temperature was 390 K while the electric heater was switched on, see Table 1).

Both phosphors were of similar thickness and showed no significant temperature differences compared to each other. It is also noteworthy, that temperatures from Fig. 11a and b before fuel termination agree very well with corresponding averaged temperatures, measured earlier during the same engine run, see Figs. 4b and 5. While averaged phosphor temperatures at 5 CAD in Figs. 4b and 5 showed a slight difference between the phosphor gas- and wall side (below one standard deviation, i.e. overlapping error bars), Fig. 11a and b concludes in accordance with findings from Fig. 10, that these differences were not significant as long as coating thicknesses remained below 20 µm.

4. Conclusions

This work is a continuation of efforts to provide experimental data for the distortion of temperature readings by thick phosphor coatings in unsteady combustion environments. Experiments determining surface temperatures in a HCCI engine were performed using two different phosphors and a range of film thicknesses from 5 to 72 µm. These phosphor films were coated on a quartz liner for optical access from two opposite sides of the coating.

Spray coatings ⩽20 µm did not show thermal gradients across the surface normal axis and are assumed to reflect the actual surface temperature without- or with only little distortion in the experiments presented here and environments of similar thermal conditions. Environments with higher thermal gradients, both spatially and temporally, are likely to require thinner phosphor coatings for accurate surface temperature measurements.

The thinnest films that could be produced using an airbrush had a thickness in the order of 5 µm and offered very weak phosphorescence signals. In order to achieve a thinner phosphor film it is advised to rely on alternative coating techniques, like e.g. RF-sputtering, which was found to result in high phosphorescence intensities from thin film coatings [22].

Thick phosphor layers in the order of several tens of microns showed a delayed temperature response at their wall-side and

experienced a bigger temperature gradient, confirming findings made in [15] and the predictive model introduced by [16].

Cycle-to-cycle variations of the global gas temperature did not correlate with the phosphor temperatures for any of the tested coatings. Spatial variations in the local heat transfer mask the coupling between small variations in global gas temperature and local surface temperature. However, both phosphor temperatures (gas- and wall-side) did correlate very clearly with each other for film thicknesses below 20 μm.

Within this study, $CdWO_4$ and La_2O_2S:Eu, were found to behave similarly concerning temperature sensitivity and thickness dependency, giving rise to the assumption that heat capacity and conductivity constants of different phosphors in practice are similar enough to play a subordinate role compared to the film thickness.

Acknowledgments

This work was performed within the D60l-2 project, funded by Swedish Energy Agency. For further financial support the authors would also like to acknowledge the European Union Seventh Framework Programme (FP7/2007-2011) under Grant agreement no. 265861 (Helios). The authors also express their gratitude to Prof. Bengt Sundén and Helgi Fridriksson for helpful discussions.

References

[1] J. Chang, O. Güralp, Z. Filipi, D. Assanis, T. Kuo, P. Najt, R. Rask, SAE Tech. Pap. 2004-01-2996, 2004, pp. 1–18.
[2] C. Wilhelmsson, A. Vressner, P. Tunestål, B. Johansson, G. Särner, M. Aldén, SAE Tech. Pap. 2005-01-3731, 2005, pp. 1–10.
[3] J. Demuynck, M. De Paepe, R. Sierens, S. Verhelst, FISITA World Automotive Congress, Proceedings F2010-A-062, 2010, pp. 1–10.
[4] S.W. Allison, G.T. Gillies, Rev. Sci. Instrum. 68 (7) (1997) 2615–2650.
[5] S.J. Skinner, J.P. Feist, I.J.E. Brooks, S. Seefeldt, A.L. Heyes, Sens. Actuators, B 136 (2009) 52–59.
[6] N. Fuhrmann, E. Baum, J. Brübach, A. Dreizler, Rev. Sci. Instrum. 82 (10) (2011) 104903 (4pp).
[7] A.H. Khalid, K. Kontis, H. Behtash, Proceedings of the Institution of Mechanical Engineers, Part G: J. Aerosp. Eng. 224 (7) (2010) 745–755.
[8] M. Aldén, A. Omrane, M. Richter, G. Särner, Prog. Energy Combust. Sci. 37 (4) (2011) 422–461.
[9] S.W. Allison, M.R. Cates, G.T. Gillies, Rev. Sci. Instrum. 73 (4) (2002) 1832–1834.
[10] B. Atakan, C. Eckert, C. Pflitsch, Measure. Sci. Technol. 20 (7) (2009) 075304 (9pp).
[11] S.M. Goedeke, S.W. Allison, M.R. Cates, P.R. Boudreaux, R.E. Valiga, D. Mee, Proc. Int. Instrum. Sympos. 470 (2007) 443–463.
[12] N. Fuhrmann, J. Brübach, A. Dreizler, Proc. Combust. Inst. 34 (2) (2013) 3611–3618.
[13] S.F. Collins, G.W. Baxter, S.A. Wade, T. Sun, K.T.V. Grattan, Z.Y. Zhang, A.W. Palmer, J. Appl. Phys. 84 (9) (1998) 4649–4654.
[14] M. Gentleman, J. Eldridge, D. Zhu, K. Murphy, D. Clarke, Surf. Coat. Technol. 201 (7) (2006) 3937–3941.
[15] C. Knappe, P. Andersson, M. Algotsson, M. Richter, J. Lindén, M. Tunér, B. Johansson, M. Aldén, SAE Int. J. Engines 4 (1) (2011) 1689–1698.
[16] B. Atakan, D. Roskosch, Proc. Combust. Inst. 34 (2) (2013) 3603–3610.
[17] O. Güralp, P. Najt, Z. Filipi, Proceedings of the ASME 2012 Internal Combustion Engine Division Fall Technical Conference ICEF2012-92188, 2012, pp. 1–14.
[18] M. Algotsson, C. Knappe, M. Tunér, M. Richter, M. Aldén, B. Johansson, in: The Eighth Conference on Modeling and Diagnostics for Advanced Engine Systems MD1-4, 2012, pp. 482–487.
[19] F.W. Bowditch, SAE Trans. 69 (1961) 17–23.
[20] J.P. Feist, A.L. Heyes, K.L. Choy, in: 18th International Congress on Instrumentation in Aerospace simulation facilities ICIASF 99, 1999, 6.1 (7pp).
[21] A. Nebatti, C. Pflitsch, C. Eckert, B. Atakan, Prog. Org. Coat. 68 (2010) 146–150.
[22] R.M. Ranson, C.B. Thomas, M.R. Craven, Meas. Sci. Technol. 9 (1998) 1947–1950.
[23] J.E. Dec, W. Hwang, SAE Int. J. Engines 2 (1) (2009) 421–438.

Limitations of ICCD detectors and optimized 2D phosphor thermometry

Paper IV

Johannes Lindén, Christoph Knappe, Mattias Richter and Marcus Aldén

Published in: Meas. Sci. Technol. **23**(3):035201, 2012.

Meas. Sci. Technol. **23** (2012) 035201 (8pp) doi:10.1088/0957-0233/23/3/035201

Limitations of ICCD detectors and optimized 2D phosphor thermometry

J Lindén, C Knappe, M Richter and M Aldén

Division of Combustion Physics, Lund University, Box 118, S-22100 Lund, Sweden

E-mail: johannes.linden@forbrf.lth.se

Received 7 July 2011, in final form 25 October 2011
Published 25 January 2012
Online at stacks.iop.org/MST/23/035201

Abstract
This paper presents investigations on the limitations of intensified CCD (ICCD) cameras when performing quantitative 2D temperature measurements using thermographic phosphors. The temperature is evaluated using a two-color ratio technique, which demands high signal linearity of the detector. However, this work shows that the ICCD cameras used suffer from nonlinearity at levels of irradiance that do not necessarily produce particularly high count levels, i.e. well below the saturation limit of the A/D converter. For the phosphor thermometry, this results in false absolute temperature readings and decreased measurement precision. The results show that there is a useful workspace in the irradiance/camera gain combination where the detector should preferably be used. A response function for the ICCD camera used is constructed. Furthermore, in order to perform quantitative measurements, there is an upper limit of counts that should not be exceeded. This limit must be investigated for each experimental configuration since it depends on the characteristics of the specific light source and also varies between different cameras.

Keywords: laser-induced phosphorescence, thermographic phosphors, thermometry, image intensifier, ICCD detectors, saturation

(Some figures may appear in colour only in the online journal)

1. Introduction

The use of intensified CCD (ICCD) cameras is widely spread in many research disciplines. For 2D detectors such as CCD cameras, the most common intensifiers consist of three functional units: a photocathode, a microchannel plate (MCP) and a phosphor screen, see figure 1. The photocathode converts the incident photons to photoelectrons, which are accelerated by an electrical field toward the MCP. This in turn multiplies these electrons which are converted back into photons by the phosphor screen. Lastly these photons are directed to a CCD chip by either an optical fiber bundle or a lens system, and read out as a digital image. The addition of an image intensifier brings certain benefits. Primarily the MCP serves to intensify the signal several orders of magnitude, enabling detection of very weak signals. In addition, by pulsing the control voltage to either the photocathode or the MCP, the image intensifier can serve as a very fast electronic shutter, enabling time gating for short-lived signals which would otherwise have been lost in the interfering background. Furthermore, the photocathode can be made sensitive to UV radiation. Effectively, the image intensifier can frequency shift an incoming UV signal, to which the CCD itself is not sensitive, into the visible range where the CCD has a high sensitivity. Together these features make ICCD cameras very useful in pulsed laser applications, where short laser pulses, of the order of 10 ns duration, are used for visualization of various substances, either by detecting the scattered laser light itself, e.g. Rayleigh scattering, or a signal emitted from the substance induced by the laser light, e.g. laser-induced fluorescence, laser-induced phosphorescence or laser-induced incandescence.

However, it has been shown that ICCD cameras suffer from spatially non-uniform image gain factors and nonlinear response functions [1, 2]. The nonlinearity is mainly due to the onset of saturation within the MCP, when the camera is subjected to high light intensities in combination with excessive gain settings. This falloff in response, or gain saturation, has to do with the MCP recovery process and is caused by the MCP's inability to produce enough secondary electrons from the original photoelectron [3, 4]. In addition,

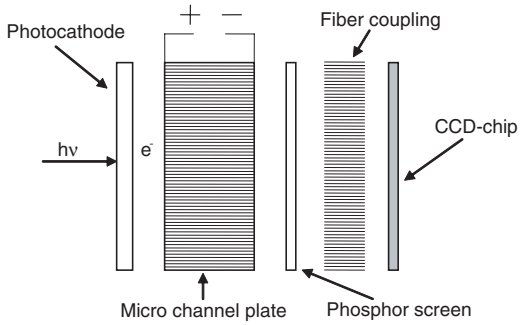

Figure 1. Principles of an image-intensified CCD camera with fiber coupling.

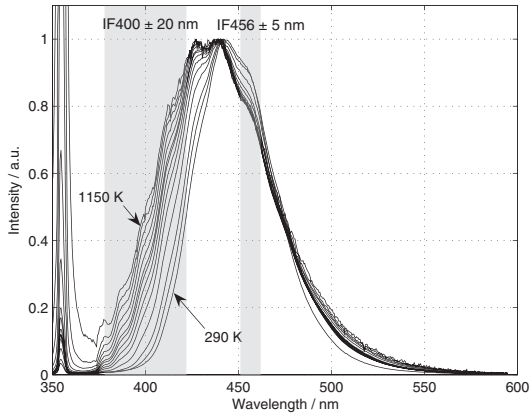

Figure 2. BAM emission spectra at different temperatures when excited with 355 nm laser radiation. The exposure time of the ICCD camera connected to the spectrometer was 8 μs. The transmission regions of the interference filters used are marked out.

bleaching of the photocathode, especially when collecting intense long-lived radiation, can also contribute to saturation. The phosphor screen can also be subject to saturation, causing a nonlinear output due to response falloff at higher intensities. Other saturations can occur after the intensifying process, i.e. in the CCD chip (filled charge wells causing blooming) and in the A/D converter, where the analog charge from the CCD is converted into digital signals. These types of saturations are usually easily avoided, since it is rather obvious when they occur.

Saturation within the intensifier is usually not a concern when performing qualitative measurements; however, quantitative measurements, and in particular the two-color ratio measurement technique, are easily affected by small nonlinearities. The presented work describes how systematic errors caused by nonlinearity due to saturation of the MCP can be avoided by operating the detectors within the proper workspace. In this context, it should be mentioned that in most practical situations it is not obvious when the MCP begins to become subject to gain saturation.

Thermographic phosphors (TPs) have been utilized in temperature measurement applications for several decades. Used for both point and two-dimensional surface measurements, TPs offer a combined temperature-sensitive range that stretches from cryogenic up to 2000 K, depending on the choice of phosphor [5–10].

The TP used in this experiment is $BaMg_2Al_{16}O_{27}$:Eu (BAM) [11]. When excited by a UV-laser pulse at 355 nm it emits broadband phosphorescence peaking at around 440 nm, with a lifetime τ of about 2 μs at room temperature. This peak broadens toward shorter wavelengths as the phosphor is heated; see figure 2. Thus, the phosphorescence intensity of the shorter wavelength side of the peak relative to the longer wavelength side of the peak will increase with temperature. Using two interference filters, one with 10 nm spectral width (FWHM) centered at 456 nm and one with 40 nm (FWHM) centered at 400 nm, a temperature sensitive intensity ratio of the phosphorescence can be determined. A pair of filtered images can be recorded by the use of either two cameras or an image-doubling device (stereoscope) [12]. Dividing the intensities in these images by each other, pixel-by-pixel, will result in a temperature-dependent ratio image. The ratios are then converted into temperatures using a predefined calibration curve derived from measurements performed in a controlled environment. Note that the procedure of utilizing signal ratios rather than absolute intensities brings an inherent advantage with this approach. The resulting ratio becomes independent of the overall phosphorescence intensity and laser excitation intensity. Hence, the technique does not require absolute homogeneous exciting laser profile, phosphor coating nor a linear relation between laser excitation and phosphorescence intensity. Despite the appearance of the spectra in figure 2, it is not recommended to use BAM for temperature measurements higher than 800 K due to degradation mechanisms [13].

The accuracy of these experiments, ideally, depends only on the accuracy of the reference thermocouples used during calibration. The precision on the other hand depends on several factors, such as the S/N ratio, flat field camera correction and the perfection of the image superposition of the two images that are to be divided. As this paper will show, both the accuracy and the precision depend on properties of the camera, which from the beginning are not obvious, but the focus will be kept on the precision.

In order to make quantitative two-color ratio measurements, it is important that the detector response is linear. The presented work shows that when performing quantitative two-color temperature measurements with TPs using a Princeton Instruments PI-MAX2 ICCD camera, it is necessary to stay below a certain count level in order to avoid nonlinear effects which would otherwise cause false absolute values and reduced precision. For the experiments performed, the trade-off between useable irradiance and gain corresponds to a number of counts less than half the numerical range of the A/D converter.

The results presented herein are valid at room temperature for the particular phosphor and individual camera used; tests must be performed with any new system in order to secure correct readouts. However, since the phosphorescence

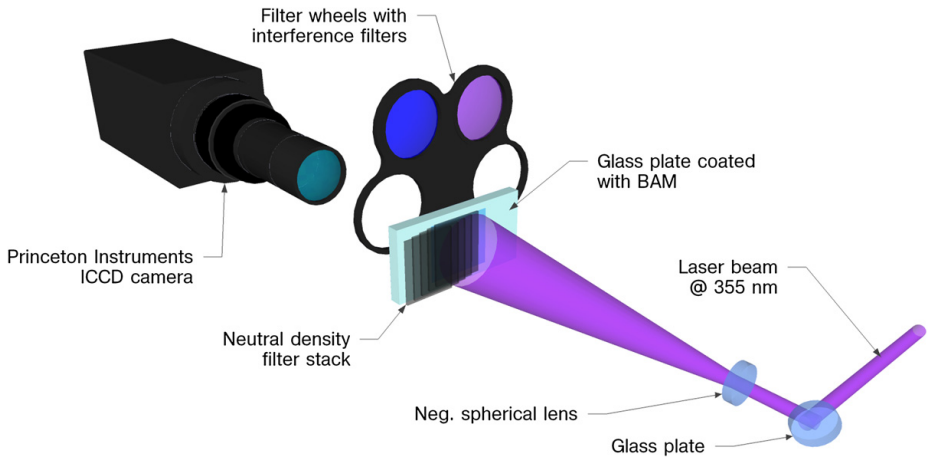

Figure 3. Experimental setup.

generally decreases with higher temperature, it is assumed that nonlinear effects due to too high irradiance will not occur once detector saturation is avoided at room temperature.

2. Experimental work

Figure 3 shows the experimental setup. The laser used is a 10 Hz pulsed Nd:YAG operating at its third harmonic, producing a wavelength of 355 nm with an energy of ∼0.5 mJ/pulse. The laser beam is directed and expanded to illuminate a glass plate surface coated with BAM. The phosphor is applied using an airbrush pen (Rich AB 300) containing a solution of the phosphor, binder (HPC) and ethanol. The thickness of the layer is approximately 10–20 μm. On the camera side of the plate, a filter wheel with appropriate filters is placed. The phosphorescence, seen through the filters, is recorded by a PI-MAX2 ICCD camera. All the measurements are performed at room temperature; thus, it is assumed that the temperature distribution across the coated phosphor surface is homogeneous.

Since this experiment focuses on the measurement error introduced by the ICCD camera rather than evaluating the overall thermometry, it is advisable to suppress extraneous error contributions. Two such errors would be incorrect image superposition and flat field correction, which would be necessary in the case of using two cameras or a stereoscope. In order to eliminate these, only one camera is used for this experiment. By switching the interference filters in front of the camera, the two images would be identical with exception to the wavelength detected and also the pixel-to-pixel variations on the CCD chip would cancel out by the image division. While this approach eliminates the source of errors caused by image superposition and flat field correction, it assumes stability in time. To reduce the influence of shot-to-shot variations in the laser profile, accumulations of ten images were made for each measurement.

As described in the setup, the filter wheel is positioned as close to the phosphor-coated surface as possible, rather than in front of the camera lens, as might be expected. The reason for this is an image distortion introduced by the design of the filters which caused displacement of the focal plane and translation of the image. Since the distortion differs between the two filters, this effect would obstruct straightforward superposition of the two images. This distortion effect would probably be eliminated by the use of higher image quality filters, which were unavailable at the time of the experiment. With the filters positioned close to the coated surface, it is impossible to illuminate the phosphor from the side facing the camera. Hence, the surface is illuminated from the backside, which requires a transparent phosphor substrate (the glass plate). The phosphor is coated on the surface facing the laser; as a result, the glass plate acts as a filter, rejecting spurious UV laser contribution to the recorded images while being transparent for the phosphorescence emission. This arrangement is limited in a realistic application due to both setup issues regarding the interference filters and restriction to measurements with more temporally stable temperatures, since the measurements cannot be performed in a single shot.

In order to investigate the linearity of the camera, different areas of the BAM-coated surface are illuminated with different laser fluences. This is achieved by using a filter stack, consisting of five identical neutral-density filters, successively partwise overlapping each other. By this approach, six different areas of the BAM-coated surface are illuminated, each with different laser fluence: one without any laser attenuation, and five with gradually increasing optical densities. The transmission of the five gradually increasing optical densities was measured to be 9%, 14%, 22%, 39% and 67%.

Figure 4 shows an example of two phosphorescence images (*a* and *b*) and the resulting ratio image (*c*) for one particular gain setting on the image intensifier (150 of 255). At this gain setting the different areas, despite illumination with different laser fluence, result in the same ratio, as can be seen in figure 4(*c*), and thus would read the same temperature as expected. For each area, the mean value and the standard deviation of the ratio is investigated. This is done for 26 different gain settings, spanning 0–250 (max value 255) in

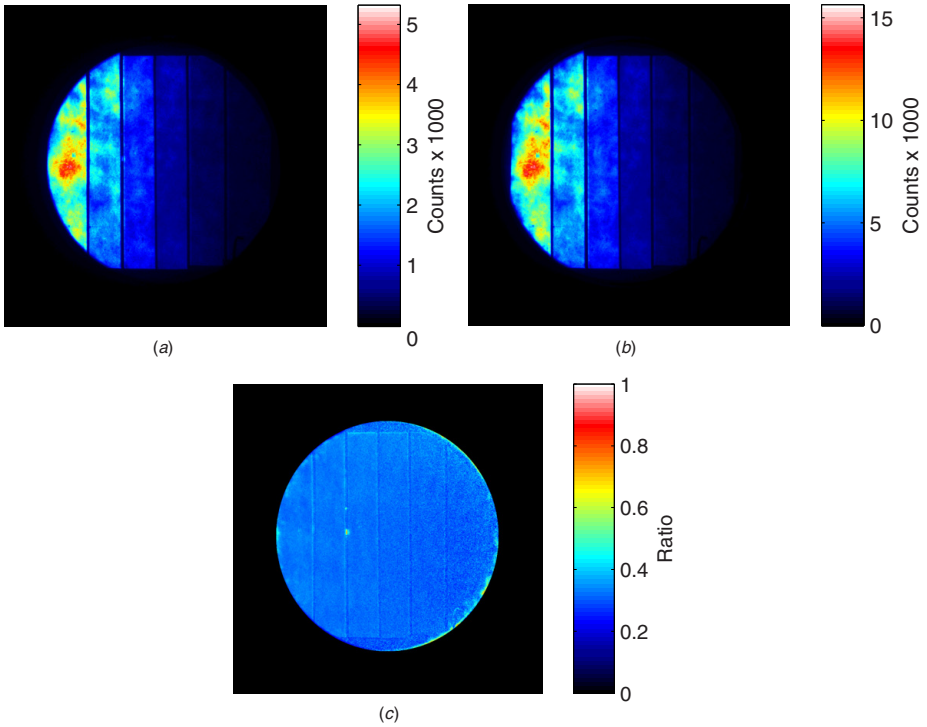

Figure 4. Example of two phosphorescence images achieved through two different interference filters ((*a*) 400 ± 20 nm, (*b*) 456 ± 5 nm) which when divided generate a ratio image (*c*).

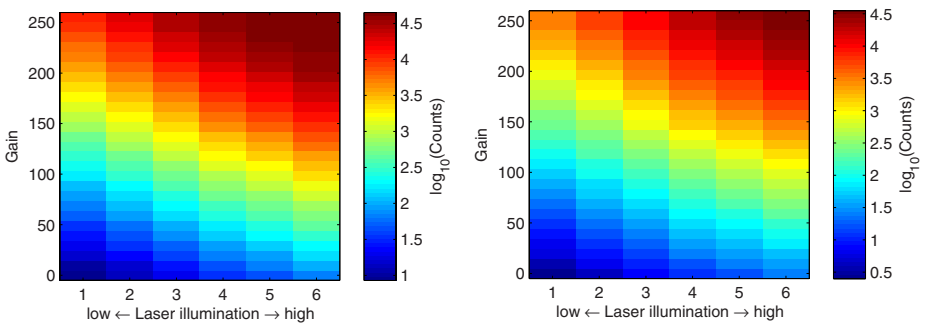

Figure 5. Mean signal in counts for the signals achieved through the IF456 filter (left) and the IF400 filter (right). Note that the count intensity scale is logarithmic.

increments of 10. With six areas of different illumination intensities, this results in 156 different gain and laser fluence combinations investigated. Prior to the experiment, the laser energy is adjusted so that, in the measurement with a gain of 250, the maximum number of counts in the area with highest intensity is just below the saturation level of the 16 bit A/D converter, i.e. 65 535 counts.

3. Results and discussion

Figure 5 displays the measured mean value, in counts, for all 156 different gain and laser fluence combinations for each filter applied (left: the 456 nm interference filter, henceforth IF456, and right: the 400 nm interference filter, henceforth IF400). Because of the exponential behavior of the camera gain, the signal intensity is displayed using a logarithmic scale. The maximum mean value from the area illuminated with highest laser fluence and amplified with the highest gain, illustrated by the upper-right corner in the IF456 chart, is 45 000 counts or $\sim 10^{4.6}$.

Figure 6 illustrates the camera's ability to reproduce the different intensities induced by the filter stack. The bars represent the measured transmission (67%, 39%, 22%, 14%

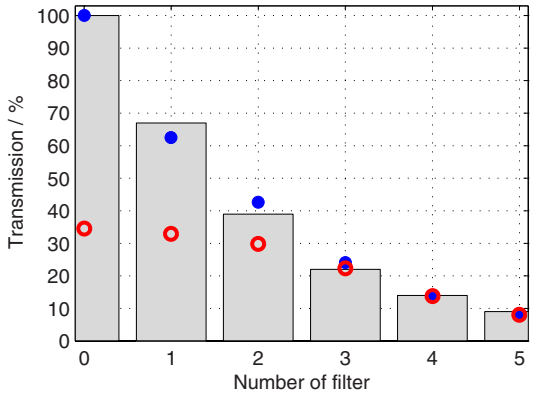

Figure 6. Measured filter stack transmission and scaled camera counts through IF456. The bars indicate the measured filter stack transmission, with values of 67%, 39%, 22%, 14% and 9%. The circles represent the normalized camera counts for gain 80 (blue, filled) and gain 250 (red unfilled).

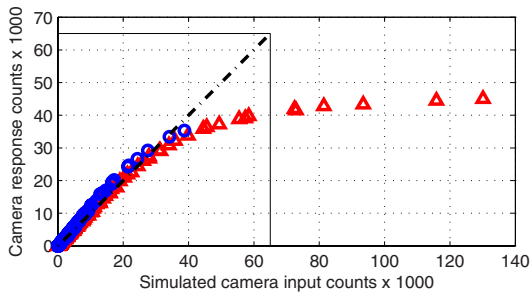

Figure 7. Camera response function for the two different filter wavelengths (IF400 blue circles; IF456 red triangles). The straight dashed line indicates the ideal linear response curve, limited to 65 000 counts by the A/D converter's bit depth.

and 9%) through the five different parts of the filter stack, in relation to 100% transmission, indicated by the first bar. The blue filled circles show the normalized average signal counts through the IF456 at gain 80, obtained from figure 5 (left). They show good agreement with the average filter transmission, indicating that the overall camera response (including the MCP) operates in its linear regime.

The red circles, on the other hand, show the normalized average signal counts at the highest gain value of 250. Here, the signal counts measured for 0, 1 and 2 filters do not reach the expected values such that the 'camera's response' is lowered to 35% only, reflecting that the ICCD camera has left its linear operating workspace. Since only the gain has changed between the two cases displayed in figure 6, while the photon flux remained constant, the saturation can be attributed to the MCP. The red circles start to differ from the expected values when less than three filters are present, where the signal level exceeded 29 000 counts or $10^{4.464}$ (corresponds to the left chart in figure 5, third column, top row). At that point, the initial amount of phosphorescence light hitting the photocathode was reduced to 22% by the filter stack.

Figure 7 utilizes all data information displayed in both charts in figure 5 to extract the camera's response function for the two investigated wavelengths: 400 and 456 nm. This is done by simulating the expected count behavior for the two charts, starting with the first column for each chart (representing five filters' transmission), assuming that each decrease in transmission through the steps of the filter stack decreases the counts with respect to the measured transmission. Since the highest count level, reached behind five filters (at a gain of 250), corresponds to approximately 10 000 counts, the whole first column in both charts in figure 5 represents data accumulated in the linear response regime.

The data displayed in figure 7 represent the overall camera response for a photocathode that operates in the linear regime. The counts through IF400 (blue circles) show a slightly steeper slope compared to those through IF456 (red triangles). This could be explained by the wavelength-dependent photocathode sensitivity which possibly emits slightly more primary electrons at 400 nm. For both wavelengths, the initial linear behavior tends to tip between 20 000 and 30 000 counts, indicating the beginning of MCP saturation. Another interesting aspect from figure 7 is that assuming a linear detector response, a measured output signal of 45 000 counts corresponds to a simulated signal level of 130 000 counts. It is remarkable that this is more than twice the numerical range of the A/D converter.

Each of the 156 count values from the IF400 image set is divided by the value from the corresponding gain and laser illumination from the IF456 image set. The result is a ratio chart illustrated by figure 8 (left), which basically could be thought of as the right chart divided by the left chart in figure 5 (if the charts in figure 5 showed the true count values and not the logarithm). The right chart in figure 8 is the same as the left, only with the ratio values translated into temperatures, using a ratio to temperature relation resulting from reference measurements done at temperatures ranging from room temperature to 500 K.

As can be seen in figure 8, the mean ratio value and hence the mean corresponding evaluated temperature are rather constant within the major part of the chart, with the exception of the upper-right corner. Despite the measurements done at constant room temperature, it is clearly seen that the evaluated temperature gives a false result and too high values are acquired for the high laser illumination and high intensifier gain. As can be seen on the right chart in figure 8, this results in a false readout of the absolute temperature, with a deviation of almost 200 K from the true value.

In terms of precision, figure 9 shows the most interesting results. It shows the spatial standard deviation, i.e. the pixel-to-pixel standard deviation, within each gain and laser illumination combination area, translated into corresponding temperature standard deviation. For BAM, the relation between temperature and ratio is rather linear within the considered temperature range, with a dT/dR relation equal to 0.0026 K^{-1}, where T is the temperature and R the ratio. To illustrate, a standard deviation in the ratio of 0.009 corresponds to a standard deviation in temperature of $0.009/0.0026 = 3.5$ K.

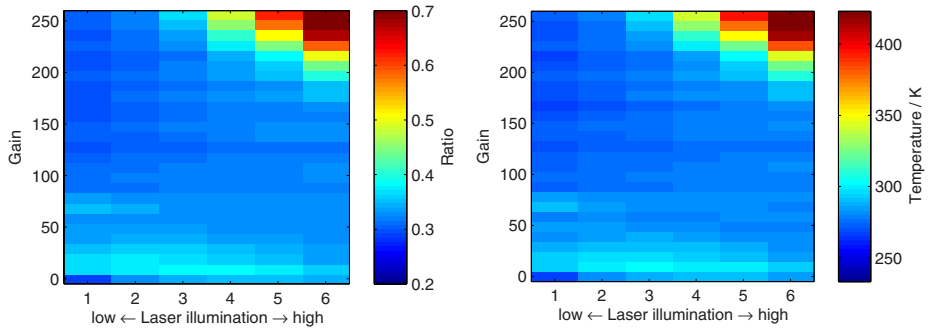

Figure 8. Evaluated ratio for all the different gains and laser illuminations (left), and corresponding values translated into temperatures (right).

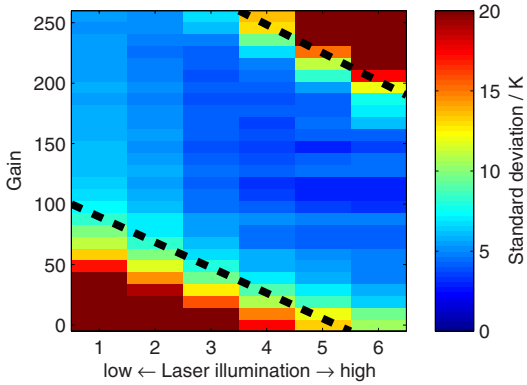

Figure 9. Evaluated spatial standard deviation within the selected areas of different gains and laser illumination, translated into standard deviation in temperature.

As can be seen in figure 9, a diagonal-shaped area, marked in between the two dashed lines, could be identified as a proper working space for higher precision measurements. Within this area, the camera exhibits a linear response independent of MCP gain or laser illumination. Below the lower line, the standard deviation becomes high simply because the S/N level is too low. The signal is still high enough to give reasonable values for the absolute temperature, as can be seen in figure 8, but the noise contribution is too high for the pixel-to-pixel precision to be sufficiently high. The number of counts at which this occurs is very low, about 30 counts per pixel.

The increase in standard deviation above the upper-dashed line indicates a more critical limitation of the camera. The value of counts where this limit is reached can be determined from figure 10, showing the spatial standard deviation of counts in each area for every gain and laser illumination combination through IF456 and IF400, respectively. In the measurements corresponding to a gain setting of 190 in the column for the highest level of laser illumination in figure 9, it can be seen that the standard deviation of the measured temperature, in other words precision, has degraded with a factor of 2 compared with the highest value achieved. Considering the left chart in figure 5, it can be determined that this condition corresponds to a count value of 26 000 through the IF456 ($10^{4.42}$). It can be clearly seen in figure 10 (left) that signal suppression is occurring under these conditions, i.e. the nonlinear regime has been entered. The standard deviation is reaching a maximum value at gain 190 and is then decreasing with higher gain, indicating that an upper limit for counts has been reached and that gain saturation will occur for higher gains and illuminations. It is notable that this saturation already occurs at count levels as low as 26 000 counts, less than half of the maximum counts of 65 535. The same effect is seen for the signals detected through the IF400 filter. In figure 10 (right), it can be seen that the value of the standard deviation reaches a maximum in the column for the highest laser illumination at a gain of 230. Considering the right chart in figure 5, it can be determined that this corresponds to a count level of about 29 000 counts ($10^{4.47}$).

Figure 9 illustrates a region identified as a useful workspace for this camera and phosphor. The upper-dashed line indicates the limit for the gain/illumination trade-off. In the left chart in figure 5, the position of the upper-dashed line in figure 9 would correspond to a count value range of 25 000–30 000 counts ($10^{4.4}$–$10^{4.5}$). Higher counts should be avoided. The fact that there is a range of gain in which the absolute evaluated temperature and precision are rather constant, regardless of laser illumination (between gain 100 and 190, see figure 9), shows that the saturation occurs after the photocathode. Hence, the strength of the light source, in itself, or the photocathode are not responsible for the saturation. However, it cannot be excluded that the saturation detected, or a portion of it, could be caused by the phosphor screen in the image intensifier. It should be mentioned that the experiments are performed using one ICCD camera and one TP only, and that the saturation limit of 25 000–30 000 counts is only valid under these conditions. However, as a precaution, an additional test was performed using a nominally identical ICCD camera and the results were very similar.

Within the useful workspace, the precision in temperature measurement spans from ± 1 to ± 10 K. This number depends on temperature and on the choice of the spatial resolution of the detection system. This relationship will be addressed in an upcoming work by the authors.

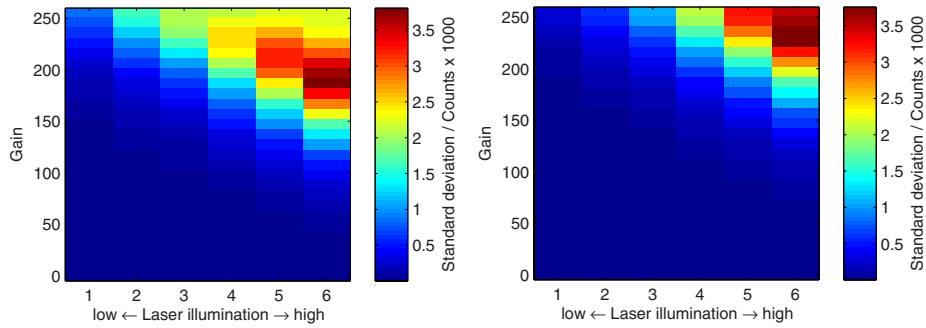

Figure 10. The spatial pixel-to-pixel standard deviation in counts for the signals achieved through the IF456 filter (left) and the IF400 filter (right) for all the different gains and laser illuminations.

This work has not only focused on the precision of measurements but has also mentioned accuracy-related issues. The authors would like to see reproducibility investigations on how the accuracy could be affected by long- and short-term drifts of cameras. Also similar investigations to the one described here, but with different types of ICCD cameras, and with different types of TPs (with different emission wavelengths and lifetimes) and at different temperatures, would be a suitable target for further investigations.

4. Conclusion

In this work, a useful workspace within the gain/illumination combination of an ICCD camera (Princeton Instruments PI-MAX2) has been identified. It has been shown that the camera used suffers from nonlinear effects due to gain saturation in the MCP, when exceeding a certain level of counts. The results show that there is a possibility of saturating the camera, and in so doing introducing nonlinearity, even though other components of the camera are not saturated. The level at which this occurs corresponds to as low as half the maximum counts allowed by the CCD chip, making the occurrence of saturation far from obvious. It is conspicuous that the count value read as 45 000 in fact represents an intensity that should actually correspond to a count value of 130 000. Another interesting conclusion drawn from figure 7, is that the nonlinearity of response has a slight dependence on the observed wavelength. In this study, two nominally identical ICCD cameras were used and showed similar results. However, each detector should be treated individually, and the behavior likely depends on the type of light source as well. This means that an investigation such as the one presented here should be done prior to any experiment involving quantitative measurements using a two-color ratio method.

To conclude, there is an upper limit of counts below which the ICCD cameras should be used in order to give reliable results. This limit is shown to be in the 25 000–30 000 count range out of a nominal 65 000 counts allowed by the 16-bit A/D converter. This level was shown to be valid for any gain.

It is inferred from our analysis that system nonlinearity is also dependent on the type of light source being investigated. In this study, the phosphorescence of BAM is detected at room temperature and at a certain distance between camera and phosphor. If cameras are to detect light at other wavelengths and with a different duration, the limitations of the ICCD cameras are likely to be different.

Acknowledgments

This work was supported by the Centre of Competence Combustion Processes and the HELIOS project within the seventh EU framework program.

References

[1] Williams T C and Shaddix C R 2007 Simultaneous correction of flat field and nonlinearity response of intensified charge-coupled devices *Rev. Sci. Instrum.* **78** 123702

[2] Montgomery D S, Drake R P, Jones B A and Wiedwald J D 1987 Flat-field response and geometric distortion measurements of optical streak cameras *Proc. SPIE* **832** 283–8

[3] Kruschwitz C A, Wu M, Moy K and Rochau G 2008 Monte Carlo simulations of high-speed, time-gated microchannel-plate-based x-ray detectors: saturation effects in dc and pulsed modes and detector dynamic range *Rev. Sci. Instrum.* **79** 10E911

[4] Wiedwald J D and Lerche R A 1987 Streak camera dynamic range and optimization *Proc. SPIE* **832** 275–82

[5] Allison S W and Gillies G T 1997 Remote thermometry with thermographic phosphors: instrumentation and applications *Rev. Sci. Instrum.* **68** 2615–50

[6] Husberg T, Girja S, Denbratt I, Omrane A, Aldén M and Engström J 2005 Piston temperature measurements by use of thermographic phosphors and thermocouples in a heavy-duty Diesel engine run under partly premixed conditions *SAE 2005-01-1646*

[7] Khalid A and Kontis K 2008 Thermographic phosphors for high temperature measurements: principles, current state of the art and recent applications *Sensors* **8** 5673–744

[8] Knappe C, Andersson P, Algotsson M, Richter M, Linden J, Alden M, Tuner M and Johansson B 2011 Laser-induced phosphorescence and the impact of phosphor coating thickness on crank-angle resolved cylinder wall temperatures *SAE Technical Paper*

[9] Seyfried H, Richter M, Nilsson K-H, Aldén M and Schmidt H 2007 Surface thermometry using laser-induced phosphorescence applied in the afterburner of an aircraft turbofan engine *Collection of Technical Papers 45th AIAA Aerospace Sciences Meeting* vol 18 pp 12794–802

[10] Aldén M, Omrane A, Richter M and Särner G 2010 Thermographic phosphors for thermometry: a survey of combustion applications *Prog. Energy Combust. Sci.* **37** 422–61

[11] Särner G, Richter M and Alden M 2008 Investigations of blue emitting phosphors for thermometry *Meas. Sci. Technol.* **19** 125304

[12] Seyfried H, Särner G, Omrane A, Richter M and Aldén M 2005 Optical diagnostics for characterization of a full-size fighter-jet after-burner *ASME GT2005-69058*

[13] Bizarri G and Moine B 2005 On BaMgAl10O17: Eu^{2+} phosphor degradation mechanism: thermal treatment effects *J. Lumin.* **113** 199–213

Investigation and compensation of the nonlinear response in photomultiplier tubes for quantitative single-shot measurements

Paper V

Christoph Knappe, Johannes Lindén, Fahed Abou Nada, Mattias Richter and Marcus Aldén

Published in: Rev. Sci. Instrum. **83**(3):034901, 2012.

Investigation and compensation of the nonlinear response in photomultiplier tubes for quantitative single-shot measurements

C. Knappe, J. Lindén, F. Abou Nada, M. Richter, and M. Aldén
Division of Combustion Physics, Lund University, Box 118, SE-221 00 Lund, Sweden

(Received 6 December 2011; accepted 23 February 2012; published online 15 March 2012)

A concept for time-sensitive optical detectors is described that shows how to confirm whether the detection device is operating in the linear response regime. By evaluating the recorded time decay of a thermographic phosphor, even weak saturation effects far from obvious situations can be identified and further related to either optical or electrical saturation. The concept has been validated by running a PMT detector close to saturation and exposing it to the optical signal decay of two different thermographic phosphors, La_2O_2S:Eu and $CdWO_4$. It was confirmed that short but intense light exposures at the beginning of an individual time decay influence the detector response for the rest of the decaying signal including temporal areas, where the anode current has dropped well below the manufacturer specified current limit. Such situations are common when applying, e.g., phosphor thermometry where it is necessary to retrieve the full decay curve from a single-shot event, i.e., standard techniques based on single-photon counting are omitted. Finally, means of compensation are introduced in order to facilitate the retrieval of useful information from the measurement data when operation in the non-linear response regime is inevitable. © *2012 American Institute of Physics*. [http://dx.doi.org/10.1063/1.3693618]

I. INTRODUCTION

The purpose of an optical detector is to convert incoming light into a measurable signal, principally electronic, which is proportional to the light intensity. While there are many different types of detectors, all are applied in one of two ways: to reproduce light intensity in a temporally resolved manner, e.g., photodiodes or photomultiplier tubes (PMTs); to integrate the light intensity over time, e.g., CCD detectors. Both applications can be used for quantitative measurements, providing that the signal response is linear (linear response region), or that corrections can be made when the input-to-output signal is nonlinear. The linear response region for detectors is often defined relative to the noise threshold and a maximum value such as anode current or digitizer limit; however, in practice, saturation effects can be seen at values much lower than these perceived extrema.

When measuring phosphorescence decay times with a PMT, for investigation of phosphor thermometry, it was found that the photomultiplier settings for gain and exposure level were linked to variations in the measured decay time, though levels were below the proscribed limits. This behavior was consistent with saturation phenomena. The purpose of this paper is to present a simple method to determine the true linear response region for any temporally resolved optical detector, as well as presenting a method to correct measurements outside the linear response region. For consideration of similar effects in integrating optical detectors see Ref. 1, where an image intensified CCD is investigated.

Photomultiplier tubes are perhaps the most widely used electronic tool in spectroscopy, having been applied in every manner of optical measurement.[2–4] The PMT provides opto-electrical conversion combined with internal electrical amplification, see Figure 1, making it suitable for low light level measurements. They are temporally resolved detectors; depending on circuitry they can resolve, in real time, the impingement of single photons on the detector, or measure continuous streams of photons. It is the ability of a PMT to operate continuously that is used in phosphor thermometry to measure the temperature dependent phosphorescence decay. For a more in-depth description of the working principles of a PMT, see Hakamata *et al.*[5] For a detailed model of photomultiplier gain, see Moatti.[6]

Significant efforts have been made to characterize nonlinearity in PMTs thus far. Sauerbrey,[7] for example, published a substantial experimental study of PMT nonlinearity in which five essentially independent sources of photomultiplier nonlinearity were measured. According to Ref. 7 some sources of PMT nonlinearity can be easily avoided as they are introduced by external circuitry connected to the PMT. Complementary to Sauerbrey's work, Aspnes and Studna[8] designed a circuit for improving photomultiplier linearity. More recent work dealt with the calibration of non-linear photomultiplier response. In 2003, Vićić *et al.*[9] used an ultraviolet pulsed-light source and determined the response of a photomultiplier within a range of light intensities from single photoelectrons up to well beyond the linear response region. Whilst

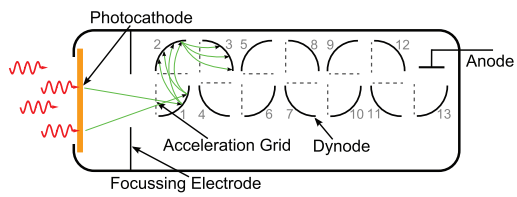

FIG. 1. Schematic construction of a PMT with 13 dynodes.

maintaining an "excellent agreement" between their measured data and the fitted model, Vićić admitted that the procedure described in Ref. 9 was "extremely computer-intensive."

It is not in the scope of this paper to present yet another in-depth discussion of PMT physics; rather, a rapid and easily accessible tool is constructed to properly evaluate the operating region of the PMT. To this end, a simple view of PMT behavior was adopted for temporally resolved, non-photon-counting instances. Ideally, the PMT response is a linear relationship between photon flux and output current. The linear response is susceptible to two independent processes that drive the PMT into the nonlinear response region when approaching saturation.[10]

The first process, photocathode bleaching, occurs when the photocathode is struck by a sufficient number of photons per time interval to deplete the valence band in the photocathode. A radial voltage drop at the photocathode is caused by large current densities and a certain time is needed for the photocathode to recover and re-enter the linear response region.

The accumulation of local electric fields inside the PMT accounts for the second process. At high gains, a space charge builds at the anode and last few dynode stages. This space charge electrically shields and decelerates advancing electrons. Hence, increasing electrical gain above a certain threshold drives the dynode chain into the saturated region. This is often considered as the major source of saturation in PMTs.[11]

The total detector response, can be understood as the product of the optical- (photocathode) and the electrical (dynode chain) response functions. These processes are not discrete, as the number of electrons arriving at the anode, and thus gain saturation, depends on the photocathode sensitivity and the amount of incoming light. Alternatively, reducing incoming light intensities will suppress the development of a space charge (as does lowering gain or applying a higher voltage across the last few dynodes). As a result, uncorrected quantitative measurements can only be performed if the PMT is operated in the linear region for both of these two responses.

Most PMTs are specified to run at a maximum DC output current of 100 μA,[5,12] which equals approximately 6×10^5 electrons/ns released at the last dynode. This current value can be understood as the absolute limit for linear dynode operation, though the photocathode may already be saturated due to the incoming light flux. According to Becker and Hickl,[13] this maximum output current can be increased almost by a factor of 1000 to around 100 mA when operating in the PMT in "pulsed" mode, mostly because the PMT can recover, to some extent, from bleaching and space charge accumulation in between two adjacent pulses.

A motivation for extending the output current beyond 100 μA is to increase the output signal: most PMTs come with a load resistance of 50 Ω, meaning that the readout instrument's input resistance has to match in order to avoid back and forth reflection ("ringing") of the signal in the cable. By Ohm's law, a current of 100 μA over 50 Ω generates a maximum voltage of 5 mV, close to the lower resolution limit of common digital oscilloscopes. This often results in unacceptably low signal/noise ratios when digitizing the analog current, without time averaging or special amplification electronics. When approaching pulse lengths of as much as a few milliseconds, as in some cases of phosphorescence, it is dubious that these enhanced limits still apply, and caution should be exercised when extending the PMT workspace by exceeding the anode's current limit.

II. DATA ACQUISITION AND EVALUATION

Temporally, resolved intensity decay curves were acquired for two different phosphors (La_2O_2S:Eu with 2 at. % Eu and $CdWO_4$) in order to generate different optical intensity time-distributions that the detector has to reproduce. The major difference between these two phosphors is an intense, short-lived, fluorescence peak, that is present for the La_2O_2S:Eu, but is missing in the $CdWO_4$ time decay (see Figure 2).

Each phosphor was excited by a 10 Hz pulsed, Q-switched and frequency tripled (355 nm, La_2O_2S:Eu) or frequency quadrupled (266 nm, $CdWO_4$) Nd:YAG laser (Quantel Brilliant B). Low laser pulse energies between 70 and 140 μJ were used in order to avoid saturating the phosphor. The resulting phosphorescence was imaged onto a photomultiplier module (Hamamatsu H6780-04) after passing an interference filter, centered at 540 nm (FWHM = 10 nm) for the La_2O_2S:Eu phosphor and 450 nm for $CdWO_4$ (FWHM = 40 nm). The filters were placed in front of the detector to eliminate spurious laser radiation and to spectrally isolate the phosphorescence emission.

In the PMT, a nominal electrical gain can be chosen within the range of 10^2 to 10^6 (Ref. 12), depending on the amount of optical signal that is available for collection. The gain number is defined by the ratio of output electrons divided by photocathode electrons. The photomultiplier output current was read out by a 350 MHz digital oscilloscope (Lecroy WaveRunner WA6030) at an input resistance of 50 Ω, allowing sampling of decay times as short as a few ns at a dynamic range of 8 bit.

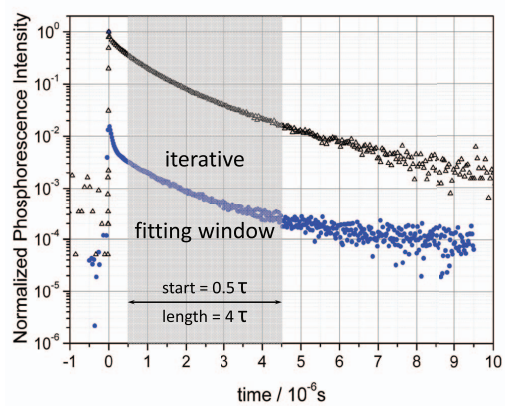

FIG. 2. A comparison of similar phosphorescence decays for La_2O_2S:Eu (at 540 nm, T = 518 K blue dots) and $CdWO_4$ (at 450 nm, T = 387 K, black triangles). The gray area indicates the time window in which the decay time is determined.

Both phosphors offer emission peaks that decay exponentially after laser excitation. The time decay can be approximated by

$$I = I_0 \cdot \exp\left(-\frac{t}{\tau}\right), \tag{1}$$

where I_0 is the initial emission intensity, t is time and τ is the decay time of the phosphorescence, i.e., the time after which the intensity has decreased to $1/e$ of the initial emission I_0.

To extract the time constant τ from the measured decay curves, a Levenberg-Marquard fitting algorithm (MATLAB) has been applied, that varies I_0 and τ and iteratively adapts the $(n+1)$th fitting window region according to the nth evaluated decay time τ_n until stability is achieved. As indicated in Figure 2 (grayed out), the fitting window was chosen to range from $0.5\tau_n$ to $4.5\tau_n$. Further details on the iterative decay time algorithm can be found in Ref. 14.

For obvious reasons, the recorded phosphorescence decay time τ is a measure of the time-distribution of the detector output signal $S_{out}(t)$. Therefore, τ is also a suitable target for analyzing the linearity of a detector's input-to-output signal conversion. In other words, the detector operates in the linear region when the evaluated decay time is purely dependent on the light source and thus insusceptible to minor changes regarding detector gain and light exposure. Consequently, the detector linearity can be analyzed either by changing the electrical amplification (gain) or by attenuating the light before it hits the detector. In case of linear operation the evaluated decay time will be constant, regardless these changes that were made on the detector side.

In a simplified approach that emphasizes how detector saturation distorts the output signal, detector response functions were simulated according to

$$S_{out}(I_{in}) = S_{max} \cdot \left[1 - \exp\left(-\frac{I_{in}}{S_{max}}\right)\right] \tag{2}$$

where I_{in} is the incoming signal intensity and S_{max} is the maximum signal output intensity. Such response curves were plotted in Figure 3(a) together with the response curve of an ideal detector indicated by the black solid line. By inserting a phosphorescence intensity distribution as I_{in} into equation (2), a distorted detector output signal can be obtained, which is shown in part (b) of Figure 3 for each corresponding response curve from Fig. 3(a). A least squares exponential fit according to equation (1) was performed within the indicated time window illustrated in grey. The graph in Figure 3(c) displays the associated decay times, which clearly depend on the saturation level, that was defined by how much the initial output (see Fig. 3(b), black curve) signal was reduced due to detector saturation in percentage.

As displayed in Figure 4, the time decays of $CdWO_4$ and La_2O_2S:Eu exhibit a strong temperature dependence between 300 K and 600 K, which makes them a sensitive remote temperature sensor, for example in engine applications.[4,15,16]

Both phosphors combined have a common range of decay times from 10 μs down to 100 ns. This broad overlap region is beneficial as it allows achieving similar decay times by keeping the two phosphors at different temperatures. This

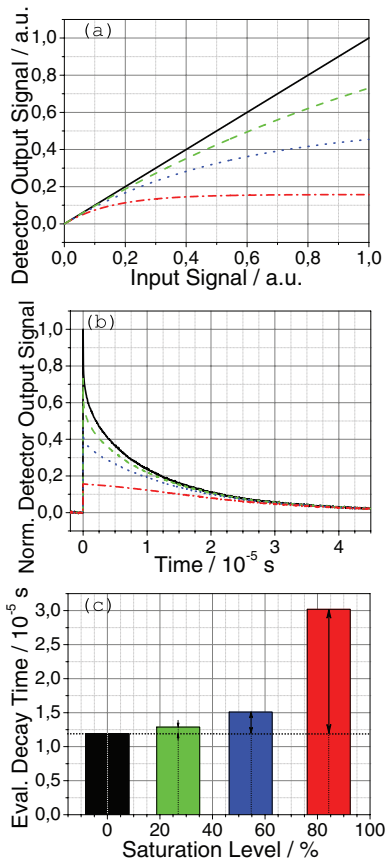

FIG. 3. Example on how different saturation states in the detector (a) change the shape of the output time-signal (b) and the evaluated decay time (c). The time decay in black corresponds to an average of 100 measured decay curves from La_2O_2S:Eu at room temperature.

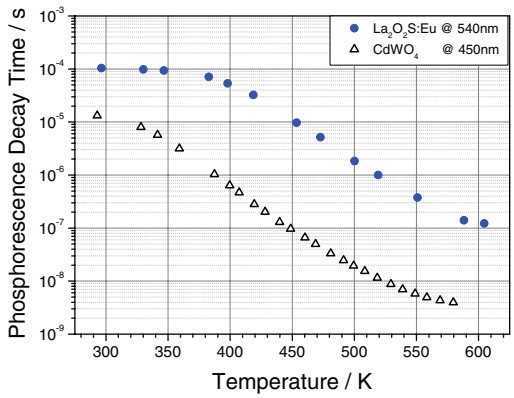

FIG. 4. Phosphorescence decay time as function of temperature for La_2O_2S:Eu and $CdWO_4$.

in turn enables the impact of an intense initial peak (present for La_2O_2S:Eu, absent for $CdWO_4$) on the detector response to be studied by comparison under otherwise similar operating conditions.

III. RESULTS

A. Saturation analysis using phosphorescence time decay

For 100 consecutive laser shots at room temperature, the La_2O_2S:Eu phosphorescence decay time τ is displayed in Figure 5(a). At a PMT gain of 4700 and mean laser pulse energy of 70 μJ, the spread in phosphorescence decay time ranges from 103.5 μs to 104.2 μs. According to the measurement data displayed in Figure 4, the spread corresponds to a temperature interval from 294 K to 299 K. What initially looks like a statistical distribution due to noise in the signal or temperature variation (see Figure 5(a)) becomes a linear trend when the measurement points are re-arranged according to the output signal voltage $S_{\text{out}}(t = 0.5\tau)$, see Figure 5(b). $S_{\text{out}}(t = 0.5\tau)$ is equal to the very first readout voltage within the fitting window, see Figure 2 for an example. Its average value is 4.75 mV, which corresponds to 95 μA in PMT output current at 50 Ω oscilloscope input resistance. The spread in voltage is about 3 % and corresponds to laser energy shot-to-shot variations that induced proportionally shifting phosphorescence yields. According to Ref. 12, an output current of 95 μA is still below the 100 μA specified limit of the cw PMT operation. However only half a decay time earlier (see Figure 2), where the phosphorescence signal coincides with spurious laser reflexes, i.e., 52 μs prior to the fitting window start position, the PMT was struck by far more photons, corresponding to 20 mA PMT output current (not shown in Figure 5) which is 200 times higher than the specified cw limit, but still only about 1/5 of what would be the limit for pulsed operation according to Ref. 13.

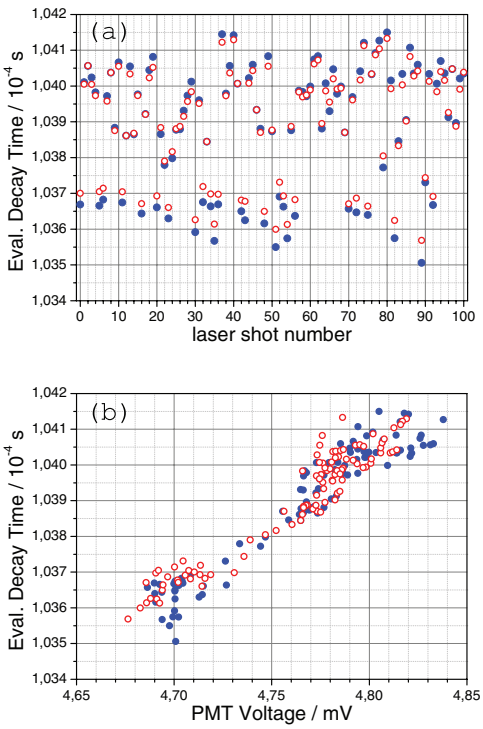

FIG. 5. La_2O_2S:Eu phosphorescence decay time at 296 K using gain 4700 and 100 consecutive laser shots at ~70 μJ (a). In graph (b), the same data has been re-arranged according to the first output voltage within the fitting window $S_{\text{out}}(t = 0.5\tau)$. Blue dots represent decay times obtained by using an iteratively changing time window (see Ref. 14) whereas the red circles illustrate the same data evaluated in a fixed time window.

The results from Figure 5 are obtained taking two different approaches: An iteratively changing fitting window that adapts its size and position according to the length of each individual decay curve (red circles) and a fixed time window for all curves, which was determined by the average iterative fitting window (blue dots). As can be seen in Figure 5, the method of data reduction has an influence on its own upon the obtained results. Similarly, it can be shown that even low level spurious background radiation can have an effect on measurement accuracy. However, being able to reproduce the intensity dependence of τ with a fixed time window is an evidence for a physical change in decay time, showing that these effects are not simply induced by evaluating different time windows. Even though the results in Figure 5(b) overlap quite nicely, the slope for the iterative time window (blue dots) is a little higher accounting for the slight differences in the window positions: Due to the slight multi-exponential time decay that characterizes phosphorescence emitted by La_2O_2S:Eu (see Figure 2), a decay time evaluated in an earlier part of the curve results in a smaller value compared to a decay time evaluated slightly later in the same curve. In summary, the trends shown in Figure 5 can clearly be interpreted as a distortion of the temporal signal shape that correlates with the amount of light hitting the PMT. The different intensities were induced by laser shot-to-shot variations and cannot be avoided, which makes this dependence a concern for any quantitative, time dependent optical measurement involving lasers. The positive slope is in agreement with what would be expected from a saturation effect (see Figure 3). However, it remains yet unclear, whether the saturation was caused by photocathode bleaching and/or by applying too high electrical amplification.

For investigating the source of saturation further, Figure 6 displays two measurement series of time decays, taken at 382 K, this time using two different gains (4700 and 7400) at constant mean laser energy of 70 μJ.

The two point clusters shown in Figure 6 correspond to the lower gain value (left) and the higher gain (right), and incorporate a series of 100 laser shots each, represented by the spread in x-direction. For a linear responding detector, the two point clusters in Figure 6 were expected to collapse in y-direction into one single decay time. Hence, PMT saturation shows its effect by linearly distributing the decay times as a function of PMT output

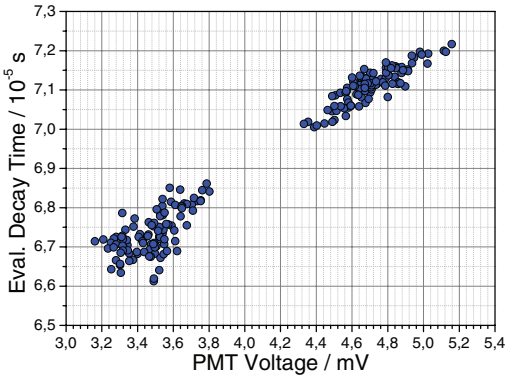

FIG. 6. La_2O_2S:Eu phosphorescence decay times at 382 K using two gains, 4700 (left group) and 7400 (right group) with 100 consecutive laser shots at ~70 μJ each. The data has been plotted as a function of the PMT Voltage $S_{out}(t = 0.5\tau)$.

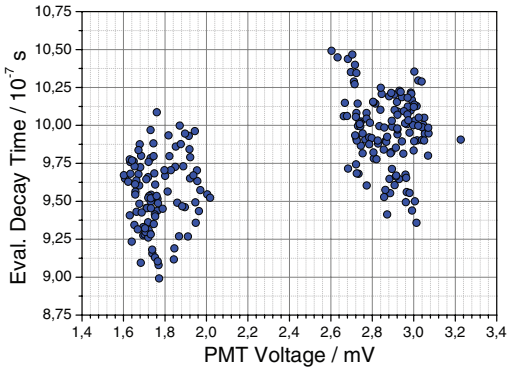

FIG. 7. La_2O_2S:Eu phosphorescence decay times at 519 K using two gains, 4700 (left) and 8400 (right), with 100 consecutive laser shots at ~ 70 μJ each.

voltage. An interesting observation is that both clusters are positioned to each other such that the individual slope from each gain measurement matches the other data cluster. In other words, the slope caused by variation from the photocathode's amount of primary electrons (shot-to-shot based) is identical to the cluster offset slope that is caused by elevating the gain. From these observations it is possible to conclude the following:

1. Since both point clusters show a non-constant decay time distribution – both gain measurement are subject to a nonlinear detector response.
2. The gain-driven cluster offset indicates electrical saturation: If the slope within each cluster was only due to photocathode saturation – the second point cluster would result in similar decay times obtained at higher output voltages, i.e., a cluster offset parallel to the x-direction.
3. The saturation seen in Figure 6 is purely gain-driven with no significant contributions of photocathode saturation, meaning that if the number of primary photoelectrons would be increased, the decay curve shape would change the same way as if the gain is increased. If also the photocathode was subject to saturation, the individual point cluster slopes would not match the gain-based cluster offset slope.

Figure 7 shows data that is similar to those that was presented in Figure 6, only this time at an elevated temperature of 519 K. The laser energy was kept low again to 70 μJ and two gain values are compared to each other (4700 and 8400).

From a comparison with Figure 6 the cluster offset slope is a factor of 84 smaller in Figure 7. Also, the relative decay time spread in each measurement increased as shorter decay times become more difficult to evaluate. Since the phosphorescence intensity decreases towards higher temperatures, the PMT voltage at gain 4700 for 382 K (see Figure 6) is almost twice as high as for 519 K (see Figure 7) for the same mean laser pulse energy. Additionally, the decay time at 519 K was 71 times shorter than for 382 K in Figure 6, reducing the mean light exposure time. Therefore less load was put on the dynode chain, which could explain the reduced cluster offset slope, seen in Figure 7.

B. Compensation approach

Operating outside the linear workspace of a detector is often required due to the higher signal intensity availed. However, the distortions in the response signal due to saturation are a source of systematic error. Nevertheless, a compensation that accounts and corrects for these effects is possible, providing systematic changes in the response are mapped into a library and thus can be sufficiently predicted. In practice, a biased result originating from a slightly saturated signal can be transformed into an unbiased result by extrapolating it towards lower signal levels into the linear operating region, using a slope proposed by the detector library. For probe techniques that rely on calibration rather than an absolute physical quantity, such as thermographic phosphorescence, the compensation is simplified because the reference is not restricted to the linear detector operating region: Any signal output can become a reference for extrapolation. For further considerations, the reference was chosen as the PMT-readout voltage $S_r(t = 0.5\tau)$ recorded over 50 Ω.

The upper part (a) of Figure 8 shows the PMT decay response slope $d\tau/dS$ for La_2O_2S:Eu decays as a function phosphorescence decay time (red circles). In graph (b) on the bottom of Figure 8, $d\tau/dS$ is presented in red as a function of temperature together with corresponding decay time values (blue dots) that were taken from the calibration curve in Figure 4. The spline interpolation (red dashed line) can be used to correct decay times obtained in the nonlinear detector regime. It refers to an output reference voltage of $S_r(t = 0.5\tau) = 4.8$ mV at the start of the decay window, for which the calibration was performed.

As the comparison between Figure 6 and 7 suggested, the slope declines for shorter time decays, probably due to the competition between saturation and space charge recovery that was briefly discussed above. The spline interpolation

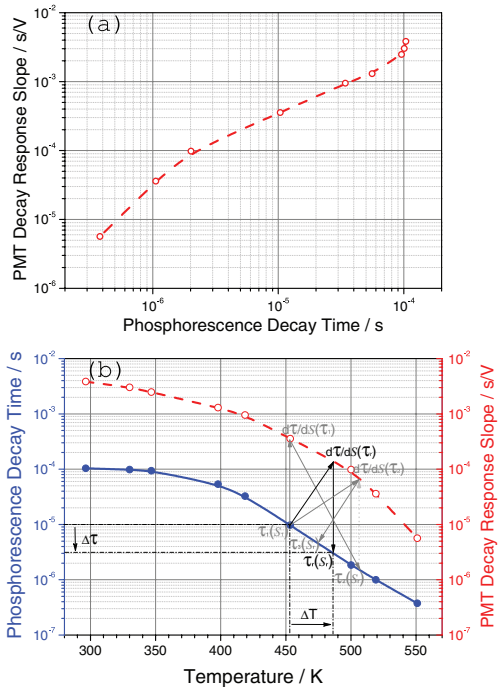

FIG. 8. PMT decay response slope for La_2O_2S:Eu (red circles) as a function of phosphorescence decay time (a) and as a function of temperature (b). The black arrows in graph (b) indicate how a measured decay time $\tau_1(S_1)$ can be iteratively corrected towards τ_r at reference signal output S_r ($< S_1$) for which the phosphor was calibrated (blue dots).

indicated in red, can further be used for compensating any obtained decay time towards the reference output voltage of $S_r(t = 0.5\tau) = 4.8$ mV, which refers to the first output voltage within the decay evaluation window. Knowing how detector distorted decay times evolve, the correction of τ_1 recorded at a output voltage of $S_1(t = 0.5\tau)$ can be performed to the reference value τ_r at reference voltage S_n according to equation (3),

$$\tau_r = \tau_1 - \left.\frac{d\tau}{dS}\right|_{\tau_r} \cdot (S_1 - S_r). \quad (3)$$

Although $d\tau/dS(\tau_r)$ is initially unknown because it requires knowledge over τ_r, it can be approached iteratively by starting with $d\tau/dS(\tau_1)$. For $d\tau/dS > 0$ and $S_1 > S_r$ it follows that $\tau_1 > \tau_r$ and $d\tau/dS(\tau_1) > d\tau/dS(\tau_r)$ as seen in Figure 8(b), meaning that the first iteration $\tau_2(S_r)$ will underestimate τ_r when correcting from S_1 against S_r. In a second iteration step, the slope $d\tau/dS(\tau_2) < d\tau/dS(\tau_r)$ can be used to correct $\tau_1(S_1)$ towards $\tau_3(S_r) < \tau_1(S_1)$, which in term is an overestimation of τ_r. Since τ_3 already is a closer estimate of τ_r compared to τ_1, the iterative solution converges oscillating towards τ_r, granted that $d\tau/dS$ is monotonic. Considering $d\tau/dS > 0$ and signal intensities smaller than the reference, i.e., $S_1 < S_r$, a similar

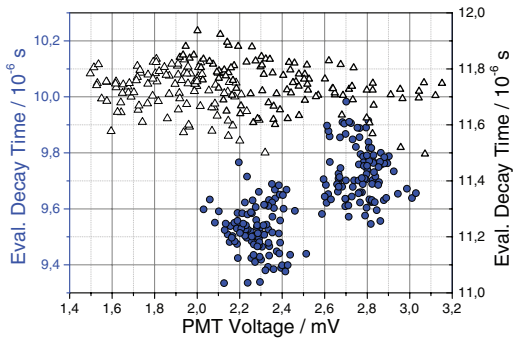

FIG. 9. Comparison of response slopes for two different phosphors (blue dots: La_2O_2S:Eu at 473 K; black triangles: $CdWO_4$ at 308 K) at similar decay times, using equal PMT gains (4700 and 6300) and laser energies that yield the same decay signal voltages.

argumentation results in τ_i converging towards $\tau_r > \tau_1$, however this time without oscillations. In summary, if measurements of a certain decay time are taken at output voltages S_1 different from the reference signal S_r for which the calibration $d\tau/dS$ (see Figure 8) was performed, the decay time has first to be corrected towards that reference signal intensity before the decay time can be converted into a temperature.

It is, however, important that the PMT is corrected for the same type of signal/phosphor, as indicated by the earlier assumption that the detector might be affected by pre-existing saturation states. To test this hypothesis, the PMT was now used to detect similar time decays from La_2O_2S:Eu and $CdWO_4$ at laser energies adjusted to generate the same output current for both signals within the investigated time window. Since the gain was identical in both cases, the laser energy was adapted to compensate for the two different phosphorescence yields and to account for the spectral photocathode sensitivity within the corresponding emission wavelengths such that the same amount of primary electrons were released from the photocathode. The experiment is set up in a way that an ideal time gated PMT, switched on only during the evaluated time window, should have no means to distinguish the two different phosphorescence emissions. However the PMT used here also recorded a peak voltage prior to the evaluation window, that was about 54 times higher for the La_2O_2S:Eu phosphor than for $CdWO_4$. In Figure 9, the results for the two cases are displayed, showing a horizontal response distribution for $CdWO_4$ in contrast to the results obtained with La_2O_2S:Eu. The bigger spread in PMT voltage for $CdWO_4$ is due the higher signal yield for $CdWO_4$ that required less, and thus more unstable, laser excitation energy.

According to Figure 9, the decay time slope has drastically changed by the presence of the peak prior to the fitting window in which the decay time was evaluated. It can thus be concluded that strong and saturating peaks in the beginning have an impact on the time progression of the detected signal. As long as these peaks cannot be avoided by some sort of time-gating, detector compensation should also take into account the time dependent photon emission curve of the light source that is to be investigated.

IV. CONCLUSIONS

In this paper, a novel test procedure is described that can be used to determine the linear operating region of any optical detector, capable of performing time-resolved measurements. Additionally, information is provided on how such a detector can be operated outside the linear regime as is often required when signal decay time information must be retrieved from single-shot measurements. The procedure was applied to the extended afterglow of thermographic phosphors and compares evaluated signal decay times as a function of electrical gain and incident intensity by creating a detector response database. By evaluating and comparing the recorded time decay within the response database even weak saturation effects (far from obvious situations) can be identified and further related to either photocathode or dynode saturation.

These saturation events introduce a systematic error on quantitative measurements results. Such errors can be corrected towards a reference value from the detector's response database. The reference value needs to be part of the linear response regime in most cases. However, if the reference value is used only to calibrate another quantity – as it is for phosphor thermometry – any value from the detector response database can be chosen as a reference.

Furthermore, a comparison of the decay signals from $CdWO_4$ and La_2O_2S:Eu has shown that an accurate correction for PMT non-linearity should also consider the history of the signal, e.g., the photo-current at the start of the decay. It is thus important from a compensation point of view to use the same sort of signal for both, the actual measurement and the generation of the response database.

ACKNOWLEDGMENTS

This work was financially supported by the HELIOS research project within the 7th EU framework program for Research and Technical Development/Transportation and the research project D60, financed by the Swedish Energy Agency. The authors gratefully acknowledge A. W. Sloman for helpful discussions.

[1] J. Lindén, C. Knappe, M. Richter, and M. Aldén, Meas. Sci. Technol. **23**, 035201 (2012).
[2] M. P. Bristow, Appl. Opt. **37**, 6468 (1997).
[3] H. Bladh, J. Johnsson, and P. E. Bengtsson, Appl. Phys. B **96**, 645 (2009).
[4] C. Knappe, P. Andersson, M. Algotsson, M. Richter, J. Lindén, M. Tunér, B. Johansson, and M. Aldén, SAE Int. J. Engines **4**, 1689 (2011).
[5] T. Hakamata, H. Kume, K. Okano, K. Tomiyama, A. Kamiya, Y. Yoshizawa, H. Matsui, I. Otsu, T. Taguchi, Y. Kawai, H. Yamaguchi, K. Suzuki, S. Suzuki, T. Morita, and D. Uchizono, *Photomultiplier Tubes – Basics and Applications* (Hamamatsu Photonics K.K., Iwata City, 2007).
[6] P. Moatti, L'Onde Electrique **43**, 787 (1963).
[7] G. Sauerbrey, Appl. Opt. **11**, 2576 (1972).
[8] D. E. Aspnes and A. A. Studna, Rev. Sci. Instrum. **49**, 291 (1978).
[9] M. Vićić, L. G. Sobotka, J. F. Williamson, R. J. Charity, and J. M. Elson, Nucl. Instrum. Methods A **507**, 636 (2003).
[10] D. H. Hartman, Rev. Sc. Instrum. **49**, 1130 (1978).
[11] H. Kunz, Metrologia **5**, 88 (1969).
[12] H6780-04 PMT Datasheet, http://sales.hamamatsu.com/assets/pdf/parts_H/H6780-04.pdf.
[13] W. Becker and H. Hickl, *How (and why not) to Amplify PMT Signals* (Becker & Hickl GmbH, Berlin, 2000), http://www.becker-hickl.de/pdf/ampmt.pdf.
[14] J. Brübach, J. Janicka, and A. Dreizler, Opt. Las. Eng. **47**, 75 (2009).
[15] G. Särner, M. Richter, and M. Aldén, Meas. Sci. Technol. **19**(12), (2008).
[16] A. Omrane, G. Särner, and M. Aldén, Appl. Phys. B **79**, 431 (2004).

Comparison of photo detectors and operating conditions for decay time determination in phosphor thermometry

Christoph Knappe, Fahed Abou Nada, Mattias Richter and Marcus Aldén

Paper VI

Published in: Rev. Sci. Instrum. **83**(9):094901, 2012.

Comparison of photo detectors and operating conditions for decay time determination in phosphor thermometry

C. Knappe, F. Abou Nada, M. Richter, and M. Aldén
Division of Combustion Physics, Lund University, Box 118, SE-221 00 Lund, Sweden

(Received 5 June 2012; accepted 4 August 2012; published online 5 September 2012)

This work compares the extent of linear response regions from standard time-resolving optical detectors for phosphor thermometry. Different types of photomultipliers (ordinary and time-gated) as well as an avalanche photodiode were tested and compared using the phosphorescence decay time of cadmium tungstate ($CdWO_4$). Effects originating from incipient detector saturation are revealed as a change in evaluated phosphorescence decay time, which was found to be a more sensitive measure for saturation than the conventional signal strength comparison between in- and output. Since the decay time of thermographic phosphors is used for temperature determination systematic temperature errors in the order of several tens of Kelvins may be introduced. Saturation from the initial intensity is isolated from temporally developed saturation by varying the $CdWO_4$ decay time over the microsecond to nanosecond range, resultant of varying the temperature from 290 to 580 K. A detector mapping procedure is developed in order to identify linear response regions where the decay-to-temperature evaluations are unbiased. In addition, this mapping procedure generates a library of the degree of distortion for operating points outside of linear response regions. Signals collected in the partly saturated regime can thus be corrected to their unbiased value using this library, extending the usable detector operating range significantly. © *2012 American Institute of Physics*. [http://dx.doi.org/10.1063/1.4746990]

I. INTRODUCTION

Phosphors are ceramic materials that exhibit an extended afterglow after being optically excited. A phosphor is thermographic when the phosphorescent light emission varies as a function of temperature. Both the changes in phosphorescence decay as well as the intensity ratio of different optical regions in the emission spectra can be exploited for thermometry.[1–3]

As the decay time of a phosphor can change several orders of magnitude for a given temperature range, point measurements exploiting the time decay are often preferred over intensity-ratio based methods when high temperature precision is demanded. Consequently, recent attempts pushed the decay-time retrieval towards 2D application by either using a stack of sequentially gated CCD cameras[4] or fast framing CMOS devices.[5]

Measurement precision and accuracy in phosphor thermometry highly depends on the phosphor itself, its sensitivity to temperature changes and whether phosphorescence is affected by other interfering factors such as pressure,[6] ambient gas composition[7] or the post growth process of annealing.[8–10] In some applications the layer thickness of the phosphor may contribute as a substantial source of error[11] and also multi-exponential decays can introduce ambiguities to the retrieval of a distinct temperature.[12]

Apart from phosphor characteristics, there are other factors to consider that restrict the accuracy of phosphor thermometry. For obvious reasons, the reliability of the temperature calibration is a key feature, i.e., how well is the temperature known during calibration, how many calibration points are sufficient for a given temperature interval and whether the same decay time can be reproduced for a set of different signal intensities. The latter question is a matter of light detection and is aimed to be addressed in this paper. Previous studies have shown that detector saturation might introduce substantial systematic errors to the signal evaluation process in phosphor thermometry.[13,14] This work seeks to compare the performance of four different standard detectors under identical test conditions. Each detector was exposed to the phosphorescence of cadmium tungstate ($CdWO_4$) at five different temperatures under varying light intensities and detector gains.

II. EXPERIMENTAL

A. Selection of detectors

Four time-resolving point detectors have been chosen for comparison within this study. The selection consists of two different photomultiplier tubes (PMTs), a multi-channel plate photomultiplier tube (MCP-PMT) and a fiber-coupled avalanche photodiode (APD). One of the two PMTs can optionally be run in time-gated mode and also offers a more sensitive photocathode within the investigated wavelength range around 450 nm. The MCP-PMT could only be used in time-gated mode. However, by triggering the PMT-gate to open either 10 ns before or after the first phosphorescence photons hit the detector allowed to study the impact of an initial peak on the signal shape. Signal outputs from all detection devices were either directly coupled to a 350 MHz digital oscilloscope using an input resistance of 50 Ω, or optionally connected to an in-house made external current-to-voltage amplifier (5 MHz bandwidth). In total, seven different detector configurations were tested as listed in Table I. The gain column below represents the electrical amplification

TABLE I. Detectors and tested operating modes.

Detector type	Specific name	Mode of operation	Gain range
PMT1	H6780-04	Continuous	480–43000
PMT1	H6780-04	Cont. + amplified	42–80
PMT2	H11526-20-NF	Continuous	950–7700
PMT2	H11526-20-NF	Time-gated: +10 ns	950–7700
MCP-PMT	R5916U-50	Time-gated: −10 ns	36–3000
MCP-PMT	R5916U-50	Time-gated: +10 ns	36–3000
APD	S5343	Continuous	62–470

range that was investigated for each detector. It has been defined according to oscilloscope peak voltages ranging from less than 100 mV up to a few Volts for each temperature and detector. Maximum peak voltages varied to some degree from detector to detector due to their different specified output current limits.

B. Experimental setup

Figure 1 displays the experimental setup, which was used to compare all detectors in their individual modes of operation (see Table I). A 10 Hz pulsed Nd:YAG laser, operating at 266 nm was used as an excitation source for $CdWO_4$, that was placed in a tube furnace. $CdWO_4$ was chosen, in particular, as it emits strong- and almost single-exponential phosphorescence light, without suffering from irreversible emission changes when exposed to elevated temperatures below 600 K. Its broadband emission centered around 470 nm is temperature sensitive from room temperature up to around 580 K, offering a vast range of decay times that span from 10 μs down to less than 10 ns.

The phosphorescence was imaged onto the detector by a 300 mm quartz lens at a 90° angle to the laser path axis. A combination of a >400 nm transmission edge filter and a 450 nm bandpass filter (FWHM = 40 nm) was placed in front of the detector to suppress spurious laser radiation and to spectrally isolate the phosphorescence emission.

Two identical PMTs (H6780-04, same type as PMT1 in Table I) were added to the setup in Figure 1 for the purpose of

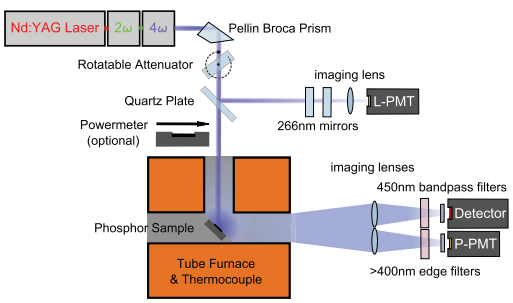

FIG. 1. Experimental setup for testing the temporal performance of a detector as a function of light intensity, gain and temperature. L- and P-PMT are two identical PMTs referencing the amount of impinging photons per time interval after being calibrated against the power meter.

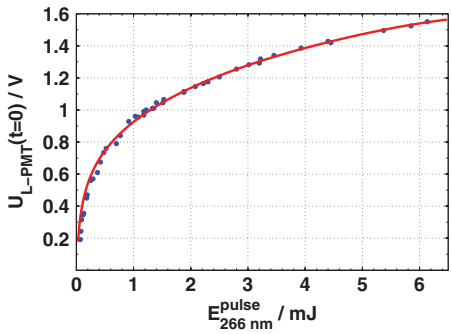

FIG. 2. Fitted correlation (red line) showing the signal peak voltage from L-PMT in as a function of Laser pulse energy. The gain of the L-PMT was set to a constant value of 6300 and additional transmission losses $T_{\text{L-PMT}}$ were introduced (see Figure 1) in order to prevent detector damage.

monitoring the phosphor's response to laser intensity changes. Keeping track on the phosphor behavior is important in order to monitor any possible phosphor-intrinsic decay-time dependence on laser irradiance (see Ref. 10) that might superpose with detector-specific results. The detector denoted as L-PMT monitors the laser pulse-to-pulse fluctuations. Once calibrated against a powermeter, it serves as a reference for the laser pulse energy, see Figure 2.

Henceforth, the laser pulse energy $E^{\text{pulse}}_{266\,\text{nm}}$ can be described as a function of the L-PMT peak voltage $U_{\text{L-PMT}}(t=0)$ using the following fitted relation:

$$E^{\text{pulse}}_{266\,\text{nm}} = F[U_{\text{L-PMT}}(t=0)] = a(e^{b\cdot U_{\text{L-PMT}}(t=0)} - 1). \quad (1)$$

The fitting constants in Eq. (1) have been obtained by a Levenberg-Marquardt fitting algorithm and are given by $a = (90 \pm 4)$ μJ and $b = (2.76 \pm 0.03)$ V^{-1}. The inverse relation of (1), i.e., $U_{\text{L-PMT}}(t=0) = F^{-1}(E^{\text{pulse}}_{266\,\text{nm}})$ is represented by a red line in Figure 2 and clearly shows a saturated behavior of the reference PMT from an early stage on.

The other reference PMT in Figure 1 (P-PMT) was placed behind identical optics as the currently investigated detector to serve as a reference for the incoming amount of light, assuming that phosphorescence was emitted isotropically from the phosphor target. Both L- and P-PMT were set to an identical gain of 6300 and relative transmission losses $T_{\text{L-PMT}}$ ($\approx 10^{-7}$) were introduced towards the laser reference in order to ensure similar peak output voltages for both references at all times.

C. Operating conditions

The total amount of phosphorescent light emitted per excitation event is a function of initial signal intensity I_0 and the phosphorescence decay time τ. It can be sufficiently described by integrating over the time-dependent phosphorescence intensity I, described by Eq. (2),

$$I = I_0 \cdot \exp\left(-\frac{t}{\tau}\right). \quad (2)$$

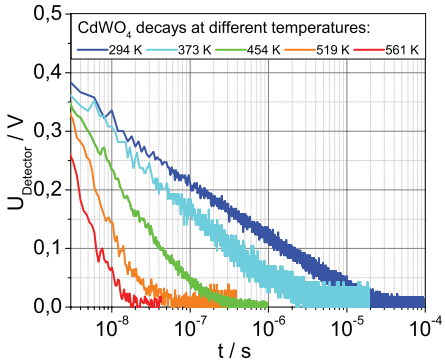

FIG. 3. Phosphorescence decay curves from $CdWO_4$ displayed at five different temperatures. As every detector yielded slightly different decays times, τ values are not explicitly given here but can be found in Figure 17 instead.

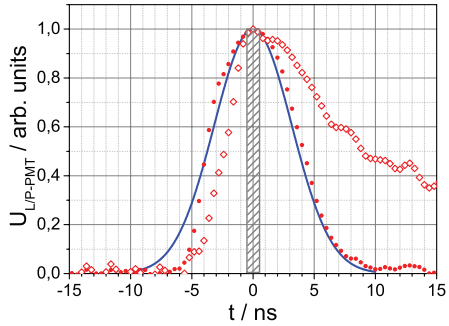

FIG. 4. Normalized signal profiles for both reference PMTs as a function of time. A Gaussian (solid blue line) has been plotted to illustrate similarities to the laser profile, expressed as solid red dots recorded by the L-PMT. The corresponding phosphorescence time response recorded by the P-PMT is represented by red hollow diamonds. A shaded box with a width of 1 ns has been centered on the signal maximum at $t = 0$.

It follows that detector saturation caused by incident light is dependent on both I_0 and τ, hence, the detector response would not only be altered by irradiances above a certain threshold ($I_0 > I_{\text{thresh}}$), but also by the time ($\sim\tau$) that the detector is exposed to elevated light intensities.

For this reason, I_0 and τ have been investigated independently by repeating each gain- and intensity variation experiment for a number of fixed phosphorescence decay times. Every detector listed in Table I was exposed to phosphorescence from a phosphor coated target kept at five specific temperatures in the tube furnace: 294, 373, 454, 519, and 561 K. Temperatures were measured using a K-type thermocouple (attached to the phosphor-coated target) and chosen such that there was a reasonable step size for the decay time in between two proximate temperatures, see Figure 3.

In order to address I_0 the authors decided to estimate the amount of photons, $N_\lambda^{\text{P-PMT}}[\text{U}_{\text{P-PMT}}(t=0)]$, reaching the detector within a time window of $\Delta t = 1$ ns, using the reference voltage from the P-PMT and the energy calibration from (1). The center of this time window coincides with the registered signal peak value of the phosphorescence curve ($t = 0$), as seen in Figure 4.

The laser pulse profile in Figure 4 is essentially a Gaussian function with a full width half maximum (FWHM) of fitted to be 7.46 ns. This is slightly broader compared to the laser manufacturer specification value of 6 ns because the reference detectors are partly saturated and have a limited signal rise time of 750 ps. Taking into account the radiant photocathode sensitivity being a function of wavelength λ ($S_{450\text{ nm}}/S_{266\text{ nm}} \approx 1.23$, see Ref. 15), the number of phosphorescence photons $N_\lambda^{\text{P-PMT}}$ arriving at $t = (0 \pm 0.5)$ ns can be estimated by Eq. (3):

$$N_\lambda^{\text{P-PMT}}[U_{\text{P-PMT}}(t=0)] \approx \frac{S_{266\,\text{nm}}}{S_\lambda} \cdot 2\sqrt{\frac{\ln 2}{\pi}} \cdot \frac{F[U_{\text{P-PMT}}(t=0)]}{E_\lambda^{\text{photon}}} \cdot \frac{\Delta t}{\text{FWHM}} \cdot T_{\text{L-PMT}}. \quad (3)$$

The Appendix covers a derivation of Eq. (3) as well as an error estimation for $N_\lambda^{\text{P-PMT}}$.

As the laser energy is scanned from 15 μJ to 5 mJ using an adjustable attenuator (see Figure 1), the phosphorescence intensity changes proportionally allowing the investigation of each detector's response to various intensities at several gain settings (see Table I). Figure 5 supports this approach as it shows a largely linear relation between the laser energy ($\sim$L-PMT signal) and phosphorescence signal (P-PMT) due to the fact that both reference detectors saturate similarly. However, some minor deviations from linearity can be observed at low laser energies.

III. RESULTS AND DISCUSSION

The phosphorescence decay time was evaluated based on a least squares fit algorithm (Levenberg-Marquardt) to a single-exponential function, see Eq. (1). To avoid contributions from changing fitting window positions to the evaluated results, a fixed evaluation time window was chosen for each temperature. However, the window size was adapted

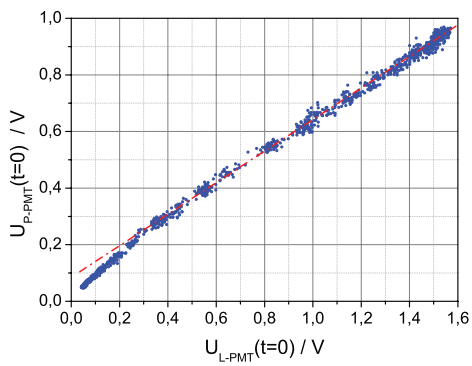

FIG. 5. Reference PMT peak signal voltages at gain 6300 corresponding to a full laser excitation energy scan from 15 μJ to 5 mJ at room temperature.

TABLE II. Fitting time window positions after the initial signal peak as a function of temperature.

Temperature / K	Start / s	Stop / s
294	10^{-8}	5×10^{-5}
373	10^{-8}	1×10^{-5}
454	10^{-8}	8×10^{-7}
519	10^{-8}	1.5×10^{-7}
561	10^{-8}	8×10^{-8}

according to the temperature in order to capture large parts of the decay, see Table II.

One exception from Table II has been made for the case of external current-to-voltage amplification: Due to the limited bandwidth of the amplifier the start of the evaluation window was set to 60 ns instead of 10 ns.

For obvious reasons, the recorded phosphorescence decay time is a measure of the time-distribution of the detector output signal: An ideal optical detector having a linear response should reproduce similar signal shapes leading to constant decay times, regardless the amount of incident light or the extent of internal signal amplification. This ideal case, however, is often far from reality as the authors have shown in Ref. 14. Two normalized decay curves displayed in Figure 6 have been measured from the same phosphorescence signal at room temperature using two different gain settings for the detector. Within the same observation window the evaluated decay time from PMT1 varied from 11 μs to 23 μs, i.e., more than a factor of two due to a change in detector gain. This behavior is supported by Figure 2, which indicated the nonlinear signal response of a similar PMT during laser energy calibration.

Figure 7 illustrates how the evaluated decay time varies as a function of gain setting and phosphorescence intensity at constant temperature. It has been produced without using the reference PMTs and displays the detector peak voltage $U_{\text{Detector}}(t = 0)$ instead of photon number on the x axis. The phosphorescence has been varied within the same intensity range for each detector gain. Also, the y axis displays the gain

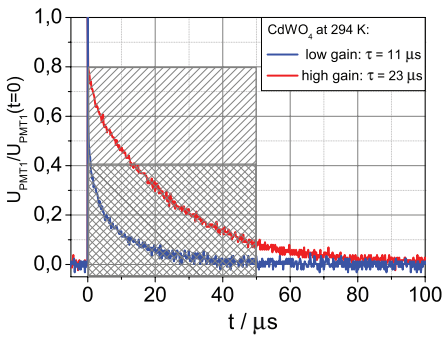

FIG. 6. Normalized time response of $CdWO_4$ phosphorescence, observed at 294 K by PMT1 using two different gain settings. The decay-time observation window for each curve has been indicated by the shaded boxes according to Table II.

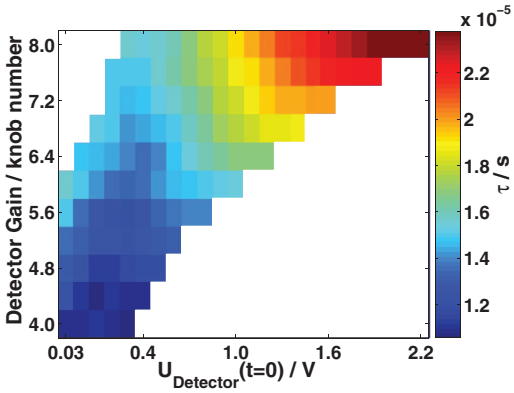

FIG. 7. Decay-time response surface of PMT1 at 294 K, shown in its original axes, gain knob number and detector peak voltage.

readout value as arbitrary unit "knob number" and translates into the control voltage for the detector. Using data sheets provided by the manufacturers (see Ref. 15), this control voltage has been converted into actual gain values later on to allow a more general gain comparison between different detectors. $U_{\text{Detector}}(t = 0)$ is dependent on both incident light flux and detector gain, leaving large matrix parts empty in Figure 7. It is thus impossible to distinguish effects from gain and incident light on the detected decay time from this plot. However, Figure 7 offers the clear advantage of showing actual reading values, allowing the experimenter to judge stability towards changes in operating condition while performing measurements. It is interesting to note that varying signal intensities in experiments cannot be compensated by changing the detector gain without affecting the decay signal shape. This comes clear when following a constant peak voltage across several gain columns with respect to the decay time, for example at $U_{\text{Detector}}(t = 0) = 0.3$ V.

Figure 8 shows the detector response surface for PMT1 at 373 K, now displayed as a function of gain and photon number according to Eq. (3). The evaluated decay time is

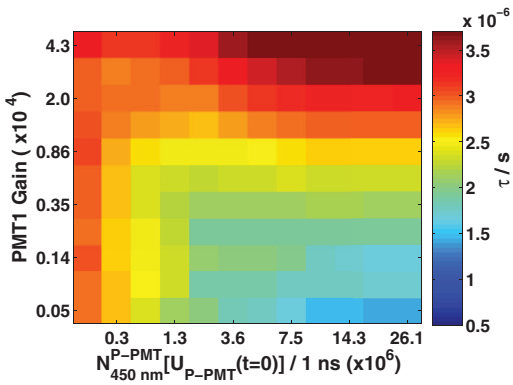

FIG. 8. Response surface of PMT1 at 373 K.

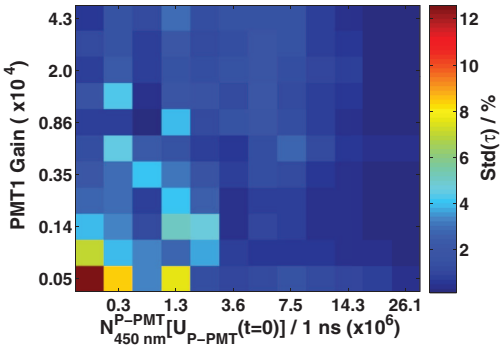

FIG. 9. Decay time standard deviation at 373 K using PMT1, normalized by the value of each matrix element in Figure 8.

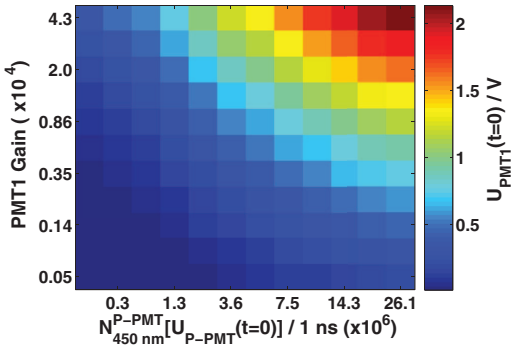

FIG. 11. Detector peak voltage of PMT1 during gain/intensity response tests at 373 K.

represented by a color scale as a function of gain and photon impingement within 1 ns at signal peak levels. Every matrix element contains contributions of 10–500 single decays, each evaluated individually before averaging. In the upper right region at high gains and photon numbers the evaluated decays are longer. As this behavior changes with gain, it can be identified as a detector artifact, caused by saturation. The lower right area in Figure 8 has a rather constant decay-time distribution, which is desirable for phosphorescence measurements. For low light exposures, there is a lifetime gradient visible that is gain-independent. It will be discussed in the context of further findings later on.

Figure 9 provides information on the measurement precision within this study. It shows the decay time standard deviation of the response matrix in Figure 8 normalized by each individual pixel average. Except for the lower left corner in Figure 9, where weak signals were recorded due to low light intensities and gains, the standard variation is well below 5%. It indicates the results to be reproducible to a large degree, which has also been confirmed by direct comparison with repeated measurements.

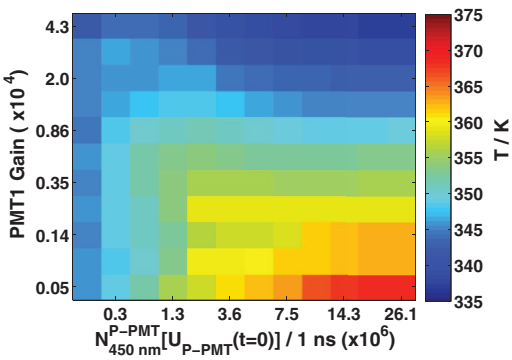

FIG. 10. Artificial temperatures, calculated from Figure 8 using previous temperature calibration data. The actual phosphor temperature was kept constant at 373 K.

Figure 10 uses a temperature calibration of $CdWO_4$, produced within a previous study (see Ref. 14) in order to calculate artificial temperatures from the detector matrix in Figure 8. It should be highlighted at this point, that all measurement data from Figure 10 has been acquired at a constant temperature of 373 K and that the temperature distribution shown is a consequence of nonlinear measurement response. The temperature distribution observed from Figure 10 spans across 40 K, which represents more than 13% of the phosphor's original temperature sensitivity range. Furthermore, $CdWO_4$ has a decay-time characteristic that changes 3 orders of magnitude within a temperature interval of merely 300 K. Since artificial temperatures, retrieved by temperature calibration curves highly depend on the sensitivity of the phosphor, it should be noted that most other phosphors are less sensitive than $CdWO_4$ and will thus exhibit an even higher spread of artificial temperatures.

Figure 11 displays the detector peak voltage of PMT1 during the acquisition of a response matrix at 373 K (see Figure 8). The signal peak voltage reaches a maximum of 2 V in the upper right corner of the plot. However, more than half the data points from Figure 11 were derived from signals with peak voltages of 500 mV or below, i.e., output values that previously in Figure 2 seemed to correspond to a linear detector response. In contrast, Figures 8 and 10 indicate vast decay-time gradients from these regions demonstrating superior sensitivity for highlighting detector nonlinearities.

Figure 12 shows the same detector arrangement as in Figure 8, now tested at 561 K. Lower phosphorescence quantum yields at elevated temperatures caused the last photon number column to be empty. The two elements that made an exception contain just a single decay each, caused by random laser fluctuation. Also the area of saturation in the upper right corner retreated to some extent, which is likely to be caused by shorter decays limiting the space charge build-up time at the end of the dynode chain.[16–18] The lifetime gradient for low light intensities (present in Figure 8) has vanished and some elements at low gains and intensities remained empty due to signal-to-noise (S/N) issues at shorter decays.

In Figure 13 another PMT (PMT2) was exposed to phosphorescence radiation at 373 K. The gain range was

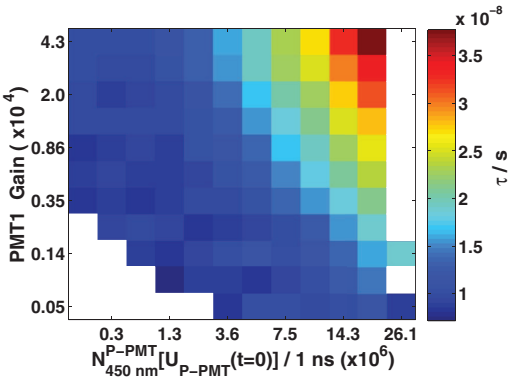

FIG. 12. Response surface of PMT1 at 561 K.

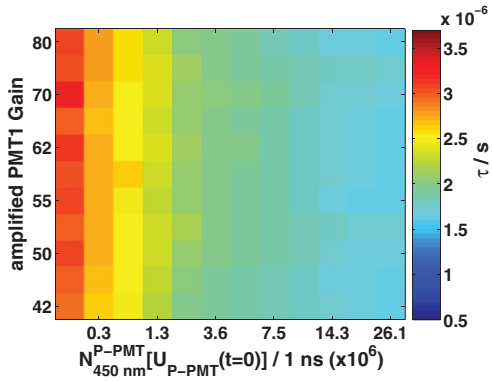

FIG. 14. Response surface of PMT1 (amplified) recorded at 373 K.

chosen smaller this time in order to limit signal output currents. PMT2 had a significantly higher sensitivity around 450 nm compared to PMT1. The upper gain region ended at 7700, which is where PMT1 in Figure 8 still was not influenced by the saturated region of high gain and intensity. In accordance to these results, Figure 13 does not show any saturation limits for the high signal regions, which makes it a preferable device for phosphor thermometry in comparison to PMT1.

However, the lifetime gradient for the low light level region is still present and stretches across the same range of intensities as observed with PMT1, i.e., for excitation energies lower than 30 μJ (peak phosphorescence $<1.3 \times 10^6$ photons/ns). This might suggest the phosphor as a possible cause, which is supported by the deviation from a linear relation at low laser energies between the two reference PMTs in Figure 5. Moreover, similar findings have been reported by Ref. 10, showing the phosphorescence decay time of another phosphor, Mg_4FGeO_6:Mn, decreasing for increasing laser excitation energies. PMT2 has another advantage, which is being capable of operating in time-gated mode. This enables suppression of fluorescence peaks that might superimpose with incipient phosphorescence, allowing a more efficient utilization of the dynamic output range.[14] Since the saturated region was not reached during experiments with PMT2, time-gated results showed very little variation to the presented plots.

Using PMT1 together with the external current-to-voltage amplifier resulted in reasonable signal levels at much lower PMT gain settings, but came at the cost of reduced temporal resolution. This helps avoiding detector saturation as seen in Figure 14, but also bandwidth-limits the retrieval of shorter decays, i.e., the amplifier confines the detection limit at high temperatures rather than the phosphor.

Figure 15 presents the detector response surface of the MCP-PMT at 373 K, with the gate opening 10 ns prior to the phosphorescence onset. Even though output currents have been four times higher for the MCP-PMT compared to PMT1 (Figure 8), this device seems not to be affected by high signal saturation. Therefore, cutting off the first intense part of the phosphorescence by triggering the gate to open 10 ns after the signal's peak voltage did not show a significant difference.

Finally, Figure 16 displays decay-time results, accumulated by using the APD at 373 K. A significant amount of data for the low light intensities has been rejected by the

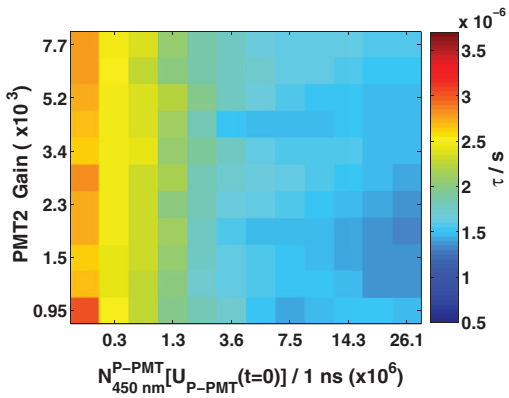

FIG. 13. Response surface of PMT2 at 373 K.

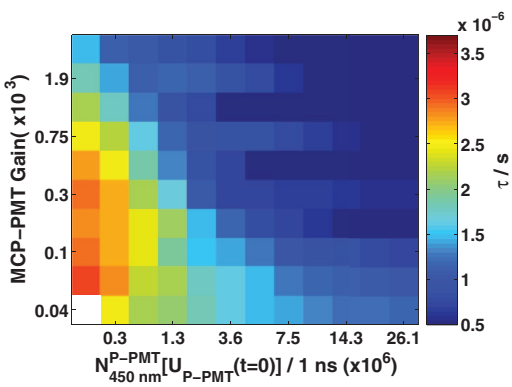

FIG. 15. Response surface of MCP-PMT at 373 K, triggered 10 ns before the signal arrived.

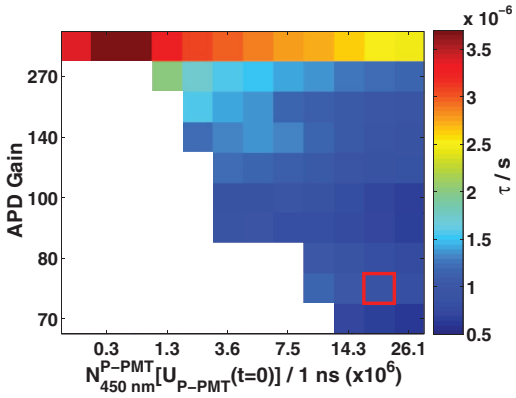

FIG. 16. Response surface of APD at 373 K.

S/N-criteria during evaluation. This is mainly due to the comparatively high transmission losses in the optical fiber coupling. In addition, the moderate gain range accessible for the APD contributed to recorded signal intensities being less than $\frac{1}{2}$ compared to the other detectors. Other than that, the evaluated decay time seems to be stable for the majority of the displayed workspace, except for the row where the gain was highest. This feature at maximum gain appears for all other temperatures that the APD has experienced and indicates that the APD has approached its global gain limit.

In Figure 17 temperature calibration curves for $CdWO_4$ are plotted, showing evaluated decays for five temperatures from all four detectors under investigation.

Since the decay-time distribution within one response surface can vary to a substantial extent, the points displayed in Figure 17 only describe data from a single fixed matrix element (fixed gain and light intensity). In order to represent a fairly linear part of the workspace as well as having data available for most of the detectors the chosen element corresponds to the second lowest gain at second highest light exposure, i.e., originates from the lower right corner of each surface plot (see red square in Figure 16).

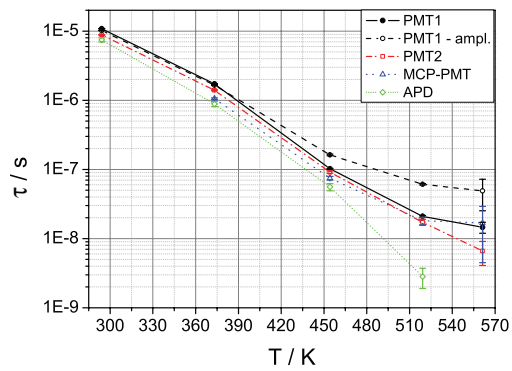

FIG. 17. Temperature calibration points for all detectors from a fixed response matrix element. Error bars indicate one standard deviation from the mean value.

The external amplification of the PMT1 signal shows a systematic effect on the evaluated lifetime. The loss in bandwidth forced the evaluation window to start later in the decay curve at 60 ns compared to the other detectors. This, accompanied with the slight multi-exponential phosphorescence behavior of $CdWO_4$, accounts for the prolonged decay times that were evaluated here. The result is decreased temperature sensitivity and the inability to measure accurate decays shorter than the signal broadening that is caused by the 5 MHz limited amplifier bandwidth.

For the MCP-PMT the lowest temperature is missing. This is due to the fact that the maximum gate length was restricted to 10 μs, corresponding to only 1/5 of the sampling time used for the other detectors (see Table II).

The APD proved to exhibit the highest lifetime sensitivity within all investigated detectors. However, the low signal output appeared to be one major restriction leaving no useful data for the highest temperature case.

For clarity, the two operational modes, where the first 10 ns were cut off by time-gating, were omitted. They carried no further relevant information, but were slightly shifted towards longer decays. The change in decay time can be attributed to the slight multi-exponential shape of $CdWO_4$ phosphorescence accompanied by a fitting window that shifted 10 ns towards a later part of the decay curve.

IV. CONCLUSIONS

Evaluated exponential decays from laser-induced phosphorescence proved to be strongly biased by incoming light intensity, electrical gain and individual properties of each photo detector. It was shown that phosphorescence intensity variations in experiments cannot generally be compensated by adjusting the detector gain without affecting the calculated decay time. Under the investigated operating conditions, the evaluated decay time most commonly varies by a factor of two across an individual response matrix. These response matrices were found to be much more sensitive to nonlinearities than what had been a corresponding signal strength comparison between in- and output (compare Figures 2 and 8). In some cases the maximum decay time can be as much as six times longer than its minimum counterpart for a given temperature (see Figure 15). Clearly, variations of this magnitude add decisive distortions to temperature readings in phosphor thermometry, making detector linearity a key aspect for applications with varying signal intensities. Especially, deviations of signal intensities between calibration and experiment may inflict major systematic temperature errors if detectors are operated outside their linear workspace. Longer decay curves were in general more distorted by gain- and light variations than shorter decay curves at higher temperatures.

All detectors that were involved in this study showed a declining decay-time gradient, visible within the first four intensity columns. The gradient vanished as temperatures rose and the signal decays became shorter. This behavior will be subject for further investigation and is suspected to be phosphor related, as suggested by its gain- and detector independence.

PMT2 (gateable) achieved the best performance amongst all tested devices, providing a large linear workspace without being compromised by additional bandwidth limitations of an external amplifier. Its capability to operate time-gated has not proved its full potential in combination with $CdWO_4$, but is believed to improve linearity for phosphors that exhibit strong fluorescence peaks along with the phosphorescent decay, as proposed in Ref. 14. The MCP-PMT could only run in time-gated mode and the maximum gate length was limited to 10 μs, which is a drawback for phosphors with longer decay times. Performing external signal amplification proved to be useful, helping to limit signal saturation in the conventional PMT (PMT1) while maintaining reasonable signal outputs. Its limited bandwidth, however, affected the detection sensitivity for decays, shorter than 200 ns (see Figure 17). The APD's capability to reproduce short decays is superior to any other detector within this comparison study. Nevertheless, signals acquired with the avalanche photodiode exhibited the lowest signal intensities and originated from a very limited gain range. Yet, the former drawback might be of individual nature as the design of the APD's external housing demanded fiber-optical signal collection, accompanied by relatively high coupling losses.

In summary, this study presents a concept of mapping individual detector responses to gain- and light level variations. It can be used for creating a library of decay response curves allowing to correct evaluated decays from measurements performed outside the linear workspace.

ACKNOWLEDGMENTS

This work was financially supported by the HELIOS research project within the European Union's (EU) 7th Framework program for Research and Technical Development/Transportation (Contract No. 030696) and the D60L-2 project financed by the Swedish Energy Agency. The authors would like to acknowledge Ronald Whiddon for helpful discussions.

APPENDIX: DERIVATION AND ERROR ESTIMATION OF $N_\lambda^{\text{P-PMT}}$

This section covers a step-by-step derivation of $N_\lambda^{\text{P-PMT}}$, followed by an error estimation. Figure 4 serves as a starting point indicating that $U_{\text{L-PMT}}(t)$ essentially is a Gaussian function with a full width half maximum of around FWHM = 6 ns. It is assumed that $U_{\text{L-PMT}}(t)$ is proportional to the optical Power $P(t)$ of the laser pulse, followed by the conclusion that the time integral over $U_{\text{L-PMT}}(t)$ can be normalized by a factor f_n to correspond to the laser pulse energy:

$$E_{266\,\text{ns}}^{\text{pulse}} = f_n \int_{-\infty}^{\infty} U_{\text{L-PMT}}(t)\mathrm{d}t = \int_{-\infty}^{\infty} P(t)\mathrm{d}t = \frac{E_{266\,\text{ns}}^{\text{pulse}}}{\sigma\sqrt{2\pi}} \int_{-\infty}^{\infty} e^{-\frac{1}{2}\left(\frac{t}{\sigma}\right)^2}\mathrm{d}t. \quad \text{(A1)}$$

In Eq. (A1), σ is the standard deviation and related to the full width half maximum of the Gaussian function by

$$\text{FWHM} = 2\sqrt{2\ln 2}\cdot\sigma. \quad \text{(A2)}$$

An energy fraction centered on the laser pulse maximum can be described by Eq. (A3) and further simplified if the time window Δt is reasonably small compared to the Gaussian standard deviation σ,

$$E_{266\,\text{ns}}^{\Delta t}(t=0) = \frac{E_{266\,\text{ns}}^{\text{pulse}}}{\sigma\sqrt{2\pi}} \int_{-\frac{\Delta t}{2}}^{\frac{\Delta t}{2}} e^{-\frac{1}{2}\left(\frac{t}{\sigma}\right)^2}\mathrm{d}t \overset{\Delta t \ll \sigma}{\approx} \frac{1}{\sqrt{2\pi}} \cdot E_{266\,\text{ns}}^{\text{pulse}} \cdot \frac{\Delta t}{\sigma}. \quad \text{(A3)}$$

Taking into account the calibration of $U_{\text{L-PMT}}(t=0)$ against laser pulse energy from Eq. (1) as well as replacing σ with FWHM using (A2), transforms Eq. (A3) into the following expression:

$$E_{266\,\text{ns}}^{\Delta t}[\text{U}_{\text{L-PMT}}(t=0)] \approx 2\sqrt{\frac{\ln 2}{\pi}} \cdot F[U_{\text{L-PMT}}(t=0)] \cdot \frac{\Delta t}{\text{FWHM}}. \quad \text{(A4)}$$

The energy area corresponding to (A4) is represented in Figure 4 by the shaded rectangular box. Provided that the energy of one single laser photon can be expressed by $E_{266\,\text{nm}}^{\text{photon}} = hc/\lambda_{266\,\text{nm}}$, with h representing Planck's constant and c given by the speed of light, Eq. (A4) allows estimating the amount of laser photons $N_{266\,\text{nm}}^{\text{phosphor}}$ arriving at the phosphor target within Δt,

$$N_{266\,\text{nm}}^{\text{phosphor}}[U_{\text{L-PMT}}(t=0)] \approx 2\sqrt{\frac{ln2}{\pi}} \cdot \frac{F[U_{\text{L-PMT}}(t=0)]}{E_{266\,\text{nm}}^{\text{photon}}} \cdot \frac{\Delta t}{\text{FWHM}}. \quad \text{(A5)}$$

In the next step the number of phosphorescence photons $N_\lambda^{\text{P-PMT}}$ arriving at the detector within Δt is estimated from the peak voltage $U_{\text{P-PMT}}(t=0)$ of the phosphorescence reference PMT. To do so, it is assumed that the phosphor is an isotropic light radiator with both phosphorescence detectors being placed at similar distances. Additionally, collection optics in front of both detectors are required to exhibit identical spectral transmission characteristics. These two assumptions imply that statistically the same amount of phosphorescence photons impinge on both detectors at all times permitting to focus on the P-PMT henceforth. Both reference PMTs (L- and P-) are of identical type and were set to the same constant gain of 6300. However, additional transmission losses have been introduced in front of the L-PMT to keep signal levels comparable to those recorded by the P-PMT reference, see Eq. (A6),

$$T_{\text{L-PMT}} = \frac{R_{\text{quartz}}}{T_{\text{quartz}}} \cdot T_{\text{mirror}}^2 \cdot T_{\text{lens}}. \quad \text{(A6)}$$

These transmission losses were automatically accounted by the calibration in (1), but have to be considered when comparing peak voltages from both reference detectors. Consequently, a correction as described in (A7) is needed.

$$N_\lambda^{\text{P-PMT}}[U_{\text{P-PMT}}(t=0)] = N_\lambda^{\text{phosphor}}[U_{\text{P-PMT}}(t=0)] \cdot T_{\text{L-PMT}}. \quad \text{(A7)}$$

Finally, the spectral radiant sensitivity of the photocathode S_λ (unit: mA/W) needs to be considered since phosphorescence appears red-shifted relative to its laser radiation. For convenience it was previously assumed in (A7) that the phosphorescence wavelength was identical to the laser wavelength such that no wavelength correction was needed as yet. S_λ determines the amount of cathode current I_{cathode} resulting from the transfer of optical power at a given wavelength to the photocathode. The output voltage is related to the cathode current via the load resistance R_{load} and gain as described in Eq. (A8),

$$U_{\text{L/P-PMT}}(t) = I_{\text{anode}}(t) \cdot R_{\text{load}} = I_{\text{cathode}}(t) \cdot \text{gain} \cdot R_{\text{load}}. \tag{A8}$$

It should be mentioned that in case of saturation the gain factor can be a function of the cathode current and due to accumulation of space charge even be a function of earlier gains and cathode currents. Since the amount of photons, needed for a given cathode current is wavelength dependent, the photon numbers for different wavelengths translate into each other according to Eq. (A9),

$$I_{\text{cathode}} = S_{\lambda_1} \cdot \frac{N_{\lambda_1}}{\Delta t} \cdot E_{\lambda_1}^{\text{photon}} = S_{\lambda_2} \cdot \frac{N_{\lambda_2}}{\Delta t} \cdot E_{\lambda_2}^{\text{photon}}$$

$$\Rightarrow N_{\lambda_2} = \frac{S_{\lambda_1}}{S_{\lambda_2}} \cdot \frac{E_{\lambda_1}^{\text{photon}}}{E_{\lambda_2}^{\text{photon}}} \cdot N_{\lambda_1}. \tag{A9}$$

Finally, inserting (A5) and (A7) into (A9) provides an estimate for the number of phosphorescence photons arriving at the detector within a time window Δt centered around $t = 0$:

$$N_\lambda^{\text{P-PMT}}[U_{\text{P-PMT}}(t=0)] \approx \frac{S_{266\,\text{nm}}}{S_\lambda} \cdot 2\sqrt{\frac{\ln 2}{\pi}} \cdot \frac{F[U_{\text{P-PMT}}(t=0)]}{E_\lambda^{\text{photon}}} \cdot \frac{\Delta t}{\text{FWHM}} \cdot T_{\text{L-PMT}}. \tag{A10}$$

In order to estimate the propagated measurement uncertainty $\Delta N_\lambda^{\text{P-PMT}}$ from (A10) all individual errors (listed in Table III) need to be taken into consideration.

Δt, given by the sampling rate, was assumed to be a fixed value without error. However, the PMT readout voltage is indirectly related to Δt and ΔFWHM, because $\Delta U_{\text{P-PMT}}$ comprises the deviation of the Gaussian from its peak value within Δt as well as the fact that sampling points are unlikely to hit the exact center of the laser pulse. The latter of these two errors counteracts the former one. The wavelength error $\Delta\lambda$ was given by two standard deviations, assuming that the spectral bandpass filter has a Gaussian spectral transmittance with FWHM = 40 nm. Certainly, ΔT_{loss} has the biggest impact on measurement uncertainty (see Table III). Its value has been calculated by propagating uncertainties from individual transmission objects, listed in Eq. (A6). The reason for ΔT_{loss} being in the order of 23% can be attributed mainly to the two mirror transmissions, each having a relative uncertainty of around 10% due to their very low transmission value of around $T_{\text{mirror}} = 1.875 \times 10^{-3}$. The total measurement uncertainty is described by Eq. (A11) and has been plotted in Figure 18 using the values from Table III,

$$\Delta N_\lambda^{\text{P-PMT}} = N_\lambda^{\text{P-PMT}} \cdot \left[\left(\frac{\Delta S_{266\,\text{nm}}}{S_{266\,\text{nm}}} \right)^2 + \left(\frac{\Delta S_\lambda}{S_\lambda} \right)^2 + \left(\frac{\Delta \text{FWHM}}{\text{FWHM}} \right)^2 + \left(\frac{\Delta\lambda}{\lambda} \right)^2 + \left(\frac{\Delta T_{\text{L-PMT}}}{T_{\text{L-PMT}}} \right)^2 + \left(\frac{\Delta a}{a} \right) + \left(1 + \frac{a}{F} \right)^2 \cdot (\Delta b^2 \cdot U_{\text{P-PMT}}^2 + \Delta U_{\text{P-PMT}}^2 \cdot b^2)^2 \right]^{\frac{1}{2}}. \tag{A11}$$

Figure 18 displays the number of photons calculated as a function of $U_{\text{P-PMT}}(t = 0)$ together with the measurement uncertainty to be seen as error bars. Measurement points have been chosen to match the photon axis from all response surface plots.

TABLE III. Individual error estimates of all quantities in Eq. (A10).

Description	Symbol	Value	Error value	Unit
Radiant cathode sensitivity	$S_{266\,\text{nm}}$	43	1	mA/W
Radiant cathode sensitivity	$S_\lambda(\lambda = 450\,\text{nm})$	53	1	mA/W
Fitting constant from *F*, Eq. (1)	a	90.0	3.8	μJ
Fitting constant from *F*, Eq. (1)	b	2.759	3.0×10^{-2}	V^{-1}
P-PMT readout voltage	$U_{\text{P-PMT}}$	Variable	1.26	% (V)
Phosphorescence wavelength	λ	450	34	nm
Photon time window	Δt	1	0	ns
Laser pulse width	FWHM	6	1.15	ns
Optical transmission infront of L-PMT	T_{loss}	9.2	2.1	10^{-8}

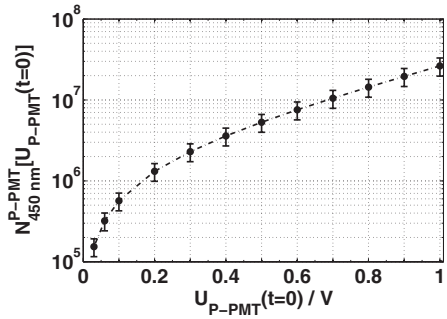

FIG. 18. Photon number as a function of P-PMT peak voltage showing intervals of uncertainty, calculated by Eq. (A11).

[1] S. W. Allison and G. T. Gillies Rev. Sci. Instrum. **68**, 2615 (1997).
[2] A. H. Khalid and K. Kontis, Sensors **8**(9), 5673 (2008).
[3] M. Aldén, A. Omrane, M. Richter, and G. Särner, Prog. Energy Combust. Sci. **37**(4), 422 (2011).
[4] A. Omrane, F. Ossler, and M. Aldén, Proc. Combust. Inst. **29**, 2653 (2002).
[5] T. Kissel, E. Baum, A. Dreizler, and J. Brübach, Appl. Phys. B **96**, 731 (2009).
[6] Y. R. Chen and K. L. Bray, Phys. Rev. B **56**, 10882 (1997).

[7]J. Brübach, A. Dreizler, and J. Janicka, Meas. Sci. Technol. **18**, 764 (2007).
[8]S. W. Allison, D. L. Beshears, T. Bencic, W. A. Hollerman, and P. Boudreaux, "Development of temperature-sensitive paints for high temperature aeropropulsion applications," AIAA Paper No. 2001-3528, 2001.
[9]R. M. Ranson, C. B. Thomas, and M. R. Craven, Meas. Sci. Technol. **9**, 1947 (1998).
[10]J. Brübach, J. P. Feist, and A. Dreizler, Meas. Sci. Technol. **19**, 025602 (2008).
[11]C. Knappe, P. Andersson, M. Algotsson, M. Richter, J. Lindén, M. Aldén, M. Tunér, and B. Johansson, SAE Int. J. Engines **4**, 1689 (2011).
[12]J. R. Lakowicz, *Principles of Fluorescence Spectroscopy* (Springer Science + Business Media, New York, 2006), p. 141.
[13]J. Lindén, C. Knappe, M. Richter, and M. Aldén, Meas. Sci. Technol. **23**, 035201 (2012).
[14]C. Knappe, J. Lindén, F. Abou Nada, M. Richter, and M. Aldén, Rev. Sci. Instrum. **83**, 034901 (2012).
[15]See http://sales.hamamatsu.com/assets/pdf/parts_H/H6780-04.pdf for H6780-04 PMT Datasheet.
[16]R. W. Engstrom, J. Opt. Soc. Am. **37**, 420 (1947).
[17]D. H. Hartman, Rev. Sci. Instrum. **49**, 1130 (1978).
[18]H. Kunz, Metrologia **5**, 88 (1969).

Precision in 2D temperature measurements using the thermographic phosphor BAM

Johannes Lindén, Christoph Knappe, Mattias Richter and Marcus Aldén

Paper VII

Published in: Meas. Sci. Technol. **23**(8):085205, 2012.

IOP Publishing Measurement Science and Technology
Meas. Sci. Technol. **23** (2012) 085205 (9pp) doi:10.1088/0957-0233/23/8/085205

Precision in 2D temperature measurements using the thermographic phosphor BAM

J Lindén, C Knappe, M Richter and M Aldén

Division of Combustion Physics, Lund University, Box 118, S-22100, Lund, Sweden

E-mail: johannes.linden@forbrf.lth.se

Received 23 March 2012, in final form 22 May 2012
Published 28 June 2012
Online at stacks.iop.org/MST/23/085205

Abstract
Investigation of optimized spatial precision for surface temperature measurements is performed. The temperature is measured by means of two-color ratio imaging with ICCD cameras, using the thermographic phosphor BAM. The precision in temperature is put in relation to the spatial resolution, two quantities which involve a trade-off in this case: the more spatial smoothing the better precision, but also the worse spatial resolution. Two different setups are used in order to investigate the influence of laser shot-to-shot variations, the flat-field correction and image registration process on the precision. In order to achieve high precision it is crucial to operate the ICCD cameras with a gain setting that does not introduce nonlinearity effects at the present level of irradiance. The results provide guidance on the precision to be expected from surface temperature measurements using the two-color ratio technique in combination with thermographic phosphors and also confirm the importance of highly stable and linear ICCD detectors. At room temperature and low spatial resolution the precision is evaluated to 0.4%.

Keywords: laser-induced phosphorescence, thermographic phosphors, thermometry, ICCD detectors

(Some figures may appear in colour only in the online journal)

1. Introduction

Thermographic phosphors have been a subject for development of thermometry techniques for several decades and are used in many applications, e.g., combustion research on reciprocating engines and gas turbines [1–6]. By utilizing the phosphorescence temperature sensitivity, measurements can be done over a wide range of temperatures, depending on the choice of phosphor. The phosphorescence from thermographic phosphors shows temperature dependence in two ways: both the spectral profile and/or the lifetime of the phosphorescence may change with temperature. The former property is often used for two-dimensional (2D) surface measurements using ICCD (intensified charge coupled device) cameras and the latter for point measurements using photomultiplier tubes for detection. This paper will consider the former technique.

When performing 2D surface temperature measurements using thermographic phosphors, either two cameras or one camera equipped with a stereoscope is used, in order to capture two images of the probed area [7]. The two images are obtained through different optical filters, which are chosen with respect to the spectral properties of the phosphor used. As the temperature changes, the intensity through the different filters will change, relative to each other. The relation between the different wavelength intensities is dependent on temperature, and thus, by dividing one image by the other, pixel by pixel, a ratio map of the surface is achieved. This ratio is translated into temperature by the use of a pre-defined ratio-to-temperature relation constructed from calibration measurements at controlled reference temperatures.

The precision achieved when performing 2D temperature measurements using thermographic phosphors is often estimated on the basis of the signal-to-noise ratio (S/N), the

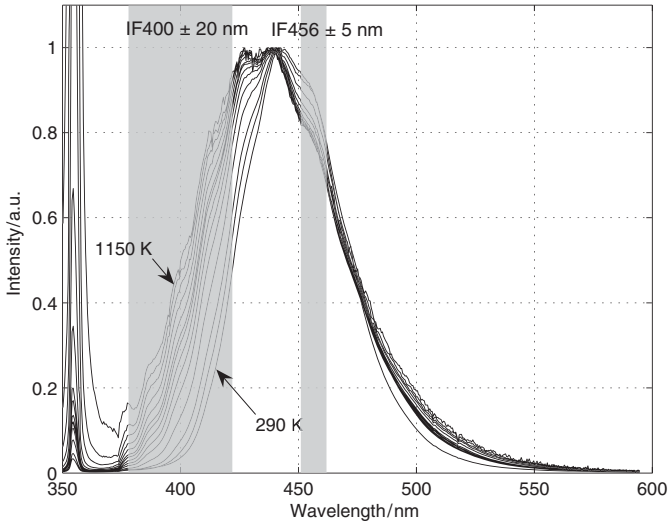

Figure 1. BAM emission spectrum at different temperatures when excited with 355 nm laser radiation. The exposure time of the ICCD camera connected to the spectrometer is 8 μs. The spectral properties of the interference filters used are marked out.

temperature sensitivity of the phosphor or the temporal and spatial repeatability. The amount of statistics varies, and the precision is seldom put in relation to the spatial resolution. The precision of the measured temperature depends on several factors. The most decisive one is of course how sensitive to temperature variations the phosphor is in the investigated temperature range, i.e. the change in spectral ratio as a function of temperature change.

Other factors that influence the precision are background and flat-field corrections, i.e. compensating for dc light contributions and pixel-to-pixel sensitivity variations on the CCD chip, respectively. In this work, it is experienced that the exposure time affected the flat field and by extension both accuracy and precision. Therefore, care needs to be taken when recording the flat-field image regarding the gain and exposure time settings. Other properties of the detection systems can also affect the precision, such as drift in sensitivity over time or nonlinear effects of ICCD cameras, which is especially crucial in two-color ratio techniques [8–11]. A final factor that affects precision is the quality of the image registration process, where geometric image correction such as warping and alignment is needed to ensure that corresponding pixels in the two images contain data from the same point in the image plane. This is done in order to superimpose the two images and generate an intensity ratio image. Here, software smoothing of the phosphorescence images before division would enhance the precision in temperature, since the precision of the overlap becomes less critical.

This paper describes the variations of the pixel-to-pixel precision (spatial precision) of the temperature at various spatial resolutions using the thermographic phosphor $BaMg_2Al_{16}O_{27}$:Eu (BAM), a blue emitting phosphor when illuminated with UV light, and Princeton PIMAX-II ICCD cameras.

BAM emits a spectrally broad phosphorescence peak around 440 nm, which broadens toward shorter wavelengths with increasing temperature, see figure 1. The phosphorescence has a constant lifetime of about 2 μs at room temperature up to about 700 K and decreases to about 10 ns at 1150 K. With two interference filters, one 10 nm wide (FWHM) centered at 456 nm and one 40 nm wide (FWHM) centered at 400 nm, a temperature-dependent intensity relation can be observed, when the phosphorescence intensity at 400 nm increases with temperature relative to the phosphorescence emission at 456 nm. The selection of wavelength and the spectral width of the interference filters were optimized using a simulation based on the measured emission spectra [12]. Dividing the intensity in these images by each other, pixel by pixel, will result in a temperature-dependent ratio image. These ratios are then translated into temperature using a pre-defined calibration curve achieved from measurements performed in controlled environments. The resulting ratio, and thus the resulting temperature, then becomes independent of the overall phosphorescence intensity and laser excitation intensity. BAM exhibits temperature sensitivity from room temperature up to 1150 K [12]. However, degradation at elevated temperatures may restrict its use for thermometry to below 800 K [13]. BAM is commercially used as the blue emitting component in fluorescent lamps and plasma display panels [14].

2. Experimental work

Performing 2D temperature measurements using the approach described above includes several sources of error. Such error can be caused by using a stereoscope, as it may introduce artifacts due to internal reflections and, as mentioned above,

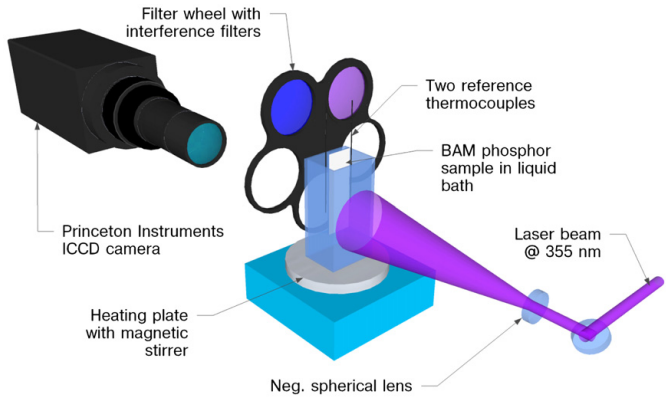

Figure 2. Experimental setup for the single-camera experiment.

by image processing such as image registration and flat-field corrections.

The experiment presented here is performed in two setups, neither of which uses a stereoscope. The first uses only one camera, in front of which the filters are switched. There is thus no need for either image registration or flat-field correction in this case. However, with this setup, measurements cannot be performed in a single shot, making it more sensitive to shot-to-shot laser energy fluctuations and temperature variations. In the second setup, two cameras and a cubic beam splitter mirror are used, and measurements can be performed in a single shot. These two different setups are used in order to investigate the impact of image registration, flat-field corrections and shot-to-shot variations on the calculated temperature field.

For both setups a 10 Hz pulsed Nd:YAG laser, working at its third harmonic and producing laser emission at 355 nm, is used to excite the phosphor. Because of the high quantum efficiency of BAM (80%–95%) [13, 15, 16], the laser power required is very low, <1 mJ. Considering the expansion of the laser beam, enhanced using a negative lens, the fluence illuminating the measured surface is calculated to be about 5 μJ cm^{-2}.

Since the aim of this study is to investigate the measurement precision of the 2D phosphor thermometry technique, it is crucial to establish a reference surface with an even temperature distribution. For this purpose, the phosphorescent material is coated onto a thin glass plate (1 mm) that is joined together with another glass plate to form a hermetically sealed cell with the phosphor between the two glass plates. This cell is then submerged in a liquid bath. The liquid, with high heat capacity, will disperse heat and buffer against rapid temperature variations. At lower temperatures, i.e. between 273 and 373 K, water is used as the dispersing fluid. To extend the temperature range complementary measurements are performed with glycerol, which has a boiling point of 563 K. The liquid bath is placed on an electrical heating plate equipped with a magnetic stirrer. Due to the limited capacity of the heater the maximum temperature achieved is 470 K. The temperature in the bath is measured with two K-type thermocouples, providing an accuracy of $\pm$1.5 K within the observed temperature range. The calibrated thermocouples will act as a reference in this study; hence, the accuracy of the temperatures retrieved from the phosphor measurements will never be better than the accuracy of the thermocouples. However, as this study focuses on the precision, the absolute temperature is only of secondary importance. In order to verify any potential offset for the thermocouple readings an initial measurement is performed in an ice-bath (273 K). During a measurement the temperature from the two thermocouples was logged and thanks to the magnetic stirrer the standard deviation of the temperature stayed below 0.2 K during all measurements.

Figure 2 shows the first experimental setup, using only one camera. The laser beam is guided and expanded via a mirror and lens system to illuminate the thermographic phosphor inside the cell. A filter wheel loaded with the mentioned filters is located on the camera side of the liquid bath. The reason for the position of the filter wheel, close up to the liquid bath and not immediately in front of the camera lens, is an image distortion caused by the internal design of the filters. With the filters directly in front of the camera, both focus and image positions on the camera chip change with different filters. By placing the filters close to the surface to be measured, these effects are minimized. With this filter position the phosphor sample needs to be illuminated from the backside, the reason for the phosphor being coated onto a glass plate.The phosphorescence seen through the filters is captured by a PIMAX II ICCD camera (Princeton Instruments).

Figure 3 shows the experimental setup for the dual-camera setup, involving two nominally identical PIMAX II ICCD cameras. A cubic beam splitter allows the cameras to observe the target from virtually identical positions. The cubic beam splitter was preferable to a semi-transparent optical flat mirror, because of the risk of artifacts caused by internal reflections in the mirror. In contrast to the single-camera setup, the phosphor cell is illuminated from the front, with a slight angle. This is possible in this setup since the interference filters are now placed at the very front of the cameras.

For both setups, the cameras are trigged by the laser and the exposure time is set to 5 μs. Phosphorescence images of

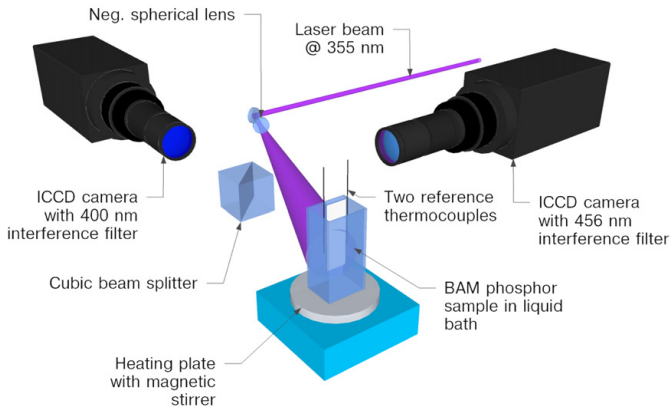

Figure 3. Experimental setup for the dual-camera experiment.

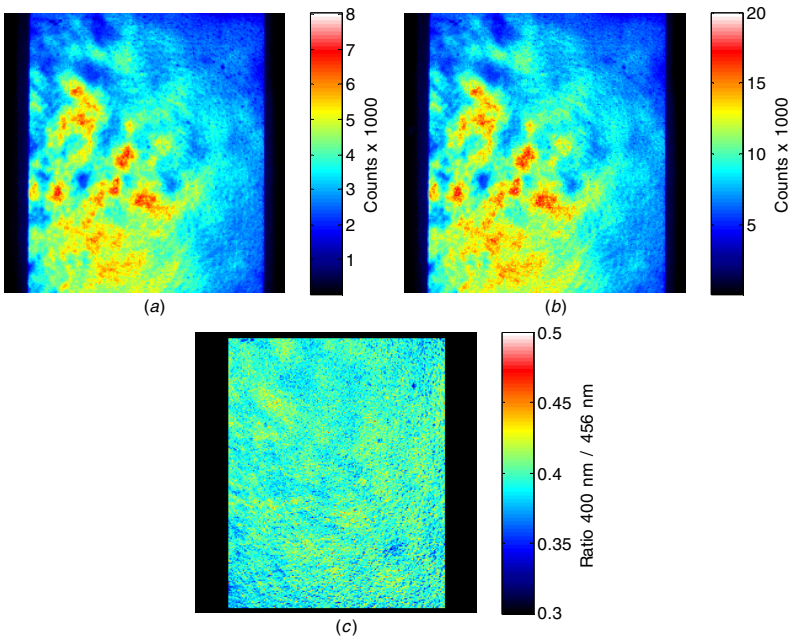

Figure 4. Examples of measurement images at 334 K done with the single-camera setup. Phosphorescence at 400 nm (*a*), at 456 nm (*b*) and the resulting ratio image (*c*). The phosphorescence images are ten averaged images.

the coated surface are recorded at different temperatures in the range from 279 to 470 K.

After stabilization at the desired liquid temperature, ten images through each filter and ten background images are recorded. The ten images are software averaged before being processed. The read-out noise is considered not to be a problem, since the phosphorescence signal is very high. For the dual-camera setup the images taken using the different filters are recorded simultaneously, while for the single-camera setup they are recorded in sequence, by rotating the filter wheel.

3. Data post processing

After background subtraction (and for the dual-camera setup, flat-field correction and image transformation registration) the images taken using the different filters are treated as described above, generating a ratio image, R. The procedure is illustrated in equation (1) for the single-camera setup and equation (2) for the dual-camera setup:

$$R = \frac{I_{400} - \mathrm{BG}_{400}}{I_{456} - \mathrm{BG}_{456}}, \tag{1}$$

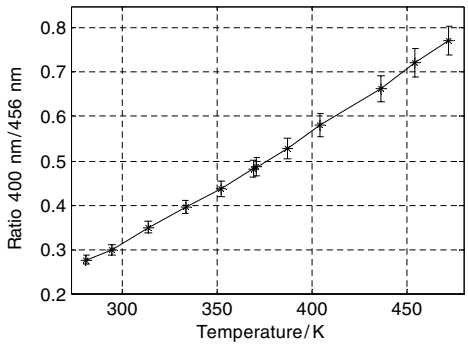

Figure 5. Relation between temperature and the phosphorescence ratio achieved using the single-camera setup. The error bars indicate the spatial standard deviation of the ratio.

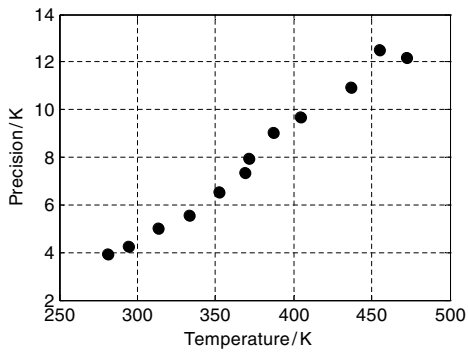

Figure 6. Evaluated precision versus temperature of data achieved using the single-camera setup.

$$R = \frac{I_{400} - \mathrm{BG}_{400}}{\mathrm{FF}_{400}} \Big/ \frac{I_{456} - \mathrm{BG}_{456}}{\mathrm{FF}_{456}}, \qquad (2)$$

where I is the phosphorescence image, BG is the background image and FF is the flat-field image. The subscript indicates the phosphorescence wavelength observed, and hence which camera is being used. For the dual-camera setup, the denominator is subject to an image registration transformation.

The mean value and spatial standard deviation of the ratio are evaluated within an area of about 1000 × 850 pixels, corresponding to an object area of about 2.8 × 2.4 cm^2.

Prior to division, the individual images from each camera are smoothed through software Gaussian filtering using MATLAB. This makes the precision of the overlapping of the two images less critical, and hence the precision of the ratio is increased, but at the expense of decreased spatial resolution.

In addition to the measurements, an image of a resolution test target is recorded, in order to measure the spatial resolution. By repeating the software filtering on the image of the resolution test target, a measure of the spatial resolution for the smoothed spectral ratio images is achieved. This procedure is repeated with different strengths of the software Gaussian filtering, resulting in a relation between precision and spatial resolution.

For the dual-camera setup, a reference grid image and a reference flat-field image are recorded for each camera. The grid image is used to construct an image transform in MATLAB in order to accomplish a proper pixel-by-pixel overlap, prior to image division. In this study, a transparent film with reference points and symbols is attached to the phosphor-coated glass plate while submerged in the liquid bath. In order to achieve as good image registration as possible, it is important to use a grid reference image with clearly distinct patterns of small structures with high contrast. By experience it is recommended to use grid patterns of small points rather than i.e. check patterns.

The flat-field reference image is used to compensate for pixel-to-pixel sensitivity variations of the CCD caused by all camera components, such as optics, image intensifier and detector chip. Because of varying pixel sensitivity for different wavelengths, the flat-field image, as the grid image, needs to be obtained with the filters in place. An ideal flat-field image is a completely uniform surface light source, best achieved by using an integrating sphere, with its aperture placed at the image plane of the camera. In this case, the flat field is generated by a tungsten halogen lamp at 3300 K mounted to a 250 mm integrating sphere with a 65 mm diameter output aperture. When achieving the flat-field image, the gain settings are kept the same as when recording the measurement images and the gate width of the cameras is adjusted so that the number of counts is similar to those in the measurement images. Before using the flat-field images they are normalized by dividing by their maximum value, according to

$$\mathrm{FF} = \frac{\mathrm{FF}_{\mathrm{raw}} - \mathrm{BG}_{\mathrm{raw}}}{\mu}, \qquad (3)$$

where μ is the maximum value within $\mathrm{FF}_{\mathrm{raw}}$–$\mathrm{BG}_{\mathrm{raw}}$.

4. Results and discussion

Figure 4 shows an example of the results of a measurement in water at 334 K using the single-camera setup. Figures 4(*a*) and (*b*) show the phosphorescence observed through the 400 nm interference filter (henceforth IF400) and through the 456 nm interference filter (henceforth IF456), respectively. After background subtraction, figure 4(*a*) is divided by 4(*b*) and the ratio image 4(*c*) is achieved. Pixels outside the selected area are masked out. As can be seen, despite the inhomogeneity of the phosphorescence intensity, seen in figure 4(*a*) and 4(*b*), the ratio image becomes very homogenous. This illustrates the inherent advantage of the two-color ratio approach, as the technique does not require an absolutely homogeneous excitation laser profile, phosphor coating or a linear relation between laser excitation and phosphorescence intensity.

Ratio images similar to that in figure 4(*c*) are generated at 12 different temperatures spanning from 281 to 473 K. For each ratio image, the mean value and spatial standard deviation of the ratio within the selected area (about 850 000 pixels) are evaluated. Figure 5 shows the resulting relation between the temperature and the ratio with the error bars indicating the spatial standard deviation of the ratio.

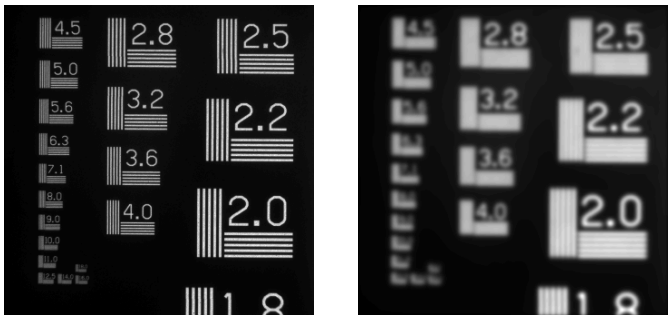

Figure 7. An image of a resolution test target before software filtering (left) resulting in a spatial resolution of 11 lines mm^{-1}, and after software filtering (right) where the target has been subjected to a spatial smoothing applying a software Gaussian filter of pixel size 50 × 50 and a sigma value of 7, resulting in a spatial resolution of 2.2 lines mm^{-1}.

As can be seen, the relation is close to linear. The slope of a fitted line gives the temperature sensitivity of the phosphor. The values in figure 5 give that the slope, and hence the sensitivity of BAM, is 0.0026 K^{-1}. The spatial standard deviation of the ratio within the selected area at room temperature is ±0.011, giving a precision of ±4.2 K, or 1.4 %.

As can be seen in figure 5, the error bars increase with temperature. Figure 6 illustrates this increase in spatial standard deviation, or degradation in precision, as the temperature increases from 281 to 473 K.

The precision at the lowest temperature of 281 K is ± 3.9 K, or 1.4%, while at the highest temperature of 473 K it is ± 12 K, or 2.6%.

The precisions in figure 6 will be increased if the original phosphorescence images are subjected to spatial smoothing, using software Gaussian filtering, since this will decrease the standard deviation caused by the shot noise. A spatial smoothing, as such, simulates in a way a lower spatial resolution, but also how pixel binning would increase the S/N ratio. An image of a resolution test target, see figure 7, is subject to the same treatment in order to quantify this reduction of resolution.

Before division, the phosphorescence images are processed with a software Gaussian filter of different strengths, smoothing out the resulting ratio image. With increasing strength the spatial resolution decreases, while the precision increases. This is illustrated by figure 8, showing the relation between the gain in precision and the loss in resolution at three different temperatures.

As can be seen, the precision at low temperature (281 K), at the highest resolution (11 lines mm^{-1}), is ± 3.9 K, or 1.4%. As the phosphorescence images are subjected to smoothing filtering, the resolution decreases gradually to 2 lines mm^{-1}, and the precision is increased to ± 1.7 K, or 0.6%. Similarly, for measurements done at high temperature, 455 K, the precision spans from ± 12.5 K, or 2.8 %, at highest resolution, to ± 6.5 K, or 1.4 %, at lowest resolution. Accordingly, in the case of the single-camera setup, the precision varies from 0.6% to 2.8%, depending on absolute temperature and resolution.

Concerning the dual-camera setup an example of a measurement done in water with the temperature of 331 K

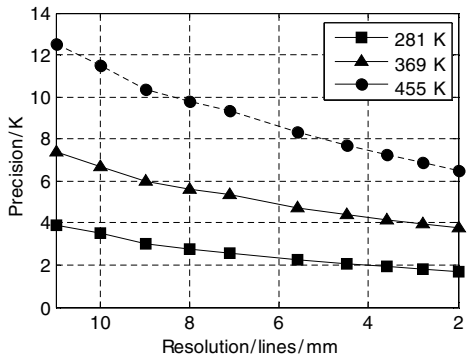

Figure 8. Relation between precision and resolution at three different temperatures.

is shown in figure 9. In contrast to the single-camera setup, the phosphorescence images here need to be flat-field corrected. Furthermore, one of the images, in this case IF456, is subjected to an image registration transform, in order to optimize image superimposition. Figure 9(*c*) shows the resulting ratio image of IF400 divided by IF456.

As in the case of the single-camera setup, the ratio image is very homogeneous, despite the inhomogeneity of the phosphorescence images. For each temperature, the mean value and spatial standard deviation of the ratio are evaluated.

Figure 10 shows the relation between the ratio and temperature for BAM, also this is close to linear. However, the slope is different, 0.005 K^{-1}, from that in the single-camera setup. This is due to the different conditions for which the two phosphorescence images are achieved, compared to the case where only one camera is used. The two cameras might have different sensitivities, the cubic beam splitter might separate the light not precisely 50/50 at the present wavelengths, etc. However, because of this, the evaluated spatial standard deviation is also somewhat different. At room temperature it is ±0.015, giving a precision of ± 3 K, or 1%, slightly better than for the single-camera setup.

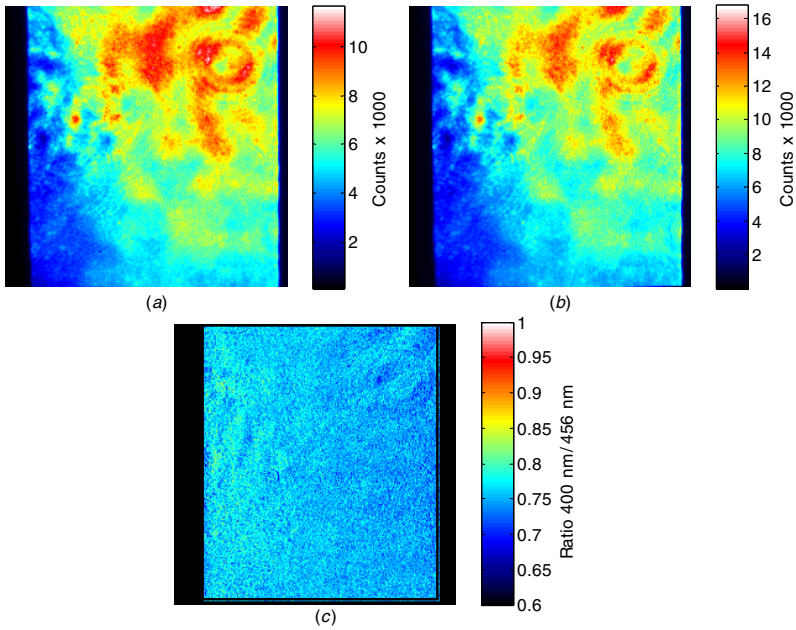

Figure 9. Examples of measurement images at 331 K done with the dual-camera setup. Phosphorescence at 400 nm (*a*), at 456 nm (*b*) and the resulting ratio image (*c*). The phosphorescence images are ten averaged images.

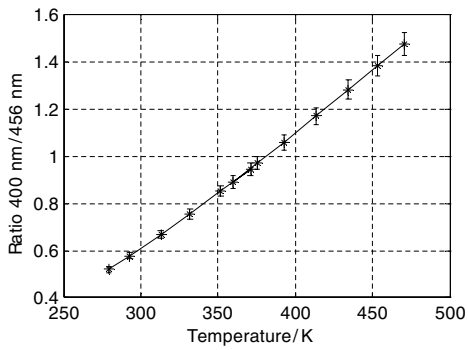

Figure 10. Relation between the phosphorescence ratio and temperature for the dual-camera setup.

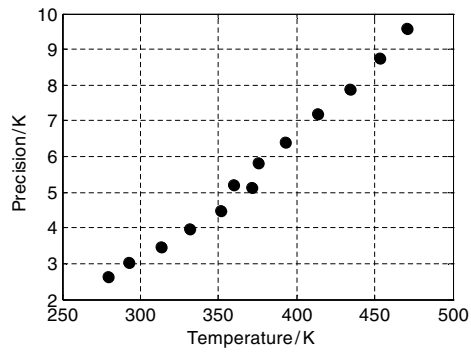

Figure 11. Evaluated precision versus temperature of data achieved using the dual-camera setup.

Figure 11 shows the increasing spatial standard deviation, or degradation in precision, with temperature from 280 to 471 K.

As can be seen, there is a discontinuity between the measurements at 360 and 370 K. This is the overlap of the measurements performed in water (280–370 K) and in glycerol (360–470 K). The reason for the discontinuity is a drift over time in one of the ICCD cameras. It is aggravated between 360 and 370 K due to a 3 h delay between continuous water and glycerol measurement sequences. During this break the local sensitivity of one of the cameras drifted, causing a gradient offset across the chip, causing this degradation in precision. This instability in the cameras is hardly notable in other applications, and indicates how easily affected this two-color ratio method is by small variations in, e.g., linearity or detector drift.

It is the authors' belief that the detector drift is, at least generally, associated with the loss in precision. This long term detector drift is a possible explanation of the increasing slope in figure 11, and without the drift, the trend would have been more linear and the slope less steep, i.e. the precision at higher temperatures would have been better than that seen in figure 11. Since Särner *et al* have shown that the phosphorescence lifetime of BAM does not decrease

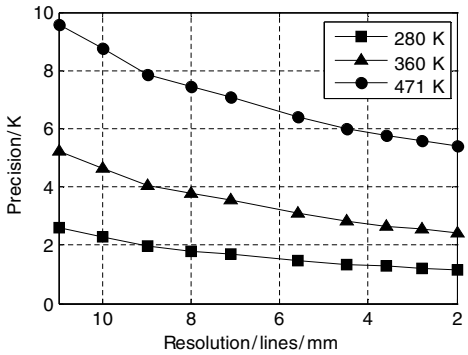

Figure 12. The increase in precision with decreasing resolution for three different temperature measurements with the dual-camera setup, i.e. with two cameras.

appreciably before 700 K, it follows that loss in accumulated signal intensity is not believed to be the reason for the decrease in precision [12].

From figure 11, it can be seen that the precision at the lowest temperature (280 K) is ±2.6 K, or 0.9%, and at the highest temperature (471 K) is ±9.6 K, or 2%. Figure 12 illustrates how this precision is improved when the phosphorescence images are subjected to spatial smoothing using Gaussian filter routines.

For the lowest temperature, the precision is increased to ±1.2 K, or 0.4%, as the resolution is decreased to 2 lines mm^{-1}. For the highest temperature, the precision is increased to ±5.4 K, or 1.2 %. Accordingly, in the case of the dual-camera setup, the precision varies from 0.4% to 2%, depending on absolute temperature and resolution. This is an improvement over the single-camera experiment results, with precision spanning from 0.6% to 2.8 %, despite both flat-field and image registrations being needed for the dual-camera experiment. The explanation for this is that, in the single-camera experiment, the phosphorescence images were recorded by different laser shots, introducing errors caused by laser shot-to-shot variations, even though these variations were determined to be very small during the experiments. It is these shot-to-shot variations that cause the deviation of especially the second last point in figure 6.

Additionally, the evaluation of the results from the dual-camera experiment is compared with those without flat-field correction. This results in a precision span from 2.3% to 5.1%, that is, a degradation of about 2–3 percentage points, indicating the importance of flat-field corrections in this particular case.

5. Conclusions

In this work, the precision in 2D temperature measurements using the thermographic phosphor BAM in the range from about 280 to 470 K has been investigated. The purpose of this work was to evaluate the technique of 2D phosphor thermometry on surfaces concerning precision, something that to the knowledge of the authors is lacking in the field today. The main contribution of the work is to provide guidance on the precision to be expected from 2D surface temperature measurements, using the two-color ratio technique with thermographic phosphors. The precision was put in relation to the spatial resolution, since better precision is possible at the expense of resolution. Depending on temperature and resolution, the precision ranges from 0.4% at the lowest temperature with the lowest investigated resolution, corresponding to 2 lines mm^{-1}, to 2.8% at the highest temperature with highest resolution of 11 lines mm^{-1}. This emphasizes the potential of precision in the 2D phosphor thermometry, since the temperature sensitivity of BAM is by no means remarkable, with the ratio spanning over a factor of 3 in the investigated temperature range. For example, Särner *et al* have demonstrated that the ratio of ZnO:Zn spans over one order of magnitude in the same temperature interval [12]. The sensitivity of ZnO:Zn, i.e. the slope in a corresponding chart such as figure 5 or 10, would be 2×10^{-8} K^{-1}, compared to 0.0025 K^{-1} for BAM. The resulting precision depends of course on the value of the standard deviation of the ratio in a measurement as such, but this high sensitivity indicates the potential of ZnO:Zn as a sensor for 2D temperature measurements.

The measurements have been performed in two different setups: one using only one ICCD camera and one using two. The results were similar for both setups, but precision slightly improved when two cameras were used. The conditions that differ for the two setups were the use of flat-field correction and image registration transformation in the dual-camera setup. The uncertainties that are introduced by the laser shot-to-shot variations are thus found to be greater than the uncertainties introduced by the proper use of an image registration procedure; hence, in terms of precision it is thus preferable to achieve the data single shot.

The impact of excluding flat-field correction on the precision was a degradation of about 2–3 percentage points in this particular case.

One final conclusion from the work carried out is the importance of stable detectors. Even small drifts and instabilities may affect the results significantly.

Acknowledgments

This work was supported by the D60 project within the Swedish Energy Agency, Centre of Competence Combustion Processes and the HELIOS project within the seventh EU framework program.

References

[1] Allison S W and Gillies G T 1997 Remote thermometry with thermographic phosphors: instrumentation and applications *Rev. Sci. Instrum.* **68** 2615–50

[2] Brübach J, Feist J P and Dreizler A 2008 Characterization of manganese-activated magnesium fluorogermanate with regards to thermographic phosphor thermometry *Meas. Sci. Technol.* **19** 025602

[3] Husberg T, Girja S, Denbratt I, Omrane A, Aldén M and Engström J 2005 Piston temperature measurements by

use of thermographic phosphors and thermocouples in a heavy-duty diesel engine run under partly premixed conditions *SAE* 2005-01-1646

[4] Khalid A and Kontis K 2008 Thermographic phosphors for high temperature measurements: principles, current state of the art and recent applications *Sensors* **8** 5673–744

[5] Aldén M, Omrane A, Richter M and Särner G 2010 Thermographic phosphors for thermometry: a survey of combustion applications *Prog. Energy Combust. Sci.* **37** 422–61

[6] Seyfried H, Richter M, Nilsson K-H, Aldén M and Schmidt H 2007 Surface thermometry using laser-induced phosphorescence applied in the afterburner of an aircraft turbofan engine *Collection of Technical Papers—45th AIAA Aerospace Sciences Meeting* vol 18 pp 12794–802

[7] Seyfried H, Särner G, Omrane A, Richter M and Aldén M 2005 Optical diagnostics for characterization of a full-size fighter-jet after-burner *ASME Conf. Proc.* pp 813–9

[8] Kruschwitz C A, Wu M, Moy K and Rochau G 2008 Monte Carlo simulations of high-speed, time-gated microchannel-plate-based x-ray detectors: saturation effects in dc and pulsed modes and detector dynamic range *Rev. Sci. Instrum.* **79** 10E911

[9] Lindén J, Knappe C, Mattias R and Marcus A 2012 Limitations of ICCD detectors and optimized 2D phosphor thermometry *Meas. Sci. Technol.* **23** 035201

[10] Wiedwald J D and Lerche R A 1987 Streak camera dynamic range and optimization *Proc. SPIE* **832** 275–82

[11] Williams T C and Shaddix C R 2007 Simultaneous correction of flat field and nonlinearity response of intensified charge-coupled devices *Rev. Sci. Instrum.* **78** 123702

[12] Särner G, Richter M and Alden M 2008 Investigations of blue emitting phosphors for thermometry *Meas. Sci. Technol.* **19** 125304

[13] Bizarri G and Moine B 2005 On $BaMgAl_{10}O_{17}:Eu^{2+}$ phosphor degradation mechanism: thermal treatment effects *J. Lumin.* **113** 199–213

[14] Shionoya S, Yamamoto H and Yen W M 2007 *Phosphor Handbook* (Boca Raton, FL: CRC Press)

[15] Do Y R and Bae J W 2000 Application of photoluminescence phosphors to a phosphor-liquid crystal display *J. Appl. Phys.* **88** 4660–5

[16] Ravichandran D, Johnson S T, Erdei S, Roy R and White W B 1999 Crystal chemistry and luminescence of the Eu^{2+}-activated alkaline earth aluminate phosphors *Displays* **19** 197–203

Enhanced color ratio calibration approach for two-dimensional surface thermometry using laser-induced phosphorescence

Christoph Knappe, Johannes Lindén, Mattias Richter and Marcus Aldén

Paper VIII

Published in: Meas. Sci. Technol. **24**(8):085202, 2013.

Meas. Sci. Technol. **24** (2013) 085202 (11pp) doi:10.1088/0957-0233/24/8/085202

Enhanced color ratio calibration for two-dimensional surface thermometry using laser-induced phosphorescence

C Knappe, J Lindén, M Richter and M Aldén

Department of Physics, Division of Combustion Physics, Lund University, Box 118 SE-221 00 Lund, Sweden

E-mail: christoph.knappe@forbrf.lth.se

Received 2 March 2013, in final form 27 April 2013
Published 2 July 2013
Online at stacks.iop.org/MST/24/085202

Abstract
An alternative concept for calibrating spectral image intensity ratios is described, which provides simple, but effective means of compensation for systematic errors, caused by nonlinearities in signal detection. The method relies on image segmentation by means of signal thresholds, where pixels are organized into different subgroups according to their corresponding signal count value. Instead of defining one global spectral ratio per calibration temperature, the phosphor-coated target surface is illuminated inhomogeneously and resulting image ratios are calibrated individually for each pixel intensity subgroup. This allows the exploitation of high intensity regions on the camera chip which offer great precision advantages, but suffer from systematic errors caused by signal nonlinearities. Temperature calibration data of $BaMg_2Al_{16}O_{27}$:Eu in the temperature range between 270 and 470 K was used to assess and compare the potential of both calibration approaches. In comparison to the conventional, e.g. global calibration approach, accuracy improvements of up to 39% were gained even while keeping average signal intensities below 15% of the detector's full dynamic range. Image ratio evaluations, based on segregated pixel subgroups, could help improve measurement accuracy also for other techniques, relying on the calibration of measured quantities. In two-dimensional phosphor thermometry, it helps bridge the current precision gap between two-color ratio methods and more elaborate lifetime-imaging approaches.

Keywords: laser-induced phosphorescence, thermographic phosphors, thermometry, ICCD detectors, BAM

(Some figures may appear in colour only in the online journal)

1. Introduction

Laser-induced phosphorescence (LIP) is a remote measurement technique for determining temperatures in gases, liquids and on surfaces with high temporal resolution [1–3]. The principle of LIP is based on activator-doped ceramic materials, known as thermographic phosphors (TPs). These phosphors exhibit temperature-dependent radiation characteristics, when optically excited by ultraviolet light. In order to identify unknown temperatures in an experiment, it is necessary to calibrate a TP under controlled conditions against a specific range of temperatures. TPs offer a combined sensitive measurement range that stretches from cryogenic temperatures up to 2000 K, depending on the choice of phosphor [4, 5].

Mainly, two temperature sensitive radiation properties are exploited in phosphor thermometry, the intensity–time dependence and the spectral intensity distribution of the phosphorescence signal [1, 2, 6].

1. The intensity–time dependence can be described by an exponential decay and varies within time scales from milli- to nanoseconds. This method offers a high degree of measurement precision as the decay time can change several orders of magnitude within a temperature interval over just a few hundred Kelvins. While temperature

determination using the phosphorescence decay time is a well-established technique when using point detectors, the retrieval of two-dimensional (2D) decay rate information is still a cumbersome undertaking, limited to fast framing devices, such as CMOS cameras or CCD camera stacks [7–11]. At present, CMOS cameras have frame rates that can be extended to a few hundred kHz at reduced spatial resolution. This translates into a minimum time interval of 1 to 10 μs in-between two consecutive camera images. Since current CMOS cameras cannot resolve decay rates in the sub-microsecond regime, temporal resolution and the dynamic range of measurable decay times (i.e. temperature sensitivity) is limited. Stacked CCD camera systems operate in burst mode with full image resolution. They do not suffer from these restrictions, because the trigger sequence for gating individual camera image intensifiers can be chosen freely. However, since each camera can only be triggered once per phosphorescence decay, the number of sampling points per curve is usually low, meaning effectively that the measurement precision is prone to signal noise.

2. Another characteristic commonly used for phosphor thermometry is the temperature-dependent distribution of spectral components in the phosphorescence signal. In various applications, the integrated intensity ratio of two separate regions from the phosphorescence emission spectrum is used for this purpose [4, 12–14]. Using this technique, 2D temperature maps can be retrieved by recording two pictures simultaneously, detected through two different spectral bandpass filters. After image background- and flat field corrections, the images need to be compared on a pixel-to-pixel basis in order to derive a temperature from individual signal intensity ratios. However, the intensity ratio usually does not change many orders of magnitude with temperature, meaning that it often provides inferior measurement precision, compared to the decay time approach commonly used in point measurements in combination with photomultiplier tubes or photodiodes [3].

Previous work has shown that nonlinearities in the detection line can be a major compromising factor for measurement accuracy in time- and intensity-based LIP likewise [15–19]. This study investigates a new intensity ratio calibration method for enhanced 2D temperature precision and accuracy. The aim is to compensate for phosphor and camera nonlinearities when measuring temperatures of inhomogeneously illuminated objects. For an ideal (i.e. linear) detector, the overall sensitivity does not change as a function of light intensity. Consequently, the spectral ratio between two integrated wavelength segments is often regarded as an intensity-independent quantity—a considerable advantage in most realistic measurement scenarios.

Figure 1 shows measured pixel response counts from a conventional intensified CCD camera (ICCD; PIMAX II, Princeton Instruments) as a function of a simulated and linearized signal scale. This scale was achieved using a set of intensity and gain variations by normalizing all image counts against the lowest camera gain. Further details on this can be found in [17]. Two different wavelengths are displayed, $\lambda_{400} = (400 \pm 20)$ nm (blue circles) and $\lambda_{456} = (456 \pm 5)$ nm (red triangles). The count ratio of both colors is displayed by a black line (right y-axis), indicating that the camera exhibits a spectral sensitivity distribution that varies with signal level.

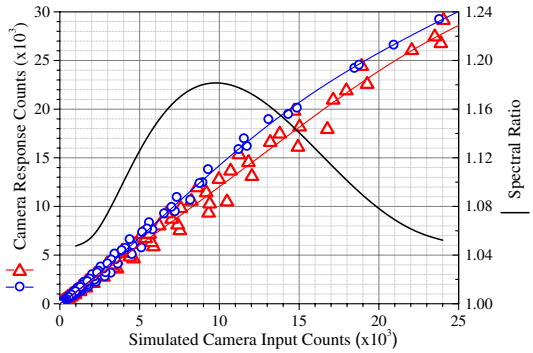

Figure 1. Camera response function for two different filter wavelengths (blue circles: $\lambda_{400} = (400 \pm 20)$ nm; red triangles: $\lambda_{456} = (456 \pm 5)$ nm), data taken from [17]. The black line (right y-axis) indicates the spectral ratio $C(\lambda_{400})/C(\lambda_{456})$ as a function of camera counts.

Even though the two wavelengths only differ about 50 nm from each other and seem to have a close to linear response up to approximately 15 000 counts out of 65 000, the relative spectral sensitivity of the camera varies by approximately 11% in total and interferes with spectral changes from observed measurement objects, such as present in an LIP experiment.

The basic idea behind this paper is therefore to compare the conventional phosphor calibration using one single, averaged spectral ratio per temperature with a set of ratio calibrations that are signal-intensity dependent. The latter method can be understood as an approach to compensate for the variations of the spectral ratio, seen in figure 1, by breaking the camera image up into several signal intensity intervals that are temperature calibrated individually.

It is anticipated, that a calibration performed this way would yield enhanced measurement accuracy as nonlinearities from the phosphor and the signal detection apparatus are partially compensated. More generally, the procedure described in this work should be applicable to enhance the evaluation accuracy of other measurement techniques employing ratios of distributed image intensities recorded by nonlinear detectors. Examples of such possible future applications are two-color pyrometry, two-line-atomic fluorescence techniques and temperature measurements based on LIF of, e.g., acetone or toluene.

2. Experimental details

2.1. Thermographic phosphor

The TP used in this study is denoted as $BaMg_2Al_{16}O_{27}$:Eu (BAM), a blue emitting phosphor with a high phosphorescence

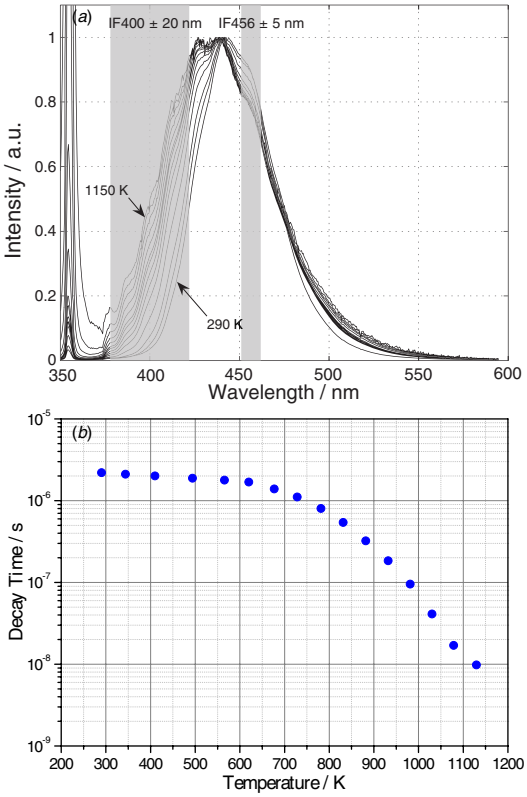

Figure 2. (*a*) Normalized emission spectra of BAM after optical excitation at 355 nm for a range of temperatures. Positions and widths of optical bandpass filters used for the two-color ratio are indicated as gray areas. They are identical to the filters used for figure 1. (*b*) Temporal response of BAM as a function of temperature.

yield and a distinct spectral response to temperature changes [20]. Figure 2 shows the spectral intensity distribution of BAM after pulsed laser excitation at 355 nm.

Increasing temperatures cause the overall phosphorescence intensity to decrease and the emission to broaden toward the blue spectral region. This means, that the phosphorescence intensity of the shorter wavelength side will increase with temperature relative to the longer wavelength side. A temperature sensitive ratio of integrated phosphorescence intensities can be determined using two interference filters: one centered at 400 nm and having a full width half maximum (FWHM) of 40 nm and the other one centered at 456 nm with a FWHM of 10 nm. The phosphorescence has a constant lifetime of about 2 μs from room temperature up to about 700 K and then decreases to about 10 ns at 1150 K. When exposed to an air atmosphere and temperatures above 670 K, BAM suffers from thermal degradation causing a permanent change of irradiation characteristics [20]. Therefore, this work only considers a limited temperature range, stretching from room temperature up to about 470 K.

2.2. Apparatus

This study uses experimental data, which were gathered under idealized measurement conditions during a previously published investigation [21]. This earlier work considered the tradeoff between image resolution and spatial pixel variation on a set of two-color ratio images, recorded at several constant temperatures using a phosphor-coated surface.

A schematic sketch of the experimental setup can be seen in figure 3. Pulsed laser light originating from a frequency tripled Nd:YAG laser, was expanded using a spherical negative lens ($f = -40$ mm) in order to illuminate a BAM-coated surface object. The laser fired ten shots per second at 355 nm with a pulse duration of 6 ns. Since BAM offers a high phosphorescence yield, the overall laser fluence interacting with the phosphor was kept at a low average value of 5 μJ cm^{-2}, such that the effect of optically induced heating was minimized.

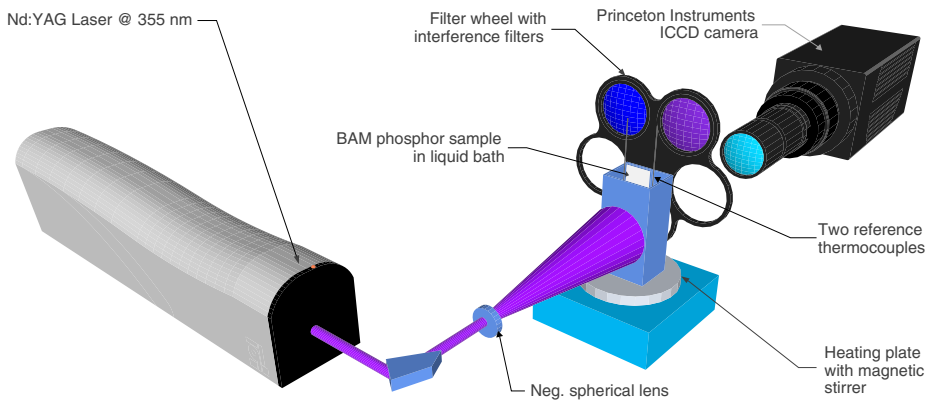

Figure 3. Experimental setup for controlled 2D surface temperature calibration of BAM.

In order to control the surface temperature, the phosphor coating was sealed in between two quartz plates and then submerged into an electrically heated liquid bath. Compared to ambient air, the liquid had a high thermal conductivity and heat capacity, helping to disperse heat and buffer against rapid temperature variations. Water was used for temperatures between 273 and 373 K, whereas glycerol enabled an extension of the temperature range beyond the boiling point of water up to around 470 K, which was the upper temperature limit possible to achieve with the electrical heater. Two K-type reference thermocouples were attached to the sample at different heights (one on each side). Both thermocouples have a temperature accuracy of $\pm$ 1.5 K, according to manufacturer specifications, which was verified by pre-tests in iced and boiling water. A magnetic stirrer provided sufficient agitation to create a homogeneous temperature profile across the measurement surface. The deviation between both thermocouples was measured continuously and stayed below $\pm$0.2 K during the experiments, indicating a fairly flat temperature distribution across the target surface.

Phosphorescence images were captured by a PI-MAX II ICCD camera (Princeton Instruments), placed behind interchangeable optical filters (see figure 2 for filter details). The camera was triggered by the laser with an exposure time set to 5 μs. When the temperature had stabilized, ten images from each filter as well as ten background images were recorded in a sequence. In order to compensate for laser shot-to-shot variations, an average image was created for each set of sequential accumulation. Temperature changes during the sequential data accumulation could pose a potential threat to the overall measurement accuracy, because image accumulations for the two-color ratio were not recorded simultaneously. However, the temperature was constantly monitored and a full data acquisition could be performed in less than a minute at a given temperature, such that the influence of temporal and spatial temperature changes is regarded as negligible.

2.3. Calculus

An advantage of using one camera instead of two in this kind of investigation is given by the lack of necessity for several steps of data corrections and therefore avoiding the introduction of additional error sources. Alongside DC-background corrections (also required when using one camera), a two-camera-setup would require additional post-processing steps, such as image registrations and flat field corrections. Those become obsolete when performing experiments and *in-situ* calibrations using just one camera[1]. Hence, two-color ratios R_i from spectrally filtered and, as in our case, pre-averaged raw images I_λ were retrieved directly after subtracting background values DC_λ in every pixel i, as given in the following equation:

$$R_i = \left(\frac{I_{\lambda_1} - DC_{\lambda_1}}{I_{\lambda_2} - DC_{\lambda_2}} \right)_i . \quad (1)$$

[1] In order to correct for non-uniform pixel intensities and increase measurement precision, a flat field correction is strongly advised whenever *in-situ* calibrations are unfeasible.

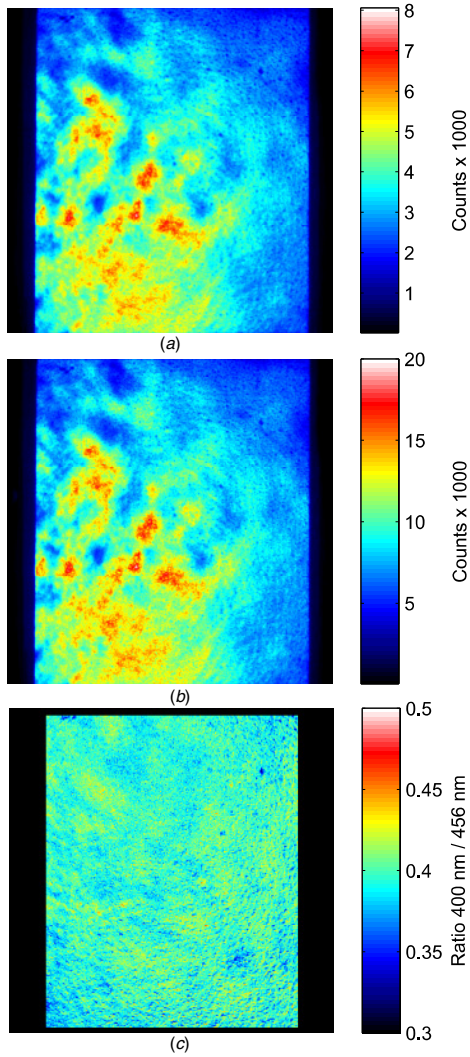

Figure 4. Examples of measurement images at 334 K. The upper two images show background-corrected phosphorescence intensities, averaged over ten laser shots: (*a*) 400 nm center wavelength, (*b*) 456 nm center wavelength. (*c*) The resulting ratio image.

The subscript λ represents the center wavelength of the spectral filters that cut out parts of the phosphorescence spectrum. Calculations were performed from a matrix of 1000×850 camera pixels, corresponding to an object area of about 2.8×2.4 cm^2. An example for the creation of a ratio image according to equation (1) can be seen in figure 4, using phosphorescence images at 334 K. The ratio image 4(*c*) appears largely insensitive to the inhomogeneous illumination pattern on the phosphor sample (see figures 4(*a*) and (*b*)).

For a camera image containing N pixels, the average, background-corrected signal intensity, given for a specific filter wavelength λ, can be expressed as

$$I_{\lambda\mathrm{corr}} = \frac{1}{N}\sum_{i=1}^{N}(I_\lambda - DC_\lambda)_i. \quad (2)$$

Assuming one constant temperature $T = T_0$ over the entire phosphor sample in each measurement, a pixel-averaged image ratio $R(T_0)$ can be calculated as

$$R(T_0) = \frac{1}{N}\sum_{i=1}^{N} R_i(T_0) = \frac{1}{N}\sum_{i=1}^{N}\left(\frac{I_{\lambda_1}(T_0) - DC_{\lambda_1}(T_0)}{I_{\lambda_2}(T_0) - DC_{\lambda_2}(T_0)}\right)_i. \quad (3)$$

The measurement precision $\Delta R_{\mathrm{prec}}(T_0)$ at a given temperature T_0 was defined by the spatial standard deviation as

$$\Delta R_{\mathrm{prec}}(T_0) = \sqrt{\frac{1}{N-1}\sum_{i=1}^{N}(R(T_0) - R_i(T_0))^2}. \quad (4)$$

Given a certain temperature relation of the two-color ratio expressed by M coefficients a_i, i.e. $R_{\mathrm{model}}(T) = R_{\mathrm{model}}(T, a_1, \ldots, a_M)$, the calibration model accuracy $\Delta R_{\mathrm{acc}}(T_0)$ can be expressed as

$$\Delta R_{\mathrm{acc}}(T_0) = R_{\mathrm{model}}(T_0,\ a_1, \ldots,\ a_M) - R(T_0), \quad (5)$$

where $\Delta R_{\mathrm{acc}}(T_0)$ is the absolute ratio offset from the calibrated ratios against the fitted model. It gives as such an estimation for the quality of the fit. ΔR_{acc} is positive when the model overpredicts the measured ratio $R(T_0)$, and negative for underpredicted ratios.

In order to retrieve a temperature from the two-color ratio, $R_{\mathrm{model}}(T)$ needs to be inverted into $T_{\mathrm{model}}(R)$. The ratio precision then translates into temperature precision $\Delta T_{\mathrm{prec}}(R(T_0))$ according to the following equation:

$$\Delta T_{\mathrm{prec}}(R(T_0)) = \left|\frac{\partial T_{\mathrm{model}}(R)}{\partial R}\right|_{|R(T_0)|}\cdot \Delta R_{\mathrm{prec}}(T_0). \quad (6)$$

Similar to the ratio accuracy, the model's temperature accuracy was defined by the capability of the modeled temperature relation $T_{\mathrm{model}}(R)$ to reproduce a calibration temperature T_0 using the calibrated ratio $R(T_0)$:

$$\Delta T_{\mathrm{acc}}(R(T_0)) = T_{\mathrm{model}}(R(T_0)) - T_0, \quad (7)$$

where $\Delta T_{\mathrm{acc}}(R(T_0))$ is the absolute temperature offset from the model against the calibrated temperature; it is positive when the model overpredicts the calibration temperature and negative for underpredicted temperatures.

3. Results

3.1. Conventional calibration results

In this section the temperature precision and accuracy of the conventional ratio calibration method is discussed, based on the experiments described in section 2.2. Figure 5 shows I_λ ($\lambda_1 = 400$ nm, $\lambda_2 = 456$ nm) and R as a function of temperature T over the entire measurement range.

A clear difference in optical transmission can be observed from the camera count levels when interchanging the ambient liquid. Dependent on the temperature, BAM phosphorescence

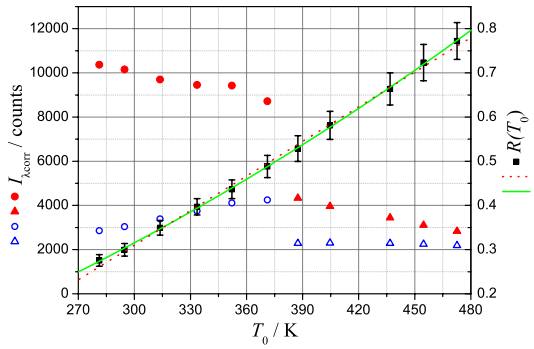

Figure 5. Two-color ratio of BAM as a function of temperature. For each temperature, the average intensity of two spectrally distinct camera images is shown (blue hollow markers: $\lambda_1 = 400$ nm, red filled markers: $\lambda_2 = 456$ nm). Dots correspond to measurements in water, whereas triangles originate from a glycol bath, showing a lower light transmission. The right y-axis is connected to the spectral ratio (black squares). Error bars correspond to the precision of R. The red dotted line shows a linear fit for $R(T_0)$, whereas the green solid line corresponds to a quadratic fit.

in the presence of water resulted in 1.6 to 2 times more signal intensity as when compared to glycerol. This loss in signal is governed by a difference in the absorption coefficient at the excitation wavelength. According to figure 5, increasing temperatures caused the spectral part centered at 400 nm (blue markers) to increase relative to the phosphorescence section around 456 nm. Hence, a temperature dependent, pixel averaged two-color ratio was obtained in figure 5 (see black squares), using equation (3).

The ratio–temperature dependence in figure 5 was fitted in two different ways: the first approach (red dotted line in figure 5) describes the relation between temperature and two-color ratio linearly, using a slope factor $a_2 = (261.0 \pm 4.3) \times 10^{-5}$ K^{-1} and a displacement constant of $a_1 = (-47.2 \pm 1.6) \times 10^{-2}$, as

$$R^{\mathrm{lin}}_{\mathrm{model}}(T) = a_2 \cdot T + a_1 \Rightarrow T^{\mathrm{lin}}_{\mathrm{model}}(R(T_0)) = \frac{R(T_0) - a_1}{a_2}. \quad (8)$$

The second approach (green solid line in figure 5) uses a quadratic least-squares fit instead, see (9), and resulted in the fitting constants $a_3 = (22.5 \pm 2.7) \times 10^{-7}$ K^{-2}, $a_2 = (9.1 \pm 2.1) \times 10^{-4}$ K^{-1} and $a_1 = (-16.1 \pm 3.9) \times 10^{-2}$:

$$R^{\mathrm{quad}}_{\mathrm{model}}(T) = a_3 \cdot T^2 + a_2 \cdot T + a_1 \Rightarrow T^{\mathrm{quad}}_{\mathrm{model}}(R(T_0)) = \frac{\sqrt{a_2^2 + 4a_3(R(T_0) - a_1)} - a_2}{2a_3}. \quad (9)$$

While the two-color ratio precision is given by the ratio standard deviation of all pixels within one image, see (4), the ratio accuracy comprehends the ability of the fitted model to reproduce calibrated ratios using corresponding calibration temperatures. The ratio precision as well as a comparison of both models (8) and (9) regarding their ratio accuracy can be seen in figure 6.

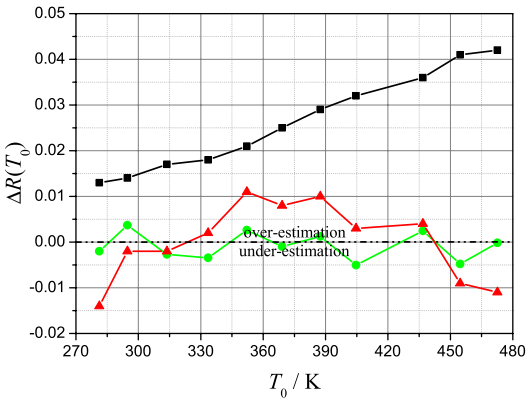

Figure 6. Two-color ratio precision (black squares) and accuracy described as a function of temperature. The red triangles describe the ratio accuracy for the linear model (8), whereas the green dots show the accuracy of the quadratic model, see equation (9). The black dotted line marks values with $\Delta R(T_0) = 0$.

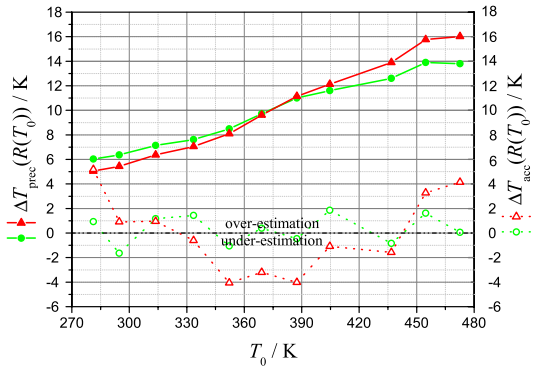

Figure 7. Temperature precision (filled markers) and accuracy (hollow markers) for the two-color ratio of BAM, expressed as a function of temperature. The red triangles correspond to the linear fitted model (8) and the green dots correspond to the quadratic model (9).

The quadratic model (green dots) shows a clear advantage over the linear model (red triangles), being almost three times as accurate as the linear model on average. However, it is obvious from figure 6 that the uncertainty of R is limited by its precision $\Delta R_{\mathrm{prec}}(T_0)$. This confirms earlier results showing the benefit of spatial noise-filtering as long as image resolution is sufficient [21].

In order to calculate the temperature precision $\Delta T_{\mathrm{prec}}(R(T_0))$ from the ratio precision $\Delta R_{\mathrm{prec}}(T_0)$, model equations (8) and (9) are inserted in (6), yielding equation (10) for the linear case and equation (11) using the quadratic model:

$$\Delta T^{\mathrm{lin}}_{\mathrm{prec}}(R(T_0)) = \frac{\Delta R_{\mathrm{prec}}(T_0)}{a_2} \tag{10}$$

$$\Delta T^{\mathrm{quad}}_{\mathrm{prec}}(R(T_0)) = \frac{\Delta R_{\mathrm{prec}}(T_0)}{\sqrt{a_2^2 + 4a_3(R(T_0) - a_1)}}. \tag{11}$$

Figure 7 shows a comparison between the linear model (red triangles, (8)) and the quadratic model (green dots, (9)) for the two-color ratio of BAM regarding temperature precision (filled markers) and accuracy (hollow markers). The temperature precisions were calculated using (10) and (11) whereas the accuracies were derived from inserting equations (8) and (9) into (7).

In the uncertainty scale of temperature, the choice of fitting model to describe the relation between calibration temperature and averaged image ratio influences not only the accuracy, but also the temperature precision, see equations (10) and (11). In figure 7, the quadratic model showed a weaker temperature dependence compared to the linear model, with a slightly inferior precision at low calibration temperatures. On average, however, the temperature precision of the quadratic model is 0.2 K higher, spanning from 6 K up to 14 K across a temperature interval of 200 K. Similar to the ratio accuracy in figure 6, the quadratic model showed a clear temperature accuracy improvement over the linear model, with an average offset of 1 K instead of 3 K. Also in the temperature scale the overall measurement uncertainty is limited by precision, caused by the spread of pixel ratios across each calibration image. Due to its superiority, only the quadratic model will be considered henceforth.

3.2. Shortcomings of the conventional ratio calibration approach

Figure 8 shows R, the two-color pixel ratio of BAM expressed as a function of $I_{400\mathrm{corr}}$, the background-corrected pixel intensity from the 400 nm centered camera image. Two calibration temperatures are shown: 8(*a*) corresponds to a measurement in water at 371 K, whereas 8(*b*) corresponds to an image from BAM submerged in a glycol bath at 473 K.

A higher ratio variation is visible at the beginning of both plots in figure 8, where signal intensities are low and image noise has a higher impact on the pixel ratio. There is a clear precision benefit of working at higher signal levels: theoretically, it can be shown that $\Delta R_{\mathrm{prec}} \sim I^{-\frac{1}{2}}$, assuming that both spectral intensities are proportional to each other. The entire spread of ratios within one image stretches from 0.29 to 0.71 and 0.55 to 1.05 in figures 8(*a*) and (*b*), respectively. Using equation (9) this corresponds to a very high virtual temperature range stretching from 291 to 451 K and 393 to 558 K in figures 8(*a*) and (*b*), respectively. Using only the uppermost 10% of the camera counts of each image, the total temperature spread related to pixel ratio variations decreases from 160 to 30 K and 165 to 50 K in figures 8(*a*) and (*b*), respectively. These variations, however, are mainly based on camera noise and stand in no physical relation to the true temperature variation across the phosphor sample, which was measured to be smaller than 1 K according to the attached thermocouples. Another observation from figure 8 is the ratio going up for increasing camera counts, just as predicted from figure 1 for count values below 10 000. This result can be attributed to the nonlinear

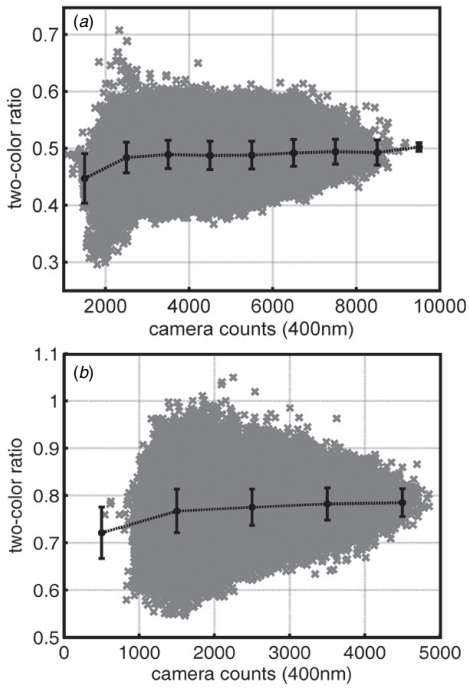

Figure 8. Two-color pixel ratio of BAM (×) expressed as a function of the background-corrected pixel intensity from the 400 nm centered camera image at (*a*) $T = 371$ K (water) and (*b*) $T = 473$ K (glycol). The black dots correspond to the ratio average within an intensity interval of ± 500 counts. The error bars show the ratio precision, expressed as one standard deviation.

signal response of the camera, which gains importance when data images possess a high dynamic range. Consequently, there is a clear potential precision- and accuracy-wise to calibrate two-color ratios separately according to the absolute count value in each pixel.

(1) The overall temperature accuracy across each camera image would improve, if ratio calibrations also consider intensity-dependent ratio drifts (see figures 1 and 8), caused by nonlinear camera behavior.
(2) Ratio precision improves significantly with higher signal levels. However, high signal levels suffer from camera-intrinsic nonlinearities, resulting in systematic ratio drifts. These require corrections such as provided by signal intensity-dependent ratio calibrations.
(3) An intensity-dependent temperature precision would be more true to the actual ratio variations, showing better precision for pixels with higher count values (see figure 8).

3.3. Intensity-compensated calibration results

In this section, a new approach for ratio calibrations is proposed, that evaluates pixel ratios individually based on their signal intensity. For that, each image recorded through the 400 nm bandpass filter undergoes a histogram analysis in order to sort all pixels into subgroups according to their count value. Each subgroup k had a width of 1000 counts and a center count value of $500 \times (2k–1)$, i.e. the first subgroup covers all pixels within the interval from 1 to 1000 counts, the second subgroup goes from 1001 to 2000 counts, etc. In the following, the variable k is added as an additional dependent quantity whenever pixel subgroups are referred to.

For further illustration, figure 9 shows an example of a background-corrected camera image, recorded at 455 K.

Figure 9(*b*) shows an altered version of the original data image (*a*). The idea is to illustrate the distribution of pixel subgroups across one image example. As can be seen from the histogram in figure 9(*d*), there were nine subgroups assigned to the data image. In figure 9(*b*), all pixel values from (*a*) were set to the center value of each subgroup in order to provide a specific color (count value) for each group. In general it can be assumed that the second image recorded around 456 nm shows a similar relative distribution of pixel intensities. Based on that assumption, the decision of breaking up the calibration into several image segments in this work was entirely governed by the signal intensity intervals which were created as subgroups from the 400 nm camera image. It should be noted, however, that ratios used for calibration in each subgroup were, of course, based on the original data image, e.g. figure 9(*a*).

Figure 10 shows such temperature calibrations of two-color image ratios arranged into several pixel count subgroups. Each subgroup has a center count value k ranging from 500 to 7500 pixel counts (referring to the image centered at $\lambda_1 = 400$ nm), dividing each image into eight subgroups with an interval width of 1000 counts. The trends from figure 10 reconfirm temperature examples, shown earlier in figure 8: due to the nonlinearities during light detection, the average image ratios increase with increasing camera counts. This behavior is visible for all calibrated temperatures.

Ratio–temperature relations from each pixel subgroup in figure 10 were fitted individually using the quadratic polynomial, described in equation (9). All resulting fitting constants are listed in table 1, including the conventional calibration results, which were discussed in section 3.1.

In figure 7, the conventional calibration was assessed using a quadratic polynomial model in order to convert averaged image ratios $R(T_0)$ into temperatures. The model's overall temperature accuracy $\Delta T_{\mathrm{acc}}(R(T_0))$ turned out to lie within a range of -2 to 2 K. However, it should be stressed that this accuracy only describes the ability of the conventional model to reconvert the averaged image ratio back into calibration temperatures T_0. The accuracy of individual pixel ratios is further degraded by both noise-based random data spread and an intensity-dependent detector response. Shortcomings of the conventional calibration are first revealed, when the conventional model (first row in table 1) is used to re-assess the temperature accuracy of several pixel subgroups $\Delta T_{\mathrm{acc}}(R(T_0, k))$, see figure 11. This time, the accuracy error is confined between the boundaries of -27 to 12 K, i.e. a factor of 10 larger than before. Systematic errors are especially large for subgroups of low k values, which already in figure 10 showed a large deviation from the mean image ratio. Figure 11 visualizes

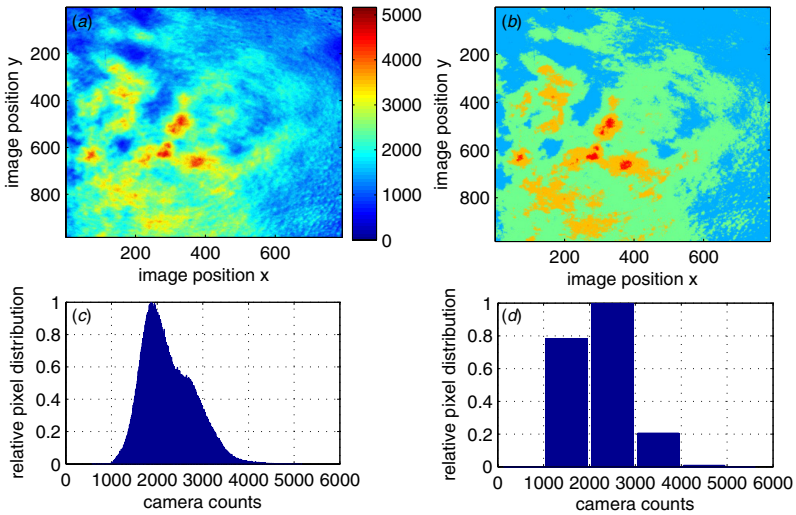

Figure 9. (*a*) Camera image of BAM at 455 K, recorded with a 400 nm bandpass filter and averaged over ten laser shots. The upper right image (*b*) shows an altered image of (*a*), where all pixels within one subgroup have been set to the group's center count value. The axes express horizontal and vertical pixel positions and the color bar expresses the count number. (*c*) and (*d*) represent histograms of (*a*) and (*b*), showing the relative distribution of pixel counts across the image.

Table 1. Fitting constants for ratio–temperature calibrations according to model equation (9). The letter k describes the center value for each fitted pixel subgroup.

k	a_3 (mK^{-2})	Δa_3 (mK^{-2})	a_2 (mK^{-1})	Δa_2 (mK^{-1})	a_3	Δa_3	R^2
All	2.25	0.28	0.91	0.21	−0.161	0.039	0.9925
500	3.34	1.74	−0.20	1.30	0.050	0.239	0.9925
1500	4.27	1.05	−0.58	0.80	0.099	0.147	0.9963
2500	2.64	0.38	0.65	0.28	−0.118	0.052	0.9995
3500	2.09	0.51	1.12	0.39	−0.208	0.072	0.9992
4500	2.32	0.75	0.95	0.57	−0.177	0.104	0.9982
5500	4.50	0.55	−0.60	0.40	0.092	0.073	0.9995
6500	0.46	1.88	2.08	1.20	−0.344	0.198	0.9988
7500	1.25	3.15	1.57	2.20	−0.262	0.368	0.9995

thus the inability of one generalized ratio calibration to yield accurate temperature results.

The accuracy benefit, achieved by calibrating each pixel-intensity subgroup individually is shown in figure 12, where the differences in absolute accuracy between individual subgroup models $\Delta T_{\mathrm{acc}}(R(T_0, k), k)$ and the generalized model $\Delta T_{\mathrm{acc}}(R(T_0, k))$ are plotted against calibration temperature.

Calibrating image sections separately according to their signal intensity yielded an average accuracy improvement of 2.70 K amongst all pixel subgroups. This value seems small, but has to be seen in relation to the average accuracy error of 4.38 K of the generalized model. Consequently, the calibration model accuracy was enhanced by 40% in this particular measurement example. The biggest improvement, i.e. 24 K, was gained for very low camera counts $k = 500$, at a calibration of temperature 455 K.

Figure 13(*a*) shows the absolute precision of image ratios when the image is divided into several pixel subgroups. These values increase proportionally with the absolute ratio values because higher temperatures are accompanied by generally weaker phosphorescence signals. At constant temperatures, higher count levels show significantly better precision, see also figure 8. The relative ratio precision is largely independent of temperature and is thus shown in figure 13(*b*). Subgroups for k values of 2500 and higher are noticed to have a better precision over the entire sample compared to the average precision of 5.13 $\pm$ 0.39%, indicated by the red lines. A calibration that is split up into several subgroups is capable of utilizing the precision benefits that come with high camera signals without suffering from systematic errors due to detector nonlinearities. On that account, the segregated calibration described here now allows the end user to advance toward the semi-saturated response region with all its precision benefits, an operating region which earlier had to be avoided.

When comparing the impact of the ratio precision upon temperature using values from figures 6, 13(*a*) and table 1 in equation (11), again, precision improvements start showing for k values of 2500 counts and above compared to the generalized model. In figure 14, the temperature precision of

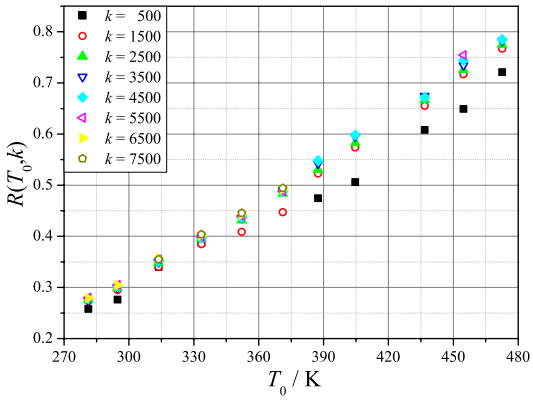

Figure 10. Intensity-dependent two-color ratios of BAM shown as a function of temperature. Eight different pixel subgroups are shown each having an interval width of ± 500 counts. The legend associates the center count value of each subgroup with different marker symbols.

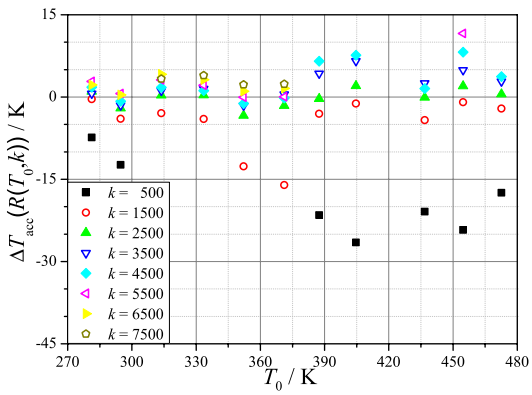

Figure 11. Temperature accuracy of the conventional calibration model when applied to individual pixel subgroups. The legend associates the center count value of each subgroup with different marker symbols.

the segregated subgroup model for $k \leqslant 1500$ is much worse compared to the overall temperature precision. However, this does not mean that the segregated model performs worse than the conventional model, but only reflects the highly increased data spread more accurately that is present at low signal levels (see also figure 8).

Figure 15 concludes the improvements in measurement uncertainty that are applied by introducing a segregated calibration model. A comparison of relative temperature precision (left *y*-axis, filled markers) and temperature accuracy (right *y*-axis, hollow markers) is made and shown for individual pixel subgroups. With increasing signal counts, the temperature precision improves from 4% down to less than 2%, whereas the temperature precision for the conventional model per definition is constant across the entire image and thus yielded an average value of around 2.6% (see

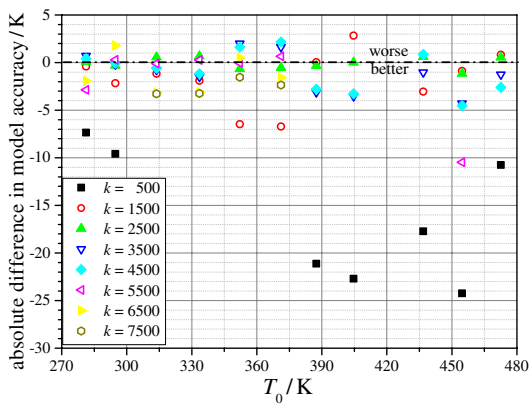

Figure 12. Absolute difference in temperature accuracy comparing one general calibration model with calibrations of individual pixel subgroups. Negative *y*-axis values indicate an improvement of accuracy whereas positive values show a decrease in temperature accuracy.

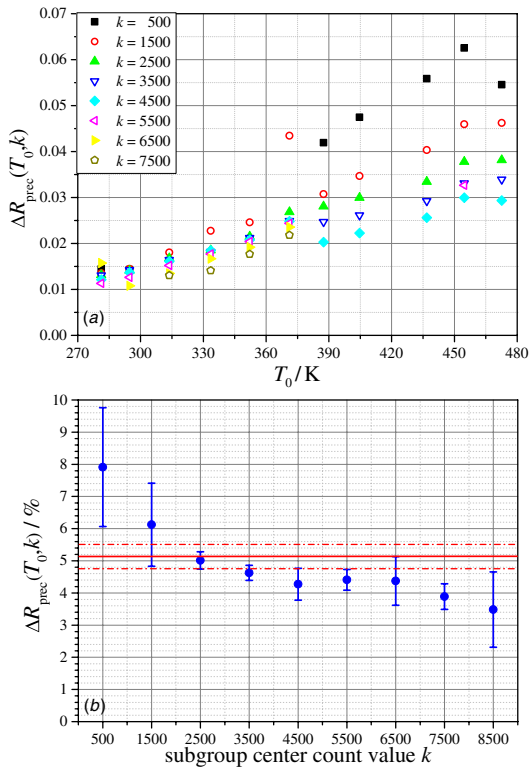

Figure 13. (*a*) Temperature dependence of the absolute image ratio precision for different subgroups *k*. (*b*) Relative ratio precision in percent averaged over all temperatures and shown as a function of pixel subgroup. The red line shows the relative ratio precision over the entire dataset. Error bars and red dash-dotted lines indicate one standard deviation due to contributions from different calibration temperatures.

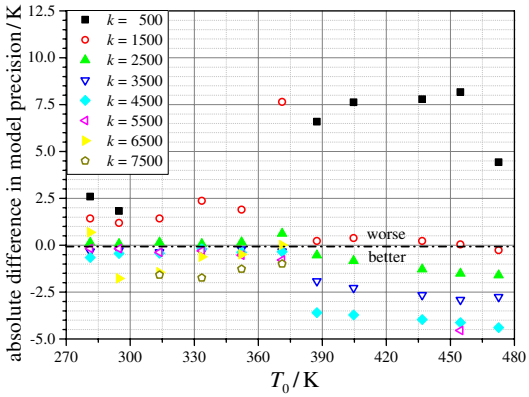

Figure 14. Absolute difference in temperature precision comparing one general calibration model with calibrations of individual pixel subgroups. Negative values show an improvement of measurement precision.

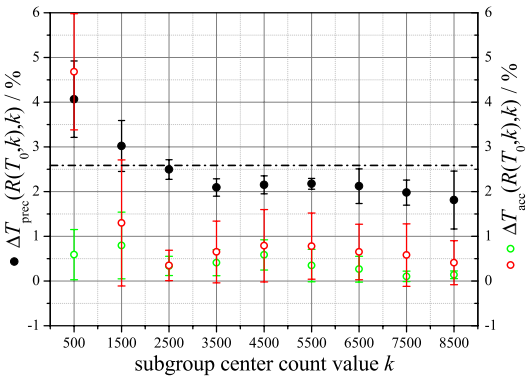

Figure 15. Relative temperature precision (right y-axis) and model accuracy (left y-axis) of the conventional calibration in comparison to the model used to describe pixel subgroups k individually. The horizontal dash-dotted line represents the conventional calibration precision, compared to the filled markers indicating the precision of individual subgroups. Hollow markers correspond to the relative accuracy (red color—conventional model, green color—subgroup model). Error bars indicate one standard deviation, due to contributions from different calibration temperatures.

dash-dotted line). As for the accuracy, the conventional model was tested for individual subgroups (red circles) and compared with the subgroup-specific models (green circles). The segregated subgroup model performs much better than the conventional model, staying always below 1% in this measurement example. For the case of $k = 500$, the relative error has decreased by almost a factor of 8 on average.

Finally, figure 16 shows performance examples for both calibrations in direct comparison using pixel ratios taken at $T_0 = 281$ and 455 K.

Intensity-dependent image segments were separated into subgroups k and averaged, before reconversion into temperature scale. When using individual calibration

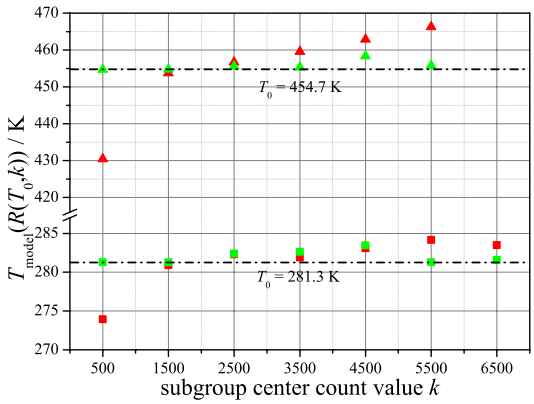

Figure 16. Temperature accuracy comparison of the conventional- (red markers) and the intensity-dependent (green markers) calibration model using image ratios of two calibrated temperatures, 281 and 455 K (horizontal lines).

parameters for each pixel subgroup $T_{model}(R(T_0, k), k)$, indicated by green markers, the temperature derived by the average ratio value does not deviate more than 4 K (corresponds to an error of 1%) from measured calibration temperature. These deviations reflect the minimized discrepancy between the model and the measured value that was found during the least-squares fitting process.

Camera-internal response nonlinearities caused a signal intensity-dependent downwards drift of pixel ratios, averaged individually for each subgroup (see figure 8). This is reflected by the upwards drift of temperatures (red markers) for increasing count values, when reconverted by the fitting function $T_{model}(R(T_0, k))$ of the conventional calibration model. Deviations up to 25 K, i.e. 6%, occur, originating mainly from camera nonlinearities and, to some extent, from a difference of least-squares distances to the fitted models.

Conclusions

A new temperature calibration concept for 2D camera image ratios has been introduced in this study. This segregated subgroup calibration model proved to enhance the accuracy for 2D temperature maps, retrieved from spectral image ratios. The number of subgroups can be adjusted according to individual detector responses and signal ranges for providing improved compensation results whilst keeping computational efforts low. During calibration a signal with high dynamic range is needed, but can be easily achieved by inhomogeneous light illumination, such as provided by a Gaussian laser beam, magnified in size to cover the entire calibration surface.

A measurement example, using the TP BAM within a calibrated temperature range from 280 to 470 K showed an average accuracy enhancement of 39% compared to the conventional calibration approach, where no attention was paid to the signal intensity on the camera chip. Also, the segregated subgroup calibration allowed better insight into the signal intensity dependence of the temperature precision,

showing much better precision for high signal intensities. At 455 K, for example, increasing the average camera count by 5000 gained a precision improvement of 13 K (see figure 14).

Whilst the measurement presented here was originally aimed at avoiding nonlinearities by keeping average signal count levels below 10 000 out of 65 000 camera counts, the true potential of the segregated subgroup calibration lies in utilizing the high intensity region on the camera chip, where data precision drastically improves but measurement accuracy is compromised by detection nonlinearities. Previously this response region, which as in our case covers most of the camera's dynamic range, had best be avoided or needed camera specific data corrections from elaborate pre-studies. The segregated subgroup calibration, however, provides simple but versatile means of compensation for local and temporal intensity drifts regardless of the detector being used. Its benefits are not restricted to phosphor thermometry only, but could enhance the overall evaluation accuracy and precision of other measurement techniques that rely on signal calibration using nonlinear detectors.

Acknowledgments

This work was performed within the D60l-2 project, founded by Swedish Energy Agency. For further financial support the authors would also like to acknowledge the European Union Seventh Framework Programme (FP7/2007-2011) under grant agreement no. 265861 (Helios).

References

[1] Khalid A and Kontis K 2008 Thermographic phosphors for high temperature measurements: principles, current state of the art and recent applications *Sensors* **8** 5673–744

[2] Aldén M, Omrane A, Richter M and Särner G 2011 Thermographic phosphors for thermometry: a survey of combustion applications *Prog. Energy Combust. Sci.* **37** 422–61

[3] Brübach J, Pflitsch C, Dreizler A and Atakan B 2013 On surface temperature measurements with thermographic phosphors: a review *Prog. Energy Combust. Sci.* **39** 37–60

[4] Krauss R H, Hellier R G and McDaniel J C 1994 Surface temperature imaging below 300 K using La_2O_2S:Eu *Appl. Opt.* **33** 3901–4

[5] Cates M R, Allison S W, Jaiswal S L and Beshears D L 2003 YAG:Dy and YAG:Tm fluorescence to 1700 °C *49th Int. Instrumentation Symp., Instrumentation, Systems, and Automation Soc. (Orlando, FL)* pp 389–400

[6] Allison S W and Gillies G T 1997 Remote thermometry with thermographic phosphors: instrumentation and applications *Rev. Sci. Instrum.* **68** 2615–50

[7] Omrane A, Ossler F and Aldén M 2002 Two-dimensional temperature measurements of burning materials *Proc. Combust. Inst.* **29** 2653–9

[8] Omrane A, Särner G and Aldén M 2004 2D-temperature imaging of single droplets and sprays using thermographic phosphors *Appl. Phys.* B **79** 431–4

[9] Kissel T, Brübach J and Dreizler A 2008 Thermometry of surfaces: application of a high speed camera as a detector for laser-induced phosphorescence *Laser Appl. to Chemical, Security and Environmental Analysis (St Petersburg, FL)* doi:10.1364/LACSEA.2008.LWB5

[10] Someya S, Uchida M, Tominaga K, Terunuma H, Li Y and Okamoto K 2011 Lifetime-based phosphor thermometry of an optical engine using a high-speed CMOS camera *Int. J. Heat Mass Transfer* **54** 3927–32

[11] Fuhrmann N, Schild M, Bensing D, Kaiser S A, Schulz C, Brübach J and Dreizler A 2012 Two-dimensional cycle-resolved exhaust valve temperature measurements in an optically accessible internal combustion engine using thermographic phosphors *Appl. Phys.* B **106** 945–51

[12] Goss L P, Smith A A and Post M E 1989 Surface thermometry by laser-induced fluorescence *Rev. Sci. Instrum.* **60** 3702–6

[13] Edge A C, Laufer G and Krauss R H 2000 Surface temperature-field imaging with laser-induced thermographic phosphorescence *Appl. Opt.* **39** 546–53

[14] Brübach J, Patt A and Dreizler A 2006 Spray thermometry using thermographic phosphors *Appl. Phys.* B **83** 499–502

[15] Williams T C and Shaddix C R 2007 Simultaneous correction of flat field and nonlinearity response of intensified charge-coupled devices *Rev. Sci. Instrum.* **78** 123702

[16] Kissel T, Baum E, Dreizler A and Brübach J 2009 Two-dimensional thermographic phosphor thermometry using a CMOS high speed camera system *Appl. Phys.* B **96** 731–4

[17] Lindén J, Knappe C, Richter M and Aldén M 2012 Limitations of ICCD detectors and optimized 2D phosphor thermometry *Meas. Sci. Technol.* **23** 035201

[18] Knappe C, Lindén J, Abou Nada F, Richter M and Aldén M 2012 Investigation and compensation of the nonlinear response in photomultiplier tubes for quantitative single-shot measurements *Rev. Sci. Instrum.* **83** 034901

[19] Knappe C, Abou Nada F, Richter M and Aldén M 2012 Comparison of photo detectors and operating conditions for decay time determination in phosphor thermometry *Rev. Sci. Instrum.* **83** 094901

[20] Bizarri G and Moine B 2005 On $BaMgAl_{10}O_{17}:Eu^{2+}$ phosphor degradation mechanism: thermal treatment effects *J. Lumin.* **113** 199–213

[21] Lindén J, Knappe C, Richter M and Aldén M 2012 Precision in 2D temperature measurements using the thermographic phosphor BAM *Meas. Sci. Technol.* **23** 085205

A library-based algorithm for evaluation of luminescent decay curves by shape recognition in time domain phosphor thermometry

Christoph Knappe, Kristin Pfeiffer, Mattias Richter and Marcus Aldén

Paper IX

Published online: J. Therm. Anal. Calorim. 1-10, August 11, 2013, in press.

J Therm Anal Calorim
DOI 10.1007/s10973-013-3337-3

A library-based algorithm for evaluation of luminescent decay curves by shape recognition in time domain phosphor thermometry

Christoph Knappe · Kristin Pfeiffer · Mattias Richter · Marcus Aldén

Received: 16 May 2013 / Accepted: 12 July 2013

Abstract This work describes and characterizes an algorithm for the nonambiguous reduction of multiexponentially decaying luminescence signals to scalar values of corresponding calibration temperatures. Previous evaluation schemes in phosphor thermometry make use of an intermediate step, where data reduction is achieved by fitting a model equation to phosphorescence decays in order to translate one or more fitting parameters into temperature. However, every slight mismatch between model equation and experimental data may lead to substantial errors in connection to noise-related inaccuracies during the retrieval of adequate fitting windows. Additionally, there is a need for fitting windows, capable of automatically adapting to largely varying signal time scales. In this context, the authors propose to set the fitting window length according to the time where the signal falls below a given percentage of the initial intensity. In comparison to fitting windows, defined by multiple decay times, modeling results suggest substantial precision benefits for as long as signal-to-noise ratios stay above 4. Nevertheless, by comparing signal shapes of measured curves directly with a library of temperature-calibrated decay signals, all necessary assumptions on the mathematical description of measured signals become redundant and evaluation errors connected to uncertain fitting windows are largely circumvented. Resulting capabilities of the proposed signal shape recognition method (SSR) in terms of temperature precision and accuracy were compared to a conventional least-squares fitting approach, using a set of temperature-calibrated phosphorescence decay signals from $CdWO_4$. Accordingly, the SSR algorithm was found to reduce statistical temperature errors by at least 9 %.

Keywords Multiexponential decay · Lifetime · Decay time · Phosphor thermometry · Thermographic phosphors · Laser-induced phosphorescence

C. Knappe (✉) · K. Pfeiffer · M. Richter · M. Aldén
Division of Combustion Physics, Department of Physics, Lund University, Box 118, 22100 Lund, Sweden
e-mail: christoph.knappe@forbrf.lth.se

Introduction

First-order differential equations are among the most common equations in physics. They apply when the rate of increase or decrease of a certain function $I(t)$ of time is proportional to the value itself. The general solution for functions that satisfy first-order differential equations is given by an exponential decay, see Eq. (1), where I_0 is the decay amplitude, $1/\tau$ is the decay rate, and B is a constant baseline offset.

$$I(t) = I_0 \cdot \exp\left(-\frac{t}{\tau}\right) + B \tag{1}$$

The amplitude of the exponential decay usually corresponds to the initial concentration of the decaying species, and the decay rate is frequently determined by the energy change involved in the transition from one state of the system into another. The analysis of exponential decays is usually straight forward, unless experimental signals are measured that comprise a sum of several exponential components. One example of practical relevance is the analysis of luminescent decays from laser-induced phosphorescence. The photo-physics of laser-induced phosphorescence is very complex and to this point not fully understood. However, upon temperature calibration in a controlled environment, the decay characteristics of thermographic phosphors can be utilized for remote thermometry [1–4]. Different thermographic phosphors

Published online: 11 August 2013

combined together allow for measurements across a large temperature interval, ranging from cryogenic temperatures all the way up to approximately 2,000 K [5, 6].

Phosphor scientists usually are confronted with the decision whether to evaluate multiexponential decays and find a way of distinctively assigning the calibration temperature to a number of model parameters or whether evaluation windows can be chosen such that the decay time of a monoexponential model can be attributed to the temperature instead.

Since the signal ratio between two or more decay constants increases with time, the probability for resolving two similar decay constants from a measured signal increases, if decay transients are monitored for as long as the signal amplitude exceeds the noise level. In practical applications, however, the signal-to-noise ratio (SNR) rarely exceeds 100 and is often limited by the experimental equipment. An experimental setup using an 8-bit oscilloscope digitizer, for example, is incapable of exceeding a SNR of $2^8 = 256$. In this example, it is therefore not meaningful to record decay transients for time spans longer than $\ln(256) \approx 5.5$ decay times, unless signals are averaged over time. An attempt to resolve individual decay constants beyond the resolution limits will result in ambiguous and unreliable results because a variation in one of the decay rates might be compensated by another amplitude variation and vice versa [7]. Due to this restriction, practically affecting most experimental situations, multiexponential analysis of decay rates offers very limited versatility for phosphor thermometry and is thus rarely employed.

Another more frequently used approach is the fitting of a monoexponential model to experimental decay transients, where the decay time τ can be easily attributed to a corresponding calibration temperature. However, due to a mismatch of recorded signals and such a simplified model, the choice of evaluation window gains vital importance as it directly influences the fitted parameter values. In an attempt to solve this problem, an algorithm was carefully described and characterised by Brübach et al. [8] who proposed to relate the fitting window boundaries iteratively to evaluated decay time constants from a previous iteration step. In the particular case of their study, it was proposed to start evaluating after one decay time and end the iterative fitting window after four decay times. The authors of [8] have stated later, that these limits have to be found individually for different phosphors and detection systems [4].

Although, there are algorithms that do not require initially guessed fitting parameters, several comparative publications [9–12] came to the conclusion that the best measurement precision was offered by a Levenberg–Marquardt (LM) algorithm [13, 14]. Ballew evaluated the precision of Ashworth's rapid lifetime determination (RLD) method using two contiguous areas and found, that a precision-optimized fitting window for monoexponential decay time analysis spans over 2.5τ [11]. At that point, the decay signal has decreased to 8.2 % of its initial value. Shorter windows having a length of 2τ and 1.5τ would end accordingly after the signal intensity has decreased to 13.5 %, and 22.3 %.

In Fig. 1, corresponding evaluation window lengths were applied to a luminescent decay from cadmium tungstate ($CdWO_4$) in order to demonstrate the mismatch between data signal and individually fitted models. Cadmium tungstate is a phosphorescent material that can be used for remote thermometry and has been previously applied in a number of applications [15–17]. The signal displayed in Fig. 1 is recorded at a temperature of $T = 326$ K and fitted to monoexponential models according to Eq. (1). All fitting windows start 10 ns after the initial peak, i.e., slightly after the excitation laser pulse has passed. The end of each window is indicated by vertical dashed lines in Fig. 1. At first glance, the fitted curves in Fig. 1 appear very similar to each other and seem to follow the measured signal reasonably well. However, asymmetric distributions of fitting residuals, as displayed in Fig. 1, suggest that a monoexponential model does not represent the measured data signal to a satisfactory extent. Mismatches between model and data values arise from the multiexponential character of the recorded signal.

As a consequence, it turns out that evaluated decay time values are largely dependent on the fitting window dimensions. Figure 2 shows the dependence of decay time (evaluated from the data displayed in Fig. 1) as a function of fitting window length. In each chosen time window, a

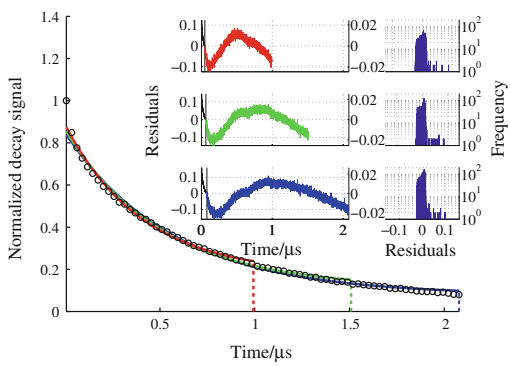

Fig. 1 Residuals of a monoexponential LM fit, applied to the decay signal of $CdWO_4$ at $T = 326$ K. Different fitting window lengths, which end after the signal has decreased to 22.3 % (*red*), 13.5 % (*green*), and 8.2 % (*blue*) are indicated by *vertical*, *dashed lines*. Corresponding fitting residuals and residual histograms are displayed in the *upper right corner*. (Color figure online)

LM monoexponential fit was adapted to the curve in order to compare evaluated signal decay times. Extending fitting windows further toward the tail of the curve means that longer decay time components gain more influence over the fitted function, and therefore results in longer monoexponential decay times. Although, the same curve was evaluated several times and different fits from Fig. 1 are hard to tell apart from each other, the evaluated decay time in Fig. 2 shifted by as much as a 300 % due to changing fitting windows.

Because decay signals from $CdWO_4$ grow shorter for increasing temperatures, these decay time variations can be directly translated into the temperature scale. The evaluated temperature stretches over an interval of more than 40 K in the case of Fig. 2, when compared to a temperature calibration where fitting windows were not varied accordingly. Since there is only one calibration temperature at which the signal was measured, these temperature changes can be interpreted as systematic errors. Depending on the multiexponential character of the signal shape and the sensitivity of a chosen thermographic phosphor, temperature errors induced by fitting window may vary from application to application. Other sources, for instance, use a different phosphor in their measurement setup and report errors in the order of 10 K [8].

This work presents an alternative SSR method for temperature determination based on phosphorescence decay curves. It offers accurate results while being largely insusceptible for systematic errors, caused by variations in the observation window.

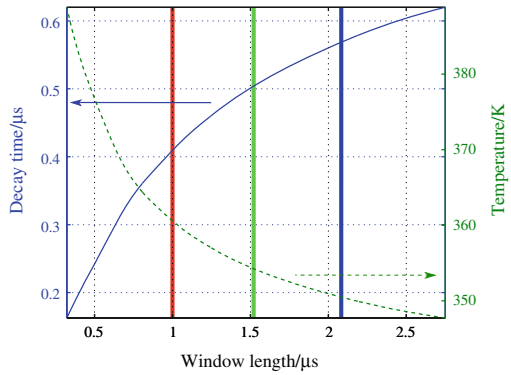

Fig. 2 Decay times and corresponding temperatures for a decay signal of $CdWO_4$ at $T = 326$ K, estimated with an LM fit to a monoexponential model are displayed as a function of different fitting windows. Colored vertical lines correspond to evaluation window examples, chosen for comparison in Fig. 1

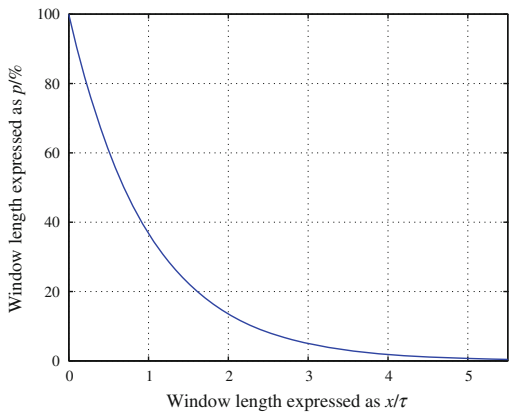

Fig. 3 Multiples of decay times converted into an intensity percentage fraction of a monoexponential decay curve according to Eq. (2)

Fitting window considerations

Figures 1 and 2 demonstrate the existence of temperature errors that stem from variations in the fitting window. In order to estimate a realistic measure for fitting window variations, the precision needs to be considered, which is achieved for defining the boundaries of fitting windows based on individual decay curves. In recent research, it became common practice to determine observation windows by multiples of decay times, as proposed by [8]. For a noise-free monoexponential transient with zero background signal, the relation between multiple decay times x and the remaining percentage fraction p of the initial intensity can be expressed by Eq. (2) and is illustrated in Fig. 3.

$$p = 100\ \mathrm{e}^{-x} \tag{2}$$

As evaluation window dimensions for functional fittings have to be found for individual and noisy decay signals, the repeatability of fitting windows is primarily governed by the SNR of the measured data and the signal positions that were chosen to define the window boundaries. Figure 4 presents the simulation results, obtained from adding random Gaussian noise to simulated monoexponential decay curves. While the beginning of the observation window was fixed to $t_{\mathrm{start}} = 10$ ns after the initial peak, the end of the window was defined by the time t_{stop}, for which the signal underruns a certain percentage value p of the intensity $I_{\mathrm{w0}} = I(t_{\mathrm{start}})$. In contrast to suggestions made in [8], the authors chose a fixed starting time for the evaluation window, shortly after the laser peak. This yielded higher window stability and, in addition, allowed the exploitation of signal parts which are still high above

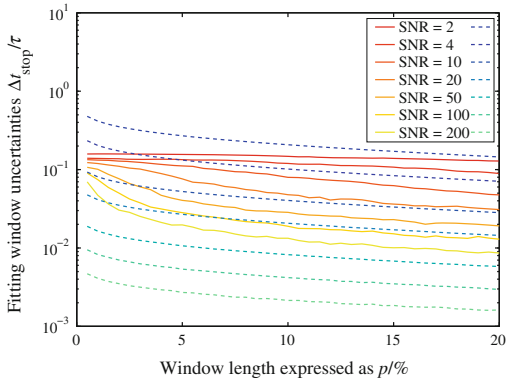

Fig. 4 Fitting window uncertainties, expressed as standard deviation of t_{stop} and normalized by the signal's decay time (*y-axis*). The results stem from simulated monoexponential decay transients with added Gaussian noise. The *x-axis* defines the choice of fitting window lengths, represented by a percentage value that corresponds to either multiples of decay times (*solid, reddish lines*) or intensity thresholds that the signal underruns after a certain time (*dashed, bluish lines*). (Color figure online)

the noise level.[1] The window end t_{stop} was determined either by setting the length to a multiple of decay times (solid lines, reddish colors), evaluated from a least-squares fit over the entire signal, or by finding a curve position for which the signal falls below a certain percentage value (dashed lines, bluish colors). For the sake of comparison, also decay time multiples were expressed as threshold percentages (see *x*-axis of Fig. 3) using the conversion represented by equation (2).

It should be noted that the time position t_{stop}, which terminates the evaluation window, was calculated in the following way: Instead of only picking the first data value that underruns the threshold intensity $p/100 \cdot I_{w0}$, also the position of the last data point above the threshold was used in order to calculate the mean time value from both data points. This limits the effect of noisy signals falling systematically earlier below the intensity threshold. However, such a mean time value might still be biased by the accidental choice of outlier points which might lie far off the actual threshold intersection. It therefore seems prudent to iterate and find the second point below and the second last point above the threshold instead. This process reduces the time difference between both data points in each iteration step. The authors decided to continue this iteration until the time difference is minimized, such that the process is terminated just before the ith point below the threshold lies after the ith last point above the intensity threshold for the first time. Finally, the value for t_{stop} is calculated from the mean time value in the last iteration step. Such a condition for terminating the evaluation window offers enhanced stability against the influence of signal noise and outliers. In addition, this method requires significantly less computational efforts compared to alternative of noise-reduction algorithms, such as smoothing filters or curve fitting approaches.

The comparison of two different definitions for setting equally long fitting windows in Fig. 4 can be summarized as follows: For very noisy signals with SNR in the order of 2, the decay time method delivers superior precision over the entire interval of window lengths. At SNR = 4, the percentage method is superior to the decay time method as long as observation windows stay reasonably short, i.e., $p \geq 4$–5 % (windows shorter than 3τ). At SNR in the order of 10, the percentage method is superior already over the entire range of investigated fitting windows. In fact, precision values were achieved that were not even matched by the decay time method operating at a SNR of 20. A SNR of 100 is necessary for the decay time method, in order to achieve a window precision, which is similar to the one achieved by the percentage method at SNR = 20.

Experimental decay transients used in this study possessed a SNR between 40 and 70. In order to provide a fair comparison between the conventional LM algorithm and our new library-based SSR method, the percentage method was used henceforth in order to limit the variations of the fitting window length.

Experimental data

For construction of a temperature calibration database, a $CdWO_4$-coated sample was continuously heated in a calibration oven at a rate of 2 degrees per minute. Decay curves were recorded every second and automatically matched to thermocouple temperatures. Further details on the automated calibration procedure can be found in [18]. The phosphor sample was excited by a 10 Hz pulsed Nd:YAG laser, operating at its fourth harmonic at 266 nm. Figure 5 shows a conventional temperature calibration, with decay times evaluated from the signal transients by fitting Eq. (1) to an evaluation window, determined by the percentage method. The threshold intensity that terminated the fitting window was set to 8.2 % of the initial signal level. Existing baseline offsets at the end of each signal vector were subtracted prior to evaluation. Within a temperature range of 295–565 K, the evaluated decay time of $CdWO_4$ varied from 2.6 ns to 2.4 µs.

[1] Some phosphor coatings may exhibit thermal history effects in the initial part of the decay, which become annealed after long thermal exposures. Hence, there are cases where selecting a fitting window that begins further from the start of the decay might be a prudent choice.

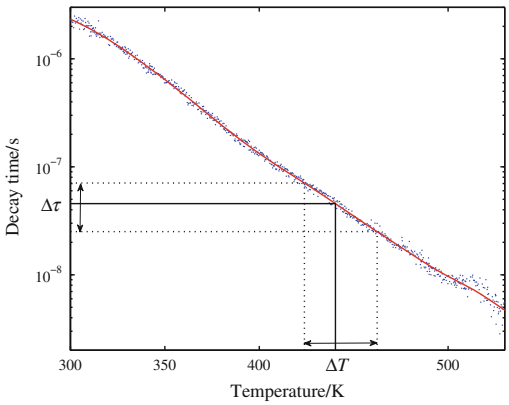

Fig. 5 Decay times from a temperature calibration of $CdWO_4$ at an emission wavelength of 450 nm (*blue dots*). The *red line* indicates a smoothing spline interpolation to the data points. (Color figure online)

Library-based algorithm of signal shape recognition (SSR algorithm)

This section describes an alternative method for temperature determination that is largely insensitive to variations of the observation window. The proposed SSR algorithm compares the shape of phosphorescence time transients with a number of decay signals from a temperature calibration measurement. A generalized flow chart helping to explain the algorithm is presented in Fig. 6.

In an initial step, the measured signal is offset-corrected and normalized to 1 at the start of the evaluation window, i.e., 10 ns after the peak signal. The entire calibration database was previously normalized this way such that the differences between the signal and individual calibration curves can be compared in terms of signal shape. In a subsequent step, a limited temperature interval ΔT for the shape comparison has to be estimated, which is large enough to contain the signal's real temperature by all means. Alternatively, each signal could be compared with the entire calibration dataset. This, however, could be very time-consuming and is only meaningful if temperature calibrations were performed in few discrete temperature steps. In the present work, ΔT was found using a range of decay times $\Delta\tau$, see Fig. 5. Temperature steps were small enough to allow $\Delta\tau$ to be defined by ± 2.5 % of the signal's logarithmic decay time. All n calibration curves within this interval are then compared with the measured signal, e.g., see Fig. 7.

Figure 7 illustrates a comparison example, showing the sample curve (red) together with the shortest calibration curve (blue) from the chosen interval ΔT. The vertical dashed line indicates the end of the observation window and was always fixed to the length of the shortest calibration curve within ΔT. This criterion was set in order to maintain the longest possible constant window during the comparison of transient shapes. An interpolating algorithm ensured that both signal and all calibration curves possessed m vector elements within the observation window. This allowed the comparison of signal shapes using the sum of squares ssq, calcualted for the difference between signal vector Y and calibration curve vector y, see Eq. (3). In addition, the ssq was divided by the number of elements m, which gives the mean-squared distance ssq_m.

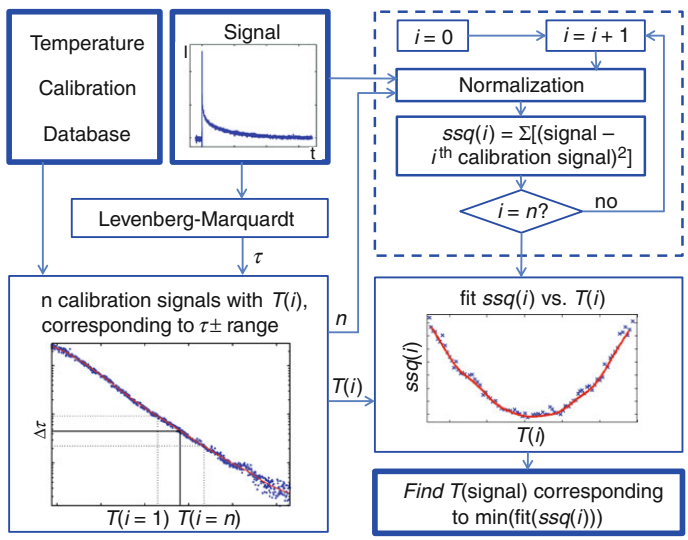

Fig. 6 Flow chart describing the basic working principle of the SSR algorithm

$$\mathrm{ssq_m} = \frac{1}{m}\mathrm{ssq} = \frac{1}{m}\sum_{j=1}^{m}\left(y_j - Y_j\right)^2 \quad (3)$$

Since each calibration curve of the database is assigned to a temperature value, the mean-squared distance for each comparison can be plotted as a function of temperature, as represented by the crosses in the example, shown in Fig. 8.

The mismatch between two compared signals is large and results in higher $\mathrm{ssq_m}$ values if the signal shapes differ substantially from each other. A minimum of $\mathrm{ssq_m}$ is reached for the closest match of signal shapes between the measured signal and a calibration curve. By applying a fit to all points (x) in Fig. 8, a global minimum can be found which then corresponds to the signal's temperature, evaluated by the SSR algorithm. For comparison, the real temperature for the signal in Fig. 8 was measured by a thermocouple and indicated by a vertical dashed line.

Local variations of ssq values in Fig. 8 are mainly caused by errors during the overlap of measurement signal and calibration curve, i.e., errors during baseline corrections and amplitude normalization. Since any of these errors induces a systematic residual increase, lower points (o) in Fig. 8 are deemed to be more reliable estimates for the mean-squared distance. In order to verify this assumption, two different fitting strategies are followed in Fig. 8: In one case, all points (x) were fitted, which is shown by a green dashed line. In another case, only the lower $\mathrm{ssq_m}$ values (o) were selected for the fitting process, which resulted into a fit described by the red solid line. The latter option was found to yield more reliable results in general.

The reduction of noise ripples in signal transients by means of filtering or averaging could contribute in decreasing local variations of $\mathrm{ssq_m}$ values, seen in Fig. 8. In the present work, the influence of a sliding average, applied to the calibration database was tested as a possibility to increase the precision of curve overlaps. Averaging curves of different temperatures, however, could create additional errors caused by introducing a higher degree of multiexponentiality to all calibration curves. Figure 9 shows the average temperature precision and accuracy of the SSR algorithm, applied over the entire $CdWO_4$ calibration. The parameter N in Fig. 9 denotes the amount of neighboring curves that were added to each calibration

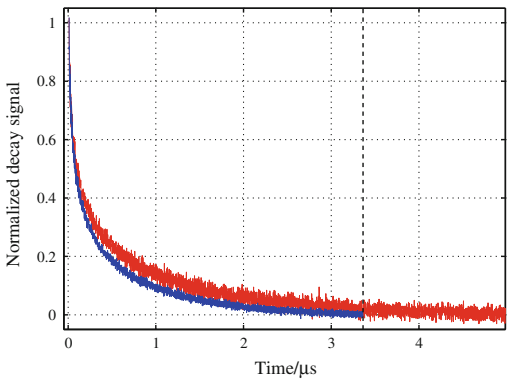

Fig. 7 Normalized measured sample curve (*red*) compared to a normalized calibration curve (*blue*). The *vertical dashed line* indicates the end of the observation window, which was set to the length of the shortest calibration curve within ΔT. (Color figure online)

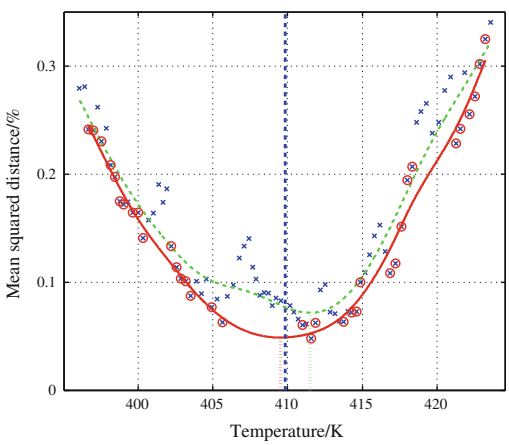

Fig. 8 Mean-squared distance of the measured sample signal from $CdWO_4$ at 409.8 K compared to a set of averaged calibration curves. The *green dashed line* corresponds to a fit that takes all data points into account, whereas the *red line* only considers lower points (o). (Color figure online)

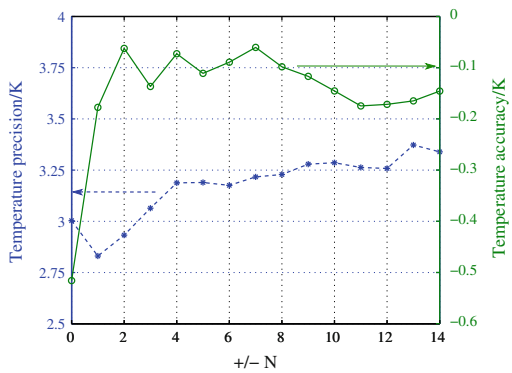

Fig. 9 Overall temperature precision (*dashed line*) and accuracy (*solid line*) as a function of averaging N neighboring calibration curves prior to the step of signal shape comparison. Trends are based on averages over the entire calibration database of $CdWO_4$, seen in Fig. 5

curve. Values for $N = 1$ or 2 suggest a good compromise between overall measurement precision and accuracy in the particular case of this calibration database.

Computation time is an important parameter for practical applications, such as real-time temperature evaluations. The speed of the presented SSR algorithm was therefore compared relative to a conventional method, relying on a single least-squares fit with the LM algorithm. It turned out that the SSR algorithm in its current form takes about ten times longer to perform (500 ms per curve). This is somewhat slower, but still competitive with the iterative approach from Ref. [8], taking 4–8 iterations usually, before stability is reached (200–400 ms). The SSR speed is much dependent on the number of calibration curves that are compared per signal. Since the present code is still under development, no regard was paid to the computation speed as yet. However, in order to demonstrate the theoretically achievable performance limit, a speed-optimized version of the SSR algorithm was built. It contained all necessary evaluation steps, i.e.:

- Offset correction and normalization of the measured signal,
- Decay time evaluation of the measured signal using the RLD algorithm [11],
- Comparison with all calibration signals within a given decay time range,
- Evaluation of residuals between measured signal and individual calibration curves,
- And fitting the residual minimum, in order to retrieve the signal's temperature.

Instead of reading out calibration curves from files and correcting them every single time they were needed for comparison, the entire calibration database was now stored on memory as a matrix. This allowed much quicker data access and the matrix notation enabled residuals to be calculated simultaneously instead of using for-loops. This speeded up the algorithm substantially, as the comparison shows in Fig. 10.

The time-optimized SSR algorithm may not yield the full precision offered by the original algorithm, but indicates its possible potential for use in real-time applications. Depending on the amount of compared signal curves, one SSR evaluation could be performed 4–12 times faster as one single LM fit. Hence, the achieved computational speed between 4.2 and 12.5 ms per signal would more than suffice for real-time thermal sensing on low-end computer hardware.

Results and discussion

Monoexponential models often fail to describe a measured signal to a satisfactory extent and may induce errors, connected to the precision of fitting window dimensions

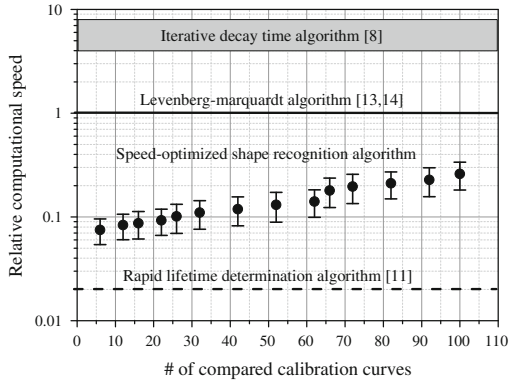

Fig. 10 Relative comparison of computation efforts for several standard algorithms used in phosphor thermometry. The Levenberg–Marquardt algorithm needed ≈50 ms for a least-squares fit of ≈1,000 data points (low-end hardware)

(see residuals in Fig. 1). In contrast to conventional curve fitting approaches, residuals of two similar signals, identified by the SSR algorithm, should be equally distributed.

In Fig. 11 , the decay transients of the two separately acquired data curves were matched ($CdWO_4$ at 326 K). In analogy to Fig. 1, the residuals between the curves were compared within the three previously defined observation windows. As expected, all residuals and histograms show symmetrical distributions around zero, regardless the choice of fitting window. Hence, the dependence of the window length is expected to be largely eliminated.

As pointed out before, it is important for conventional evaluation schemes that the exact same fitting window is applied to calibration and experiment when a monoexponential model is fitted to multiexponential decays. As soon

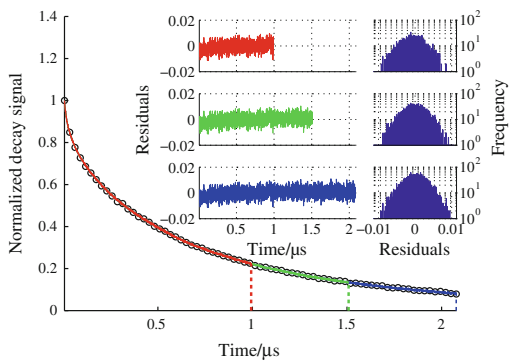

Fig. 11 Two separately achieved decay signals from $CdWO_4$ at $T = 326$ K and corresponding residuals to the match of the curves, observed for different window lengths, which end after the signal has decreased to 22.3 % (*red*), 13.5 % (*green*), and 8.2 % (*blue*). (Color figure online)

as the size of observation window differs between measurement and calibration, systematic errors in the temperature reading are induced. Consequences of this are illustrated in Fig. 12, where deviations from the calibrated temperature are shown for three different cases. During this investigation, each curve from a calibration dataset was once and individually removed from the calibration and instead treated as a measurement signal. While the evaluation of calibration signals was based on one particular fitting window definition, each measurement signal was evaluated using three different windows, resulting in three different decay times. Accordingly, three artificial temperatures were found per curve. In the first case, indicated by the blue stars in Fig. 12, the calibration, as well as the measured curve, was evaluated until the signal has decreased to 8.2 % of its initial value I_{W0}. As the evaluation of the calibration curve and the measured curve was defined using equal window positions, the resulting temperature deviation is fluctuating around zero. Within the observed temperature range of 300–530 K, the standard deviation of the temperature is about 3 K.

In the other two cases, the end of the fitting window for the calibration curves was kept at 8.2 % of I_{W0}, but the window length of the measured signal was decreased. The end of the window was set to the point of time, where the signal has decreased either to 13.5 % (green crosses) or to 22.3 % (red circles) of its initial value I_{W0}. As Fig. 12 illustrates, the temperature deviation changes for different fitting windows. For low temperatures, i.e., longer decay times, the evaluated temperature accuracy decreases. At room temperature, the offset from the true temperature is almost 52 K (red circles) and 25 K (green crosses). Temperatures have been overestimated as a result of capturing only the short-lived part of the signal. At higher temperatures, the accuracy did not change; however, a poorer precision was achieved. Observed effects become more pronounced as the difference in window size increases. The overall standard deviation of the temperature fit increases from 3.0 to 3.97 K (green crosses) and 5.33 K (red circles) as the fitting window for the measured curve becomes shorter.

For the SSR algorithm, this dependence on applying the same evaluation window is not nearly as critical. As illustrated in Fig. 13, the temperature deviation is fluctuating around zero for all three cases, indicating high measurement accuracy regardless of any fitting window constraints.

The high spread in the temperature deviations at around 300 K occurs partially due to the lack of calibration data below 295 K. This forces the best match between calibration and signal to occur on the edge of the compared interval and decreases the chances of finding a pronounced and reliable minimum. Nevertheless, variations in the low-temperature region are still of comparable magnitude to the elevated data spread, observed in Fig. 12 for the conventional algorithm.

Over the calibrated temperature region from 300 to 530 K, the temperature precision obtained from the SSR algorithm decreases somewhat as the observation window becomes shorter. Standard deviations were found to be 2.75 K, with the window ending at 8.2 % of I_{W0}; 3.0 K, with the window ending at 13.5 %; and 3.43 K for observation windows ending at 22.3 %. It has thus been proven that the SSR algorithm also offers slightly better

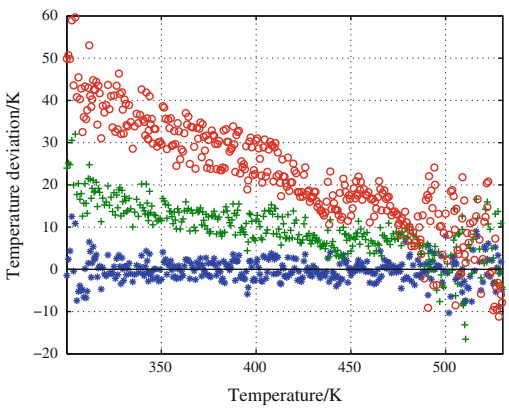

Fig. 12 Residuals of temperatures, that were evaluated with a LM fit to a monoexponential model, to the original temperatures measured by a thermocouple. The observation window during temperature calibration ended at 8.2 % of I_{W0}. The window length during the temperature measurement varied from 8.2 % (*blue stars*) and 13.5 % (*green crosses*) to 22.3 % (*red circles*). (Color figure online)

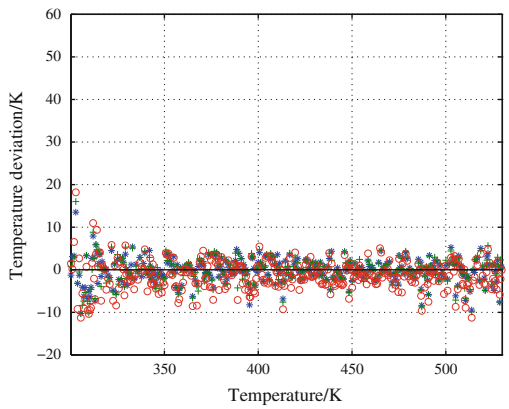

Fig. 13 Residuals of temperatures, which are determined with the SSR algorithm, to the original temperatures measured by a thermocouple. The observation window during temperature calibration ended at 8.2 % of I_{W0}. The window length during the temperature measurement varied from 8.2 % (*blue stars*) and 13.5 % (*green crosses*) to 22.3 % (*red circles*). (Color figure online)

temperature precision for a given set of measured data in comparison to the conventional fitting approach. For the three observed scenarios, the temperature precision improved by 9, 32, and 55 %.

One final investigation in this work seeks to compare the performance of the SSR algorithm with the conventional LM fitting approach in case of using a calibration library with limited temperature resolution. For this purpose, a calibration database was used which consisted of 21 fixed temperatures across the temperature-sensitive range of $CdWO_4$. Individual calibration points were equally spaced and separated by steps of ca. 13 K. At each temperature, an average decay transients was calculated, consisting of 100 recorded signals. Fitting windows again started at 10 ns after the initial peak and ended at 8.2 % of I_{W0}. It is legitimate to wonder in which ways such a limited database of calibrated transient shapes (21 temperatures available) constrains an algorithm, based on signal comparison. Hence, the temperature precision was compared to a conventional LM fitting approach by identifying all decay curves from the continuous calibration database (shown in Fig. 5) with temperatures derived from the fixed point calibration. The SSR algorithm was this time modified to compare each data signal with the entire fixed point calibration in order to provide an adequate number of points for the fit of residuals.

Evaluated results (not shown here) suggest, that the SSR algorithms fails to find adequate temperature values between the first two and the last two fixed calibration points. This drawback was somewhat expected since a minimum cannot be defined precisely close to the boundaries of the calibration. When excluding these outer parts and instead focusing on the temperature-sensitive range of the calibration, a temperature precision of 3.9 K was achieved for the SSR algorithm. The same data analyzed by the LM algorithm yielded a slightly better precision of 3.5 K in comparison. Both methods suffer from decreased measurement precision as a result of using a fixed point calibration, which is why performing a continuous and automated temperature calibration, such as proposed in [18] is advisable. Except from expected difficulties arising close to the calibration boundaries, the SSR algorithm performed surprisingly well in connection to discrete calibration libraries. The precision was found to be roughly 1/3 of the temperature step size and turned out to be just 11 % larger than results obtained from a conventional LM fitting scheme.

Conclusions

A library-based algorithm for phosphor thermometry using luminescent decay transients was described and characterized. Instead of fitting a monoexponential model to multiexponential signals, the algorithm compares measured signal shapes with a previously established calibration database in order to convert signals into reliable temperature values.

The presented SSR algorithm needed about 500 ms per temperature evaluation on low-end computer hardware, which is about 10× longer than a classical LM fit requires. However, there is potential for drastic speed improvements, showing the SSR algorithm being capable of performing up to 12 times faster than a single-exponential fit according to Levenberg–Marquardt.

A continuous data set of temperature-calibrated signals, measured from $CdWO_4$ phosphorescence temperature was used to assess the temperature accuracy and precision in a comparative study. Accordingly, results revealed that the SSR method is far less dependent on the length of the fitting window compared to conventional least-squares decay time evaluation techniques.

Noise-induced fitting window variations can be reasonably constrained by choosing a fixed starting time and defining the window end by either decay time multiples (for SNR of 4 or less) or a corresponding signal threshold.

One significant advantage of the SSR algorithm is the flexibility of being able to handle almost any kind of measurement signal without introducing ambiguities, arising from mismatches between a theoretical model and experimentally measured signals. The avoidance of intermediate fitting quantities, such as exponential decay times, reduces the amount of potential error sources. This was reflected by the obtained measurement precisions, which were ≥9 % higher as corresponding results obtained by a least-squares fitting approach. The SSR algorithm is also capable of handling discretized fixed point calibrations, but suffers from a lack of comparable signals resulting in inferior precision, when compared to conventional least-squares fitting approaches.

In general, the overall measurement precision increased as the observation window extended further toward the signal tail. Furthermore, a semi-continuous temperature calibration demonstrated the advantages for measurement precision over classical discrete calibrations: The precision improved by more than 41 % for the shape matching algorithm and more than 17 % for the conventional evaluation approach.

Acknowledgements For financial support the authors would like to acknowledge the European Union Seventh Framework Programme (FP7/2007–2011) under grant agreement no. 265861 (Helios).

References

1. Allison SW, Gillies GT. Remote thermometry with thermographic phosphors: instrumentation and applications. Rev Sci Instrum. 1997;68:2615–50.

2. Khalid AH, Kontis K. Thermographic phosphors for high temperature measurements: principles, current state of the art and recent applications. Sensors. 2008;8:5673–744.
3. Aldén M, Omrane A, Richter M, Särner G. Thermographic phosphors for thermometry: a survey of combustion applications. Prog Energy Combust. 2011;37:422–61.
4. Brübach J, Pflitsch C, Dreizler A, Atakan B. On surface temperature measurements with thermographic phosphors: a review. Prog Energ Combust. 2013;39:37–60.
5. Krauss RH, Hellier RG, McDaniel JC. Surface temperature imaging below 300 K using La_2O_2S:eu. Appl Opt. 1994;33:3901–4.
6. Cates MR, Allison SW, Jaiswal SL, Beshears DL. YAG:dy and YAG:Tm fluorescence to 1700 °C. Proc Int Instrum Symp. 2003;49:389–400.
7. Istratov A, Vyvenko O. Exponential analysis in physical phenomena. Rev Sci Instrum. 1999;70:1233–57.
8. Brühbach J, Janicka J, Dreizler A. An algorithm for the characterisation of multi-exponential decay curves. Opt Las Eng. 2009;47:75–9.
9. Dowell LD, Gillies GT. Errors caused by baseline offset and noise in the estimation of exponential lifetimes. Rev Sci Instrum. 1991;62:242–3.
10. Ballew RM, Demas JN. An error analysis of the rapid lifetime determination method for the evaluation of single exponential decays. Anal Chem. 1989;61:30–3.
11. Ballew RM, Demas JN. Error analysis of the rapid lifetime determination method for single exponential decays with a non-zero baseline. Anal Chim Acta. 1991;245:121–7.
12. Rosso L, Fernicola V. Time- and frequency-domain analyses of fluorescence lifetime for temperature sensing. Rev Sci Instrum. 2006;77:034901.
13. Levenberg K. A method for the solution of certain non-linear problems in least squares. Quart J Appl Math. 1944;2:164–8.
14. Marquardt DW. An algorithm for least-squares estimation of non linear parameters. J Soc Ind Appl Math. 1963;11:431–41.
15. Knappe C, Lindén J, Abou Nada F, Richter M, Aldén M. Investigation and compensation of the nonlinear response in photomultiplier tubes for quantitative single-shot measurements. Rev Sci Instrum. 2012;83:034901.
16. Knappe C, Lindén J, Abou Nada F, Richter M, Aldén M. Comparison of photo detectors and operating conditions for decay time determination in phosphor thermometry. Rev Sci Instrum. 2012;83:094901.
17. Knappe C, Algotsson M, Andersson P, Richter M, Tunér M, Johansson B, Aldén M. Thickness dependent variations in surface phosphor thermometry during transient combustion in an HCCI engine. Combust Flame. 2013;160:1466–75.
18. Abou Nada F, Knappe C, Xu X, Richter M, Aldén M. Development of an automatic routine for thermographic phosphors calibration. submitted to Meas. Sci. Instrum. 2013.

LUND UNIVERSITY

Lund Reports on Combustion Physics, LRCP–169
ISBN 978–91–7473–615–1 (printed)
ISBN 978–91–7473–616–8 (pdf)
ISSN 1102–8718
ISRN LUTFD2/TFCP–169–SE
Tryckeriet i E-huset, Lund 2013